

**Goal-Oriented Space-Time Adaptivity
for a Multirate Approach to
Coupled Flow and Transport**

Von der Fakultät für Maschinenbau und Bauingenieurwesen
der Helmut-Schmidt-Universität / Universität der Bundeswehr Hamburg
zur Erlangung des akademischen Grades Doktor der Naturwissenschaften (Dr. rer.
nat.) genehmigte

DISSERTATION

vorgelegt von

Marius Paul Bruchhäuser
aus Fulda

Hamburg 2022

Gutachter:

Prof. Dr. Markus Bause

Helmut-Schmidt-Universität / Universität der Bundeswehr Hamburg, Deutschland

Prof. Dr. Florin A. Radu

Universität Bergen, Norwegen

Tag der mündlichen Prüfung: 19. Juli 2022

**Goal-Oriented Space-Time Adaptivity
for a Multirate Approach to
Coupled Flow and Transport**

Doctoral Thesis

approved by the Department of Mechanical and Civil Engineering
of the Helmut-Schmidt-University /
University of the German Federal Armed Forces Hamburg
for obtaining the academic degree of Doktor der Naturwissenschaften (Dr. rer. nat.)

presented by

Marius Paul Bruchhäuser
from Fulda

Hamburg 2022

Referees:

Prof. Dr. Markus Bause

Helmut-Schmidt-University / University of German Federal Armed Forces Hamburg,
Germany

Prof. Dr. Florin A. Radu

University of Bergen, Norway

Day of the completion of the oral examination: 19.07.2022

For Laura and August

Acknowledgment

Die Mathematik als Fachgebiet ist so ernst, dass man keine Gelegenheit versäumen sollte, dieses Fachgebiet unterhaltsamer zu gestalten.

Blaise Pascal

The present thesis was developed in the course of my activity as a research associate at the Chair of Numerical Mathematics at Helmut-Schmidt-University/University of the German Federal Armed Forces Hamburg. During this time, many people supported my way, whom I would like to express my appreciation in the following.

First of all, I would like to express my heartfelt gratitude to my supervisor Markus Bause for giving me the opportunity to write my thesis on this interesting research topic. Thank you for pointing out the essential objectives of this work and always having an open door for *multi(rate)*-ple questions, *goal-oriented* discussions and any kind of *stabilizing* support. Moreover, I am grateful for the possibility to attend international conferences in order to present some results of my work, as well as the help in gaining experiences in research and teaching. Furthermore, I wish to thank Florin A. Radu for reviewing my thesis, his comments and remarks helped to improve this work. I would also like to thank him for organizing research stays in Bergen, Norway, including social and sporting events.

Furthermore, I would like to thank all of my colleagues of the Numerical Mathematics Group, especially Uwe Köcher, with whom I have shared my office and who introduced me into his software and to his way of implementing code very efficiently. I would also like to thank him for countless expedient discussions and for answering any questions, be it on mathematical topics, software implementation or other things. I am also thankful to Karina for numerous coffee breaks being an excellent discussion partner regarding topics besides mathematics.

Last but by no means least, I want to thank my family, especially my wife Laura and my son August for their endless love and encouragement. Writing this thesis would not have been possible without your special support. Thank you for always cheering me up and teaching me to enjoy everyday occurrences. I am blessed to share my life with you.

Marius Paul Bruchhäuser
Hamburg, July 2022

Zusammenfassung

In dieser Arbeit wird ein zeitliches Multi-Raten Konzept kombiniert mit zielorientierter Fehlerkontrolle basierend auf der Dual Weighted Residual (DWR) Methode für ein gekoppeltes Strömungs- und Transportproblem entwickelt. Das Transportproblem wird durch eine Konvektions-Diffusions-Reaktionsgleichung mit hochdynamischem Zeitverhalten repräsentiert, wohingegen das Strömungsproblem durch zähfließende, zeitabhängige Stokes Gleichungen modelliert wird. Dies erfordert den Einsatz von adaptiven Multi-Raten Methoden, um die unterschiedlichen charakteristischen Zeitskalen der beiden Teilprobleme adäquat auflösen zu können. Zudem wird das Transportproblem als konvektionsdominant angesehen und zu diesem Zweck mithilfe der Streamline Upwind Petrov Galerkin (SUPG) Methode stabilisiert. Für beide Probleme wird als zeitliches Diskretisierungsverfahren eine unstetige Galerkin Methode $dG(r)$ mit beliebigem Polynomgrad $r \geq 0$ und als örtliches Diskretisierungsverfahren eine stetige Galerkin Methode $cG(r)$ mit beliebigem Polynomgrad $p \geq 1$ verwendet. Für eine effiziente numerische Behandlung solch stabilisierter multiphysikalischer Probleme, deren Teilprobleme unterschiedliche Dynamiken hinsichtlich ihrer charakteristische Zeitskalen aufweisen, sind adaptive Gitterverfeinerungsstrategien unumgänglich. Vor diesem Hintergrund werden in dieser Arbeit a posteriori Fehlerschätzer basierend auf der DWR Methode für beide Teilprobleme hergeleitet. Diese Fehlerschätzer, gemessen in physikalisch relevanten Zielgrößen, werden in räumliche und zeitliche Anteile aufgeteilt, sodass ihre lokalisierten Repräsentanten als zellweise Fehlerindikatoren für räumliche und zeitliche Gitterverfeinerung genutzt werden können. Im Hinblick auf eine effiziente numerische Approximation gekoppelter Probleme sind adaptive Verfeinerungsstrategien umso wichtiger, will man hierbei nicht nur wissen, in welcher Region das jeweilige Gitter verfeinert werden soll, sondern auch welches der beiden Teilprobleme stärker zum Gesamtfehler beiträgt und somit mit größerer Genauigkeit zu lösen ist.

Um das Zusammenspiel von Stabilisierung und Fehlerkontrolle zu analysieren, werden zunächst stationäre und zeitabhängige konvektionsdominante Transportprobleme mit fest vorgegebener Konvektion behandelt. Hierzu werden zahlreiche Vergleichsstudien im Hinblick auf unterschiedliche Ansätze für das duale Problem sowie unterschiedliche Approximationstechniken für räumliche und zeitliche Gewichtungsfaktoren durchgeführt. Die Resultate dienen als Grundlage für das anschließend betrachtete gekoppelte Problem.

Für die Implementierung werden sogenannte Raum-Zeit Slabs basierend auf Tensor-Produkten verwendet, welche Galerkin Diskretisierungen mit beliebigem Polynomgrad in Raum und Zeit ermöglichen. Diese Slabs bilden eine Diskretisierung des Raum-Zeit-Gebiets und werden in einem Listen-Objekt gespeichert, was ein einfaches und effizientes Hinzufügen von weiteren Slabs im Sinne einer adaptiven Gitterverfeinerung zulässt.

Die Eigenschaften des vorgestellten Konzepts werden anhand von akademischen Testbeispielen, konvektionsdominanten Benchmarks sowie physikalischer Anwendungsbeispiele in zwei und drei Raumdimensionen untersucht. In numerischen Beispielen werden Konvergenzstudien sowie numerische Effizienz- und Stabilisierungsuntersuchungen des zugrundeliegenden Algorithmus durchgeführt.

Abstract

In this work, we develop and analyze a multirate in time approach for coupled flow and transport problems combined with goal-oriented error control based on the Dual Weighted Residual (DWR) method. The transport problem is represented by means of a convection-diffusion-reaction equation involving high dynamic behavior in time, whereas the flow problem is modeled by a viscous time-dependent Stokes flow problem. Thus, adaptive multirate methods have to be used in order to resolve the different characteristic time scales of the subproblems in an appropriate way. In addition, the transport problem is supposed to be convection-dominated and thus stabilized using the streamline upwind Petrov Galerkin (SUPG) method. Both subproblems are discretized using a discontinuous Galerkin method $dG(r)$ with an arbitrary polynomial degree $r \geq 0$ in time and a continuous Galerkin method $cG(p)$ with an arbitrary polynomial degree $p \geq 1$ in space. For the efficient numerical simulation of stabilized multi-physics problems whose dynamics run on different characteristic time scales, it is indisputable that adaptive mesh refinement strategies in space and time are necessary. With this in mind, we derive a posteriori error estimators based on the DWR method for both the transport as well as the Stokes flow problem. These error estimators, measured in goal quantities of physical interest, are splitted into spatial and temporal amounts such that their localized forms can be used as cell-wise error indicators for the adaptive mesh refinement process in space and time. With regard to an efficient numerical approximation of coupled problems, such adaptive strategies become even more crucial since one does not only need indicators that tell in which part of the respective domain the solutions have to be improved, but also which of the subproblems contributes more to the overall error and thus needs to be solved more accurately.

In order to analyze the interaction of stabilization and error control, we first deal with the case of stationary and time-dependent convection-dominated transport problems using fixed given convection fields. Here, several comparative studies regarding different approaches for the dual problem as well as the approximation of spatial and temporal weights, being part of the error estimators, are performed. This serves to gain knowledge and use the results with regard to the case of investigating coupled problems.

For the practical realization of the underlying approach we introduce the concept of space-time slabs that are based on tensor-product spaces which allow for arbitrary degree Galerkin discretizations in space and time. These slabs build a decomposition of the global space-time domain being stored within a so-called list object which enables for an easy and efficient involvement of additional slabs in the course of adaptive refinement.

The performance properties of the approach are studied by means of academic test cases, well-known benchmarks for convection-dominated problems as well as examples of physical relevance in two and three space dimensions. In numerical examples we study convergence, computational efficiency and stability of the underlying space-time adaptive algorithm.

Contents

1	Introduction and State of the Art	1
1.1	Different Characteristic Time Scales - Multirate in Time Schemes	2
1.2	Different Characteristic Spatial Scales - Convection-Dominated Problems	3
1.3	Efficient and Accurate Computations of Goal Quantities - Dual Weighted Residual Method	4
1.4	Overall Approach of this Work - Stabilization and Error Control . . .	5
1.5	Outline	6
2	Notation and Mathematical Tools	9
2.1	Basic Notation	9
2.1.1	Function Spaces	9
2.1.2	Space-Time Function Spaces	13
2.1.3	Finite Element Spaces	15
2.2	Variational Time Discretization	20
2.2.1	Continuous in Time Petrov-Galerkin Method	22
2.2.2	Discontinuous in Time Galerkin Method	24
2.3	Theoretical Results	26
2.4	Residual-Based Stabilization	30
2.5	Goal-Oriented A Posteriori Error Control	32
3	Goal-Oriented Error Control for Steady-State Convection-Dominated Problems	37
3.1	Stabilized Variational Discretization in Space	39
3.2	A FSTD and FDTS Approach for the Dual Problem	41
3.2.1	A FSTD Dual Weighted Residual Approach	42
3.2.2	A FDTS Dual Weighted Residual Approach	45

3.3	Practical Aspects	49
3.3.1	Approximation of the Weights	49
3.3.2	Adaptive Solution Algorithms	52
3.3.2.1	A FSTD Adaptive Solution Algorithm	52
3.3.2.2	A FDTS Adaptive Solution Algorithm	55
3.4	Both Approaches by Numerical Comparison	57
3.4.1	Hump with Circular Layer - Comparison of Approaches and Approximation Techniques for Weights	57
3.4.2	Step with Interior Layer - Different Goal Functionals	66
3.4.3	Domain with Interior Channel - 3d Problem of Physical Relevance	72
3.4.4	Final Summary	74
4	Goal-Oriented Error Control for Time-Dependent Convection-Dominated Problems	75
4.1	Stabilized Space-Time Discretizations	78
4.1.1	Discretization in Time	79
4.1.2	Discretization in Space	81
4.1.3	Stabilization	82
4.2	DWR-Based A Posteriori Error Estimation	84
4.2.1	Derivation of the Dual Schemes	85
4.2.1.1	Discontinuous in Time Discretization	85
4.2.1.2	Continuous in Time Discretization	88
4.2.2	Derivation of an A Posteriori Error Estimator	90
4.2.2.1	Discontinuous in Time Discretization	91
4.2.2.2	Continuous in Time Discretization	99
4.3	Practical Aspects	103
4.3.1	Representation as a Time Marching Scheme	103
4.3.1.1	Primal and Dual $cG(p)$ - $dG(r)$ Time Marching Schemes	104
4.3.1.2	Primal and Dual $cG(p)$ - $cG(r)$ Time Marching Schemes	109
4.3.2	Localization and Evaluation of the Error Estimators	115
4.3.2.1	Discontinuous in Time Discretization	115
4.3.2.2	Approximation of the Temporal Weights	117
4.3.2.3	Continuous in Time Discretization	122
4.3.3	Space-Time Adaptive Algorithm	123
4.4	Implementation and Software Architecture	128
4.4.1	Implementation of Space-Time Tensor-Product Spaces	128

4.4.2	Involvement of Slabs	132
4.4.3	Solution Mesh Transfer	133
4.4.4	Software Architecture and Underlying Data Structures	135
4.5	Numerical Examples	139
4.5.1	Rotating Hill - Convergence Behavior and Independence of Error Indicators	140
4.5.2	Rotating Hill with Changing Orientation - Comparison of Approximation Techniques for Temporal Weights	143
4.5.3	Moving Hump with Circular Layer - Stability and Robustness for a Convection-Dominated Benchmark	150
4.5.4	Final Summary	160
5	Multirate Goal-Oriented Error Control for Coupled Flow and Transport Problems	161
5.1	Stabilized Space-Time Discretizations	168
5.1.1	Multirate in Time Approach	168
5.1.2	Discretization in Time	169
5.1.3	Discretization in Space	172
5.1.4	Stabilization of the Transport Problem	174
5.2	A Posteriori Error Estimation for a Coupled Flow and Transport Problem	175
5.2.1	An A Posteriori Error Estimator for the Transport Problem	175
5.2.1.1	Derivation of the Dual Schemes	177
5.2.1.2	Derivation of an A Posteriori Error Estimator	180
5.2.2	An A Posteriori Error Estimator for the Stokes Flow Problem	185
5.2.2.1	Derivation of the Dual Schemes	187
5.2.2.2	Derivation of an A Posteriori Error Estimator	189
5.3	Practical Aspects	193
5.3.1	Representation as a Time Marching Scheme	193
5.3.1.1	Time Marching Schemes for the Transport Problem	194
5.3.1.2	Time Marching Schemes for the Stokes Flow Problem	197
5.3.2	Localization and Evaluation of the Error Estimators	199
5.3.2.1	Localized Error Indicators of the Transport Problem	199
5.3.2.2	Localized Error Indicators of the Stokes Flow Problem	203
5.3.3	Implementation of Multirate Aspects	206
5.3.4	Application Scenarios of a Multirate-DWR Concept	211

5.3.4.1	General Multirate-DWR Algorithm for Coupled Problems	212
5.3.4.2	Transport-Oriented Multirate-DWR Algorithm for Coupled Problems	216
5.3.4.3	Implemented Multirate-DWR Algorithm for Coupled Problems	220
5.4	Numerical Examples	225
5.4.1	Higher-Order Space-Time Convergence Studies	226
5.4.2	Space-Time Adaptivity Studies for Coupled Problems	232
5.4.3	Transport in a Channel	242
5.4.4	Final Summary	257
6	Conclusion and Outlook	259
6.1	Summary	259
6.2	Extensions and Future Work	261
	Abbreviations	265
	Bibliography	267

Chapter 1

Introduction and State of the Art

In recent years, the coupling of multi-physics and multi-scale problems has particularly attracted researchers' interest; cf., e.g., [111, 89, 94, 10]. Some of the main challenges that are accompanied by an efficient and accurate numerical simulation for these type of problems can be stated as the following:

- Different characteristic time scales: Multirate in time schemes.
- Different characteristic spatial scales: Layers and sharp moving fronts.
- Efficient and accurate computations of goal quantities: DWR error control.

To overcome the difficulties described above, we develop and analyze in the underlying work a **multirate in time approach for coupled flow and transport problems combined with goal-oriented error control based on the Dual Weighted Residual (DWR) method**. The transport problem is represented by a convection-dominated convection-diffusion-reaction equation involving high dynamic behavior in time, whereas the flow problem is modeled by a viscous time-dependent Stokes flow problem. For instance, such multi-physics systems are used to model species or heat transport in a creeping viscous fluid. Beyond that, such systems of coupled flow and transport serve as prototype models for applications in several branches of natural and engineering sciences, for instance, contaminant transport and degradation in the subsurface, groundwater contamination, reservoir simulation, fluid-structure interaction, thermal and mass transport in deformable porous media or thermal expansion in solid mechanics; cf., e.g., [133, 63, 184, 152, 9, 38]. In the following, we address the above mentioned challenges in greater detail.

1.1 Different Characteristic Time Scales - Multirate in Time Schemes

With regard to coupled problems, one of the main challenges lies in the treatment of different natural time scales related to the underlying subproblems. Usually, these characteristic time scales differ by orders of magnitude and thus involve suitable approaches having regard to the different dynamics in time. Their efficient numerical simulation with regard to the temporal discretization does not become feasible without using techniques adapted to these characteristic scales that resolve the solution components on their respective time length by an appropriate adaptation of the time steps sizes. Such methods are referred to as *multirate in time* (for short, multirate) schemes. Initially, they were introduced for the numerical approximation to systems of ordinary differential equations in [90, 95], “*using larger stepsizes for those variables in a system that have a behavior which is slow compared to the fastest variables*”¹. With regard to parabolic problems, multirate methods were developed in [164, 165], and regarding hyperbolic conservation laws they were investigated in [62, 60]. Moreover, multirate schemes regarding convection-diffusion problems can be found in [172]. Some recent results including, for example, propagation in porous media, poroelasticity models, coupled flow with geomechanics, air pollution modeling, fluid-structure interaction, and others, can be found in [111, 89, 94, 10, 166, 191]. For a general review of multirate methods including the development over the last two decades as well as a list of references we refer to [94, 88].

With regard to our coupled model problem, we assume a high time-dynamic, i.e. fast moving process modeled by a convection-diffusion-reaction transport equation such that the underlying temporal mesh is discretized using smaller time step sizes compared to a slowly moving process modeled by a viscous Stokes flow problem. Our motivation comes from the definition of so-called characteristic times for the two subproblems that serve as quantities to measure the underlying dynamics in time and that have their origin in the field of natural science and engineering sciences, cf., e.g., [93, 146]. These characteristic times provide the basis for the initial temporal mesh discretization related to the respective subproblem and indicate which of the two problems has to be refined stronger in the course of the simulation.

¹cited from [90]

1.2 Different Characteristic Spatial Scales - Convection-Dominated Problems

For the sake of physical realism, the transport problem is supposed to be convection-dominated by assuming high Péclet numbers that are characterized by small diffusion relative to the convection, cf. [53, 116]. The solutions of such convection-dominated problems are typically characterized by the occurrence of sharp moving fronts and interior or boundary layers. The key challenge for the accurate numerical approximation of these solutions is thus the development of discretization schemes with the ability to capture strong gradients of solutions without producing spurious oscillations or smearing effects. With regard to an accurate and efficient approximation, strong efforts and great progress were made from the second half of the last century to nowadays, especially in the pioneering works of the 1980's (cf., e.g., [49, 109]). In this context, the application of stabilization techniques is a typical approach to overcome non-physical effects. Some of the most common stabilization techniques are, for instance, the *streamline upwind Petrov Galerkin* (for short, SUPG) method [106, 49] and the very close but more general *Galerkin least squares* (for short, GLS) method [107, 108], both belonging to the family of residual-based stabilization techniques. In addition and in contrast, as belonging to the family of adding symmetric stabilized terms, the *local projection stabilization* (for short, LPS) method [33, 34, 23] and the *continuous interior penalty* (for short, CIP) method [54] should be named. For a general review of stabilization techniques we refer to, e.g., [162, 116, 175, 148]. As shown in a comparative study for time-dependent convection-diffusion-reaction equations in [58] and [120, 121], respectively, stabilization techniques on globally refined meshes fail to avoid oscillations even after tuning the underlying stabilization parameters. As further shown in [120], an alternative in reducing oscillations is obtained by using *flux-corrected transport* (for short, FCT) schemes (also referred to as *algebraic flux correction* (for short, AFC) schemes) [43, 139, 132], that work on the algebraic level. Instead of modifying the bilinear form of a finite element method (for short, FEM), as done by the aforementioned stabilization approaches, here the linear system arising from a FEM discretization is modified by adding discrete diffusion to the system matrix and appropriate anti-diffusive fluxes to the right hand side, cf., e.g., [148]. Recently, numerical analyses of these methods were introduced and applied to steady convection-diffusion-reaction equations; cf. [24, 25]. In [42], an *hp*-adaptive FCT algorithm for unsteady convection equations is presented. Although these FCT schemes show a significant reduction of the unphysical oscillations, smearing effects still arise

and can be observed; cf. [42, 120]. Similar results have been perceived in three dimensions; cf. [121]. A further alternative approach was recently proposed in [148], using a higher order symmetric interior penalty discontinuous Galerkin discretization including a diffusive L^2 -projection for investigating steady-state groundwater flow and solute transport problems. Moreover, a comparison to the most common SUPG stabilization approach can be found there.

A further challenge in view of convection-dominated problems is the existence of robust a posteriori error analyses with respect to the small perturbation parameter. A semi-robust a posteriori error estimator was derived in the energy norm for steady-state convection-diffusion equations in [179]. To get a robust error estimate, later on, the author added the dual norm of the convective derivative to the energy norm in [181]. An extension of this approach to evolutionary problems was given in [182]. A further robust error bound albeit in the so-called SUPG norm given by Eq. (2.19) was established for the stationary case in [119]. Recently, in [18], a DWR-type robust residual-based a posteriori error bound for the SUPG method in the energy norm was proposed for the stationary case. For time-dependent convection-diffusion problems, robust a posteriori estimators measuring the error in a space-time mesh-dependent dual norm can be found in [65]. For more details and further references we refer to [119, 18] for the steady-state case and to [65, 84] for time-dependent problems, respectively.

1.3 Efficient and Accurate Computations of Goal Quantities - Dual Weighted Residual Method

For the efficient numerical simulation of multi-physics problems handling the challenges described above, it is indisputable that adaptive mesh refinement strategies in space and time are necessary. One possible technique for those adaptive strategies is goal-oriented a posteriori error control based on the *Dual Weighted Residual* (for short, DWR) method [35, 36, 20]. For a review of a posteriori error estimation techniques for finite element methods in general and automatic mesh generation we refer, for instance, to the monographs [4, 178, 180]. Within the DWR approach the error is estimated in an arbitrary user-chosen goal functional of physical relevance. Such a goal functional can be any kind of output values, for instance, the deformation of a solid-point, the computation of a drag or lift coefficient in flows around obstacles, the computation of a mean normal flux across boundaries or simply the error control with respect to some global norm such as the energy norm or the L^2 -norm,

cf., e.g., [160] and [20, Sec. 3.2]. To get an error representation with respect to this goal functional, an additional dual problem has to be solved. This *dual* solution is then used for *weighting* the influence of the 'local' *residuals* on the error in the underlying goal quantity. In the last two decades this method has become very popular and was applied to a huge field of mathematical models based on partial differential equations, including fluid mechanics [31, 46, 37], wave propagation [21], structural mechanics [156], fluid-structure interaction [159, 183, 186, 160], eigenvalue problems [100], optimization problems [144], goal-oriented adaptive modeling [45], and many others. For a review including detailed lists of references regarding different model problems we refer to [36, 20, 160]. Early studies with regard to steady-state convection-diffusion transport problems have been considered in [155, 103] as well as [36, Section 3.3], and limited to the one-dimensional case in [131]. With regard to time-dependent convection-diffusion-reaction equations this approach together with SUPG stabilization has been investigated in [169]. The DWR approach together with the LPS method was applied to the steady-state Navier-Stokes equations in [31] as well as together with the LPS and SUPG method to the nonstationary Navier-Stokes equations in [167, 40]. With regard to an efficient numerical approximation of coupled problems, adaptive strategies become even more crucial since one does not only need indicators that tell in which part of the domain the solutions have to be improved, but also which of the subproblems contributes more to the overall error, and thus needs to be solved more accurately, cf., e.g., [133, 45, 111, 186, 185, 159]. Moreover, by an increasing complexity with regard to an efficient handling of the underlying discretization parameters in space and time for both subproblems, an adaptive algorithm that handles these parameters automatically by means of an a posteriori error estimator seems to be predestined.

1.4 Overall Approach of this Work - Stabilization and Error Control

In this work, we combine the DWR approach together with SUPG stabilization for several classes of convection-dominated problems, starting with the steady-state case of convection-diffusion-reaction equations, followed by the time-dependent case for this type of equations to finally end up with the above indicated case of a convection-diffusion-reaction transport problem coupled with a time-dependent Stokes flow problem. In the course of this, we focus on the interaction of stabilization and goal-oriented error control in order to obtain error representations in space and time that serve as

local indicators for the adaptive mesh refinement process within the underlying algorithm. In this context, we investigate these error representations with regard to reliability, efficiency and accuracy reasons. We aim to reduce sources of inaccuracies and non-sharp estimates within the error representation as far as possible in order to avoid numerical artefacts. Even though several investigations have been done with regard to convection-dominated problems, recently, in [116], the authors stated numerous problems that are still unresolved in this field of research. In particular, with respect to accuracy and efficiency we still expect potential for improvements considering relatively high Péclet numbers. To this end, we compare different derivation approaches for the dual problem, different approximation approaches for the spatial and temporal weights, as well as arbitrary polynomial degrees within the discretizations in space and time.

For the practical realization of the space-time adaptive process, we introduce an implementation approach using tensor-product spaces for the discretization of the global space-time domain. These spaces are referred to as space-time slabs being stored in a list object which enables for an easy and efficient involvement of additional slabs in the course of adaptive refinement. This approach was developed by U. Köcher and is here extended to the underlying types of model problems, cf. [129, 29, 52].

In numerical examples we study the performance properties of our multirate approach by means of academic test cases, well-known benchmarks for convection-dominated problems as well as examples of physical relevance in two and three space dimensions. We study convergence, computational efficiency and stability of the underlying space-time adaptive algorithm, investigating different goal functionals and several pairs of finite element spaces in space and time used for the approximation of the underlying primal and dual problems. Thereby, we focus particularly on the interaction of stability and error control with regard to accuracy and efficiency reasons.

1.5 Outline

This work is organized as follows. In **Chapter 2** we introduce the basic notation and main concepts used throughout this thesis involving some general results as well as an overview of residual-based stabilization and goal-oriented error control.

In **Chapter 3** we derive goal-oriented error representation formulas based on the DWR method for a linear stationary transport problem. We investigate two possible approaches for the derivation of the dual problem including two different ways to approximate the spatial weights occurring within the error representations,

respectively. Several comparative studies regarding the different approaches for the dual problem as well as the different approximation techniques for the weights are done in the numerical examples section. Furthermore, these comparative studies serve as basis for the upcoming chapters regarding time-dependent and coupled problems.

Based on the results of Ch. 3, we extend these concepts in **Chapter 4** to the case of time-dependent transport problems. Here, the error representation formula is separated into amounts of the temporal and spatial discretization error which serve as local error indicators for adaptive mesh refinement in space and time. Again, different approximation techniques are discussed and investigated, this time with respect to the temporal weights. An important issue of this chapter is given by explaining some details about the practical realization of the underlying concepts for goal-oriented space-time adaptivity. Furthermore, we give insight into some implementational aspects of the underlying software architecture. In numerical examples we illustrate and investigate the performance properties of the underlying algorithm for time-dependent problems including convergence studies, independence of temporal and spatial error indicators, computational efficiency as well as stability properties.

Using the knowledge and results of the previous two chapters, the main focus of this work is on **Chapter 5** considering a multirate in time approach in view of goal-oriented error control based on the DWR method for a coupled flow and transport problem. This multirate approach assumes different characteristic time scales for the underlying subproblems and thus employs different time step sizes for the respective temporal discretizations. Splitted error representation formulas in space and time are derived for both the transport and Stokes flow problem. Furthermore, different application scenarios with regard to different intentions for the underlying space-time adaptive algorithm are presented and discussed. In numerical examples we validate our higher-order space-time implementations and investigate the performance properties of the implemented algorithm with regard to the new multirate in time approach. These examples gain from the results, for instance, with regard to the approximation of the spatial and temporal weights or the equilibration of the temporal and spatial error indicators obtained in Ch. 3 and 4, respectively.

Finally, in **Chapter 6** we summarize with conclusions and give some outlook for future work and possible extensions.

Chapter 2

Notation and Mathematical Tools

In this chapter, we present the notation and main concepts used throughout this work. This involves for one thing a theoretical framework including some basic notation, the definition of function spaces and their associated norms as well as some theoretical results. On the other hand, we introduce the general concepts of residual-based stabilization as well as goal-oriented error control.

2.1 Basic Notation

Throughout this work, we assume the following properties with regard to a space-time domain $Q = \Omega \times I$.

Assumption 2.1 (Space-Time Domain)

Let $Q = \Omega \times I$ be a space-time domain (sometimes also referred to as space-time cylinder), where $\Omega \subset \mathbb{R}^d$, with $d = 2$ or $d = 3$, is a polygonal or polyhedral bounded domain with Lipschitz boundary $\partial\Omega$, cf. Def. 2.10 in Sec. 2.3 for a precise definition, and $I = (t_0, T)$, $0 \leq t_0 < T < \infty$, is a bounded time interval. The outer unit normal vector to the boundary $\partial\Omega$ is denoted by \mathbf{n} .

If not explicitly indicated, we assume homogeneous Dirichlet boundary conditions throughout all presented problems within this work. Nevertheless, we will refer to nonhomogeneous Dirichlet and Neumann boundary conditions in due time.

2.1.1 Function Spaces

In a first part, we present some well-known general function spaces. For more details we refer to standard literature, for instance, like [81], [96], [2] or [61]. The standard

Lebesgue space $L^p(\Omega)$, $1 \leq p < \infty$, being defined by

$$L^p(\Omega) := \left\{ f : \Omega \rightarrow \mathbb{R} \mid \int_{\Omega} |f(\mathbf{x})|^p d\mathbf{x} < \infty \right\},$$

consists of all measurable functions f which are Lebesgue integrable on Ω up to the power p . For $p = \infty$, this space is

$$L^\infty(\Omega) := \left\{ f : \Omega \rightarrow \mathbb{R} \mid |f(\mathbf{x})| < \infty \text{ almost everywhere in } \Omega \right\}.$$

The space $L^p(\Omega)$ is a Banach space equipped with the norm

$$\|f\|_{L^p(\Omega)} := \begin{cases} \left(\int_{\Omega} |f(\mathbf{x})|^p d\mathbf{x} \right)^{\frac{1}{p}} & \text{if } 1 \leq p < \infty, \\ \text{ess sup}_{\mathbf{x} \in \Omega} |f(\mathbf{x})| & \text{if } p = \infty. \end{cases}$$

For $p = 2$, the space $L^2(\Omega)$ is a Hilbert space with the inner product

$$(f, g)_{L^2(\Omega)} := \int_{\Omega} f(\mathbf{x})g(\mathbf{x})d\mathbf{x}.$$

For the sake of clarity, we will simply use (\cdot, \cdot) to denote the inner product of $L^2(\Omega)$ as well as $\|\cdot\|$ for the associated L^2 -norm throughout this work. Next, we introduce the Sobolev space $W^{m,p}(\Omega)$, $m \in \mathbb{N} \cup \{0\}$, $1 \leq p \leq \infty$, by

$$W^{m,p}(\Omega) := \left\{ f \in L^p(\Omega) \mid \partial^\alpha f \in L^p(\Omega) \forall \alpha \text{ with } |\alpha| \leq m \right\},$$

consisting of all functions in $L^p(\Omega)$ whose distributional derivatives of order up to m belong to $L^p(\Omega)$. Here, $\alpha = (\alpha_1, \dots, \alpha_d) \in \mathbb{N}^d$ is a multi-index with

$$|\alpha| := \sum_{i=1}^d \alpha_i, \quad \partial^\alpha f := \frac{\partial^{|\alpha|} f}{\partial x_1^{\alpha_1} \dots \partial x_d^{\alpha_d}}.$$

The space $W^{m,p}(\Omega)$ is a Banach space equipped with the norm

$$\|f\|_{W^{m,p}(\Omega)} := \begin{cases} \left(\sum_{|\alpha| \leq m} \|\partial^\alpha f\|_{L^p(\Omega)}^p \right)^{\frac{1}{p}} & \text{if } 1 \leq p < \infty, \\ \max_{|\alpha| \leq m} \|\partial^\alpha f\|_{L^\infty(\Omega)} & \text{if } p = \infty. \end{cases}$$

For $p = 2$, the space $H^m(\Omega) := W^{m,2}(\Omega)$ is a Hilbert space with the inner product

$$(f, g)_{H^m(\Omega)} := \sum_{|\alpha| \leq m} (\partial^\alpha f, \partial^\alpha g).$$

Furthermore, we introduce the following semi-norm by means of

$$|f|_{W^{m,p}(\Omega)} := \begin{cases} \left(\sum_{|\alpha|=m} \|\partial^\alpha f\|_{L^p(\Omega)}^p \right)^{\frac{1}{p}} & \text{if } 1 \leq p < \infty, \\ \max_{|\alpha|=m} \|\partial^\alpha f\|_{L^\infty(\Omega)} & \text{if } p = \infty. \end{cases}$$

In the case of d -dimensional vector functions the corresponding spaces are denoted by $L^p(\Omega)^d$, $W^{m,p}(\Omega)^d$ and $H^m(\Omega)^d$. These spaces are equipped with the usual product norm and the norms and inner products are denoted in an analogous way as for the scalar functions.

The space $C^k(\Omega)$, $k \in \mathbb{N} \cup \{0\}$, being defined by

$$C^k(\Omega) := \left\{ f : \Omega \rightarrow \mathbb{R} \mid f \text{ } k\text{-times continuously differentiable on } \Omega \right\},$$

consists of all functions whose derivatives up to order k are continuous on Ω . We set

$$C(\Omega) := C^0(\Omega), \quad C^\infty(\Omega) := \bigcap_{k \in \mathbb{N} \cup \{0\}} C^k(\Omega).$$

In this sense, the space $C^k(\bar{\Omega})$, $k \in \mathbb{N} \cup \{0\}$, consists of all functions from $C^k(\Omega)$ whose derivatives up to order k possess continuous extensions onto $\bar{\Omega}$. It is a Banach space with the norm

$$\|f\|_{C^k(\bar{\Omega})} := \max_{|\alpha| \leq k} \sup_{\mathbf{x} \in \bar{\Omega}} |\partial^\alpha f(\mathbf{x})|.$$

The space $C_c^\infty(\Omega)$ is defined by

$$C_c^\infty(\Omega) := \left\{ f \in C^\infty(\Omega) \mid \text{supp}(f) \subset \Omega \right\},$$

consisting of infinitely often differentiable functions with compact support in Ω . Here, $\text{supp}(v)$ is given by

$$\text{supp}(f) := \overline{\{\mathbf{x} \in \Omega \mid f(\mathbf{x}) \neq 0\}} \subset \Omega.$$

The Sobolev space $W_0^{m,p}(\Omega)$ is defined as the completion of $C_c^\infty(\Omega)$ in the norm of $W^{m,p}(\Omega)$

$$W_0^{m,p}(\Omega) := \overline{C_c^\infty(\Omega)}^{\|\cdot\|_{W^{m,p}(\Omega)}}.$$

For $p = 2$ we write $H_0^m(\Omega) := W_0^{m,2}(\Omega)$. Finally, the space $W^{-m,q}(\Omega)$, $m \in \mathbb{N} \cup \{0\}$, $p \in (1, \infty)$, $p^{-1} + q^{-1} = 1$, being defined by

$$W^{-m,q}(\Omega) := \left\{ g \in (C_c^\infty(\Omega))' \mid \|g\|_{W^{-m,q}(\Omega)} < \infty \right\},$$

consists of all distributions which are defined on $W^{m,p}(\Omega)$. Here, $(C_c^\infty(\Omega))'$ is the set of all distributions and the norm $\|\cdot\|_{W^{-m,q}(\Omega)}$ is given by

$$\|g\|_{W^{-m,q}(\Omega)} := \sup_{\varphi \in C_c^\infty(\Omega), \varphi \neq 0} \frac{\langle g, \varphi \rangle}{|\varphi|_{W^{m,p}(\Omega)}},$$

where $\langle g, \varphi \rangle$ can be understood as the application of a distribution φ to a function $g \in C_c^\infty(\Omega)$. $W^{-m,q}(\Omega)$ can be identified with the dual space of $W_0^{m,p}(\Omega)$. In particular, the dual space of $H_0^m(\Omega)$ is denoted by $H^{-m}(\Omega)$. In the course of this, we introduce the following definition.

Definition 2.1 (Useful Spaces in Chapter 3)

When dealing with the convection-diffusion-reaction equation in Ch. 3, the following function spaces are of fundamental importance.

$$V := W_0^{1,2}(\Omega) = H_0^1(\Omega),$$

$$V' := H^{-1}(\Omega),$$

$$H := W^{0,2}(\Omega) = L^2(\Omega).$$

Furthermore, in the context of dealing with flow problems, we introduce the following space of functions with weak divergence. For more details we refer to, for instance, [112, Ch. 3]. The space $H(\operatorname{div}, \Omega)$ being defined by

$$H(\operatorname{div}, \Omega) := \left\{ \mathbf{f} \in L^2(\Omega)^d \mid \nabla \cdot \mathbf{f} \in L^2(\Omega) \right\},$$

consists of all vector fields in $L^2(\Omega)$ where the divergence belongs also to $L^2(\Omega)$. The space $H(\operatorname{div}, \Omega)$ is a Hilbert space with the inner product and the induced norm, respectively,

$$(\mathbf{f}, \mathbf{g})_{H(\operatorname{div}, \Omega)} := (\mathbf{f}, \mathbf{g}) + (\nabla \cdot \mathbf{f}, \nabla \cdot \mathbf{g}),$$

$$\|\mathbf{f}\|_{H(\operatorname{div}, \Omega)} := \left(\|\mathbf{f}\|^2 + \|\nabla \cdot \mathbf{f}\|^2 \right)^{\frac{1}{2}}.$$

In addition, the space of weakly divergence-free functions is defined by

$$V_0 = V_{\operatorname{div}}(\Omega) := \left\{ \mathbf{f} \in V^d = H_0^1(\Omega)^d \mid (\nabla \cdot \mathbf{f}, q)_{L^2(\Omega)} = 0 \ \forall q \in L_0^2(\Omega) \right\},$$

with $L_0^2(\Omega) := \left\{ q \in L^2(\Omega) \mid \int_\Omega q \, d\mathbf{x} = 0 \right\}$. The divergence of the functions from $V_{\operatorname{div}}(\Omega)$ vanishes in the sense of $L^2(\Omega)$, i.e., it is $\nabla \cdot \mathbf{v} = 0$ almost everywhere in Ω . Finally, another space of divergence-free functions is defined by

$$H_{\operatorname{div}}(\Omega) := \left\{ \mathbf{f} \in H(\operatorname{div}, \Omega) \mid \nabla \cdot \mathbf{f} = 0 \text{ and } \mathbf{f} \cdot \mathbf{n} = 0 \text{ on } \partial\Omega \text{ in the sense of traces} \right\}.$$

We will conclude this section remarking that for bounded domains with Lipschitz boundary, it can be shown that $H_{\text{div}}(\Omega)$ is the closure of $C_{0,\text{div}}^\infty(\Omega)$, cf. [112, Ch. 3] or rather [59, Prop. 1.8] or [171, Ch.II, Lemma 2.5.3].

2.1.2 Space-Time Function Spaces

For some Banach space X , the time dependent space $L^p(I; X)$, $1 \leq p \leq \infty$, being defined by

$$L^p(I; X) := \left\{ f : I \rightarrow X \mid \|f(t)\|_{L^p(I; X)}^p < \infty \right\},$$

consists of all L^p -integrable functions f from I into X . This is a Banach space equipped with the norm

$$\|f\|_{L^p(I; X)} := \begin{cases} \left(\int_I \|f(t)\|_X^p dt \right)^{\frac{1}{p}} & \text{if } 1 \leq p < \infty, \\ \text{ess sup}_{t \in \Omega} \|f(t)\|_X & \text{if } p = \infty. \end{cases}$$

These spaces may be comprehended as Bochner spaces by means of a derivation via the Bochner integral. For more details to the derivation of these spaces, we refer to, e.g., [81, 61, 187, 56, 13, 170, 14, 130].

Similar to the space $C^k(\bar{\Omega})$, we denote by $C^k(\bar{I}; X)$, $k \in \mathbb{N} \cup \{0\}$, the space of all functions from \bar{I} into X that are k -times continuously differentiable on I and whose derivatives $\partial_t^j f(t)$, $0 \leq j \leq k$, up to order k possess continuous extensions onto \bar{I} . Again, this is a Banach space equipped with the norm

$$\|f\|_{C^k(\bar{I}; X)} := \max_{0 \leq j \leq k} \sup_{t \in \bar{I}} \|\partial_t^j f(t)\|_X.$$

We set $C(\bar{I}; X) := C^0(\bar{I}; X) = \left\{ f : \bar{I} \rightarrow X \mid f \text{ is continuous} \right\}$ with the corresponding norm

$$\|f\|_{C(\bar{I}; X)} := \sup_{t \in \bar{I}} \|f(t)\|_X.$$

As before, we let $C_c^\infty(I; X)$ be the space of infinitely often differentiable functions with compact support.

Finally, we introduce an important space when dealing with time-dependent problems in Ch. 4 and Ch. 5. Thereby, we follow the lines of [61, Ch. XVIII], assuming the following.

Assumption 2.2 (Gelfand-Triple)

Let V, H be two real, separable Hilbert spaces with related inner products and norms

denoted by $(\cdot, \cdot)_V, \|\cdot\|_V$ and $(\cdot, \cdot)_H, \|\cdot\|_H$, respectively. Further, we suppose that V is dense in H so that, by identifying H and its dual space H' , we have the continuous embedding

$$V \hookrightarrow H \hookrightarrow V',$$

where V' denotes the dual space of V and each space is dense in the following. Such a triple (V, H, V') is also known as a Gelfand-triple, cf., e.g., [163, Ch.7.2]. Well-known examples for these spaces are $V = H_0^1(\Omega), V' = H^{-1}(\Omega)$, and $H = L^2(\Omega)$, as introduced in Assumption 2.1.

Then, for spaces V and V' fulfilling Assumption 2.2, we may introduce the following space

$$W(I; V, V') := \left\{ w \in L^2(I; V) \mid \partial_t w \in L^2(I; V') \right\}.$$

This is a Hilbert space equipped with the norm (cf. [61, Prop. 6 in Ch. XVIII])

$$\|w\|_W := (\|w\|_{L^2(I; V)}^2 + \|\partial_t w\|_{L^2(I; V')}^2)^{\frac{1}{2}} = \left(\int_I \{ \|w(t)\|_V^2 + \|\partial_t w(t)\|_{V'}^2 \} dt \right)^{\frac{1}{2}}.$$

In the following, we present some properties concerning regularity of elements of the space $W(I; V, V')$.

Theorem 2.1 *The space $W(I; V, V')$ is continuously embedded in $C(\bar{I}; H)$*

$$W(I; V, V') \hookrightarrow C(\bar{I}; H).$$

Proof. The proof can be found in the literature, for instance, in [61, Thm. 1 in Ch. XVIII] or [188, Prop. 23.23 (ii)]. \square

Remark 2.1 *As a consequence of Thm. 2.3 (trace theorem) and Thm. 2.1, for a function $w \in W(I; V, V')$, with $\bar{I} \subset \mathbb{R}$, we may speak of the traces $w(t_0 = 0), w(T) \in H$. This is of importance when dealing with initial ($w(0)$) or final ($w(T)$) conditions within the variational formulations of the so-called primal and dual problems in the course of this thesis.*

Lemma 2.1 *The space $C_c^\infty(I; V)$ is dense in $W(I; V, V')$.*

Proof. The proof can be found in the literature, for instance, in [138, Thm. 2.1] or [61, Lemma 1 in Ch. XVIII]. Moreover, a slightly different proof can be found in [79, Thm. 64.36]. \square

Corollary 2.1 *The space $W(I; V, V')$ is dense in $L^2(I; V)$.*

Proof. Since there holds $W(I; V, V') \subset L^2(I; V)$ and since $C_c^\infty(I; V)$ is dense in $L^2(I; V)$ (cf., e.g., [56, Prop. 1.4.17] or [13, Ch. 1.1]), the assertion of Corollary 2.1 directly follows by Lemma 2.1 and an embedding argument. \square

Theorem 2.2 (Green's Formula or, more simply, Integration by Parts)

We assume $\bar{I} = [0, T] \subset \mathbb{R}$. Then, there holds for $u, v \in W(I; V, V')$

$$\int_0^T (\partial_t u(t), v(t)) dt = \int_0^T (u(t), -\partial_t v(t)) dt + (u(T), v(T)) - (u(0), v(0)).$$

Proof. The proof can be found in the literature, for instance, in [61, Thm. 2 in Ch. XVIII] or [188, Prop. 23.23 (iv)]. \square

In the course of this, we introduce the following definitions.

Definition 2.2 (Useful Space in Chapter 4)

When dealing with time-dependent convection-diffusion-reaction equations in Ch. 4, the following function space is of fundamental importance.

$$\mathcal{V} := W(I; H_0^1(\Omega), H^{-1}(\Omega)) = \left\{ v \in L^2(I; H_0^1(\Omega)) \mid \partial_t v \in L^2(I; H^{-1}(\Omega)) \right\}.$$

Definition 2.3 (Useful Spaces in Chapter 5)

When dealing with coupled flow and transport problems in Ch. 5, the following function spaces are of fundamental importance.

$$\begin{aligned} \mathcal{X} &:= W(I; H_0^1(\Omega), H^{-1}(\Omega)) = \left\{ v \in L^2(I; H_0^1(\Omega)) \mid \partial_t v \in L^2(I; H^{-1}(\Omega)) \right\}, \\ \mathcal{Y}_1 &:= W(I; H_0^1(\Omega)^d, H^{-1}(\Omega)^d) = \left\{ \mathbf{v} \in L^2(I; H_0^1(\Omega)^d) \mid \partial_t \mathbf{v} \in L^2(I; H^{-1}(\Omega)^d) \right\}, \\ \mathcal{Y}_2 &:= \left\{ v \in L^2(I; L_0^2(\Omega)) \right\}, \text{ with } L_0^2(\Omega) = \left\{ q \in L^2(\Omega) \mid \int_\Omega q \, d\mathbf{x} = 0 \right\}, \\ \mathcal{Y} &:= \mathcal{Y}_1 \times \mathcal{Y}_2. \end{aligned}$$

2.1.3 Finite Element Spaces

This section is inspired by [167, Sec. 3.2]. Generally speaking, the derivation of finite element spaces is closely linked to the decomposition of the underlying domain Ω .

Assumption 2.3 (Decomposition of Spatial Domain Ω)

Let \mathcal{T}_h be a decomposition (hereinafter also called triangulation) of the domain Ω introduced in Assumption 2.1 into disjoint elements or cells K , such that $\bar{\Omega} = \bigcup_{K \in \mathcal{T}_h} \bar{K}$. We denote the diameter of a cell by the cell-wise constant function $h|_K = h_K := \text{diam}(K)$. The maximum cell diameter h is then given by $h := \max_{K \in \mathcal{T}_h} h_K$. Here, we choose the elements $K \in \mathcal{T}_h$ to be quadrilaterals for $d = 2$ and hexahedrals for $d = 3$. We assume the decomposition to be regular (cf. Def. 2.5), but allowing hanging nodes (cf. Rem. 2.2). Furthermore, the decomposition is assumed to be organized in a patch-wise manner (cf. Def. 2.6).

The shape of the elements K in Assumption 2.3 is due to the fact that our implementations are based on the open source finite element library `deal.II`, cf. [16, 22], dealing with those element types only. To specify the above introduced elements as well as the decomposition, we present some definitions, that can be found in standard literature like [48], [57], or [105].

Definition 2.4 (Finite Element) Let $K \in \mathbb{R}^n$ be a bounded closed set with nonempty interior and piecewise smooth boundary (element domain). Then, K is called a **finite element** if the following is given:

- (i) A set of **nodal variables** $\mathcal{N} = \{N_1, N_2, \dots, N_R\}$.
- (ii) \mathcal{Q} be a finite-dimensional space of polynomial functions $p : K \rightarrow \mathbb{R}$ such that

$$\forall c_1, \dots, c_R \in \mathbb{R} \exists_1 p \in \mathcal{Q} : p(N_r) = c_r \quad (r = 1, \dots, R).$$

This is referred to as the space of **shape functions**.

Definition 2.5 (Regularity) A decomposition \mathcal{T}_h of a domain $\Omega \subset \mathbb{R}^d$, $d = 2, 3$, is called **regular** if the following conditions are fulfilled:

- (i) $\bar{\Omega} = \bigcup_{K \in \mathcal{T}_h} \bar{K}$.
- (ii) $K_1 \cap K_2 = \emptyset$ for all elements $K_1, K_2 \in \mathcal{T}_h$ with $K_1 \neq K_2$.
- (iii) Any edge ($d = 2$) or face ($d = 3$) of any element $K_1 \in \mathcal{T}_h$ is either a subset of the boundary $\partial\Omega$ or an edge ($d = 2$) or a face ($d = 3$) of another element $K_2 \in \mathcal{T}_h$.

Remark 2.2 (Hanging Nodes) *In order to facilitate adaptive mesh refinement, the third condition of Def. 2.5 has to be weakened in the following sense. We allow the usage of so-called **hanging nodes**, cf. [55], which means that an element is allowed to have one node variable located on the middle of its edge ($d = 2$) or face ($d = 3$) shared with neighboring elements, but none on an edge ($d = 2$) or a face ($d = 3$) shared with the boundary $\partial\Omega$. Note that there are two types of hanging nodes in three dimensions (on edges or faces), while in two dimensions there is only one type of hanging nodes (only on edges), cf. Fig.2.1 as well as [167, 20]. We point out that the global conformity of the finite element approach is still preserved since the unknowns (degrees of freedom) at such hanging nodes are eliminated by interpolation between the neighboring 'regular' nodes (degrees of freedom). Hence, hanging nodes actually do not carry any degrees of freedom, cf. [20] and [55] for more details in this concept.*

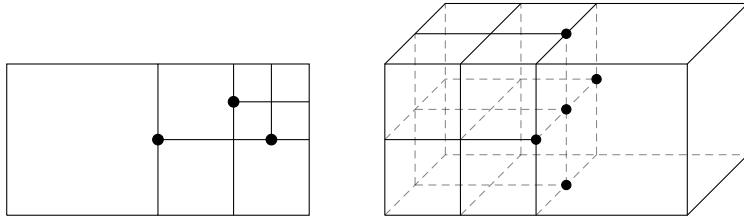


Figure 2.1: Exemplary two- and three-dimensional elements with hanging nodes, cf. [167, Fig.3.2].

Furthermore, we introduce the following property of a decomposition \mathcal{T}_h , cf. [167].

Definition 2.6 (Patch-Wise Decomposition) *A decomposition \mathcal{T}_h of a domain $\Omega \subset \mathbb{R}^d$, $d = 2, 3$, is organized in a **patch-wise** manner if the following holds true. The decomposition \mathcal{T}_h is obtained by uniform refinement of a coarser decomposition \mathcal{T}_{2h} , such that it is always possible to combine four ($d = 2$) or eight ($d = 3$) adjacent elements of \mathcal{T}_h to obtain one element of \mathcal{T}_{2h} . Such macro-elements are called **patches**, cf. Fig.2.2.*

Next, we define the discrete finite element space V_h^p , following standard literature like [57] or [48], by

$$V_h^p := \left\{ v \in V \cap C(\bar{\Omega}) \mid v|_K \in \mathcal{Q}_h^p(K), \forall K \in \mathcal{T}_h \right\}, \quad (2.1)$$

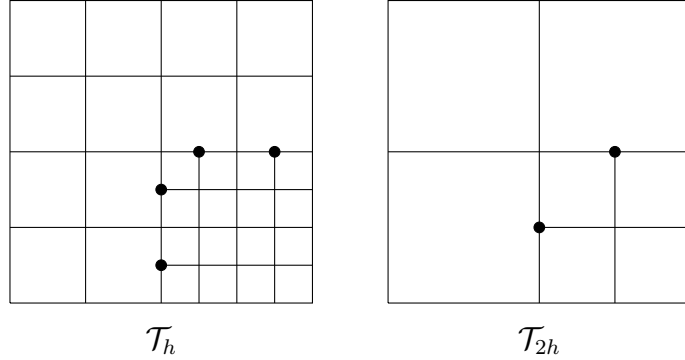


Figure 2.2: Exemplary two-dimensional decomposition \mathcal{T}_h (with hanging nodes) organized in a patch-wise manner with corresponding coarser decomposition \mathcal{T}_{2h} , cf. [167, Fig.3.3].

where the space $\mathcal{Q}_h^p(K)$ is obtained using the transformation $\mathcal{T}_K : \hat{K} \rightarrow K$, cf. Fig. 2.3, defined by

$$\mathcal{Q}_h^p(K) := \left\{ v : K \rightarrow \mathbb{R} \mid v \circ \mathcal{T}_h \in \hat{\mathcal{Q}}_h^p(\hat{K}) \right\}. \quad (2.2)$$

To specify the space $\mathcal{Q}_h^p(K)$, we introduce the standard Lagrange finite element space $\hat{\mathcal{Q}}_h^p(\hat{K})$ of tensor product polynomials up to degree p on the reference element $\hat{K} = [0, 1]^d$, $d = 2, 3$, given as

$$\hat{\mathcal{Q}}_h^p(\hat{K}) := \text{span} \left\{ \prod_{i=1}^d \hat{x}_i^{\alpha_i} \mid \alpha_i \in \{0, 1, \dots, p\} \right\}.$$

For the lowest order case, $p = 1$, we get the following space of bi-linear ($d = 2$) or tri-linear ($d = 3$) functions

$$\hat{\mathcal{Q}}_h^1(\hat{K}) := \text{span} \{1, \hat{x}_1, \hat{x}_2, \hat{x}_1 \hat{x}_2\} \quad (d = 2),$$

$$\hat{\mathcal{Q}}_h^1(\hat{K}) := \text{span} \{1, \hat{x}_1, \hat{x}_2, \hat{x}_3, \hat{x}_1 \hat{x}_2, \hat{x}_1 \hat{x}_3, \hat{x}_2 \hat{x}_3, \hat{x}_1 \hat{x}_2 \hat{x}_3\} \quad (d = 3).$$

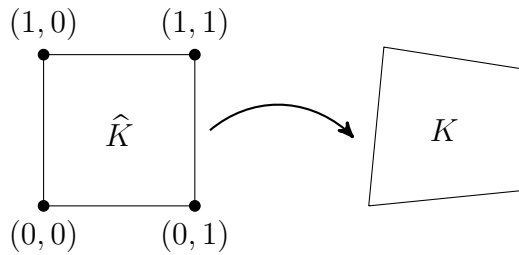


Figure 2.3: Exemplary bi-linear transformation \mathcal{T}_K from the reference element $\hat{K} = [0, 1]^2$ to an element K , cf. [167, Fig.3.4].

If the transformation \mathcal{T}_K itself is contained in $\widehat{\mathcal{Q}}_h^p(\widehat{K})$, the resulting finite element space is called *isoparametric*. We note that the discrete finite element space V_h^p is conforming, i.e., $V_h^p \in V$ by construction, cf., e.g., [57] for more details.

We close this section with some classical assumptions with regard to the geometry of the elements belonging to a decomposition \mathcal{T}_h , cf. [167] and [47].

Definition 2.7 (Quasi-Uniformity) *A family of decompositions \mathcal{T}_h is called **quasi-uniform** if there is a constant κ such that the following conditions are fulfilled:*

(i) *For each transformation $\mathcal{T}_K : \widehat{K} \rightarrow K$ there holds*

$$\frac{\sup \left\{ \|\nabla \cdot \mathcal{T}_K(\widehat{\mathbf{x}})\mathbf{x}\| \mid \widehat{\mathbf{x}} \in \widehat{K}, \|\mathbf{x}\| = 1 \right\}}{\inf \left\{ \|\nabla \cdot \mathcal{T}_K(\widehat{\mathbf{x}})\mathbf{x}\| \mid \widehat{\mathbf{x}} \in \widehat{K}, \|\mathbf{x}\| = 1 \right\}} \leq \kappa \quad \forall K \in \bigcup_h \mathcal{T}_h.$$

(ii) *With the diameter ϱ_K of the biggest ball inscribed into the element K there holds*

$$\frac{h_K}{\varrho_K} \leq \kappa \quad \forall K \in \bigcup_h \mathcal{T}_h.$$

Definition 2.8 (Uniformity) *A quasi-uniform family of decompositions \mathcal{T}_h is called **uniform** if there is a constant κ such that*

$$\frac{h}{\varrho_K} \leq \kappa \quad \forall K \in \bigcup_h \mathcal{T}_h.$$

It is well-known that the approximation error of finite elements can be estimated by interpolation errors using the lemmas of Lax-Milgram and C ea, cf., e.g., [154]. For continuous functions $v \in C(\bar{\Omega})$ the point-wise interpolation operator $I_h : C(\bar{\Omega}) \rightarrow V_h^p$ is well-defined. Then, this interpolation operator satisfies the following approximation properties stated in the following lemma, cf. [167]:

Lemma 2.2 *Let \mathcal{T}_h be a quasi-uniform family of decompositions of the domain Ω and V_h^p be the space of isoparametric finite elements of order p . Then, there exists a constant C , only depending on Ω and p , such that for $v \in H^m(\Omega)$ with $2 \leq m \leq p+1$ and $0 \leq j \leq m$ there holds*

$$\|v - I_h v\|_{H^j(\Omega)} \leq C h^{m-j} \|v\|_{H^m(\Omega)}.$$

Proof. The proof can be found in the literature, for instance, in [47]. □

2.2 Variational Time Discretization

In this section, we introduce the families of continuous and discontinuous variational time discretization methods. Many of these variational time discretization schemes are algebraically equivalent to well-known ordinary differential equation integrators such as the forward or backward Euler method, the Crank-Nicolson method, explicit and implicit Runge-Kutta methods and many more, cf., e.g., [8, 79]. In general, for the temporal discretization with regard to ordinary differential equations we refer to [80] using continuous Galerkin methods and to [64] using discontinuous Galerkin methods, respectively. Furthermore, a more detailed derivation of the concepts for continuous and discontinuous variational time discretization schemes can be found, for instance, in the textbooks [77, 174, 79]. The following course of action is inspired by [128, Sec. 3.2] and [167, Sec. 1], respectively.

Using finite element methods for the temporal variable can be traced back to the end of the 1960's and early 1970's, when crucial developments on variational formulation for time integration were proposed in the treatises [15, 87, 151, 110]. Since then, numerous applications of space-time Galerkin methods can be found in the literature, cf., e.g., [157, 134, 19, 86, 44]. A short review of the development can be found, e.g., in [190, Sec. 1]. In particular, with regard to parabolic problems having relevance to the underlying thesis, we refer to the works [174, 149, 75, 135, 19, 70, 71, 72, 73, 74, 6, 7, 142]. Furthermore, using space-time Galerkin methods in the context of goal-oriented adaptive mesh refinement, we refer, e.g., to [36, 98, 143, 168, 40].

In the scope of this thesis, the main advantage of using space-time finite element discretizations lies in enabling duality based, goal-oriented a posteriori error control allowing for high efficient adaptive mesh refinement, cf. also the following Sec. 2.5. Moreover, using finite elements for the discretization of the temporal variable offers further advantages. For example, compared to finite difference methods, a more flexible location of the degrees of freedom is possible. In addition, the proved concepts from the variational discretization in space can be easily adopted to time such as the concepts of hp -adaptivity, multiscale and upsampling techniques. Variational formulations in space and time are obtained that might be advantageous with regard to stability and a priori as well as a posteriori error analyses. Finally, the construction of higher-order approximations in time by using a post-processing approach is straightforward, cf., for instance, [78], [30] [29].

Throughout this work, when dealing with variational time discretizations, we assume the following for the underlying time interval.

Assumption 2.4 (Decomposition of Time Interval I)

Let $I = (t_0, T)$, $0 \leq t_0 < T < \infty$, be a bounded time interval. We decompose the closure of the time interval $\bar{I} = [0, T]$ into not necessarily equidistant, left-open subintervals $I_n := (t_{n-1}, t_n]$, $n = 1, \dots, N$, with $0 =: t_0 < t_1 < \dots < t_N := T$ being a set of time points of \bar{I} .

As our implementation is based on using space-time tensor product spaces for the discretization of the space-time domain Q defined in Assumption 2.1, we introduce the following concept of space-time slabs. This concept is described in detail in Sec. 4.4 and illustrated by Figs. 2.4 and 4.5, respectively. Thereby, the specification of the temporal triangulation is very similar to the spatial version described in Assumption 2.3.

Assumption 2.5 (Space-Time Slabs, cf. Figs. 2.4 and 4.5)

Since the set of time subintervals I_n in Assumption 2.4 is finite and countable, a separation of the global space-time domain $Q = \Omega \times I$ into a partition of space-time slabs $\hat{Q}_n = \Omega \times I_n$ is reasonable. The time domain of each space-time slab \hat{Q}_n is then discretized using a one-dimensional triangulation $\mathcal{T}_{\tau,n}$ for the closure of the subinterval $\bar{I}_n = [t_{n-1}, t_n]$, such that $\bar{I}_n = \bigcup_{K_n \in \mathcal{T}_{\tau,n}} \bar{K}_n$. This allows to have more than one cell in time on a slab \hat{Q}_n and a different number of cells in time of pairwise different slabs \hat{Q}_i and \hat{Q}_j , $1 \leq i, j \leq N$. Furthermore, let \mathcal{F}_τ be the set of all interior time points given as

$$\mathcal{F}_\tau := (\{t_1, \dots, t_N\} \cup \{t \in \partial K_n \mid K_n \in \mathcal{T}_{\tau,n}\}) \setminus \{0, T\},$$

with $1 \leq n \leq N$, where we denote the interior time points of the above union by $t_{\mathcal{F}}$, using $t_{\mathcal{F},n_\ell}$ and $t_{\mathcal{F},n}$ for the left and right end of the cell in time K_n , respectively. The commonly used time step size τ_K is here the diameter or length of the cell in time K_n of $\mathcal{T}_{\tau,n}$ and the global time discretization parameter τ is the maximum time step size τ_K of all cells in time of all slabs \hat{Q}_n , $1 \leq n \leq N$.

Finally, using the spatial triangulation $\mathcal{T}_{h,n}$ given in Assumption 2.3 on each slab \hat{Q}_n , $1 \leq n \leq N$, we end up with the separation of the implemented space-time slabs

$$Q_n = \mathcal{T}_{h,n} \times \mathcal{T}_{\tau,n}.$$

For reasons of clarity and as usual for an element in space $K \in \mathcal{T}_h$, we do not introduce an additional index for the number of cells in time on a single slab as well as for the interior time points here and in the following, although such an index can be used to distinguish between two cells in time belonging to the same slab or between two interior time points as illustrated in Fig. 2.4 and Fig. 2.5, respectively.

Remark 2.3 Restricting in Assumption 2.5 the temporal triangulation $\mathcal{T}_{\tau,n}$ within a single slab Q_n to consist of only one cell in time allows to interpret this cell K_n as the time subinterval I_n defined in Assumption 2.4. Then, the time step size τ_K corresponds to the length of the subinterval I_n given by $t_n - t_{n-1}$.

Moreover, we point out that the decomposition into the space-time slabs described in Assumption 2.5, using discontinuous test spaces as defined in Eq. (2.9), is conform with the approach of a so-called time marching scheme (TMS), independent of the number of cells in time used within a single slab. More precisely, the arising huge system of the finite element method in time can be decoupled into N independent subproblems, which have to be solved on the respective slabs Q_n , $n = 1, \dots, N$, cf. also Sec.4.3.1.

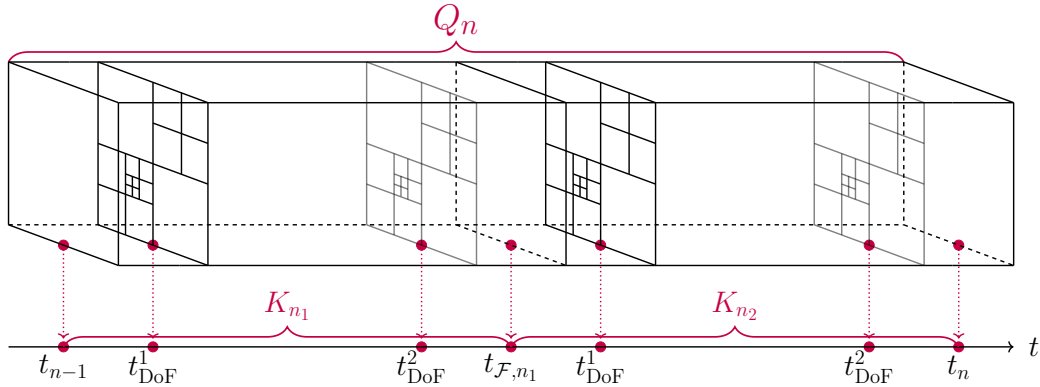


Figure 2.4: Illustration of a space-time slab with a temporal triangulation consisting of two cells in time, exemplary for a discontinuous Galerkin dG(1) time discretization generated with two Gaussian quadrature points. The two degrees of freedom (DoF) time points on each cell in time are the support points for the temporal basis functions. Each of the cells in time has the same adaptively refined spatial triangulation.

2.2.1 Continuous in Time Petrov-Galerkin Method

The idea behind the continuous in time Petrov-Galerkin method (cG(r) method) is to consider a trial space composed of continuous, piecewise polynomial functions in time of degree r , $r \geq 1$, and a test space composed of discontinuous, piecewise polynomial functions of degree $(r - 1)$. This leads to a conforming approximation in time; cf., e.g., [79, Ch. 69]. The origin of this method goes back to the work of Aziz and Monk [19], although not under this name.

For a continuous in time discretization, we define the finite-dimensional continuous time-discrete function space by means of

$$\mathcal{V}_\tau^{\text{cG}(r)} := \left\{ v_\tau \in C(\bar{I}; X) \mid v_\tau|_{K_n} \in \mathcal{P}_\tau^r(\bar{K}_n; X), K_n \in \mathcal{T}_{\tau,n}, n = 1, \dots, N \right\}, \quad (2.3)$$

consisting of piecewise polynomials of degree r in time with values in X . Here, $\mathcal{P}_\tau^r(\bar{K}_n; X)$ denotes the space of all polynomials in time up to degree $r, r \geq 1$, with values in some Banach space X . On each cell in time K_n , the piecewise polynomials v_τ in $\mathcal{V}_\tau^{\text{cG}(r)}$ can be represented by

$$v_\tau|_{K_n}(t) := \sum_{\iota=0}^r V_n^\iota \xi_{n,\iota}(t), \quad (2.4)$$

with time-independent coefficient functions $V_n^\iota \in X$ and appropriate basis functions from $\mathcal{P}_\tau^r(\bar{K}_n; \mathbb{R})$ in time. To specify these basis functions, we introduce the continuous in time function space

$$\mathcal{X}_\tau^r := \left\{ \xi \in C(I; \mathbb{R}) \mid \xi|_{K_n} \in \mathcal{P}_\tau^r(\bar{K}_n; \mathbb{R}), K_n \in \mathcal{T}_{\tau,n}, n = 1, \dots, N \right\} \subseteq L^2(I; \mathbb{R}). \quad (2.5)$$

The basis functions in \mathcal{X}_τ^r are determined using the well-known technique from the finite element method in space, i.e. we define reference basis functions on the reference cell or interval $\hat{I} := [0, 1]$ and represent them through a domain transformation \mathcal{Y}_n on the cell in time K_n . Therefore, let $\mathcal{Y}_n : \hat{I} \rightarrow \bar{K}_n$ be an affine mapping defined by

$$\mathcal{Y}_n(\hat{t}) := \tau_n \hat{t} + t_{\mathcal{F},n_\ell}, \quad \forall \hat{t} \in \hat{I}, t_{\mathcal{F},n_\ell} \in \partial K_n, K_n \in \mathcal{T}_{\tau,n}, n = 1, \dots, N,$$

and $\mathcal{Y}_n^{-1} : \bar{K}_n \rightarrow \hat{I}$ be the inverse mapping of \mathcal{Y}_n , defined by

$$\mathcal{Y}_n^{-1}(t) := \frac{t - t_{\mathcal{F},n_\ell}}{\tau_n}, \quad \forall t \in \bar{K}_n, t_{\mathcal{F},n_\ell} \in \partial K_n, K_n \in \mathcal{T}_{\tau,n}, n = 1, \dots, N.$$

Here, $t_{\mathcal{F},n_\ell} \in \partial K_n$ represents the left end of the cell in time K_n as introduced in Assumption 2.5. The space \mathcal{X}_τ^r contains globally $1 + r \cdot N_c$ independent C^0 -continuous basis functions on \bar{I} , where N_c denotes here the total number of cells in time summed up over all time subintervals. Locally, this space can be expressed by $r + 1$ independent polynomials basis functions on each cell in time K_n , i.e.

$$\begin{aligned} \mathcal{X}_\tau^r := & \text{span} \left\{ \xi_{n,\iota} \in L^2(I; \mathbb{R}) \mid \xi_{n,\iota}|_{K_n} \in \mathcal{P}_\tau^r(\bar{K}_n; \mathbb{R}), n = 1, \dots, N, \iota = 0, \dots, r \right\} \\ & \cap \left\{ \xi \in C(I; \mathbb{R}) \mid \xi|_{K_n} \in \mathcal{P}_\tau^r(\bar{K}_n; \mathbb{R}), n = 1, \dots, N \right\}, \end{aligned} \quad (2.6)$$

represented by

$$\xi_{n,\iota}(t) = \begin{cases} \widehat{\xi}_\iota(\Upsilon_n^{-1}(t)) \in \mathcal{P}_\tau^r(\widehat{I}; \mathbb{R}), & t \in \bar{K}_n, \\ 0, & t \notin \bar{K}_n, \end{cases} \quad (2.7)$$

such that the continuity in time of \mathcal{X}_τ^r from Eq. (2.5) is fulfilled, i.e. the two functions $\xi_n, \xi_{n+1} \in \mathcal{X}_\tau^r$ belonging to two consecutive cells in time, represented by the basis given in Eq. (2.6), must hold $\xi_n(t_{\mathcal{F}}^-) = \xi_{n+1}(t_{\mathcal{F}}^+)$ for all interior time points $t_{\mathcal{F}} \in \mathcal{F}_\tau$. Here, the reference basis functions $\widehat{\xi}_\iota, \iota = 0, \dots, r$, from Eq. (2.7) may now be determined as the standard Lagrange basis functions equivalently to the approach used for the spatial discretization, cf. Sec. 2.1.3. Thus, each reference basis function $\widehat{\xi}_\iota$ is uniquely defined by $r + 1$ nodal conditions

$$\widehat{\xi}_\iota(\Upsilon_n^{-1}(t_{n,\mu})) = \delta_{\mu,\iota}, \quad \mu, \iota = 0, \dots, r,$$

with the Kronecker symbol $\delta_{\mu,\iota}$ and appropriate interpolation points $t_{n,\mu}$ depending on the underlying quadrature rule used for the numerical approximation of the time integrals. Consequently, on each cell in time K_n , a trial function of temporal polynomial degree r has $r + 1$ degrees of freedom. But due to the continuity constraints on the left endpoints, the number of degrees of freedom that have to be determined on each cell in time K_n reduces to r . Thus, it is sufficient to choose the test space having one polynomial degree less than the trial space. More precisely, we choose the test space $\mathcal{V}_\tau^{\text{dG}(r-1)}$ as given in Eq. (2.9), consisting of piecewise polynomials of degree $r - 1$ in time with values in X .

2.2.2 Discontinuous in Time Galerkin Method

The discontinuous in time Galerkin method (dG(r) method) approximates the solution in time with piecewise polynomials of degree $r, r \geq 0$. Thereby, the solution in time may be discontinuous between two slabs and, in particular, between two cells in time, cf. Fig. 2.5, which leads to a nonconforming time approximation; cf., e.g., [79, Ch. 69]. The first dG method was introduced by Reed and Hill [157], where the first error analysis can be found in the work of LeSaint and Raviart [134].

We define the limits $v_\tau(t_{\mathcal{F}}^\pm)$ from above and below of a time-discrete globally discontinuous function v_τ as well as their jump at an interior time point $t_{\mathcal{F}}$ by

$$v_\tau(t_{\mathcal{F}}^\pm) := \lim_{t \rightarrow t_{\mathcal{F}}^\pm} v_\tau(t), \quad [v_\tau]_{t_{\mathcal{F}}} := v_\tau(t_{\mathcal{F}}^+) - v_\tau(t_{\mathcal{F}}^-). \quad (2.8)$$

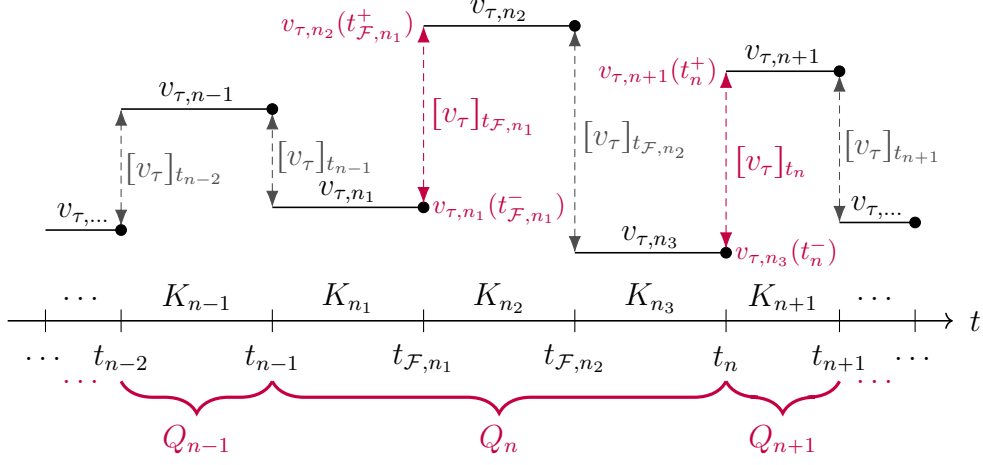


Figure 2.5: Illustration of jumps of a discontinuous in time function v_τ at interior time points including a jump between two consecutive cells in time ($[v_\tau]_{t_{\mathcal{F},n_1}}$) as well as a jump between two consecutive slabs ($[v_\tau]_{t_n}$), exemplary for a discontinuous Gelerkin dG(0) time discretization. Note that $t_n, 1 \leq n \leq N$, are included in the set of interior time points \mathcal{F}_τ introduced in Assumption 2.5.

Next, we define the finite-dimensional discontinuous time-discrete function space by means of

$$\mathcal{V}_\tau^{\text{dG}(r)} := \left\{ \begin{array}{l} v_\tau \in L^2(I; X) \mid v_\tau|_{K_n} \in \mathcal{P}_\tau^r(K_n; X), \\ v_\tau(0) \in X, K_n \in \mathcal{T}_{\tau,n}, n = 1, \dots, N \end{array} \right\}, \quad (2.9)$$

consisting of piecewise polynomials of degree r in time with values in X . Here, $\mathcal{P}_\tau^r(K_n; X)$ denotes the space of polynomials in time up to degree $r, r \geq 0$, with values in some Banach space X . The trial functions are chosen globally time-discontinuous but piecewise continuous within K_n , i.e. on each cell in time K_n they are considered as polynomials of degree r . More precisely, on each cell in time K_n , the piecewise polynomials v_τ in $\mathcal{V}_\tau^{\text{dG}(r)}$ can be represented by

$$v_\tau|_{K_n}(t) := \sum_{\iota=0}^r V_n^\iota \zeta_{n,\iota}(t), \quad (2.10)$$

with time-independent coefficient functions $V_n^\iota \in X$ and appropriate basis functions from $\mathcal{P}_\tau^r(K_n; \mathbb{R})$ in time. To specify these basis functions, we introduce the discontinuous in time function space

$$\mathcal{Y}_\tau^r := \left\{ \zeta \in L^2(I; \mathbb{R}) \mid \zeta|_{K_n} \in \mathcal{P}_\tau^r(\bar{K}_n; \mathbb{R}), \zeta(0) \in \mathbb{R}, K_n \in \mathcal{T}_{\tau,n}, n = 1, \dots, N \right\}. \quad (2.11)$$

The basis functions in \mathcal{Y}_τ^r are again determined using the well-known technique from the finite element method in space, i.e. we define reference basis functions on the reference cell or interval $\hat{I} := [0, 1]$ and represent them through a domain transformation

Υ_n on the cell in time K_n , analogous to the continuous approach above. Then, the space \mathcal{Y}_τ^r contains $r + 1$ independent basis functions on each cell in time K_n , given by

$$\mathcal{Y}_\tau^r := \text{span} \left\{ \zeta_{n,\ell} \in L^2(I; \mathbb{R}) \mid \zeta_{n,\ell}|_{K_n} \in \mathcal{P}_\tau^r(\bar{K}_n; \mathbb{R}), \right. \\ \left. \zeta_{n,\ell}(0) \in \mathbb{R}, n = 1, \dots, N, \ell = 0, \dots, r \right\}, \quad (2.12)$$

represented by

$$\zeta_{n,\ell}(t) = \begin{cases} \hat{\zeta}_\ell(\Upsilon_n^{-1}(t)) \in \mathcal{P}_\tau^r(\hat{I}; \mathbb{R}), & t \in \bar{K}_n, \\ 0, & t \notin \bar{K}_n. \end{cases} \quad (2.13)$$

Here, the reference basis functions $\hat{\zeta}_\ell, \ell = 0, \dots, r$, from Eq. 2.13 may now be determined as the standard Lagrange basis functions equivalently to the approach used for the spatial discretization, cf. Sec. 2.1.3. Thus, each reference basis function $\hat{\zeta}_\ell$ is uniquely defined by $r + 1$ nodal conditions

$$\hat{\zeta}_\ell(\Upsilon_n^{-1}(t_{n,\mu})) = \delta_{\mu,\ell}, \quad \mu, \ell = 0, \dots, r,$$

with the Kronecker symbol $\delta_{\mu,\ell}$ and appropriate interpolation points $t_{n,\mu}$. Consequently, on each cell in time K_n , a trial function of temporal polynomial degree r has $r + 1$ degrees of freedom. Due to the absence of continuity constraints on the left endpoints of the cells in time K_n , one has to determine $r + 1$ degrees of freedom on each cell in time K_n . The test space is chosen having the same polynomial degree than the trial space to guarantee a uniquely determination of the unknowns in time, i.e. the test space is also given by $\mathcal{V}_\tau^{\text{dG}(r)}$.

2.3 Theoretical Results

In the theory of weak or variational solutions, the solution of a partial differential equation is searched in an appropriate Sobolev space. Thereby, the solution has to satisfy certain boundary conditions of the underlying boundary value problem. However, since the boundary of a domain is a manifold of dimension $(d - 1)$, and consequently it has Lebesgue measure zero, one has to clarify how a function from a Sobolev space is defined on this manifold. This definition will be given in the so-called trace theorem. Therefore, we need the following terms.

Definition 2.9 (Boundary of Class $\mathbf{C}^{k,\alpha}$) *A bounded domain $\Omega \subset \mathbb{R}^d$ and its boundary $\partial\Omega$ are of class $\mathbf{C}^{k,\alpha}$, $0 \leq \alpha \leq 1$, if for all $\mathbf{x}_0 \in \partial\Omega$ there is a ball $B(\mathbf{x}_0, r), r > 0$, and a bijective map $\varphi : B(\mathbf{x}_0, r) \rightarrow U \subset \mathbb{R}^d$ such that*

- (i) $\varphi(B(\mathbf{x}_0, r) \cap \Omega) \subset \mathbb{R}_+^d$,
- (ii) $\varphi(B(\mathbf{x}_0, r) \cap \partial\Omega) \subset \partial\mathbb{R}_+^d$,
- (iii) $\varphi \in C^{k,\alpha}(B(\mathbf{x}_0, r))$, $\varphi^{-1} \in C^{k,\alpha}(U)$, are Hölder continuous.

Consequently, $\partial\Omega$ is locally the graph of a function with $d - 1$ arguments.

A function u is called Hölder continuous if

$$\|u\|_{C^{k,\alpha}(\Omega)} := \sum_{|\alpha| \leq k} \|\partial^\alpha u\|_{C(\bar{\Omega})} + \sum_{|\alpha| \leq k} [\partial^\alpha u]_{C^{0,\alpha}(\bar{\Omega})} < \infty,$$

where

$$[\partial^\alpha u]_{C^{0,\alpha}(\bar{\Omega})} = \sup_{\mathbf{x}, \mathbf{y} \in \Omega} \left\{ \frac{|u(\mathbf{x}) - u(\mathbf{y})|}{|\mathbf{x} - \mathbf{y}|^\alpha} \right\}.$$

Next, we define a special and well-known class within the above defined boundary classes, that will be assumed for all problems investigated in this work.

Definition 2.10 (Lipschitz Boundary) Assume $\Omega \subset \mathbb{R}^d$ and its boundary $\partial\Omega$ are of class $C^{0,1}$, which simply means the map in Def.2.9 is Lipschitz continuous. Such a boundary is called **Lipschitz boundary** and the domain is called Lipschitz domain.

Remark 2.4 An important feature of a Lipschitz boundary is that the outer normal vector is defined almost everywhere at the boundary and it is almost everywhere continuous.

Theorem 2.3 (Trace Theorem) Let $\Omega \subset \mathbb{R}^d$, $d \geq 2$, be a bounded open set with Lipschitz boundary $\partial\Omega$. Then, there exists a unique linear continuous operator $\gamma : W^{1,p}(\Omega) \rightarrow L^p(\Omega)$, $1 \leq p < \infty$ such that

$$\gamma v = v|_{\partial\Omega} \text{ for each } v \in C(\bar{\Omega}) \cap W^{1,p}(\Omega),$$

with $W^{1,p}(\cdot)$ and $L^p(\cdot)$ being defined in Sec. 2.1.1. The operator γ is called trace or trace operator.

Proof. The proof can be found in the literature, for instance, in [2, 81, 137]. \square

Goal-oriented a posteriori error control within the DWR-approach is based on the solution of an additional dual or adjoint problem. Within this framework, seeking a stationary point of a differentiable functional plays a key role; cf. [36, Chapter 2]. Therefore, we introduce the following definition of derivatives. For further details to these definitions, we refer, e.g., to [39, 11, 189]. We assume X, Y and Z to be arbitrary Banach spaces.

Definition 2.11 (Gâteaux and Fréchet Derivative) Let $f : U(x) \subseteq X \rightarrow Y$ be a function defined on an open set in a Banach space X with values in another Banach space Y . The function f is called **Gâteaux differentiable** at a point x if there exists a bounded linear operator $T_x : X \rightarrow Y$ such that $\forall v \in X$,

$$\lim_{t \rightarrow 0} \frac{f(x + tv) - f(x)}{t} = T_x v. \quad (2.14)$$

The operator T_x is called the **Gâteaux derivative** of f at x and is denoted by $D_f(x)$ or $f'(x)$. If the limit in (2.14) exists uniformly for v in the unit sphere of X , we say that f is **Fréchet differentiable** at x , and $D_f(x)$ is then called the **Fréchet derivative** of f at x . Again, we also write $f'(x)$ instead of $D_f(x)$.

Remark 2.5 Let us remark some aspects about Def. 2.11.

- The distinction between the two definitions of differentiability above is made by how the limit is taken, more precisely the limit in the Fréchet case only depends on the norm of y , i.e., the difference can be expressed as follows:

$$\forall \varepsilon > 0, \forall v \neq 0, \exists \delta = \delta(\varepsilon, v) : \|f(x + tv) - f(x) - tT_v\| \leq \varepsilon |t| \text{ whenever } |t| < \delta,$$

$$\forall \varepsilon > 0, \exists \delta = \delta(\varepsilon) : \|f(x + v) - f(x) - T_v\| \leq \varepsilon \|v\| \text{ whenever } \|v\| < \delta,$$

where the first line corresponds to the Gâteaux differentiability and the second one corresponds to the Fréchet differentiability; cf., e.g., [11].

- If f is Lipschitz and it holds $\dim(X) < \infty$, then the notion of Gâteaux and Fréchet differentiability coincide; cf., e.g. [11, Prop. A.4].
- If for some fixed v the limits

$$\partial_v f(x) := \left. \frac{d}{dt} \right|_{t=0} f(x + tv) = \lim_{t \rightarrow 0} \frac{f(x + tv) - f(x)}{t} \quad (2.15)$$

exists, we say f has a directional derivative at x in the direction v . Hence, f is Gâteaux differentiable at x if and only if all the directional derivatives $\partial_v f(x)$ exist and form a bounded linear operator $D_f(x) : v \mapsto \partial_v f(x)$; cf., e.g., [39].

- An equivalent way to write that $D_f(x)$ is the Fréchet derivative of f at x is

$$f(x + y) - f(x) - D_f(x)y + o(\|y\|),$$

where we set $y = tv$ and note that $t \rightarrow 0$ if and only if $y \rightarrow 0$; cf., e.g., [11].

- In general, the $(n + 1)$ th Fréchet derivative $D_f^{(n+1)}(x)$ of f at the point x can be defined through induction by means of the following formula:

$$D_f^n(x + y)y_1 \cdots y_n - D_f^n(x)y_1 \cdots y_n = D_f^{(n+1)}(x)yy_1y_2 \cdots y_n + r,$$

with the 'small' remainder

$$\sup_{\|y_j\| \leq 1, j=1, \dots, n} \|r(x; y, y_1, \dots, y_n)\| = o(\|y\|), y \rightarrow 0.$$

Here, we assume $D_f^{(n+1)}(x) : X \times \cdots \times X \rightarrow Y$ to be an $(n + 1)$ -linear bounded operator. Synonymously to above, we write $f^{(n+1)}(x)$ instead of $D_f^{(n+1)}(x)$. The existence of $D_f^{(n+1)}(x)$ implies

$$D_f^{(n+1)}(x)yy_1y_2 \cdots y_n = \left. \frac{d}{dt} \right|_{t=0} D_f^n(x + ty)y_2 \cdots y_n,$$

for all $y_1, \dots, y_n \in X$, where $n = 1, 2, \dots$; cf., e.g., [189].

- A function which is Fréchet differentiable at a point is continuous there, but this is not the case for Gâteaux differentiable functions (even in the finite dimensional case). For example, the function $f : \mathbb{R}^2 \rightarrow \mathbb{R}$ defined by $f(0, 0) = 0$ and $f(x, y) = x^4y/(x^6 + y^3)$ for $x^2 + y^2 > 0$ has 0 as its Gâteaux derivative at the origin, but fails to be continuous there; cf., e.g. [11].

Since the Euler Lagrange method of constraint optimization, using a so-called Lagrangian functional $\mathcal{L} : X \times X \rightarrow \mathbb{R}$, is an essential component of this work, we transfer the notion of a directional derivative given in the third point of Rem. 2.5 within the following definition.

Definition 2.12 (Partial Fréchet Derivative) *Let*

$$f : U(x, y) \subseteq X \times Y \rightarrow Z$$

be a map defined on an open set of the point $(x, y) \in X \times Y$ with values in a further Banach space Z . Let y be fixed and set $g(y) := f(w, y)$. If g is Fréchet differentiable in the sense of Def. 2.11 at the point x , then we define the **partial Fréchet derivative** $f_x(x, y)$ through

$$f_x(x, y) := g'(x).$$

The partial Fréchet derivative $f_y(x, y)$ is defined similarly.

Proposition 2.1 *Let $f : U(x, y) \subseteq X \times Y \rightarrow Z$ be given in Def. 2.12. If f has a Fréchet derivative at the point $(x, y) \in X \times Y$, then the partial Fréchet derivatives $f_x(x, y), f_y(x, y)$ also exist and*

$$f'(x, y)(h, k) = f_x(x, y)(h) + f_y(x, y)(k) \quad \forall h \in X, k \in Y .$$

Proof. The proof of Prop. 2.1 can be found in the literature, for instance, in [189].
□

Remark 2.6 *An analogous result to Prop. 2.1 holds true if f has a Gâteaux derivative at the point $(x, y) \in X \times Y$, where then $f_x(x, y)$ and $f_y(x, y)$ denote the directional derivatives according to the third point of Rem. 2.5 with respect to the first or second argument, respectively. Exemplary, the definition of $f_x(x, y)$ is given by*

$$f_x(x, y)(v) := \lim_{t \rightarrow 0} \frac{f(x + tv, y) - f(x, y)}{t}, \quad v \in X.$$

2.4 Residual-Based Stabilization

The numerical approximation of *convection-dominated* problems is associated with several challenges. The solutions of these problems are typically characterized by the occurrence of sharp moving fronts and interior or boundary layers. The key challenge for an accurate numerical approximation of these solutions is thus the development of discretization schemes with the ability to capture strong gradients without producing spurious oscillations or smearing effects. An important issue to overcome these difficulties are stabilization concepts. As general surveys about stabilization methods as well as an overview of related references, we refer, e.g., to the monographs [162, 175] as well as the recently published review [116], respectively. With regard to convection-diffusion equations, a comparative study of stabilization concepts can be found in the contributions [58, 120, 121, 175].

Throughout this work, we use the so-called *streamline upwind Petrov-Galerkin* (SUPG) method, introduced by Hughes and Brooks [106, 49], to stabilize our transport problems. This method is a well-known residual-based stabilization technique for finite element approximations, that adds weighted residuals to the usual Galerkin finite element method. Therefore, it is also known as *streamline diffusion finite element method* (SDFEM), cf., e.g., [162, Chapter III.3.2.1]. There are many examples in the literature, where this stabilization technique is applied to stationary (cf., e.g., [106, 147, 82, 115, 83, 117, 114, 119, 18]) and nonstationary (cf., e.g., [120, 121, 167, 118, 84, 85, 116]) convection-diffusion problems.

In order to clarify how the weighted residuals are added, we consider, by way of example, the following convection-diffusion-reaction equation.

$$-\varepsilon \Delta u + \mathbf{b} \cdot \nabla u + \alpha u = f \text{ in } \Omega, \quad u = 0 \text{ on } \partial\Omega, \quad (2.16)$$

where $\Omega \subset \mathbb{R}^d$, with $d = 2$ or $d = 3$, is a polygonal or polyhedral bounded domain with Lipschitz boundary $\partial\Omega$. A detailed investigation of the equation above is done in Chapter 3. We restrict ourselves to a very general manner in this section, skipping some mathematical details in the following. Here, ε is a constant positive diffusion coefficient, \mathbf{b} is a convection field, α is a reaction coefficient, and f is a given outer source of the unknown scalar quantity u . We start with a weak formulation of the convection-diffusion-reaction equation (2.16), assuming that \mathbf{b} , α and f are sufficiently smooth with $\alpha - \frac{1}{2} \nabla \cdot \mathbf{b} > 0$:

Find $u \in V := H_0^1(\Omega)$ such that

$$A(u)(\varphi) := (\varepsilon \nabla u, \nabla \varphi) + (\mathbf{b} \cdot \nabla u, \varphi) + (\alpha u, \varphi) = (f, \varphi) =: F(\varphi) \quad \forall \varphi \in V. \quad (2.17)$$

Let $V_h^p \subset V$ be a conforming finite element space defined in Eq. (2.1) of Sec. 2.1.3. Then, assuming that the solution u of (2.17) is regular, in the sense that

$$-\varepsilon \Delta u + \mathbf{b} \cdot \nabla u + \alpha u = f \text{ in } L^2(K) \quad \forall K \in \mathcal{T}_h,$$

the SUPG stabilized scheme is given by

$$A_S(u)(\varphi_h) = F_S(\varphi_h) \quad \forall \varphi_h \in V_h^p,$$

where

$$\begin{aligned} A_S(u)(\varphi) &:= (\varepsilon \nabla u, \nabla \varphi) + (\mathbf{b} \cdot \nabla u, \varphi) + (\alpha u, \varphi) \\ &\quad + \sum_{K \in \mathcal{T}_h} \delta_K (-\varepsilon \Delta u + \mathbf{b} \cdot \nabla u + \alpha u, \mathbf{b} \cdot \nabla \varphi)_K, \\ F(\varphi) &:= (f, \varphi) + \sum_{K \in \mathcal{T}_h} \delta_K (f, \mathbf{b} \cdot \nabla \varphi)_K. \end{aligned}$$

Here, $(\cdot, \cdot)_K$ denotes the inner product of $L^2(K)$ as given in Sec. 2.1.1, where K is a disjoint element of a decomposition \mathcal{T}_h of the domain Ω . Furthermore, δ_K is a user-chosen constant stabilization parameter, that will be specified in Remark 3.2. Since in general $\Delta u_h \notin L^2(\Omega)$ but $\Delta u_h \in L^2(K)$ for each K , one has to calculate Δu_h elementwise. Finally, the SUPG stabilized discrete scheme reads as

Find $u_h \in V_h^p$ such that

$$A_S(u_h)(\varphi_h) = F_S(\varphi_h) \quad \forall \varphi_h \in V_h^p. \quad (2.18)$$

At the end of this section we want to introduce a natural norm for proving stability and error estimates for convection-dominated problems. This norm is referred to as *SUPG-norm*. For some general results regarding this norm we refer, for instance, to the general survey [162].

$$\|v\|_{SUPG} := \left(\sum_{K \in \mathcal{T}_h} \|\sqrt{\varepsilon} \nabla v\|_{L^2(\Omega)^d}^2 + \|\sqrt{\alpha} v\|_{L^2(\Omega)}^2 + \delta_K \|\mathbf{b} \cdot \nabla v\|_{L^2(\Omega)}^2 \right)^{\frac{1}{2}}. \quad (2.19)$$

2.5 Goal-Oriented A Posteriori Error Control

A posteriori error estimation is traditionally based on error control with respect to some global norm, for instance, the generic energy or the L^2 -norm. For a general review of a posteriori error estimation techniques for finite element methods we refer, for instance, to the monographs [178, 180, 4]. However, in many applications it might be useful to compute more locally defined quantities, for example a drag or lift coefficient in flows around obstacles, a mean normal flux across boundaries or a solution just in certain subsets of the whole domain. Broadly speaking, this is what *goal-oriented* a posteriori error control stands for.

The general approach of goal-oriented a posteriori error control is based on exploiting a 'duality-argument' well-known from the *a priori* error analysis for finite element methods. This idea goes back to the 1990's, where C. Johnson and his collaborators, cf. [122, 123, 124, 125], derived computable bounds on a given norm of the error based on the finite element approximations of the underlying partial differential equation of interest; cf. [101] for more details. Based on this, two *a posteriori* error bounds were derived. A so-called *unweighted* or *Type II* a posteriori error bound that is based, inter alia, on strong stability results for the underlying dual problem and do not depend explicitly on the dual solution; cf. [76] as well as the references therein for a general review to this approach. In contrast, a so-called *weighted* or *Type I* a posteriori error bound retains the dual solution within the a posteriori error bound and is thus explicitly depending on the dual solution, cf. the works [35, 36, 20] for a general review to this approach.

The latter approach is referred to as the Dual Weighted Residual (DWR) method introduced by Becker and Rannacher in [35, 36]. This method is a main component of the underlying work and will be introduced in the following. This is done in a very general way, which means we will skip some mathematical details here in order to focus on the basic idea of this approach. For further details about this method, we refer to the monographs [20, 36].

Goal-oriented a posteriori error control within the DWR-approach aims at the control of an error in an arbitrary user-chosen goal functional J of physical interest. To get an error representation with respect to this goal functional, an additional dual problem has to be solved. This *dual* solution is used for *weighting* the influence of the 'local' *residuals* on the error in the goal quantity $J(\cdot)$ in the following way:

$$|J(e)| \leq \sum_{n=1}^N \sum_{K_n \in \mathcal{T}_{\tau,n}} \sum_{K \in \mathcal{T}_{h,n}} |\rho_{K_n,K}^n(u_{\tau h})| |\omega_{K_n,K}^n(z)|. \quad (2.20)$$

Here, $e = u - u_{\tau h}$ denotes the discretization error of the original so-called *primal* problem, $\rho_{K_n,K}$ denotes the related local primal residuals and the 'weights' are identified by $\omega_{K_n,K}$, depending on the exact dual solution z . In practice, the exact dual solution is usually not explicitly known. Therefore, the information about z has to be obtained either through *a priori* analysis in form of bounds for z in certain Sobolev norms or through approximating the dual problem numerically obtaining a fully discrete solution z_h . For further information, particularly about the a priori approach, we refer to [20, Chapter 3]. Of course, solving the dual problem numerically is associated with additional numerical costs. There are two main approaches used in the literature how to approximate the unknown exact solution z , namely the approximation by *higher-order interpolation* or the approximation by *higher-order finite elements*; cf. Sec. 3.3.1. Furthermore, but less common, is the approximation by difference quotients as well as the approximation by local residual problems. For a review to all of these approximation approaches we refer to [20, Chapter 4] or [36, Sec. 5], respectively.

In order to give an understanding to the proceeding of the DWR method, we consider the following simple example adopted from [20, Chapter 1.4]. Consider the 'continuous' and 'discrete' primal problems of finding $u, u_h \in \mathbb{R}^n$ from

$$Au = b, \quad A_h u_h = b_h, \quad (2.21)$$

where we assume $A, A_h \in \mathbb{R}^{n \times n}$ to be regular matrices, $b, b_h \in \mathbb{R}^n$ are vectors and h is a parameter indicating the quality of approximation, i.e., $A_h \rightarrow A$ and $b_h \rightarrow b$, as $h \rightarrow 0$. Moreover, we introduce the *discretization error* $e := u - u_h$ as well as the 'primal' *residual* $\rho := b - Ax_h$. Then, the classical a posteriori error analysis uses the relation

$$Ae = Ax - Ax_h = b - Ax_h = \rho,$$

to derive an a posteriori error bound involving a 'continuous' stability constant:

$$\|e\| \leq c_S \|\rho\|, \quad c_S := \|A^{-1}\|.$$

In the context of Galerkin finite element methods for linear partial differential equations the relation above is also known as *Galerkin orthogonality*. As already mentioned, on the contrary the DWR method aims to estimate the error also with respect to arbitrary moments of the solution. Therefore, a 'duality-argument' well-known from the error analysis of Galerkin methods is used. Assume that we want to estimate the value of the linear goal functional $J(\cdot)$ with

$$J(e) = J(u) - J(u_h) = (e, j),$$

for some given $j \in \mathbb{R}^n$. For the determination of this error, we consider the solution $z \in \mathbb{R}^n$ of the to problem (2.21) associated dual (or adjoint) problem

$$A^*z = j. \tag{2.22}$$

This leads us to the identity about the error

$$J(e) = (e, j) = (e, A^*z) = (Ae, z) = (\rho, z),$$

and finally to the 'weighted' a posteriori error estimate

$$|J(e)| \leq \sum_{i=1}^n |\rho_i| |z_i|. \tag{2.23}$$

The advantage of using the 'weights' z_i is that they tell us about the influence of the 'local' primal residuals ρ_i on the error in the goal quantity $J(\cdot)$.

So far, we assumed the goal functional J as well as the primal and dual problem to be linear. In the case of a nonlinear goal quantity, or at least a nonlinear primal problem, it is useful to embed the DWR approach into an optimal control problem. This nonlinear approach is based on [20, Chapter 6], where a detailed derivation can be found. In order to derive an error representation in terms of the goal quantity $J(\cdot)$, we employ the Euler-Lagrange method of constrained optimization. For some given functional $J : V \rightarrow \mathbb{R}$ we consider solving

$$J(u) = \min\{J(v), v \in V, \text{ where } A(v)(\varphi) = F(\varphi) \forall \varphi \in V\}. \tag{2.24}$$

Here, the constraint $A(u)(\varphi) = F(\varphi)$ corresponds to the original primal problem, where $A : V \times V \rightarrow \mathbb{R}$ is assumed to be a semilinear form (linear in the second argument), $F : V \rightarrow \mathbb{R}$ is assumed to be a linear form representing the force term, and $J : V \rightarrow \mathbb{R}$ is assumed to be the goal functional, not necessarily linear, defined on some function space V . Furthermore, we assume the existence of the *Gâteaux*

derivatives, defined in Sec. 2.3, of A and J up to order three. An error representation similar to Eq. (2.23) is then derived with the help of the following definition of the so-called *Lagrangian* functional $\mathcal{L} : V \times V \mapsto \mathbb{R}$.

$$\mathcal{L}(u, z) := J(u) + F(z) - A(u)(z),$$

where we refer to $z \in V$ as the *dual* variable (*adjoint* variable or *Lagrange multiplier*). Note that seeking a stationary point $\{u, z\} \in V \times V$ of $\mathcal{L}(\cdot, \cdot)$ is given by the condition

$$\mathcal{L}'(u, z)(\psi, \varphi) = 0 \quad \forall \{\psi, \varphi\} \in V \times V, \quad (2.25)$$

where \mathcal{L}' denotes the so-called Gâteaux derivatives defined in Def. 2.11, or, equivalently, by the system of equations

$$\begin{aligned} A'(u)(\psi, z) &= J'(u)(\psi) & \forall \psi \in V, \\ A(u)(\varphi) &= F(\varphi) & \forall \varphi \in V. \end{aligned} \quad (2.26)$$

Here, the second equation of (2.26) corresponds to the original primal problem, whereas the first equation of (2.26) yields the dual problem. This approach will be used to derive an error representation within Chapter 4 and Chapter 5.

Chapter 3

Goal-Oriented Error Control for Steady-State Convection-Dominated Problems

In this chapter, we present the application of goal-oriented error control based on the Dual Weighted Residual method to stationary convection-dominated problems. These problems are also referred to as *singularly perturbed problems*, since they depend on a small positive perturbation parameter ε and their solutions approach a discontinuous limit as this parameter approaches zero, cf. [162] for further details as well as Sec. 2.4 for an introduction and the challenges of those problems. There are numerous examples in various fields of application of these problems, for instance, the propagation of temperature within a fluid or solid, the distribution of a concentration of electrons in models of semiconductor designs or the distribution of a liquid pollution on the surface of a river, to name just a few.

We restrict ourselves to stationary convection-dominated problems first, since the focus of this chapter is on the interaction of stabilization and error control. For this purpose, we investigate two possible approaches for the dual problem including two different ways to get the dual solution, respectively. Furthermore, this serves as a comparative numerical study for time-dependent and coupled problems considered in Ch. 4 and Ch. 5, respectively.

We start by introducing the convection-diffusion-reaction equation together with some global assumptions and general concepts including the underlying variational formulation. Then, we present the discretization scheme in space as well as the stabilized version of this scheme. Afterwards, we present two different approaches for the dual problem and derive a respective local error representation formula in terms of a goal quantity $J(\cdot)$. The chapter is closed by some numerical examples given in

Sec. 3.4, in which we present the adaptive algorithm and perform several numerical comparative studies for the presented approaches. Some parts of this chapter have been published by the author et al. in [50].

As a prototype of convection-dominated problems we consider the steady linear convection-diffusion-reaction equation.

Problem 3.1 (Convection-Diffusion-Reaction Equation) Find u from

$$\begin{aligned} -\nabla \cdot (\varepsilon \nabla u) + \mathbf{b} \cdot \nabla u + \alpha u &= f \text{ in } \Omega, \\ u &= 0 \text{ on } \partial\Omega, \end{aligned} \quad (3.1)$$

where $\Omega \subset \mathbb{R}^d$, with $d = 2$ or $d = 3$, is a polygonal or polyhedral bounded domain with Lipschitz boundary $\partial\Omega$. Here, $0 < \varepsilon \ll 1$ is a small, constant positive diffusion coefficient, $\mathbf{b} \in (H^1(\Omega))^d \cap (L^\infty(\Omega))^d$ is the flow field or convection field, $\alpha \in L^\infty(\Omega)$ is the reaction coefficient, and $f \in L^2(\Omega)$ is a given outer source of the unknown scalar quantity u . Furthermore, we assume that one of the following conditions is fulfilled:

$$\nabla \cdot \mathbf{b}(\mathbf{x}) = 0 \text{ and } \alpha(\mathbf{x}) \geq 0, \text{ or } \alpha(\mathbf{x}) - \frac{1}{2} \operatorname{div} \mathbf{b}(\mathbf{x}) \geq c_0 > 0 \quad \forall \mathbf{x} \in \Omega. \quad (3.2)$$

Remark 3.1 The unknown u in a singularly perturbed problem depends, of course, on the perturbation parameter ε , cf., e.g. [162]. To simplify the notation, we just write $u(\mathbf{x})$ instead of, for instance, $u(\mathbf{x}, \varepsilon)$ or $u_\varepsilon(\mathbf{x})$.

For the sake of simplicity, Problem 3.1 is equipped with homogeneous Dirichlet boundary conditions. In our numerical examples in Sec. 3.4, we also consider other types of boundary conditions. In Rem. 3.3 and 3.4, the incorporation of nonhomogeneous Dirichlet and Neumann boundary conditions, respectively, is briefly addressed; cf., e.g., [20, 92] with regard to these types of boundary conditions.

It is well known that Problem 3.1 along with condition (3.2) admits a unique weak solution $u \in V := H_0^1(\Omega)$ that satisfies the following variational formulation; cf., e.g. [162, 81, 12, 119].

Problem 3.2 (Variational Formulation Primal Problem) Find $u \in V$ such that

$$A(u)(\varphi) = F(\varphi) \quad \forall \varphi \in V, \quad (3.3)$$

where the bilinear form $A : V \times V \rightarrow \mathbb{R}$ and the linear form $F : V \rightarrow \mathbb{R}$ are

$$A(u)(\varphi) := (\varepsilon \nabla u, \nabla \varphi) + (\mathbf{b} \cdot \nabla u, \varphi) + (\alpha u, \varphi), \quad (3.4)$$

$$F(\varphi) := (f, \varphi). \quad (3.5)$$

Here and in the following, (\cdot, \cdot) is the inner product of $L^2(\Omega)$ and $\|\cdot\|$ the associated L^2 -norm with $\|v\| = (v, v)^{\frac{1}{2}} = (\int_{\Omega} |v|^2 d\mathbf{x})^{\frac{1}{2}}$ as defined in Sec. 2.1.

3.1 Stabilized Variational Discretization in Space

In this section, we present the stabilized spatial discretization of the convection-diffusion-reaction equation (3.1). For this reason, we use the concepts introduced in Sec. 2.1.3, where all details can be found that are not specified in the following. We start with the spatial discretization of Eq. (3.1), denoted by $cG(p)$, using Lagrange type finite element spaces of continuous functions that are piecewise polynomials of degree $p \geq 1$. For this discretization in space, we consider a decomposition \mathcal{T}_h as given in Assumption 2.3. Then, using the discrete finite element space $V_h^p \subset V$, defined in (2.1) in Sec. 2.1.3, we find a Galerkin approximation u_h as the solution of the following discrete problem.

Problem 3.3 (Discretization in Space: Primal Problem) *Find $u_h \in V_h^p$ such that*

$$A(u_h)(\varphi_h) = F(\varphi_h) \quad \forall \varphi_h \in V_h^p, \quad (3.6)$$

where the bilinear form $A(\cdot)(\cdot)$ and the linear form $F(\cdot)$ are defined by Eq. (3.4) and Eq. (3.5), respectively.

In this work, we focus on convection-dominated problems with small diffusion parameter ε . Then, the finite element approximation needs to be stabilized in order to reduce spurious and non-physical oscillations of the discrete solution arising close to layers. Here, we apply the streamline upwind Petrov-Galerkin (SUPG) method, that was introduced in Sec. 4.1.3. Existing a priori error analysis ensure its convergence in the natural norm of the scheme including the control of the approximation error in streamline direction; cf. [162, Thm. 3.27]. The stabilized variant of the discrete scheme (3.6) then reads as follows.

Problem 3.4 (Stabilized Primal Problem) *Find $u_h \in V_h^p$ such that*

$$A_S(u_h)(\varphi_h) = F_S(\varphi_h) \quad \forall \varphi_h \in V_h^p, \quad (3.7)$$

where the stabilized bilinear form $A_S(\cdot)(\cdot)$ and the stabilized linear form $F_S(\cdot)$ are given by

$$A_S(u_h)(\varphi_h) := A(u_h)(\varphi_h) + S_A(u_h)(\varphi_h), \quad (3.8)$$

$$F_S(\varphi_h) := F(\varphi_h) + S_F(\varphi_h), \quad (3.9)$$

and the stabilization bilinear form $S_A : V \times V \rightarrow \mathbb{R}$ and the stabilization linear form $S_F : V \rightarrow \mathbb{R}$, respectively, are defined by

$$S_A(u_h)(\varphi_h) := \sum_{K \in \mathcal{T}_h} \delta_K (-\nabla \cdot (\varepsilon \nabla u_h) + \mathbf{b} \cdot \nabla u_h + \alpha u_h, \mathbf{b} \cdot \nabla \varphi_h)_K. \quad (3.10)$$

$$S_F(\varphi_h) := \delta_K (f, \mathbf{b} \cdot \nabla \varphi_h). \quad (3.11)$$

The evidence of the existence of a solution of Problem 3.4 can be found, for instance, in [127, 141, 102, 27].

In the next section, more precisely in Sec. 3.2.1, we will derive an error representation formula in terms of a goal quantity $J(\cdot)$. Therefore, we additionally have to assume that the analytical solution $u \in V$ to (3.3) satisfies the following identity:

$$A_S(u)(\varphi) = F_S(\varphi) \quad \forall \varphi \in V. \quad (3.12)$$

This can be guaranteed by

$$u \in \hat{V} := \left\{ \hat{v} \in H_0^1(\Omega) \mid (\nabla \cdot (\varepsilon \nabla \psi))_K \in L^2(K) \quad \forall K \in \mathcal{T}_h \right\}.$$

In addition, with regard to the definition of $A_S(\cdot)(\cdot)$ and $F_S(\cdot)$ in (3.8) and (3.9), respectively, we note that the stabilization forms $S_A(\cdot)(\cdot)$ and $S_F(\cdot)$ must satisfy the following consistency condition

$$S_A(u)(\varphi) = S_F(\varphi) \quad \forall \varphi \in V. \quad (3.13)$$

Based on (3.12), we derive the following Galerkin orthogonality property.

$$A_S(u - u_h)(\varphi_h) = 0 \quad \forall \varphi_h \in V_h^p. \quad (3.14)$$

Remark 3.2 *The proper choice of the stabilization parameters δ_K is an important issue in the application of the SUPG approach; cf. [117, 114] and the discussion therein. There are several proposals for the concrete choice of this parameter in the literature, see [113] for an overview. For the situation of steady-state convection-diffusion-reaction equations, all proposals have in common to choose $\delta_K = \mathcal{O}(h_K / \|\mathbf{b}\|_{K,\infty})$ in a convection-dominated case ($\text{Pe}_K \gg 1$) and $\delta_K = \mathcal{O}(h_K^2 / \varepsilon)$ in a diffusion-dominated case ($\text{Pe}_K \leq 1$), where*

$$\text{Pe}_K = \frac{\|\mathbf{b}\|_{K,\infty} h_K}{2p\varepsilon}$$

denotes the local Péclet number; cf. [119] for more details. In all our numerical examples investigated in Sec. 3.4, we made the experience that the simplified choice $\delta_K = O(h_K)$ provides for the best results for convection-dominated cases, which is in good agreement with the results in [118] and [104], respectively.

In the following, we introduce the dual problem outlined in Sec. 2.5, which is used for weighting the influence of the primal residuals on the discretization error in a given user-chosen goal quantity $J(\cdot)$. Therefore, following the notation in [169], in the context of stabilized finite element approximations two different approaches are possible, namely

- *First Stabilize and Then Dualize* (FSTD): In this approach the dual problem is derived with the help of the adjoint of the stabilized discrete primal operator (3.8).
- *First Dualize and Then Stabilize* (FDTS): In this approach the dual problem is derived with the help of the formal adjoint problem of the weak formulation (3.3) and the SUPG stabilization is applied to the discrete counterpart of this dual problem afterwards.

For more details about these two approaches, we refer to [169, 101, 103, 31]. In the following section, the two approaches are presented and an appropriate error representation formula is derived for both of the methods.

3.2 A FSTD and FDTS Approach for the Dual Problem

In this section, we introduce two different approaches for the derivation of the dual problem. For each of these approaches an error representation formula in terms of a goal functional $J(\cdot)$ is presented that can be used for adaptive refinement of the spatial grid within the finite element approximation of the underlying problem.

Assumption 3.1 (Goal Functional) *Let us assume $J : V \rightarrow \mathbb{R}$ to be a linear functional representing the goal quantity of physical interest. In general, this functional is given as*

$$J(\cdot) = (j_\Omega, \cdot)_\Omega + (j_{\partial\Omega}, \cdot)_{\partial\Omega}, \quad (3.15)$$

where we assume $j_\Omega \in L^2(\Omega)$ and $j_{\partial\Omega} \in L^2(\partial\Omega)$, respectively; cf. [101, 97, 91].

Note that j_Ω or $j_{\partial\Omega}$ may be zero, depending on the chosen goal quantity in which the error shall be controlled; for example $j_\Omega \equiv 0$ and $j_{\partial\Omega} \in L^2(\partial\Omega_+)$, where $\partial\Omega_+$ denotes the outflow boundary, for a goal functional aiming to control the outflow normal flux, whereas $j_\Omega \in L^2(\Omega)$ and $j_{\partial\Omega} \equiv 0$ for a goal functional aiming to control the mean value of the solution.

3.2.1 A FSTD Dual Weighted Residual Approach

The *First Stabilize and Then Dualize* (FSTD) approach is based on building the adjoint bilinearform of the stabilized discrete primal operator (3.8). Thereby, we follow the lines of [103], where this approach is derived for a linear transport equation. The FSTD approach leads to the following dual problem.

Problem 3.5 (Dual Problem) Find $z_s \in V$ such that

$$A_S(\psi)(z_s) = J(\psi) \quad \forall \psi \in \hat{V}, \quad (3.16)$$

where $J(\cdot)$ is a linear goal functional in the sense of Assumption 3.1 defined by Eq. (3.15) and $A_S(\cdot)(\cdot)$ is the stabilized bilinearform defined by Eq. (3.8).

Using the finite element space $V_h^p \subset V$, defined in Eq. (2.1) of the preceding section, the stabilized discrete formulation in space of Eq. (3.16) reads:

Problem 3.6 (Discretization in Space: Stabilized Dual Problem)

Find $z_{s,h} \in V_h^p$ such that

$$A_S(\psi_h)(z_{s,h}) = J(\psi_h) \quad \forall \psi_h \in V_h^p, \quad (3.17)$$

where $A_S(\cdot)(\cdot)$ and $J(\cdot)$ are defined by Eq. (3.8) and Eq. (3.15), respectively.

The evidence for the existence and uniqueness of a solution $z_{s,h}$ for Eq. (3.17) can be found in [169, Thm. 3.3], where coercivity and boundness of the dual bilinear form are proved with regard to the SUPG-norm defined by Eq. (2.19).

Next, we want to derive an error representation formula in terms of the goal quantity $J(\cdot)$. Therefore, we introduce the stabilized primal residual $\rho_S(u_h)(\cdot)$ defined by

$$\rho_S(u_h)(\varphi) := F_S(\varphi) - A_S(u_h)(\varphi) \quad \forall \varphi \in V. \quad (3.18)$$

Theorem 3.1 (Error Representation FSTD) *Assume $J : V \rightarrow \mathbb{R}$ to be a linear functional. Let $u \in \hat{V}$ be the solution of the 'continuous' scheme of the stabilized primal problem (3.7) and $u_h \in V_h^p$ a Galerkin approximation to u being defined by the 'discrete' stabilized primal problem (3.7) such that the Galerkin orthogonality (3.14) is fulfilled. Furthermore, let $z_s \in V$ be the solution of the dual (or adjoint) problem (3.16). Then, there holds the FSTD error representation formula*

$$J(u) - J(u_h) = \rho_S(u_h)(z_s - \tilde{z}_h) \quad \forall \tilde{z}_h \in V_h^p. \quad (3.19)$$

Proof. (cf., e.g., [169],[103],[101]) To prove the FSTD error representation formula (3.19), we first exploit the linearity of $J(\cdot)$ to get

$$J(u) - J(u_h) = J(u - u_h) = A_S(u - u_h)(z_s).$$

Using the Galerkin orthogonality property (3.14) together with (3.12) as well as the definition of the stabilized primal residual (3.18), we finally get

$$\begin{aligned} J(u) - J(u_h) &= A_S(u - u_h)(z_s) - A_S(u - u_h)(\tilde{z}_h) \\ &= A_S(u - u_h)(z_s - \tilde{z}_h) \\ &= A_S(u)(z_s - \tilde{z}_h) - A_S(u_h)(z_s - \tilde{z}_h) \\ &= F_S(z_s - \tilde{z}_h) - A_S(u_h)(z_s - \tilde{z}_h) \\ &= \rho_S(u_h)(z_s - \tilde{z}_h), \end{aligned}$$

for all $\tilde{z}_h \in V_h^p$. This proves the error representation (3.19). \square

Since we use this error representation formula for adaptive mesh refinement, we present the following localized form of result (3.19).

Theorem 3.2 (Localized Error Representation FSTD, cf. [169], Thm. 3.10)

Let the assumptions of Thm. 3.1 be satisfied. Then, the cell-wise error representation formula of (3.19) reads

$$J(u) - J(u_h) = \sum_{K \in \mathcal{T}_h} \left\{ (R(u_h), z_s - \tilde{z}_h)_K + \delta_K (R(u_h), \mathbf{b} \cdot \nabla(z_s - \tilde{z}_h))_K - (E(u_h), z_s - \tilde{z}_h)_{\partial K} \right\}. \quad (3.20)$$

The cell and edge residuals $R(u_h)$ and $E(u_h)$, respectively, are defined by

$$R(u_h)|_K := f + \nabla \cdot (\varepsilon \nabla u_h) - \mathbf{b} \cdot \nabla u_h - \alpha u_h, \quad (3.21)$$

$$E(u_h)|_\Gamma := \begin{cases} \frac{1}{2} [\varepsilon \nabla u_h] \cdot \mathbf{n} & \text{if } \Gamma \subset \partial K \setminus \partial \Omega, \\ 0 & \text{if } \Gamma \subset \partial \Omega, \end{cases} \quad (3.22)$$

where $[\nabla u_h] := \nabla u_h|_{\Gamma \cap K} - \nabla u_h|_{\Gamma \cap K'}$ defines the jump of ∇u_h over the inner edges Γ with normal unit vector \mathbf{n} pointing from K to K' .

Proof. (cf. [169]) The assertion directly follows by using the definitions of the stabilized primal bilinear operator (3.8) and the stabilized primal linear operator (3.9) as well as applying integration by parts on each cell $K \in \mathcal{T}_h$ to the diffusive term in the primal residual (3.18); cf., e.g., [20, Ch. 3]. \square

Remark 3.3 (Nonhomogeneous Dirichlet Boundary Conditions, cf. [20])

We briefly address the incorporation of further types of boundary conditions. First, we consider Problem 3.1 equipped with the nonhomogeneous Dirichlet boundary condition, i.e.,

$$-\nabla \cdot (\varepsilon \nabla u) + \mathbf{b} \cdot \nabla u + \alpha u = f \text{ in } \Omega, \quad u = u_D \text{ on } \partial\Omega,$$

for a given function $u_D \in H^{\frac{1}{2}}(\partial\Omega)$. For this, let $\tilde{u}_D \in H^1(\Omega)$ be an extension of u_D in the sense that the trace of \tilde{u}_D equals u_D on $\partial\Omega$ in accordance with the trace theorem 2.3. Further, let the discrete function $\tilde{u}_{D,h}$ be an appropriate finite element approximation of the extension \tilde{u}_D . Then, the trace on $\partial\Omega$ of $\tilde{u}_{D,h}$ represents a discretization of u_D . For instance, a nodal interpolation of u_D and an extension in the finite element space can be used. This allows to recast the weak form of Problem 3.1 and its discrete counterpart in terms of $w = u - \tilde{u}_D \in H_0^1(\Omega)$ and $w_h = u_h - \tilde{u}_{D,h} \in V_h^p \subset H_0^1(\Omega)$. The previous calculations and the derivation of the a posteriori error estimator are then done for the weak problem and its discrete counterpart rewritten in terms of w and w_h . This yields the result that

$$\begin{aligned} J(u) - J(u_h) = & \sum_{K \in \mathcal{T}_h} \left\{ (R(u_h), z_s - \tilde{z}_h)_K - \delta_K (R(u_h), \mathbf{b} \cdot \nabla (z_s - \tilde{z}_h))_K \right. \\ & \left. - (E(u_h), z_s - \tilde{z}_h)_{\partial K} \right\} - ((u_D - \tilde{u}_{D,h}), \varepsilon \nabla z_s \cdot \mathbf{n})_{\partial\Omega}, \end{aligned} \quad (3.23)$$

where $R(u_h)$ and $E(u_h)$ are given by (3.21) and (3.22), respectively, and \mathbf{n} denotes the outer unit normal vector to the boundary $\partial\Omega$.

Remark 3.4 (Neumann Boundary Conditions, cf. [20])

If Neumann boundary conditions are prescribed in Problem 3.1 on a part Γ_N of the boundary $\partial\Omega = \Gamma_D \cup \Gamma_N$, with Dirichlet part $\Gamma_D \neq \emptyset$, i.e.,

$$\varepsilon \nabla u \cdot \mathbf{n} = u_N \text{ on } \Gamma_N.$$

Then, the derivation has to be done analogously for the solution space $V = \{v \in H^1(\Omega) \mid v = 0 \text{ on } \Gamma_D\}$ and its discrete counterpart and the resulting variational

problems. The localized error representation formula (3.20) remains valid with the only modification that the edge residuals $E(u_h)$ are now defined by

$$E(u_h)|_\Gamma := \begin{cases} \frac{1}{2} \mathbf{n} \cdot [\varepsilon \nabla u_h] & \text{if } \Gamma \subset \partial K \setminus \partial \Omega, \\ 0 & \text{if } \Gamma \subset \Gamma_D, \\ u_N - \varepsilon \nabla u_h \cdot \mathbf{n} & \text{if } \Gamma \subset \Gamma_N. \end{cases} \quad (3.24)$$

3.2.2 A FDTS Dual Weighted Residual Approach

In this section, we derive an a posteriori error representation formula based on the second approach *First Dualize and Then Stabilize* (FDTS). Thereby, we follow the lines of [101, Sec. 2.1], where this approach is derived for a general case of a linear operator within an abstract framework. The FDTS approach is based on building the formal adjoint problem of the weak formulation (3.3). This leads to the following dual problem.

Problem 3.7 (Dual Problem) Find $z \in V$ such that

$$A(\psi)(z) = J(\psi) \quad \forall \psi \in V, \quad (3.25)$$

where $J(\cdot)$ is a linear goal functional in the sense of Assumption 3.1 defined by Eq. (3.15) and $A(\cdot)(\cdot)$ is the primal bilinearform defined by Eq. (3.4).

Remark 3.5 (cf. [101]) Problem 3.7 can also be identified with the adjoint bilinearform $A^*(\cdot)(\cdot)$, given by

$$A^*(z)(\psi) = A(\psi)(z) = (\varepsilon \nabla \psi, \nabla z) + (\mathbf{b} \cdot \nabla \psi, z) + (\alpha \psi, z).$$

Applying integration by parts to the convective (second) term along with the condition (3.2) yields the representation

$$A^*(z)(\psi) = (\varepsilon \nabla z, \nabla \psi) - (\mathbf{b} \cdot \nabla z, \psi) + (\alpha z, \psi). \quad (3.26)$$

We will use this version of the dual operator in the further course of this section. Furthermore, assuming that the goal functional $J(\cdot)$ is compatible with the primal problem (3.3), i.e.,

$$A(u)(z) = A^*(z)(u), \quad (3.27)$$

the dual problem (3.25) in strong form is

$$\begin{aligned} -\nabla \cdot (\varepsilon \nabla z) - \mathbf{b} \cdot \nabla z + \alpha z &= j \quad \text{in } \Omega, \\ z &= 0 \quad \text{on } \partial \Omega, \end{aligned} \quad (3.28)$$

i.e., $z \in V' := H^{-1}(\Omega)$ is the solution of the formal adjoint equation related to (3.1) with V' denoting the dual space of V .

Using the finite element space $V_h^p \subset V$, defined in Eq. (2.1) of the preceding chapter, we find the Galerkin approximation z_h as the solution of the following discrete problem.

Problem 3.8 (Discretization in Space: Dual Problem) Find $z_h \in V_h^p$ such that

$$A^*(z_h)(\psi_h) = J(\psi_h) \quad \forall \psi_h \in V_h^p, \quad (3.29)$$

where $A^*(\cdot)(\cdot)$ and $J(\cdot)$ are given by Eq. (3.26) and Eq. (3.15), respectively.

Since we deal with the case of convection-dominated problems, we need to stabilize the finite element approximation. Thus, the discrete dual problem (3.29) stabilized by the SUPG method reads as

Problem 3.9 (Stabilized Dual Problem) Find $z_h \in V_h^p$ such that

$$A_S^*(z_h)(\psi_h) = J(\psi_h) \quad \forall \psi_h \in V_h^p, \quad (3.30)$$

where the stabilized adjoint bilinear form $A_S^*(\cdot)(\cdot)$ is given by

$$A_S^*(z_h)(\psi_h) := A^*(z_h)(\psi_h) + S^*(z_h)(\psi_h), \quad (3.31)$$

and the stabilized term $S^*(z_h)(\psi_h)$ is defined by

$$S^*(z_h)(\psi_h) := \sum_{K \in \mathcal{T}_h} \delta_K^* (\nabla \cdot (\varepsilon \nabla z_h) + \mathbf{b} \cdot \nabla z_h - \alpha z_h + j_\Omega, \mathbf{b} \cdot \nabla \psi_h)_K.$$

The evidence for the existence and uniqueness of a solution z_h for Eq. (3.30) can be found in [169, Thm. 3.13], where coercivity and boundness of the stabilized dual bilinear form (3.31) are proofed with regard to the SUPG-norm defined by (2.19), neglecting the stabilized goal functional term $\sum_{K \in \mathcal{T}_h} \delta_K^* (j_\Omega, \mathbf{b} \cdot \nabla z_h)_K$ in (3.31).

Remark 3.6 We note that the SUPG stabilization is applied to the discrete dual problem (3.29) and acts in the negative direction of the flow field \mathbf{b} ; cf. Eq. (3.26). Furthermore, due to this derivation of the stabilized dual problem (3.30), the dual stabilization parameter δ_K^* is independent of the discretized primal problem (3.7) and thus allows more flexibility with regard to the adaption of the stabilization to the structure of the equation. This is in contrast to the stabilized dual problem (3.17) of the previous section, where the dual stabilization parameter equals its primal counterpart. Moreover, note that the goal functional is stabilized within the FDTS approach, cf. the definition of $S^*(\cdot)(\cdot)$ within (3.31).

Next, we derive an error representation formula in terms of the goal quantity $J(\cdot)$. Therefore, we introduce the original primal residual $\rho(u_h)(\cdot)$ defined by

$$\rho(u_h)(\varphi) := F(\varphi) - A(u_h)(\varphi) \quad \forall \varphi \in V. \quad (3.32)$$

Theorem 3.3 (Error Representation FDTs) *Assume $J : V \rightarrow \mathbb{R}$ to be a linear functional. Let $u \in V$ be the solution of the 'continuous' primal problem (3.3) and $u_h \in V_h^p$ a Galerkin approximation to u being defined by the 'discrete' stabilized primal problem (3.7) such that the Galerkin orthogonality property (3.14) is fulfilled. Furthermore, let $z \in V$ be the solution of the dual (or adjoint) problem (3.25). Then, there holds the FDTs error representation formula*

$$J(u) - J(u_h) = \rho(u_h)(z - \tilde{z}_h) - S_F(\tilde{z}_h) + S_A(u_h)(\tilde{z}_h) \quad \forall \tilde{z}_h \in V_h^p. \quad (3.33)$$

Proof. (cf., e.g., [101],[169],[103]) To prove the FDTs error representation formula (3.33), we first exploit the linearity of $J(\cdot)$, together with (3.25) to get

$$J(u) - J(u_h) = J(u - u_h) = A(u - u_h)(z).$$

Using the Galerkin orthogonality property (3.14) as well as the definition of the stabilized primal bilinearform $A_S(\cdot)(\cdot)$ given in (3.8), we get

$$\begin{aligned} J(u) - J(u_h) &= A(u - u_h)(z) - A_S(u - u_h)(\tilde{z}_h) \\ &= A(u - u_h)(z) - A(u - u_h)(\tilde{z}_h) - S_A(u - u_h)(\tilde{z}_h) \\ &= A(u - u_h)(z - \tilde{z}_h) - S_A(u_h)(\tilde{z}_h) \\ &= A(u)(z - \tilde{z}_h) - A(u_h)(z - \tilde{z}_h) - S_A(u)(\tilde{z}_h) + S_A(u_h)(\tilde{z}_h), \end{aligned}$$

for all $\tilde{z}_h \in V_h^p$. Finally, using (3.3) and (3.13) as well as the definition of the primal residual (3.32), we get

$$\begin{aligned} J(u) - J(u_h) &= F(z - \tilde{z}_h) - A(u_h)(z - \tilde{z}_h) - S_F(\tilde{z}_h) + S_A(u_h)(\tilde{z}_h) \\ &= \rho(u_h)(z - \tilde{z}_h) - S_F(\tilde{z}_h) + S_A(u_h)(\tilde{z}_h), \end{aligned}$$

for all $\tilde{z}_h \in V_h^p$. This proves the error representation (3.33). \square

Since we use this error representation formula for adaptive mesh refinement, we present the following localized form of result (3.33).

Theorem 3.4 (Localized Error Representation FDTS, cf. [169], Thm. 3.18)

Let the assumptions of Thm. 3.3 be satisfied. Then, the cell-wise error representation formula of (3.33) reads

$$J(u) - J(u_h) = \sum_{K \in \mathcal{T}_h} \left\{ (R(u_h), z - \tilde{z}_h)_K - \delta_K (R(u_h), \mathbf{b} \cdot \nabla(\tilde{z}_h))_K - (E(u_h), z - \tilde{z}_h)_{\partial K} \right\}. \quad (3.34)$$

The cell and edge residuals $R(u_h)$ and $E(u_h)$, respectively, are defined by

$$R(u_h)|_K := f + \nabla \cdot (\varepsilon \nabla u_h) - \mathbf{b} \cdot \nabla u_h - \alpha u_h, \quad (3.35)$$

$$E(u_h)|_\Gamma := \begin{cases} \frac{1}{2} \mathbf{n} \cdot [\varepsilon \nabla u_h] & \text{if } \Gamma \subset \partial K \setminus \partial \Omega, \\ 0 & \text{if } \Gamma \subset \partial \Omega, \end{cases} \quad (3.36)$$

where $[\nabla u_h] := \nabla u_h|_{\Gamma \cap K} - \nabla u_h|_{\Gamma \cap K'}$ defines the jump of ∇u_h over the inner edges Γ with normal unit vector \mathbf{n} pointing from K to K' .

Proof. (cf. [169]) The assertion directly follows by using the definitions of the primal bilinear form (3.4) and linear (3.5) as well as the definitions of the primal stabilization bilinear form (3.10) and linear form (3.11), and additionally applying integration by parts on each cell $K \in \mathcal{T}_h$ to the diffusive term in the primal residual (3.32); cf., e.g., [20, Ch. 3]. \square

Remark 3.7 Let us remark some aspects about the two approaches.

- In general, the dual solution to the two approaches may differ, depending on the choice of the bilinear form $A_S(\cdot)(\cdot)$ and the definition of the linear function $J(\cdot)$; cf. [101]. In the here presented case the difference comes through the way how the SUPG stabilization technique is incorporated into the DWR framework.
- Provided that the FSTD dual problem (3.16) has a unique solution z_s , the two dual solutions for the FDTS dual problem (3.25) and the FSTD dual problem (3.16), respectively, are identical, $z \equiv z_s$, if the solution z of the FDTS dual problem (3.25), cf. also (3.28), satisfies

$$A_S(v)(z) = J(v) \quad \forall v \in V.$$

This is accompanied with the definition of the discretization (3.7) and the functional $J(\cdot)$ to be adjoint consistent, which is often used in connection with discontinuous Galerkin finite element methods; cf. [101, Def. 1] based on [140] and

[153, Def. 2.1] for more details. Note that in our case the two dual solutions z_s and z differ due to the fact that the above described condition is obviously not fulfilled.

- Moreover, note that for the FDTS approach the first term in (3.33), more precisely the terms resulting from the primal residual (3.32) depend on the so-called weight $\omega(z) := z - \tilde{z}_h$, whereas the latter two stabilization terms S_F and S_A , respectively, only depend on \tilde{z}_h , cf. also (3.34). Then, the derivation of an upper bound on the error in the computed goal quantity $J(\cdot)$ might be suboptimal, cf. [101, Chapter 2.1] for more details about this predicament.
- In contrast, within the FSTD approach all terms present in the error representation formula (3.19), cf. also (3.20), involve the weight $\omega(z_s) := z_s - \tilde{z}_h$.
- The notes concerning nonhomogeneous Dirichlet boundary conditions and Neumann boundary conditions outlined in Rem. 3.3 and Rem. 3.4, respectively, can be transferred to the FDTS approach as well.

3.3 Practical Aspects

In this section, we give insight into some practical aspects regarding the application of the results given in Thm. 3.2 and Thm. 3.4, respectively. Thereby, we introduce two different approximation techniques to handle the weights $\omega(z_s) := z_s - \tilde{z}_h$ and $\omega(z) := z - \tilde{z}_h$ occurring in the error representation formulas (3.20) and (3.34), respectively. With this in mind, we derive some local error indicators that are used for the adaptive mesh refinement process. Finally, we present the underlying adaptive solution algorithm for the respective FSTD and FDTS approach.

3.3.1 Approximation of the Weights

To define some local error indicators, the localized error representation formulas (3.20) and (3.34), are rewritten as

$$\begin{aligned}
 J(u) - J(u_h) &= \sum_{K \in \mathcal{T}_h} \left\{ (R(u_h), \omega(z_s))_K + \delta_K (R(u_h), \mathbf{b} \cdot \nabla \omega(z_s))_K \right. \\
 &\quad \left. - (E(u_h), \omega(z_s))_{\partial K} \right\} = \eta^{\text{FSTD}} := \sum_{K \in \mathcal{T}_h} \eta_K^{\text{FSTD}}, \tag{3.37}
 \end{aligned}$$

where the cell and edge residuals are given in (3.21) and (3.22), respectively, and

$$\begin{aligned}
J(u) - J(u_h) &= \sum_{K \in \mathcal{T}_h} \left\{ (R(u_h), \omega(z))_K - \delta_K(R(u_h), \mathbf{b} \cdot \nabla \tilde{z}_h)_K \right. \\
&\quad \left. - (E(u_h), \omega(z))_{\partial K} \right\} = \eta^{\text{FDTS}} := \sum_{K \in \mathcal{T}_h} \eta_K^{\text{FDTS}}, \tag{3.38}
\end{aligned}$$

where the cell and edge residuals are given in (3.35) and (3.36), respectively. The error indicators η^{FSTD} and η^{FDTS} depend on the discrete primal solution u_h as well as on the exact dual solution z_s or z within the weights $\omega(z_s)$ or $\omega(z)$, respectively. For the application of (3.37) and (3.38) in computations, these weights have to be approximated. As mentioned in the introductory Sec. 2.5, there exist two main approaches to this approximation, which will be introduced now and compared numerically in the following section; cf., e.g., [20, Chapter 4.1] for more details about these approaches.

Approximation by Higher-Order Interpolation

The most common way to approximate the occurring weights within the DWR framework is done by using a patch-wise higher-order interpolation. Therefore, we introduce the following linear interpolation operator for approximating the weights within the localized error representation formulas (3.37) and (3.38), respectively:

$$\begin{aligned}
\omega(z_s) &= z_s - \tilde{z}_h \approx \mathbb{I}_{2h}^{(2p)} z_{s,h} - z_{s,h}, \\
\omega(z) &= z - \tilde{z}_h \approx \mathbb{I}_{2h}^{(2p)} z_h - z_h,
\end{aligned}$$

where $z_{s,h}$ and $z_h \in V_h^p$, denoting the discrete dual solution to (3.17) and (3.30), respectively. Note that this approximation is valid, since the quantity \tilde{z}_h can be chosen arbitrarily in the underlying finite element space V_h^p . Here, $\mathbb{I}_{2h}^{(2p)}$ denotes the interpolation in space operator that acts on a patched cell of size $2h$ and lifts the solution to a piecewise polynomial of degree $2p$ on the reference cell or element corresponding to the patched cell of width $2h$. Thus, the operator $\mathbb{I}_{2h}^{(2p)}$ can easily be computed if the underlying decomposition or mesh is organized in a patch-wise manner, cf. Def.2.6 in Sec. 2.1.3. Exemplarily, we present for $p = 1$ and $p = 2$ the interpolation in space operators $\mathbb{I}_{2h}^{(2)} : V_h^1 \rightarrow V_{2h}^2$ into the space of bi- or tri-quadratic trial functions and $\mathbb{I}_{2h}^{(4)} : V_h^2 \rightarrow V_{2h}^4$ into the space of bi- or tri-quartic trial functions, respectively. Note that within this approximation strategy the respective dual problem (3.17) or (3.30) is solved in the same finite element space V_h^p as used for the primal problem.

Approximation by Higher-Order Finite Elements

This approach aims to increase the influence of the weights by approximating the dual solution using higher-order finite elements. Thus, the solution of the respective dual problem (3.17) or (3.30) is solved in a finite element space that consists of polynomials that are at least of one polynomial degree higher than its primal counterpart, more precisely the discrete dual solution $z_{s,h}$ or z_h , respectively, is computed in V_h^q , $q \geq p + 1$. Therefore, we introduce the following linear restriction operator for approximating the weights within the localized error representation formulas (3.37) and (3.38), respectively:

$$\begin{aligned}\omega(z_s) &= z_s - \tilde{z}_h \approx z_{s,h} - \mathbf{R}_h^p z_{s,h}, \\ \omega(z_s) &= z - \tilde{z}_h \approx z_h - \mathbf{R}_h^p z_h,\end{aligned}$$

where $z_{s,h}$ and $z_h \in V_h^q$, $q \geq p + 1$, denoting the discrete dual solution to (3.17) and (3.30), respectively. Note that this approximation is valid, since the quantity \tilde{z}_h can be chosen arbitrarily in the underlying finite element space V_h^p . Here, \mathbf{R}_h^p denotes the restriction in space operator that acts on a spatial element or cell and restricts the solution to a polynomial of degree $p < q$ on the corresponding reference element. We note that the restriction operator in space \mathbf{R}_h^p is implemented in the `deal.II` library for dimension $d = 2, 3$ as back-interpolation operator between two finite element spaces that are here the dual finite element space and the intermediate primal finite element space.

However, approximating the dual problem by a higher-order finite element technique leads to higher computational costs as well.

Remark 3.8 *In the literature, the application of higher-order interpolation instead of higher-order finite elements is widespread within the DWR approach; cf., e.g., [20, 31, 40, 159]. Due to the specific character of convection-dominated problems such an interpolation might be defective and may lead to a loss of accuracy of the underlying error estimator. The error control needs a particular care in regions with layers and sharp fronts in order to get an accurate quantification of the numerical errors. Higher-order finite elements seem to show more stability and gain with regard to the accuracy of the error estimator, due to the more accurate approximation of the weights. This presumption is motivated by the work of Lube et. al. [141]. Therefore, within the numerical examples of Sec. 3.4 a comparative study between these two approximation techniques is done for both the FSTD approach as well as the FDTS approach to investigate these presumptions.*

For practical use of the error representations (3.37) and (3.38), respectively, the weights are approximated using the interpolation and restriction operators outlined in the above approximation techniques. With this in mind, the cell-wise contributions to the linearized error representations (3.37) and (3.38), respectively, are given by the following approximated local error indicators:

$$\begin{aligned}
\tilde{\eta}_K^{\text{FSTD,h-oIn}} &= (R(u_h), I_{2h}^{(2p)} z_{s,h} - z_{s,h})_K + \delta_K (R(u_h), \mathbf{b} \cdot \nabla (I_{2h}^{(2p)} z_{s,h} - z_{s,h}))_K \\
&\quad - (E(u_h), I_{2h}^{(2p)} z_{s,h} - z_{s,h})_{\partial K}, \\
\tilde{\eta}_K^{\text{FSTD,h-oFE}} &= (R(u_h), z_{s,h} - R_h^p z_{s,h})_K + \delta_K (R(u_h), \mathbf{b} \cdot \nabla (z_{s,h} - R_h^p z_{s,h}))_K \\
&\quad - (E(u_h), z_{s,h} - R_h^p z_{s,h})_{\partial K},
\end{aligned} \tag{3.39}$$

where the cell and edge residuals are given in (3.21) and (3.22), respectively, and

$$\begin{aligned}
\tilde{\eta}_K^{\text{FDTS,h-oIn}} &= (R(u_h), I_{2h}^{(2p)} z_h - z_h)_K - \delta_K (R(u_h), \mathbf{b} \cdot \nabla (z_h))_K \\
&\quad - (E(u_h), I_{2h}^{(2p)} z_h - z_h)_{\partial K}, \\
\tilde{\eta}_K^{\text{FDTS,h-oFE}} &= (R(u_h), z_h - R_h^p z_h)_K - \delta_K (R(u_h), \mathbf{b} \cdot \nabla (R_h^p z_h))_K \\
&\quad - (E(u_h), z_h - R_h^p z_h)_{\partial K}.
\end{aligned} \tag{3.40}$$

where the cell and edge residuals are given in (3.35) and (3.36), respectively.

3.3.2 Adaptive Solution Algorithms

In this section, we present the adaptive solution algorithms for both the FSTD as well as the FDTS approach. In the course of this, both approximation techniques for the spatial weights (h-oIn and h-oFE) are included within the presentation of the two algorithms. We start presenting the goal-oriented, adaptive solution algorithm for the *First Stabilize and Then Dualize* approach.

3.3.2.1 A FSTD Adaptive Solution Algorithm

We consider a hierarchy of sequentially refined meshes \mathcal{T}_h^ℓ , with $\ell \geq 1$ indexing the hierarchy or corresponding DWR-loop. The corresponding finite element spaces are denoted by $V_h^{p,\ell}$ and $V_h^{q,\ell}$, $q \geq p + 1$, respectively, cf. Eq. (2.1) in Sec. 2.1.3. Our FSTD adaptive algorithm based on the approximated local error indicators given by Eq. (3.39) then reads as follows.

FSTD-Algorithm: Goal-Oriented Space Adaptivity

Initialization:

- Set DWR-loop $\ell = 1$.
 - Generate the initial spatial triangulation \mathcal{T}_h^ℓ (geometrical mesh) for the goal-oriented adaptive convection-diffusion-reaction problem.
-

1. Solve the **Stabilized Primal Problem 3.4**: Find $u_h^\ell \in V_h^{p,\ell}$ such that

$$A_S(u_h^\ell)(\varphi_h) = F_S(\varphi_h) \quad \forall \varphi_h \in V_h^{p,\ell}.$$

2. **Break if the goal is reached**, i.e., for instance, $\|u - u_h^\ell\| < \mathbf{tol}$, or $\tilde{\eta}_K^{\text{FSTD,h-oIn/h-oFE}} < \mathbf{tol}$, or $\max N_{\text{DoF}}^{\text{tot}}$ is reached.
3. Solve the **Stabilized Dual Problem 3.6** depending on the underlying choice of the approximation strategy for the weights $\omega(z_s) := z_s - \tilde{z}_h$:

- (i) Approximation by **higher-order interpolation**: Find $z_{s,h}^\ell \in V_h^{p,\ell}$ such that

$$A_S(\psi_h)(z_{s,h}^\ell) = J(\psi_h) \quad \forall \psi_h \in V_h^{p,\ell}.$$

- (ii) Approximation by **higher-order finite elements**: Find $z_{s,h}^\ell \in V_h^{q,\ell}$, $q \geq p + 1$ such that

$$A_S(\psi_h)(z_{s,h}^\ell) = J(\psi_h) \quad \forall \psi_h \in V_h^{q,\ell}.$$

4. Evaluate the **FSTD a posteriori error indicator in space**, depending on the underlying choice of the approximation strategy for the weights $\omega(z_s) := z_s - \tilde{z}_h$:

- (i) $\tilde{\eta}^{\text{FSTD,h-oIn}} := \sum_{K \in \mathcal{T}_h} \tilde{\eta}_K^{\text{FSTD,h-oIn}}$,
- (ii) $\tilde{\eta}^{\text{FSTD,h-oFE}} := \sum_{K \in \mathcal{T}_h} \tilde{\eta}_K^{\text{FSTD,h-oFE}}$,

where the approximated local error indicators $\tilde{\eta}_K^{\text{FSTD,h-oIn}}$ and $\tilde{\eta}_K^{\text{FSTD,h-oFE}}$ are given in (3.39).

5. **Mark the cells $\tilde{K} \in \Omega_h^\ell$ for spatial refinement** if the corresponding $\tilde{\eta}_{\tilde{K}}^{\text{FSTD,h-oIn}}$ or $\tilde{\eta}_{\tilde{K}}^{\text{FSTD,h-oFE}}$ is in the set of θ_h^{top} percent of the worst indicators, **or**, respectively, **mark for spatial coarsening** if $\tilde{\eta}_{\tilde{K}}^{\text{FSTD,h-oIn}}$ or $\tilde{\eta}_{\tilde{K}}^{\text{FSTD,h-oFE}}$ is in the set of θ_h^{bottom} percent of the best indicators.
6. **Execute spatial refinement** under the use of mesh smoothing operators.
7. Increase ℓ to $\ell + 1$ and **return to Step 1**.

Regarding this algorithm, we note the following issues.

Remark 3.9

- *The exit condition ‘goal is reached’ in Step 2 is done at this position, since we are mainly interested in solving the primal problem in spite of the DWR framework and thus a further approximation of the dual problem is redundant if the primal solution already fulfills one of the the required condition described in Step 2. Note that the choice of only one of this conditions is done in advance of starting the algorithm.*
- *According to Step 3(ii) of the adaptive solution algorithm presented above, we use the same mesh Ω_h^ℓ for solving the primal and dual problem, more precisely we use the same triangulation for both problems, but different polynomial degrees for the underlying shape functions of the respective finite element space $V_h^{p,\ell}$ and $V_h^{q,\ell}$, $q \geq p + 1$, respectively, cf. Step 1 and Step 3(ii).*
- *The ‘marking’ strategy described in Step 5 is also referred to as a fixed fraction strategy, which can be handled by a precasted function within the underlying open source finite element library deal.II; cf. [16]. This strategy can be easily changed, for instance, to a fixed number strategy, pursuing the goal of providing predictable growth in the size of the mesh by refining and coarsening a given fraction of all cells. For more details about possible refinement strategies we refer to [20, Ch. 4.2] or the reference documentation of deal.II. Further, we note that the performance properties of adaptive algorithms are strongly affected by the marking strategy. The so-called Dörfler marking (cf. [66]) or the marking of the largest local error indicators represent further popular marking strategies. For a further discussion of this issue we refer to, e.g., [20]. We note that refinement and coarsening of quadrilateral meshes including hanging nodes takes place as stated in Fig. 3.1.*

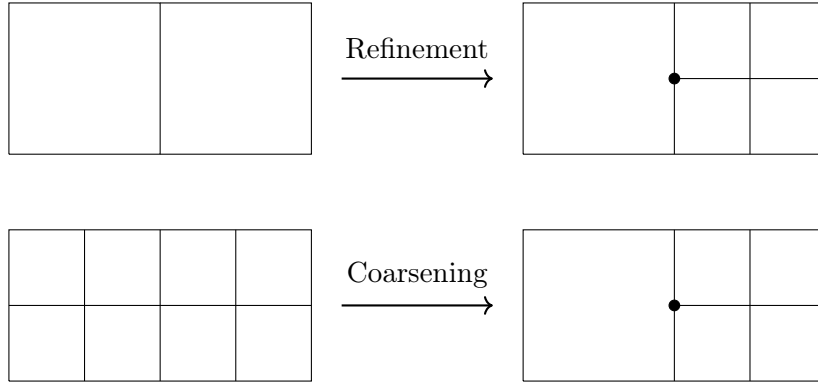


Figure 3.1: Refinement and coarsening in quadrilateral meshes, cf. [20, Fig.4.2].

- *The mesh smoothing operators can be chosen according to ensure certain properties, for instance, like seeking for isolated cells which are refined or flagged for refinement or seeking for single cells which are not refined and are surrounded by cells which are refined. For a detailed description of all possible smoothing operators we refer to the documentation of the `Triangulation` class within the reference documentation of `deal.II`; cf. [16].*

3.3.2.2 A FDTS Adaptive Solution Algorithm

We consider a hierarchy of sequentially refined meshes \mathcal{T}_h^ℓ , with $\ell \geq 1$ indexing the hierarchy or corresponding DWR-loop. The corresponding finite element spaces are denoted by $V_h^{p,\ell}$ and $V_h^{q,\ell}$, $q \geq p + 1$, respectively, cf. Eq. (2.1) in Sec. 2.1.3. Our FDTS adaptive algorithm based on the approximated local error indicators given by Eq. (3.40) then reads as follows.

FDTS-Algorithm: Goal-oriented Space Adaptivity

Initialization:

- Set DWR-loop $\ell = 1$.
- Generate the initial spatial triangulation \mathcal{T}_h^ℓ (geometrical mesh) for the goal-oriented adaptive convection-diffusion-reaction problem.

1. Solve the **Stabilized Primal Problem 3.4**: Find $u_h^\ell \in V_h^{p,\ell}$ such that

$$A_S(u_h^\ell)(\varphi_h) = F_S(\varphi_h) \quad \forall \varphi_h \in V_h^{p,\ell}.$$

2. **Break if the goal is reached**, i.e., for instance, $\|u - u_h^\ell\| < \text{tol}$,
or $\tilde{\eta}_K^{\text{FDTS,h-oIn/h-oFE}} < \text{tol}$, or $\max N_{\text{DoF}}^{\text{tot}}$ is reached.
3. Solve the **Stabilized Dual Problem 3.9** depending on the underlying choice of the approximation strategy for the weights $\omega(z) := z - \tilde{z}_h$:

- (i) Approximation by **higher-order interpolation**: Find $z_h^\ell \in V_h^{p,\ell}$ such that

$$A_S^*(z_h)(\psi_h) = J(\psi_h) \quad \forall \psi_h \in V_h^{p,\ell}.$$

- (ii) Approximation by **higher-order finite elements**: Find $z_h^\ell \in V_h^{q,\ell}$, $q \geq p + 1$ such that

$$A_S^*(z_h)(\psi_h) = J(\psi_h) \quad \forall \psi_h \in V_h^{q,\ell}.$$

4. Evaluate the **FDTS a posteriori error indicator in space**, depending on the underlying choice of the approximation strategy for the weights $\omega(z) := z - \tilde{z}_h$:

- (i) $\tilde{\eta}^{\text{FDTS,h-oIn}} := \sum_{K \in \mathcal{T}_h} \tilde{\eta}_K^{\text{FDTS,h-oIn}}$,
- (ii) $\tilde{\eta}^{\text{FDTS,h-oFE}} := \sum_{K \in \mathcal{T}_h} \tilde{\eta}_K^{\text{FDTS,h-oFE}}$,

where the approximated local error indicators $\tilde{\eta}_K^{\text{FDTS,h-oIn}}$ and $\tilde{\eta}_K^{\text{FDTS,h-oFE}}$ are given in (3.40).

5. **Mark the cells $\tilde{K} \in \Omega_h^\ell$ for spatial refinement** if the corresponding $\tilde{\eta}_{\tilde{K}}^{\text{FDTS,h-oIn}}$ or $\tilde{\eta}_{\tilde{K}}^{\text{FDTS,h-oFE}}$ is in the set of θ_h^{top} percent of the worst indicators, **or**, respectively, **mark for spatial coarsening** if $\tilde{\eta}_{\tilde{K}}^{\text{FDTS,h-oIn}}$ or $\tilde{\eta}_{\tilde{K}}^{\text{FDTS,h-oFE}}$ is in the set of θ_h^{bottom} percent of the best indicators.
6. **Execute spatial refinement** under the use of mesh smoothing operators.
7. Increase ℓ to $\ell + 1$ and **return to Step 1**.

Regarding this algorithm, we note the following issue.

Remark 3.10 *The notes outlined in Rem. 3.9 can be transferred to the FDTS-Algorithm above as well.*

3.4 Both Approaches by Numerical Comparison

In this section, we illustrate and investigate the performance properties of the proposed approaches of combining the Dual Weighted Residual method with stabilized finite element approximations for convection-dominated problems. We demonstrate the potential of the DWR method with regard to resolving solution profiles admitting sharp layers as they typically arise in convection-dominated problems. In a first example, we compare for one thing approximation techniques for the weights within the two proposed approaches, and on the other hand different pairs of finite element spaces used for solving the primal and dual problem. In a second example, we investigate the mesh adaptation processes by prescribing different goal functionals. We finish this section with an example of physical interest for a three-dimensional case. All of these examples are standard benchmark problems that are typically applied in the literature for studying convection-dominated problems. For measuring the accuracy of the underlying error estimator, we will study a so-called effectivity index,

$$\mathcal{I}_{\text{eff}} := \left| \frac{\tilde{\eta}^{\text{FSTD,h-oIn/h-oFE}}}{J(u) - J(u_h)} \right|, \text{ or else } \mathcal{I}_{\text{eff}} := \left| \frac{\tilde{\eta}^{\text{FDTS,h-oIn/h-oFE}}}{J(u) - J(u_h)} \right|, \quad (3.41)$$

as the ratio of the estimated over the exact error having regard to the different approaches and approximation techniques. Desirably, this index should be close to one. The primal and dual SUPG method stabilization parameters δ_K and δ_K^* , respectively, are given by

$$\delta_K = \delta_K^* = \delta_0 \cdot h_K, \quad 0.1 \leq \delta_0 \leq 1, \quad (3.42)$$

where h_K denotes the cell diameter of the mesh cell K , cf. Rem. 3.2. In the following, we use the abbreviations Q_p/Q_q denoting a cG(p) primal and cG(q) dual solution within a finite element space based on the family of Q_p or Q_q elements, respectively.

The software for the now following examples is called `dwr-condiffrea` being a module of our DWR software project `DTM++`. `Project/dwr` (bitbucket.org/dtmproject) developed by U. Köcher [128, 129]. It is implemented using the open source finite element library `deal.II`; cf. [16, 22]. Some of the results regarding the FDTS approach have been published by the author et al. in [50].

3.4.1 Hump with Circular Layer - Comparison of Approaches and Approximation Techniques for Weights

In a first numerical experiment, we focus on studying the accuracy of our error estimators and the impact of approximating the weights within the error representation

formulas (3.37) and (3.38), respectively. Furthermore, we compare both approaches with regard to solving the primal and dual problem by different pairs of finite element spaces based on the family of Q_k elements. For this, we investigate and compare the two algorithms presented in Sec. 3.3.2 by means of the following example.

Example 3.1 (Hump with Circular Layer, 2d) *We study Problem (3.1) with the prescribed exact solution (cf. [115, 120, 27, 3])*

$$\begin{aligned} u(\mathbf{x}) &:= u_1 \cdot u_2, \quad \mathbf{x} = (x_1, x_2)^\top \in \mathbb{R}^2, \\ u_1(\mathbf{x}) &:= 16x_1(1-x_1)x_2(1-x_2), \\ u_2(\mathbf{x}) &:= \left(\frac{1}{2} + \frac{\arctan \left[2\varepsilon^{-\frac{1}{2}} (r_0^2 - (x_1 - x_1^0)^2 - (x_2 - x_2^0)^2) \right]}{\pi} \right). \end{aligned} \quad (3.43)$$

This solution is characterized by an circular internal layer, cf. Fig. 3.2. The problem is defined in $\Omega = (0, 1)^2$ with scalars $r_0 = 0.25$, $x_1^0 = x_2^0 = 0.5$. We choose the flow field $\mathbf{b} = (2, 3)^\top$ and the reaction coefficient $\alpha = 1.0$. For the solution (3.43) the right-hand side function f is calculated from the partial differential equation. Boundary conditions are given by the exact solution. For the now following comparative study, we decided to choose a standard goal quantity, given as

$$J_{L^2}(u) = \frac{1}{\|e\|_{L^2(\Omega)}}(e, u), \quad (3.44)$$

aiming to control the global L^2 -error.

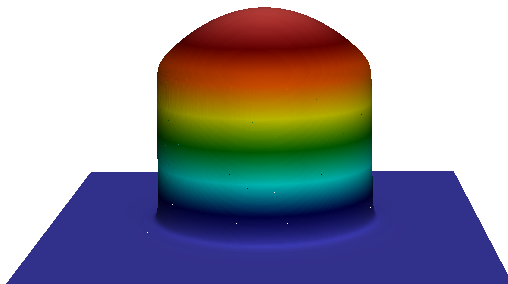


Figure 3.2: Exemplary solution profile for $\varepsilon = 10^{-6}$ for Example 3.1.

In our first test, we investigate Problem (3.1) for a fixed diffusion coefficient $\varepsilon = 1$ and without any stabilization to verify our algorithm and compare both approximation techniques for a non convection-dominated case. More precisely, we compare the approximation of the weights on the one hand by higher-order interpolation (h-oIn),

and on the other hand by higher-order finite elements (h-oFE) for both, the FSTD as well as the FDTS approach.

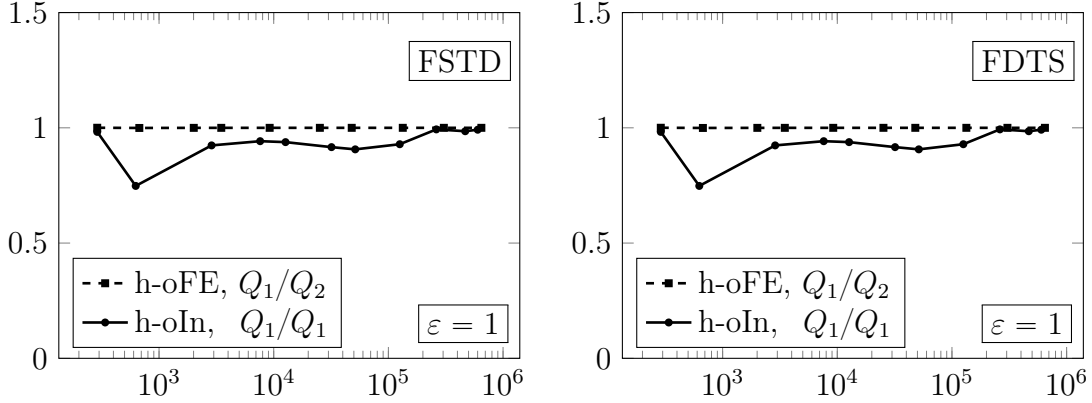


Figure 3.3: Comparison of effectivity indices (over degrees of freedom) for the FSTD approach (left) and the FDTS approach (right) without stabilization ($\delta_K = \delta_K^* = 0$), $\varepsilon = 1$, in Example 3.1. Then, both approaches (FSTD and FDTS) are identical.

Higher-Order Interpolation (Q_1/Q_1)				Higher-Order Finite Elements (Q_1/Q_2)			
N_{DoF}	$J_{L^2}(u - u_h)$	$\tilde{\eta}^{\text{FSTD/FDTS,h-oIn}}$	\mathcal{I}_{eff}	N_{DoF}	$J_{L^2}(u - u_h)$	$\tilde{\eta}^{\text{FSTD/FDTS,h-oFE}}$	\mathcal{I}_{eff}
289	9.40e-04	9.61e-04	0.98	289	9.40e-04	9.40e-04	1.00
626	3.04e-04	2.38e-04	0.74	673	3.26e-04	3.26e-04	1.00
2872	5.80e-05	5.43e-05	0.92	2008	1.24e-04	1.24e-04	1.00
7616	2.53e-05	2.41e-05	0.94	3488	6.25e-05	6.25e-05	1.00
12678	1.32e-05	1.26e-05	0.93	9218	2.30e-05	2.30e-05	1.00
31910	6.09e-06	5.81e-06	0.91	25262	9.74e-06	9.74e-06	1.00
51395	3.45e-06	3.25e-06	0.90	47902	4.28e-06	4.28e-06	1.00
261867	6.95e-07	6.94e-07	0.99	133535	1.67e-06	1.67e-06	1.00
467713	3.93e-07	3.92e-07	0.99	304606	8.39e-07	8.39e-07	1.00
601086	2.67e-07	2.67e-07	1.00	646950	3.43e-07	3.43e-07	1.00

Table 3.1: Effectivity indices with regard to higher-order interpolation versus higher-order finite elements for the FSTD/FDTS approach ($\delta_K = \delta_K^* = 0$), $\varepsilon = 1$, in Example 3.1.

We note that in a non-stabilized case, i.e. $\delta_K = \delta_K^* = 0$, both approaches are equal, cf. Rem. 3.5. Thus, it is hardly surprising that the development of the respective effectivity indices for the FSTD and the FDTS approach are exactly the same, as visualized by the left and right illustration in Fig. 3.3, respectively. While both approaches are equal with respect to a fixed approximation technique for the weights, the two approximation techniques within one of the approaches are quite different. The development of the effectivity indices for the approximation by higher-order finite elements is totally stable and exactly one from the beginning. Even though the

development of the effectivity indices for the approximation by higher-order interpolation is still close to one, it is slightly worse compared to its counterpart, cf. Fig. 3.3 and the related Table 3.1.

Hereafter, we turn to convection-dominated cases. Therefore, we consider varying diffusion coefficients that are comparatively small with respect to the convection field \mathbf{b} . Then, the finite element approximations have to be stabilized and the both approaches do not equal anymore, cf. Rem.3.7. Again, we compare both approximation techniques within the FSTD and FDTS approach.

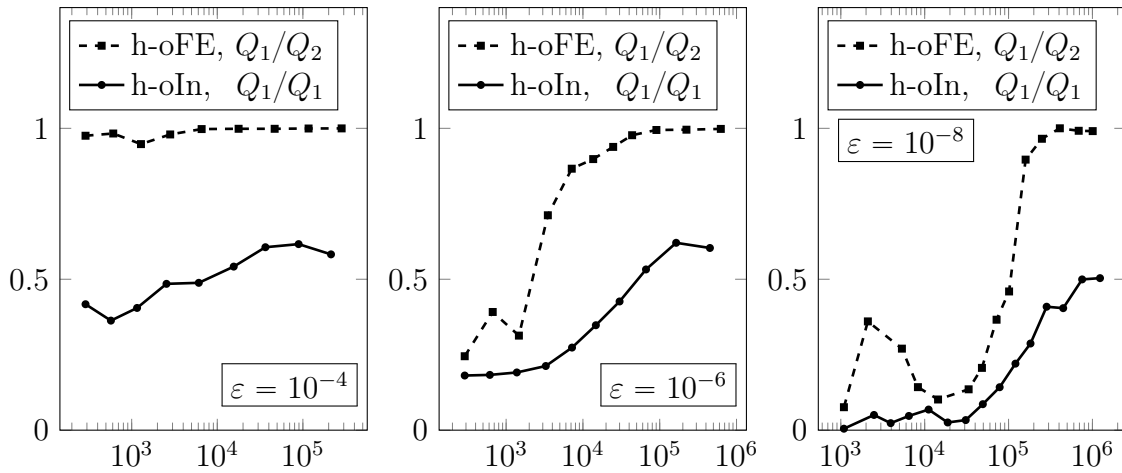


Figure 3.4: Comparison of effectivity indices (over degrees of freedom) for the FSTD approach using varying diffusion coefficients, goal (3.44), $\delta_0 = 1$, Example 3.1.

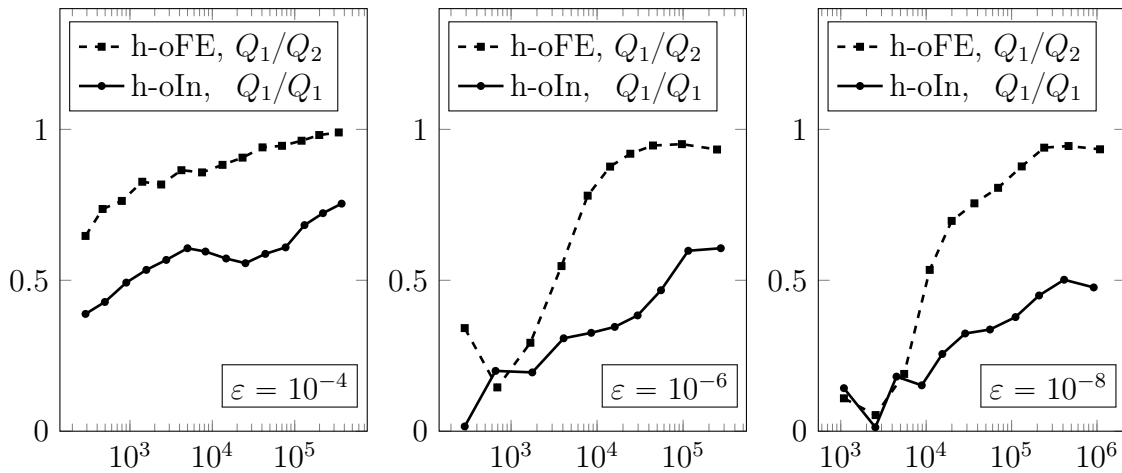


Figure 3.5: Comparison of effectivity indices (over degrees of freedom) for the FDTS approach using varying diffusion coefficients, goal (3.44), $\delta_0 = 1$, in Example 3.1.

In Fig. 3.4 and 3.5 we visualize the respective effectivity indices for varying diffusion coefficients for the FSTD and FDTS approach, respectively. For both methods,

the development of the effectivity indices is quite similar compared with respect to the same diffusion coefficient ε , but the approximation by higher-order finite elements is significantly better with regard to the accuracy and efficiency of the underlying error estimator. Furthermore, the difference of the effectivity indices with respect to the chosen approximation technique increases if ε becomes smaller. This confirms the assertion made in Rem. 3.8, obtaining better results with regard to reducing sources of inaccuracies and non-sharp estimates within the error representation by using higher-order finite elements for the approximation of the weights within convection-dominant cases. Comparing the approximation technique by higher-order finite elements with respect to both approaches, the differences are only slightly, but the FSTD approach shows marginally better results with regard to attaining the desirably value of one for the underlying effectivity index.

In the sequel, all examples are performed using the higher-order finite element approximation technique, unless otherwise specified. In the following comparative study, we investigate several combinations of polynomial orders for the finite element spaces of the primal and dual solution for a fixed diffusion coefficient of magnitude $\varepsilon = 10^{-6}$. In Fig. 3.6 and 3.7 we present the calculated effectivity indices for solving the primal and dual problem in different pairs of finite element spaces based on the family of Q_k elements for the FSTD and FDTS approach, respectively. Considering the Q_1 based approximation of the primal problem for both approaches, we note that by increasing the polynomial degree of the dual solution from Q_2 to Q_4 the desired value of one for the effectivity index is reached faster for even less degrees of freedom. This observation is reasonable, since a higher-order approximation of the dual problem is closer to its exact solution, which is part of the weights within the error representation (3.20) and (3.34), respectively. Thus, we conclude that a better approximation of the weights provides a higher accuracy of the error estimator. This observation is also confirmed by the comparison of the pairs of Q_2/Q_3 with Q_2/Q_4 based finite element spaces. Nevertheless, the difference for using higher-order finite elements for solving the dual problem is not that significant, even less if we take into account the higher computational costs for solving the algebraic form of the dual problem for an increasing order of the piecewise polynomials. Using pairs of Q_k/Q_{k+1} based elements for the approximation of the primal and dual problem, the error estimator gets worse with regard to reaching the desired value of one for increasing values of the parameter k . This observation is in good agreement with the results in [67, Example 3]. A reason for this behavior is given by the observation that for increasing values of k the mesh is less refined for the same number of degrees of

freedom. Therefore less cells are available to capture the strong gradients of the exact solution. This argues for choosing smaller values of k in the application of our DWR based approach. Overall the results for both approaches are quite similar, but again the FSTD approach shows better results with regard to attaining the desirably value of one for the underlying effectivity index.

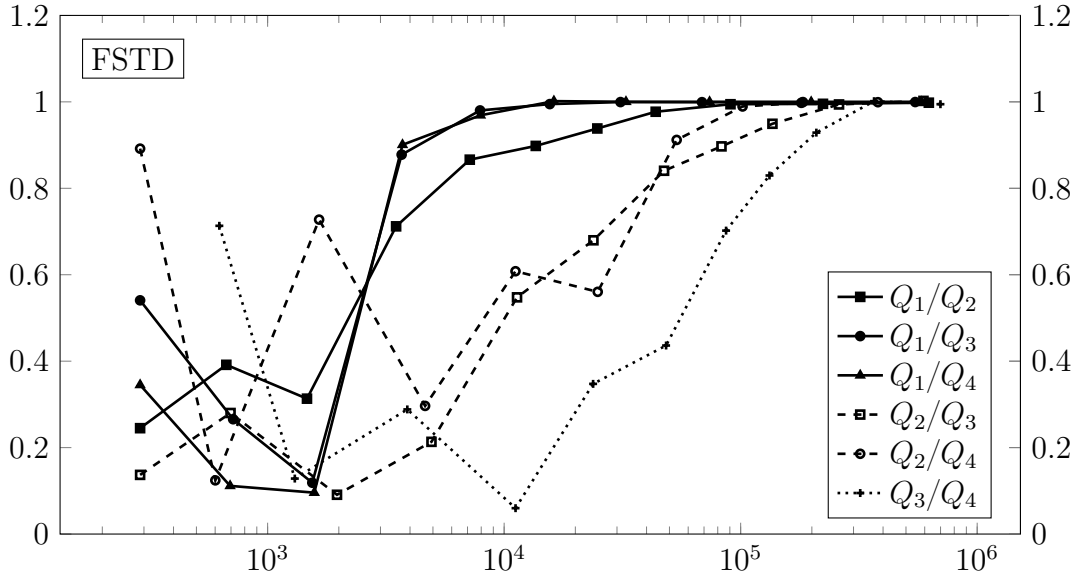


Figure 3.6: Effectivity indices over degrees of freedom for the FSTD approach using varying polynomial degrees, goal (3.44), $\varepsilon = 10^{-6}$, $\delta_0 = 1$, in Example 3.1.

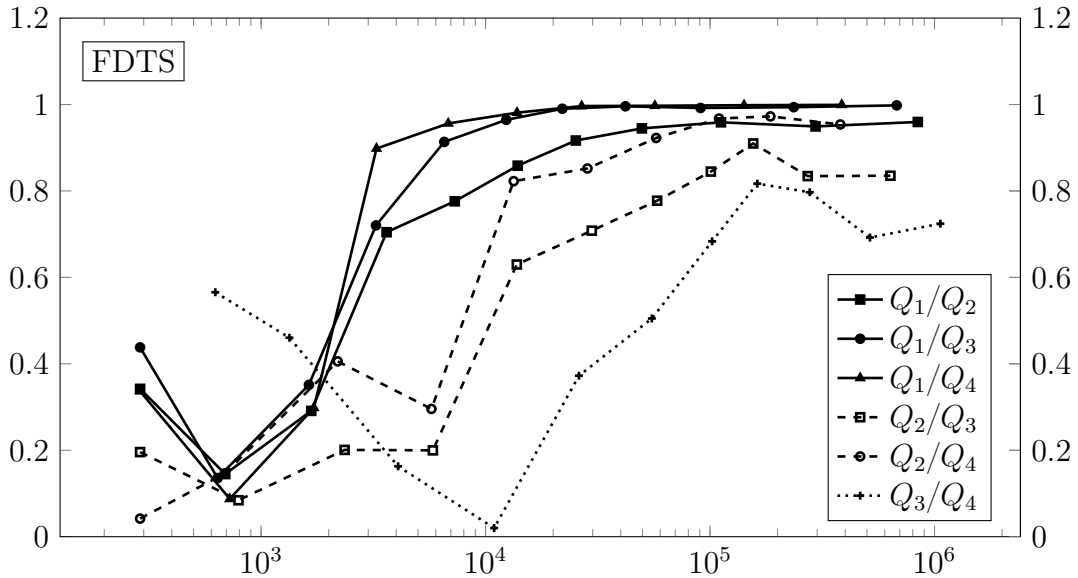


Figure 3.7: Effectivity indices over degrees of freedom for the FSTD approach using varying polynomial degrees, goal (3.44), $\varepsilon = 10^{-6}$, $\delta_0 = 1$, in Example 3.1.

In the last test case for this example, we compare the L^2 -errors on the one hand for global refinement and on the other hand for DWR adaptive mesh refinement based on the proposed approaches. Therefore, in Fig. 3.8 the convergence behavior of the proposed DWR approaches for different approximation techniques of the weights is compared with a global mesh refinement strategy. The DWR based adaptive mesh adaptation is clearly superior to the global refinement in terms of accuracy over degrees of freedom, independently of the underlying approach and approximation technique for the weights. Comparing the L^2 -error with regard to the FSTD and FDTS approach, it can be summarized that the FSTD approach shows slightly better results, cf. the blue versus the green lines. Furthermore, comparing the approximation techniques of the weights within a fixed approach, we note that again the approximation by higher-order finite elements show slightly better results compared to the approximation by higher-order interpolation, cf. the different markers for the blue as well as the green lines, respectively.

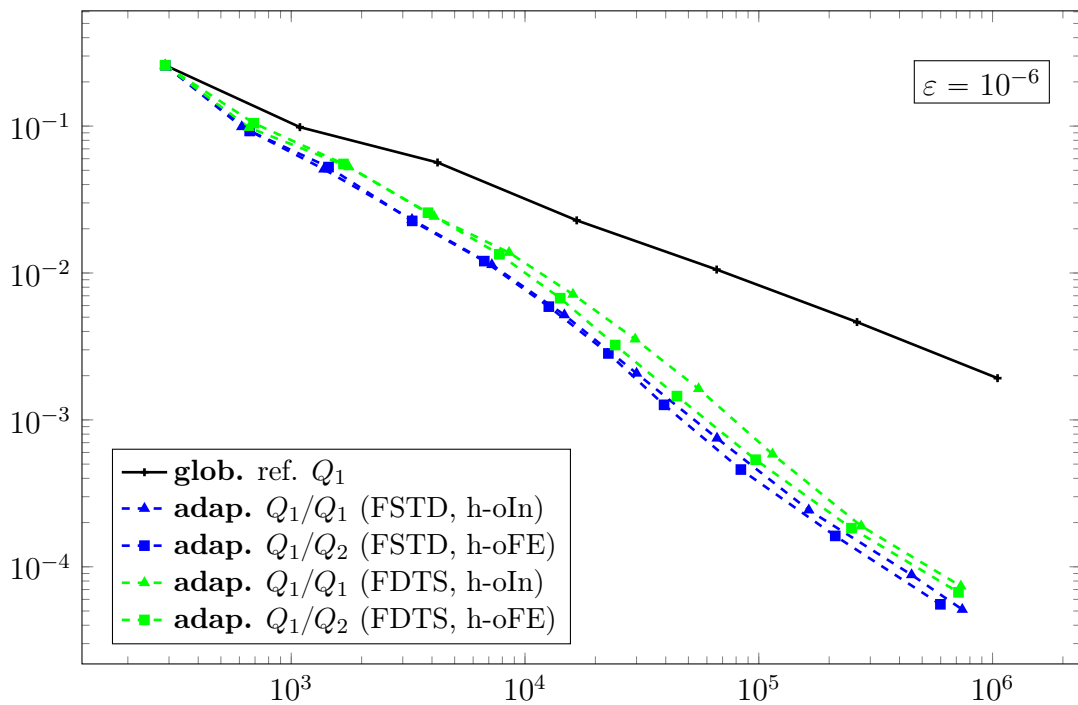
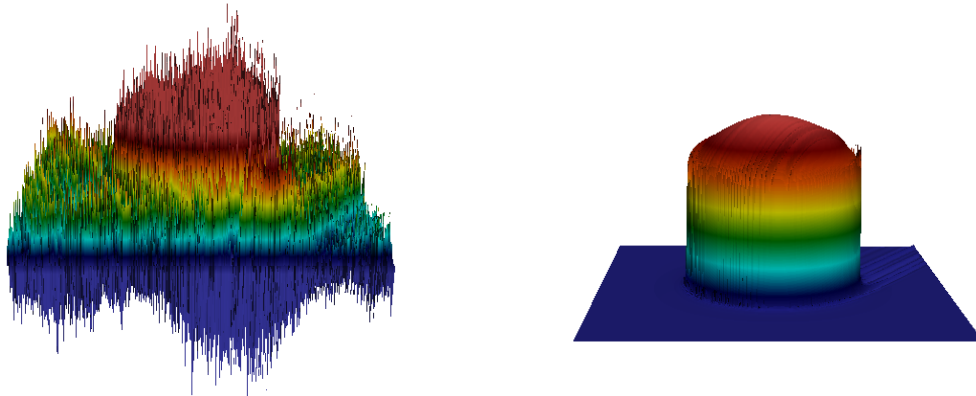


Figure 3.8: L^2 -error comparison over degrees of freedom for global and DWR adaptive mesh refinement for the FSTD and FDTS approach and different approximation techniques for the weights for fixed $\varepsilon = 10^{-6}$, $\delta_0 = 1$, in Example 3.1.

The corresponding solution profiles to the L^2 -error development given in Fig. 3.8 are visualized in Fig. 3.9 and Fig. 3.10, respectively. In Fig. 3.9 we compare the solution profile of a non-stabilized approximation (Fig. 3.9a) with an approximation

using SUPG stabilization (Fig. 3.9b) in each case on a globally refined mesh. While the non-stabilized solution approximation is strongly perturbed and overruled with occurring oscillations, the stabilized counterpart shows a significantly improvement with regard to a reduction of the oscillations. Nevertheless, the stabilized solution approximation on a uniform refined mesh still exhibits perturbations in the form of undesired oscillations within the circular layer and behind the hump in the direction of the flow field \mathbf{b} . On the contrary, all stabilized solution profiles obtained on an additionally adaptive refined mesh, as given by Figs. 3.10a–3.10d, show an almost perfect approximation of the the desired solution (cf. Fig. 3.2), independent of the approximation technique used for the weights (h-oIn versus h-oFE) and the underlying approach (FSTD or FDTS). The oscillations are completely vanished and the respective hump exhibits a smooth transition within the circular layer. This is all the more remarkable, since all solution profiles in Fig. 3.10 are obtained for even less than half of the degrees of freedom that have been used in the case of an uniformly refined mesh as given by Fig. 3.9b. Comparing the different solution profiles and related adaptively determined meshes within Fig. 3.10, the deviations are only very slightly. The approximated stabilized solution profiles show all the desired results with regard to the reduction of the oscillations, solely the respective spatial meshes exhibit minimal differences with regard to the distribution of some refined or coarsened cells within the circular layer and in the corners of the domain.



(a) Global Refinement without stabilization

(b) Global Refinement with stabilization

Figure 3.9: Solution profile without ($\delta_0 = 0$) (a) and with ($\delta_0 = 1$) (b) SUPG stabilization on a globally refined mesh with 66049 degrees of freedom for the case $\varepsilon = 10^{-6}$ in Example 3.1, using Q_1 elements.

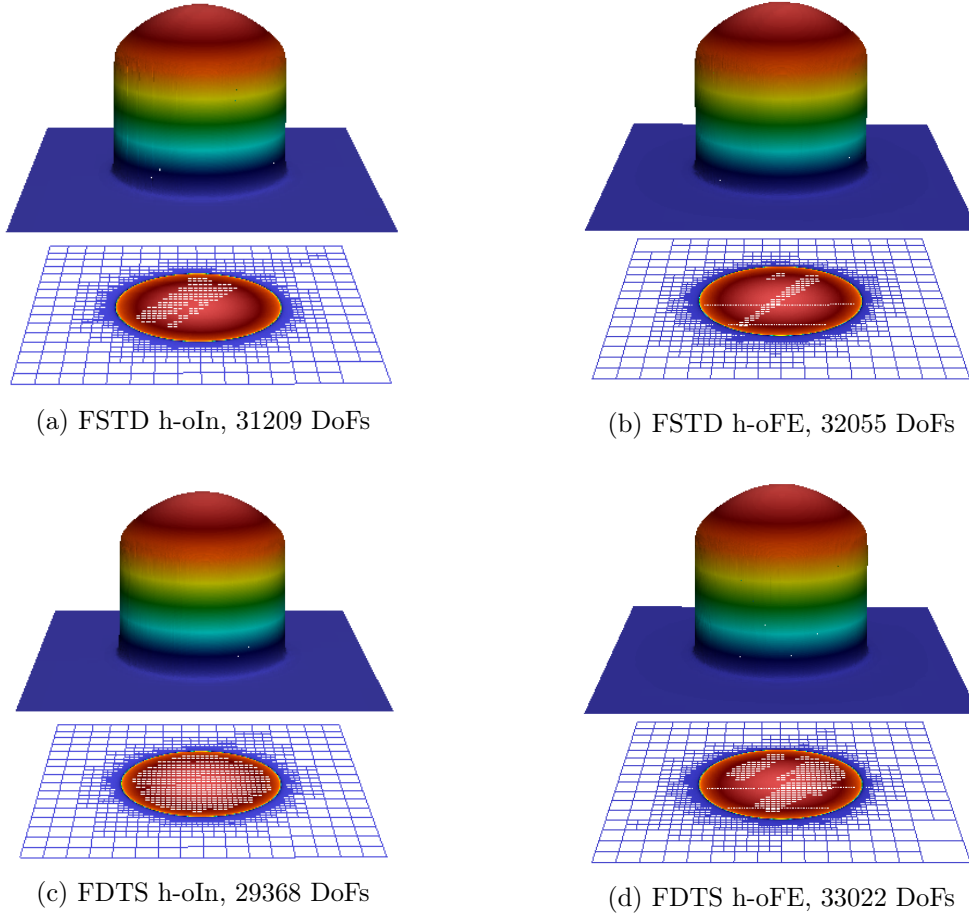


Figure 3.10: Solution profiles and related adaptively refined meshes for the FSTD and FDTS approach using both approximation techniques for the weights in each case, with goal (3.44), $\varepsilon = 10^{-6}$, $\delta_0 = 1$, in Example 3.1, using Q_1/Q_2 elements.

As an interim conclusion for the first example, we summarize the following.

Conclusion 3.1 (FSTD vs. FDTS and h-oIn vs. h-oFE)

Non-convection-dominated and thus non-stabilized case ($\varepsilon = 1$; $\delta_K = \delta_K^ = 0$):*

- Both approaches **first stabilize and then dualize** (FSTD) and **first dualize and then stabilize** (FDTS) are equal; cf. Fig. 3.3 and Rem. 3.5.
- Comparing both approximation techniques for the weights, the approximation by **higher-order finite elements** (h-oFE) provides an error estimator that is totally exact from the beginning (cf. the last column of Table 3.1) whereas the approximation by **higher-order interpolation** (h-oIn) is slightly worse. (cf. column four of Table 3.1).

Convection-dominated and thus stabilized case ($\varepsilon \ll 1; \delta_K, \delta_K^ \neq 0$):*

- *Comparing both approaches, the **FSTD** approach shows slightly better results with regard to accuracy and efficiency of the error estimator (cf. Figs. 3.4–3.7) as well as the reduction of the L^2 -error (cf. Fig. 3.8).*
- *Comparing both approximation techniques for the weights, the **h-oFE** approach is significantly better with regard to accuracy and efficiency of the underlying error estimator for increasing Péclet numbers; cf. Fig. 3.4 and 3.5. Moreover, this approximation technique shows slightly better results with regard to the reduction of the L^2 -error (cf. Fig. 3.8) compared to the **h-oIn** approach; cf. Fig. 3.8.*
- *Increasing the polynomial order q of the finite element spaces V_h^q used for solving the dual problem for a primal solution $u_h \in V_h^p$ with a fixed polynomial degree p , $p < q$, leads to a more efficient and accurate error estimator; cf. Fig. 3.6 and 3.7. This means that a higher approximation of the weights provides a higher accuracy of the underlying error estimator. But, increasing both polynomial orders p and q , $p < q$, slows the efficiency (both approaches) and reduces the accuracy (only within FSTD approach) of the estimator compared to a lower order solutions case (compare exemplary Q_3/Q_4 with Q_2/Q_3 and Q_1/Q_2 in Fig. 3.6 and 3.7).*

3.4.2 Step with Interior Layer - Different Goal Functionals

In the next example, we investigate the mesh adaptation processes by prescribing different goal quantities for varying diffusion coefficients. Thereby, we aim to analyze the robustness of the approach with respect to the small perturbation parameter ε in (3.1). Not only in the case of convection-dominated problems, but also for numerous applications of practical interest, the investigation of local quantities are of greater interest than global ones. The DWR approach offers the appreciable advantage over standard a posteriori error estimators that an error control in an arbitrary user-chosen quantity and not only in the global L^2 norm, as used in Example 3.1, or a norm of energy type can be obtained. In the sequel, we evaluate the potential of our approach with respect to these topics for two different goal functionals, more precisely a global one that aims to control the error within the mean value as well as a local one that aims to control the error within an user-prescribed control point only.

Example 3.2 (Step with Interior Layer, 2d) We study Problem (3.1) with the prescribed exact solution (cf. [141, 169])

$$u(\mathbf{x}) = \frac{1}{2} \cdot \left(1 - \tanh \frac{2x_1 - x_2 - 0.25}{\sqrt{5\varepsilon}} \right), \quad \mathbf{x} = (x_1, x_2)^\top \in \mathbb{R}^2, \quad (3.45)$$

that is characterized by an interior layer of thickness $O(\sqrt{\varepsilon} |\ln \varepsilon|)$, cf. Fig. 3.11. The problem is defined in $\Omega = (0, 1)^2$ with the flow field given by $\mathbf{b} = \frac{1}{\sqrt{5}}(1, 2)^\top$ and the reaction coefficient given by $\alpha = 1.0$. For the solution (3.45) the right-hand side function f is calculated from the partial differential equation. The Dirichlet boundary condition is given by the exact solution. The goal quantities are chosen as

$$J_M(u) = \int_{\Omega} u \, d\mathbf{x}, \quad (3.46)$$

$$J_P(u) = u(\mathbf{x}_e), \quad (3.47)$$

acting in a global and a local sense, respectively. Here, $\mathbf{x}_e = (\frac{5}{16}, \frac{3}{8})$ is an user-prescribed control point that is located in the interior of the layer. In our computations we regularize $J_P(\cdot)$ by

$$J_{rP}(u) = \frac{1}{|B_r|} \int_{B_r} u(\mathbf{x}) \, d\mathbf{x}, \quad (3.48)$$

where the ball B_r is defined by $B_r = \{\mathbf{x} \in \Omega \mid \|\mathbf{x} - \mathbf{x}_e\| < r\}$ with small radius $r > 0$. Here, all test cases are solved by using the Q_1/Q_2 pair of finite elements for the primal and dual problem which is due to the observations depicted in Example 3.1.

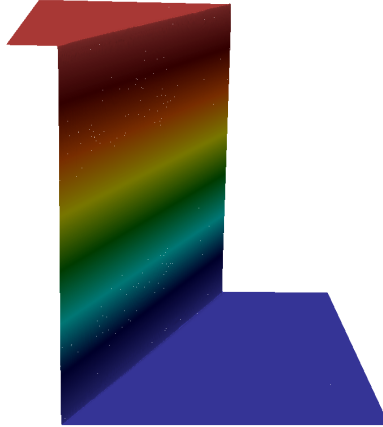


Figure 3.11: Exemplary solution profile for $\varepsilon = 10^{-6}$ for Example 3.2.

In Table 3.2, we present a comparison of the FSTD and FDTS approach with regard to the development of the effectivity indices as well as the exact and estimated errors for the global goal quantity (3.46) and varying diffusion coefficients. For both

$\varepsilon = 10^{-4}$							
FSTD				FDTS			
N_{DoF}	$J_M(u - u_h)$	$\tilde{\eta}^{\text{FSTD,h-oFE}}$	\mathcal{I}_{eff}	N_{DoF}	$J_M(u - u_h)$	$\tilde{\eta}^{\text{FDTS,h-oFE}}$	\mathcal{I}_{eff}
289	5.57e-04	6.07e-04	1.08	289	5.57e-04	5.28e-04	0.94
607	1.11e-04	1.19e-04	1.07	553	2.38e-04	4.33e-04	1.82
1040	4.48e-05	3.99e-05	0.89	1136	4.74e-05	4.56e-05	0.96
1824	7.08e-06	8.39e-06	1.18	2520	1.40e-05	1.57e-05	1.13
5705	3.80e-06	6.42e-06	1.69	3394	4.43e-06	8.38e-06	1.89
14080	1.63e-06	1.81e-06	1.11	14087	1.87e-06	2.09e-06	1.12
32672	4.60e-07	4.59e-07	1.00	38452	2.10e-07	2.15e-07	1.02
73612	4.14e-08	4.27e-08	1.03	71285	1.07e-07	8.66e-08	0.81
$\varepsilon = 10^{-6}$							
FSTD				FDTS			
N_{DoF}	$J_M(u - u_h)$	$\tilde{\eta}^{\text{FSTD,h-oFE}}$	\mathcal{I}_{eff}	N_{DoF}	$J_M(u - u_h)$	$\tilde{\eta}^{\text{FDTS,h-oFE}}$	\mathcal{I}_{eff}
289	2.28e-04	2.61e-04	1.14	289	2.28e-04	1.27e-04	0.56
516	1.73e-04	1.33e-04	0.76	543	7.49e-04	5.30e-04	0.71
981	7.20e-05	6.98e-05	0.97	1020	5.78e-05	7.09e-05	1.23
1669	5.23e-05	4.25e-05	0.81	1875	8.68e-05	4.87e-05	0.56
3049	7.74e-06	7.42e-06	0.96	3796	3.43e-06	2.69e-06	0.78
12787	5.41e-06	4.93e-06	0.91	16139	1.08e-06	1.82e-06	1.69
29258	1.23e-06	1.53e-06	1.24	30740	8.45e-07	1.10e-06	1.31
69282	6.27e-07	6.08e-07	0.97	60675	5.61e-07	6.62e-07	1.18

Table 3.2: Selected effectivity indices for the comparison of the FSTD and FDTS approach using a higher-order finite element approximation for the weights (Q_1/Q_2) , varying diffusion parameters ε , goal quantity (3.46), $\delta_0 = 0.1$, in Example 3.2.

approaches the effectivity indices are close to one for an increasing number of degrees of freedom, while the error is reduced significantly. The same was done for a more challenging error control of a point-value, given by Eq. (3.48), which, however, can be expected to be of higher interest in practice. The results for this local goal quantity are summarized in Table 3.3. Again, the effectivity indices nicely converge to one for an increasing number of degrees of freedom for both approaches. Moreover, the expected convergence behavior is robust with respect to the small diffusion parameter ε . We note that in the case of a point-value error control the goal functional lacks the regularity of the right-hand side term in the dual problem that is typically needed to ensure the existence and regularity of weak solutions; cf. [81, Chapter 6.2]. However, no impact of this lack of regularity is observed in the computational studies. Thus, for both goal quantities a robust convergence behavior is ensured within the considered

$\varepsilon = 10^{-4}$							
FSTD				FDTS			
N_{DoF}	$J_{rP}(u - u_h)$	$\tilde{\eta}^{\text{FSTD,h-oFE}}$	\mathcal{I}_{eff}	N_{DoF}	$J_{rP}(u - u_h)$	$\tilde{\eta}^{\text{FDTS,h-oFE}}$	\mathcal{I}_{eff}
289	5.64e-02	5.26e-02	0.93	289	5.64e-02	3.07e-02	0.54
564	6.68e-02	4.04e-02	0.60	555	2.71e-02	2.05e-02	0.76
1144	1.17e-02	9.84e-03	0.84	1156	7.35e-03	6.77e-03	0.92
2626	6.35e-04	6.43e-04	1.01	3792	1.76e-04	2.12e-04	1.20
11587	6.86e-06	6.67e-06	0.97	11305	6.14e-06	7.95e-06	1.29
24124	1.23e-06	-1.29e-06	1.04	16678	2.59e-06	2.86e-06	1.10
40508	4.04e-07	4.32e-07	1.06	47689	9.20e-07	9.25e-07	1.01
74171	2.38e-07	2.41e-07	1.01	69216	7.86e-07	8.53e-07	1.09
$\varepsilon = 10^{-6}$							
FSTD				FDTS			
N_{DoF}	$J_{rP}(u - u_h)$	$\tilde{\eta}^{\text{FSTD,h-oFE}}$	\mathcal{I}_{eff}	N_{DoF}	$J_{rP}(u - u_h)$	$\tilde{\eta}^{\text{FDTS,h-oFE}}$	\mathcal{I}_{eff}
289	5.50e-02	6.11e-02	1.11	289	5.50e-02	3.68e-02	0.67
549	2.82e-02	3.91e-02	1.39	558	3.68e-02	3.01e-02	0.82
1261	3.71e-02	4.64e-02	1.25	1902	7.31e-02	4.45e-02	0.61
4207	4.80e-02	5.87e-02	1.22	4312	4.44e-02	5.49e-02	1.23
9671	3.05e-02	3.28e-02	1.08	10105	2.51e-02	2.90e-02	1.16
22440	6.41e-03	6.60e-03	1.03	23112	5.02e-03	5.31e-03	1.06
49129	1.08e-03	1.09e-03	1.01	51260	9.50e-04	1.02e-03	1.08
70866	6.63e-04	6.61e-04	1.00	73768	4.98e-04	5.82e-04	1.17

Table 3.3: Selected effectivity indices for the comparison of the FSTD and FDTS approach using a higher-order finite element approximation for the weights (Q_1/Q_2) , varying diffusion parameters ε , goal quantity (3.47), $\delta_0 = 0.1$, in Example 3.2.

test case for the two different approaches.

In Figure 3.12 we visualize the computed solution profiles and adaptive meshes for an error control based on the local goal quantity $J_{rP}(\cdot)$ and the global goal quantity $J_M(\cdot)$, respectively, for both approaches in the final DWR iteration step for $\varepsilon = 10^{-6}$. This test case nicely illustrates the potential of the DWR approach. For the point-value error control the refined mesh cells are located close to the specified point of interest and along those cells that affect the point-value error by means of transport in the direction of the flow field \mathbf{b} . Furthermore, mesh cells without strong impact on the solution close to the control point are coarsened further. Even though a rough approximation of the sharp interface is obtained in downstream direction of the control point, in its neighborhood an excellent approximation of the sharp layer is ensured by the approach. A high economical mesh along with a high quality in

the computation of the user-specified goal quantity is thus obtained. In contrast to this, the global error control of $J_M(\cdot)$ provides a good approximation of the solution in the whole domain by adjusting the mesh along the complete layer. Comparing the spatial meshes for the local (3.12a and 3.12b) as well as global (3.12c and 3.12d) goal quantity with regard to the both approaches, we note that the difference is only slightly in each case.

Comparing both approaches for all presented test cases within Example 3.1 and 3.2, the following can be summarized with reference to Conclusion 3.1.

Conclusion 3.2 (FSTD vs. FDTS under Different Goal Functionals)

Both approaches yield to efficient and accurate results for solving convection-dominated problems. They are robust with respect to vanishing diffusion parameters and different types of goal quantities, cf. Tables 3.2 and 3.3. Nevertheless, for all test cases the FSTD approach shows slightly better results with regard to attaining the desirably value of one for the underlying effectivity index compared to the FDTS approach.

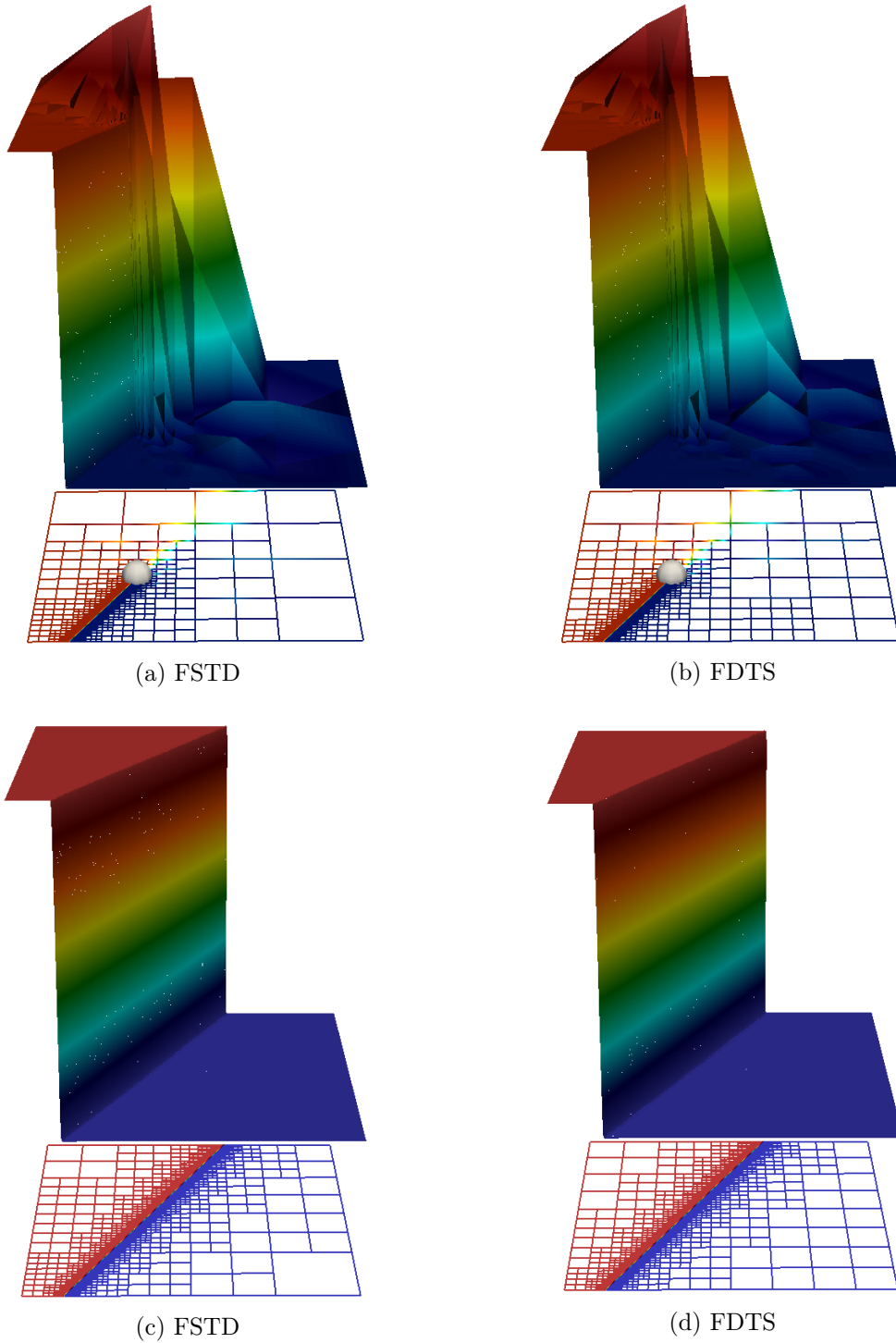


Figure 3.12: Point-value error control by J_{rP} (3.47) for FSTD approach (3.12a) and FDTS approach (3.12b) as well as global error control by J_M (3.46) for FSTD approach (3.12c) and FDTS approach (3.12d) using Q_1/Q_2 elements, $\varepsilon = 10^{-6}$, $\delta_0 = 0.1$, in Example 3.2.

3.4.3 Domain with Interior Channel - 3d Problem of Physical Relevance

We close this chapter with an example of physical interest for a three-dimensional case with unknown exact solution and a convection field \mathbf{b} depending on the space variable \mathbf{x} . Due to the results obtained above, we apply the FSTD approach for this test case only. Furthermore, since the exact solution is unknown, we do not consider effectivity indices or convergence rates here. This example is rather intended to show the potential of the DWR approach with regard to obtaining economical meshes even in a three-dimensional case. Imagine a species entering a domain and being transported through a channel. The specie's concentration is supposed to be controlled on a certain inner domain Ω_{in} only. To model this scenario, we consider the following example.

Example 3.3 (Domain with Interior Channel, 3d) *We study Problem (3.1) on the unit cube $\Omega = (0, 1)^3$, $\varepsilon = 10^{-6}$, $\alpha = 1$, $\mathbf{b} = (-x_2, x_1, 0)^\top$ and $f \equiv 0$. The boundary conditions are given by $\frac{\partial u}{\partial n} = 0$ on $\partial\Omega_N = \{\mathbf{x} \in \partial\Omega \mid x_1 = 0\}$, $u = 1$ on $\partial\Omega_{D_1} = \{\mathbf{x} \in \partial\Omega \mid 0.4 \leq x_1 \leq 0.6, x_2 = 0, 0.4 \leq x_3 \leq 0.6\}$, and $u = 0$ on $\partial\Omega_{D_2} = \partial\Omega \setminus \{\partial\Omega_N \cup \partial\Omega_{D_1}\}$. Thus, by the boundary part $\partial\Omega_{D_1}$ we model an inflow region (area) where the transport quantity modelled by the unknown u is injected; cf. Fig. 3.13. $\partial\Omega_N$ models an outflow boundary. Prescribing a homogeneous Dirichlet condition on $\partial\Omega_{D_2}$ is only done for the sake of simplicity. The goal functional aims at the control of the solution's mean value in a smaller, inner domain $\Omega_{in} = [0, 0.1] \times [0.4, 0.6] \times [0.4, 0.6]$ close to the outflow boundary, and is given by*

$$J_{iM}(u) = \int_{\Omega_{in}} u \, d\mathbf{x}. \quad (3.49)$$

In the context of applications, the transport quantity u is thus measured and controlled in the small region of interest Ω_{in} .

In Fig. 3.13, we illustrate the computed adaptively generated meshes for some of the DWR iteration steps. For visualization purposes, two surfaces with corresponding mesh distribution are shown for each of the grids, the bottom surface and the surface in the domain's center with respect to the x_3 direction. We note that the postprocessed solutions are visualized on a grid for the respective surfaces. The cells on the surfaces are triangular-shaped since the underlying visualization software `ParaView` is based on triangular-shaped elements. Similar to the previous test case of a point-value error control, the refinement is located on those cells that contribute to the

mean value error control. Here, the cells close to the two inner layers aligned in the flow direction \mathbf{b} are strongly refined. This refinement process is obvious since the inner and control domain Ω_{in} is chosen to have exactly the same dimensions as the channel-like extension of the boundary segment $\partial\Omega_{D_1}$ along the flow direction into the domain Ω . Outside the inner domain Ω_{in} and the channel-like domain of transport the mesh cells are coarsened for an increasing number of DWR iteration steps.

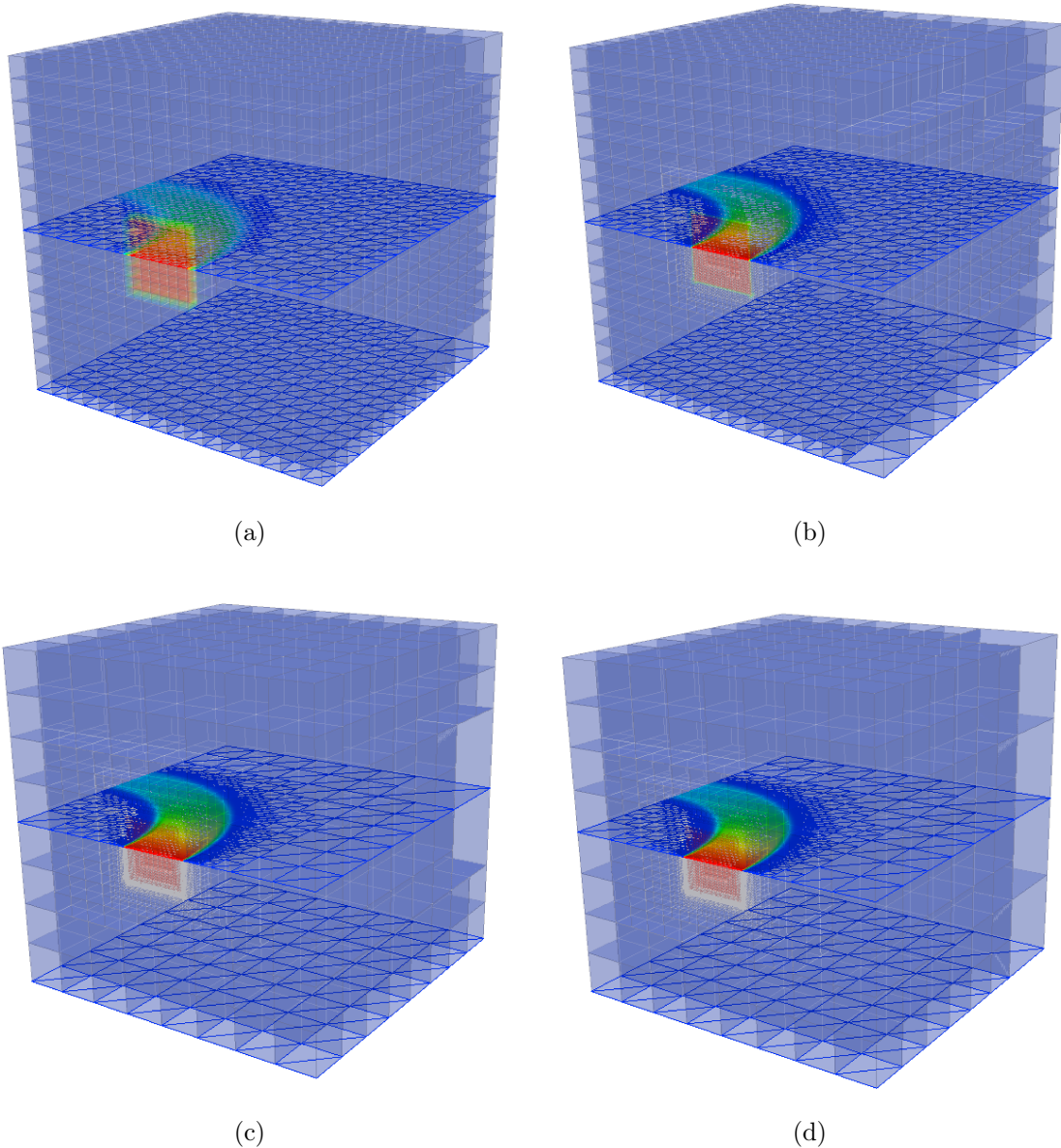


Figure 3.13: Adaptive spatial meshes after first (3.13a), third (3.13b), fifth (3.13c) and seventh (3.13d) iteration step of the DWR approach with coarsening and refinement, goal functional J_{iM} (3.49), $\varepsilon = 10^{-6}$, $\delta_0 = 1$, in Example 3.3.

Conclusion 3.3 (Efficient Mesh, 3d Case)

*We obtain very economical spatial meshes in the course of the refinement process even in **three space dimensions** regarding a **local** acting goal functional (3.49); cf. Fig. 3.13a–3.13d.*

3.4.4 Final Summary

With reference to the specific results outlined in Conclusions 3.1 and 3.2, we summarize the following. Error control for convection-dominated problems needs a particular care in regions with layers and sharp fronts in order to get an accurate quantification of the numerical errors. All examples could prove that spurious oscillations that typically arise in numerical approximations of convection-dominated problems could be reduced significantly. Robust effectivity indices that are almost one were obtained for different goal quantities. Sources of inaccuracies and non-sharp estimates were reduced and numerical artefacts were prevented mostly. The efficiency of the proposed approaches was demonstrated for two and even three space dimensions. Both approaches yield to efficient and accurate results for solving convection-dominated problems, whereas the FSTD approach showed slightly better results with regard to the so-called effectivity index as well as the reduction of the L^2 -error. In addition, the approximation using a higher-order finite element approach for the weights was significantly better than the common used approximation by higher-order interpolation with regard to accuracy and efficiency of the underlying error estimator as well as again the reduction of the L^2 -error.

Chapter 4

Goal-Oriented Error Control for Time-Dependent Convection-Dominated Problems

In this chapter, we present the application of goal-oriented error control based on the Dual Weighted Residual method to time-dependent convection-dominated transport problems. Generally spoken, these problems model the behavior of scalar quantities, like temperature, concentrations etc., that are transported within a flow field (convection), that undergo molecular transport (diffusion), and that might interact (react) with each other, cf., e.g., [116, 162]. There are several applications in many branches of technology to these problems, for instance, water pollution problems, the simulation of oil extraction from underground reservoirs, flows in chemical reactors or convective heat transport problems with large Péclet numbers, cf. [162] and the references therein. For a short review of convection-dominated problems including a list of references we refer to the main introduction. Furthermore, convection-dominated transport may be considered as a challenging subproblem in coupled problems, for instance, contaminant transport and degradation in the subsurface or the Biot's equations in poromechanics in which coupled transport with flow, chemical reaction and mechanical response in porous media is considered. In this sense, the present chapter can be seen as a transition transferring the knowledge and results of the previous chapter (Ch. 3) to time-dependent problems, and simultaneously serving as a preparation for the upcoming chapter (Ch. 5) dealing with coupled flow and transport problems.

We start by introducing the time-dependent convection-diffusion-reaction equation together with some global assumptions and general concepts including the underlying variational formulation. Then, we present the stabilized space-time discretiza-

tion schemes including a continuous (cG) as well as discontinuous (dG) discretization in time. Afterwards, we present the derivation of the related dual problems and splitted a posteriori error estimators with regard to both time discretizations. An important issue of this chapter takes the subsequent description of some practical aspects with regard to the underlying concepts of goal-oriented adaptivity as well as software architecture. Thereby, we introduce time marching schemes for the primal and dual problem, derive localized forms of the error estimators including different approaches for approximating the occurring temporal weights and present the goal-oriented space-time adaptive algorithm. Moreover, some implementational aspects and issues of the software are presented. The chapter is closed by some numerical experiments, in which we illustrate and investigate the performance properties of the underlying algorithm for time-dependent problems including convergence studies, independence of temporal and spatial error indicators, computational efficiency as well as stability properties.

Some parts of this chapter have been published by the author et al. in [51] and [129]. In this chapter we consider the following time-dependent convection-diffusion-reaction equation.

Problem 4.1 (Time-dependent Convection-Diffusion-Reaction Equation)

Find u from

$$\begin{aligned}
\partial_t u - \nabla \cdot (\varepsilon \nabla u) + \mathbf{b} \cdot \nabla u + \alpha u &= f \quad \text{in } Q = \Omega \times I, \\
u &= u_D \quad \text{on } \Sigma_D = \Gamma_D \times I, \\
\varepsilon \nabla u \cdot \mathbf{n} &= u_N \quad \text{on } \Sigma_N = \Gamma_N \times I, \\
u(0) &= u_0 \quad \text{on } \Sigma_0 = \Omega \times \{0\},
\end{aligned} \tag{4.1}$$

in the space-time domain Q , where $\Omega \subset \mathbb{R}^d$, with $d = 2$ or $d = 3$, is a polygonal or polyhedral bounded domain with Lipschitz boundary $\partial\Omega$ and $I = (0, T)$, $0 < T < \infty$, is a finite time interval. Here, $\partial\Omega = \Gamma_D \cup \Gamma_N$, $\Gamma_D \neq \emptyset$ denotes the partition of the boundary with outer unit normal vector \mathbf{n} , where Γ_D denotes the Dirichlet part and Γ_N the Neumann part, respectively. To ensure the well-posedness of Problem 4.1 we assume that $0 < \varepsilon \leq 1$ is a constant diffusion coefficient, $\mathbf{b} \in L^\infty(I; W^{1,\infty}(\Omega)^d)$ is the flow field or convection field, $\alpha \in L^\infty(I; L^\infty(\Omega))$ is a non-negative ($\alpha > 0$) reaction coefficient, $u_0 \in L^2(\Omega)$ is a given initial condition, $f \in L^2(I; H^{-1}(\Omega))$ is a given source of the unknown scalar quantity u , $u_D \in L^2(I; H^{\frac{1}{2}}(\Gamma_D))$ is a given function specifying the Dirichlet boundary condition, and $u_N \in L^2(I; H^{-\frac{1}{2}}(\Gamma_N))$ is a given function specifying the Neumann boundary condition.

Furthermore, it will be assumed that either $\nabla \cdot \mathbf{b}(\mathbf{x}, t) = 0$ and $\alpha(\mathbf{x}, t) \geq 0$, or there exists a positive constant c_0 such that

$$\alpha(\mathbf{x}, t) - \frac{1}{2} \operatorname{div} \mathbf{b}(\mathbf{x}, t) \geq c_0 > 0 \quad \forall (\mathbf{x}, t) \in \bar{\Omega} \times \bar{I},$$

which are standard assumptions for convection-dominated equations of type (4.1), cf., e.g., [3].

Henceforth, for the sake of simplicity, we deal with homogeneous Dirichlet boundary values $u_D = 0$ on $\Gamma_D = \partial\Omega$ only. In our numerical examples in Sec. 4.5, we also consider more general boundary conditions, whose incorporation is straightforward, as outlined in Rem. 4.14; cf., e.g., [92].

For the corresponding variational formulation we introduce the following function spaces as given in Def. 2.1 and Def. 2.2, respectively, of Sec. 2.1.

$$\begin{aligned} \mathcal{V} &:= \left\{ v \in L^2(I; V) \mid \partial_t v \in L^2(I; H^{-1}(\Omega)) \right\}, \\ V &:= H_0^1(\Omega). \end{aligned} \tag{4.2}$$

Problem 4.2 (Variational Formulation Primal Problem) Find $u \in \mathcal{V}$ such that

$$A(u)(\varphi) = F(\varphi) \quad \forall \varphi \in \mathcal{V}, \tag{4.3}$$

where the bilinear form $A : \mathcal{V} \times \mathcal{V} \rightarrow \mathbb{R}$ and the linear form $F : \mathcal{V} \rightarrow \mathbb{R}$ are defined by

$$A(u)(\varphi) := \int_I \{(\partial_t u, \varphi) + a(u)(\varphi)\} dt + (u(0), \varphi(0)), \tag{4.4}$$

$$F(\varphi) := \int_I (f, \varphi) dt + (u_0, \varphi(0)), \tag{4.5}$$

with the inner bilinear form $a : V \times V \rightarrow \mathbb{R}$, given by

$$a(u)(\varphi) := (\varepsilon \nabla u, \nabla \varphi) + (\mathbf{b} \cdot \nabla u, \varphi) + (\alpha u, \varphi). \tag{4.6}$$

We note that the initial condition is incorporated into the variational problem here.

Proposition 4.1 (Well-Posedness) Assume that $f \in L^2(I; H^{-1}(\Omega))$, $u_0 \in L^2(\Omega)$, $u_D \in L^2(I; H^{\frac{1}{2}}(\partial\Omega))$, $\varepsilon, \alpha \in L^\infty(I; L^\infty(\Omega))$, and $\mathbf{b} \in L^\infty(I; W^{1,\infty}(\Omega)^d)$. Then, the model problem (4.3) is well-posed.

Proof. The proof can be found in the literature, for instance, in [136, Thm. 2.1], [61, Thm. 2 in Ch. XVIII], [81, Ch. 7.1] or [79, Thm. 65.9]. \square

Remark 4.1 (Regularity) *With regard to sufficient regularity of the solution and test function we note the following.*

- *Beyond the assumption $u \in \mathcal{V}$ which is sufficient within the framework of the DWR approach, the existence of a sufficiently regular solution, such that all of the arguments and terms used below are well-defined, is tacitly assumed without mentioning explicitly all technical assumptions about the data and coefficients here. Technical details can be found, for instance, in [162, 116].*
- *We note that in Problem 4.2 it is sufficient to require the test functions φ to be in $L^2(I; V)$. Nevertheless, since \mathcal{V} is dense in $L^2(I; V)$ with respect to the norm of $L^2(I; V)$ (cf. Corollary 2.1 in Sec. 2.1.2 of Ch. 2) and with regard to the derivation of the so-called dual problems in the framework of the DWR approach, we deliberately decide to choose the test functions $\varphi \in \mathcal{V}$ here. Furthermore, we note that the expression $u(0)$ make sense for a function $u \in \mathcal{V}$, cf. Rem. 2.1 in Sec. 2.1.2.*

The weak formulation, given by Problem 4.2, is now the starting point for the variational discretization in space and time. Thereby, we start with the discretization in time leading to a finite set of coupled PDEs which is then discretized in space using the concepts introduced in Chapter 2. This approach is sometimes called Rothe’s method in the literature, cf. [79, Rem. 69.1]. For adaptivity reasons, it is desirable to allow the spatial meshes to change in time. This approach is referred to as the concept of dynamic meshes, cf. [168, 167]. For more details about the implementation features we refer to Sec. 4.4.

4.1 Stabilized Space-Time Discretizations

In this section, we describe the discretization in space and time of the weak formulation, given by Problem 4.2, by means of Galerkin finite element methods. We start with the semi-discretization in time by means of a continuous Petrov-Galerkin method as well as a discontinuous Galerkin method as introduced in Sec. 2.2. Afterwards, we present the stabilized discretization in space of the arising semi-discrete problems using continuous Galerkin finite element methods as introduced in Sec. 2.1.3. Here, we are using the approach of space-time slabs including a temporal triangulation that is allowed to have more than one cell in time on an associated time subinterval, cf. Assumption. 2.5. Therefore, the following considerations are done with respect to such

a cell in time (here denoted by K_n). Restricting the temporal triangulation to only one cell in time leads to the classical considerations with respect to a subinterval I_n , cf. Rem. 2.3.

4.1.1 Discretization in Time

For the discretization in time we assume a decomposition of the time interval I into subintervals I_n as given in Assumption 2.4. Thus, a separation of the global space-time domain $Q = \Omega \times I$ into a partition of space-time slabs $\hat{Q}_n = \Omega \times I_n$ is feasible, using a one-dimensional triangulation $\mathcal{T}_{\tau,n}$ (including cells in time K_n) for the discretization in time on each slab \hat{Q}_n as well as a set of all interior time points \mathcal{F}_τ as introduced in Assumption 2.5. In this sense, we introduce the finite-dimensional continuous time-discrete function space

$$\mathcal{V}_\tau^{\text{cG}(r)} := \left\{ v_\tau \in C(\bar{I}; V) \mid v_\tau|_{K_n} \in \mathcal{P}_\tau^r(\bar{K}_n; V), K_n \in \mathcal{T}_{\tau,n}, n = 1, \dots, N \right\}, \quad (4.7)$$

and the finite-dimensional discontinuous time-discrete function space

$$\mathcal{V}_\tau^{\text{dG}(r)} := \left\{ v_\tau \in L^2(I; V) \mid v_\tau|_{K_n} \in \mathcal{P}_\tau^r(K_n; V), \right. \\ \left. v_\tau(0) \in L^2(\Omega), K_n \in \mathcal{T}_{\tau,n}, n = 1, \dots, N \right\}, \quad (4.8)$$

as introduced in general by Eq. 2.3 and Eq. 2.9, respectively. In the following, we present the time-discrete variational schemes using the continuous in time Petrov-Galerkin method as well as the discontinuous in time Galerkin method. For more details about these methods including, for instance, the composition of the respective shape functions or the concept on the reference interval, we refer to Sec. 2.2.

Continuous in Time Petrov-Galerkin Method

The continuous in time Petrov-Galerkin method (cG(r)) method) approximates the solution in time continuously with piecewise polynomials of degree r , $r \geq 1$. It is referred to as Petrov-Galerkin method since the trial and test space are chosen differently. Let $\mathcal{V}_\tau^{\text{cG}(r)}$, given by Eq. (4.7), and $\mathcal{V}_\tau^{\text{dG}(r-1)}$, given by Eq. (4.8), be the finite-dimensional time-discrete trial and test space, respectively. Then, the continuous time-discrete variational approximation of Problem 4.2 reads as follows.

Problem 4.3 (Continuous Time-Discrete Scheme: cG(r))

Find $u_\tau \in \mathcal{V}_\tau^{\text{cG}(r)}$ such that

$$A_\tau^{\text{cG}}(u_\tau)(\varphi_\tau) = F_\tau(\varphi_\tau) \quad \forall \varphi_\tau \in \mathcal{V}_\tau^{\text{dG}(r-1)}, \quad (4.9)$$

where the bilinear form $A_\tau^{\text{cG}}(\cdot)(\cdot)$ and the linear form $F_\tau(\cdot)$ are given by

$$A_\tau^{\text{cG}}(u_\tau)(\varphi_\tau) := \sum_{n=1}^N \sum_{K_n \in \mathcal{T}_{\tau,n}} \int_{K_n} \{(\partial_t u_\tau, \varphi_\tau) + a(u_\tau)(\varphi_\tau)\} dt \quad (4.10)$$

$$+ (u_\tau(0), \varphi_\tau(0^+)),$$

$$F_\tau(\varphi_\tau) := \sum_{n=1}^N \sum_{K_n \in \mathcal{T}_{\tau,n}} \int_{K_n} (f, \varphi_\tau) dt + (u_0, \varphi_\tau(0^+)), \quad (4.11)$$

with the inner bilinear form $a(\cdot)(\cdot)$ being defined by Eq. (4.6).

Discontinuous in Time Galerkin Method

The discontinuous in time Galerkin method (dG(r) method) approximates the solution in time with piecewise polynomials of degree $r, r \geq 0$. The members of this method are characterized as discontinuous Galerkin methods since the trial space is chosen discontinuous in time here. Thus, the solution in time is allowed to be discontinuous between two slabs and, in particular, between two cells in time within a slab, but piecewise continuous within a single cell in time, cf. Fig. 2.5. In this sense, we define the limits $u_\tau(t_{\mathcal{F}}^\pm)$ from above and below as well as their jump at $t_{\mathcal{F}} \in \mathcal{F}_\tau$ by means of

$$u_\tau(t_{\mathcal{F}}^\pm) := \lim_{t \rightarrow t_{\mathcal{F}}^\pm} u_\tau(t), \quad [u_\tau]_{t_{\mathcal{F}}} := u_\tau(t_{\mathcal{F}}^+) - u_\tau(t_{\mathcal{F}}^-),$$

with \mathcal{F}_τ denoting the set of all interior time points given as

$$\mathcal{F}_\tau := (\{t_1, \dots, t_N\} \cup \{t \in \partial K_n \mid K_n \in \mathcal{T}_{\tau,n}\}) \setminus \{0, T\}.$$

Let $\mathcal{V}_\tau^{\text{dG}(r)}$, given by Eq. (4.8), be the common finite-dimensional time-discrete trial space and test space. Then, the discontinuous time-discrete variational approximation of Problem 4.2 reads as follows.

Problem 4.4 (Discontinuous Time-Discrete Scheme: dG(r))

Find $u_\tau \in \mathcal{V}_\tau^{\text{dG}(r)}$ such that

$$A_\tau^{\text{dG}}(u_\tau)(\varphi_\tau) = F_\tau(\varphi_\tau) \quad \forall \varphi_\tau \in \mathcal{V}_\tau^{\text{dG}(r)}, \quad (4.12)$$

where the linear form $F_\tau(\cdot)$ is defined by Eq. (4.11) and the bilinear form $A_\tau^{\text{dG}}(\cdot)(\cdot)$ is given by

$$A_\tau^{\text{dG}}(u_\tau)(\varphi_\tau) := \sum_{n=1}^N \sum_{K_n \in \mathcal{T}_{\tau,n}} \int_{K_n} \{(\partial_t u_\tau, \varphi_\tau) + a(u_\tau)(\varphi_\tau)\} dt \quad (4.13)$$

$$+ \sum_{t_{\mathcal{F}} \in \mathcal{F}_\tau} ([u_\tau]_{t_{\mathcal{F}}}, \varphi_\tau(t_{\mathcal{F}}^+)) + (u_\tau(0^+), \varphi_\tau(0^+)),$$

with the inner bilinear form $a(\cdot)(\cdot)$ being defined by Eq. (4.6).

4.1.2 Discretization in Space

In this section, we describe the Galerkin finite element approximation in space of the semi-discrete Problems 4.3 and 4.4, respectively. Thereby, we use the concepts introduced in Sec. 2.1.3, where all details can be found that are not specified in the following. We use Lagrange type finite element spaces of continuous functions that are piecewise polynomials. For the discretization in space, we consider a separation $Q_n = \mathcal{T}_{h,n} \times \mathcal{T}_{\tau,n}$, where $\mathcal{T}_{h,n}$ build a decomposition of the domain Ω into disjoint spatial elements K as given in Assumption 2.3 and 2.5, respectively. Our mesh adaptation process includes locally refined cells, which is enabled by allowing so-called hanging nodes. For this purpose, we assume the decomposition $\mathcal{T}_{h,n}$ (in the following also referred to as spatial triangulation) to be regular and organized in a patch-wise manner, cf. Def. 2.5 and Def. 2.6, respectively. We point out that the global conformity of the finite element approach is preserved since the unknowns at such hanging nodes are eliminated by interpolation between the neighboring 'regular' nodes, cf. Rem. 2.2.

So far, the spaces $\mathcal{V}_\tau^{\text{cG}(r)}$ and $\mathcal{V}_\tau^{\text{dG}(r)}$ still contain the continuous spatial space $V = H_0^1(\Omega)$. Thus, we introduce the discrete finite element spaces $V_h^{p,n} \subset V$ on $\mathcal{T}_{h,n}$, $n = 1, \dots, N$, with V_h^p being defined by Eq. (2.1) in Sec. 2.1.3. Now, by replacing V by $V_h^{p,n}$ in the definition of the semi-discrete function spaces $\mathcal{V}_\tau^{\text{cG}(r)}$ and $\mathcal{V}_\tau^{\text{dG}(r)}$, respectively, we obtain the fully discrete function spaces

$$\begin{aligned} \mathcal{V}_{\tau h}^{\text{cG}(r),p} &:= \left\{ v_{\tau h} \in \mathcal{V}_\tau^{\text{cG}(r)} \mid v_{\tau h}|_{K_n} \in \mathcal{P}_\tau^r(\bar{K}_n; V_h^{p,n}), K_n \in \mathcal{T}_{\tau,n}, n = 1, \dots, N \right\}, \\ \mathcal{V}_{\tau h}^{\text{dG}(r),p} &:= \left\{ v_{\tau h} \in \mathcal{V}_\tau^{\text{dG}(r)} \mid v_{\tau h}|_{K_n} \in \mathcal{P}_\tau^r(K_n; V_h^{p,n}), \right. \\ &\quad \left. v_{\tau h}(0) \in V_h^{p,1}, K_n \in \mathcal{T}_{\tau,n}, n = 1, \dots, N \right\}, \end{aligned} \quad (4.14)$$

with $\mathcal{V}_{\tau h}^{\text{cG}(r),p} \subset \mathcal{V}_\tau^{\text{cG}(r)}$ and $\mathcal{V}_{\tau h}^{\text{dG}(r),p} \subset \mathcal{V}_\tau^{\text{dG}(r)}$. We note that the spatial finite element space $V_h^{p,n}$ is allowed to be different on all slabs Q_n which is natural in the context of a discontinuous Galerkin approximation of the time variable and allows for dynamic mesh changes in time. Then, the fully discrete continuous in time as well as discontinuous in time schemes of Problem 4.2 can be easily obtained from the cG(r) and dG(r) semi-discretization schemes, given by Eq. (4.9) and Eq. (4.12), respectively, by simply adding the additional index h to the variables and by replacing the respective semi-discrete spaces by the above defined fully discrete counterparts. For the sake of completeness, the fully discrete continuous in time scheme then reads as follows.

Problem 4.5 (Fully Discrete Continuous in Time Scheme: cG(p)-cG(r))

Find $u_{\tau h} \in \mathcal{V}_{\tau h}^{\text{cG}(r),p}$ such that

$$A_{\tau}^{\text{cG}}(u_{\tau h})(\varphi_{\tau h}) = F_{\tau}(\varphi_{\tau h}) \quad \forall \varphi_{\tau h} \in \mathcal{V}_{\tau h}^{\text{dG}(r-1),p}, \quad (4.15)$$

with $A_{\tau}^{\text{cG}}(\cdot)(\cdot)$ and $F_{\tau}(\cdot)$ being defined by Eq. (4.10) and Eq. (4.11), respectively.

Finally, the fully discrete discontinuous in time scheme then reads as follows.

Problem 4.6 (Fully Discrete Discontinuous in Time Scheme: cG(p)-dG(r))

Find $u_{\tau h} \in \mathcal{V}_{\tau h}^{\text{dG}(r),p}$ such that

$$A_{\tau}^{\text{dG}}(u_{\tau h})(\varphi_{\tau h}) = F_{\tau}(\varphi_{\tau h}) \quad \forall \varphi_{\tau h} \in \mathcal{V}_{\tau h}^{\text{dG}(r),p}, \quad (4.16)$$

with $A_{\tau}^{\text{dG}}(\cdot)(\cdot)$ and $F_{\tau}(\cdot)$ being defined by Eq. (4.13) and Eq. (4.11), respectively.

Remark 4.2 The notations cG(p)-dG(r) and cG(p)-cG(r) for a space-time finite element Galerkin discretization with continuous piecewise polynomials of degree p in space and discontinuous (dG) or continuous (cG), respectively, piecewise polynomials of degree r in time is taken from [77, 40].

4.1.3 Stabilization

In this work, we focus on convection-dominated problems with small diffusion parameter ε . Then, the finite element approximation needs to be stabilized in order to reduce spurious and non-physical oscillations of the discrete solution arising close to layers. Here, we apply the streamline upwind Petrov-Galerkin (SUPG) method [106, 49], that was introduced in Sec. 2.4. Existing convergence analyses in the natural norm of the underlying scheme including local and global error bounds can be found, for instance, in [147] and [162, Ch. III.4.3]. The stabilized variant of the fully discrete continuous in time scheme (cG(p)-cG(r) scheme), given by Problem 4.5, then reads as follows.

Problem 4.7 (Stabilized cG(p)-cG(r) Scheme)

Find $u_{\tau h} \in \mathcal{V}_{\tau h}^{\text{cG}(r),p}$ such that

$$A_S^{\text{cG}}(u_{\tau h})(\varphi_{\tau h}) = F_{\tau}(\varphi_{\tau h}) \quad \forall \varphi_{\tau h} \in \mathcal{V}_{\tau h}^{\text{dG}(r-1),p}, \quad (4.17)$$

where the linear form $F_{\tau}(\cdot)$ is defined by Eq. (4.11) and the stabilized bilinear form $A_S^{\text{cG}}(\cdot)(\cdot)$ is given by

$$A_S^{\text{cG}}(u_{\tau h})(\varphi_{\tau h}) := A_{\tau}^{\text{cG}}(u_{\tau h})(\varphi_{\tau h}) + S_A^{\text{cG}}(u_{\tau h})(\varphi_{\tau h}). \quad (4.18)$$

Here, the SUPG stabilization bilinear form $S_A^{\text{cG}}(\cdot)(\cdot)$ is defined by

$$\begin{aligned} S_A^{\text{cG}}(u_{\tau h})(\varphi_{\tau h}) &:= \sum_{n=1}^N \sum_{K_n \in \mathcal{T}_{\tau,n}} \int_{K_n} \sum_{K \in \mathcal{T}_{h,n}} \delta_K(r(u_{\tau h}), \mathbf{b} \cdot \nabla \varphi_{\tau h})_K dt \\ &+ \sum_{K \in \mathcal{T}_{h,1}} \delta_K(u_{\tau h}(0) - u_0, \mathbf{b} \cdot \nabla \varphi_{\tau h}(0^+))_K, \end{aligned} \quad (4.19)$$

where δ_K is the so-called stabilization parameter (cf. Rem. 4.3) and the residual term $r(\cdot)$ is given by

$$r(u_{\tau h}) := \partial_t u_{\tau h} - \nabla \cdot (\varepsilon \nabla u_{\tau h}) + \mathbf{b} \cdot \nabla u_{\tau h} + \alpha u_{\tau h} - f. \quad (4.20)$$

In contrast, the stabilized variant of the fully discrete discontinuous in time scheme (cG(p)-dG(r) scheme), given by Problem 4.6, reads as:

Problem 4.8 (Stabilized cG(p)-dG(r) Scheme)

Find $u_{\tau h} \in \mathcal{V}_{\tau h}^{\text{dG}(r),p}$ such that

$$A_S^{\text{dG}}(u_{\tau h})(\varphi_{\tau h}) = F_{\tau}(\varphi_{\tau h}) \quad \forall \varphi_{\tau h} \in \mathcal{V}_{\tau h}^{\text{dG}(r),p}, \quad (4.21)$$

where the linear form $F_{\tau}(\cdot)$ is defined by Eq. (4.11) and the stabilized bilinear form $A_S^{\text{dG}}(\cdot)(\cdot)$ is given by

$$A_S^{\text{dG}}(u_{\tau h})(\varphi_{\tau h}) := A_{\tau}^{\text{dG}}(u_{\tau h})(\varphi_{\tau h}) + S_A^{\text{dG}}(u_{\tau h})(\varphi_{\tau h}). \quad (4.22)$$

Here, the SUPG stabilization bilinear form $S_A^{\text{dG}}(\cdot)(\cdot)$ is defined by

$$\begin{aligned} S_A^{\text{dG}}(u_{\tau h})(\varphi_{\tau h}) &:= \sum_{n=1}^N \sum_{K_n \in \mathcal{T}_{\tau,n}} \int_{K_n} \sum_{K \in \mathcal{T}_{h,n}} \delta_K(r(u_{\tau h}), \mathbf{b} \cdot \nabla \varphi_{\tau h})_K dt \\ &+ \sum_{t_{\mathcal{F}} \in \mathcal{F}_{\tau}} \sum_{K \in \mathcal{T}_{h,n}} \delta_K([u_{\tau h}]_{t_{\mathcal{F}}}, \mathbf{b} \cdot \nabla \varphi_{\tau h}(t_{\mathcal{F}}^+))_K \\ &+ \sum_{K \in \mathcal{T}_{h,1}} \delta_K(u_{\tau h}(0^+) - u_0, \mathbf{b} \cdot \nabla \varphi_{\tau h}(0^+))_K, \end{aligned} \quad (4.23)$$

where the residual term $r(\cdot)$ is defined by Eq. (4.20).

Remark 4.3 For time-dependent convection-diffusion-reaction problems an optimal error estimate for $\delta_K = \mathcal{O}(h_K)$ is derived in [118]. We also refer to Rem. 3.2 in Sec. 3.1 for a steady-state convection-diffusion-reaction problem.

4.2 DWR-Based A Posteriori Error Estimation

In this section, we derive an a posteriori error estimator for the stabilized continuous in time and discontinuous in time transport problems (4.17) and (4.21), respectively. This estimator measures the discretization errors in an output value J and serves as a key ingredient in setting up the adaptive algorithm described in the following section. The output value J is called goal functional and fulfills the following properties.

Assumption 4.1 (Goal Functional) *Let us assume $J : \mathcal{V} \rightarrow \mathbb{R}$ to be a linear functional representing the goal quantity of physical interest. In general, this functional is given as*

$$J(u) = \int_0^T J_1(u(t)) \, dt + J_2(u(T)), \quad (4.24)$$

where $J_1 \in L^2(I; H^{-1}(\Omega))$ and $J_2 \in H^{-1}(\Omega)$ are three times differentiable functionals defining the dual right-hand side and the dual initial at time $t = T$, respectively, where each of them may be zero; cf. also Rem. 4.5.

In practice, the quantity of interest represents, for instance, a mean value of a given functional (J_1) or a final time-point value $J_2(u(T))$; cf., e.g., [168, 36, 20].

Since we consider time-dependent problems in this chapter, we aim at controlling the respective errors due to the discretization in time as well as in space. Therefore, we split the a posteriori error representation with respect to J into the contributions

$$J(u) - J(u_{\tau h}) = J(u) - J(u_\tau) + J(u_\tau) - J(u_{\tau h}). \quad (4.25)$$

The derivation of an error estimator is based on the Euler Lagrange method of constraint optimization as introduced in Sec. 2.5, using the following functionals.

Definition 4.1 (Lagrangian Functionals)

The Lagrangian functionals $\mathcal{L} : \mathcal{V} \times \mathcal{V} \rightarrow \mathbb{R}$, $\mathcal{L}_\tau : \mathcal{V}_\tau^{\text{dG}(r)} \times \mathcal{V}_\tau^{\text{dG}(r)} \rightarrow \mathbb{R}$, $\mathcal{L}_{\tau h}^{\text{cG}} : \mathcal{V}_{\tau h}^{\text{cG}(r),p} \times \mathcal{V}_{\tau h}^{\text{dG}(r-1),p} \rightarrow \mathbb{R}$, and $\mathcal{L}_{\tau h} : \mathcal{V}_{\tau h}^{\text{dG}(r),p} \times \mathcal{V}_{\tau h}^{\text{dG}(r),p} \rightarrow \mathbb{R}$ are defined by

$$\mathcal{L}(u, z) := J(u) + F(z) - A(u)(z), \quad (4.26)$$

$$\mathcal{L}_\tau(u_\tau, z_\tau) := J(u_\tau) + F_\tau(z_\tau) - A_\tau^{\text{dG}}(u_\tau)(z_\tau), \quad (4.27)$$

$$\begin{aligned} \mathcal{L}_{\tau h}^{\text{cG}}(u_{\tau h}, z_{\tau h}) &:= J(u_{\tau h}) + F_\tau(z_{\tau h}) - A_S^{\text{cG}}(u_{\tau h})(z_{\tau h}) \\ &= \mathcal{L}(u_{\tau h}, z_{\tau h}) - \mathcal{S}^{\text{cG}}(u_{\tau h}, z_{\tau h}), \end{aligned} \quad (4.28)$$

$$\begin{aligned} \mathcal{L}_{\tau h}(u_{\tau h}, z_{\tau h}) &:= J(u_{\tau h}) + F_\tau(z_{\tau h}) - A_S^{\text{dG}}(u_{\tau h})(z_{\tau h}) \\ &= \mathcal{L}_\tau(u_{\tau h}, z_{\tau h}) - \mathcal{S}^{\text{dG}}(u_{\tau h}, z_{\tau h}), \end{aligned} \quad (4.29)$$

with

$$\mathcal{S}^{\text{cG}}(u_{\tau h}, z_{\tau h}) := S_A^{\text{cG}}(u_{\tau h})(z_{\tau h}), \quad \mathcal{S}^{\text{dG}}(u_{\tau h}, z_{\tau h}) := S_A^{\text{dG}}(u_{\tau h})(z_{\tau h}), \quad (4.30)$$

where $S_A^{\text{cG}}(\cdot)(\cdot)$ and $S_A^{\text{dG}}(\cdot)(\cdot)$ are given by Eq. (4.19) and Eq. (4.23), respectively.

Remark 4.4 *The Lagrange multipliers z , z_τ , and $z_{\tau h}$ are called dual variables in contrast to the primal variables u , u_τ , and $u_{\tau h}$, cf. [36, 40]. Furthermore, we note that by using the respective Lagrangian functionals from above, we can express the functional values of the continuous, semi-discrete, and fully discrete solution in the case of a continuous in time discretization (cG(r)) by means of*

$$\begin{aligned} J(u) &:= \mathcal{L}(u, \varphi) & \forall \varphi \in \mathcal{V}, \\ J(u_\tau) &:= \mathcal{L}(u_\tau, \varphi_\tau) & \forall \varphi_\tau \in \mathcal{V}_\tau^{\text{dG}(r-1)}, \\ J(u_{\tau h}) &:= \mathcal{L}_{\tau h}^{\text{cG}}(u_{\tau h}, \varphi_{\tau h}) & \forall \varphi_{\tau h} \in \mathcal{V}_{\tau h}^{\text{dG}(r-1), p}. \end{aligned} \quad (4.31)$$

In the case of a discontinuous in time discretization (dG(r)), we have to replace the second and third equation in (4.31) by means of

$$\begin{aligned} J(u_\tau) &:= \mathcal{L}_\tau(u_\tau, \varphi_\tau) & \forall \varphi_\tau \in \mathcal{V}_\tau^{\text{dG}(r)}, \\ J(u_{\tau h}) &:= \mathcal{L}_{\tau h}(u_{\tau h}, \varphi_{\tau h}) & \forall \varphi_{\tau h} \in \mathcal{V}_{\tau h}^{\text{dG}(r), p}. \end{aligned} \quad (4.32)$$

4.2.1 Derivation of the Dual Schemes

Since the main focus in our numerical examples in Sec. 4.5 is on a discontinuous in time discretization, we put emphasis on this time discretization from now on. In addition, we will also refer to the respective considerations using a continuous in time discretization.

4.2.1.1 Discontinuous in Time Discretization

As mentioned in the introductory Sec. 2.5, the DWR approach can be embedded into an optimal control problem by exploiting the Euler Lagrange method of constraint optimization. In this sense, we point out that the following optimality or stationary conditions, given by the directional derivatives of the Lagrangian functionals with respect to their second argument,

$$\begin{aligned} \mathcal{L}'_z(u, z)(\varphi) &= 0 & \forall \varphi \in \mathcal{V}, \\ \mathcal{L}'_{\tau, z}(u_\tau, z_\tau)(\varphi_\tau) &= 0 & \forall \varphi_\tau \in \mathcal{V}_\tau^{\text{dG}(r)}, \\ \mathcal{L}'_{\tau h, z}(u_{\tau h}, z_{\tau h})(\varphi_{\tau h}) &= 0 & \forall \varphi_{\tau h} \in \mathcal{V}_{\tau h}^{\text{dG}(r), p}, \end{aligned} \quad (4.33)$$

can be identified with determining the continuous solution u of Eq. (4.3), the semi-discrete solution u_τ of the discontinuous time-discrete scheme, given by Eq. (4.12), and the fully discrete solution $u_{\tau h}$ of the cG(p)-dG(r) discretization scheme, given by Eq. (4.21), respectively. More precisely, in Eq. (4.33) the so-called Gâteaux derivatives are used, given by Def. 2.11 in Sec. 2.3. In order to enhance understanding, we recall here its definition, exemplarily with respect to the second argument.

$$\mathcal{L}'_z(u, z)(\varphi) := \lim_{t \neq 0, t \rightarrow 0} t^{-1} \{ \mathcal{L}(u, z + t\varphi) - \mathcal{L}(u, z) \}, \quad \varphi \in \mathcal{V}.$$

In contrast, considering the directional derivatives of the Lagrangian functionals with respect to their first argument lead to the dual problems, cf., e.g., [40], given by the following optimality or stationary conditions.

$$\begin{aligned} \mathcal{L}'_u(u, z)(\psi) &= 0 \quad \forall \psi \in \mathcal{V}, \\ \mathcal{L}'_{\tau, u}(u_\tau, z_\tau)(\psi_\tau) &= 0 \quad \forall \psi_\tau \in \mathcal{V}_\tau^{\text{dG}(r)}, \\ \mathcal{L}'_{\tau h, u}(u_{\tau h}, z_{\tau h})(\psi_{\tau h}) &= 0 \quad \forall \psi_{\tau h} \in \mathcal{V}_{\tau h}^{\text{dG}(r), p}, \end{aligned} \tag{4.34}$$

More precisely, the continuous dual solution $z \in \mathcal{V}$ fulfills the following problem.

Problem 4.9 (Dual Problem) *Find $z \in \mathcal{V}$ such that*

$$A'(u)(\psi, z) = J'(u)(\psi) \quad \forall \psi \in \mathcal{V}, \tag{4.35}$$

where the adjoint bilinear form $A'(\cdot)(\cdot, \cdot)$ is given by

$$A'(u)(\psi, z) := \int_I \{ (\psi, -\partial_t z) + a'(u)(\psi, z) \} dt + (\psi(T), z(T)). \tag{4.36}$$

The right-hand side of Eq. (4.35) is given by

$$J'(u)(\psi) := \int_I J'_1(u)(\psi) dt + J'_2(u(T))(\psi(T)). \tag{4.37}$$

Remark 4.5 *We note that for the representation (4.36) of $A'(\cdot)(\cdot, \cdot)$ integration by parts in time is applied along with switching test and trial functions, given by*

$$\int_I (\partial_t \psi, z) dt = \int_I (\psi, -\partial_t z) dt + (\psi(T), z(T)) - (\psi(0), z(0)),$$

which is allowed for weak solutions $z \in \mathcal{V}$; cf., e.g., [160, 187] and Thm. 2.2 in Sec. 2.1.2 of Ch. 2. Therefore, the dual solution can be thought of running backward in time. Furthermore, we note that right-hand side as well as initial or better final data at time $t = T$ are given by the goal functional (4.24). More precisely, J_1 defines

the dual right-hand side, whereas J_2 defines the dual initial at time $t = T$. Then, as combination with the above introduced integration by parts in time there holds, cf. [160],

$$(\psi(T), z(T)) = J_2'(u(T))(\psi(T)).$$

Finally, the derivative $a'(u)(\psi, z)$ of the inner bilinear form $a(u)(z)$ in A' , defined by Eq. (4.6), admits the explicit form

$$a'(u)(\psi, z) = (\varepsilon \nabla \psi, \nabla z) + (\mathbf{b} \cdot \nabla \psi, z) + (\alpha \psi, z). \quad (4.38)$$

The second stationary condition of Eq. (4.34) yields the following dual semi-discrete discontinuous in time problem:

Problem 4.10 (Dual Discontinuous Time-Discrete Scheme: dG(r))

Find $z_\tau \in \mathcal{V}_\tau^{\text{dG}(r)}$ such that

$$A_\tau^{\text{dG}'}(u_\tau)(\psi_\tau, z_\tau) = J'(u_\tau)(\psi_\tau) \quad \forall \psi_\tau \in \mathcal{V}_\tau^{\text{dG}(r)}, \quad (4.39)$$

where the adjoint bilinear form $A_\tau^{\text{dG}'(\cdot)}(\cdot, \cdot)$ is defined by

$$\begin{aligned} A_\tau^{\text{dG}'}(u_\tau)(\psi_\tau, z_\tau) := & \sum_{n=1}^N \sum_{K_n \in \mathcal{T}_{\tau,n}} \int_{K_n} \{(\psi_\tau, -\partial_t z_\tau) + a'(u_\tau)(\psi_\tau, z_\tau)\} dt \\ & - \sum_{t_{\mathcal{F}} \in \mathcal{F}_\tau} (\psi_\tau(t_{\mathcal{F}}^-), [z_\tau]_{t_{\mathcal{F}}}) + (\psi_\tau(T^-), z_\tau(T^-)), \end{aligned} \quad (4.40)$$

with the dual inner bilinear form $a'(\cdot)(\cdot, \cdot)$ being defined by Eq. (4.38). The right-hand side of Eq. (4.39) is given by

$$J'(u_\tau)(\psi_\tau) := \sum_{n=1}^N \sum_{K_n \in \mathcal{T}_{\tau,n}} \int_{K_n} J_1'(u_\tau)(\psi_\tau) dt + J_2'(u_\tau(T^-))(\psi_\tau(T^-)). \quad (4.41)$$

The third stationary condition of Eq. (4.34) yields the dual stabilized fully discrete discontinuous in time problem:

Problem 4.11 (Dual Stabilized cG(p)-dG(r) Scheme)

Find $z_{\tau h} \in \mathcal{V}_{\tau h}^{\text{dG}(r),p}$ such that

$$A_S^{\text{dG}'}(u_{\tau h})(\psi_{\tau h}, z_{\tau h}) = J'(u_{\tau h})(\psi_{\tau h}) \quad \forall \psi_{\tau h} \in \mathcal{V}_{\tau h}^{\text{dG}(r),p}, \quad (4.42)$$

where the stabilized adjoint bilinear form $A_S^{\text{dG}'(\cdot)}(\cdot, \cdot)$ is defined by

$$A_S^{\text{dG}'}(u_{\tau h})(\psi_{\tau h}, z_{\tau h}) := A_\tau^{\text{dG}'}(u_{\tau h})(\psi_{\tau h}, z_{\tau h}) + S_A^{\text{dG}'}(u_{\tau h})(\psi_{\tau h}, z_{\tau h}), \quad (4.43)$$

with $A_\tau^{\text{dG}'(\cdot)}(\cdot, \cdot)$ given by Eq. (4.40). The right-hand side of Eq. (4.42) is given by

$$J'(u_{\tau h})(\psi_{\tau h}) := \sum_{n=1}^N \sum_{K_n \in \mathcal{T}_{\tau,n}} \int_{K_n} J'_1(u_{\tau h})(\psi_{\tau h}) dt + J'_2(u_{\tau h}(T^-))(\psi_{\tau h}(T^-)). \quad (4.44)$$

Here, the adjoint SUPG stabilization bilinear form $S_A^{\text{dG}'(\cdot)}(\cdot, \cdot)$ is defined by

$$\begin{aligned} S_A^{\text{dG}'(\cdot)}(u_{\tau h})(\psi_{\tau h}, z_{\tau h}) := & \sum_{n=1}^N \sum_{K_n \in \mathcal{T}_{\tau,n}} \int_{K_n} \sum_{K \in \overline{\mathcal{T}}_{h,n}} \delta_K \left\{ (\mathbf{b} \cdot \nabla \psi_{\tau h}, \partial_t z_{\tau h})_K \right. \\ & \left. - (\nabla \cdot (\varepsilon \nabla \psi_{\tau h}) - \mathbf{b} \cdot \nabla \psi_{\tau h} - \alpha \psi_{\tau h}, \mathbf{b} \cdot \nabla z_{\tau h})_K \right\} dt \\ & + \sum_{t_{\mathcal{F}} \in \mathcal{F}_\tau} \sum_{K \in \overline{\mathcal{T}}_{h,n}} \delta_K (\mathbf{b} \cdot \nabla \psi_{\tau h}(t_{\mathcal{F}}^-), [z_{\tau h}]_{t_{\mathcal{F}}})_K \\ & - \sum_{K \in \overline{\mathcal{T}}_{h,N}} \delta_K (\mathbf{b} \cdot \nabla \psi_{\tau h}(T^-), z_{\tau h}(T^-))_K. \end{aligned} \quad (4.45)$$

Here, again integration by parts in time is applied together with Green's formula and the condition $\nabla \cdot \mathbf{b} = 0$ as assumed in Problem 4.1.

4.2.1.2 Continuous in Time Discretization

In the case of a continuous in time cG(r) discretization, the semi-discrete solution u_τ of the cG(r) discretization in time, given by Eq. (4.9), and the fully discrete solution $u_{\tau h}$ of the cG(p)-cG(r) discretization, given by Eq. (4.17), respectively, can be identified with the following optimality or stationary conditions

$$\begin{aligned} \mathcal{L}'_z(u_\tau, z_\tau)(\varphi_\tau) &= 0 \quad \forall \varphi_\tau \in \mathcal{V}_\tau^{\text{dG}(r-1)}, \\ \mathcal{L}'_{\tau h, z}(u_{\tau h}, z_{\tau h})(\varphi_{\tau h}) &= 0 \quad \forall \varphi_{\tau h} \in \mathcal{V}_{\tau h}^{\text{dG}(r-1), p}. \end{aligned} \quad (4.46)$$

For identifying the discrete dual problems in the case of a continuous in time cG(r) discretization, the last two equations in (4.34) have to be replaced by the following stationary conditions

$$\begin{aligned} \mathcal{L}'_u(u_\tau, z_\tau)(\psi_\tau) &= 0 \quad \forall \psi_\tau \in \mathcal{V}_\tau^{\text{cG}(r)}, \\ \mathcal{L}'_{\tau h, u}(u_{\tau h}, z_{\tau h})(\psi_{\tau h}) &= 0 \quad \forall \psi_{\tau h} \in \mathcal{V}_{\tau h}^{\text{cG}(r), p}, \end{aligned} \quad (4.47)$$

that can be identified with the following semi-discrete and fully discrete continuous in time problems, respectively. Note that the role of trial and test spaces are switched.

Problem 4.12 (Dual Continuous Time-Discrete Scheme: cG(r))

Find $z_\tau \in \mathcal{V}_\tau^{\text{dG}(r-1)}$ such that

$$A_\tau^{\text{cG}'(\cdot)}(u_\tau)(\psi_\tau, z_\tau) = J'(u_\tau)(\psi_\tau) \quad \forall \psi_\tau \in \mathcal{V}_\tau^{\text{cG}(r)}, \quad (4.48)$$

where the adjoint bilinear form $A_\tau^{\text{cG}'(\cdot)}(\cdot, \cdot)$ is defined by

$$\begin{aligned} A_\tau^{\text{cG}'(\cdot)}(\psi_\tau, z_\tau) &:= \sum_{n=1}^N \sum_{K_n \in \mathcal{T}_{\tau,n}} \int_{K_n} \{(\psi_\tau, -\partial_t z_\tau) + a'(u_\tau)(\psi_\tau, z_\tau)\} dt \\ &\quad - \sum_{t_{\mathcal{F}} \in \mathcal{F}_\tau} (\psi_\tau(t_{\mathcal{F}}^-), [z_\tau]_{t_{\mathcal{F}}}) + (\psi_\tau(T^-), z_\tau(T^-)), \end{aligned} \quad (4.49)$$

with the dual inner bilinear form $a'(\cdot)(\cdot, \cdot)$ being defined by Eq. (4.38). The right-hand side of Eq. (4.48) is given by

$$J'(u_\tau)(\psi_\tau) := \sum_{n=1}^N \sum_{K_n \in \mathcal{T}_{\tau,n}} \int_{K_n} J'_1(u_\tau)(\psi_\tau) dt + J'_2(u_\tau(T))(\psi_\tau(T^-)). \quad (4.50)$$

Problem 4.13 (Dual Stabilized cG(p)-cG(r) Scheme)

Find $z_{\tau h} \in \mathcal{V}_{\tau h}^{\text{dG}(r-1),p}$ such that

$$A_S^{\text{cG}'(\cdot)}(u_{\tau h})(\psi_{\tau h}, z_{\tau h}) = J'(u_{\tau h})(\psi_{\tau h}) \quad \forall \psi_{\tau h} \in \mathcal{V}_{\tau h}^{\text{cG}(r),p}, \quad (4.51)$$

where the stabilized adjoint bilinear form $A_S^{\text{cG}'(\cdot)}(\cdot, \cdot)$ is defined by

$$A_S^{\text{cG}'(\cdot)}(u_{\tau h})(\psi_{\tau h}, z_{\tau h}) := A_\tau^{\text{cG}'(\cdot)}(u_{\tau h})(\psi_{\tau h}, z_{\tau h}) + S_A^{\text{cG}'(\cdot)}(u_{\tau h})(\psi_{\tau h}, z_{\tau h}), \quad (4.52)$$

with $A_\tau^{\text{cG}'(\cdot)}(\cdot, \cdot)$ given by Eq. (4.49). The right-hand side of Eq. (4.51) is given by

$$J'(u_{\tau h})(\psi_{\tau h}) := \sum_{n=1}^N \sum_{K_n \in \mathcal{T}_{\tau,n}} \int_{K_n} J'_1(u_{\tau h})(\psi_{\tau h}) dt + J'_2(u_{\tau h}(T))(\psi_{\tau h}(T^-)). \quad (4.53)$$

Here, the adjoint SUPG stabilization bilinear form $S_A^{\text{cG}'(\cdot)}(\cdot, \cdot)$ is defined by

$$\begin{aligned} S_A^{\text{cG}'(\cdot)}(u_{\tau h})(\psi_{\tau h}, z_{\tau h}) &:= \sum_{n=1}^N \sum_{K_n \in \mathcal{T}_{\tau,n}} \int_{K_n} \sum_{K \in \mathcal{T}_{h,n}} \delta_K \left\{ (\mathbf{b} \cdot \nabla \psi_{\tau h}, \partial_t z_{\tau h})_K \right. \\ &\quad \left. - (\nabla \cdot (\varepsilon \nabla \psi_{\tau h}) - \mathbf{b} \cdot \nabla \psi_{\tau h} - \alpha \psi_{\tau h}, \mathbf{b} \cdot \nabla z_{\tau h})_K \right\} dt \\ &\quad + \sum_{t_{\mathcal{F}} \in \mathcal{F}_\tau} \sum_{K \in \mathcal{T}_{h,n}} \delta_K (\mathbf{b} \cdot \nabla \psi_{\tau h}(t_{\mathcal{F}}^-), [z_{\tau h}]_{t_{\mathcal{F}}})_K \\ &\quad - \sum_{K \in \mathcal{T}_{h,N}} \delta_K (\mathbf{b} \cdot \nabla \psi_{\tau h}(T^-), z_{\tau h}(T^-))_K. \end{aligned} \quad (4.54)$$

Remark 4.6 We note that the discrete dual problems decouple to a time stepping method running backward in time, as given by Problem 4.12 and Problem 4.13, respectively, by switching test and trial functions with integration by parts in time as mentioned in Rem.4.5; cf. [160, Lemma 8.9].

Remark 4.7 *We note that the presented derivation of the dual schemes can be interpreted as an FSTD approach, since the continuous and discontinuous in time stabilized fully discrete schemes, given by Problem 4.11 and Problem 4.13, respectively, are derived with the help of the adjoint of the stabilized fully discrete primal operator that is included in the respective Lagrangian functionals; cf. also Sec. 3.2.1 of the previous chapter. This approach requires differentiation of the stabilization terms and may lead to numerically unstable dual problems, cf. [20, Ch. 11] and [31]. However, in our numerical examples considered in Sec. 4.5 we could not observe any stability problems with regard to the dual problem. Furthermore, we note that its counterpart, the so-called FDTs approach (cf. Sec. 3.2.2), where the dual scheme is derived with the help of the formal adjoint of the weak formulation, given by Problem 4.2, will not be explicitly dealt with in this work. This is due to the numerical results obtained in Sec. 3.4 of the previous chapter. In addition, this case was investigated by the author et al. in [51]. In this approach, the semi-discretization in time and the following stabilization of the fully discrete scheme is based on the resulting dual weak form and is thus not prescribed by the respective primal counterpart; cf. [51] for more details.*

4.2.2 Derivation of an A Posteriori Error Estimator

For the derivation of computable representations of the separated error contributions in Eq. (4.25) we need the following general result, that can be found in [167, 40].

Lemma 4.1 *Let \mathcal{Y} be a function space and L and \tilde{L} be three times Gâteaux differentiable functionals on \mathcal{Y} . We seek a stationary point y_1 of L on a subspace $\mathcal{Y}_1 \subseteq \mathcal{Y}$: Find $y_1 \in \mathcal{Y}_1$ such that*

$$L'(y_1)(\delta y_1) = 0 \quad \forall \delta y_1 \in \mathcal{Y}_1. \quad (4.55)$$

This equation is approximated by a Galerkin method using the functional \tilde{L} on a subspace $\mathcal{Y}_2 \subseteq \mathcal{Y}$. Hence, the discrete problem seeks $y_2 \in \mathcal{Y}_2$ such that

$$\tilde{L}'(y_2)(\delta y_2) = 0 \quad \forall \delta y_2 \in \mathcal{Y}_2. \quad (4.56)$$

If the continuous solution y_1 additionally fulfills

$$L'(y_1)(y_2) = 0, \quad (4.57)$$

with the approximated solution y_2 , we have the error representation

$$L(y_1) - \tilde{L}(y_2) = \frac{1}{2}L'(y_2)(y_1 - \tilde{y}_2) + \frac{1}{2}(L - \tilde{L})'(y_2)(\tilde{y}_2 - y_2) + (L - \tilde{L})(y_2) + \mathcal{R}, \quad (4.58)$$

for arbitrary $\tilde{y}_2 \in \mathcal{Y}_2$, where the remainder term \mathcal{R} is given in terms of $e := y_1 - y_2$ as

$$\mathcal{R} = \frac{1}{2} \int_0^1 L'''(y_2 + se)(e, e, e)s(s-1) ds. \quad (4.59)$$

Proof. (cf. [167, 40]) Using the main theorem of calculus, we have

$$L(y_1) - \tilde{L}(y_2) = L(y_1) - L(y_2) + (L - \tilde{L})(y_2) = \int_0^1 L'(y_2 + se)(e)ds + (L - \tilde{L})(y_2).$$

Then, employing the trapezoidal rule

$$\int_0^1 f(s)ds = \frac{1}{2}f(0) + \frac{1}{2}f(1) + \frac{1}{2} \int_0^1 f''(s) \cdot s \cdot (s-1) ds,$$

for approximating the integral, yields

$$L(y_1) - \tilde{L}(y_2) = \frac{1}{2}L'(y_2)(e) + \frac{1}{2}L'(y_1)(e) + \mathcal{R} + (L - \tilde{L})(y_2).$$

Because of the assumption (4.55) and (4.57), respectively, we have that

$$L'(y_1)(e) = 0.$$

Due to assertion (4.56), we may replace $L'(y_2)(e)$ by

$$L'(y_2)(y_1 - \tilde{y}_2) + L'(y_2)(\tilde{y}_2 - y_2) = L'(y_2)(y_1 - \tilde{y}_2) + (L - \tilde{L})'(y_2)(\tilde{y}_2 - y_2),$$

for arbitrary $\tilde{y}_2 \in Y_2$. This completes the proof. \square

Remark 4.8 *The result of Lemma 4.1 is a slight modification of the well-known general result presented in [36, Proposition 2.1] or [20, Proposition 6.1] with regard to the difference of L and \tilde{L} . This is owed to the loss of guarantee $\mathcal{Y}_2 \subseteq \mathcal{Y}_1$ in the case of a discontinuous in time $dG(r)$ discretization as well as the presence of the additional SUPG stabilization terms, cf. [167, Rem. 4.1].*

4.2.2.1 Discontinuous in Time Discretization

In the case of a discontinuous in time $dG(r)$, $r \geq 0$, discretization we apply the abstract error representation formula (4.58) to the Lagrangian functionals (4.26), (4.27) and (4.29), respectively, to derive an a posteriori error estimator in space and time. The result is summarized in the following Thm. 4.1 that is a slight modification of Thm. 5.2 in [40], where it was proved for the nonstationary Navier-Stokes equations

stabilized by local projection stabilization (LPS) [33, 34]. To proceed with our computations, we introduce the primal and dual residuals based on the semi-discrete in time schemes by means of

$$\begin{aligned}\rho_\tau(u)(\varphi) &:= \mathcal{L}'_{\tau,z}(u, z)(\varphi) = F_\tau(\varphi) - A_\tau^{\text{dG}}(u)(\varphi), \\ \rho_\tau^*(u, z)(\varphi) &:= \mathcal{L}'_{\tau,u}(u, z)(\varphi) = J'(u)(\varphi) - A_\tau^{\text{dG}'}(u)(\varphi, z).\end{aligned}\tag{4.60}$$

By using Lemma 4.1 we get the following result for the DWR-based error representation in the case of a discontinuous in time dG(r) discretization.

Theorem 4.1 (Error Representation dG(r) Time Discretization)

Let $\{u, z\} \in \mathcal{V} \times \mathcal{V}$, $\{u_\tau, z_\tau\} \in \mathcal{V}_\tau^{\text{dG}(r)} \times \mathcal{V}_\tau^{\text{dG}(r)}$, and $\{u_{\tau h}, z_{\tau h}\} \in \mathcal{V}_{\tau h}^{\text{dG}(r),p} \times \mathcal{V}_{\tau h}^{\text{dG}(r),p}$ be stationary points of $\mathcal{L}, \mathcal{L}_\tau$, and $\mathcal{L}_{\tau h}$ on the different levels of discretization, i.e.,

$$\begin{aligned}\mathcal{L}'(u, z)(\delta u, \delta z) &= \mathcal{L}'_\tau(u, z)(\delta u, \delta z) = 0 \quad \forall \{\delta u, \delta z\} \in \mathcal{V} \times \mathcal{V}, \\ \mathcal{L}'_\tau(u_\tau, z_\tau)(\delta u_\tau, \delta z_\tau) &= 0 \quad \forall \{\delta u_\tau, \delta z_\tau\} \in \mathcal{V}_\tau^{\text{dG}(r)} \times \mathcal{V}_\tau^{\text{dG}(r)}, \\ \mathcal{L}'_{\tau h}(u_{\tau h}, z_{\tau h})(\delta u_{\tau h}, \delta z_{\tau h}) &= 0 \quad \forall \{\delta u_{\tau h}, \delta z_{\tau h}\} \in \mathcal{V}_{\tau h}^{\text{dG}(r),p} \times \mathcal{V}_{\tau h}^{\text{dG}(r),p}.\end{aligned}$$

Then, for the discretization errors in space and time we get the representation formulas

$$J(u) - J(u_\tau) = \frac{1}{2}\rho_\tau(u_\tau)(z - \tilde{z}_\tau) + \frac{1}{2}\rho_\tau^*(u_\tau, z_\tau)(u - \tilde{u}_\tau) + \mathcal{R}_\tau, \tag{4.61}$$

$$\begin{aligned}J(u_\tau) - J(u_{\tau h}) &= \frac{1}{2}\rho_\tau(u_{\tau h})(z_\tau - \tilde{z}_{\tau h}) + \frac{1}{2}\rho_\tau^*(u_{\tau h}, z_{\tau h})(u_\tau - \tilde{u}_{\tau h}) \\ &\quad + \frac{1}{2}\mathcal{S}^{\text{dG}'}(u_{\tau h}, z_{\tau h})(\tilde{u}_{\tau h} - u_{\tau h}, \tilde{z}_{\tau h} - z_{\tau h}) \\ &\quad + \mathcal{S}^{\text{dG}}(u_{\tau h}, z_{\tau h}) + \mathcal{R}_h,\end{aligned}\tag{4.62}$$

with

$$\begin{aligned}\mathcal{S}^{\text{dG}'}(u_{\tau h}, z_{\tau h})(\tilde{u}_{\tau h} - u_{\tau h}, \tilde{z}_{\tau h} - z_{\tau h}) &:= \mathcal{S}_A^{\text{dG}}(u_{\tau h})(\tilde{z}_{\tau h} - z_{\tau h}) \\ &\quad + \mathcal{S}_A^{\text{dG}'}(u_{\tau h})(\tilde{u}_{\tau h} - u_{\tau h}, z_{\tau h}),\end{aligned}\tag{4.63}$$

obtained by the Gâteaux derivatives with respect to the first and second argument of $\mathcal{S}^{\text{dG}}(\cdot, \cdot)$ that is given in (4.30). Here, $\{\tilde{u}_\tau, \tilde{z}_\tau\} \in \mathcal{V}_\tau^{\text{dG}(r)} \times \mathcal{V}_\tau^{\text{dG}(r)}$, and $\{\tilde{u}_{\tau h}, \tilde{z}_{\tau h}\} \in \mathcal{V}_{\tau h}^{\text{dG}(r),p} \times \mathcal{V}_{\tau h}^{\text{dG}(r),p}$ can be chosen arbitrarily and the remainder terms \mathcal{R}_τ and \mathcal{R}_h have the same structure as the remainder term (4.59) in Lemma 4.1.

Proof. The proof is related to that one of Thm. 5.2 in [40]. Evaluating the Lagrangian functionals at the respective primal and dual solutions, there holds that (cf. Eq. (4.32) in Rem. 4.4)

$$J(u) = \mathcal{L}(u, z), \quad J(u_\tau) = \mathcal{L}_\tau(u_\tau, z_\tau), \quad J(u_{\tau h}) = \mathcal{L}_{\tau h}(u_{\tau h}, z_{\tau h}).$$

Since the additional jump terms and the initial condition in \mathcal{L}_τ vanish for a continuous solution $u \in \mathcal{V}$, we get the following representation for the temporal and spatial error, respectively,

$$J(u) - J(u_\tau) = \mathcal{L}(u, z) - \mathcal{L}_\tau(u_\tau, z_\tau) = \mathcal{L}_\tau(u, z) - \mathcal{L}_\tau(u_\tau, z_\tau), \quad (4.64)$$

$$J(u_\tau) - J(u_{\tau h}) = \mathcal{L}_\tau(u_\tau, z_\tau) - \mathcal{L}_{\tau h}(u_{\tau h}, z_{\tau h}). \quad (4.65)$$

To prove the assertion (4.61) for the temporal error, we apply Lemma 4.1 with the identifications

$$L = \mathcal{L}_\tau, \quad \tilde{L} = \mathcal{L}_\tau, \quad \mathcal{Y}_1 = \mathcal{V} \times \mathcal{V}, \quad \mathcal{Y}_2 = \mathcal{V}_\tau^{\text{dG}(r)} \times \mathcal{V}_\tau^{\text{dG}(r)}$$

to the identity (4.64). Further, we have to choose $\mathcal{Y} := \mathcal{Y}_1 + \mathcal{Y}_2$ since here $\mathcal{V}_\tau^{\text{dG}(r)} \not\subseteq \mathcal{V}$. Thus, we have to verify condition (4.57), that now reads as $\mathcal{L}'_\tau(u, z)(u_\tau, z_\tau) = 0$, or equivalently,

$$\mathcal{L}'_{\tau, u}(u, z)(u_\tau) = 0 \quad \text{and} \quad \mathcal{L}'_{\tau, z}(u, z)(z_\tau) = 0. \quad (4.66)$$

We only give the proof of the second equation in (4.66). The first one can be proved analogously. To show that $\mathcal{L}'_{\tau, z}(u, z)(z_\tau) = 0$, we rewrite this equation building the Gâteaux derivative of its definition, given by Eq. (4.27), as

$$F_\tau(z_\tau) - A_\tau^{\text{dG}}(u)(z_\tau) \stackrel{(4.11), (4.12)}{=} \sum_{n=1}^N \sum_{t_{\mathcal{F}} \in \mathcal{T}_{\tau, n}} \int_{K_n} \{(f - \partial_t u, z_\tau) - a(u)(z_\tau)\} dt = 0,$$

where we have used that the additional jump terms in \mathcal{L}_τ vanish for a continuous solution $u \in \mathcal{V}$. By construction, the continuous solution u satisfies that (satisfying $u(0) = u_0$) (cf. Eq. (4.3))

$$A(u)(\varphi) \stackrel{(4.4)}{=} \int_I \{(\partial_t u, \varphi) + a(u)(\varphi)\} dt = \int_I (f, \varphi) dt \stackrel{(4.5)}{=} F(\varphi) \quad \forall \varphi \in \mathcal{V}. \quad (4.67)$$

By Corollary 2.1 we have that \mathcal{V} is dense in $L^2(I; V)$ with respect to the norm of $L^2(I; V)$, and since no time derivatives of φ arise in (4.67), this equation is also satisfied for all $\varphi \in L^2(I; V)$. The inclusion $z_\tau \in \mathcal{V}_\tau^{\text{dG}(r)} \subset L^2(I; V)$ then implies that

the second equation in (4.66) is fulfilled. Now, applying Lemma 4.1 with the above made identifications yields that

$$\begin{aligned} J(u) - J(u_\tau) &= \mathcal{L}_\tau(u, z) - \mathcal{L}_\tau(u_\tau, z_\tau) \\ &= \frac{1}{2} \mathcal{L}'_\tau(u_\tau, z_\tau)(u - \tilde{u}_\tau, z - \tilde{z}_\tau) + \mathcal{R}_\tau. \end{aligned} \quad (4.68)$$

With the definition of the primal and dual residuals given in (4.60), Eq. (4.68) can be rewritten as

$$J(u) - J(u_\tau) = \frac{1}{2} \rho_\tau(u_\tau)(z - \tilde{z}_\tau) + \frac{1}{2} \rho_\tau^*(u_\tau, z_\tau)(u - \tilde{u}_\tau) + \mathcal{R}_\tau,$$

where the remainder term \mathcal{R}_τ is given by

$$\mathcal{R}_\tau = \frac{1}{2} \int_0^1 \mathcal{L}'''_\tau(u_\tau + se, z_\tau + se^*)(e, e, e, e^*, e^*, e^*)s(s-1) ds, \quad (4.69)$$

with the ‘primal’ and ‘dual’ errors $e := u - u_\tau$ and $e^* := z - z_\tau$, respectively. This proves the assertion (4.61).

To prove the spatial error representation (4.62), we apply Lemma 4.1 with the identifications

$$L = \mathcal{L}_\tau, \quad \tilde{L} = \mathcal{L}_{\tau h}, \quad \mathcal{Y}_1 = \mathcal{V}_\tau^{\text{dG}(r)} \times \mathcal{V}_\tau^{\text{dG}(r)}, \quad \mathcal{Y}_2 = \mathcal{V}_{\tau h}^{\text{dG}(r),p} \times \mathcal{V}_{\tau h}^{\text{dG}(r),p}$$

to Eq. (4.65). In this case, we have $\mathcal{Y}_2 \subseteq \mathcal{Y}_1$ since $\mathcal{V}_{\tau h}^{\text{dG}(r),p} \subseteq \mathcal{V}_\tau^{\text{dG}(r)}$. Hence, we can choose $\mathcal{Y} := \mathcal{Y}_1$ in Lemma 4.1 and condition (4.57) is directly satisfied. Now, applying Lemma 4.1 with these identifications implies that

$$\begin{aligned} J(u_\tau) - J(u_{\tau h}) &= \mathcal{L}_\tau(u_\tau, z_\tau) - \mathcal{L}_{\tau h}(u_{\tau h}, z_{\tau h}) \\ &= \frac{1}{2} \mathcal{L}'_\tau(u_{\tau h}, z_{\tau h})(u_\tau - \tilde{u}_{\tau h}, z_\tau - \tilde{z}_{\tau h}) \\ &\quad + \frac{1}{2} (\mathcal{L}_\tau - \mathcal{L}_{\tau h})'(u_{\tau h}, z_{\tau h})(\tilde{u}_{\tau h} - u_{\tau h}, \tilde{z}_{\tau h} - z_{\tau h}) \\ &\quad + (\mathcal{L}_\tau - \mathcal{L}_{\tau h})(u_{\tau h}, z_{\tau h}) + \mathcal{R}_h. \end{aligned} \quad (4.70)$$

Again, using the definition in (4.60) of the primal and dual residual, Eq. (4.70) can be rewritten as

$$\begin{aligned} J(u_\tau) - J(u_{\tau h}) &= \frac{1}{2} \rho_\tau(u_{\tau h})(z_\tau - \tilde{z}_{\tau h}) + \frac{1}{2} \rho_\tau^*(u_{\tau h}, z_{\tau h})(u_\tau - \tilde{u}_{\tau h}) \\ &\quad + \frac{1}{2} \mathcal{S}^{\text{dG}'}(u_{\tau h}, z_{\tau h})(\tilde{u}_{\tau h} - u_{\tau h}, \tilde{z}_{\tau h} - z_{\tau h}) \\ &\quad + \mathcal{S}^{\text{dG}}(u_{\tau h}, z_{\tau h}) + \mathcal{R}_h, \end{aligned}$$

where the remainder term \mathcal{R}_h is given by

$$\mathcal{R}_h = \frac{1}{2} \int_0^1 \mathcal{L}_\tau'''(u_{\tau h} + se, z_{\tau h} + se^*)(e, e, e, e^*, e^*, e^*)s(s-1) ds, \quad (4.71)$$

with the ‘primal’ and ‘dual’ errors $e := u_\tau - u_{\tau h}$ and $e^* := z_\tau - z_{\tau h}$. This proves the assertion (4.62). For completeness, we note that

$$\begin{aligned} \mathcal{S}^{\text{dG}'}(u_{\tau h}, z_{\tau h})(\tilde{u}_{\tau h} - u_{\tau h}, \tilde{z}_{\tau h} - z_{\tau h}) &= \mathcal{S}_u^{\text{dG}'}(u_{\tau h}, z_{\tau h})(\tilde{u}_{\tau h} - u_{\tau h}) \\ &\quad + \mathcal{S}_z^{\text{dG}'}(u_{\tau h}, z_{\tau h})(\tilde{z}_{\tau h} - z_{\tau h}). \\ &= S_A^{\text{dG}'}(u_{\tau h})(\tilde{u}_{\tau h} - u_{\tau h}, z_{\tau h}) \\ &\quad + S_A^{\text{dG}}(u_{\tau h})(\tilde{z}_{\tau h} - z_{\tau h}), \end{aligned}$$

where we have used the definition of the Gâteaux derivatives, given by Def. 2.11, cf. also Rem. 2.6, as well as the definition $\mathcal{S}^{\text{dG}}(u_{\tau h}, z_{\tau h}) := S_A^{\text{dG}}(u_{\tau h})(z_{\tau h})$, given by Eq. (4.30) with $S_A^{\text{dG}}(\cdot)(\cdot)$ and $S_A^{\text{dG}'}(\cdot)(\cdot, \cdot)$, given by Eq. (4.23) and Eq. (4.45), respectively. \square

Since both error representation formulas (4.61) and (4.62), respectively, depend on the primal as well as the dual residual, different weights depending on the primal and dual variables have to be approximated in a practical implementation, cf. Sec.3.3.1. To reduce the complexity of a practical realization, we derive a relation between the primal and dual residual depending on the different discretization levels that goes back to [36, Prop. 2.3] or [20, Prop. 6.6].

Proposition 4.2 *Let the assumptions of Thm. 4.1 be satisfied. Further, let the primal and dual residual be given by Eq. (4.60). Then there holds that*

$$\rho_\tau^*(u_\tau, z_\tau)(u - \tilde{u}_\tau) = \rho_\tau(u_\tau)(z - \tilde{z}_\tau) + \Delta\rho_\tau, \quad (4.72)$$

for all $\{\tilde{u}_\tau, \tilde{z}_\tau\} \in \mathcal{V}_\tau^{\text{dG}(r)} \times \mathcal{V}_\tau^{\text{dG}(r)}$ with the remainder term $\Delta\rho_\tau$, given by

$$\Delta\rho_\tau := \int_0^1 \{A_\tau^{\text{dG}''}(u_\tau + se)(e, e, z_\tau + se^*) - J''(u_\tau + se)(e, e)\} ds, \quad (4.73)$$

with $e := u - u_\tau$ and $e^* := z - z_\tau$.

Proof. (cf. [36, 20]) We introduce the scalar function $k(\cdot)$ by

$$k(s) := J'(u_\tau + se)(u - \tilde{u}_\tau) - A_\tau^{\text{dG}'}(u_\tau + se)(u - \tilde{u}_\tau, z_\tau + se^*),$$

where $J'(\cdot)(\cdot)$ and $A_\tau^{\text{dG}'(\cdot)}(\cdot, \cdot)$ are given by Eq. (4.37) and (4.40), respectively. Owing to the definition of the dual residual given in (4.60), we get that

$$k(0) = J'(u_\tau)(u - \tilde{u}_\tau) - A_\tau^{\text{dG}'(u_\tau)}(u - \tilde{u}_\tau, z_\tau) = \rho_\tau^*(u_\tau, z_\tau)(u - \tilde{u}_\tau).$$

Moreover, enlarging the space \mathcal{V} by $\mathcal{V} + \mathcal{V}_\tau^{\text{dG}(r)}$ we get

$$k(1) = J'(u)(u - \tilde{u}_\tau) - A_\tau^{\text{dG}'(u)}(u - \tilde{u}_\tau, z) = 0,$$

where we have used the same argument as in the proof of Thm. 4.1 for Eq. (4.66).

Furthermore, the derivative of $k(\cdot)$ is given by

$$\begin{aligned} k'(s) &= J''(u_\tau + se)(e, u - \tilde{u}_\tau) - A_\tau^{\text{dG}''(u_\tau + se)}(e, u - \tilde{u}_\tau, z_\tau + se^*) \\ &\quad - A_\tau^{\text{dG}'(u_\tau + se)}(u - \tilde{u}_\tau, e^*). \end{aligned}$$

Applying the theorem of calculus $\int_0^1 f'(s)ds = f(1) - f(0)$ as well as using Galerkin orthogonality, we get

$$\begin{aligned} \rho_\tau^*(u_\tau, z_\tau)(u - \tilde{u}_\tau) &= \rho_\tau^*(u_\tau, z_\tau)(e) = k(0) = k(0) - k(1) = - \int_0^1 k'(s) ds \\ &= \int_0^1 \left\{ A_\tau^{\text{dG}''(u_\tau + se)}(e, e, z_\tau + se^*) - J''(u_\tau + se)(e, e) \right\} ds \\ &\quad + \int_0^1 A_\tau^{\text{dG}'(u_\tau + se)}(e, e^*) ds \\ &= \Delta\rho_\tau + \rho_\tau(u_\tau)(z - \tilde{z}_\tau), \end{aligned}$$

where in the last step we have used that the last term is just the primal residual defined by Eq. (4.60), where we can substitute e^* by $z - \tilde{z}_\tau$ with an arbitrary $\tilde{z}_\tau \in \mathcal{V}_\tau^{\text{dG}(r)}$. \square

The relation between the primal and dual residual within the spatial error representation formula (4.62) needs some particular care due to the stabilization terms and is summarized in the following proposition.

Proposition 4.3 *Let the assumptions of Thm. 4.1 be satisfied. Further, let the primal and dual residual be given by Eq. (4.60). Then there holds that*

$$\rho_\tau^*(u_{\tau h}, z_{\tau h})(u_\tau - \tilde{u}_{\tau h}) = \rho_\tau(u_{\tau h})(z_\tau - \tilde{z}_{\tau h}) + \Delta\rho_{\text{SdG}} + \Delta\rho_h, \quad (4.74)$$

for all $\{\tilde{u}_{\tau h}, \tilde{z}_{\tau h}\} \in \mathcal{V}_{\tau h}^{\text{dG}(r), p} \times \mathcal{V}_{\tau h}^{\text{dG}(r), p}$ with the remainder terms $\Delta\rho_{\text{SdG}}$ and $\Delta\rho_h$ are given by, respectively,

$$\Delta\rho_{\text{SdG}} := S_A^{\text{dG}}(u_{\tau h})(\tilde{z}_{\tau h} - z_{\tau h}) - S_A^{\text{dG}'(u_{\tau h})}(\tilde{u}_{\tau h} - u_{\tau h}, z_{\tau h}), \quad (4.75)$$

$$\Delta\rho_h := \int_0^1 \left\{ A_\tau^{\text{dG}''(u_{\tau h} + se)}(e, e, z_{\tau h} + se^*) - J''(u_{\tau h} + se)(e, e) \right\} ds, \quad (4.76)$$

with $e := u_\tau - u_{\tau h}$ and $e^* := z_\tau - z_{\tau h}$.

Proof. (cf. [169]) We introduce the scalar function $k(\cdot)$ by

$$k(s) := J'(u_{\tau h} + se)(u_\tau - \tilde{u}_{\tau h}) - A_\tau^{\text{dG}'}(u_{\tau h} + se)(u_\tau - \tilde{u}_{\tau h}, z_{\tau h} + se^*),$$

where $J'(\cdot)(\cdot)$ and $A_\tau^{\text{dG}'}(\cdot)(\cdot, \cdot)$ are given by Eq. (4.37) and (4.40), respectively. By the definition of the dual residual given in (4.60) as well as the relation $\mathcal{V}_{\tau h}^{\text{dG}(r),p} \subset \mathcal{V}_\tau^{\text{dG}(r)}$, there holds that

$$\begin{aligned} k(1) &= J'(u_\tau)(u_\tau - \tilde{u}_{\tau h}) - A_\tau^{\text{dG}'}(u_\tau)(u_\tau - \tilde{u}_{\tau h}, z_\tau) = 0, \\ k(0) &= J'(u_{\tau h})(u_\tau - \tilde{u}_{\tau h}) - A_\tau^{\text{dG}'}(u_{\tau h})(u_\tau - \tilde{u}_{\tau h}, z_{\tau h}) = \rho_\tau^*(u_{\tau h}, z_{\tau h})(u_\tau - \tilde{u}_{\tau h}). \end{aligned}$$

Furthermore, the derivative of $k(\cdot)$ is given by

$$\begin{aligned} k'(s) &= J''(u_{\tau h} + se)(e, u_\tau - \tilde{u}_{\tau h}) - A_\tau^{\text{dG}''}(u_{\tau h} + se)(e, u_\tau - \tilde{u}_{\tau h}, z_\tau + se^*) \\ &\quad - A_\tau^{\text{dG}'}(u_\tau + se)(u_\tau - \tilde{u}_{\tau h}, e^*). \end{aligned}$$

Applying the theorem of calculus $\int_0^1 f'(s)ds = f(1) - f(0)$ as well as using Galerkin orthogonality, we get

$$\begin{aligned} \rho_\tau^*(u_{\tau h}, z_{\tau h})(u_\tau - \tilde{u}_{\tau h}) &= k(0) = k(0) - k(1) = - \int_0^1 k'(s) ds \\ &= \int_0^1 \left\{ A_\tau^{\text{dG}''}(u_{\tau h} + se)(e, u_\tau - \tilde{u}_{\tau h}, z_{\tau h} + se^*) \right. \\ &\quad \left. - J''(u_{\tau h} + se)(e, u_\tau - \tilde{u}_{\tau h}) \right. \\ &\quad \left. + A_\tau^{\text{dG}'}(u_{\tau h} + se)(u_\tau - \tilde{u}_{\tau h}, e^*) \right\} ds. \end{aligned} \quad (4.77)$$

Next, we apply a similar argument as used in the proof of [169, Thm.3.17]. By replacing $u_\tau - \tilde{u}_{\tau h}$ by $u_\tau - u_{\tau h}$ in the dual residual and using the dual stabilized cG(p)-dG(r) scheme, given by Eq. (4.42), together with (4.43), we get that

$$\begin{aligned} \rho_\tau^*(u_{\tau h}, z_{\tau h})(u_\tau - \tilde{u}_{\tau h}) &= J'(u_{\tau h})(u_\tau - \tilde{u}_{\tau h}) - A_\tau^{\text{dG}'}(u_{\tau h})(u_\tau - \tilde{u}_{\tau h}, z_{\tau h}) \\ &\quad + S_A^{\text{dG}'}(u_{\tau h})(\tilde{u}_{\tau h}, z_{\tau h}) - S_A^{\text{dG}'}(u_{\tau h})(\tilde{u}_{\tau h}, z_{\tau h}) \\ &\quad - J'(u_{\tau h})(u_{\tau h}) + A_\tau^{\text{dG}'}(u_{\tau h})(u_{\tau h}, z_{\tau h}) + S_A^{\text{dG}'}(u_{\tau h})(u_{\tau h}, z_{\tau h}) \\ &= \rho_\tau^*(u_{\tau h}, z_{\tau h})(u_\tau - u_{\tau h}) - S_A^{\text{dG}'}(u_{\tau h})(\tilde{u}_{\tau h} - u_{\tau h}, z_{\tau h}) \end{aligned}$$

Owing to (4.77), we obtain that

$$\begin{aligned}
\rho_\tau^*(u_{\tau h}, z_{\tau h})(u_\tau - \tilde{u}_{\tau h}) &= \int_0^1 \left\{ A_\tau^{\text{dG}''}(u_{\tau h} + se)(e, u_\tau - u_{\tau h}, z_{\tau h} + se^*) \right. \\
&\quad \left. - J''(u_{\tau h} + se)(e, u_\tau - u_{\tau h}) \right\} ds \\
&\quad + \int_0^1 A_\tau^{\text{dG}'}(u_{\tau h} + se)(u_\tau - \tilde{u}_{\tau h}, e^*) ds. \\
&\quad - S_A^{\text{dG}'}(u_{\tau h})(\tilde{u}_{\tau h} - u_{\tau h}, z_{\tau h}) \\
&= \Delta\rho_h + A_\tau^{\text{dG}}(e)(e^*) - S_A^{\text{dG}'}(u_{\tau h})(\tilde{u}_{\tau h} - u_{\tau h}, z_{\tau h}).
\end{aligned} \tag{4.78}$$

By inserting the dual stabilized cG(p)-dG(r) scheme

$$0 = A_S^{\text{dG}}(u_{\tau h})(\varphi_{\tau h}) - F_\tau(\varphi_{\tau h}) = A_\tau^{\text{dG}}(u_{\tau h})(\varphi_{\tau h}) + S_A^{\text{dG}}(u_{\tau h})(\varphi_{\tau h}) - F_\tau(\varphi_{\tau h}),$$

for all $\varphi_{\tau h} \in \mathcal{V}_{\tau h}^{\text{dG}(r),p}$, given by Eq. (4.21) together with (4.22), we can rewrite $A_\tau^{\text{dG}}(e)(e^*)$ by means of

$$\begin{aligned}
A_\tau^{\text{dG}}(e)(e^*) &= A_\tau^{\text{dG}}(u_\tau)(e^*) - A_\tau^{\text{dG}}(u_{\tau h})(e^*) = F_\tau(e^*) - A_\tau^{\text{dG}}(u_{\tau h})(e^*) \\
&= F_\tau(z_\tau) - F_\tau(z_{\tau h}) - A_\tau^{\text{dG}}(u_{\tau h})(z_\tau) + A_\tau^{\text{dG}}(u_{\tau h})(z_{\tau h}) \\
&\quad + S_A^{\text{dG}}(u_{\tau h})(z_{\tau h}) - S_A^{\text{dG}}(u_{\tau h})(z_{\tau h}) \\
&\quad + A_\tau^{\text{dG}}(u_{\tau h})(\tilde{z}_{\tau h}) + S_A^{\text{dG}}(u_{\tau h})(\tilde{z}_{\tau h}) - F_\tau(\tilde{z}_{\tau h}) \\
&= F_\tau(z_\tau - \tilde{z}_{\tau h}) - A_\tau^{\text{dG}}(u_{\tau h})(z_\tau - \tilde{z}_{\tau h}) + S_A^{\text{dG}}(u_{\tau h})(\tilde{z}_{\tau h} - z_{\tau h}) \\
&= \rho_\tau(u_{\tau h})(z_\tau - \tilde{z}_{\tau h}) + S_A^{\text{dG}}(u_{\tau h})(\tilde{z}_{\tau h} - z_{\tau h}),
\end{aligned} \tag{4.79}$$

where we have used the definition of the primal residual, given by Eq. (4.60), in the last step. Finally, substituting formula (4.79) into (4.78), we get that

$$\begin{aligned}
\rho_\tau^*(u_{\tau h}, z_{\tau h})(u_\tau - \tilde{u}_{\tau h}) &= A_\tau^{\text{dG}}(e)(e^*) - S_A^{\text{dG}'}(u_{\tau h})(\tilde{u}_{\tau h} - u_{\tau h}, z_{\tau h}) + \Delta\rho_h \\
&= \rho_\tau(u_{\tau h})(z_\tau - \tilde{z}_{\tau h}) + \Delta\rho_{S^{\text{dG}}} + \Delta\rho_h.
\end{aligned}$$

This proves (4.74). \square

By using Prop. 4.2 and 4.3 the error representation formulas (4.61) and (4.62), respectively, can be reduced by means of the following theorem.

Theorem 4.2 (Reduced Error Representation dG(r) Time Discretization)

Let the assumption of Thm. 4.1 be satisfied. Then, for the discretization errors in space and time we get the representation formulas

$$J(u) - J(u_\tau) = \rho_\tau(u_\tau)(z - \tilde{z}_\tau) + \frac{1}{2}\Delta\rho_\tau + \mathcal{R}_\tau, \tag{4.80}$$

$$J(u_\tau) - J(u_{\tau h}) = \rho_\tau(u_{\tau h})(z_\tau - \tilde{z}_{\tau h}) + S_A^{\text{dG}}(u_{\tau h})(\tilde{z}_{\tau h}) + \frac{1}{2}\Delta\rho_h + \mathcal{R}_h. \tag{4.81}$$

Here, $\tilde{z}_\tau \in \mathcal{V}_\tau^{\text{dG}(r)}$ and $\tilde{z}_{\tau h} \in \mathcal{V}_{\tau h}^{\text{dG}(r),p}$ can be chosen arbitrarily and the remainder terms $\Delta\rho_\tau$, $\Delta\rho_h$, \mathcal{R}_τ , and \mathcal{R}_h are given by the Eqs. (4.73), (4.76), (4.69), and (4.71), respectively.

Proof. The reduced temporal error representation formula (4.80) directly follows by applying Prop. 4.2 to Eq. (4.61) in Thm. 4.1.

To prove the reduced spatial error representation formula (4.81), we apply Prop. 4.3 to Eq. (4.62) in Thm. 4.1 along with the representation given by (4.63), to get

$$\begin{aligned} J(u_\tau) - J(u_{\tau h}) &= \rho_\tau(u_{\tau h})(z_\tau - \tilde{z}_{\tau h}) + S_A^{\text{dG}}(u_{\tau h})(\tilde{z}_{\tau h} - z_{\tau h}) + S_A^{\text{dG}}(u_{\tau h})(z_{\tau h}) \\ &\quad + \frac{1}{2}\Delta\rho_h + \mathcal{R}_h \\ &= \rho_\tau(u_{\tau h})(z_\tau - \tilde{z}_{\tau h}) + S_A^{\text{dG}}(u_{\tau h})(\tilde{z}_{\tau h}) + \frac{1}{2}\Delta\rho_h + \mathcal{R}_h. \end{aligned}$$

□

4.2.2.2 Continuous in Time Discretization

In the case of a continuous in time cG(r), $r \geq 1$, discretization we apply the abstract error representation formula (4.58) to the Lagrangian functionals (4.26) and (4.28), respectively, to derive an a posteriori error estimator in space and time. This time, the primal and dual residuals are given by the Gâteaux derivatives of the Lagrangian functional based on the continuous schemes, more precisely

$$\begin{aligned} \rho(u)(\varphi) &:= \mathcal{L}'_z(u, z)(\varphi) = F(\varphi) - A(u)(\varphi), \\ \rho^*(u, z)(\varphi) &:= \mathcal{L}'_u(u, z)(\varphi) = J'(u)(\varphi) - A'(u)(\varphi, z). \end{aligned} \tag{4.82}$$

By using Lemma 4.1 we get the following result for the DWR-based error representation in the case of a continuous in time cG(r) discretization; cf. Cor. 4.3 in [167].

Theorem 4.3 (Error Representation cG(r) Time Discretization)

Let $\{u, z\} \in \mathcal{V} \times \mathcal{V}$, $\{u_\tau, z_\tau\} \in \mathcal{V}_\tau^{\text{cG}(r)} \times \mathcal{V}_\tau^{\text{dG}(r-1)}$, and $\{u_{\tau h}, z_{\tau h}\} \in \mathcal{V}_{\tau h}^{\text{cG}(r),p} \times \mathcal{V}_{\tau h}^{\text{dG}(r-1),p}$ be stationary points of \mathcal{L} and $\mathcal{L}_{\tau h}^{\text{cG}}$ on the different levels of discretization, i.e.,

$$\begin{aligned} \mathcal{L}'(u, z)(\delta u, \delta z) &= 0 \quad \forall \{\delta u, \delta z\} \in \mathcal{V} \times \mathcal{V}, \\ \mathcal{L}'(u_\tau, z_\tau)(\delta u_\tau, \delta z_\tau) &= 0 \quad \forall \{\delta u_\tau, \delta z_\tau\} \in \mathcal{V}_\tau^{\text{cG}(r)} \times \mathcal{V}_\tau^{\text{dG}(r-1)}, \\ \mathcal{L}_{\tau h}^{\text{cG}'}(u_{\tau h}, z_{\tau h})(\delta u_{\tau h}, \delta z_{\tau h}) &= 0 \quad \forall \{\delta u_{\tau h}, \delta z_{\tau h}\} \in \mathcal{V}_{\tau h}^{\text{cG}(r),p} \times \mathcal{V}_{\tau h}^{\text{dG}(r-1),p}. \end{aligned}$$

Then, for the discretization errors in space and time we get the representation formulas

$$J(u) - J(u_\tau) = \frac{1}{2}\rho(u_\tau)(z - \tilde{z}_\tau) + \frac{1}{2}\rho^*(u_\tau, z_\tau)(u - \tilde{u}_\tau) + \mathcal{R}_{\tilde{\tau}}, \quad (4.83)$$

$$\begin{aligned} J(u_\tau) - J(u_{\tau h}) &= \frac{1}{2}\rho(u_{\tau h})(z_\tau - \tilde{z}_{\tau h}) + \frac{1}{2}\rho^*(u_{\tau h}, z_{\tau h})(u_\tau - \tilde{u}_{\tau h}) \quad (4.84) \\ &+ \frac{1}{2}\mathcal{S}^{\text{cG}'}(u_{\tau h}, z_{\tau h})(\tilde{u}_{\tau h} - u_{\tau h}, \tilde{z}_{\tau h} - z_{\tau h}) \\ &+ \mathcal{S}^{\text{cG}}(u_{\tau h}, z_{\tau h}) + \mathcal{R}_{\tilde{h}}, \end{aligned}$$

with

$$\begin{aligned} \mathcal{S}^{\text{cG}'}(u_{\tau h}, z_{\tau h})(\tilde{u}_{\tau h} - u_{\tau h}, \tilde{z}_{\tau h} - z_{\tau h}) &:= S_A^{\text{cG}}(u_{\tau h})(\tilde{z}_{\tau h} - z_{\tau h}) \\ &+ S_A^{\text{cG}'}(u_{\tau h})(\tilde{u}_{\tau h} - u_{\tau h}, z_{\tau h}), \end{aligned} \quad (4.85)$$

obtained by the Gâteaux derivatives with respect to the first and second argument of $\mathcal{S}^{\text{cG}}(\cdot, \cdot)$ that is given in (4.30). Here, $\{\tilde{u}_\tau, \tilde{z}_\tau\} \in \mathcal{V}_\tau^{\text{cG}(r)} \times \mathcal{V}_\tau^{\text{dG}(r-1)}$, and $\{\tilde{u}_{\tau h}, \tilde{z}_{\tau h}\} \in \mathcal{V}_{\tau h}^{\text{cG}(r), p} \times \mathcal{V}_{\tau h}^{\text{dG}(r-1), p}$ can be chosen arbitrarily and the remainder terms $\mathcal{R}_{\tilde{\tau}}$ and $\mathcal{R}_{\tilde{h}}$ have the same structure as the remainder term (4.59) in Lemma 4.1.

Proof. The proof is identical to that one of Thm. 4.1 using the following framework. Evaluating the Lagrangian functionals at the respective primal and dual solutions, there holds that (cf. Eq. (4.31) in Rem. 4.4)

$$J(u) = \mathcal{L}(u, z), \quad J(u_\tau) = \mathcal{L}(u_\tau, z_\tau), \quad J(u_{\tau h}) = \mathcal{L}_{\tau h}(u_{\tau h}, z_{\tau h}).$$

Consequently, we can write

$$J(u) - J(u_\tau) = \mathcal{L}(u, z) - \mathcal{L}(u_\tau, z_\tau), \quad (4.86)$$

$$J(u_\tau) - J(u_{\tau h}) = \mathcal{L}(u_\tau, z_\tau) - \mathcal{L}_{\tau h}^{\text{cG}}(u_{\tau h}, z_{\tau h}). \quad (4.87)$$

Then, we apply Lemma 4.1 with the settings

$$L = \mathcal{L}, \quad \tilde{L} = \mathcal{L}, \quad \mathcal{Y}_1 = \mathcal{V} \times \mathcal{V}, \quad \mathcal{Y}_2 = \mathcal{V}_\tau^{\text{cG}(r)} \times \mathcal{V}_\tau^{\text{dG}(r-1)} \quad \text{for (4.86),}$$

$$L = \mathcal{L}, \quad \tilde{L} = \mathcal{L}_{\tau h}^{\text{cG}}, \quad \mathcal{Y}_1 = \mathcal{V}_\tau^{\text{cG}(r)} \times \mathcal{V}_\tau^{\text{dG}(r-1)}, \quad \mathcal{Y}_2 = \mathcal{V}_{\tau h}^{\text{cG}(r), p} \times \mathcal{V}_{\tau h}^{\text{dG}(r-1), p} \quad \text{for (4.87).}$$

For completeness, we note that the remainder terms $\mathcal{R}_{\tilde{\tau}}$ and $\mathcal{R}_{\tilde{h}}$ are given by

$$\mathcal{R}_{\tilde{\tau}} = \frac{1}{2} \int_0^1 \mathcal{L}'''(u_\tau + se, z_\tau + se^*)(e, e, e, e^*, e^*, e^*) s(s-1) ds, \quad (4.88)$$

$$\mathcal{R}_{\tilde{h}} = \frac{1}{2} \int_0^1 \mathcal{L}'''(u_{\tau h} + se_h, z_{\tau h} + se_h^*)(e_h, e_h, e_h, e_h^*, e_h^*, e_h^*) s(s-1) ds, \quad (4.89)$$

with the ‘primal’ and ‘dual’ errors $e := u - u_\tau$, $e_h := u_\tau - u_{\tau h}$ and $e^* := z - z_\tau$, $e_h^* := z_\tau - z_{\tau h}$, respectively. Finally, the derivation of the continuous stabilization terms are given by

$$\begin{aligned} \mathcal{S}^{\text{cG}'}(u_{\tau h}, z_{\tau h})(\tilde{u}_{\tau h} - u_{\tau h}, \tilde{z}_{\tau h} - z_{\tau h}) &= \mathcal{S}_u^{\text{cG}'}(u_{\tau h}, z_{\tau h})(\tilde{u}_{\tau h} - u_{\tau h}) \\ &\quad + \mathcal{S}_z^{\text{cG}'}(u_{\tau h}, z_{\tau h})(\tilde{z}_{\tau h} - z_{\tau h}). \\ &= S_A^{\text{cG}'}(u_{\tau h})(\tilde{u}_{\tau h} - u_{\tau h}, z_{\tau h}) \\ &\quad + S_A^{\text{cG}}(u_{\tau h})(\tilde{z}_{\tau h} - z_{\tau h}), \end{aligned}$$

where we have used the definition of the Gâteaux derivatives, given by Def. 2.11, cf. also Rem. 2.6, as well as the definition $\mathcal{S}^{\text{cG}}(u_{\tau h}, z_{\tau h}) := S_A^{\text{cG}}(u_{\tau h})(z_{\tau h})$, given by Eq. (4.30), with $S_A^{\text{cG}}(\cdot)(\cdot)$ and $S_A^{\text{cG}'}(\cdot)(\cdot, \cdot)$, given by Eq. (4.19) and Eq. (4.54), respectively. \square

Similar to the discontinuous in time dG(r) discretization case, it is useful to derive a relation between the primal and dual residual given in (4.82) depending on the different discretization levels.

Proposition 4.4 *Let the assumptions of Thm. 4.3 be satisfied. Further, let the primal and dual residual be given by Eq. (4.82). Then there holds that*

$$\rho^*(u_\tau, z_\tau)(u - \tilde{u}_\tau) = \rho(u_\tau)(z - \tilde{z}_\tau) + \Delta\tilde{\rho}_\tau, \quad (4.90)$$

for all $\{\tilde{u}_\tau, \tilde{z}_\tau\} \in \mathcal{V}_\tau^{\text{cG}(r)} \times \mathcal{V}_\tau^{\text{dG}(r-1)}$ with the remainder term $\Delta\tilde{\rho}_\tau$, given by

$$\Delta\tilde{\rho}_\tau := \int_0^1 \{A''(u_\tau + se)(e, e, z_\tau + se^*) - J''(u_\tau + se)(e, e)\} ds, \quad (4.91)$$

with $e := u - u_\tau$ and $e^* := z - z_\tau$.

Proof. The proof is identical to that one of Prop. 4.2 choosing the scalar function $k(\cdot)$ as

$$k(s) := J'(u_\tau + se)(u - \tilde{u}_\tau) - A'(u_\tau + se)(u - \tilde{u}_\tau, z_\tau + se^*),$$

where $J'(\cdot)(\cdot)$ and $A'(\cdot)(\cdot, \cdot)$ are given by Eq. (4.37) and (4.36), respectively. \square

The relation between the primal and dual residual within the spatial error representation formula (4.62) needs some particular care due to the stabilization terms and is summarized in the following proposition.

Proposition 4.5 *Let the assumptions of Thm. 4.3 be satisfied. Further, let the primal and dual residual be given by Eq. (4.82). Then there holds that*

$$\rho^*(u_{\tau h}, z_{\tau h})(u_\tau - \tilde{u}_{\tau h}) = \rho(u_{\tau h})(z_\tau - \tilde{z}_{\tau h}) + \Delta\rho_{S^{\text{cG}}} + \Delta\tilde{\rho}_h, \quad (4.92)$$

for all $\{\tilde{u}_{\tau h}, \tilde{z}_{\tau h}\} \in \mathcal{V}_{\tau h}^{\text{cG}(r),p} \times \mathcal{V}_{\tau h}^{\text{dG}(r-1),p}$ with the remainder terms $\Delta\rho_{S^{\text{cG}}}$ and $\Delta\tilde{\rho}_h$ are given by, respectively,

$$\Delta\rho_{S^{\text{cG}}} := S_A^{\text{cG}}(u_{\tau h})(\tilde{z}_{\tau h} - z_{\tau h}) - S_A^{\text{cG}'}(u_{\tau h})(\tilde{u}_{\tau h} - u_{\tau h}, z_{\tau h}), \quad (4.93)$$

$$\Delta\tilde{\rho}_h := \int_0^1 \{A''(u_{\tau h} + se)(e, e, z_{\tau h} + se^*) - J''(u_{\tau h} + se)(e, e)\} ds, \quad (4.94)$$

with $e := u_\tau - u_{\tau h}$ and $e^* := z_\tau - z_{\tau h}$.

Proof. The proof is identical to that one of Prop. 4.3 choosing the scalar function $k(\cdot)$ as

$$k(s) := J'(u_{\tau h} + se)(u_\tau - \tilde{u}_{\tau h}) - A'(u_{\tau h} + se)(u_\tau - \tilde{u}_{\tau h}, z_{\tau h} + se^*),$$

where $J'(\cdot)(\cdot)$ and $A'(\cdot)(\cdot, \cdot)$ are given by Eq. (4.37) and (4.36), respectively. \square

By using Prop. 4.4 and 4.5 the error representation formulas (4.83) and (4.84), respectively, can be reduced by means of the following theorem.

Theorem 4.4 (Reduced Error Representation cG(r) Time Discretization)

Let the assumption of Thm. 4.3 be satisfied. Then, for the discretization errors in space and time we get the representation formulas

$$J(u) - J(u_\tau) = \rho(u_\tau)(z - \tilde{z}_\tau) + \frac{1}{2}\Delta\tilde{\rho}_\tau + \mathcal{R}_{\tilde{\tau}}, \quad (4.95)$$

$$J(u_\tau) - J(u_{\tau h}) = \rho(u_{\tau h})(z_\tau - \tilde{z}_{\tau h}) + S_A^{\text{cG}}(u_{\tau h})(\tilde{z}_{\tau h}) + \frac{1}{2}\Delta\tilde{\rho}_h + \mathcal{R}_{\tilde{h}}. \quad (4.96)$$

Here, $\tilde{z}_\tau \in \mathcal{V}_\tau^{\text{dG}(r-1)}$ and $\tilde{z}_{\tau h} \in \mathcal{V}_{\tau h}^{\text{dG}(r-1),p}$ can be chosen arbitrarily and the remainder terms $\Delta\tilde{\rho}_\tau$, $\Delta\tilde{\rho}_h$, $\mathcal{R}_{\tilde{\tau}}$, and $\mathcal{R}_{\tilde{h}}$ are given by the Eqs. (4.91), (4.94), (4.88), and (4.89), respectively.

Proof. The reduced temporal error representation formula (4.95) directly follows by applying Prop. 4.4 to Eq. (4.83) in Thm. 4.3.

To prove the reduced spatial error representation formula (4.96), we apply Prop. 4.5 to Eq. (4.84) in Thm. 4.3 along with the representation given by (4.85), to get

$$\begin{aligned} J(u_\tau) - J(u_{\tau h}) &= \rho(u_{\tau h})(z_\tau - \tilde{z}_{\tau h}) + S_A^{\text{cG}}(u_{\tau h})(\tilde{z}_{\tau h} - z_{\tau h}) + S_A^{\text{cG}}(u_{\tau h})(z_{\tau h}) \\ &\quad + \frac{1}{2}\Delta\tilde{\rho}_h + \mathcal{R}_{\tilde{h}} \\ &= \rho(u_{\tau h})(z_\tau - \tilde{z}_{\tau h}) + S_A^{\text{cG}}(u_{\tau h})(\tilde{z}_{\tau h}) + \frac{1}{2}\Delta\tilde{\rho}_h + \mathcal{R}_{\tilde{h}}. \end{aligned}$$

\square

4.3 Practical Aspects

In this section, we illustrate some aspects for the practical realization of the space-time adaptivity process in view of the underlying convection-diffusion-reaction transport problem. Thereby, we start with presenting time marching schemes (TMS) of the continuous and discontinuous in time stabilized fully discrete primal and dual problems, give definitions of the localized error indicators and introduce different approximation techniques for the temporal weights. Finally, we present the underlying adaptive space-time algorithm.

4.3.1 Representation as a Time Marching Scheme

As introduced in Rem. 2.3 in Sec. 2.2, the choice of a discontinuous time-discrete test space allows for rewriting the variational system as a time marching scheme. The representation as a TMS is helpful for the practical realization of the underlying problem by decoupling the original huge system into independent subproblems. In the course of this, we recall the separation of the global space-time domain $Q = \Omega \times I$ into a partition of space-time slabs $Q_n = \mathcal{T}_{h,n} \times \mathcal{T}_{\tau,n}$, where $\mathcal{T}_{h,n}$ builds a triangulation of the domain Ω and $\mathcal{T}_{\tau,n}$ builds a triangulation of the closure of the time subinterval \bar{I}_n , respectively. Since we focus on a discontinuous in time discretization in our numerical examples, we first derive the time marching schemes for the stabilized primal and dual cG(p)-dG(r) schemes, given by Problem 4.8 and Problem 4.11, respectively. The case of a continuous in time discretization including Problem 4.7 and Problem 4.13, respectively, is presented afterwards. To derive the time marching schemes, we start with representing the fully discrete functions in a spatial and temporal fashion. Next, we recall a detailed version of the stabilized discontinuous in time fully discrete scheme for the primal and dual problem. Based on this, we derive the primal and dual fully discrete cG(p)-dG(r) time marching schemes. For the derivation of the time marching schemes, we use a similar notation as used in [128], where we also refer to for more details.

By using the in Sec. 2.2 introduced definitions of the continuous and discontinuous time-discrete functions, given by Eq. (2.4) and Eq. (2.10), respectively, the fully discrete functions of the stabilized schemes may be represented by

$$\begin{aligned} v_{\tau h}^{\text{cG}}|_{K \times K_n}(\mathbf{x}, t) &:= \sum_{\iota=0}^r v_h^{n,\iota}|_K(\mathbf{x}) \xi_{n,\iota}(t), \\ v_{\tau h}^{\text{dG}}|_{K \times K_n}(\mathbf{x}, t) &:= \sum_{\iota=0}^r v_h^{n,\iota}|_K(\mathbf{x}) \zeta_{n,\iota}(t), \end{aligned} \tag{4.97}$$

where the time-independent coefficients V_n^t are replaced by $v_h^{n,t}(\mathbf{x})$ existing of coefficients for the degrees of freedom in space and appropriate basis functions, and $\xi_{n,t}(\cdot)$ and $\zeta_{n,t}(\cdot)$ are given by Eq. (2.7) and Eq. (2.13), respectively.

4.3.1.1 Primal and Dual cG(p)-dG(r) Time Marching Schemes

In the case of a discontinuous in time discretization, the primal stabilized fully discrete scheme (cf. Problem 4.8), given by

$$A_S^{\text{dG}}(u_{\tau h}^{\text{dG}})(\varphi_{\tau h}^{\text{dG}}) = F_\tau(\varphi_{\tau h}^{\text{dG}}),$$

has the following detailed representation: Find $u_{\tau h}^{\text{dG}} \in \mathcal{V}_{\tau h}^{\text{dG}(r),p}$ such that

$$\begin{aligned} & \sum_{n=1}^N \sum_{K_n \in \mathcal{T}_{\tau,n}} \int_{K_n} \sum_{K \in \mathcal{T}_{h,n}} \{(\partial_t u_{\tau h}^{\text{dG}}, \varphi_{\tau h}^{\text{dG}})_K + (\varepsilon \nabla u_{\tau h}^{\text{dG}}, \nabla \varphi_{\tau h}^{\text{dG}})_K \\ & + (\mathbf{b} \cdot \nabla u_{\tau h}^{\text{dG}}, \varphi_{\tau h}^{\text{dG}})_K + (\alpha u_{\tau h}^{\text{dG}}, \varphi_{\tau h}^{\text{dG}})_K\} dt \\ & + \sum_{n=1}^N \sum_{K_n \in \mathcal{T}_{\tau,n}} \int_{K_n} \sum_{K \in \mathcal{T}_{h,n}} \delta_K \{(\partial_t u_{\tau h}^{\text{dG}}, \mathbf{b} \cdot \nabla \varphi_{\tau h}^{\text{dG}})_K - (\nabla \cdot (\varepsilon \nabla u_{\tau h}^{\text{dG}}), \mathbf{b} \cdot \nabla \varphi_{\tau h}^{\text{dG}})_K \\ & + (\mathbf{b} \cdot \nabla u_{\tau h}^{\text{dG}}, \mathbf{b} \cdot \nabla \varphi_{\tau h}^{\text{dG}})_K + (\alpha u_{\tau h}^{\text{dG}}, \mathbf{b} \cdot \nabla \varphi_{\tau h}^{\text{dG}})_K - (f, \mathbf{b} \cdot \nabla \varphi_{\tau h}^{\text{dG}})_K\} dt \\ & + \sum_{t_{\mathcal{F}} \in \mathcal{F}_\tau} \sum_{K \in \mathcal{T}_{h,n}} ([u_{\tau h}^{\text{dG}}]_{t_{\mathcal{F}}}, \varphi_{\tau h}^{\text{dG}}(t_{\mathcal{F}}^+))_K + \sum_{t_{\mathcal{F}} \in \mathcal{F}_\tau} \sum_{K \in \mathcal{T}_{h,n}} \delta_K ([u_{\tau h}^{\text{dG}}]_{t_{\mathcal{F}}}, \mathbf{b} \cdot \nabla \varphi_{\tau h}^{\text{dG}}(t_{\mathcal{F}}^+))_K \\ & + \sum_{K \in \mathcal{T}_{h,1}} (u_{\tau h}^{\text{dG}}(0^+), \varphi_{\tau h}^{\text{dG}}(0^+))_K + \sum_{K \in \mathcal{T}_{h,1}} \delta_K (u_{\tau h}^{\text{dG}}(0^+) - u_0, \mathbf{b} \cdot \nabla \varphi_{\tau h}^{\text{dG}}(0^+))_K \\ & = \sum_{n=1}^N \sum_{K_n \in \mathcal{T}_{\tau,n}} \int_{K_n} \sum_{K \in \mathcal{T}_{h,n}} (f, \varphi_{\tau h}^{\text{dG}})_K dt + (u_0, \varphi_{\tau h}^{\text{dG}}(0^+)) \quad \forall \varphi_{\tau h}^{\text{dG}} \in \mathcal{V}_{\tau h}^{\text{dG}(r),p}. \end{aligned}$$

The integrals in time are evaluated numerically by using an $(r+1)$ -point Gauss quadrature rule on K_n , denoted by $\mathcal{Q}_{G(r+1)}^n$, that integrates polynomials up to degree $2r+1$ in time exactly; cf. [1, Ch. 25.4]. More precisely, we do a domain transformation from K_n to the reference cell or interval \hat{I} and then solve the resulting integrals in time numerically by the $(r+1)$ -point Gauss quadrature rule on \hat{I} , denoted by $\hat{\mathcal{Q}}_{G(r+1)}$. The Gauss quadrature points on \hat{I} are assumed to be of the order $0 < \hat{t}_0 < \dots < \hat{t}_r < 1$. According to this, the support points on K_n for the trial functions in \mathcal{Y}_τ^r , given by Eq. (2.12) in Sec. 2.2.2, are defined by

$$t_{n,0} := \Upsilon_n(\hat{t}_0) < \dots < t_{n,r} := \Upsilon_n(\hat{t}_r), \quad (4.98)$$

where we refer to Sec. 2.2 for a detailed definition of the mapping $\Upsilon_n(\cdot)$ as well as appropriate Lagrange type reference basis functions. In general, the source term

integral of the right-hand side cannot be evaluated exactly. Hence, we approximate this integral by means of a numerical quadrature. Hereby, we replace the source term f by its appropriate Lagrange interpolant in time $f_\tau^{\text{dG}} \in \mathcal{V}_\tau^{\text{dG}(r)}$, such that $f_\tau^{\text{dG}}|_{K_n} \in \mathcal{P}_\tau^r(K_n; L^2(\Omega))$ is represented by

$$f_\tau^{\text{dG}}|_{K_n}(t) := \sum_{\iota=0}^r F_n^\iota \zeta_{n,\iota}(t), \quad F_n^\iota := f(t_{n,\iota}), \quad (4.99)$$

using the same basis functions $\zeta_{n,\iota} \in \mathcal{Y}_\tau^r$ and support points $t_{n,\iota}$ as introduced above.

Since the right endpoints do not belong to the set of support points, the treatment of the left-side traces influences all basis functions and belonging coefficients as

$$u_{\tau h}^{\text{dG}}(t_{\mathcal{F},n_\ell}^-) := u_{\tau h}^{\text{dG}}|_{K_{n_\ell}}(t_{\mathcal{F},n_\ell}^-), \quad (4.100)$$

where K_{n_ℓ} denotes the left neighbor cell in time of K_n and $t_{\mathcal{F},n_\ell}$ denotes the left end of K_n , respectively. For the case that K_n represents the first cell in time of the current slab Q_n , the left neighbor cell in time K_{n_ℓ} is given by the last cell in time of the previous slab Q_{n-1} , cf. Fig. 2.5 for an illustration. In particular, on the first cell in time of the first slab Q_1 the left-side trace $u_{\tau h}^{\text{dG}}(t_{\mathcal{F},1_\ell}^-)$ is given by the initial condition u_0 . Since the left endpoints do not belong to the set of support points, the treatment of the right-side traces influences all basis functions and belonging coefficients as

$$u_{\tau h}^{\text{dG}}(t_{\mathcal{F},n_\ell}^+) = \sum_{\iota=0}^r u_h^{n,\iota} \zeta_{n,\iota}(t_{\mathcal{F},n_\ell}^+). \quad (4.101)$$

Thus, on a cell in time K_n the terms involving a jump in $t_{\mathcal{F},n_\ell}$ read as

$$\begin{aligned} ([u_{\tau h}^{\text{dG}}]_{t_{\mathcal{F},n_\ell}}, \varphi_{\tau h}^{\text{dG}}(t_{\mathcal{F},n_\ell}^+)) &= \sum_{\iota=0}^r \zeta_{n,\iota}(t_{\mathcal{F},n_\ell}^+) \zeta_{n,\kappa}(t_{\mathcal{F},n_\ell}^+) (u_h^{n,\iota}, \varphi_h) \\ &\quad - \zeta_{n,\kappa}(t_{\mathcal{F},n_\ell}^+) (u_{\tau h}^{\text{dG}}(t_{\mathcal{F},n_\ell}^-), \varphi_h), \\ ([u_{\tau h}^{\text{dG}}]_{t_{\mathcal{F},n_\ell}}, \mathbf{b} \cdot \nabla \varphi_{\tau h}^{\text{dG}}(t_{\mathcal{F},n_\ell}^+)) &= \sum_{\iota=0}^r \zeta_{n,\iota}(t_{\mathcal{F},n_\ell}^+) \zeta_{n,\kappa}(t_{\mathcal{F},n_\ell}^+) (u_h^{n,\iota}, \mathbf{b} \cdot \nabla \varphi_h) \\ &\quad - \zeta_{n,\kappa}(t_{\mathcal{F},n_\ell}^+) (u_{\tau h}^{\text{dG}}(t_{\mathcal{F},n_\ell}^-), \mathbf{b} \cdot \nabla \varphi_h). \end{aligned} \quad (4.102)$$

Finally, using the representation of the discontinuous in time fully discrete functions, given by Eq. (4.97), and the representation of the jump terms, given by Eq. (4.102), as well as the numerical approximation of the integrals in time by means of an $(r+1)$ -point Gauss quadrature rule, we get the following fully discrete cG(p)-dG(r) time marching scheme for Problem 4.8:

Problem 4.14 (Primal Fully Discrete Stabilized cG(p)-dG(r) TMS)

Find $u_{\tau h}^{\text{dG}}|_{K \times K_n} \in \mathcal{P}_\tau^r(K_n; V_h^{p,n})$, represented by Eq. (4.97) with coefficients $u_h^{n,\iota}$, $\iota = 0, \dots, r$, such that

$$\begin{aligned}
& \sum_{K_n \in \mathcal{T}_{\tau,n}} \sum_{\iota=0}^r \left\{ \alpha_{\kappa,\iota} \left(\sum_{K \in \mathcal{T}_{h,n}} ((u_h^{n,\iota}, \varphi_h)_K + \delta_K(u_h^{n,\iota}, \mathbf{b} \cdot \nabla \varphi_h)_K) \right) \right. \\
& \quad + \beta_{\kappa,\iota} \left(\sum_{K \in \mathcal{T}_{h,n}} ((\varepsilon \nabla u_h^{n,\iota}, \nabla \varphi_h)_K - \delta_K(\nabla \cdot (\varepsilon \nabla u_h^{n,\iota}), \mathbf{b} \cdot \nabla \varphi_h)_K) \right) \\
& \quad + \beta_{\kappa,\iota} \left(\sum_{K \in \mathcal{T}_{h,n}} ((\mathbf{b} \cdot \nabla u_h^{n,\iota}, \varphi_h)_K + \delta_K(\mathbf{b} \cdot \nabla u_h^{n,\iota}, \mathbf{b} \cdot \nabla \varphi_h)_K) \right) \\
& \quad \left. + \beta_{\kappa,\iota} \left(\sum_{K \in \mathcal{T}_{h,n}} ((\alpha u_h^{n,\iota}, \varphi_h)_K + \delta_K(\alpha u_h^{n,\iota}, \mathbf{b} \cdot \nabla \varphi_h)_K) \right) \right\} \\
& = \sum_{K_n \in \mathcal{T}_{\tau,n}} \sum_{\iota=0}^r \beta_{\kappa,\iota} \left(\sum_{K \in \mathcal{T}_{h,n}} ((f_h^{n,\iota}, \varphi_h)_K + \delta_K(f_h^{n,\iota}, \mathbf{b} \cdot \nabla \varphi_h)_K) \right) \\
& \quad + \gamma_\kappa \left(\sum_{K \in \mathcal{T}_{h,n}} ((u_{\tau h}^{\text{dG}}(t_{\mathcal{F},n_\ell}^-), \varphi_h)_K + (u_{\tau h}^{\text{dG}}(t_{\mathcal{F},n_\ell}^-), \mathbf{b} \cdot \nabla \varphi_h)_K) \right), \tag{4.103}
\end{aligned}$$

for all $\varphi_h \in V_h^{p,n}$, for all $\kappa = 0, \dots, r$, and with

$$\begin{aligned}
\alpha_{\kappa,\iota} & := (\zeta'_{n,\iota}(t), \zeta_{n,\kappa}(t))_{K_n} + \zeta_{n,\iota}(t_{\mathcal{F},n_\ell}^+) \zeta_{n,\kappa}(t_{\mathcal{F},n_\ell}^+) \\
& = \int_{\hat{I}} \hat{\zeta}'_\iota(\hat{t}) \hat{\zeta}_\kappa(\hat{t}) \, d\hat{t} + \hat{\zeta}_\iota(0) \hat{\zeta}_\kappa(0) = \sum_{\mu=0}^r \hat{w}_\mu \hat{\zeta}'_\iota(\hat{t}_\mu) \hat{\zeta}_\kappa(\hat{t}_\mu) + \hat{\zeta}_\iota(0) \hat{\zeta}_\kappa(0), \\
\beta_{\kappa,\iota} & := (\zeta_{n,\iota}(t), \zeta_{n,\kappa}(t))_{K_n} = \int_{\hat{I}} \hat{\zeta}_\iota(\hat{t}) \hat{\zeta}_\kappa(\hat{t}) \, \tau_n \, d\hat{t} = \sum_{\mu=0}^r \tau_n \hat{w}_\mu \hat{\zeta}_\iota(\hat{t}_\mu) \hat{\zeta}_\kappa(\hat{t}_\mu), \\
\gamma_\kappa & := \zeta_{n,\kappa}(t_{\mathcal{F},n_\ell}^+) = \hat{\zeta}_\kappa(0), \tag{4.104}
\end{aligned}$$

where the reference basis functions in time $\hat{\zeta}_\iota(\cdot)$, $\hat{\zeta}_\kappa(\cdot)$ are the standard Lagrange basis functions as introduced in Sec. 2.2.2, using quadrature weights \hat{w}_μ and quadrature points \hat{t}_μ from $\hat{\mathcal{Q}}_{G(r+1)}$, and with

$$u_{\tau h}^{\text{dG}}(t_{\mathcal{F},n_\ell}^-) := u_{\tau h}^{\text{dG}}|_{K_{n_\ell}}(t_{\mathcal{F},n_\ell}^-), \tag{4.105}$$

by marching sequentially through all slabs Q_n , $n = 1, \dots, N$, where on the first cell of the first slab Q_1 the left-side trace $u_{\tau h}^{\text{dG}}(t_{\mathcal{F},1_\ell}^-) = u_0$ is used to include the initial value.

Remark 4.9 We note that compared to the continuous in time case, given by Problem 4.16, there appears an additional term within the definition of $\alpha_{\kappa,\iota}$ in Eq. (4.104) due to the jump terms, given by Eq. (4.102). Furthermore, we note that by approximating the temporal integrals in Problem 4.14 for the case $r = 0$ by the right-sided box rule

$$\int_{K_n} f(t) \, dt \approx \tau_n f(t_{\mathcal{F},n}),$$

the $cG(p)$ - $dG(0)$ TMS is algebraically equivalent to the well-known backward Euler scheme, where $t_{\mathcal{F},n}$ represents here the right end of the cell in time K_n .

Next, we deal with the derivation of the time marching scheme for the dual problem. The dual discontinuous in time stabilized fully discrete scheme (cf. Problem 4.11), given by

$$A_S^{\text{dG}'}(u_{\tau h}^{\text{dG}})(\psi_{\tau h}^{\text{dG}}, z_{\tau h}^{\text{dG}}) = \sum_{n=1}^N \sum_{K_n \in \mathcal{T}_{\tau,n}} \int_{K_n} J_1'(u_{\tau h}^{\text{dG}})(\psi_{\tau h}^{\text{dG}}) dt + J_2'(u_{\tau h}^{\text{dG}}(T^-))(\psi_{\tau h}^{\text{dG}}(T^-)),$$

has the following detailed representation: Find $z_{\tau h}^{\text{dG}} \in \mathcal{V}_{\tau h}^{\text{dG}(r),p}$ such that

$$\begin{aligned} & \sum_{n=1}^N \sum_{K_n \in \mathcal{T}_{\tau,n}} \int_{K_n} \sum_{K \in \mathcal{T}_{h,n}} \{(\psi_{\tau h}^{\text{dG}}, -\partial_t z_{\tau h}^{\text{dG}})_K + (\varepsilon \nabla \psi_{\tau h}^{\text{dG}}, \nabla z_{\tau h}^{\text{dG}})_K \\ & + (\mathbf{b} \cdot \nabla \psi_{\tau h}^{\text{dG}}, z_{\tau h}^{\text{dG}})_K + (\alpha \psi_{\tau h}^{\text{dG}}, z_{\tau h}^{\text{dG}})_K\} dt \\ & + \sum_{n=1}^N \sum_{K_n \in \mathcal{T}_{\tau,n}} \int_{K_n} \sum_{K \in \mathcal{T}_{h,n}} \delta_K \{(\mathbf{b} \cdot \nabla \psi_{\tau h}^{\text{dG}}, \partial_t z_{\tau h}^{\text{dG}})_K - (\nabla \cdot (\varepsilon \nabla \psi_{\tau h}^{\text{dG}}), \mathbf{b} \cdot \nabla z_{\tau h}^{\text{dG}})_K \\ & + (\mathbf{b} \cdot \nabla \psi_{\tau h}^{\text{dG}}, \mathbf{b} \cdot \nabla z_{\tau h}^{\text{dG}})_K + (\alpha \psi_{\tau h}^{\text{dG}}, \mathbf{b} \cdot \nabla z_{\tau h}^{\text{dG}})_K\} dt \\ & - \sum_{t_{\mathcal{F}} \in \mathcal{F}_{\tau}} \sum_{K \in \mathcal{T}_{h,n}} (\psi_{\tau h}^{\text{dG}}(t_{\mathcal{F}}^-), [z_{\tau h}^{\text{dG}}]_{t_{\mathcal{F}}})_K + \sum_{t_{\mathcal{F}} \in \mathcal{F}_{\tau}} \sum_{K \in \mathcal{T}_{h,n}} \delta_K (\mathbf{b} \cdot \nabla \psi_{\tau h}^{\text{dG}}(t_{\mathcal{F}}^-), [z_{\tau h}^{\text{dG}}]_{t_{\mathcal{F}}})_K \\ & + \sum_{K \in \mathcal{T}_{h,N}} (\psi_{\tau h}^{\text{dG}}(T^-), z_{\tau h}^{\text{dG}}(T^-))_K - \sum_{K \in \mathcal{T}_{h,N}} \delta_K (\mathbf{b} \cdot \nabla \psi_{\tau h}^{\text{dG}}(T^-), z_{\tau h}^{\text{dG}}(T^-))_K \\ & = \sum_{n=1}^N \sum_{K_n \in \mathcal{T}_{\tau,n}} \int_{K_n} J_1'(u_{\tau h}^{\text{dG}})(\psi_{\tau h}^{\text{dG}}) dt + J_2'(u_{\tau h}^{\text{dG}}(T^-))(\psi_{\tau h}^{\text{dG}}(T^-)), \quad \forall \psi_{\tau h}^{\text{dG}} \in \mathcal{V}_{\tau h}^{\text{dG}(r),p}. \end{aligned}$$

Again, the integrals in time are evaluated numerically by using an $(r+1)$ -point Gauss quadrature rule on K_n in the same fashion as described above. Since, in general, the dual problem is solved running backward in time, the observations with regard to the primal problem above have to be modified contrarily within the following manner. Since the left endpoints do not belong to the set of support points, the treatment of the right-side traces influences all basis functions and belonging coefficients as

$$z_{\tau h}^{\text{dG}}(t_{\mathcal{F},n}^+) := z_{\tau h}^{\text{dG}}|_{K_{n_r}}(t_{\mathcal{F},n}^+), \quad (4.106)$$

where K_{n_r} denotes the right neighbor cell in time of K_n and $t_{\mathcal{F},n}$ denotes the right end of K_n , respectively. For the case that K_n represents the last cell in time of the current slab Q_n , the right neighbor cell in time K_{n_r} is given by the first cell in time of the subsequent slab Q_{n+1} , cf. Fig. 2.5 for an illustration. In particular, on the last cell

in time of the last slab Q_N the right-side trace $z_{\tau h}^{\text{dG}}(t_{\mathcal{F},n}^+)$ is given by the dual initial at time $t = T$, denoted by z_T and depending on the choice of the goal functional J , cf. Rem.4.5.

Since the right endpoints do not belong to the set of support points, the treatment of the left-side traces influences all basis functions and belonging coefficients as

$$z_{\tau h}^{\text{dG}}(t_{\mathcal{F},n}^-) = \sum_{\iota=0}^r z_h^{n,\iota} \zeta_{n,\iota}(t_{\mathcal{F},n}^-). \quad (4.107)$$

Thus, on a cell in time K_n the terms involving a jump in $t_{\mathcal{F},n}$ read as

$$\begin{aligned} (\psi_{\tau h}^{\text{dG}}(t_{\mathcal{F},n}^-), [z_{\tau h}^{\text{dG}}]_{t_{\mathcal{F},n}}) &= \zeta_{n,\kappa}(t_{\mathcal{F},n}^-)(\psi_h, z_{\tau h}^{\text{dG}}(t_{\mathcal{F},n}^+)) \\ &\quad - \sum_{\iota=0}^r \zeta_{n,\kappa}(t_{\mathcal{F},n}^-) \zeta_{n,\iota}(t_{\mathcal{F},n}^-) (\psi_h, z_h^{n,\iota}), \\ (\mathbf{b} \cdot \nabla \psi_{\tau h}^{\text{dG}}(t_{\mathcal{F},n}^-), [z_{\tau h}^{\text{dG}}]_{t_{\mathcal{F},n}}) &= \zeta_{n,\kappa}(t_{\mathcal{F},n}^-) (\mathbf{b} \cdot \nabla \psi_h, z_{\tau h}^{\text{dG}}(t_{\mathcal{F},n}^+)) \\ &\quad - \sum_{\iota=0}^r \zeta_{n,\kappa}(t_{\mathcal{F},n}^-) \zeta_{n,\iota}(t_{\mathcal{F},n}^-) (\mathbf{b} \cdot \nabla \psi_h, z_h^{n,\iota}). \end{aligned} \quad (4.108)$$

Finally, using the representation of the discontinuous in time fully discrete functions, given by Eq. (4.97), and the representation of the jump terms, given by Eq. (4.108), as well as the numerical approximation of the integrals in time by means of an $(r + 1)$ -point Gauss quadrature rule, we get the following dual fully discrete cG(p)-dG(r) time marching scheme for Problem 4.11, cf. Rem. 4.6:

Problem 4.15 (Dual Fully Discrete Stabilized cG(p)-dG(r) TMS)

Find $z_{\tau h}^{\text{dG}}|_{K \times K_n} \in \mathcal{P}_\tau^r(K_n; V_h^{p,n})$, represented by Eq. (4.97) with coefficients $z_h^{n,\iota}$, $\iota = 0, \dots, r$, such that

$$\begin{aligned} &\sum_{K_n \in \mathcal{T}_{\tau,n}} \sum_{\iota=0}^r \left\{ \alpha_{\kappa,\iota} \left(\sum_{K \in \mathcal{T}_{h,n}} (- (\psi_h, z_h^{n,\iota})_K + \delta_K (\mathbf{b} \cdot \nabla \psi_h, z_h^{n,\iota})_K) \right) \right. \\ &\quad + \beta_{\kappa,\iota} \left(\sum_{K \in \mathcal{T}_{h,n}} ((\varepsilon \nabla \psi_h, \nabla z_h^{n,\iota})_K - \delta_K (\nabla \cdot (\varepsilon \nabla \psi_h), \mathbf{b} \cdot \nabla z_h^{n,\iota})_K) \right) \\ &\quad + \beta_{\kappa,\iota} \left(\sum_{K \in \mathcal{T}_{h,n}} ((\mathbf{b} \cdot \nabla \psi_h, z_h^{n,\iota})_K + \delta_K (\mathbf{b} \cdot \nabla \psi_h, \mathbf{b} \cdot \nabla z_h^{n,\iota})_K) \right) \\ &\quad \left. + \beta_{\kappa,\iota} \left(\sum_{K \in \mathcal{T}_{h,n}} ((\alpha \psi_h, z_h^{n,\iota})_K + \delta_K (\alpha \psi_h, \mathbf{b} \cdot \nabla z_h^{n,\iota})_K) \right) \right\} \\ &= \sum_{K_n \in \mathcal{T}_{\tau,n}} \sum_{\iota=0}^r \beta_{\kappa,\iota} \sum_{K \in \mathcal{T}_{h,n}} J_1|_K(u_h^{n,\iota})(\psi_h) \\ &\quad + \gamma_\kappa \sum_{K \in \mathcal{T}_{h,n}} ((\psi_h, z_{\tau h}^{\text{dG}}(t_{\mathcal{F},n}^+))_K - \delta_K (\mathbf{b} \cdot \nabla \psi_h, z_{\tau h}^{\text{dG}}(t_{\mathcal{F},n}^+))_K), \end{aligned} \quad (4.109)$$

for all $\psi_h \in V_h^{p,n}$, for all $\kappa = 0, \dots, r$, and with

$$\begin{aligned}
\alpha_{\kappa,\iota} &:= (\zeta_{n,\kappa}(t), \zeta'_{n,\iota}(t))_{K_n} - \zeta_{n,\kappa}(t_{\mathcal{F},n}^-) (\zeta_{n,\iota}(t_{\mathcal{F},n}^-)) \\
&= \int_{\hat{I}} \hat{\zeta}_\kappa(\hat{t}) \hat{\zeta}'_\iota(\hat{t}) d\hat{t} - \hat{\zeta}_\kappa(1) \hat{\zeta}'_\iota(1) = \sum_{\mu=0}^r \hat{w}_\mu \hat{\zeta}_\kappa(\hat{t}_\mu) \hat{\zeta}'_\iota(\hat{t}_\mu) - \hat{\zeta}_\kappa(1) \hat{\zeta}'_\iota(1), \\
\beta_{\kappa,\iota} &:= (\zeta_{n,\kappa}(t), \zeta_{n,\iota}(t))_{K_n} = \int_{\hat{I}} \hat{\zeta}_\kappa(\hat{t}) \hat{\zeta}_\iota(\hat{t}) \tau_n d\hat{t} = \sum_{\mu=0}^r \tau_n \hat{w}_\mu \hat{\zeta}_\kappa(\hat{t}_\mu) \hat{\zeta}_\iota(\hat{t}_\mu), \\
\gamma_\kappa &:= \zeta_{n,\kappa}(t_{\mathcal{F},n}^-) = \hat{\zeta}_\kappa(1),
\end{aligned} \tag{4.110}$$

where the reference basis functions in time $\hat{\zeta}_\iota(\cdot), \hat{\zeta}_\kappa(\cdot)$ are the standard Lagrange basis functions as introduced in Sec. 2.2.2, using quadrature weights \hat{w}_μ and quadrature points \hat{t}_μ from $\hat{\mathcal{Q}}_{G(r+1)}$, and with

$$z_{\tau h}^{\text{dG}}(t_{\mathcal{F},n}^+) := z_{\tau h}^{\text{dG}}|_{K_{n_r}}(t_{\mathcal{F},n}^+), \tag{4.111}$$

by marching sequentially through all slabs $Q_n, n = N, \dots, 1$, where on the last cell in time of the last slab Q_N the right-side trace $z_{\tau h}^{\text{dG}}(t_{\mathcal{F},N}^+) = z_T$ is introduced to include the dual initial at time $t = T$ which depends on the choice of the underlying goal functional J as outlined in Rem.4.5.

4.3.1.2 Primal and Dual cG(p)-cG(r) Time Marching Schemes

For the sake of completeness, we present the primal and dual time marching schemes in the case of a continuous in time discretization. The primal continuous in time stabilized fully discrete scheme (cf. Problem 4.7), given by

$$A_S^{\text{cG}}(u_{\tau h}^{\text{dG}})(\varphi_{\tau h}^{\text{dG}}) = F_\tau(\varphi_{\tau h}^{\text{dG}}),$$

has the following detailed representation: Find $u_{\tau h}^{\text{cG}} \in \mathcal{V}_{\tau h}^{\text{cG}(r),p}$ such that

$$\begin{aligned}
&\sum_{n=1}^N \sum_{K_n \in \mathcal{T}_{\tau,n}} \int_{K_n} \sum_{K \in \mathcal{T}_{h,n}} \{(\partial_t u_{\tau h}^{\text{cG}}, \varphi_{\tau h}^{\text{dG}})_K + (\varepsilon \nabla u_{\tau h}^{\text{cG}}, \nabla \varphi_{\tau h}^{\text{dG}})_K \\
&+ (\mathbf{b} \cdot \nabla u_{\tau h}^{\text{cG}}, \varphi_{\tau h}^{\text{dG}})_K + (\alpha u_{\tau h}^{\text{cG}}, \varphi_{\tau h}^{\text{dG}})_K\} dt \\
&+ \sum_{n=1}^N \sum_{K_n \in \mathcal{T}_{\tau,n}} \int_{K_n} \sum_{K \in \mathcal{T}_{h,n}} \delta_K \{(\partial_t u_{\tau h}^{\text{cG}}, \mathbf{b} \cdot \nabla \varphi_{\tau h}^{\text{dG}})_K - (\nabla \cdot (\varepsilon \nabla u_{\tau h}^{\text{cG}}), \mathbf{b} \cdot \nabla \varphi_{\tau h}^{\text{dG}})_K \\
&+ (\mathbf{b} \cdot \nabla u_{\tau h}^{\text{cG}}, \mathbf{b} \cdot \nabla \varphi_{\tau h}^{\text{dG}})_K + (\alpha u_{\tau h}^{\text{cG}}, \mathbf{b} \cdot \nabla \varphi_{\tau h}^{\text{dG}})_K - (f, \mathbf{b} \cdot \nabla \varphi_{\tau h}^{\text{dG}})_K\} dt \\
&+ \sum_{K \in \mathcal{T}_{h,1}} (u_{\tau h}^{\text{cG}}(0), \varphi_{\tau h}^{\text{dG}}(0^+))_K + \sum_{K \in \mathcal{T}_{h,1}} \delta_K (u_{\tau h}^{\text{cG}}(0) - u_0, \mathbf{b} \cdot \nabla \varphi_{\tau h}^{\text{dG}}(0^+))_K \\
&= \sum_{n=1}^N \sum_{K_n \in \mathcal{T}_{\tau,n}} \int_{K_n} \sum_{K \in \mathcal{T}_{h,n}} (f, \varphi_{\tau h}^{\text{dG}})_K dt + (u_0, \varphi_{\tau h}^{\text{dG}}(0^+)) \quad \forall \varphi_{\tau h}^{\text{dG}} \in \mathcal{V}_{\tau h}^{\text{dG}(r-1),p}.
\end{aligned}$$

The integrals in time are evaluated numerically by using an r -point Gauss quadrature rule on \bar{K}_n , denoted by $\mathcal{Q}_{G(r)}^n$. This quadrature rule integrates polynomials up to degree $2r - 1$ in time exactly; cf. [1, Ch. 25.4]. More precisely, we do a domain transformation from K_n to the reference cell or rather interval \hat{I} and then solve the resulting integrals in time numerically by the r -point Gauss quadrature rule on \hat{I} , denoted by $\hat{\mathcal{Q}}_{G(r)}$. The Gauss quadrature points on \hat{I} are assumed to be of the order $0 < \hat{t}_0 < \dots < \hat{t}_{r-1} < 1$. According to this, the support points on K_n for the trial functions in \mathcal{X}_τ^r , given by Eq. (2.6) in Sec. 2.2.1, are defined by

$$t_{n,0} := \Upsilon_n(0), \quad t_{n,1} := \Upsilon_n(\hat{t}_0) < \dots < t_{n,r} := \Upsilon_n(\hat{t}_{r-1}), \quad (4.112)$$

where we refer to Sec. 2.2 for a detailed definition of the mapping $\Upsilon_n(\cdot)$ as well as appropriate Lagrange type reference basis functions. In general, the source term integral of the right-hand side cannot be evaluated exactly. For the sake of simplicity, we assume f to be continuous in time, otherwise a different discretization has to be applied to the right-hand side integral. Hence, we approximate this integral by means of the same numerical quadrature as above. Hereby, we replace the source term f by its appropriate Lagrange interpolant in time $f_\tau^{\text{cG}} \in \mathcal{V}_\tau^{\text{cG}(r)}$, such that $f_\tau^{\text{cG}}|_{K_n} \in \mathcal{P}_\tau^r(\bar{K}_n; L^2(\Omega))$ is represented by

$$f_\tau^{\text{cG}}|_{K_n}(t) := \sum_{\iota=0}^r F_n^\iota \xi_{n,\iota}(t), \quad F_n^\iota := f(t_{n,\iota}), \quad (4.113)$$

using the same basis functions $\xi_{n,\iota}(\cdot) \in \mathcal{X}_\tau^r$ and support points $t_{n,\iota}$ as introduced above. The choice for determining the basis functions in \mathcal{X}_τ^r as Lagrange type basis functions defined over the support points, given by Eq. (4.112), allows for an easy treatment of the initial and continuity condition since the left endpoints of the cells in time K_n are included in the set of support points and only one basis function is non-zero in each support point.

Now, using the representation of the continuous and discontinuous in time fully discrete functions, given by Eq. (4.97), as well as the numerical approximation of the integrals in time by means of an r -point Gauss quadrature rule, we get the following fully discrete cG(p)-cG(r) time marching scheme for Problem 4.7:

Problem 4.16 (Primal Fully Discrete Stabilized cG(p)-cG(r) TMS)

Find $u_{\tau h}^{\text{cG}}|_{K \times K_n} \in \mathcal{P}_\tau^r(\bar{K}_n; V)$, represented by Eq. (4.97) with coefficients $u_h^{n,\iota}$, $\iota = 0, \dots, r$, such that

$$\begin{aligned}
& \sum_{K_n \in \mathcal{T}_{\tau,n}} \sum_{\iota=0}^r \left\{ \alpha_{\kappa,\iota} \left(\sum_{K \in \mathcal{T}_{h,n}} ((u_h^{n,\iota}, \varphi_h)_K + \delta_K(u_h^{n,\iota}, \mathbf{b} \cdot \nabla \varphi_h)_K) \right) \right. \\
& \quad + \beta_{\kappa,\iota} \left(\sum_{K \in \mathcal{T}_{h,n}} ((\varepsilon \nabla u_h^{n,\iota}, \nabla \varphi_h)_K - \delta_K(\nabla \cdot (\varepsilon \nabla u_h^{n,\iota}), \mathbf{b} \cdot \nabla \varphi_h)_K) \right) \\
& \quad + \beta_{\kappa,\iota} \left(\sum_{K \in \mathcal{T}_{h,n}} ((\mathbf{b} \cdot \nabla u_h^{n,\iota}, \varphi_h)_K + \delta_K(\mathbf{b} \cdot \nabla u_h^{n,\iota}, \mathbf{b} \cdot \nabla \varphi_h)_K) \right) \\
& \quad \left. + \beta_{\kappa,\iota} \left(\sum_{K \in \mathcal{T}_{h,n}} ((\alpha u_h^{n,\iota}, \varphi_h)_K + \delta_K(\alpha u_h^{n,\iota}, \mathbf{b} \cdot \nabla \varphi_h)_K) \right) \right\} \\
& = \sum_{K_n \in \mathcal{T}_{\tau,n}} \sum_{\iota=0}^r \beta_{\kappa,\iota} \left(\sum_{K \in \mathcal{T}_{h,n}} ((f_h^{n,\iota}, \varphi_h)_K + \delta_K(f_h^{n,\iota}, \mathbf{b} \cdot \nabla \varphi_h)_K) \right), \tag{4.114}
\end{aligned}$$

for all $\varphi_h \in V_h^{p,n}$, for all $\kappa = 1, \dots, r$, and with

$$\begin{aligned}
\alpha_{\kappa,\iota} & := (\xi'_{n,\iota}(t), \zeta_{n,\kappa}(t))_{I_n} = \int_{\hat{I}} \hat{\xi}'_\iota(\hat{t}) \hat{\zeta}_\kappa(\hat{t}) \, d\hat{t} = \sum_{\mu=0}^{r-1} \hat{w}_\mu \hat{\xi}'_\iota(\hat{t}_\mu) \hat{\zeta}_\kappa(\hat{t}_\mu), \\
\beta_{\kappa,\iota} & := (\xi_{n,\iota}(t), \zeta_{n,\kappa}(t))_{I_n} = \int_{\hat{I}} \hat{\xi}_\iota(\hat{t}) \hat{\zeta}_\kappa(\hat{t}) \tau_n \, d\hat{t} = \sum_{\mu=0}^{r-1} \tau_n \hat{w}_\mu \hat{\xi}_\iota(\hat{t}_\mu) \hat{\zeta}_\kappa(\hat{t}_\mu), \tag{4.115}
\end{aligned}$$

where the reference basis functions in time $\hat{\xi}_\iota(\cdot), \hat{\zeta}_\kappa(\cdot)$ are the standard Lagrange basis functions as introduced in Sec. 2.2.2, using quadrature weights \hat{w}_μ and quadrature points \hat{t}_μ from $\hat{Q}_{G(r)}$, and with

$$u_h^{n,0} := \begin{cases} u_0, & \text{if } K_n \text{ is the first cell in time of } Q_1, \\ u_{\tau h}^{\text{cG}}|_{K_{n_\ell}}(t_{\mathcal{F},n_\ell}), & \text{else,} \end{cases} \tag{4.116}$$

by marching sequentially through all subintervals $I_n, n = 1, \dots, N$. Here, K_{n_ℓ} denotes the left neighbor cell in time of K_n and $t_{\mathcal{F},n_\ell}$ denotes the left end of K_n , respectively. Additionally, due to the fact that the initial condition is incorporated into the variational formulation, the following condition has to be satisfied on the first cell of Q_1 :

$$\sum_{\iota=0}^r \xi_{1,\iota}(0) \zeta_{1,\kappa}(0^+) \sum_{K \in \mathcal{T}_{h,1}} (u_h^{1,\iota}, \varphi_h)_K = \zeta_{1,\kappa}(0^+) \sum_{K \in \mathcal{T}_{h,1}} (u_0, \varphi_h)_K,$$

for all $\kappa = 0, \dots, r$.

Remark 4.10 We note that by approximating the temporal integrals in Problem 4.16 for the case $r = 1$ by the trapezoidal rule

$$\int_{K_n} f(t) dt \approx \frac{\tau_n}{2} (f(t_{\mathcal{F},n_\ell}) + f(t_{\mathcal{F}})),$$

one obtains a variant of the well-known Crank-Nicolson scheme, where $t_{\mathcal{F},n_\ell}$ and $t_{\mathcal{F},n}$ represent here the left and right end of the cell in time K_n , respectively.

Next, we deal with the derivation of the time marching scheme for the dual problem. The dual continuous in time stabilized fully discrete scheme (cf. Problem 4.13), given by

$$A_S^{\text{cG}'}(u_{\tau h}^{\text{cG}})(\psi_{\tau h}^{\text{cG}}, z_{\tau h}^{\text{dG}}) = \sum_{n=1}^N \sum_{K_n \in \mathcal{T}_{\tau,n}} \int_{K_n} J_1'(u_{\tau h}^{\text{cG}})(\psi_{\tau h}^{\text{cG}}) dt + J_2'(u_{\tau h}^{\text{cG}}(T))(\psi_{\tau h}^{\text{cG}}(T^-)),$$

has the following detailed representation: Find $z_{\tau h}^{\text{dG}} \in \mathcal{V}_{\tau h}^{\text{dG}(r-1),p}$ such that

$$\begin{aligned} & \sum_{n=1}^N \sum_{K_n \in \mathcal{T}_{\tau,n}} \int_{K_n} \sum_{K \in \mathcal{T}_{h,n}} \{ (\psi_{\tau h}^{\text{cG}}, -\partial_t z_{\tau h}^{\text{dG}})_K + (\varepsilon \nabla \psi_{\tau h}^{\text{cG}}, \nabla z_{\tau h}^{\text{dG}})_K \\ & + (\mathbf{b} \cdot \nabla \psi_{\tau h}^{\text{cG}}, z_{\tau h}^{\text{dG}})_K + (\alpha \psi_{\tau h}^{\text{cG}}, z_{\tau h}^{\text{dG}})_K \} dt \\ & + \sum_{n=1}^N \sum_{K_n \in \mathcal{T}_{\tau,n}} \int_{K_n} \sum_{K \in \mathcal{T}_{h,n}} \delta_K \{ (\mathbf{b} \cdot \nabla \psi_{\tau h}^{\text{cG}}, \partial_t z_{\tau h}^{\text{dG}})_K - (\nabla \cdot (\varepsilon \nabla \psi_{\tau h}^{\text{cG}}), \mathbf{b} \cdot \nabla z_{\tau h}^{\text{dG}})_K \\ & + (\mathbf{b} \cdot \nabla \psi_{\tau h}^{\text{cG}}, \mathbf{b} \cdot \nabla z_{\tau h}^{\text{dG}})_K + (\alpha \psi_{\tau h}^{\text{cG}}, \mathbf{b} \cdot \nabla z_{\tau h}^{\text{dG}})_K \} dt \\ & - \sum_{t_{\mathcal{F}} \in \mathcal{F}_\tau} \sum_{K \in \mathcal{T}_{h,n}} (\psi_{\tau h}^{\text{cG}}(t_{\mathcal{F}}^-), [z_{\tau h}^{\text{dG}}]_{t_{\mathcal{F}}})_K + \sum_{t_{\mathcal{F}} \in \mathcal{F}_\tau} \sum_{K \in \mathcal{T}_{h,n}} \delta_K (\mathbf{b} \cdot \nabla \psi_{\tau h}^{\text{cG}}(t_{\mathcal{F}}^-), [z_{\tau h}^{\text{dG}}]_{t_{\mathcal{F}}})_K \\ & + \sum_{K \in \mathcal{T}_{h,N}} (\psi_{\tau h}^{\text{cG}}(T^-), z_{\tau h}^{\text{dG}}(T^-))_K - \sum_{K \in \mathcal{T}_{h,N}} \delta_K (\mathbf{b} \cdot \nabla \psi_{\tau h}^{\text{cG}}(T^-), z_{\tau h}^{\text{dG}}(T^-))_K \\ & = \sum_{n=1}^N \sum_{K_n \in \mathcal{T}_{\tau,n}} \int_{K_n} J_1'(u_{\tau h}^{\text{cG}})(\psi_{\tau h}^{\text{cG}}) dt + J_2'(u_{\tau h}^{\text{cG}}(T))(\psi_{\tau h}^{\text{cG}}(T^-)), \quad \forall \psi_{\tau h}^{\text{cG}} \in \mathcal{V}_{\tau h}^{\text{cG}(r),p}. \end{aligned}$$

Again, the integrals in time are evaluated numerically by using an r -point Gauss quadrature rule on \bar{K}_n in the same fashion as described above. But since in general the dual problem is solved running backward in time and the role of trial and test spaces are switched, some observations with regard to the primal problem above have to be modified within the following manner.

The support points on K_n are defined by

$$t_{n,0} := \mathcal{T}_n(\hat{t}_0) < \dots < t_{n,r-1} := \mathcal{T}_n(\hat{t}_{r-1}), \quad t_{n,r} := \mathcal{T}_n(1), \quad (4.117)$$

where we refer to Sec. 2.2 for a detailed definition of $\mathcal{T}_n(\cdot)$ as well as appropriate Lagrange type reference basis functions. Since the right endpoints of the cells in time K_n are included in the set of support points and only one basis function is non-zero in each support point, the treatment of the left-side traces influences all basis functions and belonging coefficients as

$$z_{\tau h}^{\text{dG}}(t_{\mathcal{F},n}^-) = \sum_{\iota=0}^{r-1} z_h^{n,\iota} \zeta_{n,\iota}(t_{\mathcal{F},n}^-). \quad (4.118)$$

Since the left endpoints do not belong to the set of support points, the treatment of the right-side traces influences all basis functions and belonging coefficients as

$$z_{\tau h}^{\text{dG}}(t_{\mathcal{F},n}^+) := z_{\tau h}^{\text{dG}}|_{K_{n_r}}(t_{\mathcal{F},n}^+), \quad (4.119)$$

where K_{n_r} denotes the right neighbor cell in time of K_n and $t_{\mathcal{F},n}$ denotes the right end of K_n , respectively. For the case that K_n represents the last cell in time of the current slab Q_n , the right neighbor cell in time K_{n_r} is given by the first cell in time of the next slab Q_{n+1} , cf. Fig. 2.5 for an illustration. In particular, on the last cell in time of the last slab Q_N the right-side trace $z_{\tau h}^{\text{dG}}(t_{\mathcal{F},N}^+)$ is given by the dual initial at time $t = T$, denoted by z_T and depending on the choice of the goal functional J , cf. Rem.4.5.

Thus, on a cell in time K_n the terms involving a jump in $t_{\mathcal{F},n}$ read as

$$\begin{aligned} (\psi_{\tau h}^{\text{cG}}(t_{\mathcal{F},n}^-), [z_{\tau h}^{\text{dG}}]_{t_{\mathcal{F},n}}) &= \xi_{n,\kappa}(t_{\mathcal{F},n}^-)(\psi_h, z_{\tau h}^{\text{dG}} t_{\mathcal{F},n}^+) \\ &\quad - \sum_{\iota=0}^{r-1} \xi_{n,\kappa}(t_{\mathcal{F},n}^-) \zeta_{n,\iota}(t_{\mathcal{F},n}^-) (\psi_h, z_h^{n,\iota}), \\ (\mathbf{b} \cdot \nabla \psi_{\tau h}^{\text{dG}}(t_{\mathcal{F},n}^-), [z_{\tau h}^{\text{dG}}]_{t_{\mathcal{F},n}}) &= \xi_{n,\kappa}(t_{\mathcal{F},n}^-) (\mathbf{b} \cdot \nabla \psi_h, z_{\tau h}^{\text{dG}}(t_{\mathcal{F},n}^+)) \\ &\quad - \sum_{\iota=0}^{r-1} \xi_{n,\kappa}(t_{\mathcal{F},n}^-) \zeta_{n,\iota}(t_{\mathcal{F},n}^-) (\mathbf{b} \cdot \nabla \psi_h, z_h^{n,\iota}), \end{aligned} \quad (4.120)$$

Finally, using the representation of the continuous and discontinuous in time fully discrete functions, given by Eq. (4.97), and the representation of the jump terms, given by Eq. (4.120), as well as the numerical approximation of the integrals in time by means of an r -point Gauss quadrature rule, we get the following dual fully discrete cG(p)-cG(r) time marching scheme for Problem 4.13, cf. Rem. 4.6:

Problem 4.17 (Dual Fully Discrete Stabilized cG(p)-cG(r) TMS)

Find $z_{\tau h}^{\text{dG}}|_{K \times K_n} \in \mathcal{P}_\tau^{r-1}(K_n; V_h^{p,n})$, represented by Eq. (4.97) with coefficients $z_h^{n,\iota}$, $\iota = 0, \dots, r-1$, such that

$$\begin{aligned}
& \sum_{K_n \in \mathcal{T}_{\tau,n}} \sum_{\iota=0}^{r-1} \left\{ \alpha_{\kappa,\iota} \left(\sum_{K \in \mathcal{T}_{h,n}} \left(-(\psi_h, z_h^{n,\iota})_K + \delta_K(\mathbf{b} \cdot \nabla \psi_h, z_h^{n,\iota})_K \right) \right) \right. \\
& \quad + \beta_{\kappa,\iota} \left(\sum_{K \in \mathcal{T}_{h,n}} \left((\varepsilon \nabla \psi_h, \nabla z_h^{n,\iota})_K - \delta_K(\nabla \cdot (\varepsilon \nabla \psi_h), \mathbf{b} \cdot \nabla z_h^{n,\iota})_K \right) \right) \\
& \quad + \beta_{\kappa,\iota} \left(\sum_{K \in \mathcal{T}_{h,n}} \left((\mathbf{b} \cdot \nabla \psi_h, z_h^{n,\iota})_K + \delta_K(\mathbf{b} \cdot \nabla \psi_h, \mathbf{b} \cdot \nabla z_h^{n,\iota})_K \right) \right) \\
& \quad \left. + \beta_{\kappa,\iota} \left(\sum_{K \in \mathcal{T}_{h,n}} \left((\alpha \psi_h, z_h^{n,\iota})_K + \delta_K(\alpha \psi_h, \mathbf{b} \cdot \nabla z_h^{n,\iota})_K \right) \right) \right\} \\
& = \sum_{K_n \in \mathcal{T}_{\tau,n}} \sum_{\iota=0}^{r-1} \beta_{\kappa,\iota} \sum_{K \in \mathcal{T}_{h,n}} J_1|_K(u_h^{n,\iota})(\psi_h) \\
& \quad + \gamma_\kappa \sum_{K \in \mathcal{T}_{h,n}} \left((\psi_h, z_{\tau h}^{\text{dG}}(t_{\mathcal{F},n}^+))_K - \delta_K(\mathbf{b} \cdot \nabla \psi_h, z_{\tau h}^{\text{dG}}(t_{\mathcal{F},n}^+))_K \right),
\end{aligned} \tag{4.121}$$

for all $\psi_h \in V_h^{p,n}$, for all $\kappa = 0, \dots, r$, and with

$$\begin{aligned}
\alpha_{\kappa,\iota} & := (\xi_{n,\kappa}(t), \zeta'_{n,\iota}(t))_{K_n} - \xi_{n,\kappa}(t_{\mathcal{F},n}^-)(\zeta_{n,\iota}(t_{\mathcal{F},n}^-)) \\
& = \int_{\hat{I}} \hat{\xi}_\kappa(\hat{t}) \hat{\zeta}'_\iota(\hat{t}) \, d\hat{t} - \hat{\xi}_\kappa(1) \hat{\zeta}_\iota(1) = \sum_{\mu=0}^r \hat{w}_\mu \hat{\xi}_\kappa(\hat{t}_\mu) \hat{\zeta}'_\iota(\hat{t}_\mu) - \hat{\xi}_\kappa(1) \hat{\zeta}_\iota(1), \\
\beta_{\kappa,\iota} & := (\xi_{n,\kappa}(t), \zeta_{n,\iota}(t))_{K_n} = \int_{\hat{I}} \hat{\xi}_\kappa(\hat{t}) \hat{\zeta}_\iota(\hat{t}) \, \tau_n \, d\hat{t} = \sum_{\mu=0}^r \tau_n \hat{w}_\mu \hat{\xi}_\kappa(\hat{t}_\mu) \hat{\zeta}_\iota(\hat{t}_\mu), \\
\gamma_\kappa & := \xi_{n,\kappa}(t_n) = \hat{\xi}_\kappa(1),
\end{aligned} \tag{4.122}$$

where the reference basis functions in time $\hat{\zeta}_\iota(\cdot)$, $\hat{\zeta}'_\iota(\cdot)$ are the standard Lagrange basis functions as introduced in Sec. 2.2.2, using quadrature weights \hat{w}_μ and quadrature points \hat{t}_μ from $\hat{Q}_{G(r)}$, and with

$$z_{\tau h}^{\text{dG}}(t_{\mathcal{F},n}^+) := z_{\tau h}^{\text{dG}}|_{K_{n_r}}(t_{\mathcal{F},n}^+), \tag{4.123}$$

by marching sequentially through all slabs Q_n , $n = N, \dots, 1$, where on the last cell in time of the last slab Q_N the right-side trace $z_{\tau h}^{\text{dG}}(t_{\mathcal{F},N}^+) = z_T$ is introduced to include the dual initial at time $t = T$ which depends on the choice of the underlying goal functional J as outlined in Rem. 4.5.

4.3.2 Localization and Evaluation of the Error Estimators

The error representation formulas derived in Sec. 4.2.2 lead to a posteriori error estimators in space and time, in the following denoted by η_h and η_τ , respectively. These estimators serve for one thing as a quantitative estimation of the respective discretization error within the goal quantity J , and on the other hand as indicators for adaptive mesh refinement in space and time. For the latter case, we present a localized form of the reduced error representation formulas obtained in Thm. 4.2 and Thm. 4.4, respectively, that are used as error indicators within the practical realization of the adaptive mesh refinement process. These localized error indicators include unknown solutions as well as so-called weights that have to be approximated by an appropriate technique similar to the steady-state case considered in Chapter 3. While the spatial approximation of the weights is done in the same way as introduced in Sec. 3.3.1, we outline the temporal approximation of the weights in further detail in the following.

4.3.2.1 Discontinuous in Time Discretization

Neglecting the remainder terms in Theorem 4.2, we get the following error representation formulas in space and time.

$$\begin{aligned}
 J(u) - J(u_\tau) &\approx \rho_\tau(u_\tau)(z - \tilde{z}_\tau) & =: \eta_\tau^{\text{dG}} &= \sum_{n=1}^N \eta_\tau^{\text{dG},n}, \\
 J(u_\tau) - J(u_{\tau h}) &\approx \rho_\tau(u_{\tau h})(z_\tau - \tilde{z}_{\tau h}) + S_A^{\text{dG}}(u_{\tau h})(\tilde{z}_{\tau h}) & =: \eta_h^{\text{dG}} &= \sum_{n=1}^N \eta_h^{\text{dG},n}.
 \end{aligned} \tag{4.124}$$

Here, the local error indicators in time $\eta_\tau^{\text{dG},n}$ and space $\eta_h^{\text{dG},n}$, respectively, with regard to a single slab $Q_n = \mathcal{T}_{h,n} \times \mathcal{T}_{\tau,n}$, $n = 1, \dots, N$, are given by

$$\begin{aligned}
 \eta_\tau^{\text{dG},n} &= \sum_{K_n \in \mathcal{T}_{\tau,n}} \int_{K_n} \sum_{K \in \mathcal{T}_{h,n}} \left\{ (R(u_\tau), z - \tilde{z}_\tau)_K - (E(u_\tau), z - \tilde{z}_\tau)_{\partial K} \right\} dt \\
 &\quad - \sum_{t_{\mathcal{F},n_\ell} \in \mathcal{F}_{\tau,n}} \sum_{K \in \mathcal{T}_{h,n}} \left([u_\tau]_{t_{\mathcal{F},n_\ell}}, z(t_{\mathcal{F},n_\ell}^+) - \tilde{z}_\tau(t_{\mathcal{F},n_\ell}^+) \right)_K, \\
 \eta_h^{\text{dG},n} &= \sum_{K_n \in \mathcal{T}_{\tau,n}} \int_{K_n} \sum_{K \in \mathcal{T}_{h,n}} \left\{ (R(u_{\tau h}), z_\tau - \tilde{z}_{\tau h})_K - \delta_K(R(u_{\tau h}), \mathbf{b} \cdot \nabla \tilde{z}_{\tau h})_K \right. \\
 &\quad \left. - (E(u_{\tau h}), z_\tau - \tilde{z}_{\tau h})_{\partial K} \right\} dt \\
 &\quad - \sum_{t_{\mathcal{F},n_\ell} \in \mathcal{F}_{\tau,n}} \sum_{K \in \mathcal{T}_{h,n}} \left([u_{\tau h}]_{t_{\mathcal{F},n_\ell}}, z_\tau(t_{\mathcal{F},n_\ell}^+) - \tilde{z}_{\tau h}(t_{\mathcal{F},n_\ell}^+) \right)_K \\
 &\quad + \sum_{t_{\mathcal{F},n_\ell} \in \mathcal{F}_{\tau,n}} \sum_{K \in \mathcal{T}_{h,n}} \left([u_{\tau h}]_{t_{\mathcal{F},n_\ell}}, \mathbf{b} \cdot \nabla \tilde{z}_{\tau h}(t_{\mathcal{F},n_\ell}^+) \right)_K,
 \end{aligned} \tag{4.125}$$

where the cell and edge residuals $R(\cdot)$ and $E(\cdot)$, respectively, are given by

$$R(\varphi)|_K := f - \partial_t \varphi + \nabla \cdot (\varepsilon \nabla \varphi) - \mathbf{b} \cdot \nabla \varphi - \alpha \varphi, \quad (4.126)$$

$$E(\varphi)|_\Gamma := \begin{cases} \frac{1}{2} \mathbf{n} \cdot [\varepsilon \nabla \varphi] & \text{if } \Gamma \subset \partial K \setminus \partial \Omega, \\ 0 & \text{if } \Gamma \subset \partial \Omega, \end{cases} \quad (4.127)$$

with $[\nabla \varphi] := \nabla \varphi|_{\Gamma \cap K} - \nabla \varphi|_{\Gamma \cap K'}$ denoting the spatial jump of $\nabla \varphi$ over the inner edges Γ with normal unit vector \mathbf{n} pointing from cell K to K' . Here, $\mathcal{F}_{\tau, n}$ denotes the set of interior time points belonging to slab Q_n with $t_{\mathcal{F}, n_\ell}$ denoting the left end of the cell in time K_n .

Remark 4.11 *Let us remark some aspects about the error indicators.*

- *We have neglected the remainder terms in (4.124) as well as in the effective numerical computation of the error indicators due to their higher-order character compared to the remaining terms; cf. [20, Rem. 6.5]. Nevertheless, an actual upper bound on the error may be violated when these additional terms are significant, at least for low numbers of degrees of freedom, as it was pointed out in [5] and [150] by taking these terms into account.*
- *The additional terms including the spatial edge terms $E(\cdot)$ appear by applying integration by parts on each spatial cell $K \in \mathcal{T}_{h, n}$ to the diffusive term in the primal residual; cf., for instance, [20, Ch. 3].*
- *Here and in the numerical examples we only deal with the reduced form of the error estimators as given in Thm. 4.2. The reason for this is a significant reduction of the implementational complexity compared to the form given in Thm. 4.1, where the respective error estimators additionally depend on the dual residual including further weights that have to be approximated.*
- *The local error indicators $\eta_\tau^{\text{dG}, n}$ and $\eta_h^{\text{dG}, n}$ relate here to a slab Q_n . This is due to the fact that in most cases of our numerical examples we restrict each single slab Q_n to consist of only one cell in time, which equals a decomposition of the time interval into subintervals I_n solely. Of course, a localization on a single temporal cell in time K_n is possible including a refinement strategy related to specific cells in time of the underlying triangulation $\mathcal{T}_{\tau, n}$ in contrast to a refinement strategy that concerns the respective slabs, cf. the underlying algorithm given in Sec. 4.3.3 as well as the description of the implementational aspects given in Sec. 4.4.*

For the numerical evaluation of the temporal and spatial error indicators given by Eq. (4.125), the integrals in time have to be approximated by an appropriate quadrature rule. This quadrature rule is depending on the approximation approach used for the temporal weights and will be specified below. Furthermore, the occurring weights, i.e. $z - \tilde{z}_\tau$ and $z_\tau - \tilde{z}_{\tau h}$, have to be approximated in an appropriate way, whereby the approximation of the ‘spatial’ weights $z_\tau - \tilde{z}_{\tau h}$ can be handled by one of the techniques introduced in Sec. 3.3.1 for the case of a steady-state problem. Since \tilde{z}_τ can be chosen arbitrarily in the corresponding space $\mathcal{V}_\tau^{\text{dG}(r)}$, the weights $z - \tilde{z}_\tau$ are essentially interpolation errors; cf. [40]. The approximation of these interpolation errors can be handled by one of the following techniques.

4.3.2.2 Approximation of the Temporal Weights

Similar to the approximation of the spatial weights introduced in Sec. 3.3.1, there exists several techniques for approximating the temporal weights as well, of which we present two in the following; cf. [36] for more details and alternative approaches.

Approximation by Higher-Order Extrapolation

One possible technique to approximate the occurring temporal weights within the DWR framework is given by using a higher-order reconstruction of the fully discrete solutions. Therefore, we introduce the following operator for approximating the temporal weights within the localized error indicators, given by Eq. (4.125):

$$z - \tilde{z}_\tau \approx E_\tau^{r+1} z_\tau - z_\tau.$$

Here, E_τ^{r+1} denotes the extrapolation in time operator that acts on a cell in time of size τ and lifts the solution to a piecewise polynomial of degree $(r + 1)$ in time.

We note that the additional solution for the (local) extrapolation in time on a specific cell in time is here interpolated from the previous cell in its right end that is then combined with the current solution evaluated either in Gauss or Gauss-Lobatto quadrature points, cf. Fig. 4.1 and Fig. 4.2, respectively. On the first slab Q_1 the initial condition or the fully discrete solution evaluated at the initial time point t_0 is used.

Furthermore, we point out that within this approximation strategy the respective dual problem is solved in the same finite element space $\mathcal{V}_\tau^{\text{dG}(r)}$ as used for the primal problem. The described approach is similar to that one used in [40] for a dG(r) discretization up to $r = 1$, but we point out that it works for an arbitrary degree discontinuous Galerkin time discretization of the primal problem.

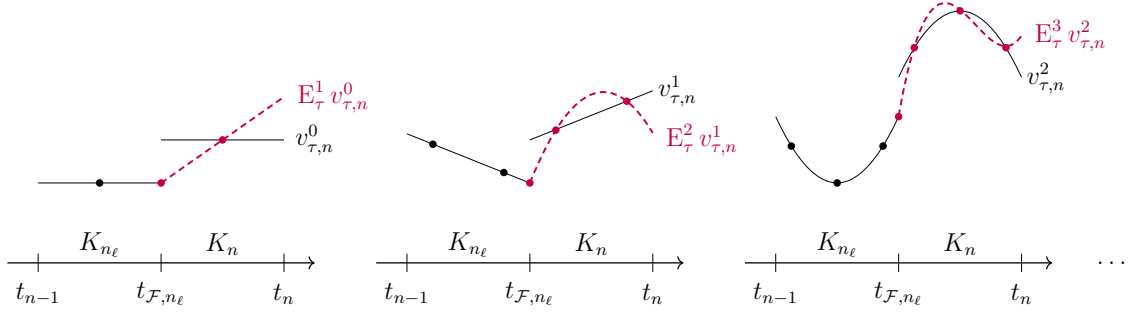


Figure 4.1: Extrapolation of a discontinuous constant (left), linear (middle) and quadratic (right) in time function on an exemplary cell in time K_n using Gauss quadrature points.

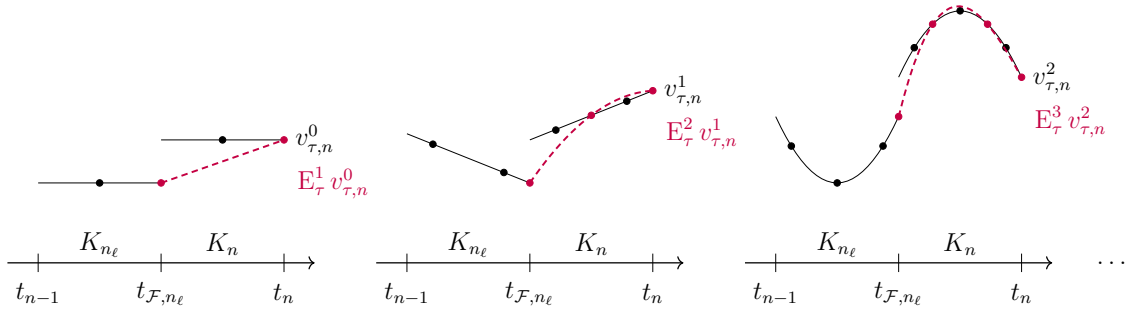


Figure 4.2: Extrapolation of a discontinuous constant (left), linear (middle) and quadratic (right) in time function on an exemplary cell in time K_n using Gauss-Lobatto quadrature points.

Approximation by Higher-Order Finite Elements

This approach aims to increase the influence of the weights by approximating the dual solution using higher-order finite elements. Thus, the solution of the respective dual problem is solved in a finite element space that consists of polynomials that are at least of one polynomial degree higher than its primal counterpart, more precisely the discrete dual solution z_τ is computed in $\mathcal{V}_\tau^{\text{dG}(s)}$, $s \geq r + 1$. Therefore, we introduce the following restriction operator in time for approximating the temporal weights within the localized error indicators given by Eq. (4.125):

$$z - \tilde{z}_\tau \approx z_\tau - \mathbf{R}_\tau^r z_\tau,$$

Note that this approximation is valid, since the quantity \tilde{z}_τ can be chosen arbitrarily in the underlying finite element space $\mathcal{V}_\tau^{\text{dG}(s)}$. Here, \mathbf{R}_τ^r denotes the restriction in time operator that acts on a cell in time of size τ and restricts the solution to a polynomial of degree $r < s$; cf. Fig. 4.3.

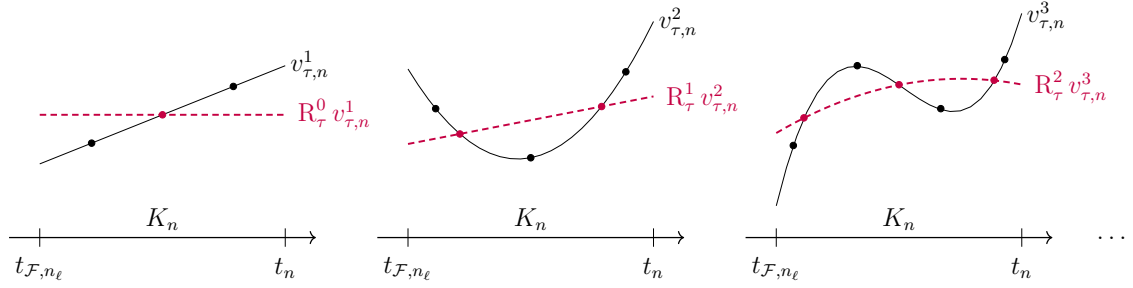


Figure 4.3: Restriction of a discontinuous linear (left), quadratic (middle) and cubic (right) in time function on an exemplary cell in time K_n using Gauss quadrature points.

Remark 4.12 *Let us remark some aspects about the temporal weights.*

- *For the approach of using the solution from the left neighbor cell in time within the higher-order extrapolation technique, the following has to be observed. If K_n represents the first cell in time of the current slab Q_n , an additional interpolation between the two spatial triangulations used on Q_{n-1} and Q_n , respectively, is necessary, since in practice the ‘unknown’ solutions are replaced by the computed fully discrete ones, cf. Eq. (4.128) as well as Sec.4.4.3. In particular, on the first cell in time of the first slab Q_1 the solution from the left neighbor cell in time is given by the initial condition u_0 , which is incorporated by an interpolation using the same spatial triangulation as on Q_1 .*
- *We note that the restriction operator in time R_{τ}^r within the higher-order finite elements technique is implemented in our software since deal.II is currently not able to operate on $(d+1)$ -dimensional tensor-product solutions. This is done by a Lagrangian interpolation in time to the primal space of the dual solution and an additional interpolation back to the dual space.*

Due to the results obtained for a comparative study of the approximation techniques for the case of a steady-state problem in Sec. 3.4, we only deal with the case of using higher-order finite elements for approximating the spatial weights here, cf. Sec. 3.3.1 for more details about this approximation technique. However, the temporal weights are approximated by one of the techniques described above using the abbreviations ‘hoEx-G’, ‘hoEx-GL’ and ‘hoFE’ denoting the approximation by higher-order extrapolation using Gauss or Gauss-Lobatto quadrature points and the approximation by higher-order finite elements, respectively.

Now, the last step in making the error indicators computable is to replace all unknown solutions appearing either in the weights or in the residuals by the computed fully discrete solutions, i.e. we approximate

$$\begin{aligned}
\eta_\tau^{\text{dG}} &= \rho_\tau(u_\tau)(z - \tilde{z}_\tau) \approx \rho_\tau(u_{\tau h})(\mathbf{E}_\tau^{r+1} z_{\tau h} - z_{\tau h}), \text{ or} \\
\eta_\tau^{\text{dG}} &= \rho_\tau(u_\tau)(z - \tilde{z}_\tau) \approx \rho_\tau(u_{\tau h})(z_{\tau h} - \mathbf{R}_\tau^r z_{\tau h}), \text{ and} \\
\eta_h^{\text{dG}} &= \rho_\tau(u_{\tau h})(z_\tau - \tilde{z}_{\tau h}) + S_A^{\text{dG}}(u_{\tau h})(\tilde{z}_{\tau h}) \\
&\approx \rho_\tau(u_{\tau h})(z_{\tau h} - \mathbf{R}_h^p z_{\tau h}) + S_A^{\text{dG}}(u_{\tau h})(\mathbf{R}_h^p z_{\tau h}),
\end{aligned} \tag{4.128}$$

where the restriction in space operator \mathbf{R}_h^p is introduced in Sec. 3.3.1. Finally, this leads to the following approximated local error indicators in time ($\tilde{\eta}_\tau^{\text{dG,hoEx},n}$ or $\tilde{\eta}_\tau^{\text{dG,hoFE},n}$) and space, respectively, ($\tilde{\eta}_h^{\text{dG},n}$) with regard to a single slab $Q_n = \mathcal{T}_{h,n} \times \mathcal{T}_{\tau,n}$, $n = 1, \dots, N$.

$$\begin{aligned}
\tilde{\eta}_\tau^{\text{dG,hoEx},n} &= \sum_{K_n \in \mathcal{T}_{\tau,n}} \int_{K_n} \sum_{K \in \mathcal{T}_{h,n}} \left\{ (R(u_{\tau h}), \mathbf{E}_\tau^{r+1} z_{\tau h} - z_{\tau h})_K \right. \\
&\quad \left. - (E(u_{\tau h}), \mathbf{E}_\tau^{r+1} z_{\tau h} - z_{\tau h})_{\partial K} \right\} dt \\
&\quad - \sum_{t_{\mathcal{F},n_\ell} \in \mathcal{F}_{\tau,n}} \sum_{K \in \mathcal{T}_{h,n}} \left([u_{\tau h}]_{t_{\mathcal{F},n_\ell}}, \mathbf{E}_\tau^{r+1} z_{\tau h}(t_{\mathcal{F},n_\ell}^+) - z_{\tau h}(t_{\mathcal{F},n_\ell}^+) \right)_K, \\
\tilde{\eta}_\tau^{\text{dG,hoFE},n} &= \sum_{K_n \in \mathcal{T}_{\tau,n}} \int_{K_n} \sum_{K \in \mathcal{T}_{h,n}} \left\{ (R(u_{\tau h}), z_{\tau h} - \mathbf{R}_\tau^r z_{\tau h})_K \right. \\
&\quad \left. - (E(u_{\tau h}), z_{\tau h} - \mathbf{R}_\tau^r z_{\tau h})_{\partial K} \right\} dt \\
&\quad - \sum_{t_{\mathcal{F},n_\ell} \in \mathcal{F}_{\tau,n}} \sum_{K \in \mathcal{T}_{h,n}} \left([u_{\tau h}]_{t_{\mathcal{F},n_\ell}}, z_{\tau h}(t_{\mathcal{F},n_\ell}^+) - \mathbf{R}_\tau^r z_{\tau h}(t_{\mathcal{F},n_\ell}^+) \right)_K, \\
\tilde{\eta}_h^{\text{dG},n} &= \sum_{K_n \in \mathcal{T}_{\tau,n}} \int_{K_n} \sum_{K \in \mathcal{T}_{h,n}} \left\{ (R(u_{\tau h}), z_{\tau h} - \mathbf{R}_h^p z_{\tau h})_K \right. \\
&\quad \left. - \delta_K (R(u_{\tau h}), \mathbf{b} \cdot \nabla \mathbf{R}_h^p z_{\tau h})_K - (E(u_{\tau h}), z_{\tau h} - \mathbf{R}_h^p z_{\tau h})_{\partial K} \right\} dt \\
&\quad - \sum_{t_{\mathcal{F},n_\ell} \in \mathcal{F}_{\tau,n}} \sum_{K \in \mathcal{T}_{h,n}} \left([u_{\tau h}]_{t_{\mathcal{F},n_\ell}}, z_{\tau h}(t_{\mathcal{F},n_\ell}^+) - \mathbf{R}_h^p z_{\tau h}(t_{\mathcal{F},n_\ell}^+) \right)_K \\
&\quad + \sum_{t_{\mathcal{F},n_\ell} \in \mathcal{F}_{\tau,n}} \sum_{K \in \mathcal{T}_{h,n}} \left([u_{\tau h}]_{t_{\mathcal{F},n_\ell}}, \mathbf{b} \cdot \nabla \mathbf{R}_h^p z_{\tau h}(t_{\mathcal{F},n_\ell}^+) \right)_K,
\end{aligned} \tag{4.129}$$

where the cell and edge residuals $R(\cdot)$ and $E(\cdot)$ are defined by Eqs. (4.126) and (4.127), respectively. Here, the integrals in time are evaluated numerically by using an $(r+2)$ -point Gauss-Lobatto quadrature rule for the approximation case hoEx-G, an $(r+1)$ -point Gauss quadrature rule for the case hoEx-GL, and an $(r+2)$ -point Gauss quadrature rule for the case hoFE, respectively.

Remark 4.13 *As outlined in [40, Rem. 3.2], the approximation of the unknown solutions by means of the computed fully discrete ones within the residuals may seem to be critical, at least for the point of linearization. As a remedy, one could also use an approximation technique as described above. However, our numerical examples show that this additional effort is not necessary to obtain quantitatively good results. In addition, this observation is substantiated by the fact that the approximation of the linearization point introduces an additional error which usually is of higher order, which can be seen as follows. The introduced error can be expressed as*

$$\mathcal{L}'_\tau(v_\tau)(v - \tilde{v}_\tau) - \mathcal{L}'_\tau(v_{\tau h})(v - \tilde{v}_\tau) = \int_0^1 \mathcal{L}''_\tau(v_{\tau h} + s(v_\tau - v_{\tau h}))(v_\tau - v_{\tau h}, v - \tilde{v}_\tau) \, ds,$$

where $v = \{u, z\}$, $v_\tau = \{u_\tau, z_\tau\}$, and $v_{\tau h} = \{u_{\tau h}, z_{\tau h}\}$. Now, by choosing for instance an appropriate interpolant for v_τ , this identity shows that the discussed approximation introduces an error of the order $\mathcal{O}(h^2\tau)$, whereas the total discretization error usually is not better than $\mathcal{O}(h^2 + k)$ in the case of a cG(1)dG(0) discretization. For more details on this issue, we refer to [40], [143] and [168], respectively.

Remark 4.14 (Boundary Conditions) *In the case of nonhomogeneous Dirichlet boundary conditions, the following additional terms have to be added to the respective equations in (4.129):*

$$\begin{aligned} & \sum_{K_n \in \mathcal{T}_{\tau,n}} \int_{K_n} -((u_D - \tilde{u}_{D,\tau}), \varepsilon \nabla z_{\tau h} \cdot \mathbf{n})_{\Gamma_D} \, dt, \\ & \sum_{K_n \in \mathcal{T}_{\tau,n}} \int_{K_n} -((\tilde{u}_{D,\tau} - \tilde{u}_{D,\tau h}), \varepsilon \nabla z_{\tau h} \cdot \mathbf{n})_{\Gamma_D} \, dt, \end{aligned} \tag{4.130}$$

where the semi-discrete function $\tilde{u}_{D,\tau}$ and the fully discrete function $\tilde{u}_{D,\tau h}$, respectively, are appropriate finite element approximations of the extension \tilde{u}_D in the sense that the trace of \tilde{u}_D equals u_D on Γ_D ; cf. also Rem. 3.3 in Ch. 3.

If Neumann boundary conditions are prescribed in Problem 4.1 on a part $\Sigma_N = \Gamma_N \times I$ of the boundary $\partial\Omega = \Gamma_D \cup \Gamma_N$, with Dirichlet part $\Gamma_D \neq \emptyset$, i.e.,

$$\varepsilon \nabla u \cdot \mathbf{n} = u_N \text{ on } \Sigma_N = \Gamma_N \times I.$$

Then, the edge residuals $E(u_{\tau h})$ used in (4.129) have to be modified in the following way, cf. also Rem. 3.4 in Ch. 3:

$$E(u_{\tau h})|_\Gamma := \begin{cases} \frac{1}{2} \mathbf{n} \cdot [\varepsilon \nabla u_{\tau h}] & \text{if } \Gamma \subset \partial K \setminus \partial\Omega, \\ 0 & \text{if } \Gamma \subset \partial\Gamma_D, \\ g_N - \varepsilon \nabla u_{\tau h} \cdot \mathbf{n} & \text{if } \Gamma \subset \partial\Gamma_N. \end{cases} \tag{4.131}$$

4.3.2.3 Continuous in Time Discretization

For the sake of completeness, we present here the approximated local error indicators in time and space for the case of a continuous in time discretization. Neglecting the remainder terms in Theorem 4.4, we get the following error representation formulas in space and time:

$$\begin{aligned}
J(u) - J(u_\tau) &\approx \rho(u_\tau)(z - \tilde{z}_\tau) & =: \eta_\tau^{\text{cG}} &= \sum_{n=1}^N \eta_\tau^{\text{cG},n}, \\
J(u_\tau) - J(u_{\tau h}) &\approx \rho(u_{\tau h})(z_\tau - \tilde{z}_{\tau h}) + S_A^{\text{cG}}(u_{\tau h})(\tilde{z}_{\tau h}) & =: \eta_h^{\text{cG}} &= \sum_{n=1}^N \eta_h^{\text{cG},n}.
\end{aligned} \tag{4.132}$$

Here, the local error indicators in time $\eta_\tau^{\text{cG},n}$ and space $\eta_h^{\text{cG},n}$, respectively, with regard to a single slab $Q_n = \mathcal{T}_{h,n} \times \mathcal{T}_{\tau,n}$, $n = 1, \dots, N$, are given by

$$\begin{aligned}
\eta_\tau^{\text{cG},n} &= \sum_{K_n \in \mathcal{T}_{\tau,n}} \int_{K_n} \sum_{K \in \mathcal{T}_{h,n}} \left\{ (R(u_\tau), z - \tilde{z}_\tau)_K - (E(u_\tau), z - \tilde{z}_\tau)_{\partial K} \right\} dt, \\
\eta_h^{\text{cG},n} &= \sum_{K_n \in \mathcal{T}_{\tau,n}} \int_{K_n} \sum_{K \in \mathcal{T}_{h,n}} \left\{ (R(u_{\tau h}), z_\tau - \tilde{z}_{\tau h})_K - \delta_K(R(u_{\tau h}), \mathbf{b} \cdot \nabla \tilde{z}_{\tau h})_K \right. \\
&\quad \left. - (E(u_{\tau h}), z_\tau - \tilde{z}_{\tau h})_{\partial K} \right\} dt,
\end{aligned} \tag{4.133}$$

where the cell and edge residuals $R(\cdot)$ and $E(\cdot)$ are given by Eq. (4.126) and Eq. (4.127), respectively, and with $u_\tau(0) = u_{\tau h}(0) = u_0$ fulfilling the initial condition.

For the numerical evaluation of the temporal and spatial error indicators given by Eq. (4.133), the integrals in time have to be approximated by an appropriate quadrature rule. Again, this quadrature rule is depending on the approximation approach used for the temporal weights as specified in the discontinuous in time case.

Replacing the unknown solutions appearing either in the weights or in the residuals by the computed fully discrete solutions, we get the following approximation of the error representation formulas in space and time:

$$\begin{aligned}
\eta_\tau^{\text{cG}} &= \rho(u_\tau)(z - \tilde{z}_\tau) \approx \rho(u_{\tau h})(E_\tau^{r+1} z_{\tau h} - z_{\tau h}), \text{ or} \\
\eta_\tau^{\text{cG}} &= \rho(u_\tau)(z - \tilde{z}_\tau) \approx \rho(u_{\tau h})(z_{\tau h} - R_\tau^r z_{\tau h}), \text{ and} \\
\eta_h^{\text{cG}} &= \rho(u_{\tau h})(z_\tau - \tilde{z}_{\tau h}) + S_A^{\text{cG}}(u_{\tau h})(\tilde{z}_{\tau h}) \\
&\approx \rho(u_{\tau h})(z_{\tau h} - R_h^p z_{\tau h}) + S_A^{\text{cG}}(u_{\tau h})(R_h^p z_{\tau h}),
\end{aligned} \tag{4.134}$$

with the same restriction in space and in time operators R_h^p and R_τ^r , respectively, as used in the case of a discontinuous in time discretization and appropriate extrapolation in time operators $E_\tau^{\text{cG},r+1}$ that are build in the same fashion as illustrated by Fig. 4.1 and Fig. 4.2, respectively, though for continuous in time functions. Finally, this leads to the following approximated local error indicators in time

($\tilde{\eta}_\tau^{\text{cG,hoEx},n}$ or $\tilde{\eta}_\tau^{\text{cG,hoFE},n}$) and space, respectively, ($\tilde{\eta}_h^{\text{cG},n}$) with regard to a single slab $Q_n = \mathcal{T}_{h,n} \times \mathcal{T}_{\tau,n}$, $n = 1, \dots, N$.

$$\begin{aligned}
\tilde{\eta}_\tau^{\text{cG,hoEx},n} &= \sum_{K_n \in \mathcal{T}_{\tau,n}} \int_{K_n} \sum_{K \in \mathcal{T}_{h,n}} \left\{ (R(u_{\tau h}), \mathbf{E}_\tau^{\text{cG},r+1} z_{\tau h} - z_{\tau h})_K \right. \\
&\quad \left. - (E(u_{\tau h}), \mathbf{E}_\tau^{\text{cG},r+1} z_{\tau h} - z_{\tau h})_{\partial K} \right\} dt, \\
\tilde{\eta}_\tau^{\text{cG,hoFE},n} &= \sum_{K_n \in \mathcal{T}_{\tau,n}} \int_{K_n} \sum_{K \in \mathcal{T}_{h,n}} \left\{ (R(u_{\tau h}), z_{\tau h} - \mathbf{R}_\tau^r z_{\tau h})_K \right. \\
&\quad \left. - (E(u_{\tau h}), z_{\tau h} - \mathbf{R}_\tau^r z_{\tau h})_{\partial K} \right\} dt, \\
\tilde{\eta}_h^{\text{cG},n} &= \sum_{K_n \in \mathcal{T}_{\tau,n}} \int_{K_n} \sum_{K \in \mathcal{T}_{h,n}} \left\{ (R(u_{\tau h}), z_{\tau h} - \mathbf{R}_h^p z_{\tau h})_K \right. \\
&\quad \left. - \delta_K (R(u_{\tau h}), \mathbf{b} \cdot \nabla \mathbf{R}_h^p z_{\tau h})_K - (E(u_{\tau h}), z_{\tau h} - \mathbf{R}_h^p z_{\tau h})_{\partial K} \right\} dt,
\end{aligned} \tag{4.135}$$

where the cell and edge residuals $R(\cdot)$ and $E(\cdot)$ are defined by Eqs. (4.126) and (4.127), respectively. Here, the integrals in time are evaluated numerically by using an $(r+2)$ -point Gauss-Lobatto quadrature rule for the approximation case hoEx-G, an $(r+1)$ -point Gauss quadrature rule for the case hoEx-GL, and an $(r+2)$ -point Gauss quadrature rule for the case hoFE, respectively.

4.3.3 Space-Time Adaptive Algorithm

In this section, we present the space-time adaptive solution algorithm for the case of a discontinuous in time discretization and explain some details regarding its single steps. The modification in the case of a continuous in time discretization is described in Rem. 4.16 afterwards. The underlying implementational aspects and software architecture are described in the following section.

A Goal-Oriented Discontinuous in Time Adaptive Solution Algorithm

For a fully adaptive numerical approximation of Problem 4.1 the space-time domain $Q = \Omega \times I$ is divided into non-overlapping space-time slabs $Q_n^\ell = \mathcal{T}_{h,n}^\ell \times \mathcal{T}_{\tau,n}^\ell$, $n = 1, \dots, N^\ell$, as introduced in Assumption 2.5 in Sec. 2.2, where we restrict the temporal triangulations $\mathcal{T}_{\tau,n}^\ell$, $n = 1, \dots, N^\ell$, to consist of only one cell in time on each slab. Here, ℓ denotes the current DWR adaptivity loop. The fully discrete primal and dual solutions are represented by $u_{\tau h}^\ell(\mathbf{x}, t)$ and $z_{\tau h}^\ell(\mathbf{x}, t)$, respectively.

Algorithm: Goal-Oriented Discontinuous in Time Space-Time Adaptivity

Initialization: Set DWR loop $\ell = 1$ and generate the initial space-time slabs $Q_n^1 = \mathcal{T}_{h,n}^1 \times \mathcal{T}_{\tau,n}^1, n = 1, \dots, N^1$, for the time-dependent convection-diffusion-reaction problem, where we restrict the the temporal triangulations $\mathcal{T}_{\tau,n}^1$ to consist of only one cell in time for each slab $Q_n, n = 1, \dots, N^1$.

1. Solve the **Stabilized cG(p)-dG(r) Primal Problem 4.8:**

Find $u_{\tau h}^\ell \in \mathcal{V}_{\tau h}^{\text{dG}(r),p}$ such that $A_S^{\text{dG}}(u_{\tau h}^\ell)(\varphi_{\tau h}) = F_\tau(\varphi_{\tau h}) \quad \forall \varphi_{\tau h} \in \mathcal{V}_{\tau h}^{\text{dG}(r),p}$.

2. **Break if the goal is reached**, i.e., for instance, $\|u - u_{\tau h}^\ell\| < \text{tol}$, or $(\tilde{\eta}_\tau^{\text{dG}} + \tilde{\eta}_h^{\text{dG}}) < \text{tol}$, or $\max N_{\text{DoF}}^{\text{tot}}$ is reached, etc.

3. Solve the **Stabilized cG(p)-dG(r) Dual Problem 4.11** depending on the underlying choice of the approximation strategy for the temporal weights $z - \tilde{z}_\tau$:

- (i) Approximation by **higher-order extrapolation:**

Find $z_{\tau h}^\ell \in \mathcal{V}_{\tau h}^{\text{dG}(r),q}, q \geq p + 1$, such that

$$A_S^{\text{dG}'}(u_{\tau h}^\ell)(\psi_{\tau h}, z_{\tau h}^\ell) = J'(u_{\tau h}^\ell)(\psi_{\tau h}) \quad \forall \psi_{\tau h} \in \mathcal{V}_{\tau h}^{\text{dG}(r),q}.$$

- (ii) Approximation by **higher-order finite elements:**

Find $z_{\tau h}^\ell \in \mathcal{V}_{\tau h}^{\text{dG}(s),q}, s \geq r + 1, q \geq p + 1$, such that

$$A_S^{\text{dG}'}(u_{\tau h}^\ell)(\psi_{\tau h}, z_{\tau h}^\ell) = J'(u_{\tau h}^\ell)(\psi_{\tau h}) \quad \forall \psi_{\tau h} \in \mathcal{V}_{\tau h}^{\text{dG}(s),q}.$$

4. Evaluate the **a posteriori space-time error indicators** $\tilde{\eta}_\tau^{\text{dG,hoEx},n,\ell}, \tilde{\eta}_\tau^{\text{dG,hoFE},n,\ell}$ and $\tilde{\eta}_h^{\text{dG},n,\ell}$, given by Eq. (4.129), by marching sequentially through all space-time slabs $Q_n^\ell, n = 1, \dots, N^\ell$.

5. **If** $|\tilde{\eta}_\tau^{\text{dG,hoEx},\ell}| > \omega |\tilde{\eta}_h^{\text{dG},\ell}|$, or else $|\tilde{\eta}_\tau^{\text{dG,hoFE},\ell}| > \omega |\tilde{\eta}_h^{\text{dG},\ell}|, \omega \geq 1$,

temporal error dominating case:

Mark the slabs $Q_{\tilde{n}}^\ell, \tilde{n} \in \{1, \dots, N^\ell\}$, **for temporal refinement** if the corresponding $\tilde{\eta}_\tau^{\text{dG,hoEx},\tilde{n},\ell}$, or else $\tilde{\eta}_\tau^{\text{dG,hoFE},\tilde{n},\ell}$ is in the set of $\theta_\tau^{\text{top}}, 0 \leq \theta_\tau^{\text{top}} \leq 1$, percent of the worst indicators.

6. **Else if** $|\tilde{\eta}_h^{\text{dG},\ell}| > \omega |\tilde{\eta}_\tau^{\text{dG,hoEx},\ell}|$, or else $|\tilde{\eta}_h^{\text{dG},\ell}| > \omega |\tilde{\eta}_\tau^{\text{dG,hoFE},\ell}|$, $\omega \geq 1$,

spatial error dominating case:

Mark the cells $\tilde{K} \in \mathcal{T}_{h,n}^\ell$ **for spatial refinement** if the corresponding $\tilde{\eta}_h^{\text{dG},n,\ell}|_{\tilde{K}}$ is in the set of $\theta_{h,1}^{\text{top}}$ or $\theta_{h,2}^{\text{top}}$ (for a slab that is or is not marked for temporal refinement), $0 \leq \theta_{h,2}^{\text{top}} \leq \theta_{h,1}^{\text{top}} \leq 1$, percent of the worst indicators, **or**, respectively, **mark for spatial coarsening** if $\tilde{\eta}_h^{\text{dG},n,\ell}|_{\tilde{K}}$ is in the set of θ_h^{bottom} , $0 \leq \theta_h^{\text{bottom}} \leq 1$, percent of the best indicators.

7. **Else (temporal and spatial errors are equilibrated):**

Mark the slabs $Q_{\tilde{n}}^\ell$, $\tilde{n} \in \{1, \dots, N^\ell\}$, **for temporal refinement** as well as **mark the cells** $\tilde{K} \in \Omega_{h,n}^\ell$ **for spatial coarsening and refinement** as described in Step 5 and Step 6, respectively.

8. **Execute spatial refinement and/or coarsening** on all slabs under the use of mesh smoothing operators.
9. **Execute temporal refinement of slabs;** cf. Fig. 4.9.
10. Increase ℓ to $\ell + 1$ and **return to Step 1**.

Remark 4.15 *Let us remark some aspects about the space-time adaptive algorithm.*

- *The remarks outlined for a steady-state adaptive algorithm can be transferred to the space-time adaptive algorithm as well, cf. Rem. 3.9 in Chapter 3.*
- *With regard to efficiency and reliability reasons of the space-time adaptive algorithm, it is crucial that one part of the error estimator is almost independent on the refinement of the discretization with regard to the other part. More precisely, this means that the temporal error estimator $\tilde{\eta}_\tau^{\text{dG,hoEx}}$, or else $\tilde{\eta}_\tau^{\text{dG,hoFE}}$ should be (almost) independent of the spatial refinement and vice versa; cf. the results of Example 4.1 in Sec. 4.5.*
- *Moreover, it is essential to ensure an equilibrated reduction of the temporal and spatial discretization error. For this purpose, the equilibration constant ω (a value in the range of $1.5 \leq \omega \leq 3.5$ is used in our numerical experiments) is introduced in Step 5 and 6; cf. the results of Example 4.2 in Sec. 4.5.*
- *Furthermore, we point out that the marking strategy in time can be understood as a fixed-fraction strategy similar to that one used for marking the spatial cells, for more details we refer to the third note in Rem. 3.9.*

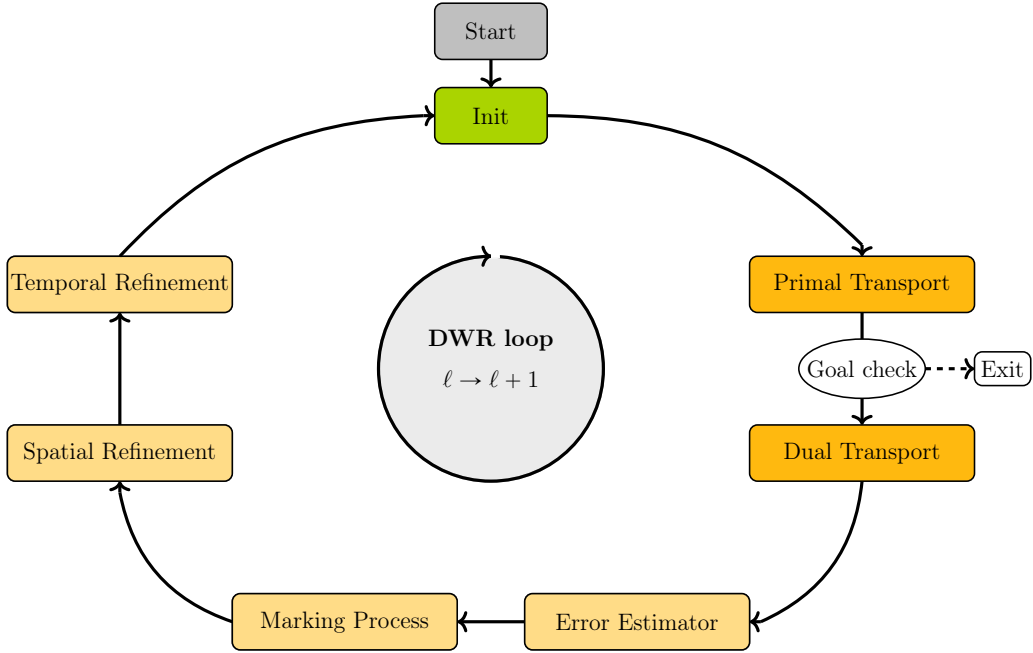


Figure 4.4: Illustration of the Goal-Oriented Discontinuous in Time Space-Time Adaptivity Algorithm. The black arrows symbolize the direction of the run, beginning with the initialization (start) of the space-time slabs.

For better clarity to the sequence of the single steps above (cf. also Fig. 4.4), we refer to the following details. The primal Problem 4.8 is solved by marching forwardly in time through all slabs (Step 1). The occurring left-side traces $u_{\tau h}(t_{\mathcal{F},n_\ell}^-)$ on $\mathcal{T}_{h,n}$ are handled by evaluating $u_{\tau h}$ on the right end of previous slab Q_{n-1} , cf. Eq. (4.105) in Problem 4.14. More precisely, we use an interpolation as described by Eq. (4.136), since the spatial triangulation used on Q_{n-1} may differ from the spatial triangulation used on the current slab Q_n in the course of adaptive mesh refinement. For more details about such a solution transfer, we refer to Sec. 4.4.3. Thereby, the initial condition u_0 is handled by an interpolation to the discrete finite element space using the same spatial triangulation $\mathcal{T}_{h,1}$ as on the first slab Q_1 . Furthermore, possible inhomogeneous Neumann boundary conditions are implemented as additional terms within the right-hand side assemblies and each system on a corresponding slab is modified such that the Dirichlet boundary conditions from Eq. (4.1) are applied strongly, cf. Rem. 4.14. More precisely, the Dirichlet boundary conditions are applied using a mapping between the degree of freedom in time and the value of the Dirichlet boundary function $u_N(\boldsymbol{x}, t)$ at the space-time degree of freedom belonging to the Dirichlet-colored boundary faces similar to the function `apply_boundary_values()` used in the `deal.II` library [17]. After the primal problem is solved, the exit condi-

tion is checked (Step 2), cf. the first note in Rem. 3.9 for the choice of the position of this exit condition.

In contrast, the dual Problem 4.11 is solved by marching backwardly in time through all slabs (Step 3). Thereby, we use the interpolation that follows the same pattern as used for the primal problem to evaluate the right-side traces $z_{\tau h}(t_{\mathcal{F},n}^+)$ on $\mathcal{T}_{h,n-1}$, cf. Eq. (4.111) in Problem 4.15. The same type of boundary coloring (either Dirichlet or Neumann type) is used for the dual problem but with homogeneous boundary value functions, even in the case of inhomogeneous primal boundary conditions. Each system is modified such that homogeneous Dirichlet boundary conditions are applied strongly to the dual solution $z_{\tau h}^\ell$.

The local error indicators $\tilde{\eta}_\tau^{\text{dG},n}$ and $\tilde{\eta}_h^{\text{dG},n}$ are computable with the primal and dual solutions as given in Eq. (4.129) (Step 4). Next, using these local error indicators on a single slab Q_n or a single spatial cell K , respectively, the marking process is done as described in Step 5-7 having regard to the balancing strategy of the temporal and spatial indicators used therein.

Finally, the execution of the refinement process is done in the following manner. We first execute the spatial refinement and/or coarsening on all slabs (Step 8). Afterwards, the refinement in time takes place as follows. If a slab Q_n is marked for temporal refinement, the corresponding just refined spatial triangulation $\mathcal{T}_{h,n}$ is copied to a new created slab Q_{n+1} (Step 9) that is mounted as the next element within a `std::list` object structure. We note that the refinement in time is done after the refinement in space since the just refined spatial triangulation $\mathcal{T}_{h,n}$ is copied to this new created slab. The process of the additional involvements of slabs is described in detail in Sec. 4.4.2, cf. also Fig. 4.9.

Remark 4.16 (Algorithm: Continuous in Time Discretization)

In the case of a continuous in time discretization the algorithm above has to be modified in the following manner:

- *Replace Problem 4.8 by Problem 4.7 in Step 1.*
- *Replace Problem 4.11 by Problem 4.13 in Step 3.*
- *Replace the a posteriori space-time error indicators $\tilde{\eta}_\tau^{\text{dG},\text{hoEx},n,\ell}$, or else $\tilde{\eta}_\tau^{\text{dG},\text{hoFE},n,\ell}$ and $\tilde{\eta}_h^{\text{dG},\ell}$ by $\tilde{\eta}_\tau^{\text{cG},\text{hoEx},n,\ell}$, or else $\tilde{\eta}_\tau^{\text{cG},\text{hoFE},n,\ell}$ and $\tilde{\eta}_h^{\text{cG},\ell}$, respectively, given by Eq. (4.135) in Step 4, and use these indicators in the following steps.*

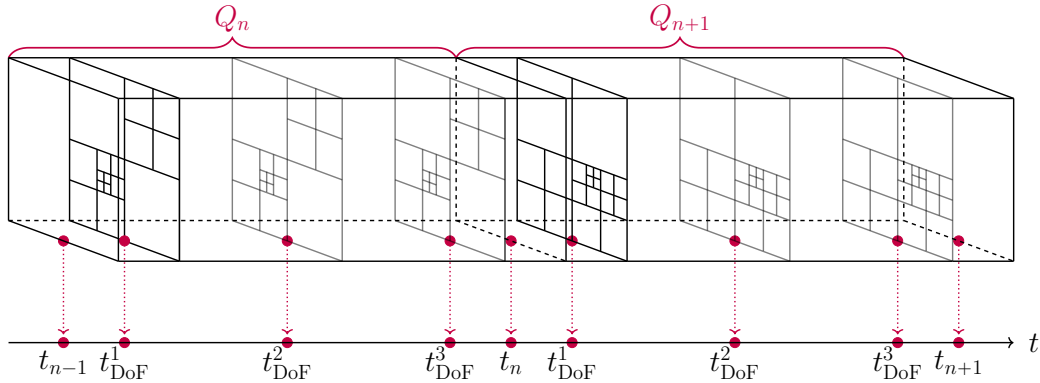


Figure 4.5: Two consecutive space-time slabs, exemplary for a discontinuous Galerkin dG(2) time discretization generated with three Gaussian quadrature points. The three degrees of freedom (DoF) time points on each slab are the support points for the temporal basis functions. Each of the illustrated slabs here consists of one cell in time and an independent and adaptively refined spatial triangulation.

4.4 Implementation and Software Architecture

In this section, we introduce some implementational aspects for the practical realization of the space-time adaptive algorithm presented in Sec. 4.3.3 and give insight into our in-house parallel frontend software DTM++, developed by U. Köcher [129], [128, Ch. 4], as well as the general framework of some specific features used thereby.

4.4.1 Implementation of Space-Time Tensor-Product Spaces

The main features of our implementation are an arbitrary degree discontinuous time discretization of the primal and dual problem as well as the approach of using space-time tensor-product spaces stored within a `std::list` object that handles the partitioning and storing of the space-time slabs. In the following, we describe the implementation of these space-time tensor-product spaces in detail.

For this purpose, the global space-time domain $Q = \Omega \times I$ is divided into non-overlapping space-time slabs $Q_n = \mathcal{T}_{h,n} \times \mathcal{T}_{\tau,n}$, $n = 1, \dots, N$, as outlined in Assumption 2.5 in Sec. 2.2. An exemplary illustration of the space-time domain that is distributed into space-time tensor-product slabs is given in Fig. 4.5, cf. also Fig. 2.4 in Sec. 2.2. On such a slab, a space-time tensor-product of finite element spaces is used. More precisely, a tensor-product of a d -dimensional, $d = 1, 2, 3$, spatial finite element space with a one-dimensional temporal finite element space is implemented. The temporal finite element space is based on a discontinuous Galerkin method of arbitrary order r on a one-dimensional triangulation $\mathcal{T}_{\tau,n}$ of $\bar{I}_n = [t_{n-1}, t_n]$, consisting

of non-overlapping elements K_n such that $\bar{I}_n = \bigcup_{K_n \in \mathcal{T}_{\tau,n}} \bar{K}_n$. On the other hand, the spatial finite element space is based on a continuous Galerkin method of arbitrary order p on a d -dimensional, $d = 1, 2, 3$, triangulation $\mathcal{T}_{h,n}$ of Ω consisting of non-overlapping elements K , such that $\bar{\Omega} = \bigcup_{K \in \mathcal{T}_{h,n}} \bar{K}$. Here, we choose the elements $K \in \mathcal{T}_{h,n}$ to be intervals for $d = 1$, quadrilaterals for $d = 2$ and hexahedra for $d = 3$, respectively. We assume the spatial triangulation to be regular, but allowing hanging nodes, cf. Rem. 2.2 in Sec. 2.1.3. Furthermore, the spatial triangulation is assumed to be organized in a patch-wise manner (cf. Def. 2.6). Thus, each computational slab Q_n can be associated with a temporal triangulation $\mathcal{T}_{\tau,n}$ and corresponding conforming finite element space \mathcal{Y}_τ^r , given by Eq. (2.11), as well as a spatial triangulation $\mathcal{T}_{h,n}$ and corresponding conforming finite element space $V_h^{p,n}$, given by Eq. (2.1), which will be used as trial and test spaces on Q_n , respectively. For the sake of implementational simplicity, we allow the spatial mesh to change between two consecutive slabs, but to be equal on all degrees of freedom in time used within one slab, cf. Fig. 4.5.

To implement the space-time tensor-product space, we start with the usual discretization for the finite element method in space having only one degree of freedom in time on each slab. We denote the number of spatial degrees of freedom by $N_{\text{DoF}}^{s,n}$ for one degree of freedom in time and the number of temporal degrees of freedom by $N_{\text{DoF}}^{t,n}$ on the n -th slab. On each slab, we generate the geometrical triangulation, i.e. a spatial mesh, and colorize the boundaries. Boundary colors can mark for instance Dirichlet type boundary conditions, Neumann type boundary conditions, etc.; cf. Fig. 4.13. Next, we initialize each slab by creating an independent copy of the generated spatial triangulation.

Then, for one degree of freedom in time on each slab, we distribute the spatial degrees of freedom and generate affine constraints objects. Remark that an affine constraints object may include information on handling degrees of freedom on hanging nodes or on Dirichlet type boundary nodes. The sparsity pattern for a sparse matrix is now generated with the geometric triangulation, the spatial degree of freedom (DoF) handler and the constraints object for one degree of freedom in time.

Next, the space-time tensor-product degrees of freedom on a slab are aligned by their local degree of freedom in time on a slab. Precisely, the first degree of freedom in time has the global number 0 and the last one has the number $N_{\text{DoF}}^{t,n} - 1$. The numbering of the local temporal degrees of freedom is increasingly ordered by their temporal mesh cell index. Remark that we have an additional one-dimensional triangulation (temporal mesh) for the time subinterval (t_{n-1}, t_n) corresponding to the

n -th slab; refer to Fig. 4.13 for details. Overall, we have $N_{\text{DoF}}^{\text{t},n}$ times $N_{\text{DoF}}^{\text{s},n}$ degrees of freedom on the n -th slab.

Next, the space-time tensor-product constraints are created by taking the original constraints object and shifting all entries accordingly such that the $N_{\text{DoF}}^{\text{t},n}$ are represented. Precisely, the spatial degrees of freedom from 0 to $N_{\text{DoF}}^{\text{s}}-1$ are associated to the first local temporal degree of freedom on a slab. If there are more than one temporal degree of freedom on a slab, the corresponding spatial degrees of freedom are shifted by the number $N_{\text{DoF}}^{\text{s},n}$ times the local temporal degree of freedom index.

For each degree of freedom in time, the sparsity pattern is now copied into the diagonal blocks for the space-time tensor product sparsity pattern. A higher-order polynomial degree in time introduces couplings between the temporal basis functions resulting in additional coupling blocks. For the case of more than one cell in time per slab, additional couplings appear for temporal derivatives between the time basis functions of two consecutive time cells, cf. Fig. 4.6 for an exemplary illustration of a primal sparsity pattern. For the primal problem, the evolution is forward in time and therefore these couplings appear in the left lower part. For the dual problem, the evolution is backward in time and therefore the coupling diagonals appear in the right upper part. Exemplary primal and dual sparsity patterns including the different locations of the coupling blocks are given in Fig. 4.7 and Fig. 4.8, respectively.

For the assembly process we can use the basis functions and their derivatives in time similar to the classical finite element approach in space. But the distribution of the local contributions must respect the order of the temporal basis functions. First, we take the mapping from a local to a global degree of freedom in space. To respect the temporal basis functions, we shift the local to global mapping accordingly by the factor of local degrees of freedom in space on a spatial cell. This results in a shift of each global degree of freedom by the factor of $N_{\text{DoF}}^{\text{s},n}$ times the global degree of freedom of the respective basis function in time. The local matrix has therefore the size of the local degrees of freedom on a spatial mesh cell times the local degrees of freedom in time on a temporal mesh cell.

In the case of more than one cell in time per slab, an additional local matrix is assembled for the coupling of the trial basis functions of the previous time cell and the test basis functions of the current time cell. This implements the negative part of the jump trace operator in time which is transferred to the right-hand side in a classical time marching approach cf. Eq. (4.105) in Problem 4.14.

Finally, the space-time constraints of the slab have to be applied to the system matrix, the solution vector and the right-hand side vector. The space-time hanging

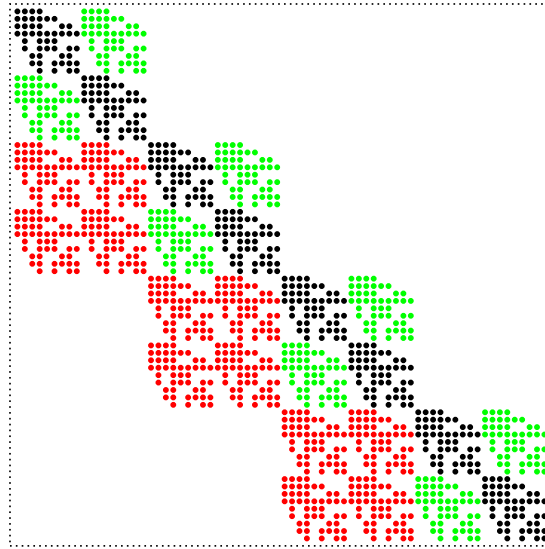


Figure 4.6: Sparsity pattern for the primal operator on a slab for $cG(1)$ - $dG(1)$ with 4 mesh cells in space and 4 mesh cells in time before condensing the Dirichlet nodes. The blocks having black dots correspond to a classical sparsity pattern for one degree of freedom in time. The blocks with green dots are additional couplings between the two time basis functions on a temporal cell. The blocks with red dots are additional couplings from the temporal jump trace operator between two time cells. The graphic is taken from [52].

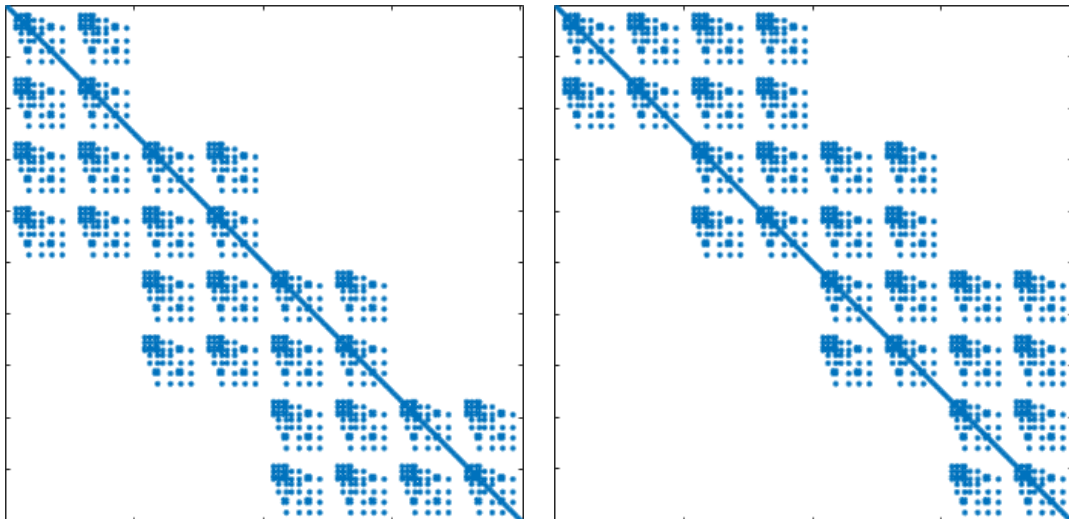


Figure 4.7: Primal and dual operator matrix sparsity patterns on a slab for $cG(1)$ - $dG(1)$ on 16 cells in space and 4 cells in time after condensing the Dirichlet nodes. The graphic is taken from [52].

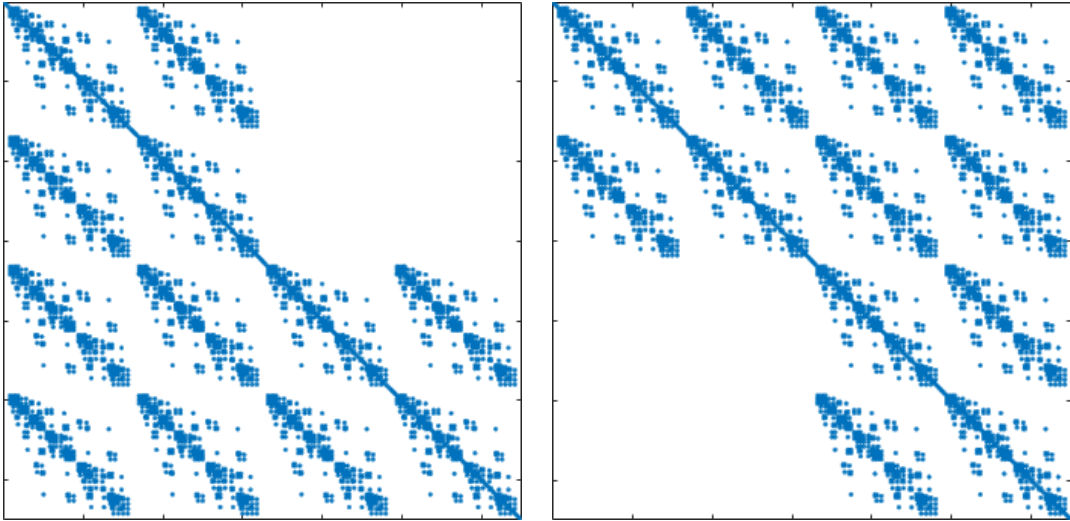


Figure 4.8: Primal and dual operator matrix sparsity patterns on a slab for cG(1)-dG(1) on 64 cells in space and 2 cells in time after condensing the Dirichlet nodes. The graphic is taken from [52].

node constraints have to be condensed in the solution vector after solving the linear system for all degrees of freedom on the slab.

4.4.2 Involvement of Slabs

The space-time tensor-product spaces described in the previous section are stored within a so-called `std::list` object, cf. Fig 4.14 of an exemplary `std::list` structure. This approach is consistent with the representation of the variational system as a TMS, since the original system decouples into subproblems on each slab, which are of less computational effort compared to solving the huge space-time system as a whole, cf. Rem. 4.17 to this issue. Moreover, the list approach allows for an easy and efficient involvement of additional slabs in the course of adaptive refinement whose process will be described in the following.

The execution of the refinement in space and time is related to the implemented tensor-product slab structure and thus takes place with regard to the following conditions. We first execute the spatial refinement and coarsening of the underlying triangulations $\mathcal{T}_{h,n}$ on all slabs. Afterwards, the refinement in time is done in the following way. If a slab Q_n is marked for temporal refinement, the corresponding just refined spatial triangulation $\mathcal{T}_{h,n}$ is copied to a new created slab Q_{n+1} that is mounted as the next element within the `std::list` structure. Thereby, the corresponding time interval $I_n^\ell := (t_{n-1}^\ell, t_n^\ell]$ is halved and within the next DWR loop ($\ell \rightarrow \ell + 1$) there holds $I_n^{\ell+1} := (t_{n-1}^{\ell+1}, t_n^{\ell+1}]$ corresponding to slab $Q_n^{\ell+1}$ with $t_{n-1}^{\ell+1} := t_{n-1}^\ell, t_n^{\ell+1} := \frac{t_{n-1}^\ell + t_n^\ell}{2}$

and $I_{n+1}^{\ell+1} := (t_n^{\ell+1}, t_{n+1}^{\ell+1}]$ corresponding to slab $Q_{n+1}^{\ell+1}$ with $t_{n+1}^{\ell+1} := t_n^\ell$, cf. Fig. 4.9 and the right part of Fig. 4.11 corresponding to a dG(0) time discretization using a Gauss quadrature rule.

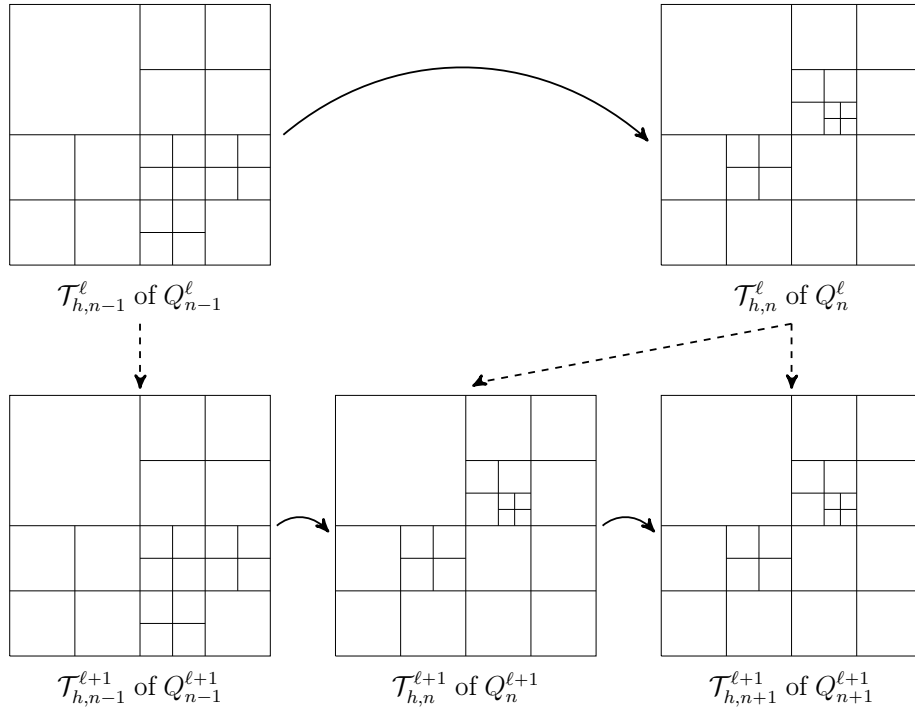


Figure 4.9: Exemplary execution of temporal refinement on a slab Q_n after spatial refinement was already executed.

Remark 4.17 *We note that the implementation of a space-time tensor product of temporal and spatial finite element spaces is general enough to allow for the computation on actual space-time meshes, i.e. the arising system on a single slab Q_n belongs to a real space-time mesh if the corresponding temporal triangulation $\mathcal{T}_{\tau,n}$ is refined at least once per slab, cf. Fig. 2.4 in Sec. 2.2. Furthermore, it is possible to use only one slab, if the choice $N^\ell = 1$ is made within the initialization step of the space-time adaptive algorithm introduced in Sec. 4.3.3, leading to a huge space-time system that has to be solved as a whole.*

4.4.3 Solution Mesh Transfer

In the context of adaptive mesh refinement for time-dependent problems, it is desirable to allow the spatial mesh to be different on all slabs Q_n , cf. Fig. 4.10. This is referred to as the concept of dynamic meshes, cf., e.g., [168, 167] for more details.

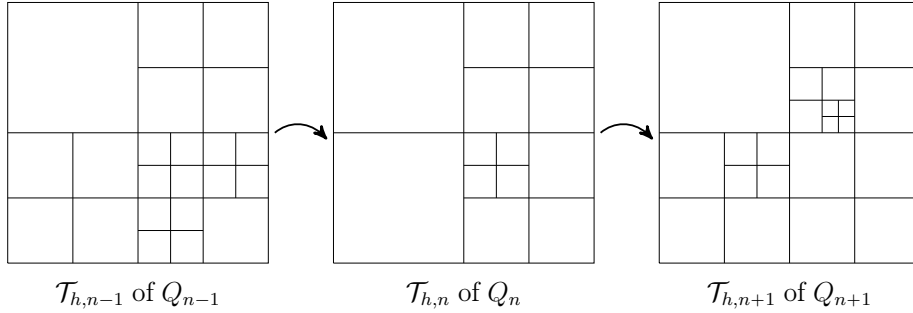


Figure 4.10: Exemplary distribution of spatial triangulations (with hanging nodes) in the course of dynamic meshes.

When dealing with computations on dynamic meshes, one of the main difficulties is the handling of a solution transfer from a spatial triangulation $\mathcal{T}_{h,n-1}$ of one slab to the spatial triangulation $\mathcal{T}_{h,n}$ of the next slab in consideration of different adaptive refinements for both meshes. More precisely, this difficulty can be reduced to the evaluation of $u_{\tau h}^{\text{dG}}(t_{\mathcal{F},n_\ell}^-)$ on $\mathcal{T}_{h,n}$ within the primal Problem 4.8 or rather Problem 4.14. In order to avoid additional computational effort as outlined in Rem. 4.18, we use for this purpose a simple interpolation of the solution from the ‘old’ mesh $\mathcal{T}_{h,n-1}$ to the current mesh $\mathcal{T}_{h,n}$ here. Then, the terms including the ‘old’ solution $u_{\tau h}^{\text{dG}}(t_{\mathcal{F},n_\ell}^-)$ on the right-hand side of Eq. (4.103) in Problem 4.14 have the following form:

$$\begin{aligned} & \gamma_\kappa \left(\sum_{K \in \mathcal{T}_h} \left((u_{\tau h}^{\text{dG}}(t_{\mathcal{F},n_\ell}^-), \varphi_h)_K + (u_{\tau h}^{\text{dG}}(t_{\mathcal{F},n_\ell}^-), \mathbf{b} \cdot \nabla \varphi_h)_K \right) \right) \\ &= \gamma_\kappa \left(\sum_{K \in \mathcal{T}_h} \left((I_h^n u_{\tau h}^{\text{dG}}(t_{\mathcal{F},n_\ell}^-), \varphi_h)_K + (I_h^n u_{\tau h}^{\text{dG}}(t_{\mathcal{F},n_\ell}^-), \mathbf{b} \cdot \nabla \varphi_h)_K \right) \right), \end{aligned} \quad (4.136)$$

where I_h^n is the interpolation operator onto the finite element space used on the current slab Q_n and $u_{\tau h}^{\text{dG}}(t_{\mathcal{F},n_\ell}^-)$ is given by Eq. (4.105). Analogous to this, the ‘old’ solution $z_{\tau h}^{\text{dG}}(t_{\mathcal{F},n}^+)$ on $\mathcal{T}_{h,n-1}$ within the dual Problem 4.11 or rather Problem 4.15 is handled, where $z_{\tau h}^{\text{dG}}(t_{\mathcal{F},n}^+)$ is given by Eq. (4.111). Note, that the dual problem is solved running backward in time. Of course, this approach entails an additional interpolation error. However, in our numerical examples in Sec. 4.5, we see that this impact is negligibly to obtain quantitatively good results.

Remark 4.18 *Since $u_{\tau h}^{\text{dG}}(t_{\mathcal{F},n_\ell}^-)$ can be thought of as previously computed data or rather as a coefficient vector with respect to the nodal basis of $V_h^{p,n-1}$, the difficulty of handling a solution transfer in general reduces to the evaluation of inner products of basis functions $\phi^{n-1} \in V_h^{p,n-1}$ with basis functions $\phi^n \in V_h^{p,n}$ given on the current spatial triangulation, cf. the right-hand side in Problem 4.14. Now, the problem is that*

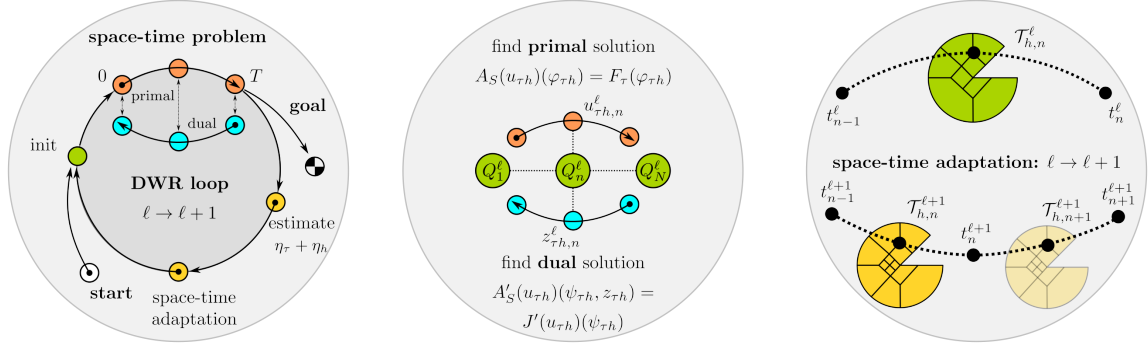


Figure 4.11: Implementation abstract of the `dwr-condiffrea` software using the DWR technique for the error estimation $\tilde{\eta}_\tau^{\text{dG}}$ and $\tilde{\eta}_h^{\text{dG}}$ (left), an exemplary forward and backward time marching step n on $(d+1)$ -dimensional space-time slabs Q_n^ℓ in the DWR loop ℓ (middle) and an exemplary space-time adaptation update of the spatial triangulation $\mathcal{T}_{h,n}^\ell \rightarrow \mathcal{T}_{h,n}^{\ell+1}$ and involvement of a further slab in the course of temporal refinement by copying $\mathcal{T}_{h,n}^{\ell+1}$ to this slab preparing the DWR loop $\ell+1$ (right). The graphic is taken from [129] and modified slightly.

the involved integrals cannot be evaluated cell-wise on the current triangulation $\mathcal{T}_{h,n}$ by simply applying quadrature rules, since we cannot guarantee ϕ^{n-1} to be smooth on each cell $K \in \mathcal{T}_{h,n}$. Thus, one has to deal with the situation to integrate shape functions defined on two different triangulations. An alternative approach to the above described interpolation is to build a temporary mesh $\mathcal{T}_{h,m}$ as the common refinement of $\mathcal{T}_{h,n-1}$ and $\mathcal{T}_{h,n}$ as proposed in [167, Sec.3.5.1]. Furthermore, a practical realization of the above mentioned integrals within the finite element library `deal.II` [17] is given in the step-28 tutorial program. For this approach it has to be assumed that all spatial meshes $\mathcal{T}_{h,n}$ are derived by adaptive refinement from a common coarse mesh $\tilde{\mathcal{T}}_h$ and each mesh itself is organized in a patch-wise manner, cf. Def. 2.6. However, this procedure is quite complex or at least effortful, since several cases for the computation on the current cell K need to be observed, namely if this cell is active on both triangulations or only on one of them and simultaneously not on the other one.

4.4.4 Software Architecture and Underlying Data Structures

In this final section, we give insight into the general framework of the underlying software architecture and present some data structures that are used to implement the space-time adaptive algorithm given in Sec. 4.3.3 including the features described in the previous sections. The software is called `dwr-condiffrea` and is a module of our in-house DWR software project `DTM++.Project/dwr` (bitbucket.org/dtmproject).

It is an extension of our former `DTM++.Project/dwr-diffusion` software [129] that is in turn related to and derived from the step-14 tutorial program code for the Laplace equation of the open source finite element library `deal.II`; cf. [17]. The `DTM++` frontend software tools are developed by Uwe Köcher designed to solve general purpose of finite element method problems using the open source `deal.II` finite element library. In addition, several backend libraries like `Trilinos` [99] or the data model and file format library `HDF5` are used; cf. [128, 129] for more details about the `DTM++` software. The software is completely written in `C++` using hierarchical object-oriented programming. It includes state-of-the-art language features from `C++.17` such as range-based loops, the `auto` specifier, reference counted dynamic memory allocation and others.

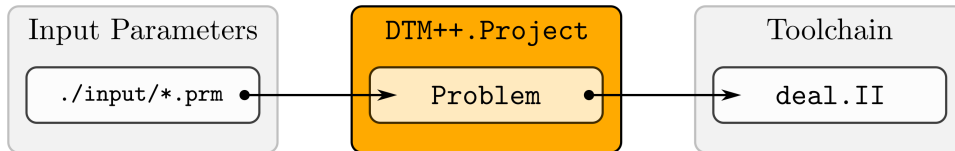


Figure 4.12: Software structure of the `DTM++.Project` module tool. The graphic is taken from [129].

The general software design is illustrated by Fig. 4.12. It is based on user-driven inputs given by simple text-based parameter input files to stake out the outer framework of the program like the choice of the spatial dimension, the desired time discretization or the goal functional used within the DWR philosophy. Furthermore, the choice of the polynomial degrees in space and time mentioned at the beginning as well as data output quantities for the primal and dual solution can be managed here. The implementation itself is done within a single central solver class template `CDR_DWR<dim>` where the respective loops of the presented algorithm given in Sec. 4.3.3 take place. This base class is inherited from `DTM::Problem` to implement a dimensionless approach with respect to the spatial variable. The structure of the solver class mimics the order given by the algorithm and the left part of Fig. 4.11, including functionalities like assembling and solving systems by using the various tools of the backend library `deal.II`. For instance, the solution transfer described in Sec. 4.4.3 that is realized by an interpolation on different spatial triangulations as given in Eq. (4.136) is done by the precasted function `interpolate_to_different_mesh()` that is implemented in the `deal.II` library; cf. the reference documentation of the `VectorTool Namespace` for more details about this function as well as [17]. All assemblers, such as for the matrices, right-hand side vectors and even the error indicators in time and

space, are using the `deal.II` workstream technology for thread-parallel and further MPI+X-parallel simulations; cf. [129] and therein the in-source `doxygen` documentation of the `DTM++.Project/dwr-diffusion` code. The assemblers are outsourced into separate classes to allow their reuse in other frameworks with minimal coding effort. Thereby, the useful and efficient auxiliary classes of the `DTM++.Project` suite are provided independently, such that the input parameter handling and data output handling must not be included into the solver class.

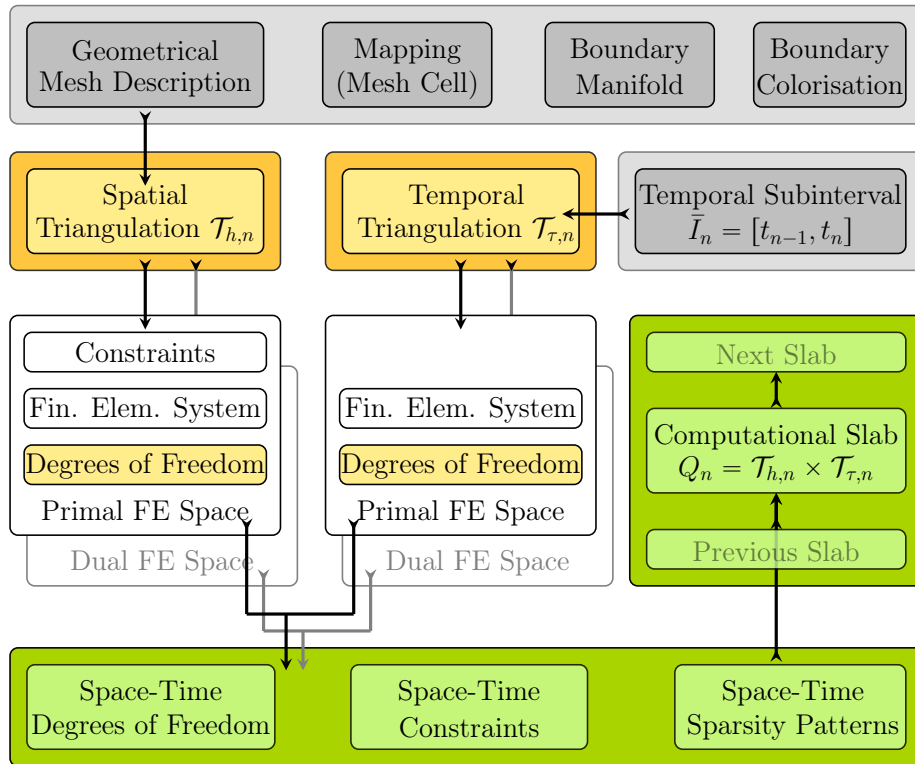


Figure 4.13: Illustration of the generation of space-time elements for tensor-product spaces on a computational slab implemented by the `DTM++::Grid_DWR` class. Remark that loop based slab data structures Q_n^ℓ is not stored for efficiency reasons. The graphic is taken from [52] and modified slightly.

The above described process of the partitioning and storing of the respective $(d+1)$ -dimensional space-time slabs by using a `std::list` approach is handled within our so-called `DTM++::Grid_DWR` class. This class is responsible for the initially chosen division N of the global space-time domain Q , storing the computational slabs $Q_n = \mathcal{T}_{h,n} \times \mathcal{T}_{\tau,n}$ as elements of this `std::list` object. Both triangulations on a single slab are shared by the primal and dual problem and the respective temporal or spatial polynomial degree can be chosen arbitrarily, cf. Fig.4.13 and [29] for further details. This enables a flexible choice of polynomial degrees in space and time and, in

addition, the realization of using an approximation by higher-order finite elements for the weights, since the dual problem can be solved using a higher polynomial degree for both space and time discretization, cf. Sec. 4.3.2. Beyond that, the `DTM++::Grid_DWR` class handles the in Sec. 4.4.2 described involvement of additional slabs in the course of adaptive temporal refinement and undertakes tasks like mapping between real and reference cell or coloring of the boundary faces by means of varying boundary conditions. As already mentioned, each of the space-time slabs consists of a separate spatial and temporal triangulation together with the respective required tools like a finite element object, a degrees of freedom (DoF) handler object as well as an possible constraints object that are used by the primal and dual problem, cf. Fig. 4.13. Note that we are using the same triangulations but different finite element and DoF handler objects for the primal and dual problem.

Besides the `DTM++::Grid_DWR` class we are using the `std::list` approach for the efficient treatment of the space-time DoF data storage management, cf. Fig. 4.14. This storage allows to efficiently iterate forwardly and backwardly in time to compute the primal and dual solutions as well as the error indicators. Keep in mind that we are solving the dual problem running backward in time and, depending on the chosen goal functional, the primal solution could be needed on the whole time interval.

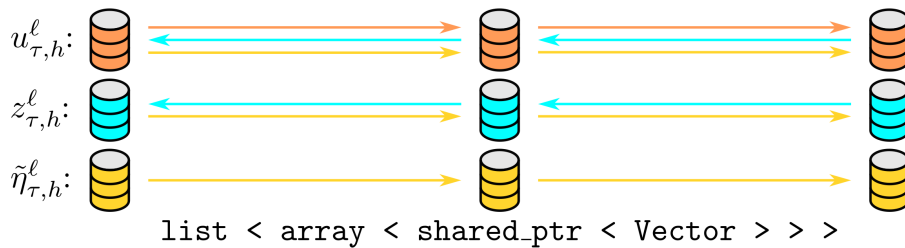


Figure 4.14: Illustration of the `DTM++::Project` data storage management. A list entry corresponds to a slab and stores a small array of shared pointer references. The large data `Vector` is stored independently and can be serialised. The graphic is taken from [129].

Remark 4.19 *The list data structure allows to efficiently iterate forwardly and backwardly to access solutions on neighboring slabs as it is needed when solving the primal and dual problem. The large data of space-time DoF vectors are accessed through a light-weighted data structure, whereby the data storage management structure only needs to store referenced counted pointers, cf. [129, Sec.2.2] for more details. This approach is even then (memory-)efficient whenever the whole primal solution $u_{\tau h}$ is needed for the right-hand side goal functional J within the dual problem, cf. Rem. 4.5. The latter case may arise in the case of nonlinear problems, cf. [40, Rem. 3.1].*

4.5 Numerical Examples

In this section, we investigate the performance properties of the proposed approach of combining the Dual Weighted Residual method with stabilized finite element approximations for time-dependent convection-dominated problems. Thereby, we study the convergence behavior, computational efficiency as well as stability properties of the underlying space-time adaptive algorithm introduced in Sec. 4.3.3.

The first example is an academic test problem with a given analytical solution to validate the correctness of the higher-order implementations in space and time regarding expected experimental orders of convergence. Additionally, this example serves to show the independency of the temporal and spatial error indicators. The second example modifies the first one with regard to more dynamic behavior in time and serves to demonstrate the performance properties of the algorithm with regard to adaptive mesh refinement in space and time. Finally, in a third example, we investigate the mesh adaptation processes concerning stability properties for a benchmark problem of convection-dominated transport.

Similar to the steady-state case, we will consider in some cases an effectivity index that thus has to be modified in the following way

$$\mathcal{I}_{\text{eff}} := \left| \frac{\tilde{\eta}_{\tau}^{\text{dG,hoEx}} + \tilde{\eta}_h^{\text{dG}}}{J(u) - J(u_{\tau h})} \right|, \quad \text{or else } \mathcal{I}_{\text{eff}} := \left| \frac{\tilde{\eta}_{\tau}^{\text{dG,hoFE}} + \tilde{\eta}_h^{\text{dG}}}{J(u) - J(u_{\tau h})} \right|, \quad (4.137)$$

defined as the ratio of the sum of the estimated errors over the exact error and depending on the underlying approximation technique used for the temporal weights. Furthermore, in the case of adaptive refinement the tuning parameters of the goal-oriented adaptive Algorithm given in Sec. 4.3.3 are chosen to balance automatically the potential misfit of the spatial and temporal errors, given by the following ranges:

$$1.5 \leq \omega \leq 3.5, \quad 0 \leq \theta_h^{\text{bottom}} \leq 0.02, \quad (4.138)$$

$$\theta_{h,1}^{\text{top}} \geq \theta_{h,2}^{\text{top}} = \frac{1}{2} \cdot \min \left\{ \left| \frac{\eta_h}{|\eta_h| + |\eta_{\tau}|} \right|, 1 \right\}, \quad \theta_{\tau}^{\text{top}} = \frac{1}{2} \cdot \min \left\{ \left| \frac{\eta_{\tau}}{|\eta_h| + |\eta_{\tau}|} \right|, 1 \right\}.$$

Finally, the SUPG method stabilization parameter δ_K is given by

$$\delta_K = \delta_0 \cdot h_K, \quad 0.1 \leq \delta_0 \leq 1, \quad (4.139)$$

where h_K denotes the cell diameter of the spatial mesh cell K , cf. Rem. 4.3. The software for the now following examples is called `dwr-condiffrea` being a module of our in-house DWR software project `DTM++.Project/dwr` (bitbucket.org/dtmproject) developed by U. Köcher [128, 129]. It is implemented using the open source finite element library `deal.II`; cf. [17]. Some of the results presented in the following have been published by the author et al. in [51] and [29].

4.5.1 Rotating Hill - Convergence Behavior and Independence of Error Indicators

In a first numerical example, we study the global space-time refinement behavior to verify the expected experimental orders of convergence and show the correctness of the higher-order implementations in space and time.

Example 4.1 (Rotating Hill)

The first example is an academic test case, in which we study Problem (4.1) with the following prescribed exact solution

$$\begin{aligned} u(\mathbf{x}, t) &:= u_1 \cdot u_2, \quad \mathbf{x} = (x_1, x_2)^\top \in \mathbb{R}^2 \text{ and } t \in \mathbb{R}, \\ u_1(\mathbf{x}, t) &:= (1 + a \cdot ((x_1 - m_1(t))^2 + (x_2 - m_2(t))^2))^{-1}, \\ u_2(\mathbf{x}, t) &:= s, \quad m_1(t) := \frac{1}{2} + \frac{1}{4} \cos(2\pi t), \quad m_2(t) := \frac{1}{2} + \frac{1}{4} \sin(2\pi t). \end{aligned} \quad (4.140)$$

This solution is characterized by a counterclockwise rotating hill whose size and gradient are depending on the scalars s, a_0 and goes back to an example used in [98, Sec. 1.4.2]. The problem is defined on $\Omega \times I := (0, 1)^2 \times (0, 1]$ with the scalars $s = 1, a_0 = 50$ such that the final position of the hill equals the initial one and its peak is close to the value 1, cf. Fig. 4.15. The right-hand side forcing term f , the nonhomogeneous Dirichlet boundary condition and the initial condition are calculated from the given analytical solution (4.140) and Eqs. (4.1). We choose the diffusion coefficient $\varepsilon = 1$, the flow field $\mathbf{b} = (2, 3)^\top$ and the reaction coefficient $\alpha = 1$. Furthermore, no stabilization ($\delta_K = 0$) is used in this test case. The goal functional is chosen to control the global $L^2(L^2)$ -error in space and time of $e := u - u_{\tau h}$, given by

$$J(u) = \frac{1}{\|e\|_{(0,T) \times \Omega}} \int_I (u, e) dt, \quad \text{with } \|\cdot\|_{(0,T) \times \Omega} = \left(\int_I (\cdot, \cdot) dt \right)^{\frac{1}{2}}. \quad (4.141)$$

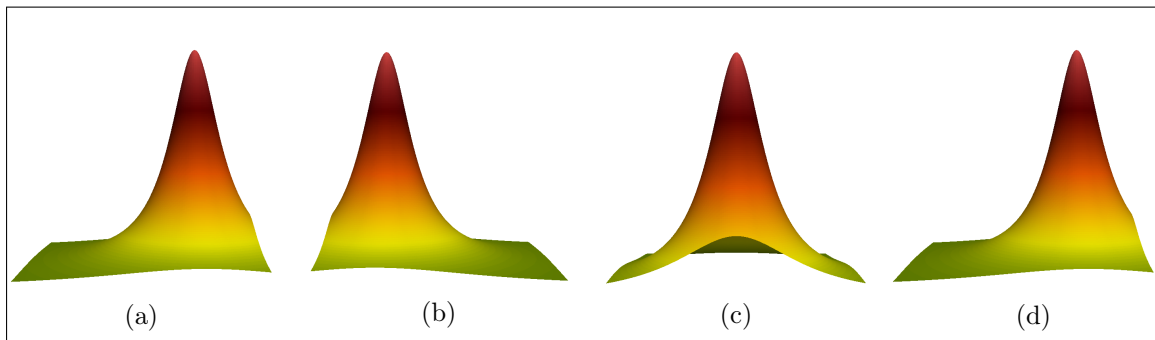


Figure 4.15: Exemplary solution profiles at time points $t_n = 0$ (a), $t_n = 0.5$ (b), $t_n = 0.75$ (c) and $t_n = 1$ (d) for Example 4.1.

ℓ	N	N_K	$N_{\text{DoF}}^{\text{tot}}$	$\ u - u_{\tau h}^{1,0}\ $	EOC	ℓ	N	N_K	$N_{\text{DoF}}^{\text{tot}}$	$\ u - u_{\tau h}^{1,1}\ $	EOC
1	4	4	36	1.4109e-01	—	1	4	4	72	1.9583e-01	—
2	8	16	200	5.9389e-02	1.25	2	8	16	400	5.8488e-02	1.74
3	16	64	1296	1.8328e-02	1.70	3	16	64	2592	1.5695e-02	1.90
4	32	256	9248	6.3123e-03	1.54	4	32	256	18496	4.3675e-03	1.85
5	64	1024	69696	2.3465e-03	1.43	5	64	1024	139392	1.1222e-03	1.96
6	128	4096	540800	9.9334e-04	1.24	6	128	4096	1081600	2.8416e-04	1.98
7	256	16384	4260096	4.5961e-04	1.11	7	256	16384	8520192	7.1620e-05	1.99

ℓ	N	N_K	$N_{\text{DoF}}^{\text{tot}}$	$\ u - u_{\tau h}^{2,2}\ $	EOC	ℓ	N	N_K	$N_{\text{DoF}}^{\text{tot}}$	$\ u - u_{\tau h}^{3,3}\ $	EOC
1	4	4	300	1.5805e-01	—	1	4	4	784	5.4849e-02	—
2	8	16	1944	1.2860e-02	3.62	2	8	16	5408	4.2480e-03	3.69
3	16	64	13872	2.3553e-03	2.45	3	16	64	40000	3.5713e-04	3.57
4	32	256	104544	3.1980e-04	2.88	4	32	256	307328	2.7199e-05	3.71
5	64	1024	811200	4.1703e-05	2.94	5	64	1024	2408704	1.7941e-06	3.92
6	128	4096	6390144	5.3032e-06	2.98	6	128	4096	19071488	1.1392e-07	3.98
7	256	16384	50725632	6.6940e-07	2.99	7	256	16384	151782400	7.1798e-09	3.99

Table 4.1: Global convergence for $u_{\tau h}^{1,0}$ in a cG(1)-dG(0), $u_{\tau h}^{1,1}$ in a cG(1)-dG(1), $u_{\tau h}^{2,2}$ in a cG(2)-dG(2) and $u_{\tau h}^{3,3}$ in a cG(3)-dG(3) primal approximation for a convection-diffusion-reaction transport problem with $\varepsilon = 1$ and $\delta_0 = 0$ for Example 4.1.

To study the global space-time refinement behavior, the solution u is approximated in different finite element spaces, starting with the lowest order case in space and time, cG(1)-dG(0), up to the space-time higher-order method cG(3)-dG(3). Here and in the following, we denote by $u_{\tau h}^{p,r}$ or $z_{\tau h}^{p,r}$ the approximated primal or dual solution obtained by using a space-time cG(p)-dG(r) method; cf. Rem. 4.2. In general, for a cG(p)-dG(r) method, measured in the $L^2(I; L^2(\Omega))$ -norm, we may expect convergence in space-time of order $\mathcal{O}(h^{p+1} + \tau^{r+1})$; cf. e.g. [174, 142]. The results of our investigations are given by Table 4.1 and nicely confirm the expected experimental orders of convergence (EOC := $-\log_2(\|e\|_\ell / \|e\|_{\ell-1})$). Here, ℓ denotes the refinement level or DWR loop, N the total cells in time, N_K the cells in space on a slab, $N_{\text{DoF}}^{\text{tot}}$ the total space-time degrees of freedom, $\|\cdot\|$ the global $L^2(L^2)$ -norm error as given in Eq. (4.141) and EOC the experimental order of convergence.

The second numerical experiment to Example 4.1 is devoted to the numerical justification of splitting the total discretization error into a temporal and spatial contribution as introduced in Eq. (4.25). Regarding efficiency and reliability reasons, it is crucial that one part of the error estimator is almost independent on the refinement of the discretization with regard to the other part. Therefore, we investigate the approximated error indicators by executing a global refinement of only one of the discretizations while the other one is kept fixed. In the course of this, both approximation techniques for the temporal weights are studied; cf. Sec. 4.3.2. In Table 4.2

			$\tilde{\eta}_\tau$					
			H-O. Extrapolation				H-O. Finite Elements	
			Gauss		Gauss-Lobatto			
ℓ	N	N_K	$u_{\tau h}^{1,0} / z_{\tau h}^{2,0}$	$u_{\tau h}^{1,1} / z_{\tau h}^{2,1}$	$u_{\tau h}^{1,0} / z_{\tau h}^{2,0}$	$u_{\tau h}^{1,1} / z_{\tau h}^{2,1}$	$u_{\tau h}^{1,0} / z_{\tau h}^{2,1}$	$u_{\tau h}^{1,1} / z_{\tau h}^{2,2}$
1	50	256	3.3016e-03	6.2584e-05	1.1947e-03	2.3387e-06	1.5890e-02	6.5242e-05
2	50	1024	3.8305e-03	2.3742e-04	1.7346e-03	1.3801e-04	3.1556e-02	2.4609e-04
3	50	4096	3.8020e-03	6.5231e-04	1.8737e-03	4.7413e-04	3.9553e-02	6.7403e-04
4	50	16384	3.7377e-03	8.5370e-04	1.8905e-03	6.5218e-04	4.1735e-02	8.8136e-04
5	50	65536	3.7161e-03	8.7429e-04	1.8926e-03	6.7606e-04	4.2276e-02	9.0240e-04

Table 4.2: Independence of the temporal error indicators $\tilde{\eta}_\tau$ on the refinement in space in consideration of approximating the temporal weights by higher-order extrapolation and higher-order finite elements with $\varepsilon = 1$ and $\delta_0 = 0$ for Example 4.1.

			$\tilde{\eta}_h$					
			H-O. Extrapolation				H-O. Finite Elements	
			Gauss		Gauss-Lobatto			
ℓ	N	N_K	$u_{\tau h}^{1,0} / z_{\tau h}^{2,0}$	$u_{\tau h}^{1,1} / z_{\tau h}^{2,1}$	$u_{\tau h}^{1,0} / z_{\tau h}^{2,0}$	$u_{\tau h}^{1,1} / z_{\tau h}^{2,1}$	$u_{\tau h}^{1,0} / z_{\tau h}^{2,1}$	$u_{\tau h}^{1,1} / z_{\tau h}^{2,2}$
1	40	4096	1.5662e-04	1.5411e-04	1.6481e-04	1.5139e-04	3.3549e-04	2.4003e-04
2	80	4096	1.8571e-04	3.3954e-04	1.8892e-04	3.3498e-04	2.7659e-04	3.7244e-04
3	160	4096	2.2249e-04	4.0984e-04	2.2392e-04	4.0326e-04	2.6611e-04	4.1197e-04
4	320	4096	2.6710e-04	4.2868e-04	2.6765e-04	4.1751e-04	2.8578e-04	4.1909e-04
5	640	4096	3.0657e-04	4.3757e-04	3.0649e-04	4.1721e-04	3.1322e-04	4.1747e-04

Table 4.3: Independence of the spatial error indicators $\tilde{\eta}_h$ on the refinement in time in consideration of approximating the temporal weights by higher-order extrapolation and higher-order finite elements with $\varepsilon = 1$ and $\delta_0 = 0$ for Example 4.1.

we present the development of the approximated temporal error indicators $\tilde{\eta}_\tau^{\text{dG,hoEx}}$, or else $\tilde{\eta}_\tau^{\text{dG,hoFE}}$ as given by the first two equations in (4.129) for a global refinement in space by using a constant number of time intervals. It can be observed that the respective temporal error indicators are almost independent of the increasing spatial refinement for all considered cases of a cG(p)-dG(r) method and both approximation techniques used for the temporal weights (columns four to seven of Table 4.2). The same holds true for the spatial error indicators. In Table 4.3 we present the related development of the approximated spatial error indicators $\tilde{\eta}_h$, as given by the last equation in (4.129), for a global refinement in time by using a constant number of space cells. Again, but this time the respective spatial error indicators are almost independent of the increasing temporal refinement for all considered cases of a cG(p)-dG(r) method and both approximation techniques used for the temporal weights (columns

four to seven of Table 4.3). Furthermore, note the good agreement of the spatial error indicators for all temporal discretizations and both approximation techniques for the temporal weights.

Conclusion 4.1 (Convergence Behavior and Independent Error Indicators)

As an interim conclusion, we summarize the following.

- The algorithm confirms the expected experimental orders of convergence in space and time $\mathcal{O}(h^{p+1} + \tau^{r+1})$; cf. Table 4.1.
- The temporal error indicators are independent of the spatial refinement and vice versa for all approximation techniques and all cases of cG(p)-dG(r) methods; cf. Table 4.2 and Table 4.3.

4.5.2 Rotating Hill with Changing Orientation - Comparison of Approximation Techniques for Temporal Weights

The second example is a modification of the first one with regard to more dynamic behavior in time.

Example 4.2 (Rotating Hill with Changing Orientation)

We study Problem (4.1) with the following prescribed exact solution

$$\begin{aligned} u(\mathbf{x}, t) &:= u_1 \cdot u_2, \quad \mathbf{x} = (x_1, x_2)^\top \in \mathbb{R}^2 \text{ and } t \in \mathbb{R}, \\ u_1(\mathbf{x}, t) &:= (1 + a \cdot ((x_1 - m_1(t))^2 + (x_2 - m_2(t))^2))^{-1}, \\ u_2(t) &:= \nu_1(t) \cdot s \cdot \arctan(\nu_2(t)), \end{aligned} \quad (4.142)$$

with $m_1(t) := \frac{1}{2} + \frac{1}{4} \cos(2\pi t)$ and $m_2(t) := \frac{1}{2} + \frac{1}{4} \sin(2\pi t)$, and, $\nu_1(\hat{t}) := -1, \nu_2(\hat{t}) := 5\pi \cdot (4\hat{t} - 1)$, for $\hat{t} \in [0, 0.5)$ and $\nu_1(\hat{t}) := 1, \nu_2(\hat{t}) := 5\pi \cdot (4(\hat{t} - 0.5) - 1)$, for $\hat{t} \in [0.5, 1)$, $\hat{t} = t - k, k \in \mathbf{N}_0$, and, scalars $s = \frac{1}{3}, a_0 = 50$. The (analytical) solution behaves as in Example 4.1, but is designed in such a way that the maximum height of the hill is compressed and the orientation of the hill changes its sign from positive to negative at $t = 0.25$ and again from negative to positive at $t = 0.75$, cf. Fig. 4.16. The problem is defined on $\Omega \times I := (0, 1)^2 \times (0, 1]$. The right-hand side forcing term f , the nonhomogeneous Dirichlet boundary condition and the initial condition are calculated from the given analytical solution (4.142) and Eqs. (4.1). We choose the diffusion coefficient $\varepsilon = 1$, the flow field $\mathbf{b} = (2, 3)^\top$ and the reaction coefficient $\alpha = 1$. Furthermore, no stabilization ($\delta_K = 0$) is used in this test case. The goal quantity is chosen to control the global $L^2(L^2)$ -error in space and time, given by Eq. (4.141).

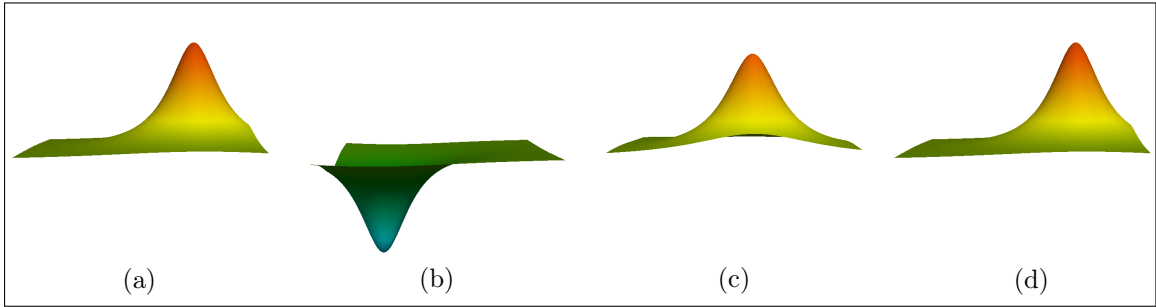


Figure 4.16: Exemplary solution profiles at time points $t_n = 0$ (a), $t_n = 0.5$ (b), $t_n = 0.8$ (c) and $t_n = 1$ (d) for Example 4.2.

In the following, we analyze the performance properties of our algorithm for varying adaptive solution approximations of the primal and dual problem with regard to the polynomial degree used in space and time including a comparison of the different approximation techniques for the temporal weights.

In Tables 4.4–4.12, we present the development of the total discretization error $J(e) = \|e\|_{(0,T)\times\Omega}$, the approximated spatial and temporal error estimators $\tilde{\eta}_h$ and $\tilde{\eta}_\tau$ as well as the effectivity index \mathcal{I}_{eff} during an adaptive refinement process for several pairs of finite element spaces. Thereby, $e^{p,r,q,s}$ or in the following a $\text{cG}(p)\text{-dG}(r)/\text{cG}(q)\text{-dG}(s)$ discretization corresponds to a primal solution approximation $u_{\tau h}^{p,r}$ in $\text{cG}(p)\text{-dG}(r)$ and dual solution approximation $z_{\tau h}^{q,s}$ in $\text{cG}(q)\text{-dG}(s)$. We distinguish between an approximation of the temporal weights by using a higher-order extrapolation strategy (Tables 4.4–4.9) or a higher-order finite elements strategy (Tables 4.10–4.12). In the former case, we further distinguish between an extrapolation using Gauss quadrature points (Tables 4.4–4.6) or Gauss-Lobatto quadrature points (Tables 4.7–4.9). Here and in the following, ℓ denotes the refinement level or DWR loop, N the total cells in time, N_K^{max} the number of cells on the finest spatial mesh within the current loop, and $N_{\text{DoF}}^{\text{tot}}$ the total space-time degrees of freedom.

Regarding the accuracy of the underlying error estimator, as given by the last column of Tables 4.4–4.12, it can be summarized that all considered $\text{cG}(p)\text{-dG}(r)/\text{cG}(q)\text{-dG}(s)$ discretizations show a good quantitative estimation of the discretization error as the respective effectivity index \mathcal{I}_{eff} is around one. With regard to efficiency reasons for a space-time adaptive algorithm, it is essential to ensure an equilibrated reduction of the temporal as well as spatial discretization error, cf. the third note in Rem. 4.15. Referring to this, we point out for all test cases a very good equilibration of the spatial and temporal error indicators $\tilde{\eta}_h$ and $\tilde{\eta}_\tau$ in the course of the refinement process (columns six and seven of Tables 4.4–4.12).

ℓ	N	N_K^{\max}	$N_{\text{DoF}}^{\text{tot}}$	$J(e^{1,0,2,0})$	$\tilde{\eta}_h$	$\tilde{\eta}_\tau^{\text{dG,hoEx-G}}$	\mathcal{I}_{eff}
1	25	16	625	2.7354e-02	1.8926e-02	5.1137e-03	0.88
2	25	40	1067	1.5713e-02	6.7241e-03	4.5785e-03	0.72
3	31	100	3039	8.7396e-03	3.0774e-03	7.3577e-03	1.19
4	37	100	3583	7.1841e-03	3.7292e-03	8.1897e-03	1.65
5	44	100	4210	6.9192e-03	3.8660e-03	5.6193e-03	1.37
6	52	160	7408	4.6584e-03	1.8486e-03	3.7331e-03	1.19
7	62	160	8864	4.5581e-03	1.8725e-03	2.7634e-03	1.01
8	88	208	15276	3.2393e-03	1.1941e-03	2.2018e-03	1.04

Table 4.4: Adaptive refinement including effectivity indices with goal quantity (4.141), $\varepsilon = 1$, $\delta_0 = 0$, and $\omega = 1.5$ for Example 4.2, using a higher-order extrapolation strategy (Gauss) for the temporal weights. $e^{1,0,2,0}$ corresponds to the primal and dual solution approximation $u_{\tau h}^{1,0}$ in cG(1)-dG(0) and $z_{\tau h}^{2,0}$ in cG(2)-dG(0), respectively.

ℓ	N	N_K^{\max}	$N_{\text{DoF}}^{\text{tot}}$	$J(e^{1,1,2,1})$	$\tilde{\eta}_h$	$\tilde{\eta}_\tau^{\text{dG,hoEx-G}}$	\mathcal{I}_{eff}
1	20	16	1000	2.4934e-02	2.5500e-02	5.5404e-04	1.04
2	20	40	1724	1.1888e-02	1.0845e-02	1.1496e-03	1.01
3	20	88	3404	7.8291e-03	6.8133e-03	1.5493e-03	1.06
4	20	148	5352	5.6387e-03	3.3423e-03	2.0080e-03	0.95
5	20	256	7600	4.8254e-03	1.6649e-03	2.5393e-03	0.87
6	37	256	14266	2.5684e-03	2.4006e-03	3.9763e-04	1.08
7	37	424	19190	2.0934e-03	1.7007e-03	4.9602e-04	1.04
8	37	724	29182	1.8398e-03	1.0117e-03	5.5312e-04	0.85

Table 4.5: Adaptive refinement including effectivity indices with goal quantity (4.141), $\varepsilon = 1$, $\delta_0 = 0$, and $\omega = 1.5$ for Example 4.2, using a higher-order extrapolation strategy (Gauss) for the temporal weights. $e^{1,1,2,1}$ corresponds to the primal and dual solution approximation $u_{\tau h}^{1,1}$ in cG(1)-dG(1) and $z_{\tau h}^{2,1}$ in cG(2)-dG(1), respectively.

ℓ	N	N_K^{\max}	$N_{\text{DoF}}^{\text{tot}}$	$J(e^{2,2,3,2})$	$\tilde{\eta}_h$	$\tilde{\eta}_\tau^{\text{dG,hoEx-G}}$	\mathcal{I}_{eff}
1	10	4	750	2.8682e-02	2.1587e-02	4.6150e-04	0.77
2	10	16	2430	1.4199e-02	3.5422e-03	4.6597e-04	0.28
3	13	40	7527	9.2277e-03	2.6691e-04	3.1271e-04	0.06
4	16	76	14970	1.4287e-03	7.2741e-04	7.7024e-04	1.04
5	20	100	23940	6.6552e-04	8.8557e-04	3.5350e-04	1.86
6	20	148	27966	5.4387e-04	6.3643e-04	4.4004e-04	1.98
7	25	208	48885	2.4309e-04	2.1829e-04	1.1789e-04	1.38
8	25	268	60963	2.1102e-04	1.3182e-04	1.3780e-04	1.27

Table 4.6: Adaptive refinement including effectivity indices with goal quantity (4.141), $\varepsilon = 1$, $\delta_0 = 0$, and $\omega = 1.5$ for Example 4.2, using a higher-order extrapolation strategy (Gauss) for the temporal weights. $e^{2,2,3,2}$ corresponds to the primal and dual solution approximation $u_{\tau h}^{2,2}$ in cG(2)-dG(2) and $z_{\tau h}^{3,2}$ in cG(3)-dG(2), respectively.

ℓ	N	N_K^{\max}	$N_{\text{DoF}}^{\text{tot}}$	$J(e^{1,0,2,0})$	$\tilde{\eta}_h$	$\tilde{\eta}_\tau^{\text{dG,hoEx-GL}}$	\mathcal{I}_{eff}
1	25	16	625	2.7354e-02	9.0916e-03	2.6871e-03	0.43
2	25	40	1067	1.6011e-02	3.5069e-03	4.1412e-03	0.48
3	31	100	2923	9.0050e-03	2.0423e-03	4.0779e-03	0.68
4	45	160	6295	4.5301e-03	1.1878e-03	1.7596e-03	0.65
5	54	244	10782	3.2418e-03	5.9727e-04	1.7663e-03	0.73
6	79	244	15737	2.5454e-03	7.1197e-04	1.1242e-03	0.72
7	96	244	19148	2.3900e-03	7.4800e-04	9.3982e-04	0.71
8	117	388	35571	1.7208e-03	4.0226e-04	9.1843e-04	0.77

Table 4.7: Adaptive refinement including effectivity indices with goal quantity (4.141), $\varepsilon = 1$, $\delta_0 = 0$, and $\omega = 1.5$ for Example 4.2, using a higher-order extrapolation strategy (Gauss-Lobatto) for the temporal weights. $e^{1,0,2,0}$ corresponds to the primal and dual solution approximation $u_{\tau h}^{1,0}$ in cG(1)-dG(0) and $z_{\tau h}^{2,0}$ in cG(2)-dG(0), respectively.

ℓ	N	N_K^{\max}	$N_{\text{DoF}}^{\text{tot}}$	$J(e^{1,1,2,1})$	$\tilde{\eta}_h$	$\tilde{\eta}_\tau^{\text{dG,hoEx-GL}}$	\mathcal{I}_{eff}
1	20	16	1000	2.4934e-02	1.4276e-02	4.2861e-04	0.59
2	20	40	1780	1.1506e-02	5.7523e-03	1.0207e-03	0.58
3	20	136	5544	5.4277e-03	1.8570e-03	2.1108e-03	0.73
4	26	220	9968	2.5790e-03	1.7388e-03	7.8413e-04	0.97
5	26	352	13836	2.0827e-03	8.8887e-04	9.6386e-04	0.89
6	32	652	33888	9.2141e-04	3.4916e-04	3.7122e-04	0.78
7	40	940	60932	6.7505e-04	3.6641e-04	3.0557e-04	1.00
8	50	1456	106980	4.6429e-04	2.5079e-04	2.1824e-04	1.01

Table 4.8: Adaptive refinement including effectivity indices with goal quantity (4.141), $\varepsilon = 1$, $\delta_0 = 0$, and $\omega = 1.5$ for Example 4.2, using a higher-order extrapolation strategy (Gauss-Lobatto) for the temporal weights. $e^{1,1,2,1}$ corresponds to the primal and dual solution approximation $u_{\tau h}^{1,1}$ in cG(1)-dG(1) and $z_{\tau h}^{2,1}$ in cG(2)-dG(1), respectively.

ℓ	N	N_K^{\max}	$N_{\text{DoF}}^{\text{tot}}$	$J(e^{2,2,3,2})$	$\tilde{\eta}_h$	$\tilde{\eta}_\tau^{\text{dG,hoEx-GL}}$	\mathcal{I}_{eff}
1	10	4	750	2.8682e-02	2.1493e-03	1.0027e-03	0.11
2	12	16	2916	7.0121e-03	4.9133e-03	1.2111e-04	0.72
3	12	76	8388	1.7267e-03	9.9659e-04	4.9147e-04	0.86
4	14	124	18588	8.7433e-04	2.8278e-04	4.3942e-04	0.82
5	16	148	24924	5.4521e-04	1.5092e-04	1.1808e-04	0.49
6	19	184	34371	3.5432e-04	8.1237e-05	9.6884e-05	0.50
7	22	220	46656	2.7304e-04	6.3655e-05	6.6686e-05	0.48
8	26	364	75660	1.3884e-04	3.7858e-05	3.5975e-05	0.53

Table 4.9: Adaptive refinement including effectivity indices with goal quantity (4.141), $\varepsilon = 1$, $\delta_0 = 0$, and $\omega = 1.5$ for Example 4.2, using a higher-order extrapolation strategy (Gauss-Lobatto) for the temporal weights. $e^{2,2,3,2}$ corresponds to the primal and dual solution approximation $u_{\tau h}^{2,2}$ in cG(2)-dG(2) and $z_{\tau h}^{3,2}$ in cG(3)-dG(2), respectively.

ℓ	N	N_K^{\max}	$N_{\text{DoF}}^{\text{tot}}$	$J(e^{1,0,2,1})$	$\tilde{\eta}_h$	$\tilde{\eta}_\tau^{\text{dG,hoFE}}$	\mathcal{I}_{eff}
1	25	16	625	2.7354e-02	2.1815e-02	1.0990e-02	1.19
2	25	40	1053	1.5764e-02	8.9839e-03	1.8929e-02	1.77
3	33	40	1409	1.2960e-02	9.9185e-03	1.0358e-02	1.56
4	42	88	3842	7.3767e-03	5.1465e-03	1.0170e-02	2.07
5	54	88	4854	6.6367e-03	5.3181e-03	6.5547e-03	1.78
6	70	160	8788	4.1634e-03	3.1242e-03	5.5366e-03	2.08
7	91	160	11395	4.0347e-03	3.0557e-03	4.0652e-03	1.76
8	105	160	16357	3.1593e-03	2.1538e-03	3.7839e-03	1.87

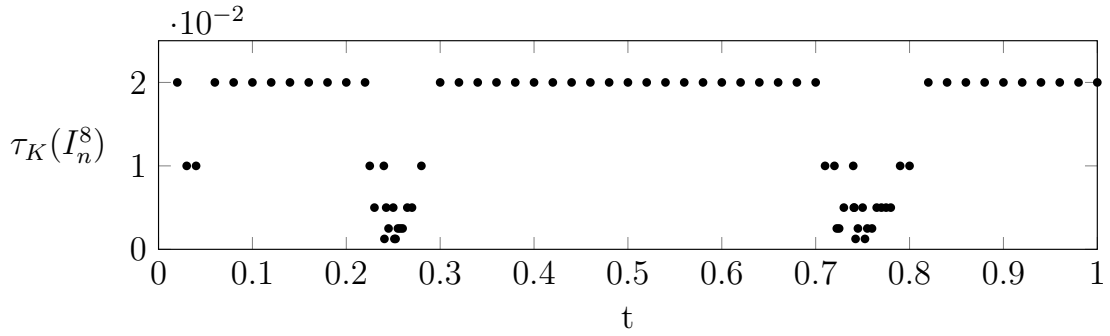
Table 4.10: Adaptive refinement including effectivity indices with goal quantity (4.141), $\varepsilon = 1$, $\delta_0 = 0$, and $\omega = 1.5$ for Example 4.2, using a higher-order finite elements strategy for the temporal weights. $e^{1,0,2,1}$ corresponds to the primal and dual solution approximation $u_{\tau h}^{1,0}$ in cG(1)-dG(0) and $z_{\tau h}^{2,1}$ in cG(2)-dG(1), respectively.

ℓ	N	N_K^{\max}	$N_{\text{DoF}}^{\text{tot}}$	$J(e^{1,1,2,2})$	$\tilde{\eta}_h$	$\tilde{\eta}_\tau^{\text{dG,hoFE}}$	\mathcal{I}_{eff}
1	20	16	1000	2.4934e-02	2.6265e-02	1.2685e-03	1.10
2	20	40	1808	1.1240e-02	1.0492e-02	2.8598e-03	1.18
3	24	160	7796	2.8027e-03	2.7916e-03	2.0501e-03	1.72
4	28	316	14340	1.5789e-03	7.0242e-04	1.4408e-03	1.35
5	33	316	16990	1.5221e-03	7.5932e-04	1.0656e-03	1.19
6	46	544	39612	8.7873e-04	4.0805e-04	5.0376e-04	1.03
7	55	820	74310	5.1495e-04	2.0234e-04	3.7718e-04	1.12
8	66	820	89752	4.8725e-04	2.0333e-04	2.5583e-04	0.94

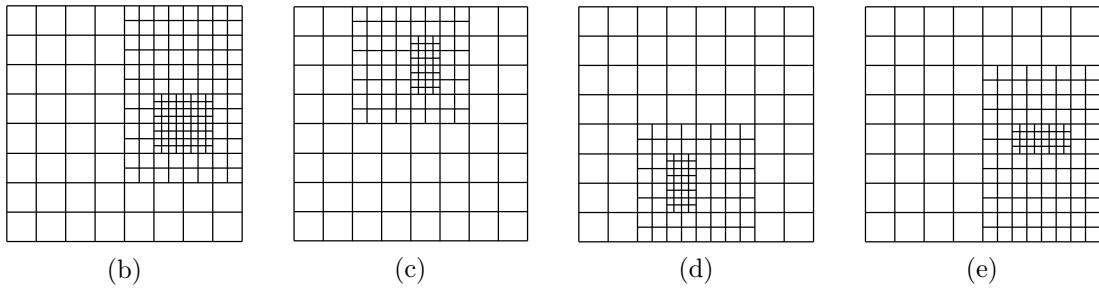
Table 4.11: Adaptive refinement including effectivity indices with goal quantity (4.141), $\varepsilon = 1$, $\delta_0 = 0$, and $\omega = 1.5$ for Example 4.2, using a higher-order finite elements strategy for the temporal weights. $e^{1,1,2,2}$ corresponds to the primal and dual solution approximation $u_{\tau h}^{1,1}$ in cG(1)-dG(1) and $z_{\tau h}^{2,2}$ in cG(2)-dG(2), respectively.

ℓ	N	N_K^{\max}	$N_{\text{DoF}}^{\text{tot}}$	$J(e^{2,2,3,3})$	$\tilde{\eta}_h$	$\tilde{\eta}_\tau^{\text{dG,hoFE}}$	\mathcal{I}_{eff}
1	10	4	750	2.8682e-02	2.1095e-02	3.2341e-03	0.84
2	10	16	2430	1.4199e-02	3.9136e-03	7.3705e-03	0.79
3	14	16	3402	7.0094e-03	6.0323e-03	3.6965e-04	0.91
4	14	28	5922	3.0814e-03	1.8958e-03	9.3145e-04	0.91
5	14	88	12432	1.6269e-03	8.3722e-04	1.7411e-03	1.58
6	20	88	18150	1.1644e-03	1.0968e-03	5.2159e-04	1.39
7	28	184	39870	4.9436e-04	5.0246e-04	6.1798e-05	1.14
8	28	256	62190	1.9469e-04	1.1485e-04	1.5513e-04	1.38

Table 4.12: Adaptive refinement including effectivity indices with goal quantity (4.141), $\varepsilon = 1$, $\delta_0 = 0$, and $\omega = 1.5$ for Example 4.2, using a higher-order finite elements strategy for the temporal weights. $e^{2,2,3,3}$ corresponds to the primal and dual solution approximation $u_{\tau h}^{2,2}$ in cG(2)-dG(2) and $z_{\tau h}^{3,3}$ in cG(3)-dG(3), respectively.



(a)



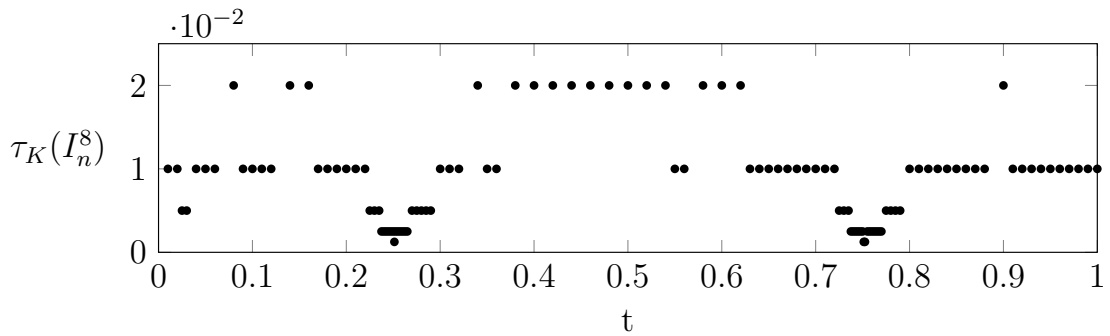
(b)

(c)

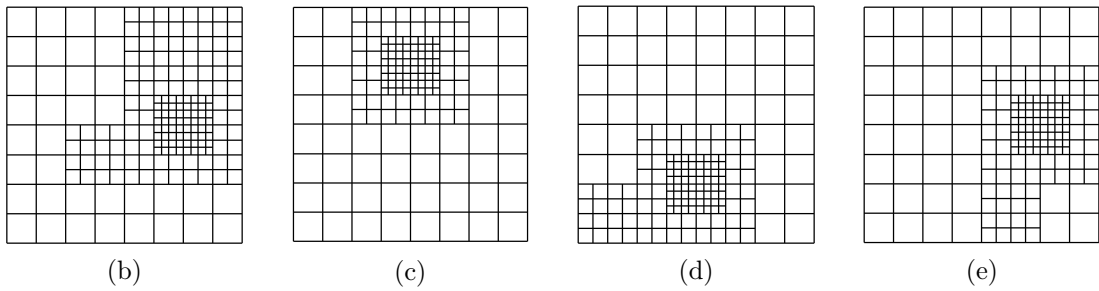
(d)

(e)

Figure 4.17: Distribution of the adaptively determined temporal step size τ_K belonging to the space-time slabs $Q_n^8 = \mathcal{T}_{h,n}^8 \times \mathcal{T}_{\tau,n}^8$ (a) and related adaptive spatial meshes at time points $t_n = 0$ (b), $t_n = 0.25$ (c), $t_n = 0.75$ (d) and $t_n = 1$ (e) corresponding to the last loop in Table 4.4.



(a)



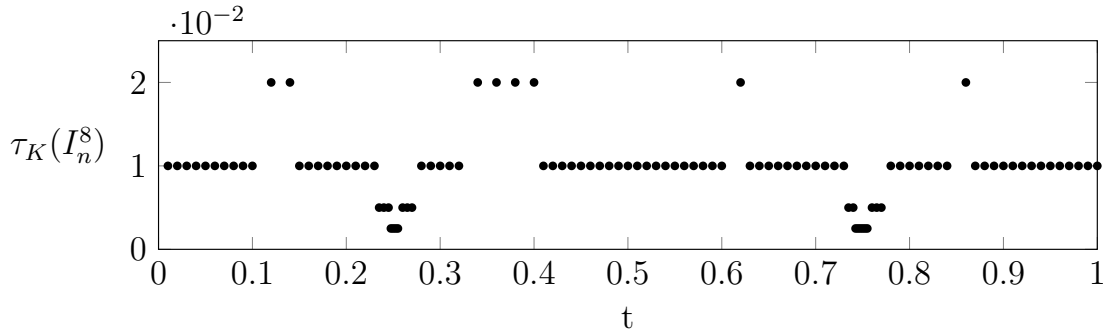
(b)

(c)

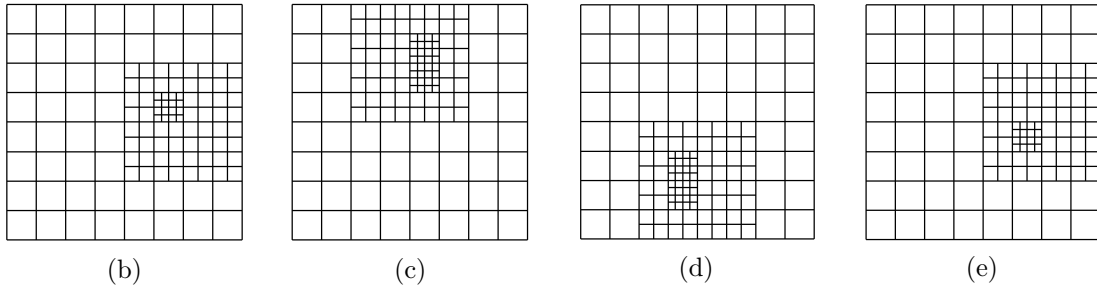
(d)

(e)

Figure 4.18: Distribution of the adaptively determined temporal step size τ_K belonging to the space-time slabs $Q_n^8 = \mathcal{T}_{h,n}^8 \times \mathcal{T}_{\tau,n}^8$ (a) and related adaptive spatial meshes at time points $t_n = 0$ (b), $t_n = 0.25$ (c), $t_n = 0.75$ (d) and $t_n = 1$ (e) corresponding to the last loop in Table 4.7.



(a)



(b)

(c)

(d)

(e)

Figure 4.19: Distribution of the adaptively determined temporal step size τ_K belonging to the space-time slabs $Q_n^8 = \mathcal{T}_{h,n}^8 \times \mathcal{T}_{\tau,n}^8$ (a) and related adaptive spatial meshes at time points $t_n = 0$ (b), $t_n = 0.25$ (c), $t_n = 0.75$ (d) and $t_n = 1$ (e) corresponding to the last loop in Table 4.10.

As mentioned before, we have modified Example 4.2 with the purpose to obtain more dynamic behavior in time in order to demonstrate the performance properties of the space-time algorithm with regard to adaptive mesh refinement. Since a goal functional (4.141) is used that acts global in space as well as in time, one would expect an almost equal distribution of the temporal step size on I for a solution that acts smooth in time. Unlike the smoothness in time, the prescribed solution (4.142) in Example 4.2 is chosen to change its orientation at $t = 0.25$ as well as $t = 0.75$, so that the expected temporal step size should be smaller close to these time points. This behavior is confirmed by the Figs. 4.17–4.19a, where the distribution of the adaptively determined time cell lengths τ_K of $\mathcal{T}_{\tau,n}^\ell$ related to the slab Q_n^ℓ over the whole time interval I is visualized for the last DWR loop, exemplary for a cG(1)-dG(0)/cG(2)-dG(0) discretization using a higher-order extrapolation approximation for the temporal weights based either on Gauss (Fig. 4.17a) or on Gauss-Lobatto (Fig. 4.18a) quadrature points and for a cG(1)-dG(0)/cG(2)-dG(1) discretization using a higher-order finite elements approximation for the temporal weights (Fig. 4.19a), respectively. In all three cases the temporal mesh is almost equally decomposed, but significantly more refined close to the time points where the hill changes its orientation ($t = 0.25$ and $t = 0.75$).

Moreover, Figs. 4.17–4.19 include the visualization of several adaptive spatial meshes at selected time points. Considering the underlying spatial meshes, we note that the total number of the spatial cells is nearly equal to each other comparing positions 4.17–4.19b with 4.17–4.19e and 4.17–4.19c with 4.17–4.19d, respectively, but the distribution of the spatial cells differs depending on the related position of the hill. Thus, for the chosen goal functional (4.141) the spatial mesh runs as expected with the rotation of the hill in a synchronous way. In addition, we note that the mesh refinement is slightly weaker at the final time point compared to the initial position. This is due to the error propagation of the underlying problem which is captured by the dual weights in the error estimate. This effect is in good agreement to the results obtained for the heat equation in [20, p. 122].

Conclusion 4.2 (Accuracy and Efficiency - hoEx-G vs. hoEx-GL vs. hoFE)

As an interim conclusion, we summarize the following.

- *All test cases end up with a very economical mesh in space and time with regard to a **global** in time acting goal functional (cf. Figs. 4.17–4.19) along with a high quality in the computation of the user-specified goal quantity; cf. the last column of Tables 4.4–4.12. This behavior is all the more remarkable since the initial space-time slabs consist of rather coarse meshes in space as well as in time.*
- *With regard to **accuracy**, all $cG(p)$ - $dG(r)$ / $cG(q)$ - $dG(s)$ discretizations show a good quantitative estimation of the discretization error, independent of the underlying approximation technique used for the temporal weights; cf. the last column of Tables 4.4–4.12.*
- *With regard to **efficiency**, all $cG(p)$ - $dG(r)$ / $cG(q)$ - $dG(s)$ discretizations show a very good equilibration of the spatial and temporal error indicators $\tilde{\eta}_h$ and $\tilde{\eta}_\tau$, independent of the underlying approximation technique used for the temporal weights; cf. the columns six and seven of Tables 4.4–4.12.*

4.5.3 Moving Hump with Circular Layer - Stability and Robustness for a Convection-Dominated Benchmark

The last example is dedicated to convection-dominated cases for a sequence of decreasing diffusion coefficients using a local goal functional. It is an extension of Example 3.1 with regard to a time-dependent solution and goes back to [120, 3].

Example 4.3 (Moving Hump with Circular Layer)

We study Problem (4.1) for a diffusive parameter dependent exact solution, given by

$$\begin{aligned} u(\mathbf{x}, t) &:= u_1 \cdot u_2, \quad \mathbf{x} = (x_1, x_2)^\top \in \mathbb{R}^2 \text{ and } t \in \mathbb{R}, \\ u_1(\mathbf{x}, t) &:= 16 \sin(\pi t) x_1 (1 - x_1) x_2 (1 - x_2), \\ u_2(\mathbf{x}) &:= \left(\frac{1}{2} + \frac{\arctan \left[2\varepsilon^{-\frac{1}{2}} (r_0^2 - (x_1 - x_1^0)^2 - (x_2 - x_2^0)^2) \right]}{\pi} \right), \end{aligned} \quad (4.143)$$

The (analytical) solution is characterized by a hump changing its height in the course of the time. The problem is defined on $\Omega \times I := (0, 1)^2 \times (0, 0.5]$ with the scalars $r_0 = 0.25$ and $x_1^0 = x_2^0 = 0.5$, such that the maximum height of the hump is reached at the final time point. The right-hand side forcing term f , the homogeneous Dirichlet boundary condition and the initial condition are calculated from the given analytical solution (4.143) and Eqs. (4.1). We choose the flow field $\mathbf{b} = (2, 3)^\top$ and the reaction coefficient $\alpha = 1$. Since this example deals with a sequence of decreasing diffusion coefficients involving high Péclet numbers as part of investigating convection-dominated problems, the finite element approximations need to be stabilized resulting in a no longer non-zero stabilization parameter $\delta_K \neq 0$ within the proposed SUPG approach as it was done in the previous two examples. The goal quantity is chosen to control the L^2 -error $e_N^-, e_N^- = u(\mathbf{x}, T) - u_{\tau h}(T^-)$, at the final time point $T = 0.5$, given by

$$J_T(u) = \frac{(u(\mathbf{x}, T), e_N^-)}{\|e_N^-\|}. \quad (4.144)$$

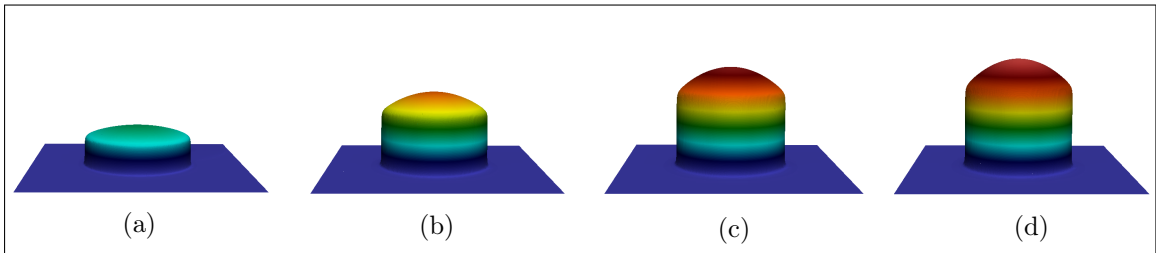


Figure 4.20: Exemplary solution profiles for $\varepsilon = 10^{-6}$ at time points $t_n = 0.125$ (a), $t_n = 0.25$ (b), $t_n = 0.375$ (c) and $t_n = 0.5$ (d) for Example 4.3.

Similar to Example 3.1 for the steady-state case, we start with a comparison of the approximation approaches for the temporal weights with regard to accuracy and efficiency reasons. More precisely, we compare the approximation by higher-order extrapolation using Gauss or Gauss-Lobatto quadrature points and the approximation by higher-order finite elements, respectively, as introduced in Sec. 4.3.2.

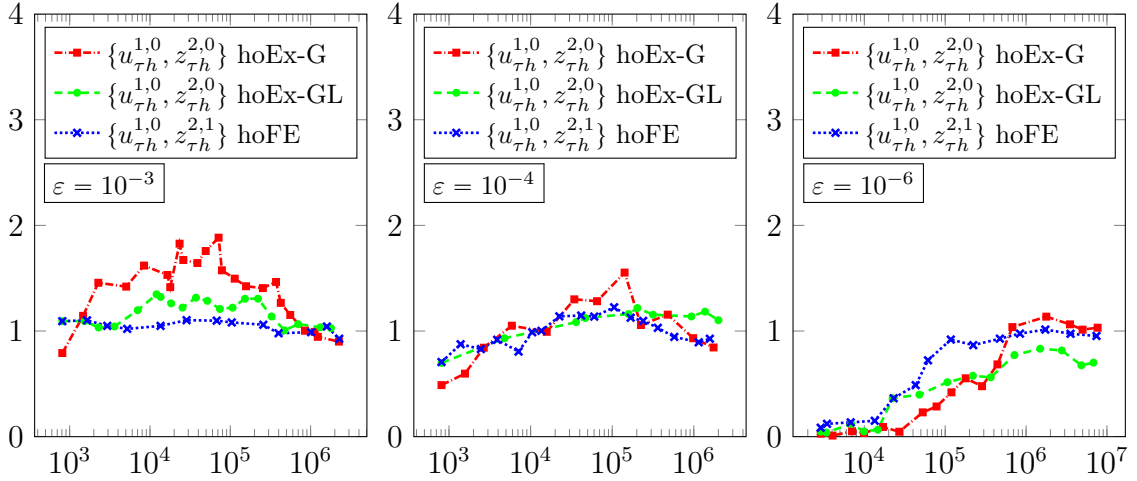


Figure 4.21: Comparison of effectivity indices (over total space-time degrees of freedom) for a sequence of decreasing diffusion coefficients ε with $\delta_0 = 1$ and $\omega = 2$ for Example 4.3. The primal solution approximation is $u_{\tau_h}^{1,0}$ in cG(1)-dG(0) and the dual solution approximations are $z_{\tau_h}^{2,0}$ in cG(2)-dG(0), $z_{\tau_h}^{2,1}$ in cG(2)-dG(1).

In Fig. 4.21, we visualize the development of the respective effectivity indices for a sequence of decreasing diffusion coefficients involving high Péclet numbers. Overall, the development as well as the actual values of the indices are similar in all considered cases of ε , but there are slight differences with regard to stability and achievement of the desired value of one. In the case of $\varepsilon = 10^{-3}$, we observe a slight overestimation of the exact error by using a higher-order extrapolation approach for the temporal weights. This observation holds true for both using Gauss (red line) or Gauss-Lobatto (green line) quadrature points. In contrast, the higher-order finite elements approach (blue line) seem to be more stable as taking values very close to one through the whole range of total space-time degrees of freedom or rather for all DWR loops within one adaptive refinement run. A similar behavior can be observed for the case of $\varepsilon = 10^{-4}$. The more challenging case of $\varepsilon = 10^{-6}$ shows a slightly different behavior compared to the other two choices of the diffusion coefficient. Here, all approximation approaches show up with small values for the respective effectivity index at the beginning. It takes some refinement processes until this value increases, cf. also Table 4.13. Again, the higher-order finite elements approach shows slightly better results with regard to the faster achievement of the desired value of one and stability as far as being close to this value. The approximation by higher-order extrapolation, however, takes more refinement levels for reaching the desired value (extrapolation based on Gauss quadrature points, red line) or rather getting at least closer to it (extrapolation based on Gauss-Lobatto quadrature points, green line). This is in good agreement to the results

obtained within the steady-state case, cf. Fig. 3.4-3.5 of Example 3.1 in Chapter 3 and the explanations therein. Nevertheless, the differences between an approximation by higher-order extrapolation or finite elements, respectively, is not that significant as it was observed for the steady-state case.

Higher-Order Extrapolation (Gauss)							
ℓ	N	N_K^{\max}	$N_{\text{DoF}}^{\text{tot}}$	$J_T(e^{1,0,2,0})$	$\tilde{\eta}_h$	$\tilde{\eta}_\tau^{\text{dG,hoEx-G}}$	\mathcal{I}_{eff}
1	10	256	2890	1.5766e-01	8.2411e-03	-3.7392e-03	0.029
7	10	1744	8812	6.5846e-02	-7.8371e-03	-2.9862e-04	0.124
12	26	2200	34330	7.1833e-02	8.0055e-05	-9.7079e-03	0.134
15	37	2200	48933	7.8090e-02	1.6105e-03	-6.1815e-03	0.059
18	55	4060	113921	3.2128e-02	8.9406e-03	-1.5898e-03	0.229
23	55	36004	364439	8.6427e-03	4.0911e-03	1.1980e-03	0.612
26	72	104800	1231580	3.9484e-03	3.0524e-03	7.1158e-04	0.953
30	108	317572	4999150	1.6206e-03	9.8061e-04	6.6106e-04	1.013
31	124	488884	7672162	1.2173e-03	6.1208e-04	6.4369e-04	1.032
Higher-Order Extrapolation (Gauss-Lobatto)							
ℓ	N	N_K^{\max}	$N_{\text{DoF}}^{\text{tot}}$	$J_T(e^{1,0,2,0})$	$\tilde{\eta}_h$	$\tilde{\eta}_\tau^{\text{dG,hoEx-GL}}$	\mathcal{I}_{eff}
1	10	256	2890	1.5766e-01	1.2740e-02	-5.2019e-03	0.048
4	12	616	5678	1.0917e-01	-1.3654e-02	-1.2161e-04	0.126
11	12	4504	22360	2.2853e-02	5.0269e-03	3.2887e-03	0.364
14	19	9340	75297	1.0323e-02	2.6713e-03	2.6807e-03	0.518
17	31	14200	220041	6.2166e-03	1.0727e-03	2.5099e-03	0.576
20	52	20872	497722	2.8948e-03	8.7129e-04	1.0268e-03	0.656
25	126	47260	2766248	9.8970e-04	2.5921e-04	5.4852e-04	0.816
27	181	59956	4828999	7.3743e-04	1.7729e-04	3.2093e-04	0.676
28	217	68128	6812307	6.1159e-04	1.5662e-04	2.7202e-04	0.701
Higher-Order Finite Elements							
ℓ	N	N_K^{\max}	$N_{\text{DoF}}^{\text{tot}}$	$J_T(e^{1,0,2,1})$	$\tilde{\eta}_h$	$\tilde{\eta}_\tau^{\text{dG,hoFE}}$	\mathcal{I}_{eff}
1	10	256	2890	1.5766e-01	1.2294e-02	1.0976e-03	0.085
7	10	1288	8132	6.4279e-02	4.3335e-03	-4.4758e-03	0.002
12	16	5788	43208	1.8951e-02	7.1073e-03	2.1344e-03	0.488
15	16	8488	74748	8.9500e-03	3.6347e-03	2.9973e-03	0.741
20	37	20428	474275	3.3894e-03	1.7497e-03	1.3950e-03	0.928
23	62	30808	1192298	1.8388e-03	9.5589e-04	8.6632e-04	0.991
24	74	40108	1731154	1.4838e-03	7.8528e-04	7.1921e-04	1.014
26	105	54892	3545763	9.8131e-04	4.3559e-04	5.2019e-04	0.974
27	126	61564	5005616	8.0768e-04	3.8737e-04	3.7806e-04	0.948

Table 4.13: Selected DWR-loops within one adaptive refinement run including effectivity indices for goal quantity (4.144), $\varepsilon = 10^{-6}$, $\delta_0 = 1$ and $\omega = 2$ for Example 4.3, using different approximation approaches for the temporal weights. $e^{1,0,2,0}$ or $e^{1,0,2,1}$ corresponds to the primal and dual solution approximation $u_{\tau h}^{1,0}$ in cG(1)-dG(0) and $z_{\tau h}^{2,0}$ in cG(2)-dG(0) or $z_{\tau h}^{2,1}$ in cG(2)-dG(1), respectively.

In Table 4.13, we present some selected DWR loops (ℓ , first column) within one adaptive refinement run for the different approximation approaches of the temporal weights, exemplary for the strongly convection-dominated case of $\varepsilon = 10^{-6}$. This table corresponds to the last plot of Fig. 4.21 and Fig. 4.22, respectively, and demonstrates the related development of the total discretization error $J_T(e) = \|e_N^-\|_\Omega$, the approximated spatial and temporal error indicators $\tilde{\eta}_h$ and $\tilde{\eta}_\tau$ as well as the effectivity index \mathcal{I}_{eff} during an adaptive run. Here, $e^{p,r,q,s}$ corresponds to a primal solution approximation $u_{\tau h}^{p,r}$ in cG(p)-dG(r) and dual solution approximation $z_{\tau h}^{q,s}$ in cG(q)-dG(s), N denotes the total cells in time, N_K^{max} the number of cells on the finest spatial mesh within the current loop, and $N_{\text{DoF}}^{\text{tot}}$ the total space-time degrees of freedom. All approaches have in common that the approximated spatial discretization error is clearly larger than its temporal counterpart at the beginning. Therefore, the algorithm orders solely spatial refinement in the first DWR loops (cf. columns one and two of Table 4.13). Similar to Example 4.2, the spatial and temporal error indicators get closer to each other in the course of the adaptive run and a very good equilibration is obtained in the final loops (cf. columns six and seven of Table 4.13). This equilibration is essential with regard to efficiency reasons for a space-time adaptive algorithm, cf. Rem. 4.15. With regard to accuracy, we observe an increase of the effectivity index in the course of the adaptive run. Thereby, the approximation by higher-order finite elements and extrapolation using Gauss quadrature points show an almost perfect approximation quality of the actual discretization error, as visible by effectivity indices very close to one (cf. the last column of Table 4.13). Although the effectivity index within the extrapolation using Gauss-Lobatto quadrature points are slightly worse, this technique still provides a good quantitative estimation of the discretization error in the course of the adaptive run.

In Fig. 4.22, we compare the L^2 -error reduction at the final time point in view of global and adaptive refinement for the same sequence of decreasing diffusion coefficients as in Fig. 4.21. As in the steady-state case, cf. Fig.3.8 of Example 3.1, the DWR-based adaptive refinement is clearly superior to the global refinement in terms of accuracy over total space-time degrees of freedom, independent of the underlying approximation technique. The difference between global and adaptive refinement increases as the diffusion coefficient decreases. Again, the differences between the respective approaches are of only marginal significance. Solely, in the case of $\varepsilon = 10^{-6}$, the approximation by higher-order extrapolation based on Gauss quadrature points shows a slower reduction compared to the other two approaches, but compared to global refinement it is still strongly superior.

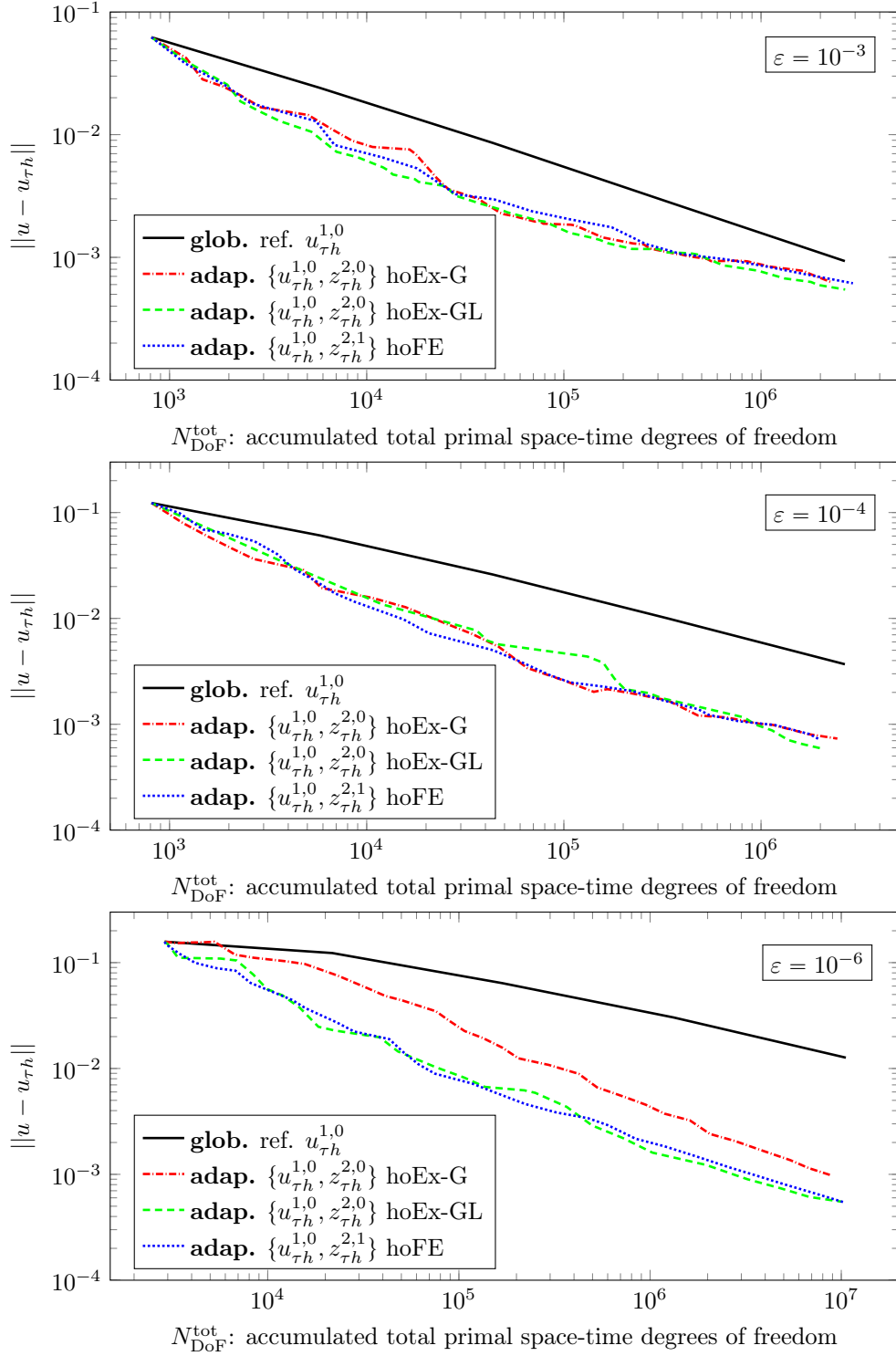
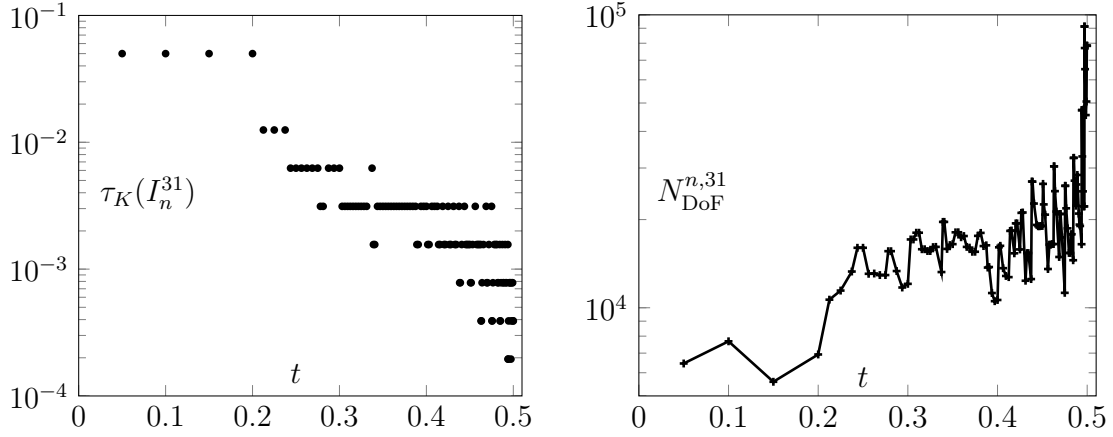


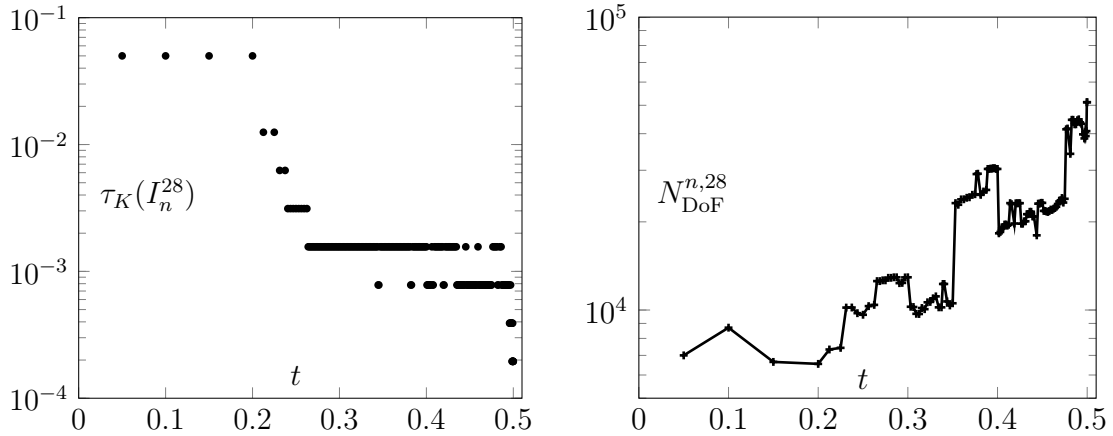
Figure 4.22: L^2 -error reduction at $T = 0.5$ in Example 4.3 for a sequence of decreasing diffusion coefficients ε with $\delta_0 = 1$ and $\omega = 2$. The primal solution approximation is $u_{\tau h}^{1,0}$ in cG(1)-dG(0) and the dual solution approximations are $z_{\tau h}^{2,0}$ in cG(2)-dG(0), $z_{\tau h}^{2,1}$ in cG(2)-dG(1).

In contrast to Example 4.2, the goal functional (4.144) acts local in time aiming to control the L^2 -error at the final time point $T = 0.5$ only. Therefore, one would expect a decrease of the temporal step size in the course of time. This behavior is confirmed by the left part of Fig. 4.23, where exemplary for the case $\varepsilon = 10^{-6}$ the distribution of the adaptively determined time cell lengths τ_K of $\mathcal{T}_{\tau,n}^\ell$ related to the slab Q_n^ℓ over the whole time interval I is visualized for the respective last DWR loop, exemplary for a cG(1)-dG(0)/cG(2)-dG(0) discretization using a higher-order extrapolation approximation for the temporal weights based either on Gauss (Fig. 4.23a(left)) or on Gauss-Lobatto (Fig. 4.23b(left)) quadrature points and for a cG(1)-dG(0)/cG(2)-dG(1) discretization using a higher-order finite elements approximation for the temporal weights (Fig. 4.23c(left)), respectively. For all approximation approaches we observe a relatively large temporal size of the first slabs whereas this size becomes much smaller in the course of time reaching the final time point $T = 0.5$. Note that the first steps are still equal to the initial distribution of the temporal mesh. Moreover, on the right part of Fig. 4.23, the related primal spatial degrees of freedom of the single slabs over the whole time interval I are depicted for the last DWR loop, denoted by $N_{\text{DoF}}^{n,\ell}$, $\ell \in \{27, 28, 31\}$. Consistently, the degrees of freedom increase in the course of time reaching the final time point.

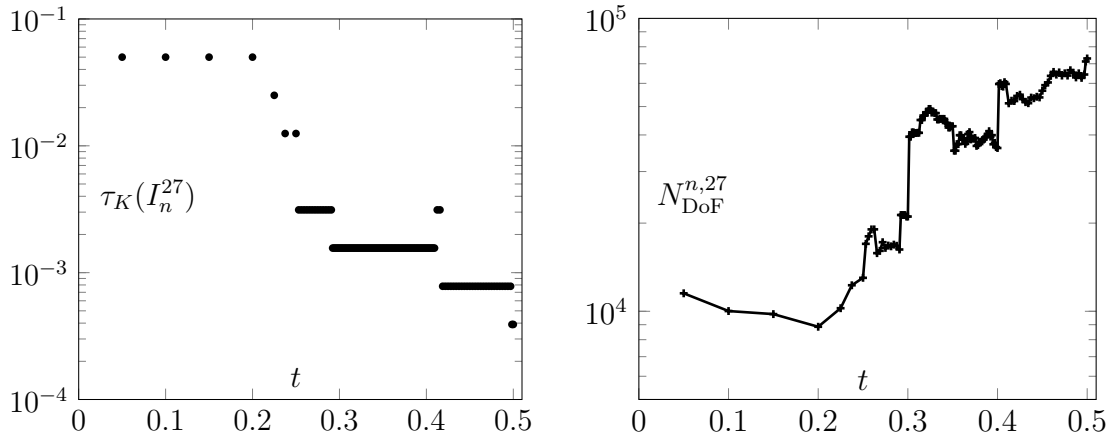
Finally, in Figs. 4.24-4.26, we present the primal solution profiles and related spatial meshes at different time points corresponding to the respective last DWR loop within Table 4.13. Considering the solution profiles at $t = 0.25$ for all approximation approaches, we observe that the respective solution is still strongly perturbed in the backward part of the hump's layer (cf. the respective value ranges with the exact minimum and maximum value of the solution u at $t = 0.25$, given by 0 and 0.705, respectively). The mesh is coarse in that part of the domain and the refinement takes mainly place on the south-western part of the circular layer due to the prescribed direction of the flow field \mathbf{b} (cf. Figs. 4.24-4.26a). For $T = 0.5$ an almost perfect solution profile is obtained for all approximation cases and the spatial mesh cells are located close to the whole circular layer and behind the hump in the north-eastern part of the domain where the direction of the flow field has an impact towards the end of time (cf. Figs. 4.24-4.26b). The mesh is considerably more refined at the final time point involving a higher number of degrees of freedom, cf. the respective right part of Fig. 4.23. Furthermore, we note that the spurious oscillations are reduced significantly and, compared to the case at $t = 0.25$, this time the respective value ranges are much closer to the exact minimum and maximum value of the solution u at $t = 0.5$, given by 0 and 0.997, respectively. Such a behavior is admissible for a



(a) Higher-order **extrapolation** using Gauss quadrature points.



(b) Higher-order **extrapolation** using Gauss-Lobatto quadrature points.



(c) Higher-order **finite elements**.

Figure 4.23: Distribution of the adaptively determined temporal step size τ_K (left) and primal spatial degrees of freedom (right) related to the space-time slabs of the different approximation approaches for the temporal weights corresponding to the respective last DWR loop in Table 4.13.

local in time acting goal functional (4.144) and nicely illustrates the potential of the DWR approach as obtaining highly economical meshes in space and time located at the time point to be controlled, whereas the solution is allowed to be of low resolution and the related meshes are notably less refined away from this time point.

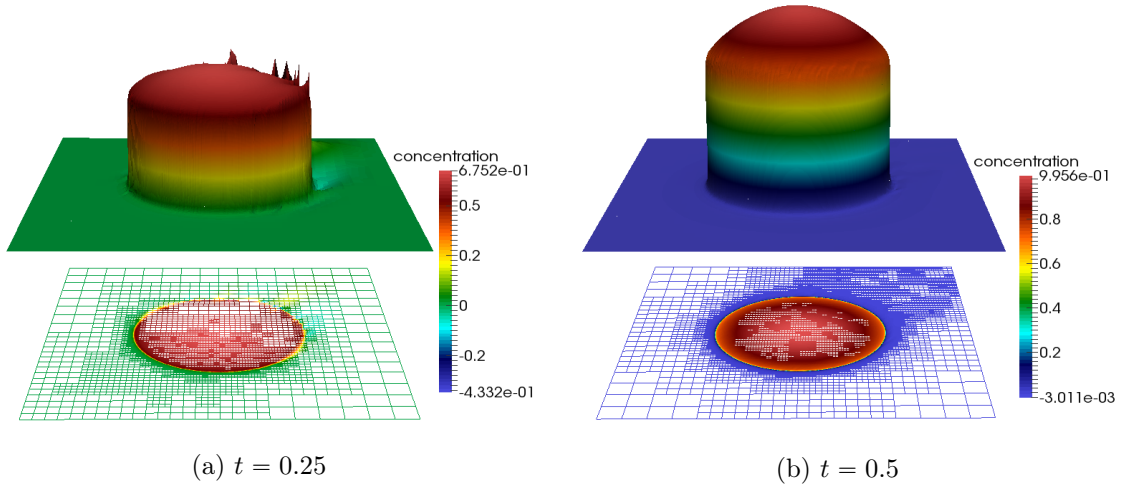


Figure 4.24: Solution profiles, value range and related adaptively refined spatial meshes at different time points within the last DWR loop $\ell = 31$ for the higher-order extrapolation approach using Gauss quadrature points with goal functional (4.144) and $\varepsilon = 10^{-6}$ for Example 4.3, using a cG(1)-dG(0)/cG(2)-dG(0) discretization.

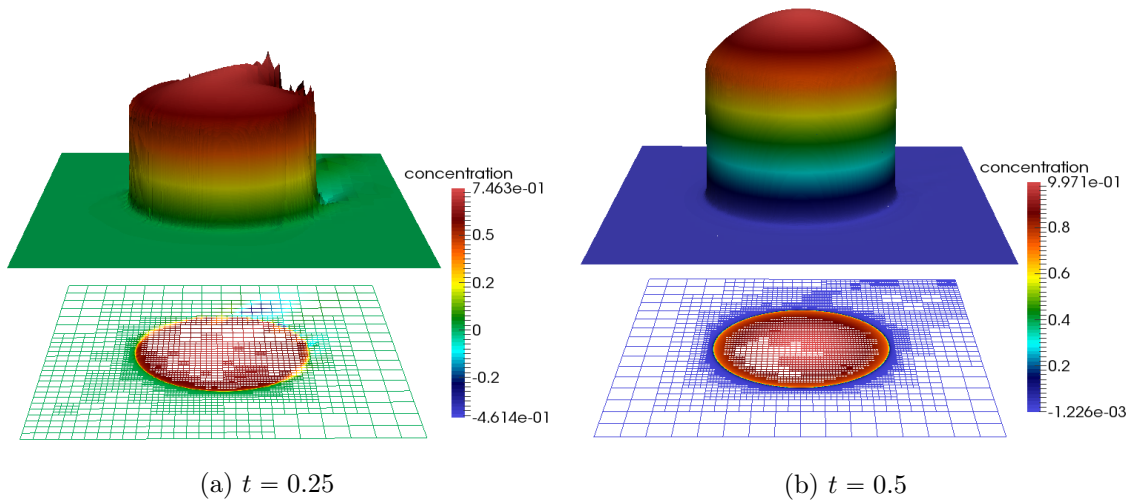


Figure 4.25: Solution profiles, value range and related adaptively refined spatial meshes at different time points within the last DWR loop $\ell = 28$ for the higher-order extrapolation approach using Gauss-Lobatto quadrature points with goal functional (4.144) and $\varepsilon = 10^{-6}$ for Example 4.3, using a cG(1)-dG(0)/cG(2)-dG(0) discretization.

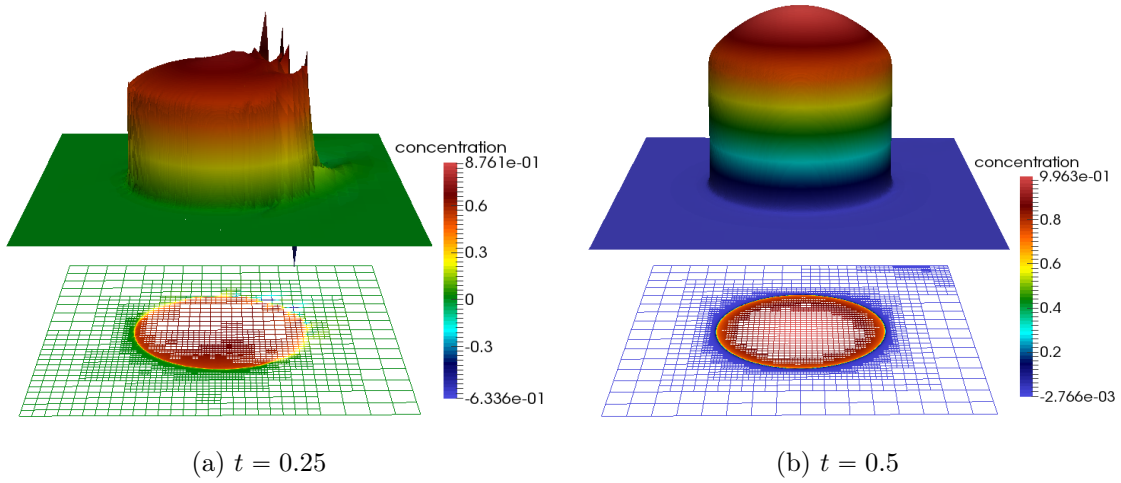


Figure 4.26: Solution profiles, value range and related adaptively refined spatial meshes at different time points within the last DWR loop $\ell = 27$ for the higher-order finite elements approach with goal functional (4.144) and $\varepsilon = 10^{-6}$ for Example 4.3, using a cG(1)-dG(0)/cG(2)-dG(1) discretization.

Conclusion 4.3 (Convection-Dominated - hoEx-G vs. hoEx-GL vs. hoFE)

As an interim conclusion, we summarize the following.

- All test cases end up with a very economical mesh in space and time with regard to a **local** in time acting goal functional, (cf. Figs. 4.23 as well as 4.24–4.26) along with a high quality in the computation of the user-specified goal quantity; cf. the last column of Table 4.13.
- Comparing the approximation techniques used for the temporal weights, the **higher-order finite elements** approach shows slightly better results with regard to **accuracy** of the underlying error estimator; cf. Fig. 4.21 as well as Table 4.13 (last column). However, the difference to the **higher-order extrapolation** approach is not that significant as in the steady-state case; cf. Conclusion 3.1 in Sec. 3.4.1.
- With regard to **efficiency**, all approximation techniques used for the temporal weights show a very good equilibration of the spatial and temporal error indicators $\tilde{\eta}_h$ and $\tilde{\eta}_\tau$, even though the approximated spatial discretization error is significantly larger than its temporal counterpart at the beginning; cf. the course of columns six and seven of Table 4.13.
- With regard to the **reduction** of the L^2 -error, the dominance of goal-oriented adaptive mesh refinement towards global refinement becomes clearer the higher

the underlying Péclet number is chosen; cf. Fig. 4.22. This holds true for all approximation techniques used for the temporal weights, although higher-order extrapolation based on Gauss quadrature points shows a slower reduction compared to the other both approaches.

4.5.4 Final Summary

With reference to the specific results outlined in Conclusions 4.1–4.3, we summarize the following. All approximation techniques yield efficient and accurate results for solving time-dependent convection-dominated problems. With regard to efficiency and reliability reasons, the independence of one part of the splitted error estimator on the refinement of the other discretization was demonstrated, cf. Table 4.2 and Table 4.3. Furthermore, very good equilibrations of the spatial and temporal error indicators were observed in the course of the refinement process, cf. Tables 4.4-4.12, and highly economical meshes in space and time were obtained with regard to the underlying goal quantity, cf. Figs. 4.17-4.19 as well as Figs. 4.23-4.26. With regard to convection-dominated cases involving stabilization, robustness of the respective approaches with respect to vanishing diffusion parameters was shown and quantitative good results for the estimation of the discretization errors were obtained, cf. Fig. 4.21 and Table 4.13. Even though the higher-order finite elements approach shows slightly better results with regard to accuracy and stability (cf. Fig. 4.21), the differences to the higher-order extrapolation approaches in all was not that significant as for the steady-state case (cf. Ch. 3), even less if we take into account the higher computational costs for solving the dual problem.

Chapter 5

Multirate Goal-Oriented Error Control for Coupled Flow and Transport Problems

In this chapter, we present the application of goal-oriented error control based on the Dual Weighted Residual method to coupled flow and transport problems using a multirate in time approach. The challenges of those problems come through different natural time scales of the underlying subproblems and their impacts regarding suitable time discretizations, cf., e.g., [111, 89, 94, 10]. An efficient numerical simulation with regard to the temporal discretization does not become feasible without using techniques adapted to these characteristic time scales that resolve the solution components on their respective time length by an adaptation of the time steps sizes. Such methods are referred to as multirate in time (for short, multirate) schemes. For a short review of multirate methods including a list of references we refer to the main introduction.

With regard to the coupled model problem, we assume a high time-dynamic, i.e. fast moving process modeled by a convection-diffusion-reaction transport equation such that the underlying temporal mesh is discretized using smaller time step sizes compared to a slowly moving process modeled by a viscous time-dependent Stokes flow problem. Our motivation comes through the definition of so-called characteristic times for the two subproblems that serve as quantities to measure the underlying dynamic in time that have their origin in the field of natural and engineering sciences, cf., e.g., [93, 146].

Imagine a slowly creeping flow in which a species is transported, for instance, a toxic, viscous fluid that runs into a strongly flowing river due to an accident within a nearby company. What are the effects of this pollution to the species living in the

river and how does the spreading takes place by the injection to the river and in the following? In practice, such a case can be modeled by a system of n transport equations representing the different species or concentrations coupled with a time-dependent Stokes flow problem characterizing the pollution, possibly given by the following coupled system

$$\begin{aligned}\partial_t u_i - \nabla \cdot (\varepsilon \nabla u_i) + \mathbf{v} \cdot \nabla u_i + r(u_i) &= g_i(\mathbf{u}, t), \quad i = 1, \dots, n, \\ \partial_t \mathbf{v} - \nu \Delta \mathbf{v} + \nabla p &= \mathbf{f}(\mathbf{u}, t), \\ \nabla \cdot \mathbf{v} &= 0.\end{aligned}$$

Such multi-physics systems of coupled flow and transport serve as prototype models for applications in several branches of natural and engineering sciences, for instance, contaminant transport and degradation in the subsurface, reservoir simulation, fluid-structure interaction, and thermal and mass transport in deformable porous media or thermal expansion in solid mechanics; cf., e.g., [133, 148, 38, 145, 152, 184, 185, 28, 41, 9].

The case of a slowly varying flow and a rapidly changing transport is ideally suitable for investigating multirate in time phenomena with regard to different time scales and the impact of adaptive mesh refinement used thereby. With regard to coupled problems, adaptive strategies become even more crucial since besides the need of error indicators that tell us in which part of the domain the solution needs to be improved one wants to know which of the subproblems contributes most to the overall error, and thus needs to be solved more accurately, cf., e.g., [133, 45, 111, 186, 185, 159]. Moreover, by an increasing complexity with regard to an efficient handling of the underlying discretization parameters in space and time for both subproblems, an adaptive algorithm that handles these parameters automatically by means of an a posteriori error estimator seems to be predestined. Beyond that, the here presented approach of the coupled system is fairly general such that it can easily be adopted to other types of problems as exemplarily described above.

This chapter is organized as follows. We start by introducing the coupled system together with some global assumptions and general concepts including the underlying variational formulation. Then, we explain our multirate in time approach for the two subproblems and present the (stabilized) space-time discretization schemes. Afterwards, we derive a posteriori error estimators for both the transport and Stokes flow problem including the introduction of the dual problems. Similar to the preceding chapters, a section regarding practical aspects follows with regard to the underlying

concepts of goal-oriented adaptivity as well as some software skills. Thereby, we introduce time marching schemes for the primal and dual problems, derive localized forms of the error estimators and present the goal-oriented space-time adaptive algorithm in different variations. The chapter is closed by some numerical experiments, in which we validate our higher-order space-time implementations and investigate the performance properties of the algorithm with regard to the new multirate in time approach. Some parts of this chapter have been published by the author et al. in [52] and [29], respectively.

Henceforth, for the sake of simplicity, we reduce the system above to the case $n = 1$, modeling, for instance, heat transport in a creeping viscous fluid. Then, the convection-diffusion-reaction transport problem coupled with time-dependent Stokes flow is given by the following model problem.

Problem 5.1 (Coupled Flow and Transport Problem)

The time dependent convection-diffusion-reaction transport problem in dimensionless form is given by

$$\begin{aligned}
\partial_t u - \nabla \cdot (\varepsilon \nabla u) + \mathbf{v} \cdot \nabla u + \alpha u &= g \quad \text{in } Q = \Omega \times I, \\
u &= u_D \quad \text{on } \Sigma_D = \Gamma_D \times I, \\
\varepsilon \nabla u \cdot \mathbf{n} &= u_N \quad \text{on } \Sigma_N = \Gamma_N \times I, \\
u(0) &= u_0 \quad \text{on } \Sigma_0 = \Omega \times \{0\},
\end{aligned} \tag{5.1}$$

for a boundary partition $\partial\Omega = \Gamma_D \cup \Gamma_N$, $\Gamma_D \neq \emptyset$ with outer unit normal vector \mathbf{n} . The convection or velocity field \mathbf{v} in the transport problem (5.1) is determined by the dimensionless Stokes flow system

$$\begin{aligned}
\partial_t \mathbf{v} - \nabla \cdot \mathbf{s}(\mathbf{v}) + \nabla p &= \mathbf{f} \quad \text{in } Q = \Omega \times I, \\
\nabla \cdot \mathbf{v} &= 0 \quad \text{in } Q = \Omega \times I, \\
\mathbf{v} &= \mathbf{v}_D \quad \text{on } \Sigma_{\text{inflow}} = \Gamma_{\text{inflow}} \times I, \\
\mathbf{v} &= \mathbf{0} \quad \text{on } \Sigma_{\text{wall}} = \Gamma_{\text{wall}} \times I, \\
\mathbf{s}(\mathbf{v}) \mathbf{n} - p \mathbf{n} &= \mathbf{0} \quad \text{on } \Sigma_{\text{outflow}} = \Gamma_{\text{outflow}} \times I, \\
\mathbf{v} &= \mathbf{v}_0 \quad \text{on } \Sigma_0 = \Omega \times \{0\},
\end{aligned} \tag{5.2}$$

for a boundary partition $\partial\Omega = \Gamma_{\text{inflow}} \cup \Gamma_{\text{wall}} \cup \Gamma_{\text{outflow}}$ which is (in general) independent from the boundary partition of the transport problem. The appropriate choice for the boundary partition and setting of the inflow profiles is standard and can be found in the literature, e.g., [79, XIV, Ch. 72], [112, Ch. 4.1].

In Eqs. (5.1) and (5.2), we denote by $Q = \Omega \times I$ the space-time domain, where $\Omega \subset \mathbb{R}^d$, with $d = 2$ or $d = 3$, is a polygonal or polyhedral bounded domain with Lipschitz

boundary $\partial\Omega$ and $I = (0, T), 0 < T < \infty$, is a finite time interval. We assume that $0 < \varepsilon \leq 1$ is a constant diffusion coefficient, $\alpha \in L^\infty(I; L^\infty(\Omega))$ is a non-negative ($\alpha > 0$) reaction coefficient, $u_0 \in L^2(\Omega)$ is a given initial condition, $g \in L^2(I; H^{-1}(\Omega))$ is a given source of the unknown scalar quantity u , $u_D \in L^2(I; H^{\frac{1}{2}}(\Gamma_D))$ is a given function specifying the Dirichlet boundary condition, and $u_N \in L^2(I; H^{-\frac{1}{2}}(\Gamma_N))$ is a given function specifying the Neumann boundary condition.

Within the flow problem the second-order tensor of symmetrized gradients $\mathbf{s}(\mathbf{v})$ is the viscous stress tensor defined as

$$\mathbf{s}(\mathbf{v}) := 2\nu \boldsymbol{\epsilon}(\mathbf{v}), \quad \boldsymbol{\epsilon}(\mathbf{v}) := \frac{1}{2}(\nabla \mathbf{v} + (\nabla \mathbf{v})^\top),$$

where $\boldsymbol{\epsilon}(\mathbf{v})$ is the (linearized) strain rate tensor and the parameter $\nu > 0$ is the dynamic or shear viscosity assumed to be constant and dimensionless here for the sake of simplicity. The gradient of the velocity is a tensor with the components

$$(\nabla \mathbf{v})_{i,j} = \partial_j v_i = \frac{\partial v_i}{\partial x_j}, \quad i, j = 1, 2, 3.$$

Furthermore, $\mathbf{f} \in L^2(I; H^{-1}(\Omega)^d)$ is a given volume force, $p \in L^2(I; L_0^2(\Omega))$ is the pressure variable, and $\mathbf{v}_0 \in H_{\text{div}}(\Omega)$ is a given initial condition, where the function spaces $L_0^2(\Omega)$ and $H_{\text{div}}(\Omega)$ are defined in Sec. 2.1.1 of Ch. 2, respectively.

Remark 5.1 (Different Forms of Viscous Term, cf. [112], Rem. 2.20)

Assume that \mathbf{v} is sufficiently smooth with $\nabla \cdot \mathbf{v} = 0$. Then, straightforward calculations, using the Theorem of Schwarz and the second equation of (5.2), give

$$\nabla \cdot (\nabla \mathbf{v}) = \Delta \mathbf{v}, \quad \nabla \cdot (\nabla \mathbf{v})^\top = \nabla(\nabla \cdot \mathbf{v}) = \begin{pmatrix} \partial_{x_1}(\nabla \cdot \mathbf{v}) \\ \partial_{x_2}(\nabla \cdot \mathbf{v}) \\ \partial_{x_3}(\nabla \cdot \mathbf{v}) \end{pmatrix} = \mathbf{0}.$$

Thus, the viscous term is equivalent to

$$-2\nu \nabla \cdot \boldsymbol{\epsilon}(\mathbf{v}) = -\nu \Delta \mathbf{v}.$$

For simplicity, we will use the latter version of the viscous term here and in the following, although the implemented version for our numerical examples in Sec. 5.4 is based on the first one.

Henceforth, for the sake of simplicity, we assume homogeneous Dirichlet boundary values $u_D = 0$ on $\Gamma_D = \partial\Omega$ in the transport problem and no-slip Dirichlet boundary values $\mathbf{v}|_{\partial\Omega} = \mathbf{0}$ in the flow problem, respectively. In our numerical examples in

Sec. 5.4 we also consider more general boundary conditions as introduced above, whose incorporation is straightforward, cf. also Rem. 4.14 and, e.g., [92].

Finally, with regard to the characteristic times mentioned in the introduction of this chapter, we assume the following.

Assumption 5.1 *The characteristic time $t_{\text{transport}}$ of the transport equation (5.1) can be comprehended as a dimensionless time variable depending on the diffusive, convective as well as reactive part and is here defined by*

$$t_{\text{transport}} := \min \left\{ \frac{L^2}{\varepsilon}; \frac{L}{V}; \frac{1}{\alpha} \right\}, \quad (5.3)$$

where L denotes the characteristic length of the domain Ω , for instance, its diameter, and V denotes a characteristic velocity of the flow field \mathbf{v} , for instance, the mean inflow velocity given by $\frac{1}{T|\Gamma_{\text{inflow}}|} \int_I \int_{\Gamma_{\text{inflow}}} \mathbf{v}_D \cdot (-\mathbf{n}) \, \text{d}t$; cf. [93, 146] for more details.

The characteristic time t_{flow} of the Stokes flow equation (5.2) is then defined by

$$t_{\text{flow}} := \frac{L}{V}, \quad (5.4)$$

with L and V being chosen as in (5.3).

With regard to the characteristic times of the two subproblems defined in Assumption 5.1, we assume that $t_{\text{transport}} \ll t_{\text{flow}}$ such that we are using a finer temporal mesh to resolve the dynamics of a faster process given by the transport equation compared to the slower process of the viscous, creeping flow. This multirate in time approach is described in detail in the following section.

For the corresponding variational formulations of the two subproblems of Problem 5.1, we introduce the following function spaces as given in Def. 2.3 of Sec. 2.1.2.

$$\begin{aligned} \mathcal{X} &:= \left\{ u \in L^2(I; X) \mid \partial_t u \in L^2(I; H^{-1}(\Omega)) \right\}, \text{ with } X := H_0^1(\Omega), \\ \mathcal{Y}_1 &:= \left\{ \mathbf{v} \in L^2(I; X^d) \mid \partial_t \mathbf{v} \in L^2(I; H^{-1}(\Omega)^d) \right\}, \\ \mathcal{Y}_2 &:= \left\{ p \in L^2(I; Y) \right\}, \text{ with } Y := L_0^2(\Omega), \\ \mathcal{Y} &:= \mathcal{Y}_1 \times \mathcal{Y}_2 = \left\{ \mathbf{u} = \{\mathbf{v}, p\} \in \mathcal{Y}_1 \times \mathcal{Y}_2 \right\}. \end{aligned} \quad (5.5)$$

Using these function spaces, the weak formulation of the transport problem (5.1) reads as follows.

Problem 5.2 (Variational Formulation Transport Problem)

For a given $\mathbf{v} \in \mathcal{Y}_1$ of Problem 5.3, find $u \in \mathcal{X}$ such that

$$A(u; \mathbf{v})(\varphi) = G(\varphi) \quad \forall \varphi \in \mathcal{X}, \quad (5.6)$$

where the bilinear form $A(\cdot; \cdot)(\cdot)$ and the linear form $G(\cdot)$ are defined by

$$A(u; \mathbf{v})(\varphi) := \int_I \{(\partial_t u, \varphi) + a(u; \mathbf{v})(\varphi)\} dt + (u(0), \varphi(0)), \quad (5.7)$$

$$G(\varphi) := \int_I (g, \varphi) dt + (u_0, \varphi(0)), \quad (5.8)$$

with the inner bilinear form $a(\cdot; \cdot)(\cdot)$ given by

$$a(u; \mathbf{v})(\varphi) := (\varepsilon \nabla u, \nabla \varphi) + (\mathbf{v} \cdot \nabla u, \varphi) + (\alpha u, \varphi). \quad (5.9)$$

Remark 5.2 (Well-Posedness and Regularity Transport) *With regard to well-posedness and sufficient regularity we assume the following.*

- The model problem (5.6) along with the conditions given in Problem 5.1 is well-posed, cf. Prop. 4.1 as well as Rem. 4.1.
- We note that in Problem 5.2 it is sufficient to require the test functions φ to be in $L^2(I; X)$. Nevertheless, since \mathcal{X} is dense in $L^2(I; X)$ with respect to the norm of $L^2(I; X)$ (cf. Corollary 2.1 in Sec. 2.1.2 of Ch. 2) and with regard to the derivation of the so-called dual problems in the framework of the DWR approach, we deliberately decide to choose the test functions $\varphi \in \mathcal{X}$ here. Furthermore, we note that the expression $u(0)$ makes sense for a function $u \in \mathcal{X}$, cf. Rem. 2.1 in Sec. 2.1.2.

Here, (\cdot, \cdot) denotes the inner product of $L^2(\Omega)$ or duality pairing of $H^{-1}(\Omega)$ with $H_0^1(\Omega)$, respectively. By $\|\cdot\|$ we denote the associated L^2 -norm as defined in Sec. 2.1.

In order to keep the treatment of the Stokes flow problem clearer and with regard to the common use of \mathbf{u} and \mathbf{z} as primal and dual variables within the DWR approach, we introduce the primal and dual variables $\mathbf{u} := \{\mathbf{v}, p\}$ and $\mathbf{z} := \{\mathbf{w}, q\}$, respectively, for the now following Stokes flow problem. The variational formulation of the Stokes flow problem (5.2) is given by the following problem.

Problem 5.3 (Variational Formulation Stokes Flow Problem)

Find $\mathbf{u} = \{\mathbf{v}, p\} \in \mathcal{Y}$ such that

$$B(\mathbf{u})(\varphi) = F(\boldsymbol{\psi}) \quad \forall \varphi = \{\boldsymbol{\psi}, \chi\} \in \mathcal{Y}, \quad (5.10)$$

where the bilinear form $B(\cdot)(\cdot)$ and the linear form $F(\cdot)$ are defined by

$$B(\mathbf{u})(\boldsymbol{\varphi}) := \int_I \{(\partial_t \mathbf{v}, \boldsymbol{\psi}) + b(\mathbf{u})(\boldsymbol{\varphi})\} dt + (\mathbf{v}(0), \boldsymbol{\psi}(0)), \quad (5.11)$$

$$F(\boldsymbol{\psi}) := \int_I (\mathbf{f}, \boldsymbol{\psi}) dt + (\mathbf{v}_0, \boldsymbol{\psi}(0)), \quad (5.12)$$

with the inner bilinear form $b(\cdot)(\cdot)$ given by

$$b(\mathbf{u})(\boldsymbol{\varphi}) := \nu(\nabla \mathbf{v}, \nabla \boldsymbol{\psi}) - (p, \nabla \cdot \boldsymbol{\psi}) + (\nabla \cdot \mathbf{v}, \chi). \quad (5.13)$$

Proposition 5.1 (Well-Posedness Stokes Flow)

Assume that $\mathbf{f} \in L^2(I; H^{-1}(\Omega)^d)$ and $\mathbf{v}_0 \in H_{\text{div}}(\Omega)$. Then, the model problem (5.10) is well-posed.

Proof. The proof can be found in the literature, for instance, in [79, Thm. 72.2]. \square

Remark 5.3 (Regularity)

Beyond the assumption $\mathbf{v} \in \mathcal{Y}_1$ which is sufficient within the framework of the DWR approach, the existence of a sufficiently regular solution is assumed such that the well-posedness of the transport problem can be ensured, cf. Prop. 4.1, and all of the arguments and terms used below are well-defined. Regularity assumptions for the Stokes flow problem in general can be found, for instance, in [79, 112, 173].

Remark 5.4 (Coupling)

The coupling of the transport problem with the time-dependent Stokes flow problem is via the convection variable \mathbf{v} of the system (5.1), (5.2). We consider for the error estimation in Sec. 5.2 a coupled system but remark that the coupling is uni-directional from the Stokes flow to the transport problem. Furthermore, we note that the statement of Rem. 5.2 can be transferred to the Stokes flow problem by replacing the corresponding spaces.

The weak formulations, given by Problem 5.2 and 5.3, respectively, are now the starting point for the variational discretizations in space and time. Thereby, we start with a discontinuous in time discretization leading to a finite set of coupled PDEs which is then discretized in space using the concepts introduced in Chapter 2. This approach is sometimes called Rothe’s method in the literature, cf. [79, Rem. 69.1]. For adaptivity reasons, it is desirably to allow the spatial meshes to change in time. This approach is referred to as the concept of dynamic meshes, cf. [168, 167]. For more details about the implementation features we refer to Sec. 4.4 of the previous chapter.

5.1 Stabilized Space-Time Discretizations

In this section, we explain our multirate in time approach and describe the discretization in space and time of the weak formulations of the transport and Stokes flow problem by means of Galerkin finite element methods. Thereby, we start with the semi-discretization in time using a discontinuous Galerkin method as introduced in Sec. 2.2. Afterwards, we present the (stabilized) discretization in space of the arising semi-discrete problems using continuous Galerkin finite element methods as introduced in Sec. 2.1.3. Here, we are using the approach of space-time slabs including a temporal triangulation that is allowed to have more than one cell in time on an associated time subinterval, cf. Assumption. 2.5. Therefore, the following considerations are done with respect to such a cell in time (here denoted by K_n). Restricting the temporal triangulation to only one cell in time leads to the classical considerations with respect to a subinterval I_n , cf. Rem. 2.3.

5.1.1 Multirate in Time Approach

For the efficient approximation of the underlying coupled problem, we use a multirate in time approach to mimic the behavior of a slowly moving fluid, that is approximated by a time-dependent Stokes solver, and a faster convection-diffusion-reaction process. Precisely, the subproblems given by (5.1) and (5.2) are considered on different time scales modeling the underlying physical processes. We initialize the temporal mesh independently for the Stokes flow and the transport problem with the following properties:

- The Stokes flow temporal mesh is coarser or equal to that of the transport problem.
- The endpoints in the temporal mesh of the Stokes solver must match with endpoints in the temporal mesh of the transport problem.

We allow for adaptive time refinements of the temporal meshes of the transport and Stokes flow problem complying the conditions above. An exemplary initialization and one manufactured refined temporal mesh are illustrated in Fig. 5.1.

For our multirate in time approach including different time scales for the two subproblems, we rely on the concepts introduced in Assumptions 2.4-2.5 in Sec. 2.2. Thus, for the multirate decoupling of the transport problem, we let $0 =: t_0^T < t_1^T < \dots < t_{N^\ell}^T := T$ a set of time points for the partition of the closure of the time domain $\bar{I} = [0, T]$ into left-open subintervals $I_n := (t_{n-1}^T, t_n^T]$, $n = 1, \dots, N^\ell$. The number

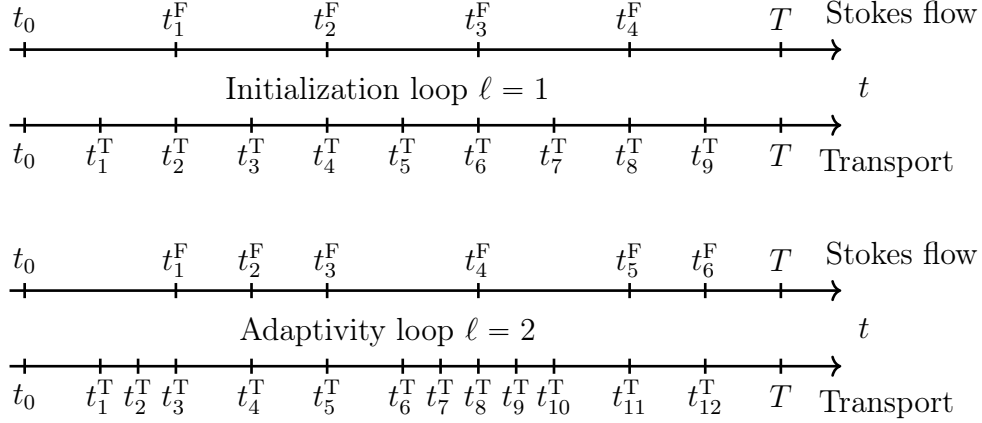


Figure 5.1: Illustration of different exemplary temporal meshes for the transport and Stokes flow solver for the initial loop and for the first adaptively refined loop.

N^ℓ depends on the adaptivity loop ℓ . Since we allow the Stokes flow problem to be solved on a different temporal mesh compared to the transport problem, we introduce an additional partition of the time domain I . Thus, for the Stokes flow problem, we let $0 =: t_0^F < t_1^F < \dots < t_{N^{\text{F},\ell}}^F := T$ a set of time points for the partition of the closure of the time domain $\bar{I} = [0, T]$ into left-open subintervals $I_n^F := (t_{n-1}^F, t_n^F]$, $n = 1, \dots, N^{\text{F},\ell}$. For simplicity of the implementation, we ensure that each element of the set $\{t_0^F, t_1^F, \dots, t_{N^{\text{F},\ell}}^F\}$ corresponds to an element of the set $\{t_0^T, t_1^T, \dots, t_{N^\ell}^T\}$. Additionally, we can approximate the transport and Stokes flow problem with an arbitrary, but different degree $r^T, r^F \geq 0$ in time. This gives us for $r^T > r^F$ an additional level of the multirate in time character between the two problems.

5.1.2 Discretization in Time

The sets of time subintervals I_n and I_n^F are finite and countable. Thus, a separation of the global space-time domain $Q = \Omega \times I$ into a partition of space-time slabs $\hat{Q}_n = \Omega \times I_n$ for the transport problem and $\hat{Q}_n^F = \Omega \times I_n^F$ for the Stokes flow problem, respectively, is reasonable, using a one-dimensional triangulation $\mathcal{T}_{\tau,n}$ (including cells in time K_n) or $\mathcal{T}_{\sigma,n}$ (including cells in time K_n^F) for the discretization in time on each slab \hat{Q}_n or \hat{Q}_n^F , $1 \leq n \leq N^\ell$, or $1 \leq n \leq N^{\text{F},\ell}$, as introduced in Assumption 2.5. Furthermore, let \mathcal{F}_τ and \mathcal{F}_σ be the sets of all interior time points given as

$$\begin{aligned} \mathcal{F}_\tau &:= (\{t_1^T, \dots, t_{N^\ell}^T\} \cup \{t \in \partial K_n \mid K_n \in \mathcal{T}_{\tau,n}\}) \setminus \{0, T\}, \\ \mathcal{F}_\sigma &:= (\{t_1^F, \dots, t_{N^{\text{F},\ell}}^F\} \cup \{t \in \partial K_n^F \mid K_n^F \in \mathcal{T}_{\sigma,n}\}) \setminus \{0, T\}. \end{aligned} \quad (5.14)$$

The commonly used time step size τ_K or σ_K is here the diameter or length of the cell in time of $\mathcal{T}_{\tau,n}$ or $\mathcal{T}_{\sigma,n}$ and the global time discretization parameter τ or σ is the

maximum time step size τ_K or σ_K of all cells in time of all slabs \hat{Q}_n or \hat{Q}_n^F , respectively.

For the discretization in time of the transport and Stokes flow problem we use a discontinuous Galerkin method dG(r) with an arbitrary polynomial degree $r \geq 0$. For more details about this method including, for instance, the composition of the respective shape functions or the concept on the reference interval, we refer to Sec. 2.2. Let $\mathcal{X}_\tau^{\text{dG}(r)}$ be the finite-dimensional discontinuous time-discrete function space for the transport problem defined by

$$\mathcal{X}_\tau^{\text{dG}(r)} := \left\{ u_\tau \in L^2(I; X) \mid u_\tau|_{K_n} \in \mathcal{P}_\tau^r(K_n; X), \right. \\ \left. u_\tau(0) \in L^2(\Omega), K_n \in \mathcal{T}_{\tau,n}, n = 1, \dots, N^\ell \right\}, \quad (5.15)$$

where $\mathcal{P}_\tau^r(K_n; X)$ denotes the space of all polynomials in time up to degree $r \geq 0$ on $K_n \in \mathcal{T}_{\tau,n}$ with values in X , as given in Eq. (2.9) in Sec. 2.2.2. For some discontinuous in time function $u_\tau \in \mathcal{X}_\tau^{\text{dG}(r)}$, we allow the left-side traces to be different from the right-side traces at some interior time point $t_{\mathcal{F}} \in \mathcal{F}_\tau$. Thus, we define the limits $u_\tau(t_{\mathcal{F}}^\pm)$ from above and below as well as their jump at $t_{\mathcal{F}}$ by means of

$$u_\tau(t_{\mathcal{F}}^\pm) := \lim_{t \rightarrow t_{\mathcal{F}}^\pm} u_\tau(t), \quad [u_\tau]_{t_{\mathcal{F}}} := u_\tau(t_{\mathcal{F}}^+) - u_\tau(t_{\mathcal{F}}^-). \quad (5.16)$$

In the same way, we define the finite-dimensional discontinuous time-discrete function space used for the Stokes flow problem by means of

$$\mathcal{Y}_\sigma^{\text{dG}(r)} := \left\{ \{\mathbf{v}_\sigma, p_\sigma\} \in L^2(I; X^d \times Y) \mid \mathbf{v}_\sigma|_{K_n^F} \in \mathcal{P}_\sigma^r(K_n^F; X^d), \mathbf{v}_\sigma(0) \in L^2(\Omega)^d, \right. \\ \left. p_\sigma|_{K_n^F} \in \mathcal{P}_\sigma^r(K_n^F; Y), K_n^F \in \mathcal{F}_{\sigma,n}, n = 1, \dots, N^{F,\ell} \right\}, \quad (5.17)$$

as well as the limits $\mathbf{v}_\tau(t_{\mathcal{F}}^\pm)$ from above and below as well as their jump at $t_{\mathcal{F}} \in \mathcal{F}_\sigma$ by means of

$$\mathbf{v}_\sigma(t_{\mathcal{F}}^\pm) := \lim_{t \rightarrow t_{\mathcal{F}}^\pm} \mathbf{v}_\sigma(t), \quad [\mathbf{v}_\sigma]_{t_{\mathcal{F}}} := \mathbf{v}_\sigma(t_{\mathcal{F}}^+) - \mathbf{v}_\sigma(t_{\mathcal{F}}^-). \quad (5.18)$$

In the following, we present the semidiscretization in time schemes of the transport and Stokes flow problem. Let $\mathcal{X}_\tau^{\text{dG}(r)}$ be the common trial and test space for the transport problem. Then, the discontinuous time-discrete variational approximation of Problem 5.2 reads as follows.

Problem 5.4 (Discontinuous Time-Discrete Transport Scheme: dG(r))

For a given $\mathbf{v}_\sigma \in \mathcal{Y}_\sigma^{\text{dG}(r)}$ of Problem 5.5, find $u_\tau \in \mathcal{X}_\tau^{\text{dG}(r)}$ such that

$$A_\tau(u_\tau; \mathbf{v}_\sigma)(\varphi_\tau) = G_\tau(\varphi_\tau) \quad \forall \varphi_\tau \in \mathcal{X}_\tau^{\text{dG}(r)}, \quad (5.19)$$

where the bilinear form $A_\tau(\cdot; \cdot)(\cdot)$ and the linear form $G_\tau(\cdot)$ are defined by

$$A_\tau(u_\tau; \mathbf{v}_\sigma)(\varphi_\tau) := \sum_{n=1}^{N^\ell} \sum_{K_n \in \mathcal{T}_{\tau,n}} \int_{K_n} \{(\partial_t u_\tau, \varphi_\tau) + a_\tau(u_\tau; \mathbf{v}_\sigma)(\varphi_\tau)\} dt \quad (5.20)$$

$$+ \sum_{t_F \in \mathcal{F}_\tau} ([u_\tau]_{t_F}, \varphi_\tau(t_F^+)) + (u_\tau(0^+), \varphi_\tau(0^+)),$$

$$G_\tau(\varphi_\tau) := \sum_{n=1}^{N^\ell} \sum_{K_n \in \mathcal{T}_{\tau,n}} \int_{K_n} (g, \varphi_\tau) dt + (u_0, \varphi_\tau(0^+)), \quad (5.21)$$

with the inner bilinear form $a_\tau(\cdot; \cdot)(\cdot)$ given by

$$a_\tau(u_\tau; \mathbf{v}_\sigma)(\varphi_\tau) := (\varepsilon \nabla u_\tau, \nabla \varphi_\tau) + (\mathbf{v}_\sigma \cdot \nabla u_\tau, \varphi_\tau) + (\alpha u_\tau, \varphi_\tau), \quad (5.22)$$

depending on the semi-discrete Stokes solution \mathbf{v}_σ .

Remark 5.5 For the error $e = u - u_\tau$ we get by subtracting Eq. (5.19) from Eq. (5.6) the identity

$$\sum_{n=1}^{N^\ell} \sum_{K_n \in \mathcal{T}_{\tau,n}} \int_{K_n} \{(\partial_t e, \varphi_\tau) + a(e; \mathbf{v}_\sigma)(\varphi_\tau)\} dt \quad (5.23)$$

$$= \sum_{t_F \in \mathcal{F}_\tau} ([u_\tau]_{t_F}, \varphi_\tau(t_F^+)) - \sum_{n=1}^{N^\ell} \sum_{K_n \in \mathcal{T}_{\tau,n}} \int_{K_n} ((\mathbf{v} - \mathbf{v}_\sigma) \cdot \nabla u, \varphi_\tau) dt,$$

with a non-vanishing right-hand side term depending on the jump terms and the error in the approximation of the flow field. Eq. (5.23) with the perturbation terms on the right-hand side replaces the standard Galerkin orthogonality of the space-time finite element approximation.

For the discontinuous in time semi-discretization of the Stokes flow problem let $\mathcal{Y}_\sigma^{\text{dG}(r)}$ be the common trial and test space. Then, the discontinuous time-discrete variational approximation of Problem 5.3 reads as follows.

Problem 5.5 (Discontinuous Time-Discrete Stokes Flow Scheme: dG(r))

Find $\mathbf{u}_\sigma = \{\mathbf{v}_\sigma, p_\sigma\} \in \mathcal{Y}_\sigma^{\text{dG}(r)}$ such that

$$B_\sigma(\mathbf{u}_\sigma)(\varphi_\sigma) = F_\sigma(\psi) \quad \forall \varphi_\sigma = \{\psi_\sigma, \chi_\sigma\} \in \mathcal{Y}_\sigma^{\text{dG}(r)}, \quad (5.24)$$

where the bilinear form $B_\sigma(\cdot, \cdot)(\cdot, \cdot)$ and the linear form $F_\sigma(\cdot)$ are defined by

$$B_\sigma(\mathbf{u}_\sigma)(\boldsymbol{\varphi}_\sigma) := \sum_{n=1}^{N^{\text{F},\ell}} \sum_{K_n^{\text{F}} \in \mathcal{T}_{\sigma,n}} \int_{K_n^{\text{F}}} \{(\partial_t \mathbf{v}_\sigma, \boldsymbol{\psi}_\sigma) + b(\mathbf{u}_\sigma)(\boldsymbol{\varphi}_\sigma)\} dt \quad (5.25)$$

$$+ \sum_{t_{\mathcal{F}} \in \mathcal{F}_\sigma} ([\mathbf{v}_\sigma]_{t_{\mathcal{F}}}, \boldsymbol{\psi}_\sigma(t_{\mathcal{F}}^+)) + (\mathbf{v}_\sigma(0^+), \boldsymbol{\psi}_\sigma(0^+)),$$

$$F_\sigma(\boldsymbol{\psi}_\sigma) := \sum_{n=1}^{N^{\text{F},\ell}} \sum_{K_n^{\text{F}} \in \mathcal{T}_{\sigma,n}} \int_{K_n^{\text{F}}} (\mathbf{f}, \boldsymbol{\psi}_\sigma) dt + (\mathbf{v}_0, \boldsymbol{\psi}_\sigma(0^+)), \quad (5.26)$$

where the inner bilinear form $b(\cdot)(\cdot)$ is given by Eq. (5.13).

5.1.3 Discretization in Space

In this section, we describe the Galerkin finite element approximation in space of the semi-discrete Problems 5.4 and 5.5, respectively. Thereby, we use the concepts introduced in Sec. 2.1.3, where all details can be found that are not specified in the following. We use Lagrange type finite element spaces of continuous functions that are piecewise polynomials. For the discretization in space, we consider a separation $Q_n = \mathcal{T}_{h,n} \times \mathcal{T}_{\tau,n}$ or $Q_n^{\text{F}} = \mathcal{T}_{h,n}^{\text{F}} \times \mathcal{T}_{\tau,n}$ as given in Assumption 2.5, where $\mathcal{T}_{h,n}$ or $\mathcal{T}_{h,n}^{\text{F}}$ build a decomposition of the domain Ω into disjoint spatial elements K or K^{F} for the transport or Stokes flow problem, respectively. Our mesh adaptation process includes locally refined cells, which is enabled by allowing so-called hanging nodes. For this purpose, we assume the decompositions $\mathcal{T}_{h,n}$ and $\mathcal{T}_{h,n}^{\text{F}}$ (in the following also referred to as spatial triangulation) to be regular and organized in a patch-wise manner, cf. Def. 2.5 and Def. 2.6, respectively. We point out that the global conformity of the finite element approach is preserved since the unknowns at such hanging nodes are eliminated by interpolation between the neighboring 'regular' nodes, cf. Rem. 2.2.

Now, using discrete finite element spaces $(V_h^{p,n})^d$ on $\mathcal{T}_{h,n}$ and $\mathcal{T}_{h,n}^{\text{F}}$, $n = 1, \dots, N^\ell$ and $n = 1, \dots, N^{\text{F},\ell}$, respectively, with V_h^p being defined by Eq. (2.1) in Sec. 2.1.3, we introduce the fully discrete function spaces for the transport and Stokes flow problem, respectively, by means of

$$\mathcal{X}_{\tau h}^{\text{dG}(r),p} := \left\{ u_{\tau h} \in \mathcal{X}_\tau^{\text{dG}(r)} \mid \begin{aligned} &u_{\tau h}|_{K_n} \in \mathcal{P}_\tau^r(K_n; H_h^{p_u,n}), \\ &u_{\tau h}(0) \in H_h^{p_u,1}, K_n \in \mathcal{T}_{\tau,n}, n = 1, \dots, N^\ell \end{aligned} \right\}, \quad (5.27)$$

$$\mathcal{Y}_{\sigma h}^{\text{dG}(r),p} := \left\{ \begin{aligned} &\{\mathbf{v}_{\sigma h}, p_{\sigma h}\} \in \mathcal{Y}_{\sigma}^{\text{dG}(r)} \Big| \mathbf{v}_{\sigma h}|_{K_n^{\text{F}}} \in \mathcal{P}_{\sigma}^r(K_n^{\text{F}}; (H_h^{p_v,n})^d), \\ &\mathbf{v}_{\sigma h}(0) \in (H_h^{p_v,1})^d, p_{\sigma h}|_{K_n^{\text{F}}} \in \mathcal{P}_{\sigma}^r(K_n^{\text{F}}; L_h^{p_p,n}), \\ &K_n^{\text{F}} \in \mathcal{T}_{\sigma,n}, n = 1, \dots, N^{\text{F},\ell} \end{aligned} \right\}, \quad (5.28)$$

with

$$H_h^{p_u,n} := V_h^{p_u,n} \cap X, \quad H_h^{p_v,n} := V_h^{p_v,n} \cap X, \quad L_h^{p_p,n} := V_h^{p_p,n} \cap Y.$$

We note that the spatial finite element space $(V_h^{p,n})^d$ is allowed to be different on all slabs Q_n or Q_n^{F} , respectively, which is natural in the context of a discontinuous Galerkin approximation of the time variable and allows for dynamic mesh changes in time. Due to the conformity of $H_h^{p_u,n}$, $H_h^{p_v,n}$ and $L_h^{p_p,n}$ we get $\mathcal{X}_{\tau h}^{\text{dG}(r),p} \subseteq \mathcal{X}_{\tau}^{\text{dG}(r)}$ and $\mathcal{Y}_{\sigma h}^{\text{dG}(r),p} \subseteq \mathcal{Y}_{\sigma}^{\text{dG}(r)}$, respectively.

The fully discrete discontinuous in time schemes of the transport problem (5.6) and Stokes flow problem (5.10) can be easily obtained now from the dG(r) semi-discretization schemes given by Eq. (5.19) and Eq. (5.24), respectively, by simply adding the additional index h to the variables and by replacing the respective semi-discrete spaces by the above defined fully discrete counterparts. For the sake of completeness, the fully discrete discontinuous in time scheme for the transport problem then reads as follows.

Problem 5.6 (Fully Discrete Transport Scheme: cG(p)-dG(r))

For a given $\mathbf{v}_{\sigma h} \in \mathcal{Y}_{\sigma h}^{\text{dG}(r),p}$ of Problem 5.7, find $u_{\tau h} \in \mathcal{X}_{\tau h}^{\text{dG}(r),p}$ such that

$$A_{\tau h}(u_{\tau h}; \mathbf{v}_{\sigma h})(\varphi_{\tau h}) = G_{\tau h}(\varphi_{\tau h}) \quad \forall \varphi_{\tau h} \in \mathcal{X}_{\tau h}^{\text{dG}(r),p}, \quad (5.29)$$

with $A_{\tau h}(\cdot; \cdot)(\cdot) = A_{\tau}(\cdot; \cdot)(\cdot)$ and $G_{\tau h}(\cdot) = G_{\tau}(\cdot)$ being defined in Eq. (5.20) and Eq. (5.21), respectively. We note that the inner bilinear form $a_{\tau h}(\cdot; \cdot)(\cdot)$ occurring in $A_{\tau h}(\cdot; \cdot)(\cdot)$ reads here as

$$a_{\tau h}(u_{\tau h}; \mathbf{v}_{\sigma h})(\varphi_{\tau h}) := (\varepsilon \nabla u_{\tau h}, \nabla \varphi_{\tau h}) + (\mathbf{v}_{\sigma h} \cdot \nabla u_{\tau h}, \varphi_{\tau h}) + (\alpha u_{\tau h}, \varphi_{\tau h}), \quad (5.30)$$

depending on the fully discrete Stokes solution $\mathbf{v}_{\sigma h}$.

The fully discrete discontinuous in time scheme for the Stokes flow problem reads as follows.

Problem 5.7 (Fully Discrete Stokes Flow Scheme: cG(p)-dG(r))

Find $\mathbf{u}_{\sigma h} = \{\mathbf{v}_{\sigma h}, p_{\sigma h}\} \in \mathcal{Y}_{\sigma h}^{\text{dG}(r),p}$ such that

$$B_{\sigma h}(\mathbf{u}_{\sigma h})(\boldsymbol{\varphi}_{\sigma h}) = F_{\sigma h}(\boldsymbol{\psi}_{\sigma h}) \quad \forall \boldsymbol{\varphi}_{\sigma h} = \{\boldsymbol{\psi}_{\sigma h}, \chi_{\sigma h}\} \in \mathcal{Y}_{\sigma h}^{\text{dG}(r),p}, \quad (5.31)$$

with $B_{\sigma h}(\cdot)(\cdot) = B_{\sigma}(\cdot)(\cdot)$ and $F_{\sigma h}(\cdot) = F_{\sigma}(\cdot)$ being defined in Eq. (5.25) and Eq. (5.26), respectively.

5.1.4 Stabilization of the Transport Problem

For the sake of physical realism, the transport problem is supposed to be convection-dominated by assuming high Péclet numbers that are characterized by the ratio of small diffusion compared to the convection field, cf. [53, 116]. Thus, the finite element approximation needs to be stabilized in order to avoid spurious and non-physical oscillations of the discrete solution arising close to sharp fronts and layers. Here, we apply the streamline upwind Petrov-Galerkin (SUPG) method [106, 49], that was introduced in Sec. 2.4. Existing convergence analyses in the natural norm of the underlying scheme including local and global error bounds can be found, for instance, in [147] and [162, Ch. III.4.3]. With this in mind, the stabilized fully discrete discontinuous in time scheme for the transport problem reads as follows.

Problem 5.8 (Stabilized Transport Scheme: cG(p)-dG(r))

For a given $\mathbf{v}_{\sigma h} \in \mathcal{Y}_{\sigma h}^{\text{dG}(r),p}$ of Problem 5.7, find $u_{\tau h} \in \mathcal{X}_{\tau h}^{\text{dG}(r),p}$ such that

$$A_S(u_{\tau h}; \mathbf{v}_{\sigma h})(\varphi_{\tau h}) = G_{\tau h}(\varphi_{\tau h}) \quad \forall \varphi_{\tau h} \in \mathcal{X}_{\tau h}^{\text{dG}(r),p}, \quad (5.32)$$

where the linear form $G_{\tau h}(\cdot) = G_{\tau}(\cdot)$ is defined by Eq. (5.21) and the stabilized bilinear form $A_S(\cdot; \cdot)(\cdot)$ is given by

$$A_S(u_{\tau h}; \mathbf{v}_{\sigma h})(\varphi_{\tau h}) := A_{\tau h}(u_{\tau h}; \mathbf{v}_{\sigma h})(\varphi_{\tau h}) + S_A(u_{\tau h}; \mathbf{v}_{\sigma h})(\varphi_{\tau h}), \quad (5.33)$$

with $A_{\tau h}(\cdot; \cdot)(\cdot) = A_{\tau}(\cdot; \cdot)(\cdot)$ being defined by Eq. (5.20) using (5.30). Here, the SUPG stabilization bilinear form $S_A(\cdot; \cdot)(\cdot)$ is defined by

$$\begin{aligned} S_A(u_{\tau h}; \mathbf{v}_{\sigma h})(\varphi_{\tau h}) := & \sum_{n=1}^{N^\ell} \sum_{K_n \in \mathcal{T}_{\tau,n}} \int_{K_n} \sum_{K \in \mathcal{T}_{h,n}} \delta_K(r(u_{\tau h}; \mathbf{v}_{\sigma h}), \mathbf{v}_{\sigma h} \cdot \nabla \varphi_{\tau h})_K dt \\ & + \sum_{t_{\mathcal{F}} \in \mathcal{F}_{\tau}} \sum_{K \in \mathcal{T}_{h,n}} \delta_K([u_{\tau h}]_{t_{\mathcal{F}}}, \mathbf{v}_{\sigma h} \cdot \nabla \varphi_{\tau h}(t_{\mathcal{F}}^+))_K \\ & + \sum_{K \in \mathcal{T}_{h,1}} \delta_K(u_{\tau h}(0^+) - u_0, \mathbf{v}_{\sigma h} \cdot \nabla \varphi_{\tau h}(0^+))_K, \end{aligned} \quad (5.34)$$

where δ_K is the so-called stabilization parameter (cf. Rem. 4.3) and the residual term $r(\cdot; \cdot)$ is given by

$$r(u_{\tau h}; \mathbf{v}_{\sigma h}) := \partial_t u_{\tau h} - \nabla \cdot (\varepsilon \nabla u_{\tau h}) + \mathbf{v}_{\sigma h} \cdot \nabla u_{\tau h} + \alpha u_{\tau h} - g. \quad (5.35)$$

Remark 5.6 For the error $e = u_\tau - u_{\tau h}$ we get by subtracting Eq. (5.32) from Eq. (5.19) the identity

$$\begin{aligned}
& \sum_{n=1}^{N^\ell} \sum_{K_n \in \mathcal{T}_{\tau,n}} \int_{K_n} \{(\partial_t e, \varphi_{\tau h}) + a(e; \mathbf{v}_{\sigma h})(\varphi_{\tau h})\} dt \\
& + \sum_{t_F \in \mathcal{F}_\tau} ([e]_{t_F}, \varphi_{\tau h}(t_F^+) + (e(0^+), \varphi_{\tau h}(0^+)) \\
& = S_A(u_{\tau h}; \mathbf{v}_{\sigma h})(\varphi_{\tau h}) - \sum_{n=1}^{N^\ell} \sum_{K_n \in \mathcal{T}_{\tau,n}} \int_{K_n} ((\mathbf{v}_\sigma - \mathbf{v}_{\sigma h}) \cdot \nabla u_\tau, \varphi_{\tau h}) dt,
\end{aligned} \tag{5.36}$$

with a non-vanishing right-hand side term depending on the stabilization and the error in the approximation of the flow field. Eq. (5.36) with the perturbation terms on the right-hand side replaces the standard Galerkin orthogonality of the space-time finite element approximation.

5.2 A Posteriori Error Estimation for a Coupled Flow and Transport Problem

In this section, we derive DWR-based a posteriori error estimators for the stabilized transport and the Stokes flow problem. With regard to practical relevance described at the beginning of this chapter, we a priori focus on the derivation of an a posteriori error estimator for the transport problem depending, among other things, on the error in the Stokes flow problem due to the coupling terms. Thereafter, we derive an a posteriori error estimator for the time-dependent Stokes flow problem.

5.2.1 An A Posteriori Error Estimator for the Transport Problem

So far, this work dealt with fixed given convection fields for steady-state and time-dependent transport problems. Here, this convection field is now determined through the coupling with the Stokes flow problem, more precisely its solution \mathbf{v} . Hence, this coupling affects the error representation formula of the transport problem by means of additionally occurring coupling terms. This is an extension compared to the former results obtained in Thm. 4.1 or rather Thm. 4.2. Nevertheless, the derivation of the error estimator for the stabilized transport equation (5.32) is similar to the course of action in the previous chapter. Based on that, we first derive the dual transport problems using the Euler Lagrange method of constraint optimization as introduced in Sec. 2.5. In a second step, we develop an a posteriori error estimator measuring the

discretization errors in an output value J . This output value is called goal functional and fulfills the following properties.

Assumption 5.2 (Goal Functional of Transport) *Let us assume $J : \mathcal{X} \rightarrow \mathbb{R}$ to be a linear functional representing the goal quantity of physical interest. In general, this functional is given as*

$$J(u) = \int_0^T J_1(u(t)) dt + J_2(u(T)), \quad (5.37)$$

where $J_1 \in L^2(I; H^{-1}(\Omega))$ and $J_2 \in H^{-1}(\Omega)$ are three times differentiable functionals defining the dual right-hand side and the dual initial at time $t = T$, respectively, where each of them may be zero; cf. also Rem. 4.5.

In practice, the quantity of interest represents, for instance, a mean value of a given functional (J_1) or a final time-point value $J_2(u(T))$; cf., e.g., [168, 36, 20].

Since we are interested in error indicators for both the spatial and the temporal mesh, we split the a posteriori error representation with respect to J into the following contributions

$$J(u) - J(u_{\tau h}) = J(u) - J(u_\tau) + J(u_\tau) - J(u_{\tau h}). \quad (5.38)$$

To derive these representations, we define the following Lagrangian functionals based on the Euler Lagrange method of constraint optimization as introduced in Sec. 2.5.

Definition 5.1 (Lagrangian Functionals of Transport) *The Lagrangian functionals $\mathcal{L} : \mathcal{X} \times \mathcal{X} \rightarrow \mathbb{R}$, $\mathcal{L}_\tau : \mathcal{X}_\tau^{\text{dG}(r)} \times \mathcal{X}_\tau^{\text{dG}(r)} \rightarrow \mathbb{R}$, and $\mathcal{L}_{\tau h} : \mathcal{X}_{\tau h}^{\text{dG}(r),p} \times \mathcal{X}_{\tau h}^{\text{dG}(r),p} \rightarrow \mathbb{R}$ are defined by*

$$\mathcal{L}(u, z; \mathbf{v}) := J(u) + G(z) - A(u; \mathbf{v})(z), \quad (5.39)$$

$$\mathcal{L}_\tau(u_\tau, z_\tau; \mathbf{v}_\sigma) := J(u_\tau) + G_\tau(z_\tau) - A_\tau(u_\tau; \mathbf{v}_\sigma)(z_\tau), \quad (5.40)$$

$$\begin{aligned} &= \mathcal{L}(u_\tau, z_\tau; \mathbf{v}_\sigma) - \sum_{t_{\mathcal{F}} \in \mathcal{F}_\tau} ([u_\tau]_{t_{\mathcal{F}}}, z_\tau(t_{\mathcal{F}}^\pm)) \\ &\quad + \sum_{n=1}^{N^\ell} \sum_{K_n \in \mathcal{T}_{\tau,n}} \int_{K_n} ((\mathbf{v} - \mathbf{v}_\sigma) \cdot \nabla u_\tau, z_\tau) dt, \end{aligned}$$

$$\mathcal{L}_{\tau h}(u_{\tau h}, z_{\tau h}; \mathbf{v}_{\sigma h}) := J(u_{\tau h}) + G_{\tau h}(z_{\tau h}) - A_S(u_{\tau h}; \mathbf{v}_{\sigma h})(z_{\tau h}) \quad (5.41)$$

$$\begin{aligned} &= \mathcal{L}_\tau(u_{\tau h}, z_{\tau h}; \mathbf{v}_{\sigma h}) - S_A(u_{\tau h}; \mathbf{v}_{\sigma h})(z_{\tau h}) \\ &\quad + \sum_{n=1}^{N^\ell} \sum_{K_n \in \mathcal{T}_{\tau,n}} \int_{K_n} ((\mathbf{v}_\sigma - \mathbf{v}_{\sigma h}) \cdot \nabla u_{\tau h}, z_{\tau h}) dt, \end{aligned}$$

where \mathcal{F}_τ denotes the set of interior time points of the temporal mesh of the transport problem, defined by the first equation in (5.14).

Remark 5.7 *The Lagrange multipliers z , z_τ , and $z_{\tau h}$ are called dual variables in contrast to the primal variables u , u_τ , and $u_{\tau h}$, cf. [36, 40]. Furthermore, by using the respective Lagrangian functionals from above, we can express the functional values of the continuous, semi-discrete, and fully discrete solution by means of*

$$\begin{aligned} J(u) &:= \mathcal{L}(u, \varphi; \mathbf{v}) & \forall \varphi \in \mathcal{X}, \\ J(u_\tau) &:= \mathcal{L}(u_\tau, \varphi_\tau; \mathbf{v}_\sigma) & \forall \varphi_\tau \in \mathcal{X}_\tau^{\text{dG}(r)}, \\ J(u_{\tau h}) &:= \mathcal{L}_{\tau h}(u_{\tau h}, \varphi_{\tau h}; \mathbf{v}_{\sigma h}) & \forall \varphi_{\tau h} \in \mathcal{X}_{\tau h}^{\text{dG}(r),p}. \end{aligned} \quad (5.42)$$

5.2.1.1 Derivation of the Dual Schemes

As mentioned in the introductory Sec. 2.5, the DWR approach may be comprehended as a constraint optimization problem in terms of exploiting the Euler Lagrange method of constraint optimization. In this sense, we point out that the following optimality or stationary conditions, given by the directional derivatives of the Lagrangian functionals with respect to their second argument,

$$\begin{aligned} \mathcal{L}'_z(u, z; \mathbf{v})(\varphi) &= 0 \quad \forall \varphi \in \mathcal{X}, \\ \mathcal{L}'_{\tau, z}(u_\tau, z_\tau; \mathbf{v}_\sigma)(\varphi_\tau) &= 0 \quad \forall \varphi_\tau \in \mathcal{X}_\tau^{\text{dG}(r)}, \\ \mathcal{L}'_{\tau h, z}(u_{\tau h}, z_{\tau h}; \mathbf{v}_{\sigma h})(\varphi_{\tau h}) &= 0 \quad \forall \varphi_{\tau h} \in \mathcal{X}_{\tau h}^{\text{dG}(r),p}, \end{aligned} \quad (5.43)$$

can be identified with determining the continuous solution u of Eq. (5.6), the semi-discrete solution u_τ of the discontinuous time-discrete transport scheme, given by Eq. (5.19), and the fully discrete solution $u_{\tau h}$ of the stabilized fully discrete cG(p)-dG(r) transport scheme, given by Eq. (5.32), respectively. More precisely, in Eq. (5.43) the so-called Gâteaux derivatives are used, given by Def. 2.11 in Sec. 2.3. In order to enhance understanding, we recall here its definition with respect to the first and second argument.

$$\begin{aligned} \mathcal{L}'_z(u, z; \mathbf{v})(\varphi) &:= \lim_{t \neq 0, t \rightarrow 0} t^{-1} \{ \mathcal{L}(u, z + t\varphi; \mathbf{v}) - \mathcal{L}(u, z; \mathbf{v}) \}, \quad \varphi \in \mathcal{X}, \\ \mathcal{L}'_u(u, z; \mathbf{v})(\psi) &:= \lim_{t \neq 0, t \rightarrow 0} t^{-1} \{ \mathcal{L}(u + t\psi, z; \mathbf{v}) - \mathcal{L}(u, z; \mathbf{v}) \}, \quad \psi \in \mathcal{X}, \end{aligned}$$

In contrast, considering the directional derivatives of the Lagrangian functionals with respect to their first argument leads to the dual problems, cf., e.g., [40], given by the

following optimality or stationary conditions.

$$\begin{aligned}
\mathcal{L}'_u(u, z; \mathbf{v})(\psi) &= 0 \quad \forall \psi \in \mathcal{X}, \\
\mathcal{L}'_{\tau, u}(u_\tau, z_\tau; \mathbf{v}_\sigma)(\psi_\tau) &= 0 \quad \forall \psi_\tau \in \mathcal{X}_\tau^{\text{dG}(r)}, \\
\mathcal{L}'_{\tau h, u}(u_{\tau h}, z_{\tau h}; \mathbf{v}_{\sigma h})(\psi_{\tau h}) &= 0 \quad \forall \psi_{\tau h} \in \mathcal{X}_{\tau h}^{\text{dG}(r), p}.
\end{aligned} \tag{5.44}$$

More precisely, the continuous dual solution $z \in \mathcal{X}$ fulfills the following problem.

Problem 5.9 (Dual Transport Problem)

For a given $\mathbf{v} \in \mathcal{Y}_1$ of Problem 5.3, find $z \in \mathcal{X}$ such that

$$A'(u; \mathbf{v})(\psi, z) = J'(u)(\psi) \quad \forall \psi \in \mathcal{X}, \tag{5.45}$$

where the adjoint bilinear form $A'(\cdot; \cdot)(\cdot, \cdot)$ is defined by

$$A'(u; \mathbf{v})(\psi, z) := \int_I \{(\psi, -\partial_t z) + a'(u; \mathbf{v})(\psi, z)\} dt + (\psi(T), z(T)). \tag{5.46}$$

The right-hand side of Eq. (5.45) is given by

$$J'(u)(\psi) := \int_I J'_1(u)(\psi) dt + J'_2(u(T))(\psi(T)). \tag{5.47}$$

Remark 5.8 Within the representation (5.46) of $A'(\cdot; \cdot)(\cdot, \cdot)$ integration by parts in time is applied, given by

$$\int_I (\partial_t \psi, z) dt = \int_I (\psi, -\partial_t z) dt + (\psi(T), z(T)) - (\psi(0), z(0)),$$

which is allowed for weak solutions $z \in \mathcal{X}$; cf., e.g., [160, 187] and Thm. 2.2 in Sec. 2.1.2 of Ch. 2. Therefore, the dual solution can be thought of running backward in time. Furthermore, we note that right-hand side as well as initial or better final data at time $t = T$ are given by the goal functional (5.37). More precisely, J_1 defines the dual right-hand side, whereas J_2 defines the dual initial at time $t = T$. Then, as combination with the above introduced integration by parts in time there holds, cf. [160],

$$(\psi(T), z(T)) = J'_2(u(T))(\psi(T)).$$

Finally, the derivative $a'(u; \mathbf{v})(\psi, z)$ of the inner bilinear form $a(u; \mathbf{v})(z)$ in A' , defined by Eq. (5.9), admits the explicit form

$$a'(u; \mathbf{v})(\psi, z) = (\varepsilon \nabla \psi, \nabla z) + (\mathbf{v} \cdot \nabla \psi, z) + (\alpha \psi, z). \tag{5.48}$$

The second stationary condition of Eq. (5.44) yields the following dual semi-discrete discontinuous in time problem:

Problem 5.10 (Dual Discontinuous Time-Discrete Transport Scheme)

For a given $\mathbf{v}_\sigma \in \mathcal{Y}_\sigma^{\text{dG}(r)}$ of Problem 5.5, find $z_\tau \in \mathcal{X}_\tau^{\text{dG}(r)}$ such that

$$A'_\tau(u_\tau; \mathbf{v}_\sigma)(\psi_\tau, z_\tau) = J'(u_\tau)(\psi_\tau) \quad \forall \psi_\tau \in \mathcal{X}_\tau^{\text{dG}(r)}, \quad (5.49)$$

where the adjoint bilinear form $A'_\tau(\cdot; \cdot)(\cdot, \cdot)$ is defined by

$$\begin{aligned} A'_\tau(u_\tau; \mathbf{v}_\sigma)(\psi_\tau, z_\tau) := & \sum_{n=1}^{N^\ell} \sum_{K_n \in \mathcal{T}_{\tau,n}} \int_{K_n} \{(\psi_\tau, -\partial_t z_\tau) + a'_\tau(u_\tau; \mathbf{v}_\sigma)(\psi_\tau, z_\tau)\} dt \\ & - \sum_{t_{\mathcal{F}} \in \mathcal{F}_\tau} (\psi_\tau(t_{\mathcal{F}}^-), [z_\tau]_{t_{\mathcal{F}}}) + (\psi_\tau(T^-), z_\tau(T^-)), \end{aligned} \quad (5.50)$$

with the dual inner bilinear form $a'_\tau(\cdot; \cdot)(\cdot, \cdot)$ being defined by Eq. (5.48) depending on the semi-discrete Stokes solution \mathbf{v}_σ . The right-hand side of Eq. (5.49) is given by

$$J'(u_\tau)(\psi_\tau) := \sum_{n=1}^{N^\ell} \sum_{K_n \in \mathcal{T}_{\tau,n}} \int_{K_n} J'_1(u_\tau)(\psi_\tau) dt + J'_2(u_\tau(T^-))(\psi_\tau(T^-)). \quad (5.51)$$

The third stationary condition of Eq. (5.44) yields the dual stabilized fully discrete discontinuous in time problem:

Problem 5.11 (Dual Stabilized Transport Scheme: cG(p)-dG(r))

For a given $\mathbf{v}_{\sigma h} \in \mathcal{Y}_\sigma^{\text{dG}(r),p}$ of Problem 5.7, find $z_{\tau h} \in \mathcal{X}_{\tau h}^{\text{dG}(r),p}$ such that

$$A'_S(u_{\tau h}; \mathbf{v}_{\sigma h})(\psi_{\tau h}, z_{\tau h}) = J'(u_{\tau h})(\psi_{\tau h}) \quad \forall \psi_{\tau h} \in \mathcal{X}_{\tau h}^{\text{dG}(r),p}, \quad (5.52)$$

where the stabilized adjoint bilinear form $A'_S(\cdot; \cdot)(\cdot, \cdot)$ is defined by

$$A'_S(u_{\tau h}; \mathbf{v}_{\sigma h})(\psi_{\tau h}, z_{\tau h}) := A'_{\tau h}(u_{\tau h}; \mathbf{v}_{\sigma h})(\psi_{\tau h}, z_{\tau h}) + S'_A(u_{\tau h}; \mathbf{v}_{\sigma h})(\psi_{\tau h}, z_{\tau h}), \quad (5.53)$$

with $A'_{\tau h}(\cdot; \cdot)(\cdot, \cdot)$ given by Eq. (5.50) including the dual inner bilinear form $a'_{\tau h}(\cdot; \cdot)(\cdot, \cdot)$ being defined by Eq. (5.48) and depending on the fully discrete Stokes solution $\mathbf{v}_{\sigma h}$. The right-hand side of Eq. (5.52) is given by

$$J'(u_{\tau h})(\psi_{\tau h}) := \sum_{n=1}^{N^\ell} \sum_{K_n \in \mathcal{T}_{\tau,n}} \int_{K_n} J'_1(u_{\tau h})(\psi_{\tau h}) dt + J'_2(u_{\tau h}(T^-))(\psi_{\tau h}(T^-)). \quad (5.54)$$

Here, the adjoint SUPG stabilization bilinear form $S'_A(\cdot; \cdot)(\cdot, \cdot)$ is defined by

$$\begin{aligned}
S'_A(u_{\tau h}; \mathbf{v}_{\sigma h})(\psi_{\tau h}, z_{\tau h}) &:= \sum_{n=1}^{N^\ell} \sum_{K_n \in \mathcal{T}_{\tau, n}} \int_{K_n} \sum_{K \in \mathcal{T}_{h, n}} \delta_K \left\{ (\mathbf{v}_{\sigma h} \cdot \nabla \psi_{\tau h}, \partial_t z_{\tau h})_K \right. \\
&\quad - (\nabla \cdot (\varepsilon \nabla \psi_{\tau h}), \mathbf{v}_{\sigma h} \cdot \nabla z_{\tau h})_K \\
&\quad + (\mathbf{v}_{\sigma h} \cdot \nabla \psi_{\tau h} + \alpha \psi_{\tau h}, \mathbf{v}_{\sigma h} \cdot \nabla z_{\tau h})_K \\
&\quad + \sum_{t_{\mathcal{F}} \in \mathcal{F}_\tau} \sum_{K \in \mathcal{T}_{h, n}} \delta_K (\mathbf{v}_{\sigma h} \cdot \nabla \psi_{\tau h}(t_{\mathcal{F}}^-), [z_{\tau h}]_{t_{\mathcal{F}}})_K \\
&\quad \left. - \sum_{K \in \mathcal{T}_{h, N}} \delta_K (\mathbf{v}_{\sigma h} \cdot \nabla \psi_{\tau h}(T^-), z_{\tau h}(T^-))_K \right\}.
\end{aligned} \tag{5.55}$$

Remark 5.9 *The discrete dual problems decouple to a time stepping method running backward in time as given by Problem 5.10 and Problem 5.11, respectively, by using integration by parts in time; cf. [160, Lemma 8.9]. Furthermore, the presented derivation of the dual schemes can be interpreted as an FSTD approach, since the stabilized fully discrete scheme given by Problem 5.11 is derived with the help of the adjoint of the stabilized fully discrete primal operator that is included in the respective Lagrangian functionals; cf. also Rem. 4.7 of the preceding chapter. For more details about the two approaches, we further refer to [169, 101, 103, 31].*

5.2.1.2 Derivation of an A Posteriori Error Estimator

For the derivation of computable representations of the separated error contributions in space and time as indicated in Eq. (5.38) we use Lemma 4.1 of the preceding chapter. Therefore, we recall the general result of this lemma, that can be found in [167, 40]. The proof can be found in the stated literature and is additionally given in Sec. 4.2.2 of Ch. 4; cf. also Rem. 4.8.

Lemma 5.1 *Let \mathcal{W} be a function space and L and \tilde{L} be three times Gâteaux differentiable functionals on \mathcal{W} . We seek a stationary point w_1 of L on a subspace $\mathcal{W}_1 \subseteq \mathcal{W}$: Find $w_1 \in \mathcal{W}_1$ such that*

$$L'(w_1)(\delta w_1) = 0 \quad \forall \delta w_1 \in \mathcal{W}_1. \tag{5.56}$$

This equation is approximated by a Galerkin method using the functional \tilde{L} on a subspace $\mathcal{W}_2 \subseteq \mathcal{W}$. Hence, the discrete problem seeks $w_2 \in \mathcal{W}_2$ such that

$$\tilde{L}'(w_2)(\delta w_2) = 0 \quad \forall \delta w_2 \in \mathcal{W}_2. \tag{5.57}$$

If the continuous solution w_1 additionally fulfills

$$L'(w_1)(w_2) = 0, \quad (5.58)$$

with the approximated solution w_2 , we have the error representation

$$L(w_1) - \tilde{L}(w_2) = \frac{1}{2}L'(w_2)(w_1 - \tilde{w}_2) + \frac{1}{2}(L - \tilde{L})'(w_2)(\tilde{w}_2 - w_2) + (L - \tilde{L})(w_2) + \mathcal{R}, \quad (5.59)$$

for arbitrary $\tilde{w}_2 \in \mathcal{W}_2$, where the remainder term \mathcal{R} is given in terms of $e := w_1 - w_2$ as

$$\mathcal{R} = \frac{1}{2} \int_0^1 L'''(w_2 + se)(e, e, e)s(s-1) ds. \quad (5.60)$$

Before proceeding with the main result, we introduce the primal and dual residuals based on the continuous and semi-discrete in time schemes by means of

$$\begin{aligned} \rho(u; \mathbf{v})(\varphi) &:= \mathcal{L}'_z(u, z; \mathbf{v})(\varphi) = G(\varphi) - A(u; \mathbf{v})(\varphi), \\ \rho^*(u, z; \mathbf{v})(\varphi) &:= \mathcal{L}'_u(u, z; \mathbf{v})(\varphi) = J'(u)(\varphi) - A'(u; \mathbf{v})(\varphi, z), \\ \rho_\tau(u; \mathbf{v}_\sigma)(\varphi) &:= \mathcal{L}'_{\tau, z}(u, z; \mathbf{v}_\sigma)(\varphi) = G_\tau(\varphi) - A_\tau(u; \mathbf{v}_\sigma)(\varphi), \\ \rho_\tau^*(u, z; \mathbf{v}_\sigma)(\varphi) &:= \mathcal{L}'_{\tau, u}(u, z; \mathbf{v}_\sigma)(\varphi) = J'(u)(\varphi) - A'_\tau(u; \mathbf{v}_\sigma)(\varphi, z). \end{aligned} \quad (5.61)$$

We apply the abstract error representation formula (5.59) to the Lagrangian functionals (5.39), (5.40) and (5.41), respectively, to derive an a posteriori error estimator for the transport problem in space and time. The result is summarized in the following Thm. 5.1 that is an extension to the result in Thm. 4.1 with regard to additionally occurring terms caused by the coupling. Furthermore, we note that the idea of the proof goes back to the result in [40, Thm. 5.2] stated for the nonstationary Navier-Stokes equations stabilized by local projection stabilization.

Theorem 5.1 (Error Representation for the Transport Problem)

Let $\{u, z\} \in \mathcal{X} \times \mathcal{X}$, $\{u_\tau, z_\tau\} \in \mathcal{X}_\tau^{\text{dG}(r)} \times \mathcal{X}_\tau^{\text{dG}(r)}$, and $\{u_{\tau h}, z_{\tau h}\} \in \mathcal{X}_{\tau h}^{\text{dG}(r), p} \times \mathcal{X}_{\tau h}^{\text{dG}(r), p}$ be stationary points of $\mathcal{L}, \mathcal{L}_\tau$, and $\mathcal{L}_{\tau h}$ on the different levels of discretization, i.e.,

$$\begin{aligned} \mathcal{L}'(u, z; \mathbf{v})(\delta u, \delta z) &= 0 \quad \forall \{\delta u, \delta z\} \in \mathcal{X} \times \mathcal{X}, \\ \mathcal{L}'_\tau(u_\tau, z_\tau; \mathbf{v}_\sigma)(\delta u_\tau, \delta z_\tau) &= 0 \quad \forall \{\delta u_\tau, \delta z_\tau\} \in \mathcal{X}_\tau^{\text{dG}(r)} \times \mathcal{X}_\tau^{\text{dG}(r)}, \\ \mathcal{L}'_{\tau h}(u_{\tau h}, z_{\tau h}; \mathbf{v}_{\sigma h})(\delta u_{\tau h}, \delta z_{\tau h}) &= 0 \quad \forall \{\delta u_{\tau h}, \delta z_{\tau h}\} \in \mathcal{X}_{\tau h}^{\text{dG}(r), p} \times \mathcal{X}_{\tau h}^{\text{dG}(r), p}. \end{aligned}$$

Additionally, there holds the Galerkin orthogonalities (5.23) and (5.36) for the error $e = u - u_\tau$ and $e = u_\tau - u_{\tau h}$, respectively. Then, there hold the following error

representation formulas for the discretization errors in space and time

$$\begin{aligned}
J(u) - J(u_\tau) &= \frac{1}{2}\rho(u_\tau; \mathbf{v})(z - \tilde{z}_\tau) + \frac{1}{2}\rho^*(u_\tau, z_\tau; \mathbf{v})(u - \tilde{u}_\tau) \\
&+ \frac{1}{2}\mathcal{D}'_\tau(u_\tau, z_\tau; \mathbf{v} - \mathbf{v}_\sigma)(\tilde{u}_\tau - u_\tau, \tilde{z}_\tau - z_\tau) \\
&+ \mathcal{D}_\tau(u_\tau, z_\tau; \mathbf{v} - \mathbf{v}_\sigma) + \mathcal{R}_\tau,
\end{aligned} \tag{5.62}$$

$$\begin{aligned}
J(u_\tau) - J(u_{\tau h}) &= \frac{1}{2}\rho_\tau(u_{\tau h}; \mathbf{v}_\sigma)(z_\tau - \tilde{z}_{\tau h}) + \frac{1}{2}\rho_\tau^*(u_{\tau h}, z_{\tau h}; \mathbf{v}_\sigma)(u_\tau - \tilde{u}_{\tau h}) \\
&+ \frac{1}{2}\mathcal{D}'_{\tau h}(u_{\tau h}, z_{\tau h}; \mathbf{v}_\sigma - \mathbf{v}_{\sigma h})(\tilde{u}_{\tau h} - u_{\tau h}, \tilde{z}_{\tau h} - z_{\tau h}) \\
&+ \mathcal{D}_{\tau h}(u_{\tau h}, z_{\tau h}; \mathbf{v}_\sigma - \mathbf{v}_{\sigma h}) + \mathcal{R}_h,
\end{aligned} \tag{5.63}$$

with

$$\begin{aligned}
\mathcal{D}_\tau(u_\tau, z_\tau; \mathbf{v} - \mathbf{v}_\sigma) &= \sum_{t_{\mathcal{F}} \in \mathcal{F}_\tau} ([u_\tau]_{t_{\mathcal{F}}}, z_\tau(t_{\mathcal{F}}^+)) \\
&- \sum_{n=1}^{N^\ell} \sum_{K_n \in \mathcal{T}_{\tau, n}} \int_{K_n} ((\mathbf{v} - \mathbf{v}_\sigma) \cdot \nabla u_\tau, z_\tau) dt, \\
\mathcal{D}_{\tau h}(u_{\tau h}, z_{\tau h}; \mathbf{v}_\sigma - \mathbf{v}_{\sigma h}) &= S_A(u_{\tau h}; \mathbf{v}_{\sigma h})(z_{\tau h}) \\
&- \sum_{n=1}^{N^\ell} \sum_{K_n \in \mathcal{T}_{\tau, n}} \int_{K_n} ((\mathbf{v}_\sigma - \mathbf{v}_{\sigma h}) \cdot \nabla u_{\tau h}, z_{\tau h}) dt,
\end{aligned} \tag{5.64}$$

and $\mathcal{D}'_\tau(\cdot, \cdot; \cdot)(\cdot, \cdot)$, $\mathcal{D}'_{\tau h}(\cdot, \cdot; \cdot)(\cdot, \cdot)$ denoting the the Gâteaux derivatives with respect to the first and second argument. Here, $\{\tilde{u}_\tau, \tilde{z}_\tau\} \in \mathcal{X}_\tau^{\text{dG}(r)} \times \mathcal{X}_\tau^{\text{dG}(r)}$, and $\{\tilde{u}_{\tau h}, \tilde{z}_{\tau h}\} \in \mathcal{X}_{\tau h}^{\text{dG}(r), p} \times \mathcal{X}_{\tau h}^{\text{dG}(r), p}$ can be chosen arbitrarily and the remainder terms \mathcal{R}_τ and \mathcal{R}_h have the same structure as the remainder term (5.60) in Lemma 5.1.

Proof. The proof is basically equal to that one of Thm. 4.1 given in Ch. 4. The difference comes through the coupling via the flow velocity field with regard to non-vanishing terms depending on the error in the approximation of this flow field within the respective Galerkin orthogonalities; cf. Rem. 5.5 and Rem. 5.6. Evaluating the Lagrangian functionals at the respective primal and dual solutions, there holds that (cf. Eq. (5.42) in Rem. 5.7)

$$J(u) = \mathcal{L}(u, z; \mathbf{v}), \quad J(u_\tau) = \mathcal{L}_\tau(u_\tau, z_\tau; \mathbf{v}_\sigma), \quad J(u_{\tau h}) = \mathcal{L}_{\tau h}(u_{\tau h}, z_{\tau h}; \mathbf{v}_{\sigma h}).$$

Thus, we get the following representation for the temporal and spatial error, respectively,

$$J(u) - J(u_\tau) = \mathcal{L}(u, z; \mathbf{v}) - \mathcal{L}_\tau(u_\tau, z_\tau; \mathbf{v}_\sigma), \quad (5.65a)$$

$$J(u_\tau) - J(u_{\tau h}) = \mathcal{L}_\tau(u_\tau, z_\tau; \mathbf{v}_\sigma) - \mathcal{L}_{\tau h}(u_{\tau h}, z_{\tau h}; \mathbf{v}_{\sigma h}). \quad (5.65b)$$

To prove the assertion (5.62) for the temporal error, we apply Lemma 5.1 with the identifications

$$L = \mathcal{L}, \quad \tilde{L} = \mathcal{L}_\tau, \quad \mathcal{W}_1 = \mathcal{X} \times \mathcal{X}, \quad \mathcal{W}_2 = \mathcal{X}_\tau^{\text{dG}(r)} \times \mathcal{X}_\tau^{\text{dG}(r)}$$

to the identity (5.65a). Further, we have to choose $\mathcal{W} := \mathcal{W}_1 + \mathcal{W}_2$ since here $\mathcal{X}_\tau^{\text{dG}(r)} \not\subseteq \mathcal{X}$. Thus, we have to verify condition (5.58), that now reads as $\mathcal{L}'(u, z; \mathbf{v})(u_\tau, z_\tau) = 0$, or equivalently,

$$\mathcal{L}'_u(u, z; \mathbf{v})(u_\tau) = 0 \quad \text{and} \quad \mathcal{L}'_z(u, z; \mathbf{v})(z_\tau) = 0. \quad (5.66)$$

We only give the proof of the second equation in (5.66). The first one can be proved analogously. To show that $\mathcal{L}'_z(u, z; \mathbf{v})(z_\tau) = 0$, we rewrite this equation building the Gâteaux derivative of its definition given by Eq. (5.39) as

$$G(z_\tau) - A(u; \mathbf{v})(z_\tau) = \int_I \{(g - \partial_t u, z_\tau) - a(u; \mathbf{v})(z_\tau)\} dt.$$

By construction, the continuous solution u satisfies that (cf. Eq. (5.6))

$$G(\varphi) - A(u; \mathbf{v})(\varphi) = \int_I \{(g - \partial_t u, \varphi) + a(u; \mathbf{v})(\varphi)\} dt = 0 \quad \forall \varphi \in \mathcal{X}. \quad (5.67)$$

By Corollary 2.1 we have that \mathcal{X} is dense in $L^2(I; X)$ with respect to the norm of $L^2(I; X)$, and since no time derivatives of φ arise in (5.67), this equation is also satisfied for all $\varphi \in L^2(I; X)$. The inclusion $z_\tau \in \mathcal{X}_\tau^{\text{dG}(r)} \subset L^2(I; X)$ then implies that the second equation in (5.66) is fulfilled. Now, applying Lemma 5.1 with the above made identifications yields

$$\begin{aligned} J(u) - J(u_\tau) &= \mathcal{L}(u, z; \mathbf{v}) - \mathcal{L}_\tau(u_\tau, z_\tau; \mathbf{v}_\sigma) \\ &= \frac{1}{2} \mathcal{L}'(u_\tau, z_\tau; \mathbf{v})(u - \tilde{u}_\tau, z - \tilde{z}_\tau) \\ &\quad + \frac{1}{2} (\mathcal{L} - \mathcal{L}_\tau)'(u_\tau, z_\tau; \mathbf{v} - \mathbf{v}_\sigma)(\tilde{u}_\tau - u_\tau, \tilde{z}_\tau - z_\tau) \\ &\quad + (\mathcal{L} - \mathcal{L}_\tau)(u_\tau, z_\tau; \mathbf{v} - \mathbf{v}_\sigma) + \mathcal{R}_\tau. \end{aligned} \quad (5.68)$$

With the definition of the primal and dual residuals based on the continuous schemes, given by the first two equations in (5.61) as well as taking into account the non-vanishing terms in Eq. (5.23) of Rem. 5.5, Eq. (5.68) can be rewritten as

$$\begin{aligned} J(u) - J(u_\tau) &= \frac{1}{2}\rho(u_\tau; \mathbf{v})(z - \tilde{z}_\tau) + \frac{1}{2}\rho^*(u_\tau, z_\tau; \mathbf{v})(u - \tilde{u}_\tau) \\ &\quad + \frac{1}{2}\mathcal{D}'_\tau(u_\tau, z_\tau; \mathbf{v} - \mathbf{v}_\sigma)(\tilde{u}_\tau - u_\tau, \tilde{z}_\tau - z_\tau) \\ &\quad + \mathcal{D}_\tau(u_\tau, z_\tau; \mathbf{v} - \mathbf{v}_\sigma) + \mathcal{R}_\tau, \end{aligned}$$

where the remainder term \mathcal{R}_τ is given by

$$\mathcal{R}_\tau = \frac{1}{2} \int_0^1 \mathcal{L}'''(u_\tau + se, z_\tau + se^*; \mathbf{v})(e, e, e, e^*, e^*, e^*)s(s-1) ds, \quad (5.69)$$

with the ‘primal’ and ‘dual’ errors $e := u - u_\tau$ and $e^* := z - z_\tau$, respectively. This proves the assertion (5.62).

To prove the spatial error representation (5.63), we apply Lemma 5.1 with the identifications

$$L = \mathcal{L}_\tau, \quad \tilde{L} = \mathcal{L}_{\tau h}, \quad \mathcal{W}_1 = \mathcal{X}_\tau^{\text{dG}(r)} \times \mathcal{X}_\tau^{\text{dG}(r)}, \quad \mathcal{W}_2 = \mathcal{X}_{\tau h}^{\text{dG}(r),p} \times \mathcal{X}_{\tau h}^{\text{dG}(r),p}$$

to Eq. (5.65b). In this case, we have $\mathcal{W}_2 \subseteq \mathcal{W}_1$ since $\mathcal{X}_{\tau h}^{\text{dG}(r),p} \subseteq \mathcal{X}_\tau^{\text{dG}(r)}$. Hence, we can choose $\mathcal{W} := \mathcal{W}_1$ in Lemma 5.1 and condition (5.58) is directly satisfied. Now, applying Lemma 5.1 with these identifications implies that

$$\begin{aligned} J(u_\tau) - J(u_{\tau h}) &= \mathcal{L}_\tau(u_\tau, z_\tau; \mathbf{v}_\sigma) - \mathcal{L}_{\tau h}(u_{\tau h}, z_{\tau h}; \mathbf{v}_{\sigma h}) \\ &= \frac{1}{2} \mathcal{L}'_\tau(u_{\tau h}, z_{\tau h}; \mathbf{v}_\sigma)(u_\tau - \tilde{u}_{\tau h}, z_\tau - \tilde{z}_{\tau h}) \\ &\quad + \frac{1}{2} (\mathcal{L}_\tau - \mathcal{L}_{\tau h})'(u_{\tau h}, z_{\tau h}; \mathbf{v}_\sigma - \mathbf{v}_{\sigma h})(\tilde{u}_{\tau h} - u_{\tau h}, \tilde{z}_{\tau h} - z_{\tau h}) \\ &\quad + (\mathcal{L}_\tau - \mathcal{L}_{\tau h})(u_{\tau h}, z_{\tau h}; \mathbf{v}_\sigma - \mathbf{v}_{\sigma h}) + \mathcal{R}_h. \end{aligned} \quad (5.70)$$

Again, using the definition of the primal and dual residuals this time based on the semi-discrete schemes, given by the last two equations in (5.61) as well as taking into account the non-vanishing terms in Eq. (5.36) of Rem. 5.6, Eq. (5.70) can be rewritten as

$$\begin{aligned} J(u_\tau) - J(u_{\tau h}) &= \frac{1}{2}\rho_\tau(u_{\tau h}; \mathbf{v}_\sigma)(z_\tau - \tilde{z}_{\tau h}) + \frac{1}{2}\rho_\tau^*(u_{\tau h}, z_{\tau h}; \mathbf{v}_\sigma)(u_\tau - \tilde{u}_{\tau h}) \\ &\quad + \frac{1}{2}\mathcal{D}'_{\tau h}(u_{\tau h}, z_{\tau h}; \mathbf{v}_\sigma - \mathbf{v}_{\sigma h})(\tilde{u}_{\tau h} - u_{\tau h}, \tilde{z}_{\tau h} - z_{\tau h}) \\ &\quad + \mathcal{D}_{\tau h}(u_{\tau h}, z_{\tau h}; \mathbf{v}_\sigma - \mathbf{v}_{\sigma h}) + \mathcal{R}_h, \end{aligned}$$

where the remainder term \mathcal{R}_h is given by

$$\mathcal{R}_h = \frac{1}{2} \int_0^1 \mathcal{L}'''_\tau(u_{\tau h} + se, z_{\tau h} + se^*; \mathbf{v}_\sigma)(e, e, e, e^*, e^*, e^*)s(s-1) ds, \quad (5.71)$$

with the ‘primal’ and ‘dual’ errors $e := u_\tau - u_{\tau h}$ and $e^* := z_\tau - z_{\tau h}$. This proves the assertion (5.63). For completeness, we state the explicit form of the Gâteaux derivatives $\mathcal{D}'_\tau(\cdot, \cdot; \cdot)(\cdot, \cdot)$ and $\mathcal{D}'_{\tau h}(\cdot, \cdot; \cdot)(\cdot, \cdot)$, respectively, given by

$$\begin{aligned}
& \mathcal{D}'_\tau(u_\tau, z_\tau; \mathbf{v} - \mathbf{v}_\sigma)(\tilde{u}_\tau - u_\tau, \tilde{z}_\tau - z_\tau) \\
&= \mathcal{D}'_{\tau, u}(u_\tau, z_\tau; \mathbf{v} - \mathbf{v}_\sigma)(\tilde{u}_\tau - u_\tau) + \mathcal{D}'_{\tau, z}(u_\tau, z_\tau; \mathbf{v} - \mathbf{v}_\sigma)(\tilde{z}_\tau - z_\tau) \\
&= \sum_{t_{\mathcal{F}} \in \mathcal{F}_\tau} ([\tilde{u}_\tau - u_\tau]_{t_{\mathcal{F}}}, z_\tau(t_{\mathcal{F}}^+)) \\
&\quad - \sum_{n=1}^{N^\ell} \sum_{K_n \in \mathcal{T}_{\tau, n}} \int_{K_n} ((\mathbf{v} - \mathbf{v}_\sigma) \cdot \nabla(\tilde{u}_\tau - u_\tau), z_\tau) dt \\
&\quad + \sum_{t_{\mathcal{F}} \in \mathcal{F}_\tau} ([u_\tau]_{t_{\mathcal{F}}}, \tilde{z}_\tau(t_{\mathcal{F}}^+) - z_\tau(t_{\mathcal{F}}^+)) \\
&\quad - \sum_{n=1}^{N^\ell} \sum_{K_n \in \mathcal{T}_{\tau, n}} \int_{K_n} ((\mathbf{v} - \mathbf{v}_\sigma) \cdot \nabla u_\tau, \tilde{z}_\tau - z_\tau) dt, \tag{5.72}
\end{aligned}$$

$$\begin{aligned}
& \mathcal{D}'_{\tau h}(u_{\tau h}, z_{\tau h}; \mathbf{v}_\sigma - \mathbf{v}_{\sigma h})(\tilde{u}_{\tau h} - u_{\tau h}, \tilde{z}_{\tau h} - z_{\tau h}) \\
&= \mathcal{D}'_{\tau h, u}(u_{\tau h}, z_{\tau h}; \mathbf{v}_\sigma - \mathbf{v}_{\sigma h})(\tilde{u}_{\tau h} - u_{\tau h}) + \mathcal{D}'_{\tau h, z}(u_{\tau h}, z_{\tau h}; \mathbf{v}_\sigma - \mathbf{v}_{\sigma h})(\tilde{z}_{\tau h} - z_{\tau h}) \\
&= S'_A(u_{\tau h}; \mathbf{v}_{\sigma h})(\tilde{u}_{\tau h} - u_{\tau h}, z_{\tau h}) \\
&\quad - \sum_{n=1}^{N^\ell} \sum_{K_n \in \mathcal{T}_{\tau, n}} \int_{K_n} ((\mathbf{v}_\sigma - \mathbf{v}_{\sigma h}) \cdot \nabla(\tilde{u}_{\tau h} - u_{\tau h}), z_{\tau h}) dt \\
&\quad + S_A(u_{\tau h}; \mathbf{v}_{\sigma h})(\tilde{z}_{\tau h} - z_{\tau h}) \\
&\quad - \sum_{n=1}^{N^\ell} \sum_{K_n \in \mathcal{T}_{\tau, n}} \int_{K_n} ((\mathbf{v}_\sigma - \mathbf{v}_{\sigma h}) \cdot \nabla u_{\tau h}, \tilde{z}_{\tau h} - z_{\tau h}) dt, \tag{5.73}
\end{aligned}$$

where we have used Def. 2.11, cf. also Rem. 2.6 and the stabilization terms $S_A(\cdot; \cdot)(\cdot)$ and $S'_A(\cdot; \cdot)(\cdot, \cdot)$ are given by Eq. (5.34) and Eq. (5.55), respectively. \square

5.2.2 An A Posteriori Error Estimator for the Stokes Flow Problem

In general, the derivation of an a posteriori error estimator for the time-dependent Stokes flow problem (5.31) is similar to the approach of the transport problem having regard to some slight modifications. The ideas and concepts are based on the work of Besier and Rannacher [40] as well as Schmich and Vexler [168], respectively, where LPS-stabilized Navier-Stokes equations and parabolic problems in general have been investigated. Consequently, we start with introducing the underlying Lagrangian

functionals to derive for one thing the dual flow problems and, for another thing, to present the splitted error representation formula for the Stokes flow problem.

As in the case of the transport problem, we first define the goal functional of the Stokes flow problem.

Assumption 5.3 (Goal Functional of Stokes Flow) *Let us assume $J : \mathcal{Y} \rightarrow \mathbb{R}$ to be a linear functional representing the goal quantity of physical interest. In general, this functional is given as*

$$J(\mathbf{u}) = \int_0^T J_1(\mathbf{u}(t))dt + J_2(\mathbf{u}(T)), \quad (5.74)$$

where $\mathbf{u} = \{\mathbf{v}, p\}$ and the single functionals $J_1 \in L^2(I; H^{-1}(\Omega)^d \times H^{-1}(\Omega))$ and $J_2 \in H^{-1}(\Omega)^d \times H^{-1}(\Omega)$ are three times differentiable functionals defining the dual right-hand side and the dual initial at time $t = T$, respectively, where each of them may be zero; cf. also Rem. 5.11.

Again, we separate the influences due to the discretization errors in space and time by splitting the a posteriori error representation with respect to J into the following contributions

$$J(\mathbf{u}) - J(\mathbf{u}_{\sigma h}) = J(\mathbf{u}) - J(\mathbf{u}_\sigma) + J(\mathbf{u}_\sigma) - J(\mathbf{u}_{\sigma h}). \quad (5.75)$$

To derive these representations we define the following Lagrangian functionals based on the Euler Lagrange method of constraint optimization as introduced in Sec. 2.5.

Definition 5.2 (Lagrangian Functionals of Stokes Flow) *With regard to the Stokes flow problem, the Lagrangian functionals $\mathcal{L} : \mathcal{Y} \times \mathcal{Y} \rightarrow \mathbb{R}$, $\mathcal{L}_\sigma : \mathcal{Y}_\sigma^{\text{dG}(r)} \times \mathcal{Y}_\sigma^{\text{dG}(r)} \rightarrow \mathbb{R}$, and $\mathcal{L}_{\sigma h} : \mathcal{Y}_{\sigma h}^{\text{dG}(r),p} \times \mathcal{Y}_{\sigma h}^{\text{dG}(r),p} \rightarrow \mathbb{R}$ are defined by*

$$\mathcal{L}(\mathbf{u}, \mathbf{z}) := J(\mathbf{u}) + F(\mathbf{w}) - B(\mathbf{u})(\mathbf{z}), \quad (5.76)$$

$$\begin{aligned} \mathcal{L}_\sigma(\mathbf{u}_\sigma, \mathbf{z}_\sigma) &:= J(\mathbf{u}_\sigma) + F(\mathbf{w}_\sigma) - B_\sigma(\mathbf{u}_\sigma)(\mathbf{z}_\sigma) \\ &= \mathcal{L}(\mathbf{u}_\sigma, \mathbf{z}_\sigma) - \sum_{t_{\mathcal{F}} \in \mathcal{F}_\sigma} ([\mathbf{v}_\sigma]_{t_{\mathcal{F}}}, \mathbf{w}_\sigma(t_{\mathcal{F}}^+)), \end{aligned} \quad (5.77)$$

$$\mathcal{L}_{\sigma h}(\mathbf{u}_{\sigma h}, \mathbf{z}_{\sigma h}) := \mathcal{L}_\sigma(\mathbf{u}_{\sigma h}, \mathbf{z}_{\sigma h}), \quad (5.78)$$

where \mathcal{F}_σ denotes the set of interior time points of the temporal mesh of the Stokes flow problem, defined by the second equation in (5.14).

Remark 5.10 *The Lagrange multipliers $\mathbf{z} = \{\mathbf{w}, q\}$, $\mathbf{z}_\sigma = \{\mathbf{w}_\sigma, q_\sigma\}$, and $\mathbf{z}_{\sigma h} = \{\mathbf{w}_{\sigma h}, q_{\sigma h}\}$ are called dual variables in contrast to the primal variables $\mathbf{u} = \{\mathbf{v}, p\}$, $\mathbf{u}_\sigma = \{\mathbf{v}_\sigma, p_\sigma\}$, and $\mathbf{u}_{\sigma h} = \{\mathbf{v}_{\sigma h}, p_{\sigma h}\}$ cf. [36, 40]. Furthermore, by using the respective Lagrangian functionals from above, we can express the functional values of the continuous, semi-discrete, and fully discrete solution by means of*

$$\begin{aligned} J(\mathbf{u}) &:= \mathcal{L}(\mathbf{u}, \boldsymbol{\varphi}) & \forall \boldsymbol{\varphi} = \{\boldsymbol{\psi}, \chi\} \in \mathcal{Y}, \\ J(\mathbf{u}_\sigma) &:= \mathcal{L}_\sigma(\mathbf{u}_\sigma, \boldsymbol{\varphi}_\sigma) & \forall \boldsymbol{\varphi}_\sigma = \{\boldsymbol{\psi}_\sigma, \chi_\sigma\} \in \mathcal{Y}_\sigma^{\text{dG}(r)}, \\ J(\mathbf{u}_{\sigma h}) &:= \mathcal{L}_{\sigma h}(\mathbf{u}_{\sigma h}, \boldsymbol{\varphi}_{\sigma h}) & \forall \boldsymbol{\varphi}_{\sigma h} = \{\boldsymbol{\psi}_{\sigma h}, \chi_{\sigma h}\} \in \mathcal{Y}_{\sigma h}^{\text{dG}(r),p}. \end{aligned} \quad (5.79)$$

5.2.2.1 Derivation of the Dual Schemes

As mentioned in the introductory Sec. 2.5, the DWR approach may be comprehended as a constraint optimization problem in terms of exploiting the Euler Lagrange method of constraint optimization. In this sense, we point out that the following optimality or stationary conditions, given by the directional derivatives of the Lagrangian functionals with respect to their second argument,

$$\begin{aligned} \mathcal{L}'_{\mathbf{z}}(\mathbf{u}, \mathbf{z})(\boldsymbol{\varphi}) &= 0 & \forall \boldsymbol{\varphi} \in \mathcal{Y}, \\ \mathcal{L}'_{\boldsymbol{\sigma}, \mathbf{z}}(\mathbf{u}_\sigma, \mathbf{z}_\sigma)(\boldsymbol{\varphi}_\sigma) &= 0 & \forall \boldsymbol{\varphi}_\sigma \in \mathcal{Y}_\sigma^{\text{dG}(r)}, \\ \mathcal{L}'_{\boldsymbol{\sigma}h, \mathbf{z}}(\mathbf{u}_{\sigma h}, \mathbf{z}_{\sigma h})(\boldsymbol{\varphi}_{\sigma h}) &= 0 & \forall \boldsymbol{\varphi}_{\sigma h} \in \mathcal{Y}_{\sigma h}^{\text{dG}(r),p}, \end{aligned} \quad (5.80)$$

can be identified with determining the continuous solutions \mathbf{u} of Eq. (5.10), the semi-discrete solutions \mathbf{u}_σ of the discontinuous time-discrete Stokes flow scheme, given by Eq. (5.24), and the fully discrete solution $\mathbf{u}_{\sigma h}$ of the fully discrete cG(p)-dG(r) Stokes flow scheme, given by Eq. (5.31), respectively. More precisely, in Eq. (5.80) the so-called Gâteaux derivatives are used, given by Def. 2.11 in Sec. 2.3. In order to enhance understanding, we recall here its definition, exemplary with respect to the second argument.

$$\mathcal{L}'_{\mathbf{z}}(\mathbf{u}, \mathbf{z})(\boldsymbol{\varphi}) := \lim_{t \neq 0, t \rightarrow 0} t^{-1} \{ \mathcal{L}(\mathbf{u}, \mathbf{z} + t\boldsymbol{\psi}) - \mathcal{L}(\mathbf{u}, \mathbf{z}) \}, \quad \boldsymbol{\varphi} \in \mathcal{Y}.$$

In contrast, considering the directional derivatives of the Lagrangian functionals with respect to their first argument leads to the dual problems, cf., e.g., [40], given by the following optimality or stationary conditions:

$$\begin{aligned} \mathcal{L}'_{\mathbf{u}}(\mathbf{u}, \mathbf{z})(\boldsymbol{\varphi}) &= 0 & \forall \boldsymbol{\varphi}, \chi \in \mathcal{Y}, \\ \mathcal{L}'_{\boldsymbol{\sigma}, \mathbf{u}}(\mathbf{u}_\sigma, \mathbf{z}_\sigma)(\boldsymbol{\varphi}_\sigma) &= 0 & \forall \boldsymbol{\varphi}_\sigma \in \mathcal{Y}_\sigma^{\text{dG}(r)}, \\ \mathcal{L}'_{\boldsymbol{\sigma}h, \mathbf{u}}(\mathbf{u}_{\sigma h}, \mathbf{z}_{\sigma h})(\boldsymbol{\varphi}_{\sigma h}) &= 0 & \forall \boldsymbol{\varphi}_{\sigma h} \in \mathcal{Y}_{\sigma h}^{\text{dG}(r),p}, \end{aligned} \quad (5.81)$$

More precisely, the continuous dual solution $\mathbf{z} = \{\mathbf{w}, q\} \in \mathcal{Y}$ fulfills the following problem.

Problem 5.12 (Dual Stokes Flow Problem)

Find $\mathbf{z} = \{\mathbf{w}, q\} \in \mathcal{Y}$ such that

$$B'(\mathbf{u})(\boldsymbol{\varphi}, \mathbf{z}) = J'(\mathbf{u})(\boldsymbol{\varphi}) \quad \forall \boldsymbol{\varphi} = \{\boldsymbol{\psi}, \chi\} \in \mathcal{Y}, \quad (5.82)$$

where the adjoint bilinear form $B'(\cdot)(\cdot, \cdot)$ is defined by

$$B'(\mathbf{u})(\boldsymbol{\varphi}, \mathbf{z}) := \int_I \{(\boldsymbol{\psi}, -\partial_t \mathbf{w}) + b'(\mathbf{u})(\boldsymbol{\varphi}, \mathbf{z})\} dt + (\boldsymbol{\psi}(T), \mathbf{w}(T)). \quad (5.83)$$

The right-hand side of Eq. (5.82) is given by

$$J'(\mathbf{u})(\boldsymbol{\varphi}) := \int_I J'_1(\mathbf{u})(\boldsymbol{\varphi}) dt + J'_2(\mathbf{u}(T))(\boldsymbol{\varphi}(T)). \quad (5.84)$$

Remark 5.11 Within the representation (5.83) of $B'(\cdot)(\cdot, \cdot)$ integration by parts in time is applied, given by

$$\int_I (\partial_t \boldsymbol{\psi}, \mathbf{w}) dt = \int_I (\boldsymbol{\psi}, -\partial_t \mathbf{w}) dt + (\boldsymbol{\psi}(T), \mathbf{w}(T)) - (\boldsymbol{\psi}(0), \mathbf{w}(0)),$$

which is allowed for weak solutions $\mathbf{z} \in \mathcal{Y}$; cf., e.g., [160, 187] and Thm. 2.2 in Sec. 2.1.2 of Ch. 2. Therefore, the dual solution can be thought of running backward in time. Furthermore, we note that right-hand side as well as initial or better final data at time $t = T$ are given by the goal functional (5.74). More precisely, J_1 defines the dual right-hand side, whereas J_2 defines the dual initial at time $t = T$. Then, as combination with the above introduced integration by parts in time there holds, cf. [160],

$$(\boldsymbol{\psi}(T), \mathbf{w}(T)) = J'_2(\mathbf{v}(T), p(T))(\boldsymbol{\psi}(T), \chi(T)).$$

Finally, the derivative $b'(\mathbf{u})(\boldsymbol{\varphi}, \mathbf{z})$ of the inner bilinear form $b(\mathbf{u})(\mathbf{z})$ in B' , defined by Eq. (5.13), admits the explicit form

$$b'(\mathbf{u})(\boldsymbol{\varphi}, \mathbf{z}) = \nu(\nabla \boldsymbol{\psi}, \nabla \mathbf{w}) - (\chi, \nabla \cdot \mathbf{w}) + (\nabla \cdot \boldsymbol{\psi}, q). \quad (5.85)$$

The second stationary condition of Eq. (5.81) yields the following dual semi-discrete discontinuous in time problem:

Problem 5.13 (Dual Discontinuous Time-Discrete Stokes Flow Scheme)

Find $\mathbf{z}_\sigma = \{\mathbf{w}_\sigma, q_\sigma\} \in \mathcal{Y}_\sigma^{\text{dG}(r)}$ such that

$$B'_\sigma(\mathbf{u}_\sigma)(\boldsymbol{\varphi}_\sigma, \mathbf{z}_\sigma) = J'(\mathbf{u}_\sigma)(\boldsymbol{\varphi}_\sigma) \quad \forall \boldsymbol{\varphi}_\sigma = \{\boldsymbol{\psi}_\sigma, \chi_\sigma\} \in \mathcal{Y}_\sigma^{\text{dG}(r)}, \quad (5.86)$$

where the adjoint bilinear form $B'_\sigma(\cdot)(\cdot, \cdot)$ is defined by

$$\begin{aligned} B'_\sigma(\mathbf{u}_\sigma)(\boldsymbol{\varphi}_\sigma, \mathbf{z}_\sigma) := & \sum_{n=1}^{N^{\text{F},\ell}} \sum_{K_n^{\text{F}} \in \mathcal{T}_{\sigma,n}} \int_{K_n^{\text{F}}} \{(\boldsymbol{\psi}_\sigma, -\partial_t \mathbf{w}_\sigma) + b'(\mathbf{u}_\sigma)(\boldsymbol{\varphi}_\sigma, \mathbf{z}_\sigma)\} dt \\ & - \sum_{t_{\mathcal{F}} \in \mathcal{F}_\sigma} (\boldsymbol{\psi}_\sigma(t_{\mathcal{F}}^-), [\mathbf{w}_\sigma]_{t_{\mathcal{F}}}) + (\boldsymbol{\psi}_\sigma(T^-), \mathbf{w}_\sigma(T^-)), \end{aligned} \quad (5.87)$$

with the dual inner bilinear form $b'(\cdot)(\cdot, \cdot)$ being defined by Eq. (5.85). The right-hand side of Eq. (5.86) is given by

$$J'(\mathbf{u}_\sigma)(\boldsymbol{\varphi}_\sigma) := \sum_{n=1}^{N^{\text{F},\ell}} \sum_{K_n^{\text{F}} \in \mathcal{T}_{\sigma,n}} \int_{K_n^{\text{F}}} J'_1(\mathbf{u}_\sigma)(\boldsymbol{\varphi}_\sigma) dt + J'_2(\mathbf{u}_\sigma(T^-))(\boldsymbol{\varphi}_\sigma(T^-)). \quad (5.88)$$

The third stationary condition of Eq. (5.81) yields the dual stabilized fully discrete discontinuous in time problem:

Problem 5.14 (Dual Fully-Discrete Stokes Flow Scheme: cG(p)-dG(r))

Find $\mathbf{z}_{\sigma h} = \{\mathbf{w}_{\sigma h}, q_{\sigma h}\} \in \mathcal{Y}_{\sigma h}^{\text{dG}(r),p}$ such that

$$B'_{\sigma h}(\mathbf{u}_{\sigma h})(\boldsymbol{\varphi}_{\sigma h}, \mathbf{z}_{\sigma h}) = J'(\mathbf{u}_{\sigma h})(\boldsymbol{\varphi}_{\sigma h}) \quad \forall \boldsymbol{\varphi}_{\sigma h} = \{\boldsymbol{\psi}_{\sigma h}, \chi_{\sigma h}\} \in \mathcal{Y}_{\sigma h}^{\text{dG}(r)}, \quad (5.89)$$

with $B_{\sigma h}(\cdot)(\cdot, \cdot) = B_\sigma(\cdot)(\cdot, \cdot)$ and $J'(\cdot)(\cdot)$ being defined in Eq. (5.87) and Eq. (5.88), respectively.

Remark 5.12 *The discrete dual problems decouple to a time stepping method running backward in time as given by Problem 5.13 and Problem 5.14, respectively, by using integration by parts in time; cf. [160, Lemma 8.9].*

5.2.2.2 Derivation of an A Posteriori Error Estimator

For the derivation of computable representations of the separated error contributions in space and time as indicated in Eq. (5.75) we use a well-known abstract result from [36].

Lemma 5.2 *Let \mathcal{W} be a function space and L be a three times Gâteaux differentiable functional on \mathcal{W} . We seek a stationary point w of L on \mathcal{W} , that is,*

$$L'(w)(\delta w) = 0 \quad \forall \delta w \in \mathcal{W}. \quad (5.90)$$

This equation is approximated by a Galerkin method using a finite-dimensional subspace $\mathcal{W}_0 \subseteq \mathcal{W}$. Hence, the discrete problem seeks $w_0 \in \mathcal{W}_0$ such that

$$L'(w_0)(\delta w_0) = 0 \quad \forall \delta w_0 \in \mathcal{W}_0. \quad (5.91)$$

Then we have for arbitrary $\tilde{w}_0 \in \mathcal{W}_0$ the error representation

$$L(w) - L(w_0) = \frac{1}{2}L'(w_0)(w - \tilde{w}_0) + \mathcal{R}, \quad (5.92)$$

where the remainder term \mathcal{R} is given in terms of $e := w - w_0$, as

$$\mathcal{R} = \int_0^1 L'''(w_0 + se)(e, e, e)s(s-1) ds. \quad (5.93)$$

Proof. The proof of Lemma 5.2 is given by setting $\tilde{L} := L$ within the proof of Lemma 4.1 in Sec. 4.2.2 of Ch. 4 and can be found, for instance, in [36, Prop. 2.1] or [20, Prop. 6.1], cf. also Rem. 4.8. \square

We apply the abstract error representation formula (5.92) to the Lagrangian functionals (5.76), (5.77) and (5.78), respectively, to derive an a posteriori error estimator for the Stokes flow problem in space and time. The idea of the proof goes back to the result in [168, Thm. 3.2], where it was stated for parabolic problems.

Before proceeding with the theorem, we introduce the primal and dual residuals based on the semi-discrete in time schemes by means of

$$\begin{aligned} \rho_\sigma(\mathbf{u})(\boldsymbol{\varphi}) &:= \mathcal{L}'_{\sigma, \mathbf{z}}(\mathbf{u}, \mathbf{z})(\boldsymbol{\varphi}) = F_\sigma(\boldsymbol{\psi}) - B_\sigma(\mathbf{u})(\boldsymbol{\varphi}), \\ \rho_\sigma^*(\mathbf{u}, \mathbf{z})(\boldsymbol{\varphi}) &:= \mathcal{L}'_{\sigma, \mathbf{u}}(\mathbf{u}, \mathbf{z})(\boldsymbol{\varphi}) = J'(\mathbf{u})(\boldsymbol{\varphi}) - B'_\sigma(\mathbf{u})(\boldsymbol{\varphi}, \mathbf{z}). \end{aligned} \quad (5.94)$$

By using Lemma 5.2 we get the following result for the DWR-based error representation in space and time for the Stokes flow problem.

Theorem 5.2 (Error Representation for the Stokes Flow Problem)

Let $\{\mathbf{u}, \mathbf{z}\} \in \mathcal{Y} \times \mathcal{Y}$, $\{\mathbf{u}_\sigma, \mathbf{z}_\sigma\} \in \mathcal{Y}_\sigma^{\text{dG}(r)} \times \mathcal{Y}_\sigma^{\text{dG}(r)}$, and $\{\mathbf{u}_{\sigma h}, \mathbf{z}_{\sigma h}\} \in \mathcal{Y}_{\sigma h}^{\text{dG}(r), p} \times \mathcal{Y}_{\sigma h}^{\text{dG}(r), p}$ be stationary points of $\mathcal{L}, \mathcal{L}_\sigma$, and $\mathcal{L}_{\sigma h}$ on the different levels of discretization, i.e.,

$$\begin{aligned} \mathcal{L}'(\mathbf{u}, \mathbf{z})(\delta \mathbf{u}, \delta \mathbf{z}) &= \mathcal{L}'_\sigma(\mathbf{u}, \mathbf{z})(\delta \mathbf{u}, \delta \mathbf{z}) = 0 \quad \forall \{\delta \mathbf{u}, \delta \mathbf{z}\} \in \mathcal{Y} \times \mathcal{Y}, \\ \mathcal{L}'_\sigma(\mathbf{u}_\sigma, \mathbf{z}_\sigma)(\delta \mathbf{u}_\sigma, \delta \mathbf{z}_\sigma) &= 0 \quad \forall \{\delta \mathbf{u}_\sigma, \delta \mathbf{z}_\sigma\} \in \mathcal{Y}_\sigma^{\text{dG}(r)} \times \mathcal{Y}_\sigma^{\text{dG}(r)}, \\ \mathcal{L}'_{\sigma h}(\mathbf{u}_{\sigma h}, \mathbf{z}_{\sigma h})(\delta \mathbf{u}_{\sigma h}, \delta \mathbf{z}_{\sigma h}) &= \mathcal{L}'_\sigma(\mathbf{u}_{\sigma h}, \mathbf{z}_{\sigma h})(\delta \mathbf{u}_{\sigma h}, \delta \mathbf{z}_{\sigma h}) \\ &= 0 \quad \forall \{\delta \mathbf{u}_{\sigma h}, \delta \mathbf{z}_{\sigma h}\} \in \mathcal{Y}_{\sigma h}^{\text{dG}(r), p} \times \mathcal{Y}_{\sigma h}^{\text{dG}(r), p}. \end{aligned}$$

Then, there hold the following error representation formulas for the discretization errors in space and time

$$J(\mathbf{u}) - J(\mathbf{u}_\sigma) = \frac{1}{2}\rho_\sigma(\mathbf{u}_\sigma)(\mathbf{z} - \tilde{\mathbf{z}}_\sigma) + \frac{1}{2}\rho_\sigma^*(\mathbf{u}_\sigma, \mathbf{z}_\sigma)(\mathbf{u} - \tilde{\mathbf{u}}_\sigma) + \mathcal{R}_\sigma, \quad (5.95)$$

$$\begin{aligned} J(\mathbf{u}_\sigma) - J(\mathbf{u}_{\sigma h}) &= \frac{1}{2}\rho_\sigma(\mathbf{u}_{\sigma h})(\mathbf{z}_\sigma - \tilde{\mathbf{z}}_{\sigma h}) + \frac{1}{2}\rho_\sigma^*(\mathbf{u}_{\sigma h}, \mathbf{z}_{\sigma h})(\mathbf{u}_\sigma - \tilde{\mathbf{u}}_{\sigma h}) \\ &+ \mathcal{R}_{\sigma h}. \end{aligned} \quad (5.96)$$

Here, $\{\tilde{\mathbf{u}}_\sigma, \tilde{\mathbf{z}}_\sigma\} \in \mathcal{Y}_\sigma^{\text{dG}(r)} \times \mathcal{Y}_\sigma^{\text{dG}(r)}$, and $\{\tilde{\mathbf{u}}_{\sigma h}, \tilde{\mathbf{z}}_{\sigma h}\} \in \mathcal{Y}_{\sigma h}^{\text{dG}(r),p} \times \mathcal{Y}_{\sigma h}^{\text{dG}(r),p}$ can be chosen arbitrarily and the remainder terms \mathcal{R}_σ and $\mathcal{R}_{\sigma h}$ have the same structure as the remainder term (5.93) in Lemma 5.2.

Proof. The proof is related to that one of Thm. 3.2 in [168]. It is basically equal to that one of Thm. 4.1 given in Ch. 4. The difference comes through the absence of stabilization terms and thus the equality of \mathcal{L}_σ and $\mathcal{L}_{\sigma h}$. Evaluating the Lagrangian functionals at the respective primal and dual solutions, there holds that (cf. Eq. (5.79) in Rem. 5.10)

$$\begin{aligned} J(\mathbf{u}) &= \mathcal{L}(\mathbf{u}, \mathbf{z}), \\ J(\mathbf{u}_\sigma) &= \mathcal{L}_\sigma(\mathbf{u}_\sigma, \mathbf{z}_\sigma), \\ J(\mathbf{u}_{\sigma h}) &= \mathcal{L}_{\sigma h}(\mathbf{u}_{\sigma h}, \mathbf{z}_{\sigma h}). \end{aligned}$$

Since the additional jump terms and the initial condition in \mathcal{L}_σ vanish for a continuous solution $\mathbf{u} = \{\mathbf{v}, p\} \in \mathcal{Y}$ and there holds $\mathcal{L}_\sigma = \mathcal{L}_{\sigma h}$ for a fully discrete solution $\mathbf{u}_{\sigma h} = \{\mathbf{v}_{\sigma h}, p_{\sigma h}\} \in \mathcal{Y}_{\sigma h}^{\text{dG}(r),p}$, we get the following representation for the temporal and spatial error, respectively,

$$\begin{aligned} J(\mathbf{u}) - J(\mathbf{u}_\sigma) &= \mathcal{L}(\mathbf{u}, \mathbf{z}) - \mathcal{L}_\sigma(\mathbf{u}_\sigma, \mathbf{z}_\sigma) \\ &= \mathcal{L}_\sigma(\mathbf{u}, \mathbf{z}) - \mathcal{L}_\sigma(\mathbf{u}_\sigma, \mathbf{z}_\sigma), \end{aligned} \quad (5.97a)$$

$$\begin{aligned} J(\mathbf{u}_\sigma) - J(\mathbf{u}_{\sigma h}) &= \mathcal{L}_\sigma(\mathbf{u}_\sigma, \mathbf{z}_\sigma) - \mathcal{L}_{\sigma h}(\mathbf{u}_{\sigma h}, \mathbf{z}_{\sigma h}) \\ &= \mathcal{L}_\sigma(\mathbf{u}_\sigma, \mathbf{z}_\sigma) - \mathcal{L}_\sigma(\mathbf{u}_{\sigma h}, \mathbf{z}_{\sigma h}). \end{aligned} \quad (5.97b)$$

To prove the assertion (5.95) for the temporal error, we apply Lemma 5.2 with the identifications

$$L = \mathcal{L}_\sigma, \quad \mathcal{W} = (\mathcal{Y} + \mathcal{Y}_\sigma^{\text{dG}(r)}) \times (\mathcal{Y} + \mathcal{Y}_\sigma^{\text{dG}(r)}), \quad \mathcal{W}_0 = \mathcal{Y}_\sigma^{\text{dG}(r)} \times \mathcal{Y}_\sigma^{\text{dG}(r)}$$

to the identity (5.97a). The above choice of \mathcal{W} is necessary since $\mathcal{Y}_\sigma^{\text{dG}(r)} \not\subseteq \mathcal{Y}$. Then, the validity of condition (5.90) can be shown by the same density argument as used

in the proof of Thm. 5.1 with the fact that \mathcal{Y} being dense in $L^2(I; H_0^1(\Omega)^d \times L_0^2(\Omega))$ given by Corollary 2.1 of Sec. 2.1.2 in Ch. 2. Now, applying Lemma 5.2 with the above made identifications yields that

$$\begin{aligned} J(\mathbf{u}) - J(\mathbf{u}_\sigma) &= \mathcal{L}_\sigma(\mathbf{u}, \mathbf{z}) - \mathcal{L}_\sigma(\mathbf{u}_\sigma, \mathbf{z}_\sigma) \\ &= \frac{1}{2} \mathcal{L}'_\sigma(\mathbf{u}_\sigma, \mathbf{z}_\sigma)(\mathbf{u} - \tilde{\mathbf{u}}_\sigma, \mathbf{z} - \tilde{\mathbf{z}}_\sigma) + \mathcal{R}_\sigma. \end{aligned} \quad (5.98)$$

With the definition of the primal and dual residuals based on the semi-discrete schemes, given by the equations in (5.94), Eq. (5.98) can be rewritten as

$$J(\mathbf{u}) - J(\mathbf{u}_\sigma) = \frac{1}{2} \rho_\sigma(\mathbf{u}_\sigma)(\mathbf{z} - \tilde{\mathbf{z}}_\sigma) + \frac{1}{2} \rho_\sigma^*(\mathbf{u}_\sigma, \mathbf{z}_\sigma)(\mathbf{u} - \tilde{\mathbf{u}}_\sigma) + \mathcal{R}_\sigma,$$

where the remainder term \mathcal{R}_σ is given by

$$\mathcal{R}_\sigma = \frac{1}{2} \int_0^1 \left\{ \mathcal{L}'''_\sigma(\mathbf{u}_\sigma + se_{\mathbf{u}}, \mathbf{z}_\sigma + se_{\mathbf{z}}^*)(e_{\mathbf{u}}, e_{\mathbf{u}}, e_{\mathbf{u}}, e_{\mathbf{z}}^*, e_{\mathbf{z}}^*, e_{\mathbf{z}}^*)s(s-1) \right\} ds, \quad (5.99)$$

with the ‘primal’ and ‘dual’ errors $e_{\mathbf{u}} := \mathbf{u} - \mathbf{u}_\sigma = \{\mathbf{v} - \mathbf{v}_\sigma, p - p_\sigma\}$ and $e_{\mathbf{z}}^* := \mathbf{z} - \mathbf{z}_\sigma = \{\mathbf{w} - \mathbf{w}_\sigma, q - q_\sigma\}$, respectively. This proves the assertion (5.95).

To prove the spatial error representation (5.96), we apply Lemma 5.2 with the identifications

$$L = \mathcal{L}_\sigma, \quad \mathcal{W} = \mathcal{Y}_\sigma^{\text{dG}(r)} \times \mathcal{Y}_\sigma^{\text{dG}(r)}, \quad \mathcal{W}_0 = \mathcal{Y}_{\sigma h}^{\text{dG}(r),p} \times \mathcal{Y}_{\sigma h}^{\text{dG}(r),p}$$

to Eq. (5.97b). In this case, we have $\mathcal{W}_0 \subseteq \mathcal{W}$ since $\mathcal{Y}_{\sigma h}^{\text{dG}(r),p} \subseteq \mathcal{Y}_\sigma^{\text{dG}(r)}$. Then, applying Lemma 5.2 with these identifications yields that

$$\begin{aligned} J(\mathbf{u}_\sigma) - J(\mathbf{u}_{\sigma h}) &= \mathcal{L}_\sigma(\mathbf{u}_\sigma, \mathbf{z}_\sigma) - \mathcal{L}_\sigma(\mathbf{u}_{\sigma h}, \mathbf{z}_{\sigma h}) \\ &= \frac{1}{2} \mathcal{L}'_\sigma(\mathbf{u}_{\sigma h}, \mathbf{z}_{\sigma h})(\mathbf{u}_\sigma - \tilde{\mathbf{u}}_{\sigma h}, \mathbf{z}_\sigma - \tilde{\mathbf{z}}_{\sigma h}) + \mathcal{R}_{\sigma h}. \end{aligned} \quad (5.100)$$

Again, using the definition of the primal and dual residuals based on the semi-discrete schemes given by the equations in (5.94), Eq. (5.100) can be rewritten as

$$J(\mathbf{u}_\sigma) - J(\mathbf{u}_{\sigma h}) = \frac{1}{2} \rho_\sigma(\mathbf{u}_{\sigma h})(\mathbf{z}_\sigma - \tilde{\mathbf{z}}_{\sigma h}) + \frac{1}{2} \rho_\sigma^*(\mathbf{u}_{\sigma h}, \mathbf{z}_{\sigma h})(\mathbf{u}_\sigma - \tilde{\mathbf{u}}_{\sigma h}) + \mathcal{R}_{\sigma h},$$

where the remainder term $\mathcal{R}_{\sigma h}$ is given by

$$\mathcal{R}_{\sigma h} = \frac{1}{2} \int_0^1 \left\{ \mathcal{L}'''_\sigma(\mathbf{u}_{\sigma h} + se_{\mathbf{u}}, \mathbf{z}_{\sigma h} + se_{\mathbf{z}}^*)(e_{\mathbf{u}}, e_{\mathbf{u}}, e_{\mathbf{u}}, e_{\mathbf{z}}^*, e_{\mathbf{z}}^*, e_{\mathbf{z}}^*)s(s-1) \right\} ds, \quad (5.101)$$

with the ‘primal’ and ‘dual’ errors $e_{\mathbf{u}} := \mathbf{u}_\sigma - \mathbf{u}_{\sigma h} = \{\mathbf{v}_\sigma - \mathbf{v}_{\sigma h}, p_\sigma - p_{\sigma h}\}$ and $e_{\mathbf{z}}^* := \mathbf{z}_\sigma - \mathbf{z}_{\sigma h} = \{\mathbf{w}_\sigma - \mathbf{w}_{\sigma h}, q_\sigma - q_{\sigma h}\}$, respectively. This proves the assertion (5.96). \square

Remark 5.13 *The above derived error representation formulas for the Stokes flow problem are based on a general goal functional in the form of Eq. (5.74) such that an error control independent of the transport problem is theoretically possible. In practice, however, especially for the case of the underlying model problem given by Prob. 5.1, one is primarily interested to control the transport problem under the condition that the influence of the error in the Stokes flow problem stays small. Here, the terms that account for this influence are given by the coupling terms in Eq. (5.64) within the error representation formulas (5.62) and (5.63), respectively, and may be interpreted as a modeling error; cf., for instance, [133]. In this case, the general right-hand side term in Eq. (5.86) within Problem 5.13 has to be modified by*

$$J'(\mathbf{u}_\sigma)(\varphi_\sigma) = \int_I (\mathbf{v} - \mathbf{v}_\sigma, u_\tau \cdot \nabla z_\tau) \, dt. \quad (5.102)$$

Likewise, for the dual fully discrete case the right-hand side term in Eq. (5.89) within Problem 5.14 has to be modified by

$$J'(\mathbf{u}_{\sigma h})(\varphi_{\sigma h}) = \int_I (\mathbf{v}_\sigma - \mathbf{v}_{\sigma h}, u_{\tau h} \cdot \nabla z_{\tau h}) \, dt. \quad (5.103)$$

5.3 Practical Aspects

In this section, we illustrate some useful aspects for the practical implementation of the adaptivity process used within the DWR framework for the specific class of coupled problems. Thereby, we present the formulation as time marching schemes for the transport and Stokes flow problem, respectively, derive localized forms of the error estimators for both problems on spatial and temporal cells, respectively, give insight into some implementational aspects regarding our multirate in time approach, and introduce the underlying adaptive space-time algorithm in different variations.

5.3.1 Representation as a Time Marching Scheme

As introduced in Sec. 2.2.2, the choice of a discontinuous time-discrete test space allows for rewriting the variational system as a time marching scheme (TMS). The representation as a TMS is helpful for the practical realization of the underlying problem by decoupling the original huge system into independent subproblems using so-called space-time slabs, cf. Sec. 4.4 and, in particular, Fig. 4.5 for more details. In the course of this, we recall the separation of the global space-time domain $Q = \Omega \times I$ into a partition of space-time slabs $Q_n = \mathcal{T}_{h,n} \times \mathcal{T}_{\tau,n}$, where $\mathcal{T}_{h,n}$ builds a triangulation

of the domain Ω and $\mathcal{T}_{\tau,n}$ builds a triangulation of the closure of the time subinterval \bar{I}_n , respectively.

Since the derivation was described explicitly in Sec. 4.3.1, we restrict ourselves to the final presentation of the time marching schemes (TMSs) here and reference to this section for more details. However, we recall the representation of the fully discrete discontinuous in time solutions given by

$$\begin{aligned} u_{\tau h}^{\text{dG}}|_{K \times K_n}(\mathbf{x}, t) &:= \sum_{\ell=0}^r u_h^{n,\ell}|_K(\mathbf{x}) \zeta_{n,\ell}(t), \\ \mathbf{v}_{\sigma h}^{\text{dG}}|_{K^{\text{F}} \times K_n^{\text{F}}}(\mathbf{x}, t) &:= \sum_{\ell=0}^r \mathbf{v}_h^{n,\ell}|_{K^{\text{F}}}(\mathbf{x}) \zeta_{n,\ell}(t), \\ p_{\sigma h}^{\text{dG}}|_{K^{\text{F}} \times K_n^{\text{F}}}(\mathbf{x}, t) &:= \sum_{\ell=0}^r p_h^{n,\ell}|_{K^{\text{F}}}(\mathbf{x}) \zeta_{n,\ell}(t), \end{aligned} \quad (5.104)$$

on an element $K \in \mathcal{T}_{h,n}$ or $K^{\text{F}} \in \mathcal{T}_{h,n}^{\text{F}}$, respectively, where $K_n \in \mathcal{T}_{\tau,n}$, $n = 1, \dots, N^\ell$, or $K_n^{\text{F}} \in \mathcal{T}_{\sigma,n}$, $n = 1, \dots, N^{\text{F},\ell}$, denotes the underlying cell in time. For more details we refer to Sec. 2.2 in Ch. 2. Here, we use the same notation as used in [128], where we also refer to for more details.

5.3.1.1 Time Marching Schemes for the Transport Problem

In the case of a discontinuous in time discretization, the TMS of the primal stabilized transport scheme given by Problem 5.8 has the following form:

Problem 5.15 (Primal stabilized TMS for the Transport Problem)

For a given $\mathbf{v}_{\sigma h} \in \mathcal{Y}_{\sigma h}^{\text{dG}(r),p}$ of Problem 5.7, represented in the form of the second equation in (5.104), find $u_{\tau h}^{\text{dG}}|_{K \times K_n} \in \mathcal{P}_\tau^r(K_n; H_h^{p_u, n})$, represented by the first equation in (5.104) with coefficients $u_h^{n,\ell}$, $\ell = 0, \dots, r$, such that

$$\begin{aligned} & \sum_{K_n \in \mathcal{T}_{\tau,n}} \sum_{\ell=0}^r \left\{ \alpha_{\kappa,\ell} \left(\sum_{K \in \mathcal{T}_{h,n}} ((u_h^{n,\ell}, \varphi_h)_K + \delta_K(u_h^{n,\ell}, \mathbf{v}_{\sigma h} \cdot \nabla \varphi_h)_K) \right) \right. \\ & \quad + \beta_{\kappa,\ell} \left(\sum_{K \in \mathcal{T}_{h,n}} ((\varepsilon \nabla u_h^{n,\ell}, \nabla \varphi_h)_K - \delta_K(\nabla \cdot (\varepsilon \nabla u_h^{n,\ell}), \mathbf{v}_{\sigma h} \cdot \nabla \varphi_h)_K) \right) \\ & \quad + \beta_{\kappa,\ell} \left(\sum_{K \in \mathcal{T}_{h,n}} ((\mathbf{v}_{\sigma h} \cdot \nabla u_h^{n,\ell}, \varphi_h)_K + \delta_K(\mathbf{v}_{\sigma h} \cdot \nabla u_h^{n,\ell}, \mathbf{v}_{\sigma h} \cdot \nabla \varphi_h)_K) \right) \\ & \quad \left. + \beta_{\kappa,\ell} \left(\sum_{K \in \mathcal{T}_{h,n}} ((\alpha u_h^{n,\ell}, \varphi_h)_K + \delta_K(\alpha u_h^{n,\ell}, \mathbf{v}_{\sigma h} \cdot \nabla \varphi_h)_K) \right) \right\} \\ & = \sum_{K_n \in \mathcal{T}_{\tau,n}} \sum_{\ell=0}^r \beta_{\kappa,\ell} \left(\sum_{K \in \mathcal{T}_{h,n}} ((g_h^{n,\ell}, \varphi_h)_K + \delta_K(g_h^{n,\ell}, \mathbf{v}_{\sigma h} \cdot \nabla \varphi_h)_K) \right) \\ & \quad + \gamma_\kappa \left(\sum_{K \in \mathcal{T}_{h,n}} ((u_{\tau h}^{\text{dG}}(t_{\mathcal{F},n_\ell}^-), \varphi_h)_K + (u_{\tau h}^{\text{dG}}(t_{\mathcal{F},n_\ell}^-), \mathbf{v}_{\sigma h} \cdot \nabla \varphi_h)_K) \right), \end{aligned} \quad (5.105)$$

for all $\varphi_h \in V_h^{p_u, n}$, for all $\kappa = 0, \dots, r$, and with

$$\begin{aligned}
\alpha_{\kappa, \iota} &:= (\zeta'_{n, \iota}(t), \zeta_{n, \kappa}(t))_{K_n} + \zeta_{n, \iota}(t_{\mathcal{F}, n_\ell}^+) \zeta_{n, \kappa}(t_{\mathcal{F}, n_\ell}^+) \\
&= \int_{\hat{I}} \hat{\zeta}'_\iota(\hat{t}) \hat{\zeta}_\kappa(\hat{t}) \, d\hat{t} + \hat{\zeta}_\iota(0) \hat{\zeta}_\kappa(0) = \sum_{\mu=0}^r \hat{w}_\mu \hat{\zeta}'_\iota(\hat{t}_\mu) \hat{\zeta}_\kappa(\hat{t}_\mu) + \hat{\zeta}_\iota(0) \hat{\zeta}_\kappa(0), \\
\beta_{\kappa, \iota} &:= (\zeta_{n, \iota}(t), \zeta_{n, \kappa}(t))_{K_n} = \int_{\hat{I}} \hat{\zeta}_\iota(\hat{t}) \hat{\zeta}_\kappa(\hat{t}) \tau_K \, d\hat{t} = \sum_{\mu=0}^r \tau_K \hat{w}_\mu \hat{\zeta}_\iota(\hat{t}_\mu) \hat{\zeta}_\kappa(\hat{t}_\mu), \\
\gamma_\kappa &:= \zeta_{n, \kappa}(t_{\mathcal{F}, n_\ell}^+) = \hat{\zeta}_\kappa(0),
\end{aligned} \tag{5.106}$$

where the reference basis functions in time $\hat{\zeta}_\iota(\cdot), \hat{\zeta}_\kappa(\cdot)$ are the standard Lagrange basis functions as introduced in Sec. 2.2.2, using quadrature weights \hat{w}_μ and quadrature points \hat{t}_μ from an $(r+1)$ -point Gauss quadrature rule on the reference cell in time $\hat{I} = [0, 1]$, denoted by $\hat{\mathcal{Q}}_{G(r+1)}$, with τ_K denoting the length of the cell in time K_n , and with

$$u_{\tau h}^{\text{dG}}(t_{\mathcal{F}, n_\ell}^-) := u_{\tau h}^{\text{dG}}|_{K_{n_\ell}}(t_{\mathcal{F}, n_\ell}^-), \tag{5.107}$$

by marching sequentially through all slabs $Q_n, n = 1, \dots, N^\ell$, where ℓ denotes the current DWR adaptivity loop. Here, K_{n_ℓ} denotes the left neighbor cell in time of K_n and $t_{\mathcal{F}, n_\ell}$ denotes the left end of K_n , respectively. For the case that K_n represents the first cell in time of the current slab Q_n , the left neighbor cell in time K_{n_ℓ} is given by the last cell in time of the previous slab Q_{n-1} , cf. Fig. 2.5 for an illustration. In particular, on the first cell in time of the first slab Q_1 the left-side trace $u_{\tau h}^{\text{dG}}(t_{\mathcal{F}, 1_\ell}^-)$ is given by the initial condition u_0 .

Remark 5.14 In general, the source term integral of the right-hand side cannot be evaluated exactly. Hence, we approximate this integral here by means of a numerical quadrature. Here, we replace the source term g by its appropriate Lagrange interpolant in time $g_\tau^{\text{dG}} \in \mathcal{X}_\tau^{\text{dG}(r)}$, such that $g_\tau^{\text{dG}}|_{K_n} \in \mathcal{P}_\tau^r(K_n; L^2(\Omega))$ is represented by

$$g_\tau^{\text{dG}}|_{K_n}(t) := \sum_{\iota=0}^r G_n^\iota \zeta_{n, \iota}(t), \quad G_n^\iota := g(t_{n, \iota}), \tag{5.108}$$

using the same basis functions $\zeta_{n, \iota}(\cdot) \in \mathcal{Y}_\tau^r$ and support points $t_{n, \iota}$ as introduced in Sec. 4.3.1.1. Finally, the time-independent coefficients G_n^ι of the Lagrange interpolants given by Eq. (5.108) are replaced in space by $g_h^{n, \iota}$, to the following fully discrete functions

$$g_{\tau h}^{\text{dG}}|_{K \times K_n}(\mathbf{x}, t) := \sum_{\iota=0}^r g_h^{n, \iota}|_K \zeta_{n, \iota}(t). \tag{5.109}$$

The TMS of the dual stabilized transport scheme given by Problem 5.11 has the following form, cf. Rem. 5.9:

Problem 5.16 (Dual stabilized TMS for the Transport Problem)

For a given $\mathbf{v}_{\sigma h} \in \mathcal{Y}_{\sigma h}^{\text{dG}(r),p}$ of Problem 5.7, represented in the form of the second equation in (5.104), find $z_{\tau h}^{\text{dG}}|_{K \times K_n} \in \mathcal{P}_\tau^r(K_n; H_h^{p_u, n})$, represented in the shape of the first equation in (5.104) with coefficients $z_h^{n,\iota}$, $\iota = 0, \dots, r$, such that

$$\begin{aligned}
& \sum_{K_n \in \mathcal{T}_{\tau,n}} \sum_{\iota=0}^r \left\{ \alpha_{\kappa,\iota} \left(\sum_{K \in \mathcal{T}_{h,n}} \left(-(\psi_h, \rho z_h^{n,\iota})_K + \delta_K(\mathbf{v}_{\sigma h} \cdot \nabla \psi_h, z_h^{n,\iota})_K \right) \right. \right. \\
& \quad + \beta_{\kappa,\iota} \left(\sum_{K \in \mathcal{T}_{h,n}} \left((\varepsilon \nabla \psi_h, \nabla z_h^{n,\iota})_K - \delta_K(\nabla \cdot (\varepsilon \nabla \psi_h), \mathbf{v}_{\sigma h} \cdot \nabla z_h^{n,\iota})_K \right) \right) \\
& \quad + \beta_{\kappa,\iota} \left(\sum_{K \in \mathcal{T}_{h,n}} \left((\mathbf{v}_{\sigma h} \cdot \nabla \psi_h, z_h^{n,\iota})_K + \delta_K(\mathbf{v}_{\sigma h} \cdot \nabla \psi_h, \mathbf{v}_{\sigma h} \cdot \nabla z_h^{n,\iota})_K \right) \right) \\
& \quad \left. + \beta_{\kappa,\iota} \left(\sum_{K \in \mathcal{T}_{h,n}} \left((\alpha \psi_h, z_h^{n,\iota})_K + \delta_K(\alpha \psi_h, \mathbf{v}_{\sigma h} \cdot \nabla z_h^{n,\iota})_K \right) \right) \right\} \\
& = \sum_{K_n \in \mathcal{T}_{\tau,n}} \sum_{\iota=0}^r \beta_{\kappa,\iota} \sum_{K \in \mathcal{T}_{h,n}} J_1'|_K(u_h^{n,\iota})(\psi_h) \\
& \quad + \gamma_\kappa \sum_{K \in \mathcal{T}_{h,n}} \left((\psi_h, z_{\tau h}^{\text{dG}}(t_{\mathcal{F},n}^+))_K - \delta_K(\mathbf{v}_{\sigma h} \cdot \nabla \psi_h, z_{\tau h}^{\text{dG}}(t_{\mathcal{F},n}^+))_K \right), \tag{5.110}
\end{aligned}$$

for all $\psi_h \in V_h^{p_u, n}$, and for all $\kappa = 0, \dots, r$, and with

$$\begin{aligned}
\alpha_{\kappa,\iota} & := (\zeta_{n,\kappa}(t), \zeta'_{n,\iota}(t))_{K_n} - \zeta_{n,\kappa}(t_{\mathcal{F},n}^-) (\zeta_{n,\iota}(t_{\mathcal{F},n}^-)) \\
& = \int_{\hat{I}} \hat{\zeta}_\kappa(\hat{t}) \hat{\zeta}'_\iota(\hat{t}) \, d\hat{t} - \hat{\zeta}_\kappa(1) \hat{\zeta}_\iota(1) = \sum_{\mu=0}^r \hat{w}_\mu \hat{\zeta}_\kappa(\hat{t}_\mu) \hat{\zeta}'_\iota(\hat{t}_\mu) - \hat{\zeta}_\kappa(1) \hat{\zeta}_\iota(1), \\
\beta_{\kappa,\iota} & := (\zeta_{n,\kappa}(t), \zeta_{n,\iota}(t))_{K_n} = \int_{\hat{I}} \hat{\zeta}_\kappa(\hat{t}) \hat{\zeta}_\iota(\hat{t}) \, \tau_K \, d\hat{t} = \sum_{\mu=0}^r \tau_K \hat{w}_\mu \hat{\zeta}_\kappa(\hat{t}_\mu) \hat{\zeta}_\iota(\hat{t}_\mu), \\
\gamma_\kappa & := \zeta_{n,\kappa}(t_{\mathcal{F},n}^-) = \hat{\zeta}_\kappa(1), \tag{5.111}
\end{aligned}$$

where the reference basis functions in time $\hat{\zeta}_\iota(\cdot)$, $\hat{\zeta}_\kappa(\cdot)$ are the standard Lagrange basis functions as introduced in Sec. 2.2.2, using quadrature weights \hat{w}_μ and quadrature points \hat{t}_μ from $\hat{\mathcal{Q}}_{G(r+1)}$, with τ_K denoting the length of the cell in time K_n , and with

$$z_{\tau h}^{\text{dG}}(t_{\mathcal{F},n}^+) := z_{\tau h}^{\text{dG}}|_{K_{n_r}}(t_{\mathcal{F},n}^+), \tag{5.112}$$

by marching sequentially through all slabs Q_n , $n = N^\ell, \dots, 1$. Here, K_{n_r} denotes the right neighbor cell in time of K_n and $t_{\mathcal{F},n}$ denotes the right end of K_n , respectively. For the case that K_n represents the last cell in time of the current slab Q_n , the right neighbor cell in time K_{n_r} is given by the first cell in time of the next slab Q_{n+1} ,

cf. Fig. 2.5 for an illustration. In particular, on the last cell in time of the last slab Q_N the right-side trace $z_{\tau_h}^{\text{dG}}(t_{\mathcal{F},N}^+)$ is given by the dual initial at time $t = T$, denoted by z_T and depending on the choice of the goal functional J or rather J_2 , cf. Rem.5.8.

5.3.1.2 Time Marching Schemes for the Stokes Flow Problem

The TMS of the primal discontinuous in time fully discrete Stokes flow scheme given by Problem 5.7 reads as

Problem 5.17 (Primal TMS for the Stokes Flow Problem)

Find the pairs $\{\mathbf{v}_{\sigma h}^{\text{dG}}|_{K^{\text{F}} \times K_n^{\text{F}}}, p_{\sigma h}^{\text{dG}}|_{K^{\text{F}} \times K_n^{\text{F}}}\} \in \mathcal{P}_\tau^r(K_n^{\text{F}}; H_h^{pv,n}) \times \mathcal{P}_\tau^r(K_n^{\text{F}}; L_h^{pp,n})$, represented in the shape of Eq. (5.104) with coefficients $\mathbf{v}_h^{m,\iota}, p_h^{n,\iota}, \iota = 0, \dots, r$, such that

$$\begin{aligned} & \sum_{K_n^{\text{F}} \in \mathcal{T}_{\sigma,n}} \sum_{\iota=0}^r \left\{ \alpha_{\kappa,\iota} \sum_{K^{\text{F}} \in \mathcal{T}_{h,n}^{\text{F}}} (\mathbf{v}_h^{m,\iota}, \boldsymbol{\psi}_h)_{K^{\text{F}}} \right. \\ & \left. + \beta_{\kappa,\iota} \sum_{K^{\text{F}} \in \mathcal{T}_{h,n}^{\text{F}}} (\nu(\nabla \mathbf{v}_h^{m,\iota}, \nabla \boldsymbol{\psi}_h)_{K^{\text{F}}} - (p_h^{m,\iota}, \nabla \cdot \boldsymbol{\psi}_h)_{K^{\text{F}}} + (\nabla \cdot \mathbf{v}_h^{m,\iota}, \chi_h)_{K^{\text{F}}}) \right\} \\ & = \sum_{K_n^{\text{F}} \in \mathcal{T}_{\sigma,n}} \sum_{\iota=0}^r \beta_{\kappa,\iota} \sum_{K^{\text{F}} \in \mathcal{T}_{h,n}^{\text{F}}} (\mathbf{f}_h^{m,\iota}, \boldsymbol{\psi}_h)_{K^{\text{F}}} + \gamma_\kappa \sum_{K^{\text{F}} \in \mathcal{T}_{h,n}^{\text{F}}} (\mathbf{v}_{\sigma h}^{\text{dG}}(t_{\mathcal{F},n_\ell}^-), \boldsymbol{\psi}_h)_{K^{\text{F}}}, \end{aligned} \quad (5.113)$$

for all $\{\boldsymbol{\psi}_h, \chi_h\} \in V_h^{pv,n} \times V_h^{pp,n}$, for all $\kappa = 0, \dots, r$, and with

$$\begin{aligned} \alpha_{\kappa,\iota} & := (\zeta'_{n,\iota}(t), \zeta_{n,\kappa}(t))_{K_n^{\text{F}}} + \zeta_{n,\iota}(t_{\mathcal{F},n_\ell}^+) \zeta_{n,\kappa}(t_{\mathcal{F},n_\ell}^+) \\ & = \int_{\hat{I}} \hat{\zeta}'_\iota(\hat{t}) \hat{\zeta}_\kappa(\hat{t}) \, d\hat{t} + \hat{\zeta}_\iota(0) \hat{\zeta}_\kappa(0) = \sum_{\mu=0}^r \hat{w}_\mu \hat{\zeta}'_\iota(\hat{t}_\mu) \hat{\zeta}_\kappa(\hat{t}_\mu) + \hat{\zeta}_\iota(0) \hat{\zeta}_\kappa(0), \\ \beta_{\kappa,\iota} & := (\zeta_{n,\iota}(t), \zeta_{n,\kappa}(t))_{K_n^{\text{F}}} = \int_{\hat{I}} \hat{\zeta}_\iota(\hat{t}) \hat{\zeta}_\kappa(\hat{t}) \, \sigma_K \, d\hat{t} = \sum_{\mu=0}^r \sigma_K \hat{w}_\mu \hat{\zeta}_\iota(\hat{t}_\mu) \hat{\zeta}_\kappa(\hat{t}_\mu), \\ \gamma_\kappa & := \zeta_{n,\kappa}(t_{\mathcal{F},n_\ell}^+) = \hat{\zeta}_\kappa(0), \end{aligned} \quad (5.114)$$

where the reference basis functions in time $\hat{\zeta}_\iota(\cdot), \hat{\zeta}_\kappa(\cdot)$ are the standard Lagrange basis functions as introduced in Sec. 2.2.2, using quadrature weights \hat{w}_μ and quadrature points \hat{t}_μ from an $(r+1)$ -point Gauss quadrature rule on the reference time cell \hat{I} , denoted by $\hat{Q}_{G(r+1)}$, with σ_K denoting the length of the cell in time K_n^{F} , and with

$$\mathbf{v}_{\sigma h}^{\text{dG}}(t_{\mathcal{F},n_\ell}^-) := \mathbf{v}_{\sigma h}^{\text{dG}}|_{K_{n_\ell}^{\text{F}}}(t_{\mathcal{F},n_\ell}^-), \quad (5.115)$$

by marching sequentially through all slabs $Q_n^{\text{F}}, n = 1, \dots, N^{\text{F},\ell}$, where ℓ denotes the current DWR adaptivity loop. Here, $K_{n_\ell}^{\text{F}}$ denotes the left neighbor cell in time of K_n^{F} and $t_{\mathcal{F},n_\ell}$ denotes the left end of K_n^{F} , respectively. For the case that K_n^{F} represents

the first cell in time of the current slab Q_n^F , the left neighbor cell in time $K_{n_\ell}^F$ is given by the last cell in time of the previous slab Q_{n-1}^F , cf. Fig. 2.5 for an illustration. In particular, on the first cell in time of the first slab Q_1^F the left-side trace $\mathbf{v}_{\sigma_h}^{\text{dG}}(t_{\mathcal{F},1}^-)$ is given by the initial condition \mathbf{v}_0 . Again, the source term integral of the right-hand side in Eq. (5.113) is handled in the same fashion as described in Rem. 5.14.

The TMS of the dual discontinuous in time fully discrete Stokes flow schemes given by Problem 5.14 has the following form, cf. Rem. 5.12.

Problem 5.18 (Dual TMS for the Stokes Flow Problem)

Find the pairs $\{\mathbf{w}_{\sigma_h}^{\text{dG}}|_{K^F \times K_n^F}, q_{\sigma_h}^{\text{dG}}|_{K^F \times K_n^F}\} \in \mathcal{P}_\tau^r(K_n^F; H_h^{pv,n}) \times \mathcal{P}_\tau^r(K_n^F; L_h^{pp,n})$, represented in the shape of Eq. (5.104) with coefficients $\mathbf{w}_h^{m,\ell}, q_h^{m,\ell}, \ell = 0, \dots, r$, such that

$$\begin{aligned} & \sum_{K_n \in \mathcal{T}_{\tau,n}} \sum_{\ell=0}^r \left\{ \alpha_{\kappa,\ell} \sum_{K \in \mathcal{T}_{h,n}} -(\boldsymbol{\psi}_h, \mathbf{w}_h^{m,\ell})_{K^F} \right. \\ & \left. + \beta_{\kappa,\ell} \sum_{K \in \mathcal{T}_{h,n}} \left(\nu(\nabla \boldsymbol{\psi}_h, \nabla \mathbf{w}_h^{m,\ell})_{K^F} - (\chi_h, \nabla \cdot \mathbf{w}_h^{m,\ell})_{K^F} + (\nabla \cdot \boldsymbol{\psi}_h, q_h^{m,\ell})_{K^F} \right) \right\} \\ & = \sum_{K_n^F \in \mathcal{T}_{\sigma,n}} \sum_{\ell=0}^r \beta_{\kappa,\ell} \sum_{K^F \in \mathcal{T}_{h,n}^F} J_1'|_{K^F}(\mathbf{u}_h^{n,\ell})(\boldsymbol{\varphi}_h) + \gamma_\kappa \sum_{K^F \in \mathcal{T}_{h,n}^F} ((\boldsymbol{\psi}_h, \mathbf{w}_{\sigma_h}^{\text{dG}}(t_{\mathcal{F},n}^+))_{K^F})_{K^F}, \end{aligned} \quad (5.116)$$

for all $\{\boldsymbol{\psi}_h, \chi_h\} \in V_h^{pv,n} \times V_h^{pp,n}$, for all $\kappa = 0, \dots, r$, and with

$$\begin{aligned} \alpha_{\kappa,\ell} & := (\zeta_{n,\kappa}(t), \zeta'_{n,\ell}(t))_{K_n^F} - \zeta_{n,\kappa}(t_{\mathcal{F},n}^-)(\zeta_{n,\ell}(t_{\mathcal{F},n}^-)) \\ & = \int_{\hat{I}} \hat{\zeta}_\kappa(\hat{t}) \hat{\zeta}'_\ell(\hat{t}) \, d\hat{t} - \hat{\zeta}_\kappa(1) \hat{\zeta}_\ell(1) = \sum_{\mu=0}^r \hat{w}_\mu \hat{\zeta}_\kappa(\hat{t}_\mu) \hat{\zeta}'_\ell(\hat{t}_\mu) - \hat{\zeta}_\kappa(1) \hat{\zeta}_\ell(1), \\ \beta_{\kappa,\ell} & := (\zeta_{n,\kappa}(t), \zeta_{n,\ell}(t))_{K_n^F} = \int_{\hat{I}} \hat{\zeta}_\kappa(\hat{t}) \hat{\zeta}_\ell(\hat{t}) \, \sigma_K \, d\hat{t} = \sum_{\mu=0}^r \sigma_K \hat{w}_\mu \hat{\zeta}_\kappa(\hat{t}_\mu) \hat{\zeta}_\ell(\hat{t}_\mu), \\ \gamma_\kappa & := \zeta_{n,\kappa}(t_{\mathcal{F},n}^-) = \hat{\zeta}_\kappa(1), \end{aligned} \quad (5.117)$$

where the reference basis functions in time $\hat{\zeta}_\ell(\cdot), \hat{\zeta}_\kappa(\cdot)$ are the standard Lagrange basis functions as introduced in Sec. 2.2.2, using quadrature weights \hat{w}_μ and quadrature points \hat{t}_μ from $\hat{Q}_{G(r+1)}$, with σ_K denoting the length of the cell in time K_n^F , and with

$$\mathbf{w}_{\sigma_h}^{\text{dG}}(t_{\mathcal{F},n}^+) := \mathbf{w}_{\sigma_h}^{\text{dG}}|_{K_{n_r}^F}(t_{\mathcal{F},n}^+), \quad (5.118)$$

by marching sequentially through all slabs $Q_n^F, n = N^{F,\ell}, \dots, 1$. Here, $K_{n_r}^F$ denotes the right neighbor cell in time of K_n^F and $t_{\mathcal{F},n}$ denotes the right end of K_n^F , respectively. For the case that K_n^F represents the last cell in time of the current slab Q_n^F , the right neighbor cell in time $K_{n_r}^F$ is given by the first cell in time of the next slab Q_{n+1}^F ,

cf. Fig. 2.5 for an illustration. In particular, on the last cell in time of the last slab Q_N^F the right-side trace $\mathbf{w}_{\sigma h}^{\text{dG}}(t_{\mathcal{F},N}^+)$ is given by the dual initial at time $t = T$, denoted by \mathbf{w}_T and depending on the choice of the goal functional J or rather J_2 , cf. Rem.5.11.

5.3.2 Localization and Evaluation of the Error Estimators

The error representation formulas derived in Sec. 5.2 lead to temporal and spatial a posteriori error estimators for the transport and for the Stokes flow problem, respectively. These estimators serve for one thing as a quantitative estimation of the discretization error within the user-chosen goal quantity J and, for another thing, as indicators for the adaptive mesh refinement process in space and time. For the latter case, we present a localized form of the error representation formulas for the transport and Stokes flow problem as obtained in Thm. 5.1 and Thm. 5.2, respectively, that are used as error indicators within the practical realization of the adaptive mesh refinement process.

5.3.2.1 Localized Error Indicators of the Transport Problem

Neglecting the remainder terms in the error representation formulas of the transport problem given by Eqs. (5.62)–(5.63) in Theorem 5.1, we get the following approximations in space and time:

$$\begin{aligned}
J(u) - J(u_\tau) &\approx \frac{1}{2}\rho(u_\tau; \mathbf{v})(z - \tilde{z}_\tau) + \frac{1}{2}\rho^*(u_\tau, z_\tau; \mathbf{v})(u - \tilde{u}_\tau) \\
&\quad + \frac{1}{2}\mathcal{D}'_\tau(u_\tau, z_\tau; \mathbf{v} - \mathbf{v}_\sigma)(\tilde{u}_\tau - u_\tau, \tilde{z}_\tau - z_\tau) \\
&\quad + \mathcal{D}_\tau(u_\tau, z_\tau; \mathbf{v} - \mathbf{v}_\sigma) \\
&=: \eta_\tau = \sum_{n=1}^N \eta_\tau^n, \\
J(u_\tau) - J(u_{\tau h}) &\approx \frac{1}{2}\rho_\tau(u_{\tau h}; \mathbf{v}_{\sigma h})(z_\tau - \tilde{z}_{\tau h}) + \frac{1}{2}\rho_\tau^*(u_{\tau h}, z_{\tau h}; \mathbf{v}_{\sigma h})(u_\tau - \tilde{u}_{\tau h}) \\
&\quad + \frac{1}{2}\mathcal{D}'_{\tau h}(u_{\tau h}, z_{\tau h}; \mathbf{v}_\sigma - \mathbf{v}_{\sigma h})(\tilde{u}_{\tau h} - u_{\tau h}, \tilde{z}_{\tau h} - z_{\tau h}) \\
&\quad + \mathcal{D}_{\tau h}(u_{\tau h}, z_{\tau h}; \mathbf{v}_\sigma - \mathbf{v}_{\sigma h}) \\
&=: \eta_h = \sum_{n=1}^N \eta_h^n.
\end{aligned} \tag{5.119}$$

Assumption 5.4 *To simplify notation while presenting a localized form of the error indicators in time η_τ^n and space η_h^n , respectively, we make the following assumptions.*

- We assume that $J_2(\cdot) = 0$ and that $J_1(\cdot)$ is given by $J_1(u(t)) := (\psi(t), j(t))$ or rather $J_1(u(t))(\psi(t)) = (\psi(t), j(t))$ for some density function $j \in L^2(I; L^2(\Omega))$, cf. Eq. (5.37).
- We only present the localized form of the residuals in (5.119) and leave all other terms untouched.

Thus, the local error indicators in time η_τ^n and space η_h^n , respectively, with regard to a single slab $Q_n = \mathcal{T}_{h,n} \times \mathcal{T}_{\tau,n}$, $n = 1, \dots, N^\ell$, are given by

$$\begin{aligned} \eta_\tau^n &= \frac{1}{2} \sum_{K_n \in \mathcal{T}_{\tau,n}} \int_{K_n} \sum_{K \in \mathcal{T}_{h,n}} \left\{ (R(u_\tau; \mathbf{v}), z - \tilde{z}_\tau)_K - (E(u_\tau), z - \tilde{z}_\tau)_{\partial K} \right\} dt \\ &+ \frac{1}{2} \sum_{K_n \in \mathcal{T}_{\tau,n}} \int_{K_n} \sum_{K \in \mathcal{T}_{h,n}} \left\{ (u - \tilde{u}_\tau, R^*(z_\tau; \mathbf{v}))_K - (u - \tilde{u}_\tau, E^*(z_\tau))_{\partial K} \right\} dt \\ &+ \frac{1}{2} \mathcal{D}'_\tau(u_\tau, z_\tau; \mathbf{v} - \mathbf{v}_\sigma)(\tilde{u}_\tau - u_\tau, \tilde{z}_\tau - z_\tau) + \mathcal{D}_\tau(u_\tau, z_\tau; \mathbf{v} - \mathbf{v}_\sigma), \end{aligned} \quad (5.120)$$

where \mathcal{D}_τ and \mathcal{D}'_τ are given by the first equation of Eq. (5.64) and Eq. (5.72), respectively, having regard to its respective localized form, and

$$\begin{aligned} \eta_h^n &= \frac{1}{2} \sum_{K_n \in \mathcal{T}_{\tau,n}} \int_{K_n} \sum_{K \in \mathcal{T}_{h,n}} \left\{ (R(u_{\tau h}; \mathbf{v}_\sigma), z_\tau - \tilde{z}_{\tau h})_K - (E(u_{\tau h}), z_\tau - \tilde{z}_{\tau h})_{\partial K} \right\} dt \\ &- \sum_{t_{\mathcal{F}} \in \mathcal{F}_{\tau,n}} \sum_{K \in \mathcal{T}_{h,n}} \left([u_{\tau h}]_{t_{\mathcal{F},n_\ell}}, z_\tau(t_{\mathcal{F},n_\ell}^+) - \tilde{z}_{\tau h}(t_{\mathcal{F},n_\ell}^+) \right)_K \\ &+ \frac{1}{2} \sum_{K_n \in \mathcal{T}_{\tau,n}} \int_{K_n} \sum_{K \in \mathcal{T}_{h,n}} \left\{ (u_\tau - \tilde{u}_{\tau h}, R^*(z_{\tau h}; \mathbf{v}_\sigma) - (u_\tau - \tilde{u}_{\tau h}, E^*(z_{\tau h}))_{\partial K} \right\} dt \\ &+ \sum_{t_{\mathcal{F}} \in \mathcal{F}_{\tau,n}} \sum_{K \in \mathcal{T}_{h,n}} (u_\tau(t_{\mathcal{F},n}^-) - \tilde{u}_{\tau h}(t_{\mathcal{F},n}^-), [z_{\tau h}]_{t_{\mathcal{F},n}})_K \\ &+ \frac{1}{2} \mathcal{D}'_{\tau h}(u_{\tau h}, z_{\tau h}; \mathbf{v}_\sigma - \mathbf{v}_{\sigma h})(\tilde{u}_{\tau h} - u_{\tau h}, \tilde{z}_{\tau h} - z_{\tau h}) \\ &+ \mathcal{D}_{\tau h}(u_{\tau h}, z_{\tau h}; \mathbf{v}_\sigma - \mathbf{v}_{\sigma h}), \end{aligned} \quad (5.121)$$

where $\mathcal{D}_{\tau h}$ and $\mathcal{D}'_{\tau h}$ are given by the second equation of Eq. (5.64) and Eq. (5.73), respectively, having regard to its respective localized form. The cell and edge residuals $R(\cdot; \cdot)$, $R^*(\cdot; \cdot)$ and $E(\cdot)$, $E^*(\cdot)$, respectively, are given by

$$R(u; \mathbf{v})|_K := g - \rho \partial_t u + \nabla \cdot (\varepsilon \nabla u) - \mathbf{v} \cdot \nabla u - \alpha u, \quad (5.122)$$

$$R^*(z; \mathbf{v})|_K := j + \rho \partial_t z + \nabla \cdot (\varepsilon \nabla z) + \mathbf{v} \cdot \nabla z - \alpha z, \quad (5.123)$$

$$E(u)|_\Gamma := \begin{cases} \frac{1}{2} \mathbf{n} \cdot [\varepsilon \nabla u] & \text{if } \Gamma \subset \partial K \setminus \partial \Omega, \\ 0 & \text{if } \Gamma \subset \partial \Omega, \end{cases} \quad (5.124)$$

$$E^*(z)|_\Gamma := \begin{cases} \frac{1}{2} \mathbf{n} \cdot [\varepsilon \nabla z] & \text{if } \Gamma \subset \partial K \setminus \partial \Omega, \\ 0 & \text{if } \Gamma \subset \partial \Omega, \end{cases} \quad (5.125)$$

with $[\nabla\varphi] := \nabla\varphi|_{\Gamma\cap K} - \nabla\varphi|_{\Gamma\cap K'}$ denoting the spatial jump of $\nabla\varphi$ over the inner edges Γ with normal unit vector \mathbf{n} pointing from cell K to K' . Here, $\mathcal{F}_{\tau,n}$ denotes the set of interior time points corresponding to slab Q_n with $t_{\mathcal{F},n_\ell}$ and $t_{\mathcal{F},n}$ denoting the left and right end of the cell in time K_n , respectively.

Remark 5.15 *Let us remark some aspects about the error indicators.*

- *The additional terms including the spatial edge terms $E(\cdot), E^*(\cdot)$ appear applying integration by parts on each spatial cell $K \in \mathcal{T}_{h,n}, n = 1, \dots, N^\ell$, to the second order terms of the primal or dual residual, respectively; cf., e.g., [20, Ch. 3].*
- *For the case of nonhomogeneous Dirichlet and Neumann boundary conditions we refer to Rem. 4.14.*
- *With regard to neglecting the remainder terms in (5.120) and (5.121), respectively, we refer to the first note in Rem. 4.11 and [20, Rem. 6.5].*
- *In the case of a non-vanishing goal functional $J_2(\cdot)$, an additional sum in the form*

$$\begin{aligned} & \sum_{K \in \mathcal{T}_{h,N}} J'_2|_K(u_\tau(T^-))(u(T^-) - \tilde{u}_\tau(T^-)), \\ & \sum_{K \in \mathcal{T}_{h,N}} J'_2|_K(u_{\tau h}(T^-))(u_\tau(T^-) - \tilde{u}_{\tau h}(T^-)), \end{aligned}$$

has to be added within the computation on the last cell in time of the last slab Q_N in Eq. (5.120) and Eq. (5.121), respectively. Obviously, this means that the final condition z_T does not vanish in this case.

So far, the localized forms of the temporal and spatial error indicators given by Eq. (5.120) and Eq. (5.121), respectively, include solutions and integrals that have to be approximated for a practical realization. In view of this, the numerical evaluation of the temporal and spatial error indicators is performed in the following fashion.

Assumption 5.5 (Approximation Techniques) *For a practical computation of the local error indicators given by Eq. (5.120) and Eq. (5.121), respectively, we introduce the following possibilities.*

- *Approximate the temporal weights $u - \tilde{u}_\tau$ and $z - \tilde{z}_\tau$, respectively, occurring in Eq. (5.120), by means of a higher-order extrapolation or finite elements approach, exemplary given by*

$$\begin{aligned} u - \tilde{u}_\tau &\approx \mathbf{E}_\tau^{r+1} u_\tau - u_\tau, \\ u - \tilde{u}_\tau &\approx u_\tau - \mathbf{R}_\tau^r u_\tau, \end{aligned} \tag{5.126}$$

using an extrapolation in time operator \mathbf{E}_τ^{r+1} or a restriction in time operator \mathbf{R}_τ^r , respectively, as introduced in Sec. 4.3.2.2. Note that within the higher-order finite elements approach the discrete dual solution z_τ has to be solved in a space $\mathcal{X}_\tau^{\text{dG}(s)}$, $s > r$, as given by Eq. (5.15).

- Approximate the spatial weights $u_\tau - \tilde{u}_{\tau h}$ and $z_\tau - \tilde{z}_{\tau h}$, respectively, occurring in Eq. (5.121), by means of a patch-wise higher-order interpolation or higher-order finite elements approach, exemplary given by

$$\begin{aligned} u_\tau - \tilde{u}_{\tau h} &\approx \mathbf{I}_{2h}^{(2p)} u_{\tau h} - u_{\tau h}, \\ u_\tau - \tilde{u}_{\tau h} &\approx u_{\tau h} - \mathbf{R}_h^p u_{\tau h}, \end{aligned} \tag{5.127}$$

using an interpolation in space operator $\mathbf{I}_{2h}^{(2p)}$ or a restriction in space operator \mathbf{R}_h^p , respectively, as introduced in Sec. 3.3.1. Note that within the higher-order finite elements approach the discrete dual solution $z_{\tau h}$ has to be solved in a space $\mathcal{X}_{\tau h}^{\text{dG}(r),q}$, $q > p$, as given by Eq. (5.27).

- Approximate the temporal velocity difference $\mathbf{v} - \mathbf{v}_\sigma$ within the coupling terms, occurring in Eq. (5.120), by one of the techniques used for the temporal weights given by

$$\begin{aligned} \mathbf{v} - \mathbf{v}_\sigma &\approx \mathbf{E}_\tau^{r+1} \mathbf{v}_\sigma - \mathbf{v}_\sigma, \\ \mathbf{v} - \mathbf{v}_\sigma &\approx \mathbf{v}_\sigma - \mathbf{R}_\tau^r \mathbf{v}_\sigma, \end{aligned} \tag{5.128}$$

with \mathbf{E}_τ^{r+1} and \mathbf{R}_τ^r acting componentwise like $\mathbf{E}_\tau^{(r+1)}$ and \mathbf{R}_τ^r , respectively.

- Approximate the spatial velocity difference $\mathbf{v}_\sigma - \mathbf{v}_{\sigma h}$ within the coupling terms, occurring in Eq. (5.121), by one of the techniques used for the spatial weights given by

$$\begin{aligned} \mathbf{v}_\sigma - \mathbf{v}_{\sigma h} &\approx \mathbf{I}_{2h}^{(2p)} \mathbf{v}_{\sigma h} - \mathbf{v}_{\sigma h}, \\ \mathbf{v}_\sigma - \mathbf{v}_{\sigma h} &\approx \mathbf{v}_{\sigma h} - \mathbf{R}_h^p \mathbf{v}_{\sigma h}, \end{aligned} \tag{5.129}$$

with $\mathbf{I}_{2h}^{(2p)}$ and \mathbf{R}_h^p acting componentwise like $\mathbf{I}_{2h}^{(2p)}$ and \mathbf{R}_h^p , respectively. Note that the solution transfer of the fully discrete solution $\mathbf{v}_{\sigma h}$ to the meshes used for the transport problem is handled by a precasted function within `deal.II` called `interpolate_to_different_mesh()`, cf. Sec. 5.3.3 for further information.

- Approximate the integrals in time by means of an appropriate quadrature rule depending on the approximation approach used for the temporal weights. More precisely, the integrals in time are evaluated numerically by using an $(r+2)$ -point

Gauss-Lobatto quadrature rule for the approximation case hoEx-G, an $(r + 1)$ -point Gauss quadrature rule for the case hoEx-GL, and an $(r + 2)$ -point Gauss quadrature rule for the case hoFE, respectively, cf. Sec. 4.3.2.2 for more details.

- Replace all unknown solutions occurring either in the residuals, weights or in the coupling depending terms by the computed fully discrete solutions $u_{\tau h}$, $z_{\tau h}$ and $\mathbf{v}_{\sigma h}$, respectively, cf. also Rem. 4.13.

5.3.2.2 Localized Error Indicators of the Stokes Flow Problem

The derivation of local error indicators for the Stokes flow problem is rather similar to the transport problem, although less complex due to missing stabilization and coupling terms. Again, neglecting the remainder terms in the error representation formulas of the Stokes flow problem given by Eqs. (5.95)–(5.96) in Theorem 5.2, we get the following approximations in space and time:

$$\begin{aligned}
J(\mathbf{u}) - J(\mathbf{u}_\sigma) &\approx \frac{1}{2}\rho_\sigma(\mathbf{u}_\sigma)(\mathbf{z} - \tilde{\mathbf{z}}_\sigma) + \frac{1}{2}\rho_\sigma^*(\mathbf{u}_\sigma, \mathbf{z}_\sigma)(\mathbf{u} - \tilde{\mathbf{u}}_\sigma) \\
&=: \eta_\sigma^F = \sum_{n=1}^{N^{F,\ell}} \eta_\sigma^{F,n}. \\
J(\mathbf{u}_\sigma) - J(\mathbf{u}_{\sigma h}) &\approx \frac{1}{2}\rho_\sigma(\mathbf{u}_{\sigma h})(\mathbf{z}_\sigma - \tilde{\mathbf{z}}_{\sigma h}) + \frac{1}{2}\rho_\sigma^*(\mathbf{u}_{\sigma h}, \mathbf{z}_{\sigma h})(\mathbf{u}_\sigma - \tilde{\mathbf{u}}_{\sigma h}) \\
&=: \eta_h^F = \sum_{n=1}^{N^{F,\ell}} \eta_h^{F,n}.
\end{aligned} \tag{5.130}$$

Maintaining the same restrictions as in Assumption 5.4, the local error indicators in time $\eta_\sigma^{F,n}$ and space $\eta_h^{F,n}$, respectively, with regard to a single slab $Q_n^F = \mathcal{T}_{h,n}^F \times \mathcal{T}_{\sigma,n}$, $n = 1, \dots, N^{F,\ell}$, are given by

$$\begin{aligned}
\eta_\sigma^{F,n} &= \frac{1}{2} \sum_{K_n^F \in \mathcal{T}_{\sigma,n}} \int_{K_n^F} \sum_{K^F \in \mathcal{T}_{h,n}^F} \left\{ (\mathbf{R}(\mathbf{u}_\sigma), \mathbf{w} - \tilde{\mathbf{w}}_\sigma)_{K^F} \right. \\
&\quad \left. - (\nabla \cdot \mathbf{v}_\sigma, q - \tilde{q}_\sigma)_{K^F} - (\mathbf{E}(\mathbf{u}_\sigma), \mathbf{w} - \tilde{\mathbf{w}}_\sigma)_{\partial K^F} \right\} dt \\
&\quad - \sum_{t_{\mathcal{F},n_\ell} \in \mathcal{F}_{\sigma,n}} \sum_{K^F \in \mathcal{T}_{h,n}^F} ([\mathbf{v}_\sigma]_{t_{\mathcal{F},n_\ell}}, \mathbf{w}(t_{\mathcal{F},n_\ell}^+) - \tilde{\mathbf{w}}_\sigma(t_{\mathcal{F},n_\ell}^+))_{K^F} \\
&\quad + \frac{1}{2} \sum_{K_n^F \in \mathcal{T}_{\sigma,n}} \int_{K_n^F} \sum_{K^F \in \mathcal{T}_{h,n}^F} \left\{ (\mathbf{v} - \tilde{\mathbf{v}}_\sigma, \mathbf{R}^*(\mathbf{z}_\sigma))_{K^F} \right. \\
&\quad \left. + (p - \tilde{p}_\sigma, \nabla \cdot \mathbf{w}_\sigma)_{K^F} - (\mathbf{v} - \tilde{\mathbf{v}}_\sigma, \mathbf{E}^*(\mathbf{z}_\sigma))_{\partial K^F} \right\} dt \\
&\quad + \sum_{t_{\mathcal{F},n} \in \mathcal{F}_{\sigma,n}} \sum_{K^F \in \mathcal{T}_{h,n}^F} (\mathbf{v}(t_{\mathcal{F},n}^-) - \tilde{\mathbf{v}}_\sigma(t_{\mathcal{F},n}^-), [\mathbf{w}_\sigma]_{t_{\mathcal{F},n}})_{K^F},
\end{aligned} \tag{5.131}$$

and

$$\begin{aligned}
\eta_h^{\mathbb{F},n} &= \frac{1}{2} \sum_{K_n^{\mathbb{F}} \in \mathcal{T}_{\sigma,n}} \int_{K_n^{\mathbb{F}}} \sum_{K^{\mathbb{F}} \in \mathcal{T}_{h,n}^{\mathbb{F}}} \left\{ (\mathbf{R}(\mathbf{u}_{\sigma h}), \mathbf{w}_{\sigma} - \tilde{\mathbf{w}}_{\sigma h})_{K^{\mathbb{F}}} \right. \\
&\quad \left. - (\nabla \cdot \mathbf{v}_{\sigma h}, q_{\sigma} - \tilde{q}_{\sigma h})_{K^{\mathbb{F}}} - (\mathbf{E}(\mathbf{u}_{\sigma h}), \mathbf{w}_{\sigma} - \tilde{\mathbf{w}}_{\sigma h})_{\partial K^{\mathbb{F}}} \right\} dt \\
&\quad - \sum_{t_{\mathcal{F},n_{\ell}} \in \mathcal{F}_{\sigma,n}} \sum_{K^{\mathbb{F}} \in \mathcal{T}_{h,n}^{\mathbb{F}}} ([\mathbf{v}_{\sigma h}]_{t_{\mathcal{F},n_{\ell}}}, \mathbf{w}_{\sigma}(t_{\mathcal{F},n_{\ell}}^+) - \tilde{\mathbf{w}}_{\sigma h}(t_{\mathcal{F},n_{\ell}}^+))_{K^{\mathbb{F}}} \\
&\quad + \frac{1}{2} \sum_{K_n^{\mathbb{F}} \in \mathcal{T}_{\sigma,n}} \int_{K_n^{\mathbb{F}}} \sum_{K^{\mathbb{F}} \in \mathcal{T}_{h,n}^{\mathbb{F}}} \left\{ (\mathbf{v}_{\sigma} - \tilde{\mathbf{v}}_{\sigma h}, \mathbf{R}^*(\mathbf{z}_{\sigma h}))_{K^{\mathbb{F}}} \right. \\
&\quad \left. + (p_{\sigma} - \tilde{p}_{\sigma h}, \nabla \cdot \mathbf{w}_{\sigma h})_{K^{\mathbb{F}}} - (\mathbf{v}_{\sigma} - \tilde{\mathbf{v}}_{\sigma h}, \mathbf{E}^*(\mathbf{z}_{\sigma h}))_{\partial K^{\mathbb{F}}} \right\} dt \\
&\quad + \sum_{t_{\mathcal{F},n} \in \mathcal{F}_{\sigma,n}} \sum_{K^{\mathbb{F}} \in \mathcal{T}_{h,n}^{\mathbb{F}}} (\mathbf{v}_{\sigma}(t_{\mathcal{F},n}^-) - \tilde{\mathbf{v}}_{\sigma h}(t_{\mathcal{F},n}^-), [\mathbf{w}_{\sigma h}]_{t_{\mathcal{F},n}})_{K^{\mathbb{F}}},
\end{aligned} \tag{5.132}$$

where the cell and edge residuals $\mathbf{R}(\cdot)$, $\mathbf{R}^*(\cdot)$ and $\mathbf{E}(\cdot)$, $\mathbf{E}^*(\cdot)$, respectively, are given by

$$\mathbf{R}(\mathbf{u}) := \mathbf{f} - \partial_t \mathbf{v} + \nabla \cdot (\nu \nabla \mathbf{v}) - \nabla p, \tag{5.133}$$

$$\mathbf{R}^*(\mathbf{z}) := \mathbf{j} + \partial_t \mathbf{w} + \nabla \cdot (\nu \nabla \mathbf{w}) + \nabla q, \tag{5.134}$$

$$\mathbf{E}^{\rho}(\mathbf{u})|_{\Gamma} := \begin{cases} \frac{1}{2}[\nu \partial_n \mathbf{v} - p \mathbf{n}] & \text{if } \Gamma \subset \partial K \setminus \partial \Omega, \\ 0 & \text{if } \Gamma \subset \partial \Omega, \end{cases} \tag{5.135}$$

$$\mathbf{E}^{\rho*}(\mathbf{z})|_{\Gamma} := \begin{cases} \frac{1}{2}[\nu \partial_n \mathbf{w} + q \mathbf{n}] & \text{if } \Gamma \subset \partial K \setminus \partial \Omega, \\ 0 & \text{if } \Gamma \subset \partial \Omega, \end{cases} \tag{5.136}$$

with $[\varphi] := \varphi|_{\Gamma \cap K} - \varphi|_{\Gamma \cap K'}$ denoting the spatial jump of φ over the inner edges Γ with normal unit vector \mathbf{n} pointing from cell K to K' . Here, $\mathcal{F}_{\sigma,n}$ denotes the set of interior time points corresponding to slab $Q_n^{\mathbb{F}}$ with $t_{\mathcal{F},n_{\ell}}$ and $t_{\mathcal{F},n}$ denoting the left and right end of the cell in time $K_n^{\mathbb{F}}$, respectively.

Remark 5.16 *Let us remark some aspects about the error indicators.*

- *Again, the additional terms including the spatial edge terms $\mathbf{E}(\cdot)$, $\mathbf{E}^*(\cdot)$ appear by applying integration by parts on each spatial cell $K^{\mathbb{F}} \in \mathcal{T}_{h,n}^{\mathbb{F}}$, $n = 1, \dots, N^{\mathbb{F},\ell}$, to the second order terms of the primal or dual residual; cf., for instance, [20, Ch. 11] and [32]. Furthermore, since we are using continuous pressure approximations in space within our numerical computations in Sec. 5.4, the pressure jump terms across inner edges vanish, $[p_{\sigma h} \mathbf{n}] \equiv [q_{\sigma h} \mathbf{n}] \equiv 0$; cf., for instance, [40] or [20, Ch. 11].*

- With regard to problem dependent boundary conditions such as so-called no-slip, inflow and outflow conditions, we refer to Rem. 4.14 and [20, Ch. 11.1].
- Furthermore, the remaining notes outlined in Rem. 5.15 can be transferred to the case of the Stokes flow problem.

So far, the localized forms of the temporal and spatial error indicators given by Eq. (5.131) and Eq. (5.132), respectively, include solutions and integrals that have to be approximated for a practical realization. In view of this, the numerical evaluation of the temporal and spatial error indicators is performed in the following way:

- Approximate the temporal weights $\mathbf{v} - \tilde{\mathbf{v}}_\sigma, p - \tilde{p}_\sigma$ and $\mathbf{w} - \tilde{\mathbf{w}}_\sigma, q - \tilde{q}_\sigma$, respectively, occurring in Eq. (5.131), by means of a higher-order extrapolation or finite elements approach, exemplary given by

$$\begin{aligned}
\mathbf{v} - \tilde{\mathbf{v}}_\sigma &\approx \mathbf{E}_\tau^{r+1} \mathbf{v}_\sigma - \mathbf{v}_\sigma, \\
\mathbf{v} - \tilde{\mathbf{v}}_\sigma &\approx \mathbf{v}_\sigma - \mathbf{R}_\tau^r \mathbf{v}_\sigma, \\
p - \tilde{p}_\sigma &\approx \mathbf{E}_\tau^{r+1} p_\sigma - p_\sigma, \\
p - \tilde{p}_\sigma &\approx p_\sigma - \mathbf{R}_\tau^r p_\sigma,
\end{aligned} \tag{5.137}$$

using an extrapolation in time operator \mathbf{E}_τ^{r+1} or a restriction in time operator \mathbf{R}_τ^r , respectively, as introduced in Sec. 4.3.2.2 and with \mathbf{E}_τ^{r+1} and \mathbf{R}_τ^r acting componentwise like $\mathbf{E}_\tau^{(r+1)}$ and \mathbf{R}_τ^r , respectively. Note that within the higher-order finite elements approach the discrete dual solution \mathbf{z}_σ has to be solved in a space $\mathcal{Y}_\sigma^{\text{dG}(s)}$, $s > r$, as given by Eq. (5.17).

- Approximate the spatial weights $\mathbf{v}_\sigma - \tilde{\mathbf{v}}_{\sigma h}, p_\sigma - \tilde{p}_{\sigma h}$ and $\mathbf{w}_\sigma - \tilde{\mathbf{w}}_{\sigma h}, q_\sigma - \tilde{q}_{\sigma h}$, respectively, occurring in Eq. (5.132), by means of a patch-wise higher-order interpolation or higher-order finite elements approach, exemplary given by

$$\begin{aligned}
\mathbf{v}_\sigma - \tilde{\mathbf{v}}_{\sigma h} &\approx \mathbf{I}_{2h}^{(2p)} \mathbf{v}_{\sigma h} - \mathbf{v}_{\sigma h}, \\
\mathbf{v}_\sigma - \tilde{\mathbf{v}}_{\sigma h} &\approx \mathbf{v}_{\sigma h} - \mathbf{R}_h^p \mathbf{v}_{\sigma h}, \\
p_\sigma - \tilde{p}_{\sigma h} &\approx \mathbf{I}_{2h}^{(2p)} p_{\sigma h} - p_{\sigma h}, \\
p_\sigma - \tilde{p}_{\sigma h} &\approx p_{\sigma h} - \mathbf{R}_h^p p_{\sigma h},
\end{aligned} \tag{5.138}$$

using an interpolation in space operator $\mathbf{I}_{2h}^{(2p)}$ or a restriction in space operator \mathbf{R}_h^p , respectively, as introduced in Sec. 3.3.1 and with $\mathbf{I}_{2h}^{(2p)}$ and \mathbf{R}_h^p acting componentwise like $\mathbf{I}_{2h}^{(2p)}$ and \mathbf{R}_h^p , respectively. Note that within the higher-order finite elements approach the discrete dual solution $\mathbf{z}_{\sigma h}$ has to be solved in a space $\mathcal{Y}_{\sigma h}^{\text{dG}(r),q}$, $q > p$, as given by Eq. (5.28).

- Approximate the integrals in time by means of an appropriate quadrature rule depending on the approximation approach used for the temporal weights. More precisely, the integrals in time are evaluated numerically by using an $(r + 2)$ -point Gauss-Lobatto quadrature rule for the approximation case hoEx-G, an $(r + 1)$ -point Gauss quadrature rule for the case hoEx-GL, and an $(r + 2)$ -point Gauss quadrature rule for the case hoFE, respectively, cf. Sec. 4.3.2.2 for more details.
- Replace all unknown solutions occurring either in the weights or residuals by the computed fully discrete solutions $\mathbf{v}_{\sigma h}, p_{\sigma h}, \mathbf{w}_{\sigma h}$ and $q_{\sigma h}$, respectively, cf. also Rem. 4.13.

5.3.3 Implementation of Multirate Aspects

In this section, we give insight into some implementational aspects with regard to our multirate in time approach for coupled problems. Most of these aspects are based on the concepts introduced in Sec. 4.4, where we refer to for all details not being specified in the following. With regard to a practical realization of our multirate in time approach for coupled flow and transport problems, the following aspects are of particular importance:

- Initialization of spatial and temporal meshes for both transport and Stokes flow problem: Space-time slabs.
- Interaction of spatial and temporal meshes between transport and Stokes flow problem: Solution mesh transfer.
- Realization of adaptive mesh refinement in space and time: Involvement of slabs.

In the following, we address the above mentioned aspects in greater detail.

Initialization of Spatial and Temporal Meshes for Transport and Flow

For an adaptive numerical approximation of Problem 5.1, the space-time domain $Q = \Omega \times I$ is divided into non-overlapping space-time slabs $Q_n = \mathcal{T}_{h,n} \times \mathcal{T}_{\tau,n}, n = 1, \dots, N$, as well as $Q_n^F = \mathcal{T}_{h,n}^F \times \mathcal{T}_{\sigma,n}, n = 1, \dots, N^F$, with $N^F \leq N$, for the transport (5.1) and Stokes flow (5.2) problem, respectively, as outlined in Assumption 2.5 in Sec. 2.2. On such a slab, a tensor-product of a d -dimensional, $d = 1, 2, 3$, spatial finite element space with a one-dimensional temporal finite element space is implemented.

An exemplary illustration of such a slab is given by Fig.2.4 in Sec. 2.2. The temporal finite element space is based on a discontinuous Galerkin dG(r) method of arbitrary order $r, r \geq 0$, whereas the spatial finite element space is based on a continuous Galerkin cG(p) method of arbitrary order $p, p \geq 1$. In this sense, we are using here and in the following the notation cG(p)-dG(r) method, cf. Rem. 4.2.

As mentioned at the beginning of this chapter, the behavior of the underlying transport and Stokes flow problem is rather contrary with regard to the processes that take place in time. In order to measure these different dynamics in time, we introduced the concept of characteristic times $t_{\text{transport}}$ and t_{flow} for the respective subproblems, cf. Assumption 5.1. Due to these characteristic times the transport and Stokes flow problem given by (5.1) and (5.2), respectively, are initialized independently on different time scales fulfilling the following conditions:

- The Stokes flow temporal mesh is coarser or equal to the transport problem.
- The endpoints in the temporal mesh of the Stokes solver must match with endpoints in the temporal mesh of the transport problem.

An exemplary initialization of the temporal meshes for the transport and Stokes flow problems are illustrated in Fig. 5.2.

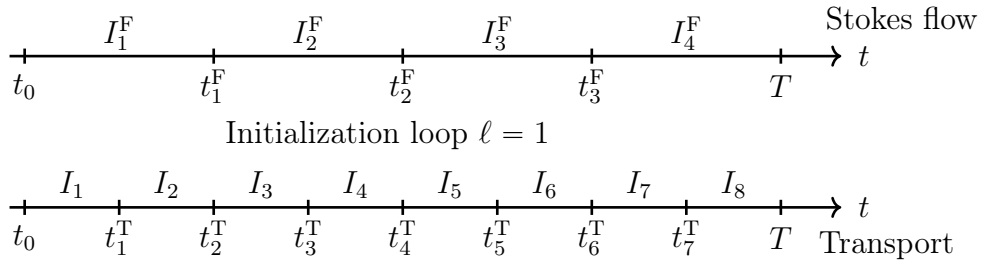


Figure 5.2: Exemplary initialization of different temporal meshes for the transport and Stokes solver.

The number of the above mentioned slabs corresponds to the number of the initial decomposition of the time interval I , as exemplarily given by Fig. 5.2, such that the closure of a subinterval $\bar{I}_n = [t_{n-1}^T, t_n^T]$ or $\bar{I}_n^F = [t_{n-1}^F, t_n^F]$ is discretized using a one-dimensional triangulation $\mathcal{T}_{\tau,n}$ or $\mathcal{T}_{\sigma,n}$, respectively. For further information to these triangulations including, e.g., their decomposition, we refer to Assumption 2.5.

With regard to the underlying spatial triangulations, we state the following. On each slab, we generate a geometrical triangulation $\mathcal{T}_{h,n}$ or $\mathcal{T}_{h,n}^F$, i.e. a spatial mesh, and colorize the respective boundaries. We choose the elements $K \in \mathcal{T}_{h,n}$ or $K^F \in \mathcal{T}_{h,n}^F$ to

be intervals for $d = 1$, quadrilaterals for $d = 2$ and hexahedrons for $d = 3$, respectively. We assume the spatial triangulations to be regular, but allowing hanging nodes, cf. Rem. 2.2 in Sec. 2.1.3. Furthermore, the spatial triangulations are assumed to be organized in a patch-wise manner (cf. Def. 2.6). For the sake of implementational simplicity, we allow the spatial mesh to change between two consecutive slabs, but to be equal on all degrees of freedom in time used within one slab, cf. Fig. 4.5. Thus, for the initialization of the spatial meshes for the transport and Stokes flow problem, we assume the following:

- The Stokes flow spatial mesh is coarser or equal to the transport problem.
- If the Stokes flow spatial mesh is coarser, the transport spatial mesh has to be emerged from the Stokes mesh in the sense of a patch-wise manner, i.e. $\mathcal{T}_{h,n}$ is obtained by uniform refinement of the coarser decomposition $\mathcal{T}_{h,n}^F$ such that it is always possible to combine four ($d = 2$) or eight ($d = 3$) adjacent elements of $\mathcal{T}_{h,n}$ to obtain one element of $\mathcal{T}_{h,n}^F$, cf. Def.2.6.

An exemplary initialization of the spatial meshes for the transport and Stokes flow problems are illustrated in Fig. 5.3.

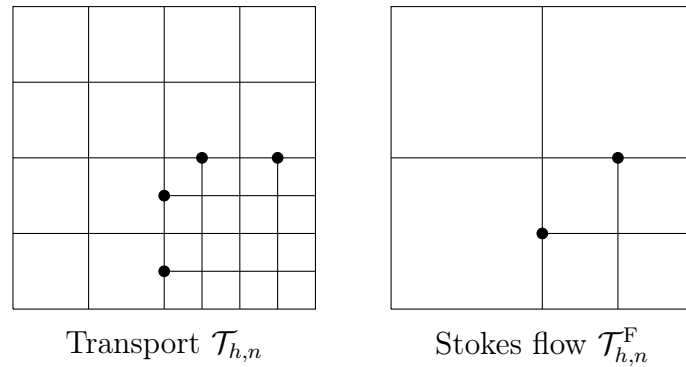


Figure 5.3: Exemplary initialization of different spatial meshes for the transport $\mathcal{T}_{h,n}$ and Stokes solver $\mathcal{T}_{h,n}^F$.

Finally, for the specific implementation process of the space-time tensor-product spaces Q_n and Q_n^F , respectively, we refer to Sec. 4.4.1.

Interaction of Spatial and Temporal Meshes between Transport and Flow

The coupling within Problem 5.1 is given via the convection variable \mathbf{v} of the system (5.1), (5.2). Thus, we need the fully discrete Stokes solution $\mathbf{v}_{\sigma h}$ for the numerical approximation of the stabilized primal and dual transport problems given by Eq. (5.32)

and Eq. (5.52), respectively. More precisely, the fully discrete Stokes solution $\mathbf{v}_{\sigma h}$ has to be transferred to the respective transport meshes in an appropriate way. This solution mesh transfer is handled in a similar fashion as described in Sec. 4.4.3 for the transfer of a solution between two consecutive slabs with different underlying spatial meshes and will be specified in the following.

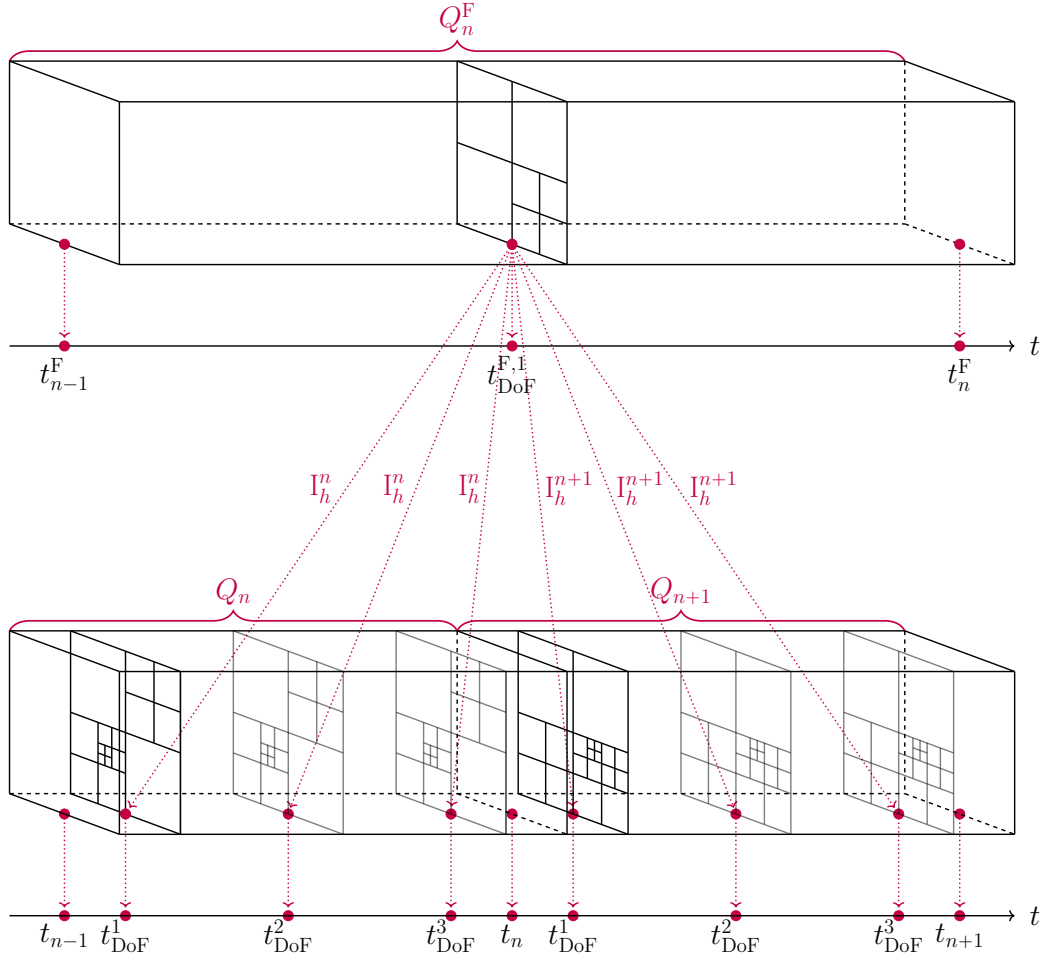


Figure 5.4: Exemplary solution mesh transfer from a Stokes flow slab Q_n^F (for a discontinuous Galerkin dG(0) time discretization generated with one Gaussian quadrature point) to transport slabs Q_n and Q_{n+1} (for a discontinuous Galerkin dG(2) time discretization generated with three Gaussian quadrature points), respectively. Each of the illustrated slabs here consists of one cell in time and an independent and adaptively refined spatial triangulation.

For the sake of simplicity, we approximate the solution $\{\mathbf{v}, p\}$ of the Stokes flow problem on each I_n^F by means of a globally piecewise constant discontinuous Galerkin (dG(0)) time approximation. Thus, in accordance with the above described conditions for the temporal discretizations of both subproblems (cf. Fig. 5.2), we simply have

to guarantee the correct choice of the corresponding Stokes flow slab when solving on the current transport slab and avoid an additional evaluation of the Stokes flow solution at the temporal degrees of freedom within the slab. For example, with regard to Fig. 5.2, for the approximation of the transport solution on I_4 (corresponding to slab Q_4) the Stokes flow solution on I_2^F (corresponding to slab Q_2^F) is needed.

The Stokes solution transfer with regard to the spatial meshes is handled by means of introducing a temporary additional Stokes triangulation build as a copy of the transport triangulation. Then, the Stokes solution is interpolated to this temporary triangulation using an interpolation operator I_h^n onto the primal or dual finite element space used on the current slab Q_n in the same way as given in Eq. (4.136). This interpolation is handled by the precasted function `interpolate_to_different_mesh()` within the `deal.II` library [17] in the same fashion as described in Sec. 4.4.3, where we refer to for further details. An exemplary solution transfer of the Stokes flow solution to the transport meshes is illustrated in Fig. 5.4. Of course, this approach entails an additional interpolation error. However, in our numerical examples in Sec. 5.4, we see that this impact as well as the restriction to a dG(0) approximation in time for the Stokes flow problem is negligibly to obtain quantitatively good results with regard to the transport solution.

Realization of Adaptive Mesh Refinement in Space and Time

A further important aspect when dealing with goal-oriented error control of coupled problems is the treatment of adaptive mesh refinement within the single subproblems as well as the question of the consequences for the respective other meshes due to these refinements. The adaptive refinement is performed cell-wise in space and time based on the local error indicators η_τ^n, η_h^n and $\eta_\sigma^{F,n}, \eta_h^{F,n}$ given by the Eqs. (5.120)–(5.121) and Eqs. (5.131)–(5.132) for the transport and Stokes flow problem, respectively. With regard to a single subproblem, the adaptive mesh refinement process including the involvement of additional space-time slabs is described in detail within the correspondent Sec. 4.4.2 given in the previous chapter. For this reason, we outline here only the main features of the framework regarding the adaptive process:

- Store the space-time slabs within a `std::list` object; cf. Fig. 4.14 of an exemplary `std::list` structure.
- Execute at first the spatial refinement and coarsening of the underlying triangulations on all slabs.

- Refine in time by involving new created slabs by copying the just refined spatial triangulation of a slab that is marked for refinement; cf. Fig. 4.9.

A detailed description of the issues above is given in Sec. 4.4.2. Finally, in order to respond the question above successfully with regard to the resulting consequences for the meshes of the other subproblem within the adaptive refinement process, we assume the following:

- Refine the transport meshes after the Stokes flow meshes.
- The endpoints in the temporal mesh of the Stokes solver match with endpoints in the temporal mesh of the transport problem; cf. the second condition for the initialization of the temporal meshes for both problems.

5.3.4 Application Scenarios of a Multirate-DWR Concept

In this section, we present various implementation scenarios in terms of different strategies with regard to goal functionals for the dual problems, approximation techniques of the weights and adaptive refinement in space and time for both the transport and Stokes flow problem. More precisely, we present the following three cases of a multirate in time approach including dual weighted residual based error estimation for coupled problems:

- General Multirate-DWR Algorithm for Coupled Problems.
- Transport-Oriented Multirate-DWR Algorithm for Coupled Problems.
- Implemented Multirate-DWR Algorithm for Coupled Problems.

Here, the first case is kept as general as possible with regard to an independent error control of the two subproblems including arbitrary goal functionals. In contrast, the transport-oriented algorithm is designed to focus on the transport equation characterized by using a specific goal functional within the dual Stokes flow problem as outlined in Rem.5.13. Finally, we present our implemented version that is inspired by the transport-oriented approach, although the strategy to gain information for the refinement of the Stokes flow meshes is a different one. This approach is used within the numerical examples given in Sec. 5.4 As introduced in the sections before, we use a multirate in time approach based on a discontinuous in time Galerkin method within all the following three application scenarios, cf. Sec.5.1.1 for the details.

5.3.4.1 General Multirate-DWR Algorithm for Coupled Problems

We start with presenting an algorithm in its most general version to demonstrate what is possible when dealing with goal-oriented adaptive mesh refinement in space and time with regard to coupled problems. This serves to provide an overview of solution approaches used for the dual problems, approximation techniques for the respective weights within the error indicators as well as refinement strategies for both the transport and Stokes flow problem with regard to different goals.

For the case of a fully adaptive space-time approximation of Problem 5.1, the space-time domain $Q = \Omega \times I$ is divided into non-overlapping space-time slabs $Q_n^\ell = \mathcal{T}_{h,n}^\ell \times \mathcal{T}_{\tau,n}^\ell, n = 1, \dots, N^\ell$, as well as $Q_n^{\text{F},\ell} = \mathcal{T}_{h,n}^{\text{F},\ell} \times \mathcal{T}_{\sigma,n}^\ell, n = 1, \dots, N^{\text{F},\ell}$, with $N^{\text{F},\ell} \leq N^\ell$, for the transport and Stokes flow problem, respectively, as introduced in Assumption 2.5 in Sec. 2.2, where ℓ denotes the current DWR adaptivity loop. For the underlying software architecture in general, we refer to Sec. 5.3.3 and Sec. 4.4, respectively, and for the effective implementation of the space-time tensor-product spaces in particular, we refer to Sec. 4.4.1.

The fully discrete primal and dual solutions of the transport problem are represented by $u_{\tau h}^\ell$ and $z_{\tau h}^\ell$, respectively. The fully discrete primal and dual solutions of the Stokes flow problem are represented by $\mathbf{u}_{\sigma h}^\ell = \{\mathbf{v}_{\sigma h}^\ell, p_{\sigma h}^\ell\}$ and $\mathbf{z}_{\tau h}^\ell = \{\mathbf{w}_{\sigma h}^\ell, q_{\sigma h}^\ell\}$, respectively.

General Multirate-DWR Algorithm for Coupled Problems

Initialization: Set DWR loop $\ell = 1$ and generate the initial space-time slabs $Q_n^1 = \mathcal{T}_{h,n}^1 \times \mathcal{T}_{\tau,n}^1, n = 1, \dots, N^1$, as well as $Q_n^{\text{F},1} = \mathcal{T}_{h,n}^{\text{F},1} \times \mathcal{T}_{\sigma,n}^1, n = 1, \dots, N^{\text{F},1}, N^{\text{F},1} \leq N^1$ for the transport and Stokes flow problem, respectively.

1. Solve the **Fully Discrete cG(p)-dG(r) Primal Stokes Flow Problem 5.7:**

Find $\mathbf{u}_{\sigma h}^\ell = \{\mathbf{v}_{\sigma h}^\ell, p_{\sigma h}^\ell\} \in \mathcal{Y}_{\sigma h}^{\text{dG}(r),p}$ such that $B_{\sigma h}(\mathbf{u}_{\sigma h}^\ell)(\varphi_{\sigma h}) = F_{\sigma h}(\varphi_{\sigma h})$,
for all $\varphi_{\sigma h} = \{\psi_{\sigma h}, \chi_{\sigma h}\} \in \mathcal{Y}_{\sigma h}^{\text{dG}(r),p}$.

2. **Break if the goal for the Stokes flow problem is reached**, i.e., for instance, $\|\mathbf{u} - \mathbf{u}_{\sigma h}^\ell\| < \text{tol}$, or $(\eta_\sigma^{\text{F},\ell} + \eta_h^{\text{F},\ell}) < \text{tol}$, or $\max N_{\text{DoF}}^{\text{tot}}$ is reached, etc.

3. Solve the **Stabilized cG(p)-dG(r) Primal Transport Problem 5.8:**

Find $u_{\tau h}^\ell \in \mathcal{X}_{\tau h}^{\text{dG}(r),p}$ such that $A_S(u_{\tau h}^\ell; \mathbf{v}_{\sigma h}^\ell)(\varphi_{\tau h}) = G_{\tau h}(\varphi_{\tau h})$,
for all $\varphi_{\tau h} \in \mathcal{X}_{\tau h}^{\text{dG}(r),p}$, using $\mathbf{v}_{\sigma h}^\ell$ from step 1.

4. **Break if the goal for the transport problem is reached**, i.e., for instance, $\|u - u_{\tau h}^\ell\| < \text{tol}$, or $(\eta_\tau^\ell + \eta_h^\ell) < \text{tol}$, or $\max N_{\text{DoF}}^{\text{tot}}$ is reached, etc.
5. Solve the **Stabilized cG(q)-dG(s) Dual Transport Problem 5.11** depending on the underlying choice of the approximation strategy for the weights:
 Find $z_{\tau h}^\ell \in \mathcal{X}_{\tau h}^{dG(s),q}$ such that $A'_S(u_{\tau h}^\ell; \mathbf{v}_{\sigma h}^\ell)(\psi_{\tau h}, z_{\tau h}^\ell) = J'(u_{\tau h}^\ell)(\psi_{\tau h})$,
 for all $\psi_{\tau h} \in \mathcal{X}_{\tau h}^{dG(s),q}$, where $s = r, q = p$ (hoEx approach) or rather $s \geq r + 1, q \geq p + 1$ (hoFE approach), using $\mathbf{v}_{\sigma h}^\ell$ from step 1, **and**
 solve the **Fully Discrete cG(q)-dG(s) Dual Stokes Flow Problem 5.14** depending on the underlying choice of the approximation strategy for the weights:
 Find $\mathbf{z}_{\sigma h}^\ell = \{\mathbf{w}_{\sigma h}^\ell, q_{\sigma h}^\ell\} \in \mathcal{Y}_{\sigma h}^{dG(s),q}$ such that $B'_{\sigma h}(\mathbf{u}_{\sigma h}^\ell)(\boldsymbol{\varphi}_{\sigma h}, \mathbf{z}_{\sigma h}^\ell) = J'(\mathbf{u}_{\sigma h}^\ell)(\boldsymbol{\varphi}_{\sigma h})$,
 for all $\boldsymbol{\varphi}_{\sigma h} = \{\boldsymbol{\psi}_{\sigma h}, \chi_{\sigma h}\} \in \mathcal{Y}_{\sigma h}^{dG(s),q}$, where $s = r, q = p$ (hoEx approach) or rather $s \geq r + 1, q \geq p + 1$ (hoFE approach).
6. Evaluate the **local a posteriori space-time error indicators** $\eta_\tau^{n,\ell}, \eta_h^{n,\ell}$ given by Eqs. (5.120), (5.121) for the **transport** problem, and $\eta_\sigma^{F,n,\ell}, \eta_h^{F,n,\ell}$ given by Eqs. (5.131), (5.132) for the **Stokes flow** problem, by marching sequentially through all space-time slabs $Q_n^\ell, n = 1, \dots, N^\ell$, and $Q_n^{F,\ell}, n = 1, \dots, N^{F,\ell}$, respectively.
7. **If** $|\eta_\sigma^{F,\ell}| + |\eta_h^{F,\ell}| > \varpi (|\eta_\tau^\ell| + |\eta_h^\ell|)$, $\varpi \geq 1$, (**Stokes flow dominating case**):
 Refine the temporal and spatial meshes of the **Stokes flow** problem as follows:
- (i) **If** $|\eta_\sigma^{F,\ell}| > \omega^F |\eta_h^{F,\ell}|$, $\omega^F \geq 1$, (**Temporal error dominating case**):
 Mark the cells $\tilde{K}_n^F \in \mathcal{T}_{\sigma,n}^\ell$ for **temporal refinement** if the corresponding $\eta_\sigma^{F,n,\ell}|_{\tilde{K}_n^F}$ is in the set of $\theta_\sigma^{\text{top}}$, $0 \leq \theta_\sigma^{\text{top}} \leq 1$, percent of the worst indicators.
- (ii) **Else if** $|\eta_h^{F,\ell}| > \omega^F |\eta_\sigma^{F,\ell}|$, $\omega^F \geq 1$, (**Spatial error dominating case**):
 Mark the cells $\tilde{K}^F \in \mathcal{T}_{h,n}^{F,\ell}$ for **spatial refinement** if the corresponding $\eta_h^{F,n,\ell}|_{\tilde{K}^F}$ is in the set of $\theta_{h,1}^{F,\text{top}}$ or $\theta_{h,2}^{F,\text{top}}$ (for a slab that includes or does not include marked cells in time), $0 \leq \theta_{h,2}^{F,\text{top}} \leq \theta_{h,1}^{F,\text{top}} \leq 1$, percent of the worst indicators, **or**, respectively, mark for **spatial coarsening** if $\eta_h^{F,n,\ell}|_{\tilde{K}^F}$ is in the set of $\theta_h^{F,\text{bottom}}$, $0 \leq \theta_h^{F,\text{bottom}} \leq 1$, percent of the best indicators.
- (iii) **Else** (**Temporal and spatial errors are equilibrated**):
 Mark the cells $\tilde{K}_n^F \in \mathcal{T}_{\sigma,n}^\ell$ for **temporal refinement** as well as **mark the cells** $\tilde{K}^F \in \mathcal{T}_{h,n}^{F,\ell}$ for **spatial coarsening and refinement** as described in Step 7(i) and Step 7(ii), respectively.

- (iv) **Execute spatial refinement and/or coarsening** on all slabs of the Stokes flow problem under the use of mesh smoothing operators.
- (v) **Execute temporal refinement** on all slabs of the Stokes flow problem.
8. **If** $|\eta_\tau^\ell| + |\eta_h^\ell| > \varpi (|\eta_\sigma^{\text{F},\ell}| + |\eta_h^{\text{F},\ell}|)$, $\varpi \geq 1$, (**Transport dominating case**):
 Refine the temporal and spatial meshes of the **transport** problem as follows:
- (i) **If** $|\eta_\tau^\ell| > \omega |\eta_h^\ell|$, $\omega \geq 1$, (**Temporal error dominating case**):
Mark the cells $\tilde{K}_n \in \mathcal{T}_{\tau,n}^\ell$ **for temporal refinement** if the corresponding $\eta_\tau^{n,\ell}|_{\tilde{K}_n}$ is in the set of θ_τ^{top} , $0 \leq \theta_\tau^{\text{top}} \leq 1$, percent of the worst indicators.
- (ii) **Else if** $|\eta_h^\ell| > \omega |\eta_\tau^\ell|$, $\omega \geq 1$, (**Spatial error dominating case**):
Mark the cells $\tilde{K} \in \mathcal{T}_{h,n}^\ell$ **for spatial refinement** if the corresponding $\eta_h^{n,\ell}|_{\tilde{K}}$ is in the set of $\theta_{h,1}^{\text{top}}$ or $\theta_{h,2}^{\text{top}}$ (for a slab that includes or does not include marked cells in time), $0 \leq \theta_{h,2}^{\text{top}} \leq \theta_{h,1}^{\text{top}} \leq 1$, percent of the worst indicators, **or**, respectively, mark **for spatial coarsening** if $\eta_h^{n,\ell}|_{\tilde{K}}$ is in the set of θ_h^{bottom} , $0 \leq \theta_h^{\text{bottom}} \leq 1$, percent of the best indicators.
- (iii) **Else** (**Temporal and spatial errors are equilibrated**):
Mark the cells $\tilde{K}_n \in \mathcal{T}_{\tau,n}^\ell$ **for temporal refinement** as well as **mark the cells** $\tilde{K} \in \mathcal{T}_{h,n}^\ell$ **for spatial coarsening and refinement** as described in Step 8(i) and Step 8(ii), respectively.
- (iv) **Execute spatial refinement and/or coarsening** on all slabs of the transport problem under the use of mesh smoothing operators.
- (v) **Execute temporal refinement** on all slabs of the transport problem.
9. **Else** (**Transport and Stokes flow errors are equilibrated**):
 Refine the temporal and spatial meshes of the **Stokes flow** and **transport** problem as described in Step 7 and Step 8, respectively.
10. Increase ℓ to $\ell + 1$ and **return to Step 1**.

Remark 5.17 *Let us remark some aspects about the multirate adaptive algorithm.*

- *The remarks outlined for the case of a steady-state and space-time adaptive algorithm given by Rem. 3.9 in Chapter 3 and Rem. 4.15 in Chapter 4, respectively, can be transferred to the above multirate algorithm for coupled problems as well.*

- *Depending on the goal that is pursued by the user, there are two possible exit conditions, one after solving the primal Stokes flow problem and one after solving the primal transport problem, respectively; cf. Step 2 and 4 of the algorithm above as well as Fig. 5.5.*
- *Besides an equilibrated reduction of the temporal and spatial discretization errors for both the transport and the Stokes flow problem, ensured by the use of equilibration constants ω and ω^F (values in the range of $1.0 \leq \omega, \omega^F \leq 3.5$ are used in our numerical experiments), respectively, within the framework of coupled problems, it is essential to know which equation contributes most to the overall error. For this purpose, the problem equilibration constant ϖ (a value in the range of $1 \leq \varpi \leq 3$ is used in our numerical experiments) is introduced in Step 7 and 8.*

For better clarity to the sequence of the single steps above, an illustration of the general algorithm is given in Fig. 5.5. The black arrows symbolize the direction of the run here, beginning with the initialization (start) of the space-time slabs for both the transport and Stokes flow problem, respectively. If an arrow is splitted this means that both actions or only one of them are possible, cf., e.g., the refinement process described by Step 7-9. We note that the actual refinement at least of the temporal mesh for the transport problem is done after the refinement of the Stokes flow problem due to guarantee the properties outlined in Sec. 5.3.3. Furthermore, we note that the dual Stokes flow problem is solved simultaneously to the dual transport one. This is only possible for a Stokes flow goal functional being independent of the primal and dual transport solutions and is in contrast to the following transport-oriented algorithm; cf. Rem. 5.13 and Fig. 5.6. We point out that it is also possible to solve the dual Stokes flow problem simultaneously to the primal transport one, but if the goal check after the latter one is positive, the solution of the dual Stokes flow problem becomes redundant.

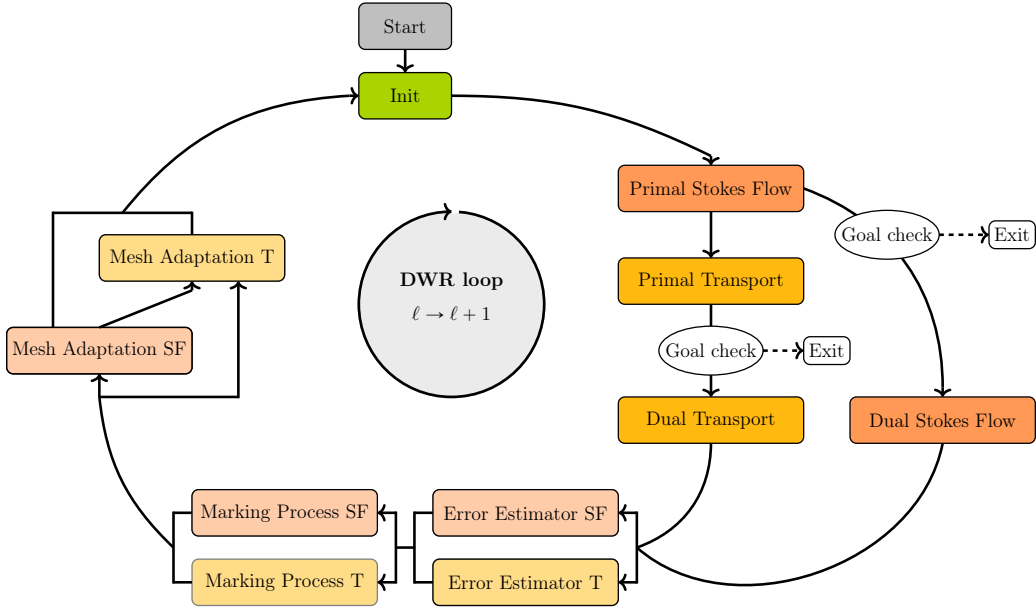


Figure 5.5: Illustration of the General Multirate-DWR Algorithm for Coupled Problems.

5.3.4.2 Transport-Oriented Multirate-DWR Algorithm for Coupled Problems

As outlined in Rem. 5.13, in a practical realization of Problem 5.1 one is rather interested to control the transport problem under the condition that the influence of the error in the Stokes flow problem is minimized. We call this case a transport-oriented approach and will specify it in the following. The main difference to the general case introduced in the previous section comes through the focus on solving the transport equation and to subordinate all other aspects to this goal. More precisely, the goal of the dual Stokes flow problem is here to account for the influence of the error in the velocity and to keep this error small due to its presence in the error representation formulas of the transport problem, cf. Eqs. (5.62)–(5.63) and, in particular, Rem. 5.13 for more details. This goal is ensured using the modified goal functionals (5.102) and (5.103), respectively, within the dual Stokes flow problem. These functionals are additionally depending on the primal and dual transport solutions with the consequence that the dual Stokes flow problem is no longer solvable simultaneously to the dual transport problem, but subsequently to that, cf. Step 5 of the following algorithm as well as Fig. 5.6. Moreover, the goal-check and respective exit condition for the Stokes flow problem are omitted here.

Since the introduction to the partition of the space-time slabs equals that one

described for the general case, we refrain to this here and refer to Sec. 5.3.4.1 instead. The fully discrete primal and dual solutions of the transport problem are represented by $u_{\tau h}^\ell$ and $z_{\tau h}^\ell$, respectively. The fully discrete primal and dual solutions of the Stokes flow problem are represented by $\mathbf{u}_{\sigma h}^\ell = \{\mathbf{v}_{\sigma h}^\ell, p_{\sigma h}^\ell\}$ and $\mathbf{z}_{\tau h}^\ell = \{\mathbf{w}_{\sigma h}^\ell, q_{\sigma h}^\ell\}$, respectively.

Transport-Oriented Multirate-DWR Algorithm for Coupled Problems

Initialization: Set DWR loop $\ell = 1$ and generate the initial space-time slabs $Q_n^1 = \mathcal{T}_{h,n}^1 \times \mathcal{T}_{\tau,n}^1$, $n = 1, \dots, N^1$, as well as $Q_n^{F,1} = \mathcal{T}_{h,n}^{F,1} \times \mathcal{T}_{\sigma,n}^1$, $n = 1, \dots, N^{F,1}$, $N^{F,1} \leq N^1$ for the transport and Stokes flow problem, respectively.

1. Solve the **Fully Discrete cG(p)-dG(r) Primal Stokes Flow Problem 5.7:**

Find $\mathbf{u}_{\sigma h}^\ell = \{\mathbf{v}_{\sigma h}^\ell, p_{\sigma h}^\ell\} \in \mathcal{Y}_{\sigma h}^{dG(r),p}$ such that $B_{\sigma h}(\mathbf{u}_{\sigma h}^\ell)(\varphi_{\sigma h}) = F_{\sigma h}(\varphi_{\sigma h})$,
for all $\varphi_{\sigma h} = \{\psi_{\sigma h}, \chi_{\sigma h}\} \in \mathcal{Y}_{\sigma h}^{dG(r),p}$.

2. Solve the **Stabilized cG(p)-dG(r) Primal Transport Problem 5.8:**

Find $u_{\tau h}^\ell \in \mathcal{X}_{\tau h}^{dG(r),p}$ such that $A_S(u_{\tau h}^\ell; \mathbf{v}_{\sigma h}^\ell)(\varphi_{\tau h}) = G_{\tau h}(\varphi_{\tau h})$,
for all $\varphi_{\tau h} \in \mathcal{X}_{\tau h}^{dG(r),p}$, using $\mathbf{v}_{\sigma h}^\ell$ from step 1.

3. **Break if the goal for the transport problem is reached**, i.e., for instance, $\|u - u_{\tau h}^\ell\| < \text{tol}$, or $(\eta_\tau + \eta_h) < \text{tol}$, or $\max N_{\text{DoF}}^{\text{tot}}$ is reached, etc.

4. Solve the **Stabilized cG(q)-dG(s) Dual Transport Problem 5.11** depending on the underlying choice of the approximation strategy for the weights:

Find $z_{\tau h}^\ell \in \mathcal{X}_{\tau h}^{dG(s),q}$ such that $A'_S(u_{\tau h}^\ell; \mathbf{v}_{\sigma h}^\ell)(\psi_{\tau h}, z_{\tau h}^\ell) = J'(u_{\tau h}^\ell)(\psi_{\tau h})$,
for all $\psi_{\tau h} \in \mathcal{X}_{\tau h}^{dG(s),q}$, where $s = r, q = p$ (hoEx approach) or rather $s \geq r + 1, q \geq p + 1$ (hoFE approach), using $\mathbf{v}_{\sigma h}^\ell$ from step 1.

5. Solve the **Fully Discrete cG(q)-dG(s) Dual Stokes Flow Problem 5.14** depending on the underlying choice of the approximation strategy for the weights:

Find $\mathbf{z}_{\sigma h}^\ell = \{\mathbf{w}_{\sigma h}^\ell, q_{\sigma h}^\ell\} \in \mathcal{Y}_{\sigma h}^{dG(s),q}$ such that

$$B'_{\sigma h}(\mathbf{u}_{\sigma h}^\ell)(\varphi_{\sigma h}, \mathbf{z}_{\sigma h}^\ell) = \sum_{n=1}^{N^{F,\ell}} \sum_{K_n^F \in \mathcal{T}_{\sigma,n}} \int_{K_n^F} (\mathbf{v}_\sigma - \mathbf{v}_{\sigma h}, u_{\tau h} \cdot \nabla z_{\tau h}) \, dt,$$

for all $\varphi_{\sigma h} = \{\psi_{\sigma h}, \chi_{\sigma h}\} \in \mathcal{Y}_{\sigma h}^{dG(s),q}$, where $s = r, q = p$ (hoEx approach) or rather $s \geq r + 1, q \geq p + 1$ (hoFE approach).

6. Evaluate the **local a posteriori space-time error indicators** $\eta_\tau^{n,\ell}, \eta_h^{n,\ell}$ given by Eqs. (5.120), (5.121) for the **transport** problem, and $\eta_\sigma^{F,n,\ell}, \eta_h^{F,n,\ell}$ given by Eqs. (5.131), (5.132) for the **Stokes flow** problem, by marching sequentially through all space-time slabs $Q_n^\ell, n = 1, \dots, N^\ell$, and $Q_n^{F,\ell}, n = 1, \dots, N^{F,\ell}$, respectively.

7. **If** $|\eta_\sigma^{F,\ell}| + |\eta_h^{F,\ell}| > \varpi (|\eta_\tau^\ell| + |\eta_h^\ell|), \varpi \geq 1$, (**Stokes flow dominating case**):

Refine the temporal and spatial meshes of the **Stokes flow** problem as follows:

(i) **If** $|\eta_\sigma^{F,\ell}| > \omega^F |\eta_h^{F,\ell}|, \omega^F \geq 1$, (**Temporal error dominating case**):

Mark the cells $\tilde{K}_n^F \in \mathcal{T}_{\sigma,n}^\ell$ **for temporal refinement** if the corresponding $\eta_\sigma^{F,n,\ell}|_{\tilde{K}_n^F}$ is in the set of $\theta_\sigma^{\text{top}}, 0 \leq \theta_\sigma^{\text{top}} \leq 1$, percent of the worst indicators.

(ii) **Else if** $|\eta_h^{F,\ell}| > \omega^F |\eta_\sigma^{F,\ell}|, \omega^F \geq 1$, (**Spatial error dominating case**):

Mark the cells $\tilde{K}^F \in \mathcal{T}_{h,n}^{F,\ell}$ **for spatial refinement** if the corresponding $\eta_h^{F,n,\ell}|_{\tilde{K}^F}$ is in the set of $\theta_{h,1}^{F,\text{top}}$ or $\theta_{h,2}^{F,\text{top}}$ (for a slab that includes or does not include marked cells in time), $0 \leq \theta_{h,2}^{F,\text{top}} \leq \theta_{h,1}^{F,\text{top}} \leq 1$, percent of the worst indicators, **or**, respectively, **mark for spatial coarsening** if $\eta_h^{F,n,\ell}|_{\tilde{K}^F}$ is in the set of $\theta_h^{F,\text{bottom}}, 0 \leq \theta_h^{F,\text{bottom}} \leq 1$, percent of the best indicators.

(iii) **Else** (**Temporal and spatial errors are equilibrated**):

Mark the cells $\tilde{K}_n^F \in \mathcal{T}_{\sigma,n}^\ell$ **for temporal refinement** as well as **mark the cells** $\tilde{K}^F \in \mathcal{T}_{h,n}^{F,\ell}$ **for spatial coarsening and refinement** as described in Step 7(i) and Step 7(ii), respectively.

(iv) **Execute spatial refinement and/or coarsening** on all slabs of the Stokes flow problem under the use of mesh smoothing operators.

(v) **Execute temporal refinement** on all slabs of the Stokes flow problem.

8. **If** $|\eta_\tau^\ell| + |\eta_h^\ell| > \varpi (|\eta_\sigma^{F,\ell}| + |\eta_h^{F,\ell}|), \varpi \geq 1$, (**Transport dominating case**):

Refine the temporal and spatial meshes of the **transport** problem as follows:

(i) **If** $|\eta_\tau^\ell| > \omega |\eta_h^\ell|, \omega \geq 1$, (**Temporal error dominating case**): :

Mark the cells $\tilde{K}_n \in \mathcal{T}_{\tau,n}^\ell$ **for temporal refinement** if the corresponding $\eta_\tau^{n,\ell}|_{\tilde{K}_n}$ is in the set of $\theta_\tau^{\text{top}}, 0 \leq \theta_\tau^{\text{top}} \leq 1$, percent of the worst indicators.

(ii) **Else if** $|\eta_h^\ell| > \omega |\eta_\tau^\ell|, \omega \geq 1$, (**Spatial error dominating case**):

Mark the cells $\tilde{K} \in \mathcal{T}_{h,n}^\ell$ **for spatial refinement** if the corresponding $\eta_h^{n,\ell}|_{\tilde{K}}$ is in the set of $\theta_{h,1}^{\text{top}}$ or $\theta_{h,2}^{\text{top}}$ (for a slab that includes or does not

include marked cells in time), $0 \leq \theta_{h,2}^{\text{top}} \leq \theta_{h,1}^{\text{top}} \leq 1$, percent of the worst indicators, **or**, respectively, mark **for spatial coarsening** if $\eta_h^{n,\ell}|_{\tilde{K}}$ is in the set of θ_h^{bottom} , $0 \leq \theta_h^{\text{bottom}} \leq 1$, percent of the best indicators.

(iii) **Else (Temporal and spatial errors are equilibrated):**

Mark the cells $\tilde{K}_n \in \mathcal{T}_{\tau,n}^\ell$ for temporal refinement as well as **mark the cells $\tilde{K} \in \mathcal{T}_{h,n}^\ell$ for spatial coarsening and refinement** as described in Step 8(i) and Step 8(ii), respectively.

(iv) **Execute spatial refinement and/or coarsening** on all slabs of the transport problem under the use of mesh smoothing operators.

(v) **Execute temporal refinement** on all slabs of the transport problem.

9. **Else (Transport and Stokes flow errors are equilibrated):**

Refine the temporal and spatial meshes of the **Stokes flow** and **transport** problem as described in Step 7 and Step 8, respectively.

10. Increase ℓ to $\ell + 1$ and **return to Step 1**.

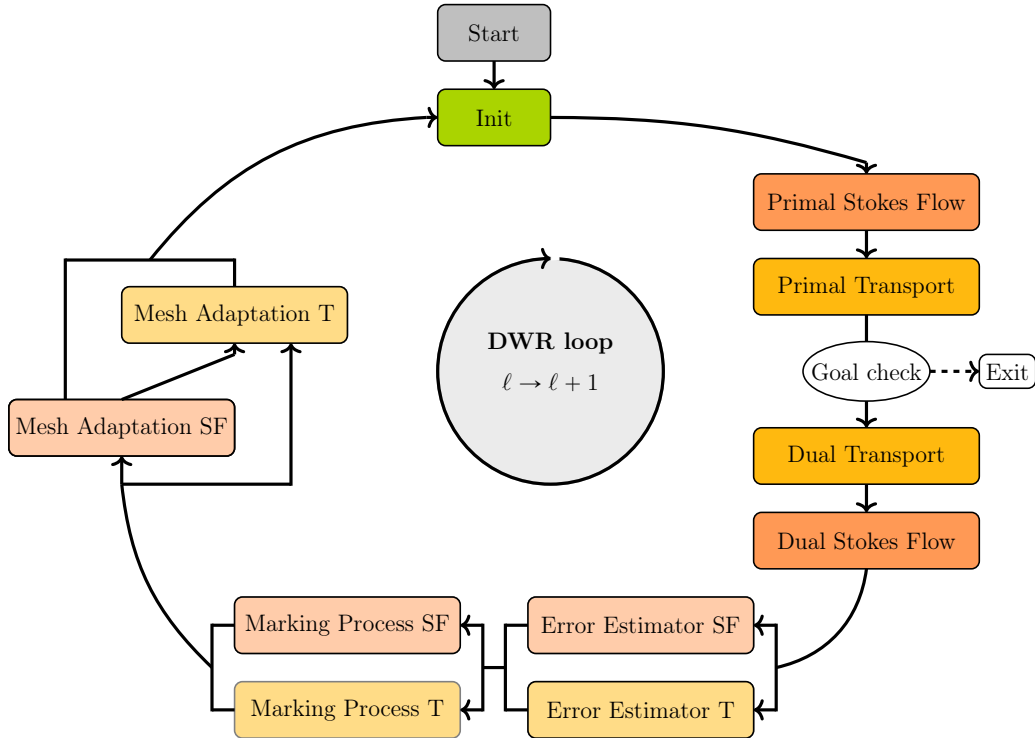


Figure 5.6: Illustration of the Transport-Oriented Multirate-DWR Algorithm for Coupled Problems.

5.3.4.3 Implemented Multirate-DWR Algorithm for Coupled Problems

In a final step, we present our implemented version of a discontinuous in time multirate DWR algorithm for coupled problems that slightly differs from the variants introduced before. In order to investigate our multirate in time approach with regard to a rapidly changing transport coupled with a slowly creeping flow, we put the focus on the space-time adaptive refinement process within the transport problem and approximate at first the Stokes flow solution on globally refined meshes in space and time. Nonetheless, in some test cases of our numerical examples we apply adaptive mesh refinement within the Stokes flow problem obtained by means of using so-called auxiliary error indicators, given by

$$\tilde{\eta}_{\sigma h}^F = \tilde{\eta}_{\sigma}^F + \tilde{\eta}_h^F = \sum_{n=1}^{N^{F,\ell}} \eta_{\sigma}^{F,n} + \sum_{n=1}^{N^{F,\ell}} \eta_h^{F,n}. \quad (5.139)$$

These indicators may represent, for instance, global or local errors in common norms or indicators of non-weighted error estimators such as the Kelly Error Estimator that is introduced in Rem. 5.19. This allows to refrain an explicit computation of the dual Stokes flow problem, cf. Fig. 5.7.

While we kept the framework of the two algorithms presented before as general as possible, we give details to the actual used approximation techniques within the numerical examples given in Sec. 5.4 in the following.

Assumption 5.6 *To compute the local transport error indicators η_{τ}^n and η_h^n given by Eq. (5.120) and (5.121), respectively, we make the following choices.*

- *Replace all unknown solutions occurring either in the weights or residuals by the approximated fully discrete solutions $u_{\tau h} \in \mathcal{X}_{\tau h}^{\text{dG}(r),p}$, $z_{\tau h} \in \mathcal{X}_{\tau h}^{\text{dG}(r),q}$, with $p < q$, and $\mathbf{v}_{\sigma h} \in \mathcal{Y}_{\sigma h}^{\text{dG}(r),p}$,*
- *Approximate the temporal weights $u - \tilde{u}_{\tau}$ and $z - \tilde{z}_{\tau}$, respectively, by means of a higher-order extrapolation using Gauss-Lobatto quadrature points given by*

$$\begin{aligned} u - \tilde{u}_{\tau} &\approx \mathbf{E}_{\tau}^{r+1} u_{\tau h} - u_{\tau h}, \\ z - \tilde{z}_{\tau} &\approx \mathbf{E}_{\tau}^{r+1} z_{\tau h} - z_{\tau h}, \end{aligned}$$

using an extrapolation in time operator \mathbf{E}_{τ}^{r+1} as introduced in Sec. 4.3.2.2. Due to this approximation technique, the integrals in time within the error indicators given by Eq. (5.120) and (5.121), respectively, are approximated by using an $(r + 1)$ -point Gauss quadrature rule; cf. Sec. 4.3.2.2 for more details.

- Approximate the spatial weights $u_\tau - \tilde{u}_{\tau h}$ by means of a patch-wise higher-order interpolation given by

$$u_\tau - \tilde{u}_{\tau h} \approx \mathbf{I}_{2h}^{(2p)} u_{\tau h} - u_{\tau h},$$

using an interpolation in space operator $\mathbf{I}_{2h}^{(2p)}$ as introduced in Sec. 3.3.1.

- Approximate the spatial weights $z_\tau - \tilde{z}_{\tau h}$ by means of a higher-order finite elements approach given by

$$z_\tau - \tilde{z}_{\tau h} \approx z_{\tau h} - \mathbf{R}_h^p z_{\tau h},$$

using a restriction in space operator \mathbf{R}_h^p as introduced in Sec. 3.3.1.

- Approximate the temporal velocity difference $\mathbf{v} - \mathbf{v}_\sigma$ by means of a higher-order extrapolation using Gauss-Lobatto quadrature points given by

$$\mathbf{v} - \mathbf{v}_\sigma \approx \mathbf{E}_\tau^{(r+1)} \mathbf{v}_\sigma - \mathbf{v}_\sigma,$$

with $\mathbf{E}_\tau^{(r+1)}$ acting componentwise like $\mathbf{E}_\tau^{(r+1)}$.

- Approximate the spatial velocity difference $\mathbf{v}_\sigma - \mathbf{v}_{\sigma h}$ by means of a patch-wise higher-order interpolation given by

$$\mathbf{v}_\sigma - \mathbf{v}_{\sigma h} \approx \mathbf{I}_{2h}^{(2p)} \mathbf{v}_{\sigma h} - \mathbf{v}_{\sigma h},$$

with $\mathbf{I}_{2h}^{(2p)}$ acting componentwise like $\mathbf{I}_{2h}^{(2p)}$. Note that the solution mesh transfer of the fully discrete solution $\mathbf{v}_{\sigma h}$ to the spatial mesh used for the transport problem is handled by a precasted function within the finite element library `deal.II` called `interpolate_to_different_mesh()`, cf. Sec. 5.3.3 for further details.

For the case of the implemented space-time approximation of Problem 5.1, the space-time domain $Q = \Omega \times I$ is divided into non-overlapping space-time slabs $Q_n^\ell = \mathcal{T}_{h,n}^\ell \times \mathcal{T}_{\tau,n}^\ell, n = 1, \dots, N^\ell$, as well as $Q_n^{\mathbf{F},\ell} = \mathcal{T}_{h,n}^{\mathbf{F},\ell} \times \mathcal{T}_{\sigma,n}^\ell, n = 1, \dots, N^{\mathbf{F},\ell}$, with $N^{\mathbf{F},\ell} \leq N^\ell$, for the transport and Stokes flow problem, respectively, as introduced in Assumption 2.5, where ℓ denotes the current DWR adaptivity loop here. For the underlying software architecture in general, we refer to Sec. 5.3.3 and Sec. 4.4, respectively, and for the effective implementation of the space-time tensor-product spaces in particular, we refer to Sec. 4.4.1. The fully discrete primal and dual solutions of the transport problem are represented by $u_{\tau h}^\ell$ and $z_{\tau h}^\ell$, respectively, and the fully discrete primal solution of the Stokes flow problem is represented by $\mathbf{u}_{\sigma h}^\ell = \{\mathbf{v}_{\sigma h}^\ell, p_{\sigma h}^\ell\}$.

Implemented Multirate-DWR Algorithm for Coupled Problems

Initialization: Set DWR loop $\ell = 1$ and generate the initial space-time slabs $Q_n^1 = \mathcal{T}_{h,n}^1 \times \mathcal{T}_{\tau,n}^1, n = 1, \dots, N^1$, as well as $Q_n^{F,1} = \mathcal{T}_{h,n}^{F,1} \times \mathcal{T}_{\sigma,n}^1, n = 1, \dots, N^{F,1}, N^{F,1} \leq N^1$ for the transport and Stokes flow problem, respectively, where we restrict $\mathcal{T}_{\tau,n}^1, \mathcal{T}_{\sigma,n}^1$ to consist of only one cell in time on each slab.

1. Solve the **Fully Discrete cG(p)-dG(r) Primal Stokes Flow Problem 5.7:**

Find $\mathbf{u}_{\sigma h}^\ell = \{\mathbf{v}_{\sigma h}^\ell, p_{\sigma h}^\ell\} \in \mathcal{Y}_{\sigma h}^{\text{dG}(r),p}$ such that $B_{\sigma h}(\mathbf{u}_{\sigma h}^\ell)(\boldsymbol{\varphi}_{\sigma h}) = F_{\sigma h}(\boldsymbol{\varphi}_{\sigma h})$,
for all $\boldsymbol{\varphi}_{\sigma h} = \{\boldsymbol{\psi}_{\sigma h}, \chi_{\sigma h}\} \in \mathcal{Y}_{\sigma h}^{\text{dG}(r),p}$.

2. Solve the **Stabilized cG(p)-dG(r) Primal Transport Problem 5.8:**

Find $u_{\tau h}^\ell \in \mathcal{X}_{\tau h}^{\text{dG}(r),p}$ such that $A_S(u_{\tau h}^\ell; \mathbf{v}_{\sigma h}^\ell)(\varphi_{\tau h}) = G_{\tau h}(\varphi_{\tau h})$,
for all $\varphi_{\tau h} \in \mathcal{X}_{\tau h}^{\text{dG}(r),p}$, using $\mathbf{v}_{\sigma h}^\ell$ from step 1.

3. **Break if the goal for the transport problem is reached**, i.e., for instance, $\|u - u_{\tau h}^\ell\| < \text{tol}$, or $(\eta_\tau + \eta_h) < \text{tol}$, or $\max N_{\text{DoF}}^{\text{tot}}$ is reached, etc.

4. Solve the **Stabilized cG(q)-dG(s) Dual Transport Problem 5.11:**

Find $z_{\tau h}^\ell \in \mathcal{X}_{\tau h}^{\text{dG}(r),q}$ such that $A'_S(u_{\tau h}^\ell; \mathbf{v}_{\sigma h}^\ell)(\psi_{\tau h}, z_{\tau h}^\ell) = J'(u_{\tau h}^\ell)(\psi_{\tau h})$,
for all $\psi_{\tau h} \in \mathcal{X}_{\tau h}^{\text{dG}(r),q}$, where $q > p, s \geq r$ using $\mathbf{v}_{\sigma h}^\ell$ from step 1.

5. Evaluate the **local a posteriori space-time error indicators** $\eta_\tau^{n,\ell}, \eta_h^{n,\ell}$ given by Eqs. (5.120), (5.121) for the **transport** problem by marching sequentially through all space-time slabs $Q_n^\ell, n = 1, \dots, N^\ell$, and the **auxiliary error indicators** $\tilde{\eta}_\sigma^{F,n,\ell}, \tilde{\eta}_h^{F,n,\ell}$ given by Eq. (5.139) for the **Stokes flow** problem, by marching sequentially through all space-time slabs $Q_n^{F,\ell}, n = 1, \dots, N^{F,\ell}$.

6. **If** $|\tilde{\eta}_{\sigma h}^{F,\ell}| = |\tilde{\eta}_\sigma^{F,\ell}| + |\tilde{\eta}_h^{F,\ell}| > \varpi (|\eta_\tau^\ell| + |\eta_h^\ell|), \varpi \geq 1$:

- (i) **Mark the slabs** $Q_{\tilde{n}}^{F,\ell}, \tilde{n} \in \{1, \dots, N^{F,\ell}\}$, **for temporal refinement** if the corresponding $\tilde{\eta}_\sigma^{F,\tilde{n},\ell}$ is in the set of $\theta_\sigma^{\text{top}}, 0 \leq \theta_\sigma^{\text{top}} \leq 1$, percent of the worst indicators.

- (ii) **Mark the cells** $\tilde{K}^F \in \mathcal{T}_{h,n}^{F,\ell}$ **for spatial refinement** if the corresponding $\tilde{\eta}_h^{F,n,\ell}|_{\tilde{K}^F}$ is in the set of $\theta_{h,1}^{F,\text{top}}$ or $\theta_{h,2}^{F,\text{top}}$ (for a slab that is or is not marked for temporal refinement), $0 \leq \theta_{h,2}^{F,\text{top}} \leq \theta_{h,1}^{F,\text{top}} \leq 1$, percent of the worst indicators, **or**, respectively, **mark for spatial coarsening** if $\tilde{\eta}_h^{F,n,\ell}|_{\tilde{K}^F}$ is in the set of $\theta_h^{F,\text{bottom}}$, $0 \leq \theta_h^{F,\text{bottom}} \leq 1$, percent of the best indicators.
- (iii) **Execute spatial refinement and/or coarsening** on all slabs of the Stokes flow problem under the use of mesh smoothing operators.
- (iv) **Execute temporal refinement** on all slabs of the Stokes flow problem.

Else:

Do not refine the temporal and spatial meshes of the Stokes flow problem and continue with Step 7.

7. Refine the temporal and spatial meshes of the **transport** problem as follows:

- (i) **If** $|\eta_\tau^\ell| > \omega |\eta_h^\ell|, \omega \geq 1$, (**Temporal error dominating case**):
Mark the slabs $Q_{\tilde{n}}^\ell, \tilde{n} \in \{1, \dots, N^\ell\}$, **for temporal refinement** if the corresponding $\eta_{\tilde{n}}^{\tau,\ell}$ is in the set of $\theta_\tau^{\text{top}}, 0 \leq \theta_\tau^{\text{top}} \leq 1$, percent of the worst indicators.
- (ii) **Else if** $|\eta_h^\ell| > \omega |\eta_\tau^\ell|, \omega \geq 1$, (**Spatial error dominating case**):
Mark the cells $\tilde{K} \in \mathcal{T}_{h,n}^\ell$ **for spatial refinement** if the corresponding $\eta_h^{n,\ell}|_{\tilde{K}}$ is in the set of $\theta_{h,1}^{\text{top}}$ or $\theta_{h,2}^{\text{top}}$ (for a slab that is or is not marked for temporal refinement), $0 \leq \theta_{h,2}^{\text{top}} \leq \theta_{h,1}^{\text{top}} \leq 1$, percent of the worst indicators, **or**, respectively, **mark for spatial coarsening** if $\eta_h^{n,\ell}|_{\tilde{K}}$ is in the set of $\theta_h^{\text{bottom}}, 0 \leq \theta_h^{\text{bottom}} \leq 1$, percent of the best indicators.
- (iii) **Else** (**Temporal and spatial errors are equilibrated**):
Mark the slabs $Q_{\tilde{n}}^\ell, \tilde{n} \in \{1, \dots, N^\ell\}$, **for temporal refinement** as well as **mark the cells** $\tilde{K} \in \mathcal{T}_{h,n}^\ell$ **for spatial coarsening and refinement** as described in Step 7(i) and Step 7(ii), respectively.
- (iv) **Execute spatial refinement and/or coarsening** on all slabs of the transport problem under the use of mesh smoothing operators.
- (v) **Execute temporal refinement** on all slabs of the transport problem.

8. Increase ℓ to $\ell + 1$ and **return to Step 1**.

Remark 5.18 *Let us remark some aspects about the implemented algorithm above.*

- *For the spatial discretization of the Stokes flow problem we are using Taylor-Hood elements Q_p/Q_{p-1} , $p \geq 2$. This choice represents conforming inf-sup stable pairs of finite element spaces, cf., e.g., [112, Sec. 4.2.1].*
- *Restricting the temporal triangulation $\mathcal{T}_{\tau,n}^\ell$ within a single slab Q_n^ℓ to consist of only one cell in time allows for interpreting this cell $K_n \in \mathcal{T}_{\tau,n}^\ell$ as the time subinterval I_n , $n = 1, \dots, N^\ell$; cf. Rem.2.3 in Sec.2.2. Then, the time step size τ_K corresponds to the length of the subinterval I_n given by $(t_n^T - t_{n-1}^T)$ and the variational system may be represented as time marching scheme (TMS) in a classical sense; cf. Sec.5.1.1. The same holds true for the decomposition of the Stokes flow problem.*
- *Nevertheless, in some numerical examples in Sec. 5.4 we use temporal triangulations consisting of more than one cell in time on a slab and compare this approach to the classical restriction to one cell described above.*

Remark 5.19 (Kelly Error Estimator) *The absence of an error estimator based on the DWR approach by means of solving an additional dual problem could be bypassed, for instance, using a so-called Kelly Error Estimator [126] that was originally developed for Laplace's equation and tries to approximate the error per cell by integration of the jump of the gradient of the solution along the faces of each cell, cf. the reference documentation of the `KellyErrorEstimator` class of the `deal.II` library for more details as well as [4] for a further discussion. The disadvantage compared to error indicators based on the DWR method is the missing weighting by means of measuring the discretization error in the goal functional which may lead to unnecessary refinement depending on the respective goal.*

Finally, for the sake of completeness, we present an illustration of the implemented algorithm in Fig. 5.7.

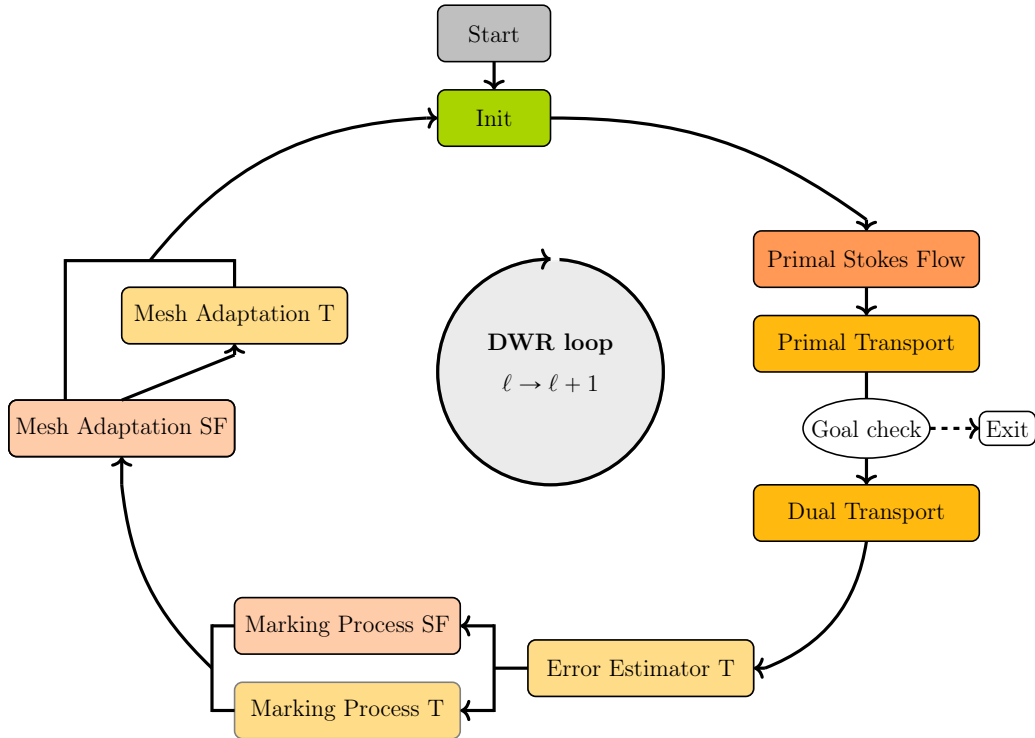


Figure 5.7: Illustration of the Implemented Multirate-DWR Algorithm for Coupled Problems.

5.4 Numerical Examples

In this section, we illustrate and investigate the performance properties of the proposed multirate in time approach combined with goal-oriented space-time adaptive error control based on the Dual Weighted Residual method for coupled flow and transport problems. More precisely, we study convergence, computational efficiency and stability of the underlying multirate adaptive algorithm introduced in Sec. 5.3.4.3.

The first example is an academic test problem with given analytical solutions to study the convergence behavior of the two subproblems and, in particular, the coupling between them. The second example serves to demonstrate the performance properties of the algorithm with regard to adaptive mesh refinement in space and time and different goal functionals. Finally, the third example is motivated by a problem of physical relevance in which we simulate a convection-dominated transport with goal-oriented adaptivity of a species through a channel with a constraint.

Here and in the following, we denote by $w_{\tau h}^{p,r}$ and $\mathbf{w}_{\sigma h}^{p,r}$, respectively, an exemplary approximated solution obtained by using a space-time cG(p)-dG(r) method; cf. Rem. 4.2. For the spatial discretization of the Stokes flow problem, we are using

Taylor-Hood elements Q_p/Q_{p-1} , $p \geq 2$. We note that this choice represents conforming inf-sup stable pairs of finite element spaces, cf., e.g., [112, Sec. 4.2.1] for more details. Similar to the previous two chapters, we will consider in some cases an effectivity index for the transport problem, as given by

$$\mathcal{I}_{\text{eff}} := \left| \frac{\eta_\tau + \eta_h}{J(u) - J(u_{\tau h})} \right|, \quad (5.140)$$

measuring the ratio of the sum of the estimated errors in space and time over the exact error. In general, the tuning parameters with regard to the adaptive mesh refinement process used in the respective algorithms given in Sec. 5.3.4 are chosen to balance automatically the potential misfit of the spatial and temporal errors. If not specified differently in the respective sections, these parameters are given by the following ranges.

$$\begin{aligned} 1.0 \leq \varpi \leq 3.0, \quad 1.0 \leq \omega \leq 3.5, \quad 0 \leq \theta_h^{\text{bottom}}, \theta_h^{\text{F,bottom}} \leq 0.02, \\ \theta_{h,1}^{\text{top}} \geq \theta_{h,2}^{\text{top}} = \frac{1}{2} \cdot \min \left\{ \left| \frac{\eta_h}{|\eta_h| + |\eta_\tau|} \right|, 1 \right\}, \quad \theta_\tau^{\text{top}} = \frac{1}{2} \cdot \min \left\{ \left| \frac{\eta_\tau}{|\eta_h| + |\eta_\tau|} \right|, 1 \right\}, \\ \theta_{h,1}^{\text{F,top}} \geq \theta_{h,2}^{\text{F,top}} = \frac{1}{2} \cdot \min \left\{ \left| \frac{\eta_h^{\text{F}}}{|\eta_h^{\text{F}}| + |\eta_\tau^{\text{F}}|} \right|, 1 \right\}, \quad \theta_\sigma^{\text{top}} = \frac{1}{2} \cdot \min \left\{ \left| \frac{\eta_\tau^{\text{F}}}{|\eta_h^{\text{F}}| + |\eta_\tau^{\text{F}}|} \right|, 1 \right\}. \end{aligned} \quad (5.141)$$

Finally, the SUPG method stabilization parameter δ_K is given by

$$\delta_K = \delta_0 \cdot h_K, \quad 0.1 \leq \delta_0 \leq 1, \quad (5.142)$$

where h_K denotes the cell diameter of the spatial mesh cell K , cf. Rem. 4.3.

The software for the now following examples is called `dwr-stokes-condiffrea` being a module of our in-house DWR software project `DTM++.Project/dwr` (bitbucket.org/dtmproject) developed by U. Köcher [128, 129]. It is implemented using the open source finite element library `deal.II`; cf. [17]. Some of the results presented in the following have been published in [52] and [29], respectively.

5.4.1 Higher-Order Space-Time Convergence Studies

In a first numerical example, we study the global space-time refinement behavior to verify the expected experimental orders of convergence and show the correctness of the higher-order implementations in space and time. We consider the following two cases, namely the case of a Stokes flow problem solved on its own as well as the case of a non-stabilized solved convection-diffusion-reaction transport problem coupled with this Stokes equation via the convection field solution $\mathbf{v}_{\sigma h}$. The latter may be compared to the results of a transport equation solved by its own with a constant convection field $\mathbf{v} = (2, 3)^\top$ that can be found in Sec. 4.5.1 of the previous chapter. For this purpose, we consider the following example.

Example 5.1 (Bechmark Stokes Flow)

The first example is an academic test case, in which we study the time dependent Stokes flow problem given by Eq. (5.2) with the prescribed exact solution (cf. [40, Example 1])

$$\begin{aligned}\mathbf{v}(\mathbf{x}, t) &:= \begin{pmatrix} \sin(t) \sin^2(\pi x_1) \sin(\pi x_2) \cos(\pi x_2) \\ -\sin(t) \sin(\pi x_1) \cos(\pi x_1) \sin^2(\pi x_2) \end{pmatrix}, \\ p(\mathbf{x}, t) &:= \sin(t) \sin(\pi x_1) \cos(\pi x_1) \sin(\pi x_2) \cos(\pi x_2),\end{aligned}\tag{5.143}$$

with $\mathbf{x} = (x_1, x_2)^\top \in \mathbb{R}^2, t \in \mathbb{R}$ and $\nabla \cdot \mathbf{v} = 0$. The viscosity is set to $\nu = 0.5$. The stream function, velocity, and pressure of the (analytical) solution (5.143) given at an exemplary time point are presented in Fig. 5.8. The problem is defined on $Q = \Omega \times I := (0, 1)^2 \times (0, 1]$. The initial and boundary conditions are given as

$$\mathbf{v} = 0 \text{ on } \Sigma_0 = \Omega \times \{0\}, \quad \mathbf{v} = 0 \text{ on } \Sigma_D = \partial\Omega \times (0, 1),$$

and the volume force term \mathbf{f} is calculated from the given analytical solution (5.143) and Eq. (5.2). The global $L^2(I; L^2(\Omega)^d)$ -norm (for short, $L^2(L^2)$ -norm) is given by

$$\|\cdot\|_{(0,T) \times \Omega} := \|\cdot\|_{L^2(I; L^2(\Omega)^d)} = \left(\int_I (\cdot, \cdot) dt \right)^{\frac{1}{2}}.\tag{5.144}$$

In general, for a cG(p)-dG(r) method, measured in the $L^2(L^2)$ -norm, we may expect convergence in space-time of order $\mathcal{O}(h^{p+1} + \tau^{r+1})$; cf., e.g., [174, 142] and, in particular, for the Stokes flow problem, e.g. [79, Rem. 73.5],[112, Corollary 4.30]. To study the global space-time refinement behavior, the solution $\{\mathbf{v}, p\}$ is approximated in different finite element spaces. More precisely, we consider the approximation of $\{\mathbf{v}, p\}$ by means of the space-time higher-order methods $\{\text{cG}(2)\text{-dG}(2), \text{cG}(1)\text{-dG}(2)\}$ and $\{\text{cG}(3)\text{-dG}(3), \text{cG}(2)\text{-dG}(3)\}$, respectively. Due to the same polynomial orders of the spatial and temporal discretizations with respect to the flow field \mathbf{v} , and lower polynomial order in space compared to in time with respect to the pressure variable p , we expect experimental orders of convergence (EOC := $-\log_2(\|e\|_\ell / \|e\|_{\ell-1})$) for \mathbf{v} of $\text{EOC}^{2,2} \approx 3$ for the cG(2)-dG(2) method and $\text{EOC}^{3,3} \approx 4$ for the cG(3)-dG(3) method, as well as $\text{EOC}^{1,2} \approx 2$ for the cG(1)-dG(2) method and $\text{EOC}^{2,3} \approx 3$ for the cG(2)-dG(3) method for p , respectively, for a global refinement convergence test. The results are given by Table 5.1 and nicely confirm the expected experimental orders of convergence. Here, ℓ denotes the refinement level, N^F the number of slabs, $K_n^{\text{F,tot}}$ the total number of cells in time, N_K^F the cells in space on a slab, $N_{\text{DoF}}^{\text{F,tot}}$ the total space-time degrees of freedom, $\|\cdot\|$ the global $L^2(L^2)$ -norm error as given in Eq. (5.144) and EOC the experimental order of convergence.

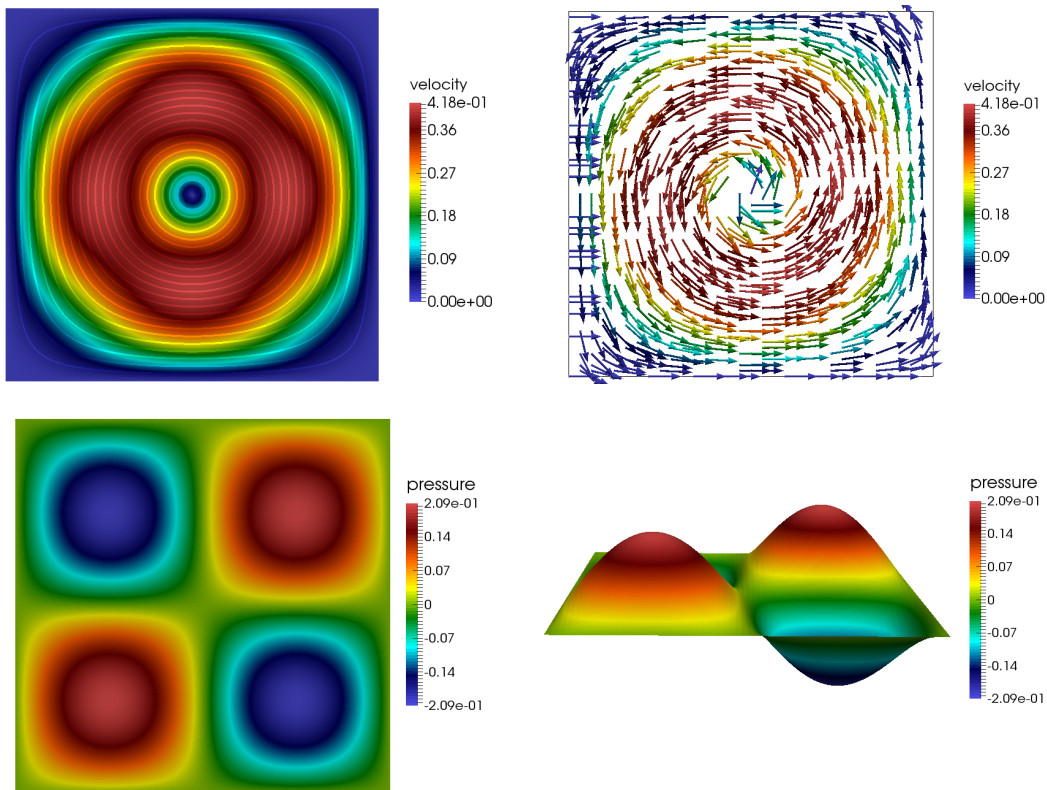


Figure 5.8: Exemplary stream function (top left) velocity (top right) and pressure (bottom) at final time point $t_N = T = 1$ for Example 5.1.

ℓ	N^F	$K_n^{F,\text{tot}}$	N_K^F	$N_{\text{DoF}}^{F,\text{tot}}$	$\ \mathbf{v} - \mathbf{v}_{\sigma h}^{2,2}\ $	EOC	$\ p - p_{\sigma h}^{1,2}\ $	EOC
1	4	4	16	2244	3.7974e-03	—	2.0593e-02	—
2	8	8	64	15816	4.4945e-04	3.08	2.5898e-03	2.99
3	16	16	256	118416	5.5129e-05	3.03	5.5087e-04	2.23
4	32	32	1024	915744	6.8603e-06	3.01	1.3405e-04	2.04
5	64	64	4096	7201344	8.5697e-07	3.00	3.3291e-05	2.01
6	128	128	16384	57115776	1.0713e-07	3.00	8.3039e-06	2.00
7	256	256	65536	454953216	1.3394e-08	3.00	2.0740e-06	2.00

ℓ	N^F	$K_n^{F,\text{tot}}$	N_K^F	$N_{\text{DoF}}^{F,\text{tot}}$	$\ \mathbf{v} - \mathbf{v}_{\sigma h}^{3,3}\ $	EOC	$\ p - p_{\sigma h}^{2,3}\ $	EOC
1	4	4	16	6704	3.0085e-04	—	3.6349e-03	—
2	8	8	64	49248	1.9122e-05	3.98	4.9603e-04	2.87
3	16	16	256	377024	1.2073e-06	3.99	4.6902e-05	3.40
4	32	32	1024	2949504	7.5829e-08	3.99	4.6449e-06	3.34
5	64	64	4096	23331584	4.7494e-09	4.00	5.3029e-07	3.13
6	128	128	16384	185599488	2.9712e-10	4.00	6.4815e-08	3.03

Table 5.1: Global convergence for $\mathbf{v}_{\sigma h}^{2,2}, p_{\sigma h}^{1,2}$ in a $\{\text{cG}(2)\text{-dG}(2), \text{cG}(1)\text{-dG}(2)\}$ and $\mathbf{v}_{\sigma h}^{3,3}, p_{\sigma h}^{2,3}$ in a $\{\text{cG}(3)\text{-dG}(3), \text{cG}(2)\text{-dG}(3)\}$ primal approximation for a time-dependent Stokes flow problem with $\nu = 0.5$ for Example 5.1. Each slab includes a temporal triangulation that consists of one cell in time.

ℓ	N^F	$K_n^{F,\text{tot}}$	N_K^F	$N_{\text{DoF}}^{F,\text{tot}}$	$\ \mathbf{v} - \mathbf{v}_{\sigma h}^{2,2}\ $	EOC	$\ p - p_{\sigma h}^{1,2}\ $	EOC
1	1	4	16	2244	3.7541e-03	—	2.0683e-02	—
2	2	8	64	15816	4.4315e-04	3.08	2.5754e-03	3.01
3	4	16	256	118416	5.4348e-05	3.03	5.4736e-04	2.23
4	8	32	1024	915744	6.7589e-06	3.01	1.3353e-04	2.04
5	16	64	4096	7201344	8.4385e-07	3.00	3.3221e-05	2.01

ℓ	N^F	$K_n^{F,\text{tot}}$	N_K^F	$N_{\text{DoF}}^{F,\text{tot}}$	$\ \mathbf{v} - \mathbf{v}_{\sigma h}^{3,3}\ $	EOC	$\ p - p_{\sigma h}^{2,3}\ $	EOC
1	1	4	16	6704	2.9764e-04	—	3.6385e-03	—
2	2	8	64	49248	1.8822e-05	3.98	4.9491e-04	2.88
3	4	16	256	377024	1.1863e-06	3.99	4.6552e-05	3.41
4	8	32	1024	2949504	7.4484e-08	3.99	4.5766e-06	3.35

Table 5.2: Global convergence for $\mathbf{v}_{\sigma h}^{2,2}, p_{\sigma h}^{1,2}$ in a $\{\text{cG}(2)\text{-dG}(2), \text{cG}(1)\text{-dG}(2)\}$ and $\mathbf{v}_{\sigma h}^{3,3}, p_{\sigma h}^{2,3}$ in a $\{\text{cG}(3)\text{-dG}(3), \text{cG}(2)\text{-dG}(3)\}$ primal approximation for a time-dependent Stokes flow problem with $\nu = 0.5$ for Example 5.1. Each slab includes a temporal triangulation that consists of four cells in time.

To verify our approach of allowing more than one cell in time on a slab including additional coupling terms appearing due to the jumps at the transition of two consecutive cells in time, we perform the same convergence test a second time using slabs whose corresponding temporal triangulations consist of four cells in time, cf. Assumption 2.5 as well as Sec. 4.4.1 and Fig.4.6 for the details of this approach. The results are given by Table 5.2 starting with only one slab within the first loop. As desired, the same orders of convergence as in Table 5.1 are obtained, albeit negligible differences are visible with regard to the respective errors in the global $L^2(L^2)$ -norm, which may depend on solving less but larger systems in the second case but we are not able to explain so far. We skipped here in each case the last two refinement loops due to the disproportionate running time compared to the known results, cf. the tremendous number of total space-time degrees of freedom ($N_{\text{DoF}}^{F,\text{tot}}$) in the last two rows of Table 5.1.

The second part of the first example now serves to verify the higher-order implementation of the coupled problem. To compare the following results to the case of a transport equation solved by its own with a constant convection field $\mathbf{v} = (2, 3)^\top$ given by Table 4.1 in Sec. 4.5.1, we are using the same (analytical) solution for the transport equation again. This case is summarized in the following example.

Example 5.2 (Rotating Hill)

We consider the Coupled Flow and Transport Problem 5.1 given by the Eqs. (5.1) and (5.2), respectively. Thereby, the time-dependent Stokes flow problem (5.2) is studied with the prescribed exact solution (5.143) as outlined in Example 5.1. Here,

the convection-diffusion-reaction transport problem given by Eq. (5.1) is studied with the prescribed exact solution (cf. [98, Sec. 1.4.2])

$$\begin{aligned} u(\mathbf{x}, t) &:= u_1 \cdot u_2, \quad \mathbf{x} = (x_1, x_2)^\top \in \mathbb{R}^2 \text{ and } t \in \mathbb{R}, \\ u_1(\mathbf{x}, t) &:= (1 + a \cdot ((x_1 - m_1(t))^2 + (x_2 - m_2(t))^2))^{-1}, \\ u_2(\mathbf{x}, t) &:= s, \quad m_1(t) := \frac{1}{2} + \frac{1}{4} \cos(2\pi t), \quad m_2(t) := \frac{1}{2} + \frac{1}{4} \sin(2\pi t). \end{aligned} \quad (5.145)$$

The (analytic) solution (5.145) mimics a counterclockwise rotating hill whose size and gradient are depending on the scalars s, a_0 . The problem is defined on $Q = \Omega \times I := (0, 1)^2 \times (0, 1]$ with the scalars $s = 1, a_0 = 50$ such that the final position of the hill equals the initial one and its peak is close to the value 1, cf. Fig. 4.15. The right-hand side forcing term g , the nonhomogeneous Dirichlet boundary condition and the initial condition are calculated from the given analytical solution (5.145) and Eqs. (5.1). We choose the diffusion coefficient $\varepsilon = 1$, the convection field \mathbf{v} is given by the exact Stokes solution (5.143) and the reaction coefficient is set to $\alpha = 1$. Since we study the global space-time refinement behavior here, we restrict the transport problem to a non-stabilized case, i.e. we set $\delta_0 := 0$ within the local SUPG stabilization parameter δ_K given by Eq. (5.142).

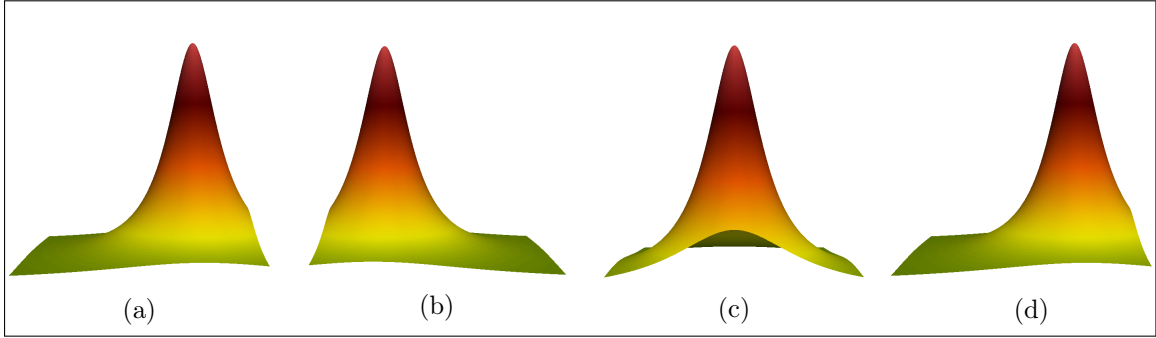


Figure 5.9: Exemplary solution profiles at time points $t_n = 0$ (a), $t_n = 0.5$ (b), $t_n = 0.75$ (c) and $t_n = 1$ (d) for Example 5.2.

With regard to the practical implementation, we note that the assembly of the transport system matrix uses the approximated fully-discrete Stokes solution \mathbf{v}_{sh} of Problem 5.7 that has to be transferred to the spatial and temporal mesh of the transport problem, cf. the last note in Assumption 5.6 as well as Sec. 5.3.3.

The global space-time refinement behavior is illustrated by Table 5.3 and nicely confirms our results with respect to the expected EOCs for the solely solved transport problem including a constant convection field $\mathbf{v} = (2, 3)^\top$ obtained by Table 4.1 in Sec. 4.5.1, cf. columns five and six of Table 5.3. Furthermore, with regard to the

ℓ	N	N_K	$N_{\text{DoF}}^{\text{tot}}$	$\ u - u_{\tau h}^{1,1}\ $	EOC	N^{F}	N_K^{F}	$N_{\text{DoF}}^{\text{F,tot}}$	$\ \mathbf{v} - \mathbf{v}_{\sigma h}^{2,0}\ $	EOC
1	4	4	72	1.8778e-01	—	4	16	748	4.5783e-03	—
2	8	16	400	5.7990e-02	1.70	8	64	5272	1.7196e-03	1.41
3	16	64	2592	1.5808e-02	1.88	16	256	39472	9.9383e-04	0.79
4	32	256	18496	4.4262e-03	1.84	32	1024	305248	5.6228e-04	0.82
5	64	1024	139392	1.1384e-03	1.96	64	4096	2400448	3.0374e-04	0.89
6	128	4096	1081600	2.8829e-04	1.98	128	16384	19038592	1.5868e-04	0.94
7	256	16384	8520192	7.2658e-05	1.99	256	65536	151651072	1.5868e-04	0.94

ℓ	N	N_K	$N_{\text{DoF}}^{\text{tot}}$	$\ u - u_{\tau h}^{2,2}\ $	EOC	N^{F}	N_K^{F}	$N_{\text{DoF}}^{\text{F,tot}}$	$\ \mathbf{v} - \mathbf{v}_{\sigma h}^{3,0}\ $	EOC
1	2	1	54	2.3725e-01	—	2	1	72	3.8910e-02	—
2	4	4	300	1.5974e-01	0.57	4	4	428	7.6009e-03	2.36
3	8	16	1944	1.2939e-02	3.60	8	16	2904	1.7488e-03	2.12
4	16	64	13872	2.3660e-03	2.45	16	64	21296	9.9237e-04	0.82
5	32	256	104544	3.2088e-04	2.88	32	256	162912	5.6213e-04	0.82
6	64	1024	811200	4.2252e-05	2.92	64	1024	1274048	3.0373e-04	0.89
7	128	4096	6390144	5.8599e-06	2.85	128	4096	10076544	1.5868e-04	0.94

Table 5.3: Global convergence for $u_{\tau h}^{1,1}$ in a cG(1)-dG(1) and $u_{\tau h}^{2,2}$ in a cG(2)-dG(2) primal solution approximation of the transport problem for Example 5.2 using $\mathbf{v}_{\sigma h}^{2,0}$ in a cG(2)-dG(0) and $\mathbf{v}_{\sigma h}^{3,0}$ in a cG(3)-dG(0) primal solution approximation of the Stokes flow problem for Example 5.1.

EOCs of the Stokes solution, we note that both approximations cG(2)-dG(0) as well as cG(3)-dG(0) are restricted through the lowest order approximation in time, cf. the last two columns of Table 5.3.

Conclusion 5.1 (Convergence Behavior Stokes Flow, Coupled Problem)

As an interim conclusion, we summarize the following.

- *The algorithm confirms the expected experimental orders of convergence in space and time $\mathcal{O}(h^{p+1} + \tau^{r+1})$ for the time-dependent Stokes flow problem (5.2) regarding one or four cells in time per slab; cf. Tables 5.1 and 5.2, respectively.*
- *The algorithm confirms the expected experimental orders of convergence in space and time $\mathcal{O}(h^{p+1} + \tau^{r+1})$ for the Coupled Flow and Transport Problem 5.1; cf. Table 5.3.*
- *The experimental orders of convergence for the Coupled Flow and Transport Problem 5.1 confirm the orders of convergence of a solely solved transport problem using a fixed convection field $\mathbf{v} = (2, 3)^\top$ that can be found in Table 4.1 of the previous chapter.*

5.4.2 Space-Time Adaptivity Studies for Coupled Problems

The second example serves to study the goal-oriented space-time adaptivity behavior of our multirate DWR algorithm introduced in Sec. 5.3.4.3. In this sense, we modify Example 5.2 of the previous section regarding more dynamic behavior in time. This modification is summarized in the following example.

Example 5.3 (Rotating Hill with Changing Orientation)

We consider the Coupled Flow and Transport Problem 5.1 given by the Eqs. (5.1) and (5.2), respectively. Thereby, the time-dependent Stokes flow problem (5.2) is studied with the prescribed exact solution (5.143) as outlined in Example 5.1. Here, the convection-diffusion-reaction transport problem given by Eq. (5.1) is now studied with the prescribed exact solution (cf. [98, Sec. 1.4.2])

$$\begin{aligned} u(\mathbf{x}, t) &:= u_1 \cdot u_2, \quad \mathbf{x} = (x_1, x_2)^\top \in \mathbb{R}^2 \text{ and } t \in \mathbb{R}, \\ u_1(\mathbf{x}, t) &:= (1 + a \cdot ((x_1 - m_1(t))^2 + (x_2 - m_2(t))^2))^{-1}, \\ u_2(t) &:= \nu_1(t) \cdot s \cdot \arctan(\nu_2(t)), \end{aligned} \quad (5.146)$$

with $m_1(t) := \frac{1}{2} + \frac{1}{4} \cos(2\pi t)$ and $m_2(t) := \frac{1}{2} + \frac{1}{4} \sin(2\pi t)$, and, $\nu_1(\hat{t}) := -1, \nu_2(\hat{t}) := 5\pi \cdot (4\hat{t} - 1)$, for $\hat{t} \in [0, 0.5)$ and $\nu_1(\hat{t}) := 1, \nu_2(\hat{t}) := 5\pi \cdot (4(\hat{t} - 0.5) - 1)$, for $\hat{t} \in [0.5, 1)$, $\hat{t} = t - k, k \in \mathbf{N}_0$, and, scalars $s = \frac{1}{3}, a_0 = 50$.

The (analytical) solution behaves as in Example 5.2, but is designed in such a way that the maximum height of the hill is compressed and the orientation of the hill changes its sign from positive to negative at $t = 0.25$ and again from negative to positive at $t = 0.75$, cf. Fig. 5.10. The problem is defined on $Q = \Omega \times I := (0, 1)^2 \times (0, 1]$. The right-hand side forcing term g , the nonhomogeneous Dirichlet boundary condition and the initial condition are calculated from the given analytical solution (5.146) and Eqs. (5.1). We choose the diffusion coefficient $\varepsilon = 1$, the convection field \mathbf{v} is given by the exact Stokes solution (5.143) and the reaction coefficient is set to $\alpha = 1$. Furthermore, no stabilization ($\delta_K = 0$) is used in this test case. The goal quantity is chosen to control the global $L^2(L^2)$ -error of $e, e = u - u_{\tau_h}$, in space and time, given by

$$J(u) = \frac{1}{\|e\|_{(0,T) \times \Omega}} \int_I (u, e) dt, \quad \text{with } \|\cdot\|_{(0,T) \times \Omega} = \left(\int_I (\cdot, \cdot) dt \right)^{\frac{1}{2}}. \quad (5.147)$$

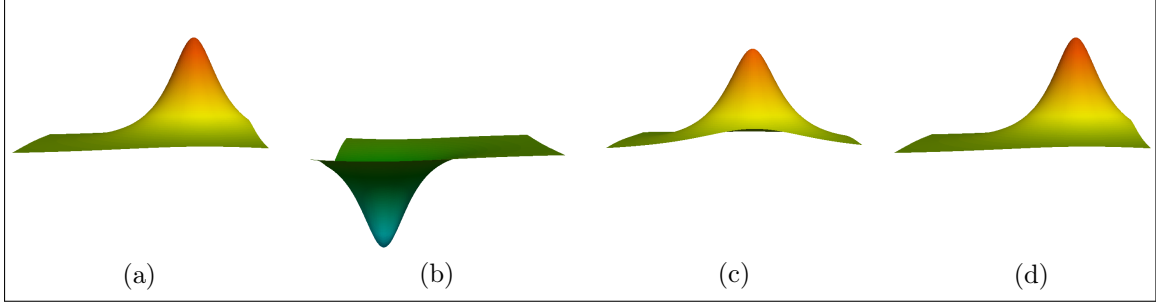


Figure 5.10: Exemplary solution profiles at time points $t_n = 0$ (a), $t_n = 0.5$ (b), $t_n = 0.8$ (c) and $t_n = 1$ (d) for Example 5.3.

In view of our multirate in time approach, we first put focus on the adaptive refinement process with respect to the temporal mesh of the transport problem using global refined meshes for the Stokes flow problem. More precisely, the transport problem is adaptively refined in space and time using an approximated Stokes solution $\mathbf{v}_{\sigma h}$ on a coarser global refined mesh in space and time. With regard to the characteristic times of the two subproblems defined in Assumption 5.1, the respective coefficients in Example 5.3 are chosen in such a way that there holds $t_{\text{transport}} < t_{\text{flow}}$. Thus, the initial space-time meshes of the transport problem are finer compared to the initial meshes of the Stokes flow problem, cf. the first rows of Tables 5.4–5.6 and the first plot of Fig. 5.11, respectively. Here, we set the auxiliary error indicators introduced in Eq. (5.139) as $\tilde{\eta}_{\sigma h}^F := \|\mathbf{v} - \mathbf{v}_{\sigma h}^{2,0}\|_{(0,T) \times \Omega}$, cf. also Step 7 of the algorithm introduced in Sec. 5.3.4.3. Thus, the temporal and spatial meshes of the Stokes flow problem are refined globally if the global $L^2(L^2)$ -error ($\|\mathbf{v} - \mathbf{v}_{\sigma h}^{p,r}\|_{(0,T) \times \Omega}$) for the Stokes flow problem is larger than its counterpart ($\|u - u_{\tau h}^{p,r}\|_{(0,T) \times \Omega}$) corresponding to the goal functional (5.147) for the transport problem, with $\mathbf{v}_{\sigma h}^{p,r}$ and $u_{\tau h}^{p,r}$ representing an approximated solution using a cG(p)-dG(r) method; cf. columns five and nine of Tables 5.4–5.6. The tuning parameters of the adaptive algorithm given in Sec. 5.3.4.3 are chosen to balance automatically the potential misfit of the spatial and temporal errors as

$$\begin{aligned}
 \theta_{h,1}^{\text{top}} &\geq \theta_{h,2}^{\text{top}} = \frac{1}{2} \cdot \left| \frac{\eta_h}{|\eta_h| + |\eta_\tau|} \right|, & \theta_h^{\text{bottom}} &= 0.02, & \theta_\tau^{\text{top}} &= \frac{1}{2} \cdot \left| \frac{\eta_\tau}{|\eta_h| + |\eta_\tau|} \right|, \\
 \theta_{h,1}^{\text{F,top}} &= \theta_{h,2}^{\text{F,top}} = 1.0, & \theta_h^{\text{F,bottom}} &= 0.0, & \theta_\sigma^{\text{top}} &= 1.0, \\
 \varpi &= 1.0, & 1.5 &\leq \omega \leq 3.0.
 \end{aligned}$$

In Tables 5.4–5.6, we present the development of the total discretization error $J(e) = \|e\|_{(0,T) \times \Omega}$ for goal functional (5.147), the spatial and temporal error indicators η_h and η_τ as well as the effectivity index \mathcal{I}_{eff} during an adaptive refinement process for

different primal and dual solution pairings $\{u_{\tau h}, z_{\tau h}\}$: $\{\text{cG}(1)\text{-dG}(0), \text{cG}(2)\text{-dG}(0)\}$, $\{\text{cG}(1)\text{-dG}(1), \text{cG}(2)\text{-dG}(1)\}$, $\{\text{cG}(2)\text{-dG}(2), \text{cG}(3)\text{-dG}(2)\}$ of the transport problem. Moreover, the development of the total discretization error $\|\mathbf{v} - \mathbf{v}_{\sigma h}^{p,r}\|_{(0,T)\times\Omega}$ (for short, in Tables 5.4–5.6 only $\|\mathbf{v} - \mathbf{v}_{\sigma h}^{p,r}\|$) for the Stokes flow solution on a global refined mesh in space and time is displayed. Here, ℓ denotes the refinement level or DWR loop, N or N^F the number of slabs, N_K^{\max} or $N_K^{F,\max}$ the number of spatial cells on the finest mesh within the current loop, and $N_{\text{DoF}}^{\text{tot}}$ or $N_{\text{DoF}}^{F,\text{tot}}$ the total space-time degrees of freedom of the transport or Stokes flow problem, respectively. Here and in the following, we use an approximation of the temporal weights by means of a higher-order extrapolation strategy using Gauss-Lobatto quadrature points, cf. Sec. 4.3.2.2 and Fig. 4.2 for the details of this approximation technique. This is due to the results regarding comparative studies of different approximation techniques performed in Sec. 4.5 of the previous chapter as well as efficiency reasons in view of reducing numerical costs compared to the higher-order finite elements approach.

Regarding the accuracy of the underlying error estimator, as given by the last column of Tables 5.4–5.6, we observe a good quantitative estimation of the discretization error as the respective effectivity indices are getting close to one in the course of the refinement process. With regard to efficiency reasons for a space-time adaptive algorithm, it is essential to ensure an equilibrated reduction of the temporal as well as spatial discretization error, cf. [40, Sec. 3.3]. Referring to this, we point out a good equilibration of the spatial and temporal error indicators η_h and η_τ in the course of the refinement process (columns ten and eleven of Table 5.4–5.6).

In Fig. 5.11, we visualize exemplarily the distribution of the adaptively determined time cell lengths τ_K of $\mathcal{T}_{\tau,n}$, used for the transport problem, as well as the distribution of the globally determined time cell lengths σ_K of $\mathcal{T}_{\sigma,n}$, used for the Stokes flow problem, over the whole time interval I for different DWR refinement loops, corresponding to Table 5.4. We point out that the respective figures corresponding to Table 5.5 and Table 5.6, respectively, show a similar distribution, albeit not explicitly displayed here. The initial temporal meshes for the transport and Stokes flow problem are chosen fulfilling the requirements presented in Sec. 5.1.1 and Fig. 5.1. While the time steps for the transport problem become smaller when the hill is changing its orientation ($t = 0.25$ and $t = 0.75$), the time steps for the Stokes flow problem stay comparatively large in the course of the refinement process, cf. the last two plots of Fig. 5.11. Away from the time points of orientation change, the temporal mesh of the transport problem is almost equally decomposed. This behavior seems natural for a global acting goal quantity (5.147) and nicely confirms our multirate in

DWR	Stokes Flow				Transport						
	N^F	$N_K^{F,\max}$	$N_{\text{DoF}}^{F,\text{tot}}$	$\ \mathbf{v} - \mathbf{v}_{\sigma_h}^{2,0}\ $	N	N_K^{\max}	$N_{\text{DoF}}^{\text{tot}}$	$J(e^{1,0,2,0})$	η_h	η_r	\mathcal{I}_{eff}
1	5	4	295	1.97e-02	10	16	250	5.25e-02	4.27e-03	3.34e-04	0.09
2				1.97e-02	10	40	438	4.68e-02	7.12e-04	3.55e-03	0.09
3				1.97e-02	14	40	616	1.73e-02	3.59e-03	1.59e-03	0.30
4	10	16	1870	4.10e-03	19	88	1913	1.10e-02	1.61e-03	3.78e-03	0.49
5				4.10e-03	26	160	4074	7.14e-03	6.66e-04	3.64e-03	0.60
6				4.10e-03	36	160	5534	5.04e-03	9.44e-04	2.59e-03	0.70
7				4.10e-03	50	268	11954	3.44e-03	4.24e-04	2.15e-03	0.75
8	20	64	13180	9.68e-04	70	268	16752	2.59e-03	5.38e-04	1.45e-03	0.77
9				9.68e-04	98	448	37900	1.84e-03	2.34e-04	1.18e-03	0.77
10	20	64	13180	9.68e-04	137	448	52937	1.40e-03	2.91e-04	8.38e-04	0.81

Table 5.4: Adaptive refinement in the transport problem (based on the DWR method) including effectivity indices for goal (5.147), with $\varepsilon = 1$, $\delta_0 = 0$, $\omega = 3$ for Example 5.3 using a Stokes solution $\mathbf{v}_{\sigma_h}^{2,0}$ related to a cG(2)-dG(0) method on global refined meshes in space and time. $e^{1,0,2,0}$ corresponds to the adaptive solution approximation $u_{\tau_h}^{1,0}$ in cG(1)-dG(0) and dual solution approximation $z_{\tau_h}^{2,0}$ in cG(2)-dG(0).

DWR	Stokes Flow				Transport						
	N^F	$N_K^{F,\max}$	$N_{\text{DoF}}^{F,\text{tot}}$	$\ \mathbf{v} - \mathbf{v}_{\sigma_h}^{2,0}\ $	N	N_K^{\max}	$N_{\text{DoF}}^{\text{tot}}$	$J(e^{1,1,2,1})$	η_h	η_r	\mathcal{I}_{eff}
1	5	4	295	1.97e-02	20	16	1000	2.55e-02	2.12e-02	1.23e-04	0.83
2				1.97e-02	20	28	1640	1.16e-02	1.28e-02	4.41e-03	1.48
3	10	16	1870	4.10e-03	20	76	2956	7.73e-03	3.99e-03	5.23e-03	1.19
4				4.10e-03	28	124	6468	4.34e-03	3.63e-03	4.31e-03	1.83
5				4.10e-03	39	172	11694	2.84e-03	2.31e-03	3.45e-03	2.02
6	20	64	13180	9.68e-04	54	232	20348	1.95e-03	8.63e-04	3.17e-03	2.07
7				9.68e-04	64	232	24600	1.89e-03	2.21e-04	1.83e-03	1.08
8				9.68e-04	75	232	28022	1.87e-03	5.16e-04	1.29e-03	0.97
9				9.68e-04	147	316	66570	1.47e-03	7.05e-04	8.05e-04	1.02
10	40	256	98680	4.69e-04	283	532	220298	8.42e-04	4.54e-04	4.15e-04	1.03

Table 5.5: Adaptive refinement in the transport problem (based on the DWR method) including effectivity indices for goal (5.147), with $\varepsilon = 1$, $\delta_0 = 0$, $\omega = 2.5$ for Example 5.3 using a Stokes solution $\mathbf{v}_{\sigma_h}^{2,0}$ related to a cG(2)-dG(0) method on a global refined mesh in space and time. $e^{1,1,2,1}$ corresponds to the adaptive solution approximation $u_{\tau_h}^{1,1}$ in cG(1)-dG(1) and dual solution approximation $z_{\tau_h}^{2,1}$ in cG(2)-dG(1).

DWR	Stokes Flow				Transport						
	N^F	$N_K^{F,\max}$	$N_{\text{DoF}}^{F,\text{tot}}$	$\ \mathbf{v} - \mathbf{v}_{\sigma_h}^{3,0}\ $	N	N_K^{\max}	$N_{\text{DoF}}^{\text{tot}}$	$J(e^{2,2,3,2})$	η_h	η_r	\mathcal{I}_{eff}
1	5	4	535	7.53e-03	10	16	2430	1.39e-02	6.21e-04	1.19e-02	0.90
2				7.53e-03	13	16	3159	5.77e-03	9.78e-03	1.43e-03	1.94
3	10	16	3630	1.53e-03	13	28	5499	2.57e-03	4.01e-03	8.09e-04	1.84
4				1.53e-03	17	76	10803	1.12e-03	1.11e-03	3.64e-04	1.31
5	20	64	26620	8.32e-04	17	88	17091	8.27e-04	6.88e-04	5.79e-04	1.53
6	40	256	203640	4.63e-04	23	100	27717	5.87e-04	3.12e-04	4.83e-04	1.35
7				4.63e-04	31	100	38145	5.06e-04	2.54e-04	3.92e-04	1.28
8				4.63e-04	50	100	63960	4.84e-04	1.71e-04	3.41e-04	1.06
9				4.63e-04	57	100	70611	4.74e-04	2.13e-04	3.24e-04	1.13
10	40	256	203640	4.63e-04	61	100	74553	5.48e-04	3.08e-04	3.16e-04	1.14

Table 5.6: Adaptive refinement in the transport problem (based on the DWR method) including effectivity indices for goal (5.147), with $\varepsilon = 1$, $\delta_0 = 0$, $\omega = 1.5$ for Example 5.3 using a Stokes solution $\mathbf{v}_{\sigma_h}^{3,0}$ related to a cG(3)-dG(0) method on a global refined mesh in space and time. $e^{2,2,3,2}$ corresponds to the adaptive solution approximation $u_{\tau_h}^{2,2}$ in cG(2)-dG(2) and dual solution approximation $z_{\tau_h}^{3,2}$ in cG(3)-dG(2).

time approach regarding an efficient temporal approximation of a rapidly changing transport coupled with a slowly varying viscous flow.

Finally, in Fig. 5.12 we present the related adaptive spatial meshes at selected time points corresponding to the the last loop in Table 5.4 and the last plot of Fig. 5.11, respectively. Considering these meshes, we note that the total number and distribution of the spatial cells is totally equal to each other comparing the initial (Fig. 5.12a) and final (Fig. 5.12d) position of the hill. The same holds true comparing the spatial meshes where the dynamics in time take place (Fig. 5.12b at $t = 0.25$ and Fig. 5.12c at $t = 0.75$), although the distribution of the cells differs here depending on the related position of the hill. Thus, for the chosen goal functional (5.144) the spatial mesh runs as expected with the rotation of the hill in a synchronous way.

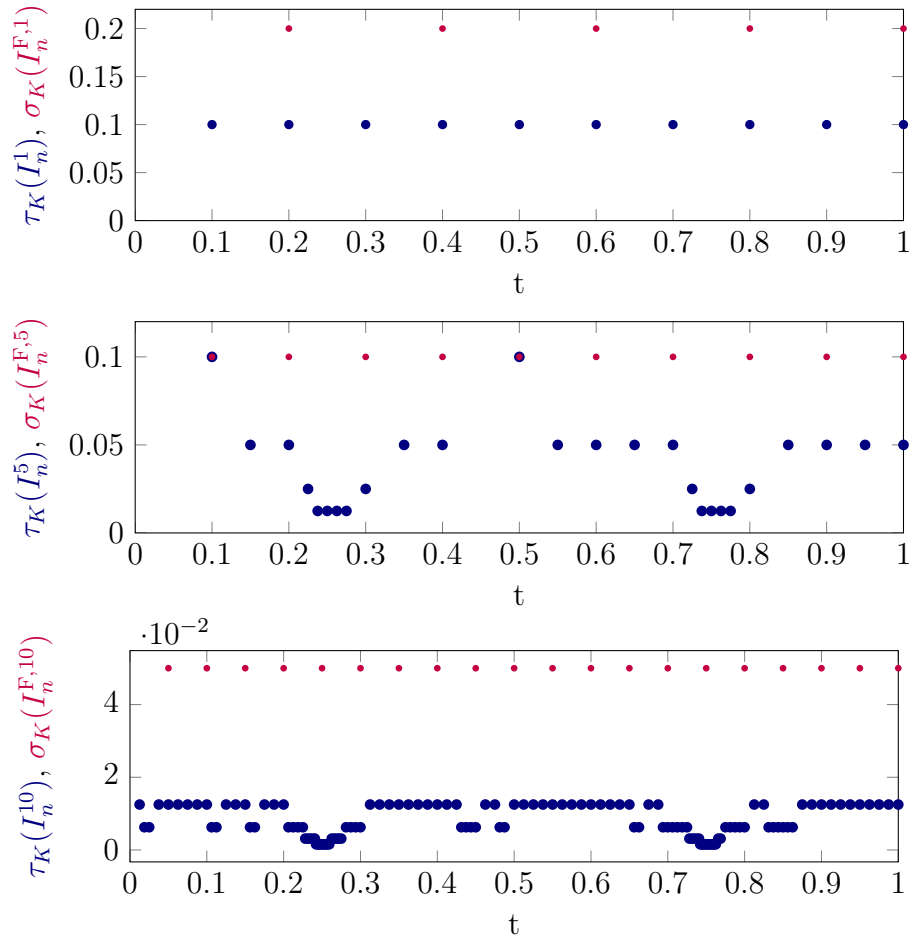


Figure 5.11: Distribution of the temporal step size τ_K of the transport problem (adaptive, based on the DWR method) and σ_K of the Stokes flow problem (global) over the time interval $I = (0, T]$ for the initial (1) and after 5 and 10 DWR-loops, corresponding to Table 5.4.

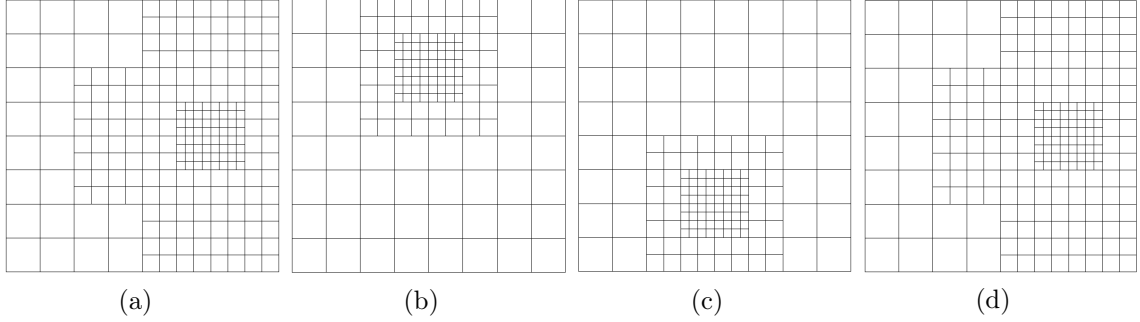


Figure 5.12: Adaptive spatial meshes of the transport problem (based on the DWR method) at time points $t_n = 0$ (a), $t_n = 0.25$ (b), $t_n = 0.75$ (c) and $t_n = 1$ (d) corresponding to the last loop in Table 5.4 and the last plot of Fig. 5.11, respectively.

The second part of the space-time adaptivity studies is devoted to a local in time acting goal functional. More precisely, this goal aims to control the L^2 -error at the final time point. Moreover, we are using adaptive spatial mesh refinement for the Stokes flow problem by means of applying a so-called Kelly Error Estimator as introduced in Rem. 5.19. This case is summarized in the following example.

Example 5.4 (Local in Time Goal Functional)

We study the Coupled Flow and Transport Problem 5.1 that is given by the Eqs. (5.1)–(5.2) with the prescribed exact solutions (5.146) and (5.143), respectively.

The problem is defined on $Q = \Omega \times I := (0, 1)^2 \times (0, 1]$. The right-hand side forcing terms, the initial and boundary conditions as well as the underlying coefficients are chosen in the same way as outlined in Example 5.1 and Example 5.3, respectively. The goal functional is chosen to control the L^2 -error $e_N^-, e_N^- = u(\mathbf{x}, T) - u_{\tau h}(T^-)$, at the final time point $T = 1.0$, given by

$$J_T(u) = \frac{(u(\mathbf{x}, T), e_N^-)}{\|e_N^-\|_T}, \quad (5.148)$$

where $\|\cdot\|_T$ denotes the L^2 -norm at the final time point T .

We approximate the primal and dual transport solutions u and z by means of a cG(1)-dG(0) and a cG(2)-dG(0) method, respectively. The primal Stokes flow solution $\{\mathbf{v}, p\}$ is approximated by using a $\{cG(2)$ -dG(0), cG(1)-dG(0) $\}$ discretization. The transport problem is adaptively refined in space and time using an approximated Stokes solution $\mathbf{v}_{\sigma h}$ on coarser global in time and adaptive in space refined meshes. The adaptivity in space with regard to the Stokes flow problem is based on non-weighted spatial error indicators $\tilde{\eta}_h^F$ obtained by means of a Kelly Error Estimator, cf. Eq. (5.139) and

Rem.5.19 for more details. Here, we set the auxiliary error indicators introduced in Eq. (5.139) as $\tilde{\eta}_{\sigma h}^F := \|\mathbf{v} - \mathbf{v}_{\sigma h}^{2,0}\|_{(0,T)\times\Omega}$, cf. also Step 7 of the algorithm introduced in Sec. 5.3.4.3. Thus, the temporal and spatial meshes of the Stokes flow problem are refined if the global $L^2(L^2)$ -error ($\|\mathbf{v} - \mathbf{v}_{\sigma h}^{2,0}\|_{(0,T)\times\Omega}$) for the Stokes flow problem is larger than the L^2 -error at the final time point T ($\|(\mathbf{x}, T) - u_{\tau h}^{1,0}(T^-)\|_T$) corresponding to the goal functional (5.148) for the transport problem; cf. columns five and nine of Table 5.7. As before, the approximation of the temporal weights is done by a higher-order extrapolation strategy using Gauss-Lobatto quadrature points, cf. Sec. 4.3.2.2. The tuning parameters with regard to the adaptive refinement process are chosen to balance automatically the potential misfit of the spatial and temporal errors as

$$\begin{aligned} \theta_{h,1}^{\text{top}} &\geq \theta_{h,2}^{\text{top}} = \frac{1}{2} \cdot \left| \frac{\eta_h}{|\eta_h| + |\eta_\tau|} \right|, & \theta_h^{\text{bottom}} &= 0.02, & \theta_\tau^{\text{top}} &= \frac{1}{2} \cdot \left| \frac{\eta_\tau}{|\eta_h| + |\eta_\tau|} \right|, \\ \theta_{h,1}^{\text{F,top}} = \theta_{h,2}^{\text{F,top}} &= 0.38, & \theta_h^{\text{F,bottom}} &= 0.02, & \theta_\sigma^{\text{top}} &= 1.0, \\ \varpi &= 1.0, & \omega &= 2.0. \end{aligned}$$

In Table 5.7, we present the development of the total discretization error $J_T(e_N^-) = \|e_N^-\|_T$ for goal functional (5.148), the spatial and temporal error indicators η_h and η_τ as well as the effectivity index \mathcal{I}_{eff} during an adaptive refinement process. Moreover, the development of the total discretization error $\|\mathbf{v} - \mathbf{v}_{\sigma h}^{p,r}\|_{(0,T)\times\Omega}$ (for short, in Table 5.7 only $\|\mathbf{v} - \mathbf{v}_{\sigma h}^{p,r}\|$) for the Stokes flow solution on a global refined mesh in time and an adaptive refined mesh in space is displayed. Again, ℓ denotes the refinement level or DWR loop, N or N^F the number of slabs, N_K^{max} or $N_K^{\text{F,max}}$ the number of spatial cells on the finest mesh within the current loop, and $N_{\text{DoF}}^{\text{tot}}$ or $N_{\text{DoF}}^{\text{F,tot}}$ the total space-time degrees of freedom of the transport or Stokes flow problem, respectively.

We observe a very good estimation of the discretization error $J_T(e)$ identified by effectivity indices close to one (cf. the last column of Table 5.7). Thus, with regard to accuracy the underlying algorithm performs very well. Moreover, well-balanced error indicators η_τ and η_h are obtained in the course of the refinement process (cf. columns ten and eleven of Table 5.7). Note the existing mismatch of these indicators at the beginning or, for instance, in the DWR loops 4, 10 or 17, such that the refinement only takes place in time here. This fact is guaranteed by the balancing parameter ω and thus ensures an equilibrated reduction of the temporal as well as spatial discretization error which is very important with regard to reliability and efficiency reasons of the underlying algorithm.

In Fig. 5.13, we visualize the distribution of the adaptively determined time cell lengths τ_K of $\mathcal{T}_{\tau,n}$, used for the transport problem, as well as the distribution of the globally determined time cell lengths σ_K of $\mathcal{T}_{\sigma,n}$, used for the Stokes flow problem,

DWR	Stokes Flow				Transport						
	N^F	$N_K^{F,\max}$	$N_{\text{DoF}}^{F,\text{tot}}$	$\ \mathbf{v} - \mathbf{v}_{\sigma h}^{2,0}\ $	N	N_K^{\max}	$N_{\text{DoF}}^{\text{tot}}$	$J_T(e^{1,0,2,0})$	η_h	η_τ	\mathcal{I}_{eff}
1	2	4	118	1.96e-02	10	16	250	2.14e-02	-1.26e-03	4.67e-02	2.12
2				1.96e-02	12	16	300	2.10e-02	5.06e-03	1.87e-03	0.33
3				1.96e-02	15	40	699	1.88e-02	3.73e-03	4.07e-03	0.41
4	4	16	748	4.58e-03	19	112	1975	1.05e-02	7.08e-04	2.97e-03	0.35
5				4.58e-03	24	112	2512	6.32e-03	1.22e-03	2.02e-03	0.51
6				4.58e-03	30	196	4374	4.29e-03	8.97e-04	3.72e-03	1.08
7	8	64	5272	1.72e-03	38	196	5688	3.10e-03	1.23e-03	2.72e-03	1.27
8				1.72e-03	48	196	7022	3.02e-03	1.25e-03	2.60e-03	1.27
9				1.72e-03	60	196	8856	2.30e-03	1.64e-03	1.28e-03	1.27
10				1.72e-03	76	268	14436	2.22e-03	8.26e-04	1.80e-03	1.18
11				1.72e-03	96	268	18040	2.05e-03	8.99e-04	1.25e-03	1.05
12				1.72e-03	121	400	31421	1.47e-03	6.71e-04	9.64e-04	1.11
13	16	208	33072	1.01e-03	153	556	52213	1.22e-03	4.30e-04	9.60e-04	1.14
14				1.01e-03	194	556	64340	1.18e-03	4.42e-04	6.89e-04	0.96
15				1.01e-03	246	1060	121064	8.30e-04	3.72e-04	4.35e-04	0.97
16	32	688	215980	5.65e-04	312	1372	197706	6.79e-04	2.43e-04	4.14e-04	0.97
17				5.65e-04	396	1744	320712	4.50e-04	1.81e-04	4.05e-04	1.30
18	64	2176	1354656	3.04e-04	502	1744	415834	4.03e-04	2.02e-04	2.14e-04	1.03
19				3.04e-04	637	2860	707155	3.56e-04	1.37e-04	2.16e-04	1.00
20	64	2176	1354656	3.04e-04	808	3484	1146746	2.74e-04	9.77e-05	1.76e-04	1.00

Table 5.7: Adaptive refinement in the transport problem (based on the DWR method) including effectivity indices for goal functional (5.147), with $\varepsilon = 1$, $\delta_0 = 0$, and $\omega = 2.0$ for Example. 5.4 using a Stokes solution $\mathbf{v}_{\sigma h}^{2,0}$ corresponding to a cG(2)-dG(0) approximation on a global refined mesh in time and adaptive refined mesh in space (based on the Kelly Error Estimator). $e^{1,0,2,0}$ corresponds to the adaptive solution approximation $u_{\tau h}^{1,0}$ in cG(1)-dG(0) and dual solution approximation $z_{\tau h}^{2,0}$ in cG(2)-dG(0).

over the whole time interval I for selected DWR refinement loops corresponding to Table 5.7. We observe a similar distribution as displayed in Fig. 5.11 corresponding to a global in time acting goal functional. But in addition, here the temporal mesh is significantly more refined reaching the final time point $T = 1$, cf. the last three plots of Fig. 5.13. This behavior is desirable since the underlying goal functional (5.148) aims to control the L^2 -error at the final time point. It is all the more remarkable that the dynamics in time arising close to the time points where the hill is changing its orientation ($t = 0.25$ and $t = 0.75$) are detected which illustrates once more the potential of the underlying algorithm with regard to obtaining efficient temporal meshes regarding different characteristic dynamics in time of the subproblems.

Finally, regarding the spatial meshes of the Stokes flow and transport problem given by Fig. 5.14, we state the following. Compared to the spatial transport meshes obtained in Fig. 5.12 corresponding to a global in time acting goal functional, we observe a similar result with regard to localization and distribution of the spatial cells, cf. Figs. 5.14e–5.14h. Additionally, a significantly stronger refinement takes place within the spatial mesh corresponding to the final time point (cf. Fig. 5.14h) in accor-

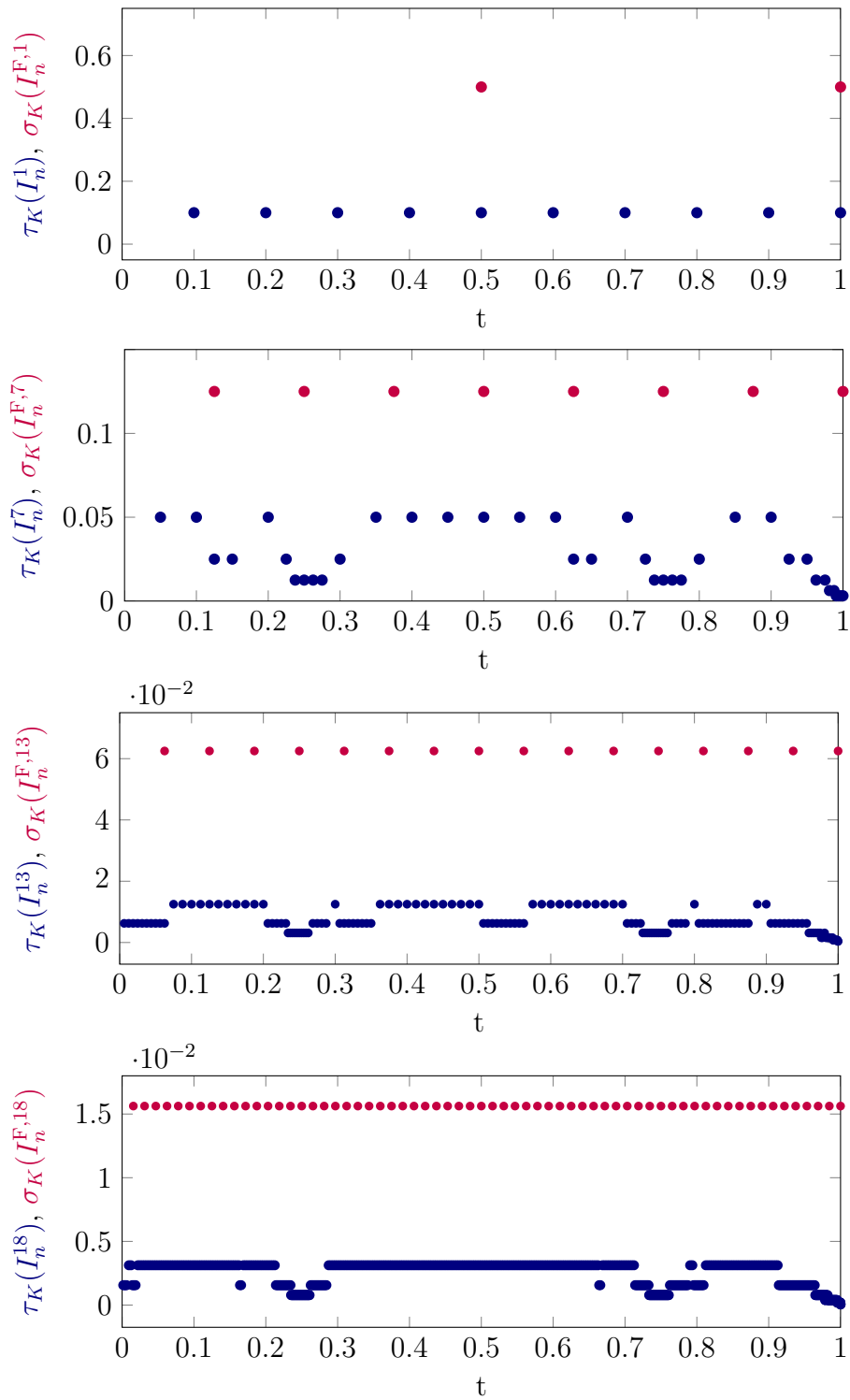


Figure 5.13: Distribution of the temporal step size τ_K of the transport problem (adaptive, based on the DWR method) and σ_K of the Stokes flow problem (global) over the time interval $I = (0, T]$ for the initial (1) and after 7, 13 and 18 DWR-loops, corresponding to Table 5.7.

dance to the underlying local in time acting goal functional (5.148) that aims at controlling the L^2 -error at the final time point. Moreover, we observe a slightly stronger spatial refinement where the dynamics in time take place (cf. Figs. 5.14f–5.14g) compared to the spatial mesh corresponding to the initial time point (cf. Fig. 5.14e). All in all, the algorithm provides very efficient spatial meshes with regard to the underlying goal functional, additionally taking into account the dynamics in time.

Regarding the spatial meshes of the Stokes flow problem obtained by using non-weighted error indicators by means of a Kelly Error Estimator, we observe an almost equal number and distribution of the spatial cells over the whole time located to the course of the stream lines of the flow field solution, cf. the upper plots in Fig. 5.8. This observation is in good agreement with the results obtained in [167, Sec. 4.7.2] using so-called heuristic error indicators, cf. [167, Sec. 4.6] for further details of this approach. Comparing the adaptive spatial meshes of the transport and Stokes flow problem obtained by different error estimators, the advantage of weighted error indicators based on the DWR method is clearly visible. Due to the user-chosen goal functional more flexibility with regard to localized interests along with economical and efficient meshes adapted to these goals is feasible.

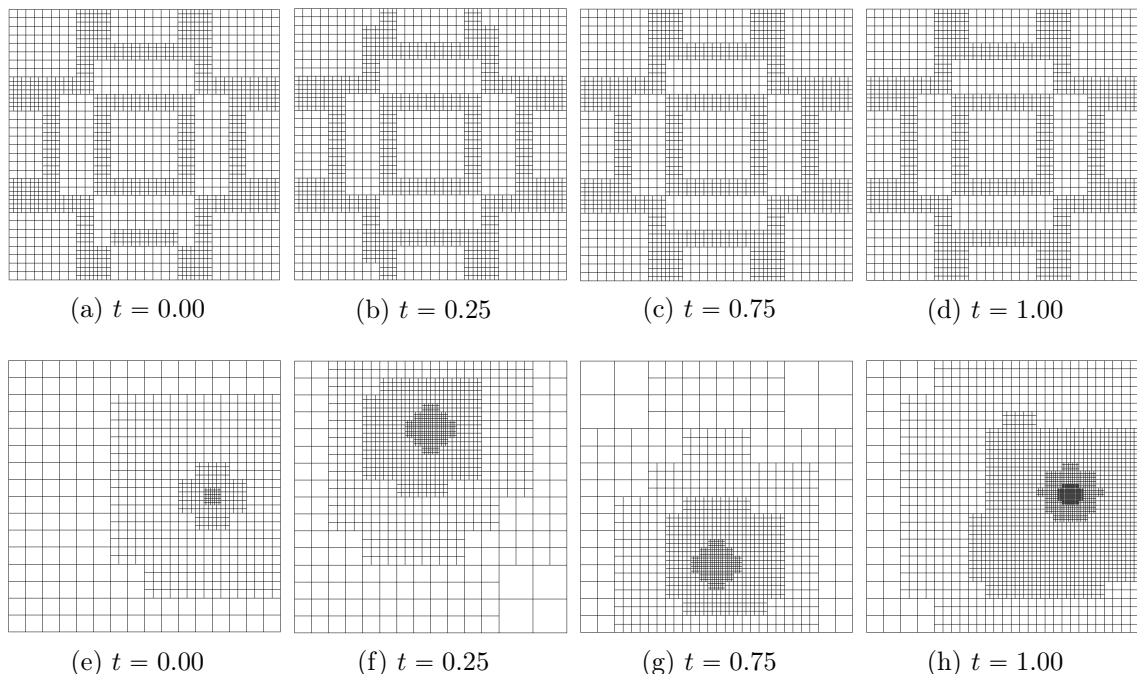


Figure 5.14: Comparison of adaptive spatial meshes at different time points for the Stokes flow (based on the Kelly Error Estimator) (top, (a)–(d)) and transport (based on the DWR method) (bottom, (e)–(h)) problem, respectively, corresponding to the last loop in Table 5.7.

Conclusion 5.2 (Accuracy and Efficiency)

As an interim conclusion, we summarize the following.

- With regard to **accuracy**, all $cG(p)$ - $dG(r)$ discretizations show a good quantitative estimation of the discretization error; cf. the last column of Tables 5.4–5.5 and Table 5.7, respectively.
- With regard to **efficiency**, all $cG(p)$ - $dG(r)$ discretizations show a very good equilibration of the spatial and temporal error indicators η_h and η_τ in the course of refinement; cf. the columns ten and eleven of Tables 5.4–5.5 and Table 5.7, respectively.
- Our **multirate in time approach** combined with goal-oriented error control based on the DWR method leads to very economical and efficient temporal meshes for both subproblems regarding both a **global** and **local** in time acting goal functional; cf. Fig. 5.11 and Fig. 5.13, respectively.
- Very economical and efficient spatial meshes having regard to a **global** as well as a **local** in time acting goal functional were obtained for the transport problem using weighted error indicators by means of the DWR approach; cf. Fig. 5.12 and Figs. 5.14e–5.14h, respectively. Moreover, economical spatial meshes having regard to the stream lines were obtained for the Stokes flow problem using non-weighted error indicators by means of a Kelly Error Estimator; cf. Figs. 5.14a–5.14d

5.4.3 Transport in a Channel

In this example, we simulate a convection-dominated transport with goal-oriented adaptivity of a species through a channel with a constraint. This scenario including unknown exact solutions is summarized in the following example.

Example 5.5 (Transport in a Channel, Steady-State Inflow v_D)

We study the Coupled Flow and Transport Problem 5.1 given by the Eqs. (5.1) and (5.2), respectively, with the following settings. The domain and its boundary colorization are presented by Fig. 5.15. Precisely, the spatial domain is composed of two unit squares and a constraint in the middle which restricts the channel height by a factor of five. In detail, $\Omega = (-1, 0) \times (-0.5, 0.5) \cup (0, 1) \times (-0.1, 0.1) \cup (1, 2) \times (-0.5, 0.5)$ with an initial cell diameter of $h = \sqrt{2 \cdot 0.025^2}$. The time domain is set to $I = (0, 2.5)$

with an initial $\tau = 0.1$ for the transport and $\sigma = 2.5$ for the Stokes flow problem for the initialization of the slabs for the first loop $\ell = 1$.

The transport of the species, which enters the domain on the left with a nonhomogeneous and time-dependent Dirichlet boundary condition and leaves the domain on the right through a homogeneous Neumann boundary condition, is driven by the convection with magnitudes between 0 and 5 as displayed in Fig. 5.16. More precisely, the Dirichlet boundary function value is homogeneous on Γ_D except for the line $(-1, -1) \times (-0.4, 0.4)$ and time $0 \leq t \leq 0.2$ where the constant value

$$u(\mathbf{x}, t) = 1$$

is prescribed on the solution. The initial value function $u_0 = 0$ as well as the forcing term $g = 0$ are homogeneous. On the left boundary Γ_{inflow} , the parabolic inflow condition \mathbf{v}_D for the Stokes flow problem is given by

$$\mathbf{v}_D(\mathbf{x}, t) = (1 - 4x_2^2, 0)^\top, \quad (5.149)$$

The diffusion coefficient has the constant and small value of $\varepsilon = 10^{-4}$, the reaction coefficient is chosen $\alpha = 0.1$ and the viscosity is set to $\nu = 1$. The local SUPG stabilization coefficient is here set to $\delta_K = \delta_0 \cdot h_K$, $\delta_0 = 0$, i.e. a vanishing stabilization here. The goal quantity is

$$J(u) = \frac{1}{|T| \cdot |\Omega|} \int_I \int_\Omega u(\mathbf{x}, t) \, d\mathbf{x} dt. \quad (5.150)$$

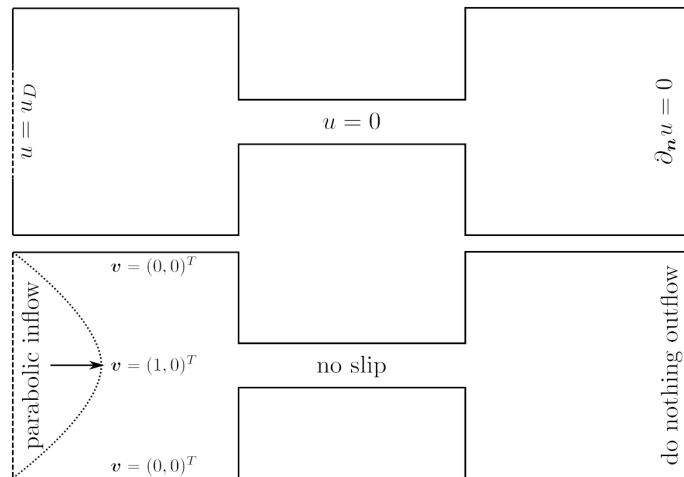


Figure 5.15: Boundary colorization for the convection-diffusion-reaction transport problem (top) and the coupled Stokes flow problem (bottom) for Example 5.5. The graphic is taken from [29].

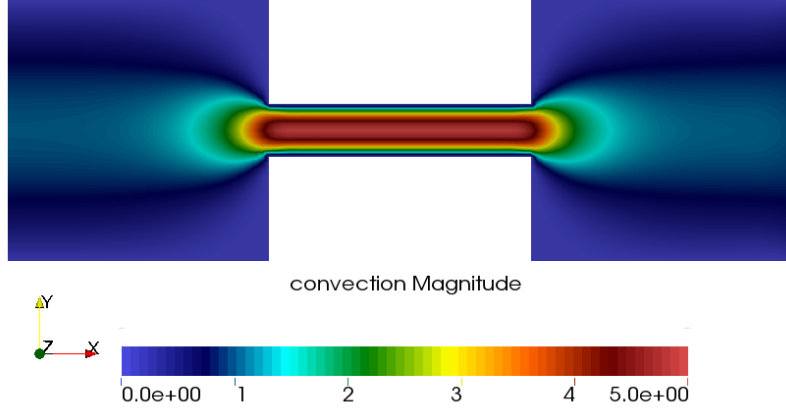


Figure 5.16: Convection $\mathbf{v}_{\sigma h}$ solution of the Stokes flow problem on one slab with a sufficiently globally refined spatial mesh with Q_2 - Q_1 finite elements for Example 5.5. On the left boundary a parabolic inflow profile in the positive x_1 -direction with unit magnitude is prescribed for the convection \mathbf{v}_D . The graphic is taken from [29].

The choice $\sigma = 2.5$ in Example 5.5 has been made to compare the results to Example 2 in [29], where a quasi-stationary Stokes flow solution \mathbf{v}_h was used. We approximate the primal transport solution $u_{\tau h}^{1,0}$ with a cG(1)-dG(0) method and the dual transport solution $z_{\tau h}^{2,0}$ with a cG(2)-dG(0) method, respectively, on adaptively refined meshes in space and time. The Stokes flow solution $\mathbf{v}_{\sigma h}^{2,0}$ is approximated with a cG(2)-dG(0) method on globally refined meshes in space and time obtained by means of weighted error indicators based on the DWR method given by Eq. (5.119). The tuning parameters with regard to the adaptive refinement process are chosen to balance automatically the potential misfit of the spatial and temporal errors as

$$\begin{aligned} \theta_{h,1}^{\text{top}} &\geq \theta_{h,2}^{\text{top}} = \frac{1}{2} \cdot \min \left\{ \left| \frac{\eta_h}{|\eta_h| + |\eta_\tau|} \right|, 1 \right\}, & \theta_h^{\text{bottom}} &= 0.02, & \theta_\tau^{\text{top}} &= \frac{1}{2} \cdot \min \left\{ \left| \frac{\eta_\tau}{|\eta_h| + |\eta_\tau|} \right|, 1 \right\}, \\ \theta_{h,1}^{\text{F,top}} &= \theta_{h,2}^{\text{F,top}} = 1.0, & \theta_h^{\text{F,bottom}} &= 0.0, & \theta_\sigma^{\text{top}} &= 0.0, \\ \varpi &= 1.0, & \omega &= 3.0. \end{aligned}$$

The solution profiles and corresponding adaptive spatial meshes of the primal transport solution $u_{\tau h}^{1,0}$ of the loop $\ell = 8$ for $t = 0.15$, $t = 0.70$, $t = 0.92$, $t = 1.33$ and $t = 2.45$ are given by Fig. 5.17. The refinement in space is adjusted to the position of the transported species within the channel. It is located to the layers of the transported species, whereas the mesh stays coarse in the non-affected area.

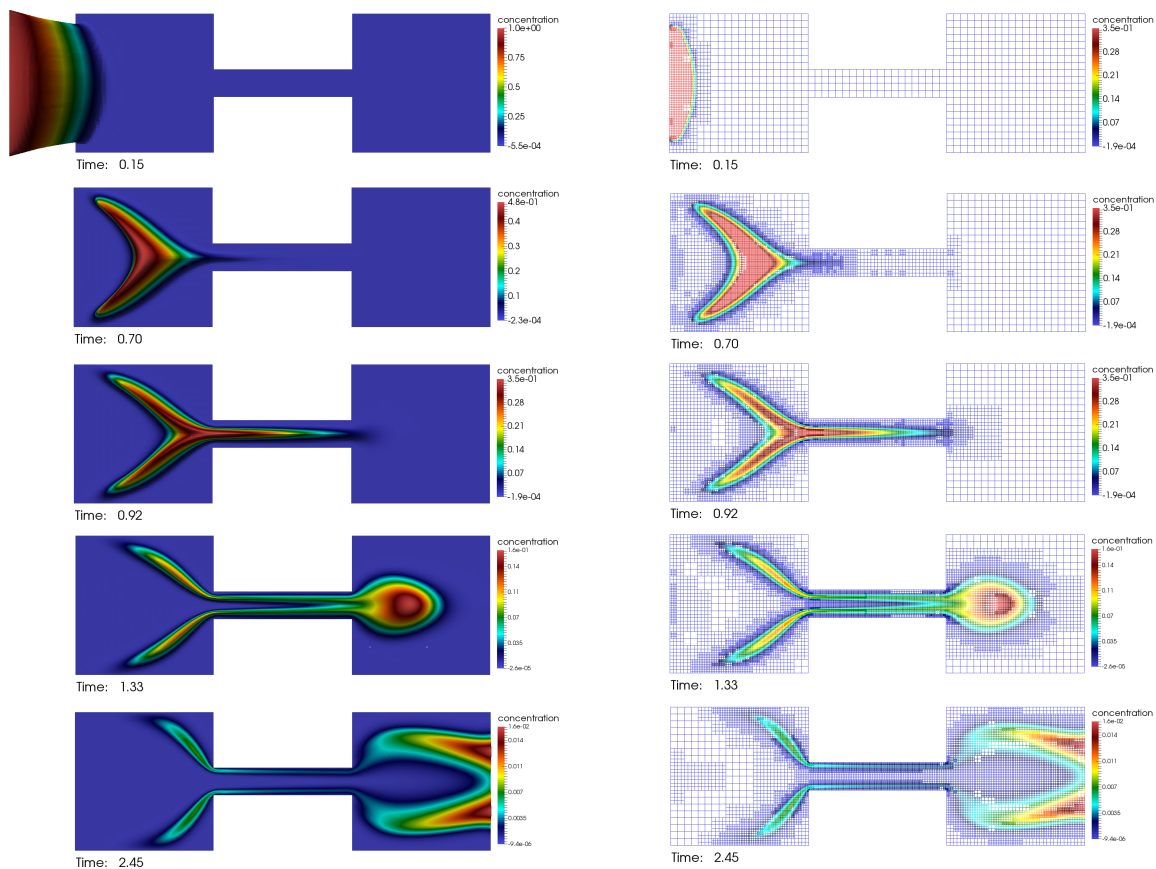


Figure 5.17: Transport solution profiles and related adaptively refined spatial meshes (based on the DWR method) with $\varepsilon = 10^{-4}$, $\delta_0 = 0.0$, and $\omega = 3.0$ at different time points corresponding to loop $\ell = 8$ for Example 5.5.

In Fig. 5.18, we present a comparative study of the solution profile and corresponding spatial meshes for $t = 0.95$ in the course of the adaptive refinement loops. For $\ell = 1, 2, 3$ obvious spurious oscillations in the left square and at the beginning of the constriction are existing, which are captured and resolved by the goal-oriented adaptivity by taking spatial mesh refinements along the layers of the transported species within the left square and within the constriction of the channel. For $\ell > 3$ the spatial refinements capture especially the solution profile fronts with strong gradients with a focus on the high-convective middle of the spatial domain. For the last loops an almost perfect solution profile is observable and the spurious oscillations occurred within the first loops are reduced significantly.

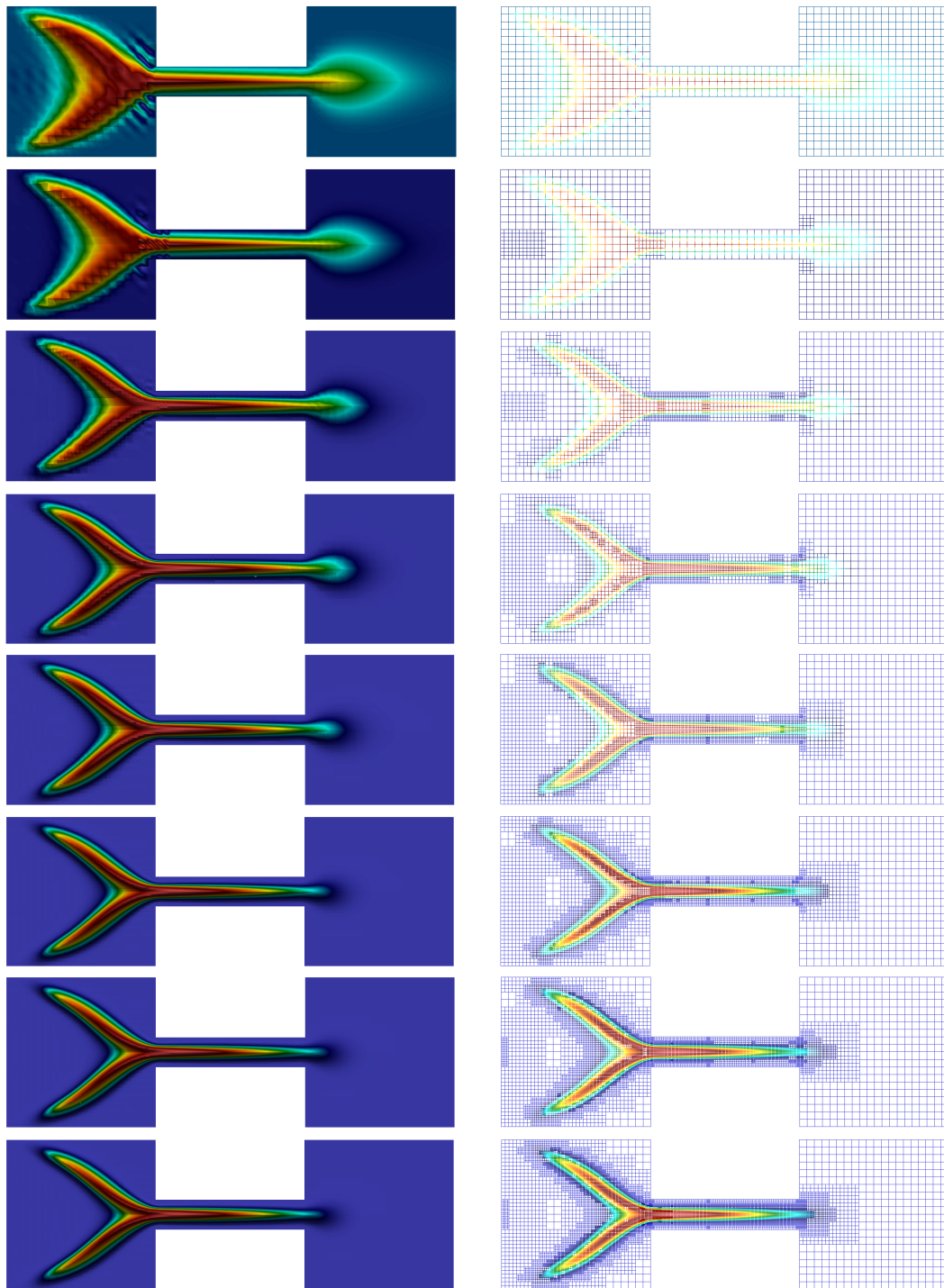


Figure 5.18: Capturing of spurious oscillations with goal-oriented adaptivity illustrated by comparative solution profiles and related adaptively refined spatial meshes (based on the DWR method) of the loops $\ell = 1 - 8$ with $\varepsilon = 10^{-4}$, $\delta_0 = 0.0$, and $\omega = 3.0$, exemplary at time point $t = 0.95$ for Example 5.5.

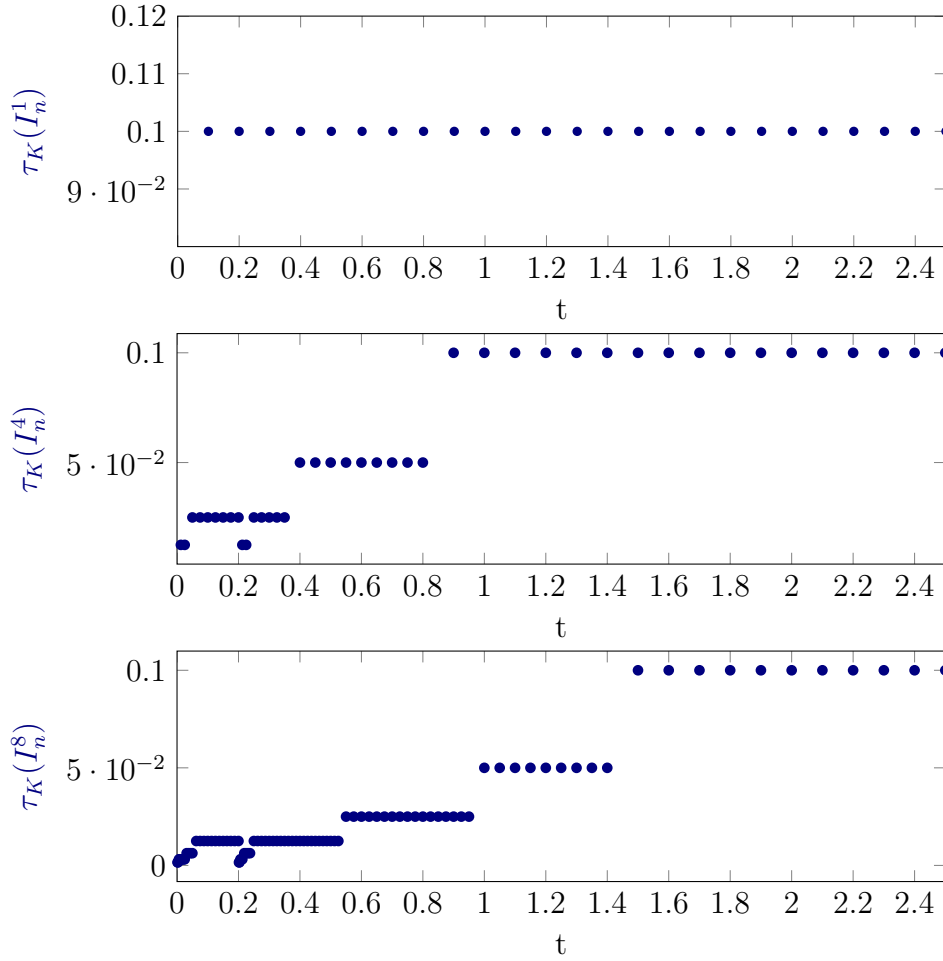


Figure 5.19: Distribution of the temporal step size τ_K of the transport problem (based on the DWR method) for a fixed $\sigma_K = 2.5$ of the Stokes flow problem over the time interval $I = (0, T]$ for the initial (1) and after 4 and 8 DWR-loops.

In Fig. 5.19, we visualize the temporal distribution of the transport problem for several DWR-loops. The time cell lengths of the Stokes flow problem is kept fixed with value $\sigma_K = 2.5$ for all DWR-loops here and thus explicitly not displayed. We observe an adaptive refinement in time at the beginning, consistent with the restriction in time of the inflow boundary condition. The closer we get to the final time point T the coarser the temporal mesh is chosen. This behavior nicely brings out the feature of automatically controlled mesh refinement of the underlying algorithm with regard to dynamics in time, note that the respective goal functional (5.150) acts global in time. The refinement in space and time is automatically balanced due to the dynamic choice of $\theta_{h,1}^{\text{top}}$, $\theta_{h,2}^{\text{top}}$ and θ_τ^{top} given by (5.141) and is illustrated by Table 5.8. Here, ℓ denotes DWR loop, N the number of slabs, N_K^{max} the number of spatial cells on the finest mesh within the current loop, and $N_{\text{DoF}}^{\text{tot}}$ the total space-time degrees of

freedom. Regarding the spatial and temporal error indicators (cf. columns five and six of Table 5.8) a good equilibration can be observed within the final loop, whereas in the first step a mismatch occurs resulting in a solely temporal refinement between $\ell = 1$ and $\ell = 2$. This behavior is desirable with regard to efficiency reasons.

ℓ	N	N_K^{\max}	$N_{\text{DoF}}^{\text{tot}}$	η_h	η_τ
1	25	880	24425	3.5795e-03	1.1452e-02
2	29	880	28333	3.8619e-03	3.2318e-03
3	32	1456	39456	2.9354e-03	5.4042e-03
4	42	2116	62528	2.5532e-03	5.2001e-03
5	51	4492	132483	2.3178e-03	5.2170e-03
6	70	7072	239266	1.8934e-03	3.8571e-03
7	79	10744	371015	1.7406e-03	2.3554e-03
8	89	15376	619071	1.6069e-03	1.2974e-03

Table 5.8: Adaptive temporal and spatial refinements for the transport problem including error indicators (based on the DWR method) in space η_h and time η_τ , respectively, $\varepsilon = 10^{-4}$, $\delta_0 = 0$, and $\omega = 3.0$ for Example 5.5.

With regard to **more dynamic in time**, we now modify Example 5.5 regarding a **time-dependent inflow** condition for the Stokes flow problem in order to investigate our multirate in time approach for the present example. This modification is summarized in the following example.

Example 5.6 (Transport in a Channel, Time-Dependent Inflow \mathbf{v}_D)

We study the Coupled Flow and Transport Problem 5.1 given by the Eqs. (5.1) and (5.2), respectively, with the same settings as outlined in Example 5.5 except for the following. On the left boundary Γ_{inflow} the inflow condition \mathbf{v}_D is now time-dependent, given by

$$\mathbf{v}_D(\mathbf{x}, t) = \begin{cases} \frac{\arctan(t)}{\pi/2} \cdot (1 - 4x_2^2, 0)^\top & \text{for } 0 \leq t \leq 0.1, \\ (1, 0)^\top & \text{for } 0.1 < t \leq T. \end{cases} \quad (5.151)$$

Moreover, for the transport problem, the Dirichlet boundary function value is homogeneous on Γ_D except for the line $(-1, -1) \times (-0.4, 0.4)$ and time $0 \leq t \leq 0.1$ where the constant value

$$u(\mathbf{x}, t) = 1$$

is prescribed on the solution.

With regard to the characteristic times of the two subproblems defined in Assumption 5.1 relating to Example 5.6, the coefficients are chosen in such a way that the

convective part of $t_{\text{transport}}$ becomes dominant towards the diffusive and reactive part and thus there holds $t_{\text{transport}} = t_{\text{flow}}$. Therefore, the time domain $I = (0, 2.5)$ is now discretized using the same initial $\tau = \sigma = 0.1$ for the transport and Stokes flow problem for the first loop $\ell = 1$, cf. the first plot in Fig. 5.20. The tuning parameters with regard to the adaptive refinement process are chosen to balance automatically the potential misfit of the spatial and temporal errors as

$$\begin{aligned} \theta_{h,1}^{\text{top}} &\geq \theta_{h,2}^{\text{top}} = \frac{1}{2} \cdot \min \left\{ \left| \frac{\eta_h}{|\eta_h| + |\eta_\tau|} \right|, 1 \right\}, & \theta_h^{\text{bottom}} &= 0.02, & \theta_\tau^{\text{top}} &= \frac{1}{2} \cdot \min \left\{ \left| \frac{\eta_\tau}{|\eta_h| + |\eta_\tau|} \right|, 1 \right\}, \\ \theta_{h,1}^{\text{F,top}} &= \theta_{h,2}^{\text{F,top}} = 1.0, & \theta_h^{\text{F,bottom}} &= 0.0, & \theta_\sigma^{\text{top}} &= 1.0 \text{ (for } 0 \leq t \leq 0.2 \text{)}, \\ \varpi &= 1.0, & \omega &= 3.0. & \theta_\sigma^{\text{top}} &= 0.0 \text{ (for } 0.2 < t \leq 2.5 \text{)}. \end{aligned}$$

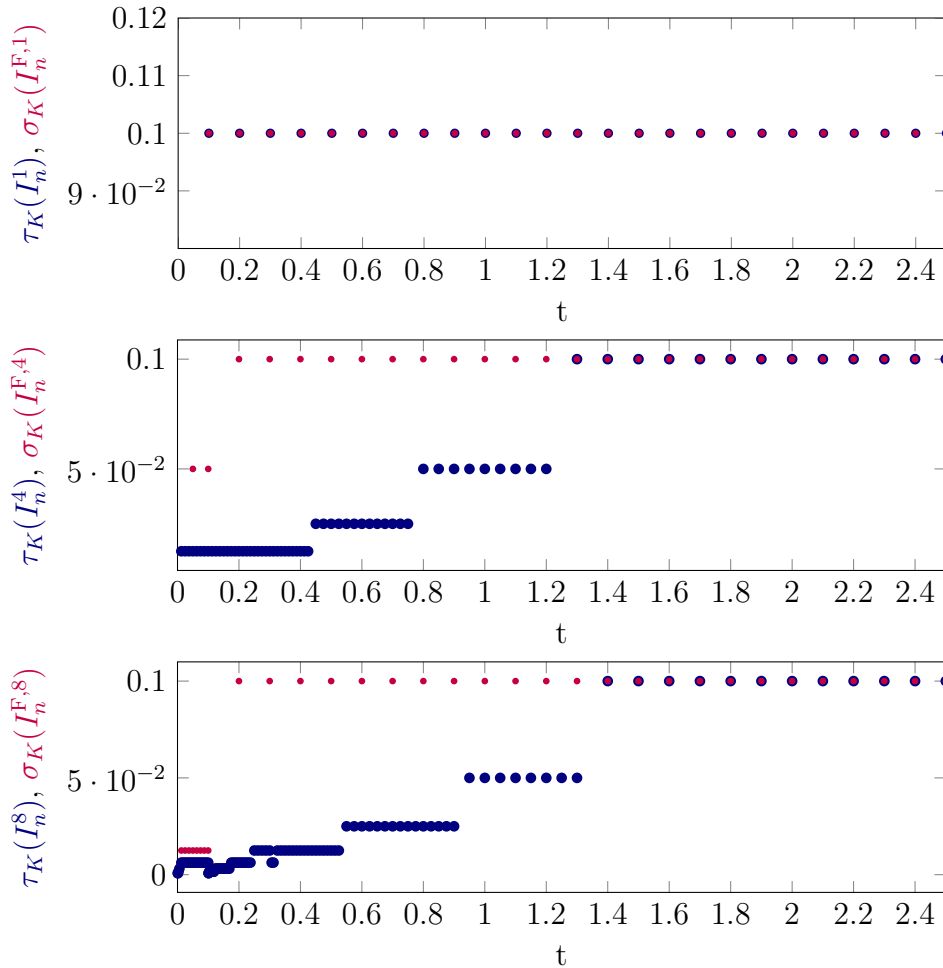


Figure 5.20: Distribution of the temporal step size τ_K of the transport problem (based on the DWR method) and σ_K of the Stokes flow problem (based on fixed, user-chosen refinement) over the time interval $I = (0, T]$ for the initial (1) and after 4 and 8 DWR-loops.

In Fig. 5.20, we visualize the distribution of the adaptively determined time cell lengths τ_K and σ_K used for the transport and Stokes flow problem, respectively, over the whole time interval I for different DWR refinement loops. We observe a similar behavior as displayed in Fig. 5.19. The temporal mesh is refined close to the time conditions of the respective inflow boundaries for both problems, where the refinement in time for the Stokes flow problem is chosen to refine those slabs related to the inflow condition (5.151) for each second DWR-loop with regard to the choice of $\theta_\sigma^{\text{top}}$ given above. Away from the temporal inflow condition both temporal meshes stay coarse. The solution profiles and corresponding adaptive spatial meshes of the primal transport solution look very similar to that obtained in the steady-state inflow case given by Figs. 5.17–5.18 and thus are not explicitly displayed here.

In a final step, we demonstrate the application and interaction of all mathematical tools and techniques developed in this work. More precisely, we investigate our **multirate in time** approach in view of focusing on the interaction of **stabilization** techniques combined with goal-oriented **error control**. For this purpose, we modify Example 5.5 to the case of a strongly convection-dominated transport problem by increasing the Péclet number by two orders of magnitude. We show that for this case a solely application of adaptive mesh refinement is no longer sufficient, but the transport problem additionally has to be stabilized in order to capture strong gradients and reduce spurious and non-physical oscillations. This is done by comparing a non-stabilized solution ($\delta_0 = 0$) with the case of a SUPG stabilized solution ($\delta_0 \neq 0$) of the transport problem. This final investigation is summarized in the following example.

Example 5.7 (Transport in a Channel, Stabilized Transport)

We study the Coupled Flow and Transport Problem 5.1 given by the Eqs. (5.1) and (5.2), respectively, with the same settings as outlined in Example 5.5 except for the following. The diffusion coefficient has the constant and small value of

$$\varepsilon = 10^{-6}.$$

The transport problem is stabilized using SUPG stabilization. Therefore, the local SUPG stabilization coefficient is here set to

$$\delta_K = \delta_0 \cdot h_K, \delta_0 = 0.1.$$

The goal functional is given by Eq. (5.150) and on the left boundary Γ_{inflow} the inflow condition \mathbf{v}_D is still time-dependent, given by Eq. (5.151).

In order to investigate the interaction of stabilization and goal-oriented error control based on the DWR approach, we focus here on the transport problem and compare the approximated solution given by the non-stabilized fully discrete scheme (5.29) with that one obtained by the SUPG stabilized fully discrete scheme (5.32), respectively. We approximate the respective primal transport solution $u_{\tau h}^{1,0}$ with a cG(1)-dG(0) method and the dual transport solution $z_{\tau h}^{2,0}$ with a cG(2)-dG(0) method, respectively, on adaptively refined meshes in space and time obtained by means of weighted error indicators based on the DWR method, given by Eq. (5.119). However, the Stokes flow solution $\mathbf{v}_{\sigma h}^{2,0}$ is approximated with a cG(2)-dG(0) method on adaptively refined meshes in space and time obtained by means of the auxiliary non-weighted error indicators based on the Kelly Error Estimator, given by Eq. (5.139). Thereby, the auxiliary spatial error indicators are determined as described in Rem. 5.19 and the temporal error indicators are set to

$$\tilde{\eta}_{\sigma}^{\text{F},n} := \sum_{K^{\text{F}} \in \mathcal{T}_{h,n}^{\text{F}}} \tilde{\eta}_h^{\text{F},n}, \quad (5.152)$$

with regard to a single slab Q_n^{F} , $n = 1, \dots, N^{\text{F}}$. The tuning parameters are chosen to balance automatically the potential misfit of the spatial and temporal errors as

$$\begin{aligned} \theta_{h,1}^{\text{top}} &\geq \theta_{h,2}^{\text{top}} = \frac{1}{2} \cdot \min \left\{ \left| \frac{\eta_h}{|\eta_h| + |\eta_{\tau}|} \right|, 1 \right\}, & \theta_h^{\text{bottom}} &= 0.02, & \theta_{\tau}^{\text{top}} &= \frac{1}{2} \cdot \min \left\{ \left| \frac{\eta_{\tau}}{|\eta_h| + |\eta_{\tau}|} \right|, 1 \right\}, \\ \theta_{h,1}^{\text{F},\text{top}} &= \theta_{h,2}^{\text{F},\text{top}} = 0.33, & \theta_h^{\text{F},\text{bottom}} &= 0.02, & \theta_{\sigma}^{\text{top}} &= 0.2, \\ \varpi &= 1.0, & \omega &= 3.0. \end{aligned}$$

With regard to the characteristic times of the two subproblems there still holds $t_{\text{transport}} = t_{\text{flow}}$ as outlined in the context of Example 5.6. Thus, the time domain $I = (0, 2.5)$ is again discretized using the same initialization for the transport and Stokes flow problem. In Fig. 5.21, we visualize the distribution of the adaptively determined time cell lengths τ_K and σ_K used for the transport and Stokes flow problem, respectively, over the whole time interval I for different DWR refinement loops. We observe a similar behavior as displayed in Fig. 5.19 and Fig. 5.20, respectively. The temporal mesh is refined close to the temporal conditions of the respective inflow boundaries for both problems. Away from the temporal inflow condition both temporal meshes stay coarse. The adaptive refinement in time for the Stokes flow problem is here based on the auxiliary indicators given by Eq. (5.152) instead of a user-chosen, fixed given refinement in each second loop as used in Example 5.6. Obtaining similar results with regard to the distribution and localization of the temporal refinement for

the Stokes flow problem as given in Fig. 5.20 validates the underlying approach for the computation of the temporal error indicators.

In Fig. 5.22, we compare the solution profiles and corresponding adaptive spatial meshes of the primal transport solution $u_{\tau h}^{1,0}$ for a non-stabilized and stabilized case, respectively, at different time points within the final DWR loop $\ell = 8$. Comparing the results of the present non-stabilized case to that one obtained by Fig. 5.17 for a lower Péclet number, it becomes clear that in the strongly convection-dominated case a solely adaptive mesh refinement without stabilization is no longer sufficient to resolve the arising layers of the transported species within the channel, especially regarding the solution profiles in the course of time; cf. the blurred solution profiles in the course of the transported species on the left part of Fig. 5.22 compared to those of Fig. 5.17. This becomes even clearer considering the exemplary side profile of the primal transport solution at time $t = 1.35$ given by the upper part of Fig. 5.23 that is strongly perturbed by means of spurious and non-physical oscillations, especially in the part of the constriction within the channel. Without additional stabilization techniques the underlying algorithm is not able to capture the strong gradients and resolve the layers and sharp moving fronts of the underlying transported species.

In contrast, regarding the stabilized solution profiles given by the right and lower part of Fig. 5.22 and Fig. 5.23, respectively, the solution profile fronts are resolved in a visibly more accurate way along with a significantly reduction of the spurious oscillations. Moreover, regarding the underlying spatial meshes, we point out that in the stabilized case the adaptive refinement is located close to the whole solution front of the underlying transported species within the channel. More precisely, we observe local refinements located in the left unit square corresponding to the wing-like fronts and behind them, within the constriction corresponding to the course of the solution profile as well as at the exit of the restriction, in particular at the corners of the exit, corresponding to the head of the solution profile.

In contrast to that, in the non-stabilized case most of the local refinement takes place at the beginning of the constriction where most of the oscillations are visible. In comparison, the remaining parts along the solution front are less refined, in particular, regarding the wing-like fronts in the left unit square. This is obvious since the goal functional (5.150) acts global in space and time and thus those parts of the error indicators are weighted stronger involving larger errors in the respective quantity.

Due to the additional stabilization along with a significantly reduction of the oscillations, the algorithm in the stabilized case is capable to distribute the refinement more evenly to the regions belonging to strong gradients of the underlying solution

profile. In summary, the stabilized solution shows a significantly improvement with regard to resolving layers and sharp moving fronts along with efficient underlying spatial meshes, even though some slight perturbations located at the course of the layers are still visibly.

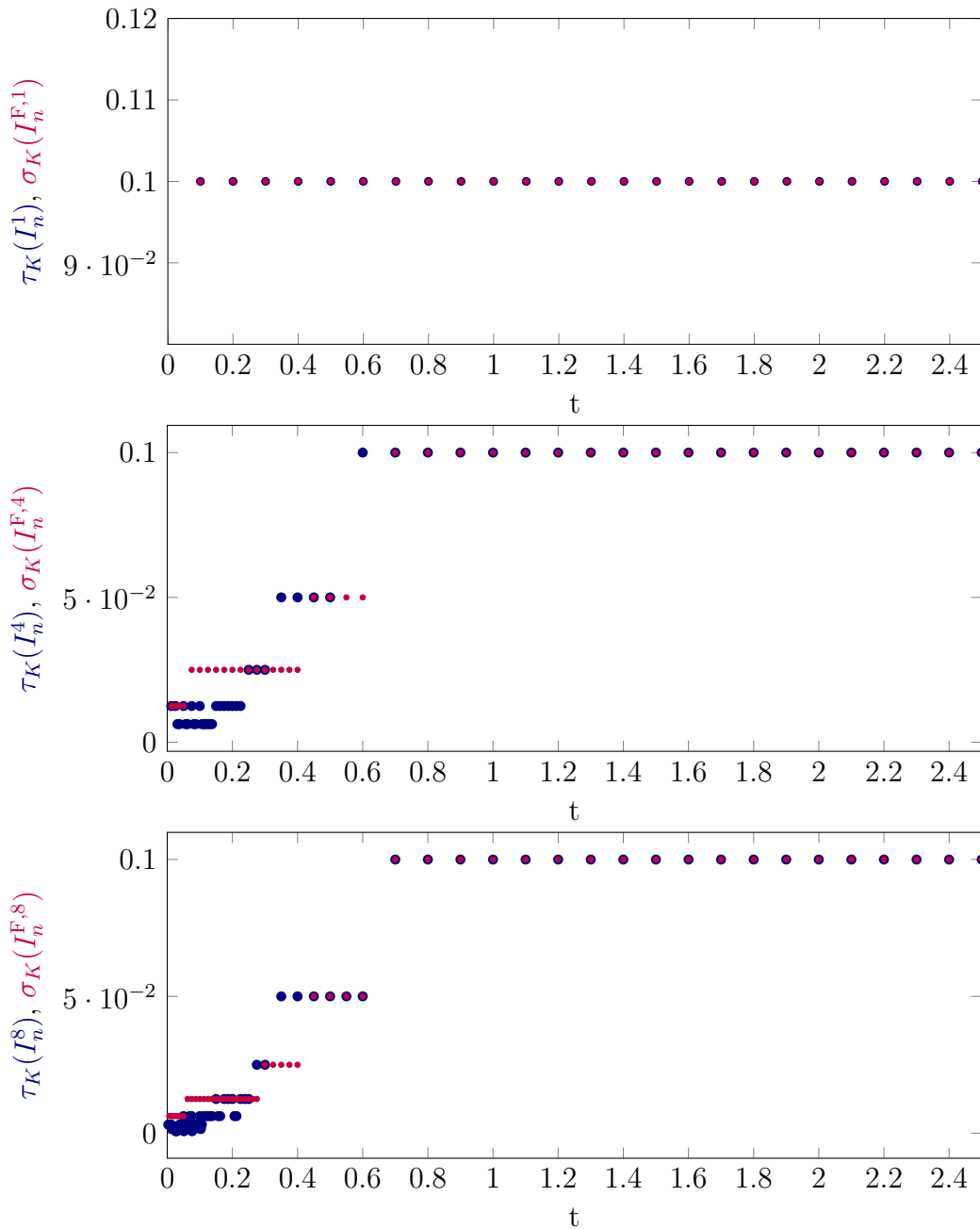


Figure 5.21: Distribution of the temporal step size τ_K of the transport problem (based on the DWR method) and σ_K of the Stokes flow problem (based on the Kelly Error Estimator) over the time interval $I = (0, T]$ for the initial (1) and after 5 and 8 DWR-loops.

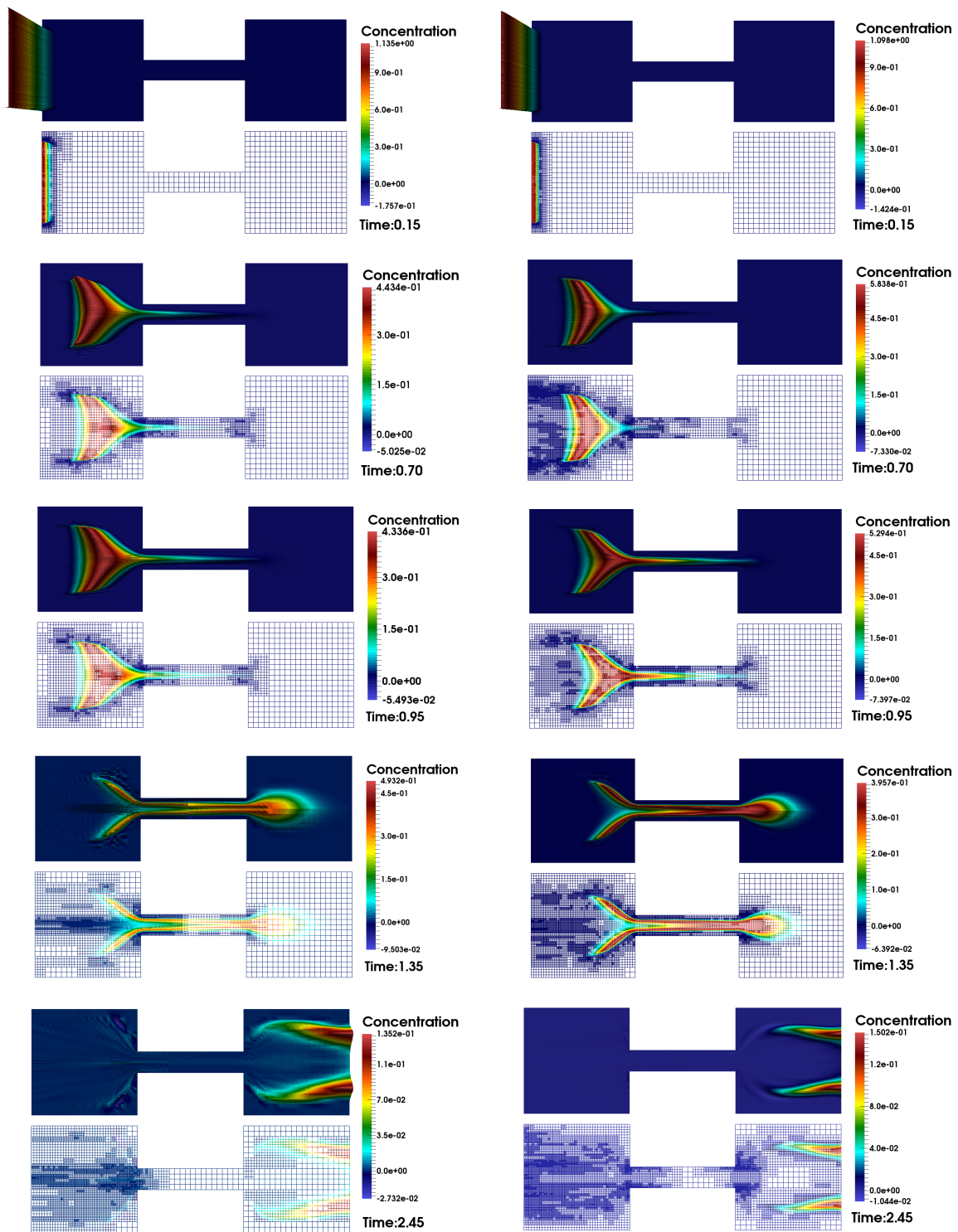
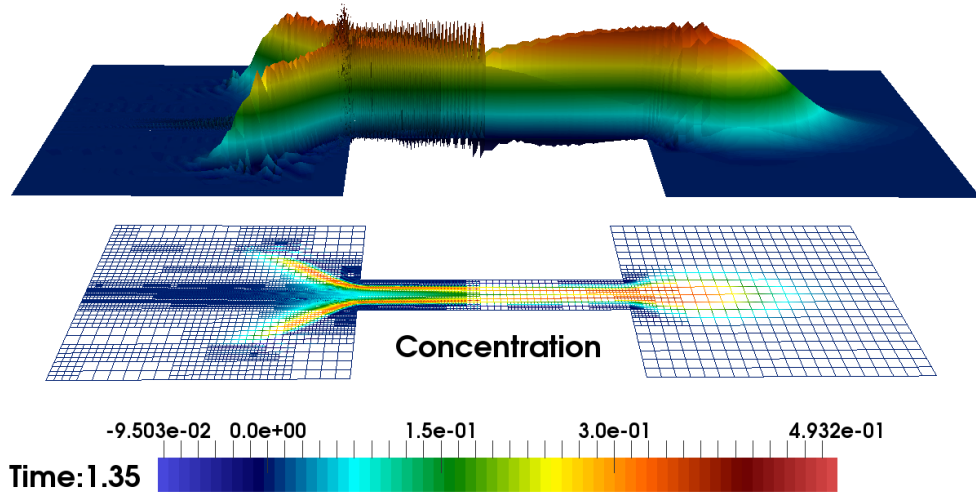
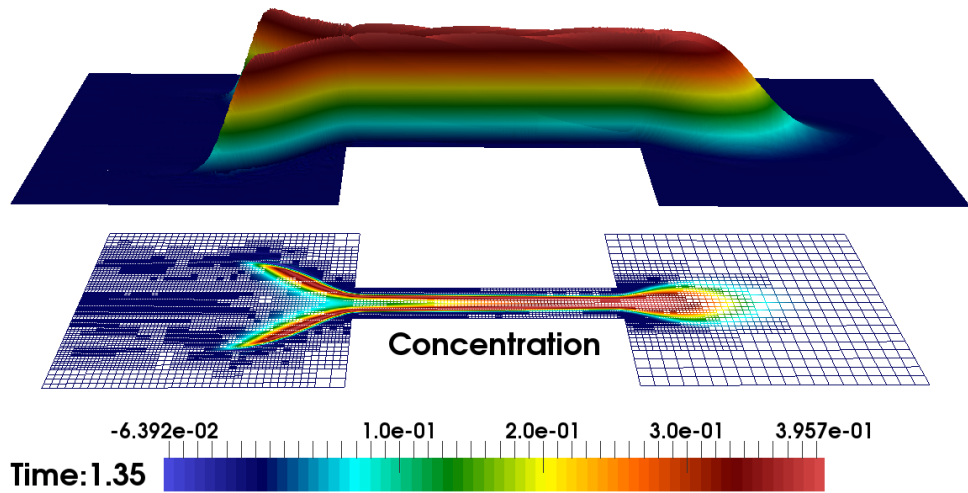


Figure 5.22: Comparison of transport solution profiles and related adaptively refined spatial meshes (based on the DWR method) without stabilization $\delta_0 = 0.0$ (left) and with SUPG stabilization $\delta_0 = 0.1$ (right) for $\varepsilon = 10^{-6}$ at different time points corresponding to loop $\ell = 8$ for Example 5.7.



(a) No Stabilization ($\delta_0 = 0.0$), 29843 spatial DoFs



(b) SUPG Stabilization ($\delta_0 = 0.1$), 27471 spatial DoFs

Figure 5.23: Comparison of side profiles for the transport solution and related adaptively refined spatial meshes (based on the DWR method) without stabilization $\delta_0 = 0.0$ (top) and with SUPG stabilization $\delta_0 = 0.1$ (bottom) for $\varepsilon = 10^{-6}$ corresponding to loop $\ell = 8$ for Example 5.7, exemplary at time point $t = 1.35$.

Finally, for the sake of completeness, we present in Fig. 5.24 the solution profile and corresponding adaptive spatial mesh of the primal Stokes flow convection solution $\mathbf{v}_{\sigma h}$ based on the Kelly Error Estimator, exemplary at time $t = 0.1$ corresponding to the time-dependence of the inflow boundary condition given by Eq. (5.151) within the final loop $\ell = 8$. The adaptive spatial refinement is located to the spreading of the convection flow field $\mathbf{v}_{\sigma h}$, cf. the upper plot of Fig. 5.24. Moreover, the spatial mesh is visibly more refined close to the corners of the entrance and exit of the

channels' constriction consistent with occurring challenges arising in such regions of the underlying meshes, cf., e.g., [168, 67].

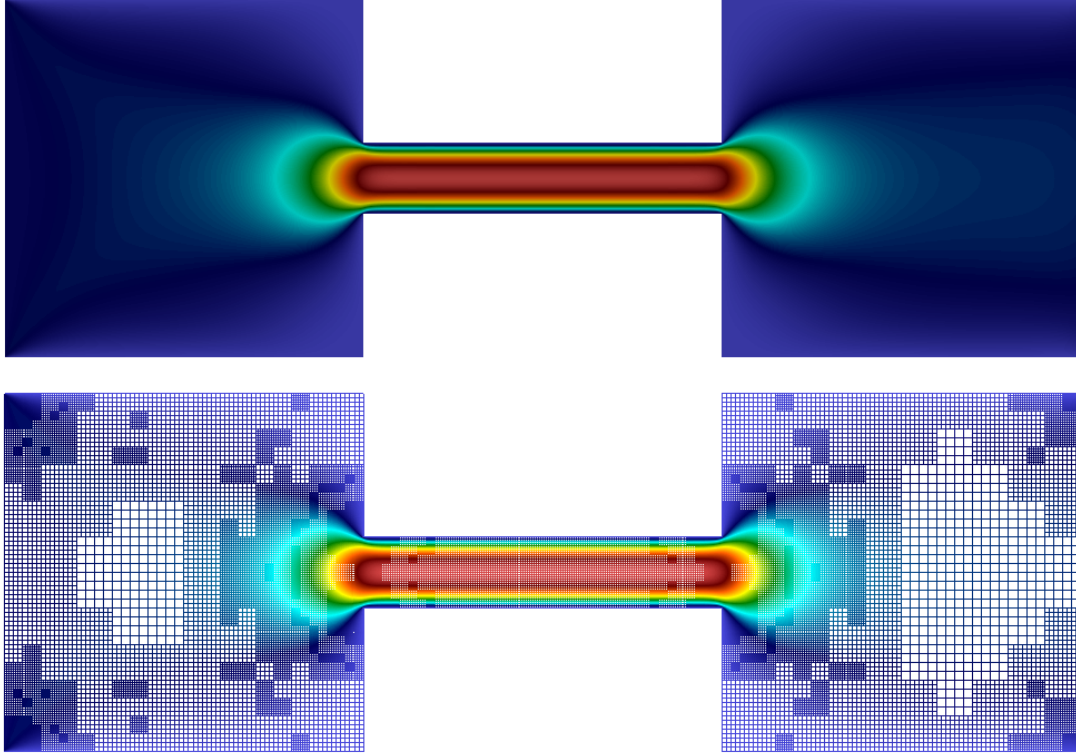


Figure 5.24: Convection \mathbf{v}_{σ_h} solution of the Stokes flow problem and related adaptively refined spatial mesh (based on the Kelly Error Estimator) with Q_2 - Q_1 finite elements and 48186 spatial DoFs, corresponding to loop $\ell = 8$ for Example 5.7, exemplary at time point $t = 0.1$. On the left boundary a time-dependent inflow profile in the positive x_1 -direction is prescribed for the convection \mathbf{v}_D given by Eq. (5.151).

Conclusion 5.3 (Accuracy and Efficiency - Convection-Dominated Case)

As an interim conclusion, we summarize the following.

- *With regard to **accuracy**, the solution profiles of the transport approximated solution u_{τ_h} show significant improvements with regard to reducing spurious unphysical oscillations close to layers in the course of the DWR refinement loops; cf. Fig. 5.18 and Figs. 5.22–5.23, respectively.*
- *With regard to **efficiency**, a very good equilibration of the spatial and temporal error indicators η_h and η_τ is obtained in the course of the DWR refinement loops; cf. the columns five and six of Table 5.8.*
- *Our **multirate in time approach** combined with goal-oriented error control based on the DWR method leads to very economical and efficient temporal*

meshes for both subproblems even in the case of convection-dominated transport. Moreover, the algorithm is able to recognize dynamics in time and thus adjusts automatically the temporal mesh refinement; cf. Figs. 5.19–5.20 as well as Fig. 5.21, respectively.

- With regard to adaptive mesh refinement in **space**, economical and efficient meshes are obtained capturing strong gradients of the transport solution and running with the position of the species within the channel; cf. Figs. 5.17–5.18 and Figs. 5.22–5.23, respectively.
- With regard to **strongly convection-dominated** cases ($\varepsilon \leq 10^{-6}$), the interaction of **stabilization** and goal-oriented **error control** becomes crucial and solely adaptive mesh refinement without stabilization is no longer sufficient, cf. Figs. 5.22–5.23. compared to Figs. 5.17–5.18, respectively.
- Finally, the auxiliary non-weighted error indicators obtained by means of the so-called Kelly Error Estimator used within the Stokes flow problem lead to reasonable meshes in space and time, cf. Fig. 5.24 and Fig. 5.21, respectively.

5.4.4 Final Summary

At the beginning of this work, we proclaimed the need of an error estimator that is able to automatically control the necessary parameters within the increasing complexity of efficiently solving coupled problems including different characteristic time scales by means of adaptive mesh refinement in space and time. For this purpose, with reference to the specific results outlined in Conclusions 5.1–5.3, we summarize the following. The underlying algorithm of our multirate in time approach combined with goal-oriented error control based on the DWR method is able to detect different dynamics in time as well as layers and sharp moving fronts of the solutions of the underlying coupled problem, and thus automatically controls the adaptive mesh refinement process by means of localized error indicators in space and time. Efficient temporal and spatial meshes were obtained even in the case of convection-dominated transport, capturing the specific dynamics in time and strong gradients of the solution profiles, respectively. This property of automatically controlling discretization parameters within the fully adaptive algorithm based on goal-oriented a posteriori error estimators was nicely confirmed considering Fig. 5.11 as well as Figs. 5.17–5.24, respectively, considering different goal functionals and test cases.

Experimental orders of convergence were verified for academic test cases for both the two subproblems as well as the coupled problem, cf. Table 4.1, Tables 5.1–5.2 and Table 5.3, respectively. With regard to reliability and accuracy reasons, effectivity indices close to one were obtained for different $cG(p)$ - $dG(r)$ discretization methods which is indicative for a good quantitative estimation of the underlying discretization errors, cf. Tables 5.4–5.6 and Table 5.7, respectively. Furthermore, with regard to efficiency reasons well-balanced error indicators in time and space were obtained in the course of the refinement process, even though these indicators differed strongly at the beginning, cf. Tables 5.4–5.6, Table 5.7 and Table 5.8, respectively. Finally, spurious oscillations that typically arise in numerical approximations of convection-dominated problems could be reduced significantly and local mesh refinements were adjusted to the position of the transported species within the channel, cf. Figs.5.17–5.18. For the case of strongly convection-dominated transport solely adaptive mesh refinement by means of goal-oriented error control was no longer sufficient to resolve solution profile fronts with strong gradients without producing spurious oscillations, but the application of additionally stabilization techniques were necessary to reduce these oscillations and obtain more accurate solution profiles.

Chapter 6

Conclusion and Outlook

6.1 Summary

In this work, we developed a fully space-time adaptive multirate approach regarding different time scales for a rapidly changing transport problem coupled with a slowly creeping Stokes flow problem. The transport problem is represented by a convection-dominated convection-diffusion-reaction equation which is for this reason stabilized using the residual-based streamline upwind Petrov Galerkin (SUPG) method. Both subproblems are discretized using a discontinuous Galerkin method $dG(r)$ with an arbitrary polynomial degree $r \geq 0$ in time and a continuous Galerkin method $cG(p)$ with an arbitrary polynomial degree $p \geq 1$ in space. Based on these discretizations, we derived goal-oriented a posteriori error representations based on the Dual Weighted Residual (DWR) method for both the transport as well as the Stokes flow problem. These error representations, measured in quantities of physical interest, are splitted into spatial and temporal amounts such that their localized forms can be used as cell-wise error indicators for the adaptive mesh refinement process in space and time. Thereby, the underlying algorithm balances these error indicators and ensures good quantitative estimation of the discretization error including an equilibrated reduction of the temporal and spatial discretization error in the course of further adaptive refinement of the respective meshes. These are important properties of the underlying algorithm with regard to reliability, efficiency and accuracy reasons.

For the practical realization of the underlying approach we introduced the concept of space-time slabs that are based on tensor-product spaces. The slabs are stored within a list object which enables for an easy and efficient involvement of additional slabs in the course of adaptive refinement and is thus governed by the concept of dynamic meshes, i.e. spatial meshes that change in time. The software is called `dwr-stokes-condiffrea` being a module of our in-house DWR software project

DTM++.Project/dwr (bitbucket.org/dtmproject) developed by U. Köcher [128, 129]. It is implemented using the open source finite element library `deal.II`; cf. [17].

In order to analyze the interaction of stabilization and error control with regard to accuracy and efficiency reasons, we considered first the case of stationary and time-dependent convection-dominated transport problems without coupling but using fixed convection fields. Furthermore, these two cases served to study and compare different approaches for obtaining the dual problem and approximating the spatial and temporal weights occurring within the error representations such that the gained knowledge could be used with regard to the case of investigating coupled problems.

The efficiency of the developed approach was demonstrated by applying it to academic test cases, well-known benchmarks for convection-dominated problems as well as examples of physical relevance in two and three space dimensions. Flexibility with regard to arbitrary polynomial degrees up to order three in space and time was shown by investigating several space-time $cG(p)$ - $dG(r)$ discretizations. In numerical examples we verified experimental orders of convergence, studied several goal quantities and demonstrated the independence of the temporal error indicators by means of spatial refinement and vice versa. Space-time adaptivity studies were investigated leading to high-efficient adaptively refined meshes in space and time. We could prove that spurious oscillations that typically arise in numerical approximations of convection-dominated problems are reduced significantly. Regarding stabilization, robustness against the choice of the underlying stabilization parameter was observed which is an important issue in view of stabilization concepts. Furthermore, effectivity indices close to one and well-balanced error indicators in space and time were obtained.

With regard to reliability, efficiency and accuracy reasons of the underlying error representations, as posed at the beginning of this work, we summarize the following. It turned out that the approximation of the spatial weights by means of a higher-order finite elements approach is significantly better regarding the accuracy of the underlying error estimator, especially for increasing Péclet numbers. An approximation comparison for the temporal weights showed only marginal better results using the higher-order finite elements approach with regard to accuracy, but the difference was not that significant as obtained for the spatial weights in the steady-state case. With regard to efficiency and reliability reasons ensured by an equilibrated reduction of the temporal and spatial discretization error, no significant differences between the approximation by higher-order extrapolation or finite elements, respectively, were observed. In view of efficiency reasons regarding the underlying numerical costs, the higher-order extrapolation approach is preferable.

6.2 Extensions and Future Work

As mentioned before, the here proposed multirate in time approach based on goal-oriented error control by means of the DWR method applied to coupled flow and transport problems is fairly general such that it serves as a prototype model that can easily be adopted to other similar types of problems in natural sciences and engineering sciences. This could be, for instance, contaminant transport and degradation in the subsurface, reservoir simulation, fluid-structure interaction, and thermal and mass transport in deformable porous media or thermal expansion in solid mechanics; cf., e.g., [133, 148, 38, 145, 152, 184, 185, 41, 9]. This work has set itself the goal to analyze the interaction of stabilization and goal-oriented error control for the case of convection-dominated transport coupled with fluid flow in order to obtain optimal cell-wise error indicators in space and time with regard to the adaptive mesh refinement process. Here, the term optimal refers to reliability, efficiency and accuracy reasons. Therefore, several comparative studies have been done regarding different approaches for obtaining the dual problem, different approximation approaches for spatial and temporal weights as well as various $cG(p)$ - $dG(r)$ discretizations with polynomial degrees up to order three in space and time.

Nevertheless, there is still potential for further improvements and extensions. A first and evident extension is to deal with nonlinear flow within the coupled system by means of the incompressible Navier-Stokes equations. The DWR approach together with the LPS method was investigated for the model of nonstationary incompressible flow on its own in [40, 167]. Furthermore, an extension to a system of transport equations as introduced at the beginning of Ch. 5 is possible and more or less straight forward. The here arising challenges in view of different underlying meshes for the respective equations of the system can be handled by means of the techniques described in Sec. 4.4.2 and Sec. 4.4.3 of the underlying work. Moreover, we point out that the application of the DWR method with regard to systems of equations is possible since the dual system is decoupled, and thus can be solved easily. With regard to combining goal quantities, here for instance for each single equation of the system, first investigations have been recently proposed under the name of a *multigoal-oriented* approach in [69, 68, 67].

With regard to convection-dominated problems, this work dealt with the SUPG stabilization method which is the most common used stabilization technique with regard to convection-dominated transport problems, cf., e.g., [116, 148]. In general, an overview of state-of-the-art results as well as open questions and problems with regard

to singular perturbed convection-diffusion-reaction equations can be found in [116, 161]. Numerical results regarding the SUPG method applied to (time-dependent) convection-diffusion-reaction equations and a comparison to other stabilization techniques as well as different approaches can be found in [120, 121, 58, 169, 148]. Moreover, combining the DWR method with stabilization concepts for the case of steady-state Navier-Stokes equations have been investigated in [31] and using the stabilization approach of the LPS method for the case of nonstationary Navier-Stokes equations in [40, 167].

Finally, we point out that the concepts of our software `dwr-stokes-condiffrea` are fairly general and thus can easily be adopted to other kind of model problems by modifying the respective parts of the model specific classes such as assemblies of system matrices or the error estimator class exemplarily. On the other hand, the proposed approach of using space-time slabs based on tensor-product spaces within a list object is universally usable. To this end, we refer to our in-house DWR software project `DTM++.Project/dwr` (bitbucket.org/dtmproject) developed by U. Köcher [128, 129], where we developed several model problem cases with regard to the DWR approach, starting from the case of a simple heat equation (`dwr-heat`) over steady-state Stokes flow problems (`dwr-stokes`) up to time-dependent convection-diffusion-reaction equations (`dwr-condiffrea`) and more. The latter was used within the numerical examples of Ch. 3 (in a steady-state and stabilized version) and Ch. 4 (in a time-dependent and stabilized version), respectively. Moreover, since our software is based on the open source finite element library `deal.II` [17], many of the underlying concepts, features and functions itself can be used that are in addition to it well documented. In this sense, our implementations can be used as starting point to incorporate the user and model problem specific issues. Despite this wide range of application scenarios, our software still has potential for further improvements. So far, we are using a direct solver for solving the linear systems. For the here considered test cases these direct solvers have been sufficient and performed very well, but with regard to the above mentioned extension to nonlinear flow or test cases in three space dimensions within the coupled problem, these solvers may quickly come up against their limits. For that reason, the application of iterative solvers such as multigrid (for short, MG) methods, for instance, the geometric multigrid (for short, GMG) method or the algebraic multigrid (for short, AMG) method, including appropriate preconditioning theory is indispensable with regard to these scenarios. With regard to time-dependent convection-diffusion equations, GMG methods have been investi-

gated in [158, 176, 177], and regarding preconditioners for a discontinuous Galerkin time-stepping method applied to parabolic equations we refer to [26].

Moreover, in view of parallel computing there exists further potential for extensions and improvements. Even though we already use some parallel concepts such as the `deal.II - WorkStream` approach within the assemblies of system matrices and right hand side vectors as well as the computation of the error indicators within our error estimator class, the concepts of parallel computing should be further incorporated with regard to efficiency reasons; cf. the reference documentation of the `WorkStream Namespace` for more details about this approach as well as [17].

Abbreviations

AFC	Algebraic Flux Correction scheme
AMG	Algebraic Multigrid method
CIP	Continuous Interior Penalty method
EOC	Experimental Order of Convergence
FCT	Flux-Corrected Transport scheme
FDTs	First Dualize and Then Stabilize approach
FEM	Finite Element Method
FSTD	First Stabilize and Then Dualize approach
GLS	Galerkin Least Squares method
G-L	Gauss-Lobatto quadrature rule
GMG	Geometric Multigrid method
h-oIn	Approximation by higher-order Interpolation in space
h-oFE	Approximation by higher-order Finite Elements in space
hoEx	Approximation by higher-order Extrapolation in time
hoEx-G	Approximation by higher-order Extrapolation in time using Gauss quadrature points
hoEx-GL	Approximation by higher-order Extrapolation in time using Gauss-Lobatto quadrature points
hoFE	Approximation by higher-order Finite Elements in time
LPS	Local Projection Stabilization method
SUPG	Streamline Upwind Petrov-Galerkin method
SDFEM	Streamline Diffusion Finite Element method
TMS(s)	Time Marching Scheme(s)

Variational Space-Time Methods

cG	continuous (in space or time) Galerkin method
dG	discontinuous (in time) Galerkin method
cG(p)	continuous in space Galerkin method of degree p
cG(r)	continuous in time (Petrov-)Galerkin method of degree r
dG(r)	discontinuous in time Galerkin method of degree r
$_G(p)_G(r)$	space-time method of degree p in space and r in time

Bibliography

- [1] Abramowitz, M., Stegun, I.A.: Handbook of mathematical functions: with formulas, graphs, and mathematical tables. "§25.4, Integration". Dover Books on Mathematics, New York (1972)
- [2] Adams, R.A.: Sobolev spaces. Academic Press, New York (1975)
- [3] Ahmed, N., John, V.: Adaptive time step control for higher order variational time discretizations applied to convection-diffusion equations. *Comput. Methods Appl. Mech. Eng.* **285**, 83–101 (2015) doi:10.1016/j.cma.2014.10.054
- [4] Ainsworth, M., Oden, J.T.: A posteriori error estimation in finite element analysis. Wiley, New York (2000)
- [5] Ainsworth, M., Rankin, R.: Guaranteed computable bounds on quantities of interest in finite element computations. *Int. J. Numer. Methods Eng.* **89**(13), 1605–1634 (2012) doi:10.1002/nme.3276
- [6] Akrivis, G., Makridakis, C.: Galerkin time-stepping methods for nonlinear parabolic equations. *ESAIM:M2AN Math. Model. Numer. Anal.* **38**(2), 261–289 (2004) doi:10.1051/m2an:2004013
- [7] Akrivis, G., Makridakis, C., Nochetto, R.H.: A posteriori error estimates for the Crank-Nicolson method for parabolic equations. *Math. Comput.* **75**(254), 511–531 (2005)
- [8] Akrivis, G., Makridakis, C., Nochetto, R.H.: Galerkin and Runge-Kutta methods: unified formulation, a posteriori error estimates and nodal superconvergence. *Numer. Math.* **118**, 429–456 (2011) doi:10.1007/s00211-011-0363-6
- [9] Allaire, G.: Homogenization of the Stokes flow in a connected porous medium. *Asymptotic Anal.* **2**(3), 203–222, (1989) doi:10.3233/ASY-1989-2302

- [10] Almani, T., Kumar, K., Dogru, A., Singh, G., Wheeler, M.F.: Convergence analysis of multirate fixed-stress split iterative schemes for coupling flow with geomechanics. *Comput. Methods Appl. Mech. Eng.* **311**, 180–207 (2016) doi:10.1016/j.cma.2016.07.036
- [11] Andrews, B., Hopper, C.: The Ricci flow in Riemannian geometry: a complete proof of the differentiable $1/4$ -pinching sphere theorem. *Lecture Notes in Math.*, vol. 2011, Springer, Heidelberg (2011) doi:10.1007/978-3-642-16286-2
- [12] Angermann, L.: Balanced a posteriori error estimates for finite-volume type discretizations of convection-dominated elliptic problems. *Computing.* **55**, 305–323 (1995) doi:10.1007/BF02238485
- [13] Arendt, W., Batty, C.J.K., Hieber, M., Neubrander, F.: Vector-valued Laplace transforms and Cauchy problems. 2nd edn. *Monographs in Mathematics*, vol. 96. Birkhäuser, Basel (2011) doi:10.1007/978-3-0348-0087-7
- [14] Arendt, W., Kreuter, M.: Mapping theorems for Sobolev spaces of vector-valued functions. *Stud. Math.* **240**, 275–299 (2018) doi:10.4064/sm8757-4-2017
- [15] Argyris, J.H., Scharpf, D.W.: Finite elements in time and space. *Aer. J. Royal Aer. Soc.* **73**, 1041–1044 (1969)
- [16] Arndt, D., Bangerth, W., Davydov, D., Heister, T., Heltai, L., Kronbichler, M., Maier, M., Pelteret, J.-P., Turcksin, B., Wells, D.: The deal.II library, version 8.5. *J. Numer. Math.* **25**(3), 137–146 (2017). doi:10.1515/jnma-2016-1045
- [17] Arndt, D., Bangerth, W., Blais, B., Fehling, M., Gassmüller, R., Heister, T., Heltai, L., Köcher, U., Kronbichler, M., Maier, M., Munch, P., Pelteret, J.-P., Proell, S., Simon, K., Turcksin, B., Wells, D., Zhang, J.: The deal.II Library, version 9.3. *J. Numer. Math.* **29**(3), 171–186 (2021). doi:10.1515/jnma-2021-0081
- [18] Avijit, D., Natesan, S.: An efficient DWR-type a posteriori error bound of SDFEM for singularly perturbed convection-diffusion PDEs. *J. Sci. Comput.* **90**(73), (2022) doi:10.1007/s10915-021-01749-9
- [19] Aziz, A.K., Monk, P.: Continuous finite elements in space and time for the heat equation. *Math. Comput.* **52**(186), 255–274 (1989) doi:10.1090/S0025-5718-1989-0983310-2

- [20] Bangerth, W., Rannacher, R.: Adaptive finite element methods for differential equations. Birkhäuser, Basel (2003)
- [21] Bangerth, W., Geiger, M., Rannacher, R.: Adaptive Galerkin finite element methods for the wave equation. *Comput. Meth. Appl. Math.* **10**(1), 3–48 (2010) doi:10.2478/cmam-2010-0001
- [22] Bangerth, W., Hartmann, R., Kanschat, G.: deal.II-A general purpose object oriented finite element library. *ACM Trans. Math. Software* **33**(4), 24/1–24/27 (2007). doi:10.1145/1268776.1268779
- [23] Barrenechea, G.R., John, V., Knobloch, P.: A local projection stabilization finite element method with vonlinear crosswind diffusion for convection-diffusion-reaction equations. *ESAIM: Math. Model. Numer. Anal.* **47**(5), 1335–1366 (2013) doi:10.1051/m2an/2013071
- [24] Barrenechea, G.R., John, V., Knobloch, P.: Some analytical results for an algebraic flux correction scheme for a steady convection-diffusion equation in one dimension. *IMA J. Numer. Anal.* **35**(4), 1729–1756 (2015) doi:10.1093/imanum/dru041
- [25] Barrenechea, G.R., John, V., Knobloch, P.: Analysis of algebraic flux correction schemes. *SIAM J. Numer. Anal.* **54**(4), 2427–2451 (2016) doi:10.1137/15M1018216
- [26] Basting, S., Bänsch, E.: Preconditioners for the discontinuous Galerkin time-stepping method of arbitrary order. *ESAIM: Math. Model. Numer. Anal.* **51**(4), 1173–1195 (2015) doi:10.1051/m2an/2016055
- [27] Bause, M., Schwegler, K.: Analysis of stabilized higher order finite element approximation of nonstationary and nonlinear convection-diffusion-reaction equations. *Comput. Methods Appl. Mech. Eng.* **209–212**, 184–196 (2012) doi:10.1016/j.cma.2011.10.004
- [28] Bause, M., Radu, F.A., Köcher, U.: Space-time finite element approximation of the Biot poroelasticity system with iterative coupling. *Comput. Methods Appl. Mech. Eng.* **320**, 745–768 (2017) doi:10.1016/j.cma.2017.03.017
- [29] Bause, M., Bruchhäuser, M.P., Köcher, U.: Flexible goal-oriented adaptivity for higher-order space-time discretizations of transport problems with coupled flow. *Comput. Math. Appl.* **91**, 17–35 (2021) doi:10.1016/j.camwa.2020.08.028

- [30] Bause, M., Köcher, U., Radu, F.A., Schieweck, F.: Post-processed Galerkin approximation of improved order for wave equations. *Math. Comput.* **89**(322), 595–627 (2020) doi:10.1090/mcom/3464
- [31] Becker, R.: An optimal-control approach to a posteriori error estimation for finite element discretizations of the Navier–Stokes equations. *East-West J. Numer. Math.* **8**, 257–274 (2000)
- [32] Becker, R.: Mesh adaptation for stationary flow control. *J. Math. Fluid Mech.* **3**, 317–341 (2001)
- [33] Becker, R., Braack, M.: A finite element pressure gradient stabilization for the Stokes equations based on local projections. *Calcolo* **38**(4), 173–199 (2001)
- [34] Becker, R., Braack, M.: A two-level stabilization scheme for the Navier-Stokes equations. In: Feistauer, M., Dolejší, V., Knobloch, P., Najzar, K. (eds.) *Numerical Mathematics and Advanced Applications. ENUMATH 2003*, Springer, Berlin, Heidelberg, 123–130 (2004)
- [35] Becker, R., Rannacher, R.: Weighted a posteriori error control in FE methods. In: Bock, H.G., Kanschä, G., Rannacher, R., Brezzi, F., Glowinski, R. (eds.) *ENUMATH 97. Proceedings of the 2nd European Conference on Numerical Mathematics and Advanced Applications*, World Scientific, Singapore, 621–637 (1998)
- [36] Becker, R., Rannacher, R.: An optimal control approach to a posteriori error estimation in finite element methods. In: Iserles, A. (ed.) *Acta Numer.*, Vol. 10, 1–102. Cambridge University Press (2001)
- [37] Becker, R., Braack, M., Rannacher, R.: On error control for reactive flow problems. In: Keil, F., Mackens, W., Voß, H., Werther, J. (eds.) *Scientific Computing in Chemical Engineering II. Computational Fluid Dynamics, Reaction Engineering, and Molecular Properties*, vol. 1, Springer, Berlin, Heidelberg 320–327 (1999) doi:10.1007/978-3-642-60185-9_37
- [38] Bengzon, F., Larson, M.G.: Adaptive finite element approximation of multiphysics problems: a fluid-structure interaction model problem. *Int. J. Numer. Methods Eng.* **84**(12), 1451–1465 (2010) doi:10.1002/nme.2945

- [39] Benyamini, Y., Lindenstrauss, J.: Geometric nonlinear functional analysis Vol. I. Amer. Math. Soc., Providence, Rhode Island (2000)
- [40] Besier, M., Rannacher, R.: Goal-oriented space-time adaptivity in the finite element Galerkin method for the computation of nonstationary incompressible flow. *Int. J. Num. Methods Fluids* **70**(9), 1139–1166 (2012) doi:10.1002/fld.2735
- [41] Biot, M.A.: General theory of three-dimensional consolidation. *J. Appl. Phys.* **12**(2), 155–164 (1941) doi:10.1063/1.1712886
- [42] Bittl, M., Kuzmin, D.: An hp-adaptive flux-corrected transport algorithm for continuous finite elements. *Computing* **95**, 27–48 (2013) doi:10.1007/s00607-012-0223-y
- [43] Boris, J.P., Book, D.L.: Flux-corrected transport. I. SHASTA, a fluid transport algorithm that works. *J. Comput. Phys.* **11**(1), 38–69 (1973) doi:10.1016/0021-9991(73)90147-2
- [44] Bottasso, C.L.: A new look at finite elements in time: a variational interpretation of Runge-Kutta methods. *Appl. Numer. Math.* **25**(4), 355–368 (1997) doi:10.1016/S0168-9274(97)00072-X
- [45] Braack, M., Ern, A.: A posteriori control of modeling errors and discretization errors. *Multiscale Model. Simul.* **1**(2), 221–238 (2003) doi:10.1137/S1540345902410482
- [46] Braak, M., Richter, T.: Solutions of 3D Navier-Stokes benchmark problems with adaptive finite elements. *Comput. Fluids* **35**(4), 372–392 (2006) doi:10.1016/j.compfluid.2005.02.001
- [47] Braess, D.: *Finite Elemente. Theorie, schnelle Löser und Anwendungen in der Elastizitätstheorie*. 5th edn. Springer, Berlin (2013)
- [48] Brenner, S.C., Scott, L.R.: *The mathematical theory of finite element methods*, Vol. 15 of Texts in Applied Mathematics. 3rd edn. Springer, New York (2008) doi:10.1007/978-0-387-75934-0
- [49] Brooks, A.N., Hughes, T.J.R.: Streamline upwind/Petrov-Galerkin formulations for convection dominated flows with particular emphasis on the incompressible Navier-Stokes equations. *Comput. Methods Appl. Mech. Eng.* **32**(1-3), 199–259 (1982) doi:10.1016/0045-7825(82)90071-8

- [50] Bruchhäuser, M.P., Schwegler, K., Bause, M.: Numerical study of goal-oriented error control for stabilized finite element methods. In: Apel, T., Langer, U., Meyer, A., Steinbach, O. (eds.), *Advanced Finite Element Methods with Applications. FEM 2017. Lect. Notes Comput. Sci. Eng.* **128**, Springer, Cham, 85–106 (2019) doi:10.1007/978-3-030-14244-5_5
- [51] Bruchhäuser, M.P., Schwegler, K., Bause, M.: Dual weighted residual based error control for nonstationary convection-dominated equations: potential or ballast?. In: Barrenechea G.R., Mackenzie, J. (eds.), *Boundary and Interior Layers, Computational and Asymptotic Methods BAIL 2018. Lect. Notes Comput. Sci. Eng.* **135**, Springer, Cham, 1–17 (2020) doi:10.1007/978-3-030-41800-7_1
- [52] Bruchhäuser, M.P., Köcher, U., Bause, M.: On the implementation of an adaptive multirate framework for coupled transport and flow. *J. Sci. Comput.*, submitted 07 Feb. 2022, 1–32 (2022). arXiv:2202.03748
- [53] Burman, E.: Robust error estimates in weak norms for advection dominated transport problems with rough data. *Math. Models Methods Appl. Sci.* **24**(13), 2663–2684 (2014) doi:10.1142/S021820251450033X
- [54] Burman, E., Hansbo, P.: Edge stabilization for Galerkin approximations of convection-diffusion-reaction problems. *Comput. Methods Appl. Mech. Eng.* **193**(15-16), 1437–1453 (2004) doi:10.1016/j.cma.2003.12.032
- [55] Carey, G.F., Oden, J.T.: *Finite elements, computational aspects, Vol. III (The Texas finite element series)*. Prentice-Hall, Englewood Cliffs, New Jersey (1984)
- [56] Cazenave, T., Haraux, A.: *An introduction to semilinear evolution equations, Oxford Lecture Ser. Math. Appl.* 13, Clarendon Press, New York (1998)
- [57] Ciarlet, P.G.: *The finite element method for elliptic problems*. North-Holland Publishing Company, Amsterdam New York Oxford (1987)
- [58] Codina, R.: Comparison of some finite element methods for solving the diffusion-convection-reaction equation. *Comput. Methods Appl. Mech. Eng.* **156**, 185–210 (1998) doi:10.1016/S0045-7825(97)00206-5
- [59] Constantin, P., Foias, C.: *Navier-Stokes equations. Chicago lectures in mathematics*. University of Chicago Press, Chicago (1988)

- [60] Constantinescu, E.M., Sandu, A.: Multirate timestepping methods for hyperbolic conservation laws. *J. Sci. Comput.* **33**, 239–278 (2007) doi:10.1007/s10915-007-9151-y
- [61] Dautray, R., Lions, J.-L.: *Mathematical analysis and numerical methods for science and technology. Vol. 5. Evolution problems I*, Springer, Berlin (2000)
- [62] Dawson, C., Kirby, R.: High resolution schemes for conservation laws with locally varying time steps. *SIAM J. Sci. Comput.* **22**(6), 2256–2281 (2001) doi:10.1137/S1064827500367737
- [63] Dawson, C., Sun, S., Wheeler, M.F.: Compatible algorithms for coupled flow and transport. *Comput. Methods Appl. Mech. Eng.* **139**(23-26), 2565–2580 (2004) doi:10.1016/j.cma.2003.12.059
- [64] Delfour, M., Hager, W., Trochu, F.: Discontinuous Galerkin methods for ordinary differential equations. *Math. Comput.* **36**(154), 455–473 (1981) doi:10.2307/2007652
- [65] Dolejší, V., Ern, A., Vohralík, M.: A framework for robust a posteriori error control in unsteady nonlinear advection-diffusion problems. *SIAM J. Numer. Anal.* **51**(2), 773–793 (2013) doi:10.1137/110859282
- [66] Dörfler, W.: A convergent adaptive algorithm for Poisson’s equation. *SIAM J. Numer. Anal.* **33**, 1106–1124 (1996) doi:10.1137/0733054
- [67] Endtmayer, B., Wick, T.: A partition-of-unity dual-weighted residual approach for multi-objective goal functional error estimation applied to elliptic problems. *Comput. Methods Appl. Math.* **17**(4), 575-599 (2017). doi:10.1515/cmam-2017-0001
- [68] Endtmayer, B., Langer, U., Wick, T.: Multigoal-oriented error estimates for non-linear problems. *J. Numer. Math.* **27**(4), 215–235 (2018) doi:10.1515/jnma-2018-0038
- [69] Endtmayer, B., Langer, U., Neitzel, I., Wick, T., Wollner, W.: Multigoal-oriented optimal control problems with nonlinear PDE constraints. *Comput. Math. Appl.* **79**(10), 3001–3026 (2020) doi:10.1016/j.camwa.2020.01.005

- [70] Eriksson, K., Johnson, C.: Adaptive finite element methods for parabolic problems. I: A linear model problem. *SIAM J. Numer. Anal.*, **28**(1), 43–77 (1991) doi:10.1137/0728003
- [71] Eriksson, K., Johnson, C.: Adaptive finite element methods for parabolic problems. II: Optimal error estimates in $L_\infty L_2$ and $L_\infty L_\infty$. *SIAM J. Numer. Anal.*, **32**(3), 706–740 (1995) doi:10.1137/0732033
- [72] Eriksson, K., Johnson, C.: Adaptive finite element methods for parabolic problems. IV: Nonlinear problems. *SIAM J. Numer. Anal.*, **32**(6), 1729–1749 (1995) doi:10.1137/0732078
- [73] Eriksson, K., Johnson, C.: Adaptive finite element methods for parabolic problems. V: Long-time integration. *SIAM J. Numer. Anal.*, **32**(6), 1750–1763 (1995) doi:10.1137/0732079
- [74] Eriksson, K., Johnson, C., Larsson, S.: Adaptive finite element methods for parabolic problems. VI: Analytic semigroups. *SIAM J. Numer. Anal.*, **35**(4), 1315–1325 (1998) doi:10.1137/S0036142996310216
- [75] Eriksson, K., Johnson, C., Thomée, V.: Time discretization of parabolic problems by the discontinuous Galerkin method. *ESAIM: Math. Model. Numer. Anal.* **19**(4), 611–643 (1985) doi:10.1051/m2an/1985190406111
- [76] Eriksson, K., Estep, D., Hansbo, P., Johnson, C.: Introduction to adaptive methods for differential equations. In: Iserles, A. (ed.), *Acta Numerica*. Cambridge University Press, Cambridge, 105–158 (1995) doi:10.1017/S0962492900002531
- [77] Eriksson, K., Estep, D., Hansbo, P., Johnson, C.: *Computational differential equations*. Cambridge University Press, Cambridge, (1996)
- [78] Ern, A., Schieweck, F.: Discontinuous Galerkin method in time combined with a stabilized finite element method in space for linear first-order pdes. *Math. Comput.* **85**, 2099–2129 (2016) doi:10.1090/mcom/3073
- [79] Ern, A., Guermond, J.-L.: *Finite elements III: First-order and time-dependent pdes*. vol. 74, *Texts in Applied Mathematics*, Springer, Cham (2021)

- [80] Estep, D., French, D.: Global error control for the continuous Galerkin finite element method for ordinary differential equations. *ESAIM: Math. Model. Numer. Anal.* **28**(7), 815–852 (1994) doi:10.1051/m2an/1994280708151
- [81] Evans, L.C.: *Partial differential equations*. American Mathematical Society, Providence, Rhode Island (2010)
- [82] Franca, L.P., Frey, S.L., Hughes, T.J.R.: Stabilized finite element methods I: application to the advective-diffusive model. *Comput. Methods Appl. Mech. Eng.* **95**, 253–271 (1992)
- [83] Franca, L.P., John, V., Matthies, G., Tobiska, L.: An inf-sup stable and residual-free bubble element for the Oseen equations. *SIAM J. Numer. Anal.* **45**, 2392–2407 (2007) doi:10.1016/0045-7825(92)90143-8
- [84] de Frutos, J., García-Archilla, B., John, V., Novo, J.: An adaptive SUPG method for evolutionary convection-diffusion equations. *Comput. Methods Appl. Mech. Eng.* **273**, 129–237 (2014) doi:10.1016/j.cma.2014.01.022
- [85] de Frutos, J., García-Archilla, B., Novo, J.: Local error estimates for the SUPG method applied to evolutionary convection-reaction-diffusion equations. *J. Sci. Comput.* **66**(2), 528–554 (2016) doi:10.1007/s10915-015-0035-2
- [86] French, D.A., Peterson, T.E.: A continuous space-time finite element method for the wave equation. *Math. Comput.* **65**(214), 491–506 (1996) doi:10.1090/S0025-5718-96-00685-0
- [87] Fried, I.: Finite element analysis of time dependent phenomena. *AIAA J.* **7**, 1170–1173 (1969) doi:10.2514/3.5299
- [88] Gander, M.J., Halpern, L.: Techniques for locally adaptive time stepping developed over the last two decades. In: Bank, R., Holst, M., Widlund, O., Xu, J. (eds.) *Domain Decomposition Methods in Science and Engineering XX*, *Lect. Notes Comput. Sci. Eng.* **91**, Springer, Berlin, Heidelberg, 377–385 (2013) doi:10.1007/978-3-642-35275-1_44
- [89] Ge, Z., Ma, M.: Multirate iterative scheme based on multiphysics discontinuous Galerkin method for a poroelasticity model. *Appl. Numer. Math.* **128**, 125–138 (2018) doi:10.1016/j.apnum.2018.02.003

- [90] Gear, C.W., Wells, D.R.: Multirate linear multistep methods. *BIT* **24**(4), 484–502 (1984) doi:10.1007/BF01934907
- [91] Giles, M.B., Pierce, N.A.: Adjoint equations in CFD: Duality, boundary conditions and solution behaviour. *AIAA Paper 97–1850* (1997) doi:10.2514/6.1997-1850
- [92] Girault, V., Raviart, P.-A.: Finite element methods for Navier-Stokes equations: Theory and algorithms. *Springer Series in Computational Mathematics*, vol. 5, Springer, Berlin, Heidelberg (1986)
- [93] Gujer, W.: *Systems analysis for water technology*. Springer, Berlin, Heidelberg (2008)
- [94] Gupta, S., Wohlmuth, B., Helmig, R.: Multi-rate time stepping schemes for hydro-geomechanical model for subsurface methane hydrate reservoirs. *Adv. Water Res.* **91**, 78–87 (2016) doi:10.1016/j.advwatres.2016.02.013
- [95] Günther, M., Rentrop, P.: Multirate ROW methods and latency of electric circuits. *Appl. Numer. Math.* **13**(1), 83–102 (1993) doi:10.1016/0168-9274(93)90133-C
- [96] Haroske, D.D., Triebel, H.: *Distributions, Sobolev spaces, elliptic equations*. European Mathematical Society, Zurich (2008)
- [97] Hartmann, R.: Adjoint consistency analysis of discontinuous Galerkin discretizations. *SIAM J. Numer. Anal.* **45**(6), 2671–2696 (2007) doi:10.1137/060665117
- [98] Hartmann, R.: A-posteriori Fehlerschätzung und adaptive Schrittweiten- und Ortsgittersteuerung bei Galerkin-Verfahren für die Wärmeleitungsgleichung. *Diploma Thesis*, Institute of Applied Mathematics, University of Heidelberg (1998)
- [99] Heroux, M.A., Bartlett, R.A., Howle, V.E., Hoekstra, R.J., Hu, J.J., Kolda, T.G., Lehoucq, R.B., Long, K.R., Pawlowski, R.P., Phipps, E.T., Salinger, A.G., Thornquist, H.K., Tuminaro, R.S., Willenbring, J.M., Williams, A., Stanley, K.S.: An overview of the Trilinos project. *ACM Trans. Math. Softw.* **31**(3), 397–423 (2005) doi:10.1145/1089014.1089021

- [100] Heuveline, V., Rannacher, R.: A posteriori error control for finite element approximations of elliptic eigenvalue problems. *J. Comput. Math. Appl.* **15**, 107–138 (2001) doi:10.1023/A:1014291224961
- [101] Houston, P.: Adjoint error estimation and adaptivity for hyperbolic problems. In: ABGRALL, R., SHU, C.-W. (eds.) *Handbook of Numerical Analysis: Handbook of Numerical Methods for Hyperbolic Problems. Applied and Modern Issues* 18. Elsevier. 233-261 (2017) doi:10.1016/bs.hna.2016.10.003
- [102] Houston, P., Süli, E.: Stabilized hp-finite element approximation of partial differential equations with nonnegative characteristic form. In: *Computing* **66**, 99–119 (2001) doi:10.1007/s006070170030
- [103] Houston, P., Rannacher, R., Süli, E.: A posteriori error analysis for stabilised finite element approximations of transport problems. *Comput. Methods Appl. Mech. Eng.* **190**, 1483–1508 (2000) doi:10.1016/S0045-7825(00)00174-2
- [104] Hsu, M.-C., Bazilevs, Y., Calo, V.M., Tezduyar, T.E., Hughes, T.J.R.: Improving stability of stabilized and multiscale formulations in flow simulations at small time steps. *Comput. Methods Appl. Mech. Eng.* **199**(13-16), 828 – 840 (2010). doi:10.1016/j.cma.2009.06.019
- [105] Hughes, T.J.R.: *The finite element method: Linear static and dynamic finite element analysis*. Dover Publications, Mineola, New York (2000)
- [106] Hughes, T.J.R., Brooks, A.N.: A multidimensional upwind scheme with no crosswind diffusion. In: Hughes, T.J.R. (ed.) *Finite Element Methods for Convection Dominated Flows, AMD*, vol. 34, Amer. Soc. Mech. Engrs. (ASME), 19–35 (1979)
- [107] Hughes, T.J.R., Franca, L.P.: A new finite element formulation for computational fluid dynamics: VII. The Stokes problem with various well-posed boundary conditions: symmetric formulations that converge for all velocity/pressure spaces *Comput. Methods Appl. Mech. Eng.* **65**(1), 85–96 (1987) doi:10.1016/0045-7825(87)90184-8
- [108] Hughes, T.J.R., Franca, L.P., Hulber, G.M.: A new finite element formulation for computational fluid dynamics: VIII. The Galerkin/least-squares method for advective-diffusive equations. *Comput. Methods Appl. Mech. Eng.* **73**(2), 173–189 (1989) doi:10.1016/0045-7825(89)90111-4

- [109] Hughes, T.J.R., Mallet, M., Mizukami, A.: A new finite element formulation for computational fluid dynamics: II. Beyond SUPG. *Comput. Methods Appl. Mech. Eng.* **54**, 341–355 (1986) doi:10.1016/0045-7825(86)90110-6
- [110] Hulme, B.L.: One-step piecewise polynomial Galerkin methods for initial value problems. *Math. Comput.* **26**, 415–426 (1972) doi:10.2307/2005168
- [111] Jammoul, M., Wheeler, M.F., Wick, T.: A phase-field multirate scheme with stabilized iterative coupling for pressure driven fracture propagation in porous media. *Comput. Math. Appl.* **91**, 176–191 (2021) doi:10.1016/j.camwa.2020.11.009
- [112] John, V.: Finite element methods for incompressible flow problems. Springer Series in Computational Mathematics, vol.51, Springer, Cham (2016)
- [113] John, V., Knobloch, P.: On spurious oscillations at layers diminishing (SOLD) methods for convection-diffusion equations: Part I – A review. *Comput. Methods Appl. Mech. Eng.* **196**(17-20), 2197–2215 (2007) doi:10.1016/j.cma.2006.11.013
- [114] John, V., Knobloch, P.: Adaptive computation of parameters in stabilized methods for convection-diffusion problems. In: Cangiani, A., Davidchack, R., Georgoulis, E., Gorban, A., Levesley, J., Tretyakov, M. (eds.) *Numerical Mathematics and Advanced Applications 2011*, Springer, Berlin, Heidelberg (2013) doi:10.1007/978-3-642-33134-3_30
- [115] John, V., Maubach, J.M., Tobiska, L.: Nonconforming streamline-diffusion-finite-element-methods for convection-diffusion problems. *Numer. Math.* **78**, 165–188 (1997) doi:10.1007/s002110050309
- [116] John, V., Knobloch, P., Novo, J.: Finite elements for scalar convection-dominated equations and incompressible flow problems: a never ending story? *Comput. Vis. Sci.* **19**, 47–63 (2018) doi:10.1007/s00791-018-0290-5
- [117] John, V., Knobloch, P., Savescu, S.B.: A posteriori optimization of parameters in stabilized methods for convection-diffusion problems - Part I. *Comput. Methods Appl. Mech. Eng.* **200**, 2916–2929 (2011) doi:10.1016/j.cma.2011.04.016
- [118] John, V., Novo, J.: Error analysis of the SUPG finite element discretization of evolutionary convection-diffusion-reaction equations. *SIAM J. Numer. Anal.* **49**(3), 1149–1176 (2011) doi:10.2307/23074327

- [119] John, V., Novo, J.: A robust SUPG norm a posteriori error estimator for stationary convection-diffusion equations. *Comput. Methods Appl. Mech. Eng.* **255**, 289–305 (2013) doi:10.1137/040604261
- [120] John, V., Schmeyer, E.: Finite element methods for time-dependent convection-diffusion-reaction equations with small diffusion. *Comput. Methods Appl. Mech. Eng.* **198**(3-4), 475–494 (2008) doi:10.1016/j.cma.2008.08.016
- [121] John, V., Schmeyer, E.: On finite element methods for 3D time-dependent convection-diffusion-reaction equations with small diffusion In: Hegarty, A., Kopteva, N., O’Riordan, E., Stynes, M. (eds.) *BAIL 2008 - Boundary and Interior Layers. Lect. Notes Comput. Sci. Eng.* **69**, Springer, Berlin, Heidelberg, 173–181 (2009) doi:10.1007/978-3-642-00605-0_13
- [122] Johnson, C.: *Numerical solution of partial differential equations by the finite element method.* Cambridge University Press, Cambridge (1988)
- [123] Johnson, C.: Adaptive finite element methods for diffusion and convection problems. *Comput. Methods Appl. Mech. Eng.* **82**, 301–322 (1990) doi:10.1016/0045-7825(90)90169-M
- [124] Johnson, C., Hansbo, P.: Adaptive finite element methods in computational mechanics. *Commun. Pure Appl. Math.* **48**, 199–243 (1995) doi:10.1016/0045-7825(92)90020-K
- [125] Johnson, C., Szepessy, A.: Adaptive finite element methods for conservation laws based on a posteriori error estimates. *Commun. Pure. Appl. Math.* **48**(3), 199–234 (1995) doi:10.1002/cpa.3160480302
- [126] Kelly, D.W., Gago, J.P. De S.R., Zienkiewicz, O.C., Babuska, I.: A posteriori error analysis and adaptive processes in the finite element method: Part I-error analysis. *Int. J. Num. Meth. Eng.* **19**, 1593–1619 (1983) doi:10.1002/nme.1620191103
- [127] Knopp, T., Lube, G., Rapin, G.: Stabilized finite element methods with shock capturing for advection-diffusion problems. *Comput. Methods Appl. Mech. Eng.* **191**, 2997–3013 (2002) doi:10.1016/S0045-7825(02)00222-0
- [128] Köcher, U.: Variational space-time methods for the elastic wave equation and the diffusion equation. Ph.D. thesis, Mech. Eng. Helmut-Schmidt-University Hamburg, (2015) urn:nbn:de:gbv:705-opus-31129

- [129] Köcher, U., Bruchhäuser, M.P., Bause, M.: Efficient and scalable data structures and algorithms for goal-oriented adaptivity of space–time FEM codes. *Software X*, 10:100239 (2019) doi:10.1016/j.softx.2019.100239
- [130] Kreuter, M.: Sobolev spaces of vector-valued functions. Master Thesis, Ulm University (2015)
- [131] Kuzmin, D., Korotov, S.: Goal-oriented a posteriori error estimates for transport problems. *Math. Comput. Simul.* **80**(8), 1674–1683 (2010) doi:10.1016/j.matcom.2009.03.008
- [132] Kuzmin, D., Turek, S.: Flux correction tools for finite elements. *J. Comput. Phys.* **175**, 525–558 (2002) doi:10.1006/jcph.2001.6955
- [133] Larson, M.G., Målquist, A.: Goal oriented adaptivity for coupled flow and transport with applications in oil reservoir simulations. *Comput. Methods Appl. Mech. Eng.* **196**, 3546–3561 (2007) doi:10.1016/j.cma.2006.10.038
- [134] Lesaint, P., Raviart, P.A.: On a finite element method for solving the neutron transport equation. In: De Boor, C. (ed.) *Mathematical Aspects of Finite Elements in Partial Differential Equations*, Academic Press, New York, 89–145 (1974) doi:10.1016/B978-0-12-208350-1.50008-X
- [135] Lewis, D.L., Lund, J., Bowers, K.L.: The space-time Sinc-Galerkin method for parabolic problems. *Int. J. Numer. Methods Eng.* **24**(9), 1629–1644 (1987) doi:10.1002/nme.1620240903
- [136] Lions, J.-L.: Quelques remarques sur les équations différentielles opérationnelles du 1er ordre. *Rend. Sem. Mat. Univ. Padova* **33**, 213–225 (1963)
- [137] Lions, J.-L., Magenes, E.: *Problèmes aux Limites non Homogènes et applications*. 1. and 2., Dunod, Paris (1968)
- [138] Lions, J.-L., Magenes, E.: *Non-homogeneous boundary value problems and applications*. Vol. 1. Springer, Berlin Heidelberg (1972)
- [139] Löhner, R., Morgan, K., Peraire, P., Vahdati, M.: Finite element flux-corrected transport (FEM-FCT) for the Euler and Navier-Stokes equations. *Int. J. Numer. Methods Fluids* **7**(10), 1093–1109 (1987) doi:10.1002/fd.1650071007

- [140] Lu, J.: An a posteriori error control framework for adaptive precision optimization using discontinuous Galerkin finite element method. Ph.D. thesis, M.I.T., (2005)
- [141] Lube, G., Rapin, G.: Residual-based stabilized higher-order fem for advection-dominated problems. *Comput. Methods Appl. Mech. Eng.* **195**, 4124–4138 (2006) doi:10.1016/j.cma.2005.07.017
- [142] Matthies, G., Schieweck, F.: Higher order variational time discretizations for nonlinear systems of ordinary differential equations. Preprint no. 23/2011, Fakultät für Mathematik, Otto-von-Guericke-Universität Magdeburg (2011)
- [143] Meidner, D.: Adaptive space-time finite element methods for optimization problems governed by nonlinear parabolic systems. Ph.D. thesis, University of Heidelberg (2007) doi:10.11588/heidok.00008272
- [144] Meidner, D., Vexler, B.: Adaptive space-time finite element methods for parabolic optimization problems. *SIAM J. Control Optim.* **46**(1), 116–162 (2007) doi:10.1137/060648994
- [145] Mikelić, A., Wheeler, M.F.: Convergence of iterative coupling for coupled flow and geomechanics. *Comput. Geosci.* **17**, 479–496 (2013) doi:10.1007/s10596-012-9318-y
- [146] Morgenroth, E.: How are characteristic times (τ_{char}) and non-dimensional numbers related. (2015)
<https://ethz.ch/content/dam/ethz/special-interest/baug/ifu/water-management-dam/documents/education/Lectures/UWM3/SAMM.HS15.Handout.CharacteristicTimes.pdf>, accessed 20 April 2022
- [147] Nävert, U.: A finite element method for convection-diffusion problems. Ph.D. thesis, Chalmers University of Technology (1982)
- [148] Ngo, A.Q.T., Bastian, P., Ippisch, O.: Numerical solution of steady-state groundwater flow and solute transport problems: Discontinuous Galerkin based methods compared to the Streamline Diffusion approach. *Comput. Methods Appl. Mech. Eng.* **294**, 331–358 (2015) doi:10.1016/j.cma.2015.06.008
- [149] Nguyen H., Reynen J.: A space-time least-square finite element scheme for advection-diffusion equations. *Comput. Methods Appl. Mech. Eng.* **42**(3), 331–342 (1984) doi:10.1016/0045-7825(84)90012-4

- [150] Nochetto, R.H., Veerer, A., Verani, M.: A safeguarded dual weighted residual method. *IMA J. Numer. Anal.* **29**(1), 126–140 (2009) doi:10.1093/imanum/drm026
- [151] Oden, J.T.: A general theory of finite elements. II. Applications. *Int. J. Numer. Methods Eng.* **1**(3), 247–259 (1969) doi:10.1002/nme.1620010304
- [152] Odsæter, L.H., Kvamsdal, T., Larson, M.G.: A simple embedded discrete fracture-matrix model for a coupled flow and transport problem in porous media. *Comput Methods Appl. Mech. Eng.* **343**, 572–601 (2019) doi:10.1016/j.cma.2018.09.003
- [153] Oliver, T.A., Darmofal, D.L.: Analysis of dual-consistency for discontinuous Galerkin discretizations of source terms. *SIAM J. Numer. Anal.* **47**(5), 3507–3525 (2009) doi:10.1137/080721467
- [154] Quarteroni, A., Valli, A.: Numerical approximation of partial differential equations, Vol. 23 of Springer series in computational mathematics. Springer, Berlin, Heidelberg (1994)
- [155] Rannacher, R.: A posteriori error estimation in least-squares stabilized finite element schemes. *Comput. Methods Appl. Mech. Eng.* **166**, 99–114 (1998) doi:10.1016/S0045-7825(98)00085-1
- [156] Rannacher, R., Suttmeier, F.T.: A posteriori error estimation and mesh adaptation for finite element models in elasto-plasticity. *Comput. Methods Appl. Mech. Eng.* **176**, 333–361 (1999) doi:10.1016/S0045-7825(98)00344-2
- [157] Reed, W.H., Hill, T.R.: Triangular mesh methods for the neutron transport equation. Tech. Report LA-UR-73-479, Los Alamos Scientific Laboratory, (1973)
- [158] Rhebergen S., van der Vegt, J.J.W., van der Ven, H.: Multigrid optimization for space-time discontinuous Galerkin discretizations of advection dominated flows. In: Kroll, N., Bieler, H., Deconinck, H., Couaillier, V., van der Ven, H., Sørensen, K. (eds.) *ADIGMA - A European Initiative on the Development of Adaptive Higher-Order Variational Methods for Aerospace Applications. Notes on Numerical Fluid Mechanics and Multidisciplinary Design*, vol. 113. Springer, Berlin, Heidelberg, 257–269 (2010) doi:10.1007/978-3-642-03707-8_18

- [159] Richter, T.: Goal-oriented error estimation for fluid–structure interaction problems. *Comput. Methods Appl. Mech. Eng.* **223–224**, 28–42 (2012) doi:10.1016/j.cma.2012.02.014
- [160] Richter, T.: Fluid–structure interactions: Models, analysis and finite elements, *Lect. Notes Comput. Sci. Eng.* **118**, Springer, Berlin (2017)
- [161] Roos, H.-G., Stynes, M.: Some open questions in the numerical analysis of singularly perturbed differential equations. *Comput. Methods Appl. Math.* **15**(4), 531–550 (2015) doi:10.1515/cmam-2015-0011
- [162] Roos, H.-G., Stynes, M., Tobiska, L.: Robust numerical methods for singularly perturbed differential equations. Springer, Berlin (2008)
- [163] Roubíček, T.: Nonlinear partial differential equations with applications. 2nd edn. Birkhäuser, Basel (2013)
- [164] Savcenco, V., Hundsdorfer, W., Verwer, J.: A multirate time stepping strategy for parabolic PDE. Tech. Report MAS-E0516, Centrum voor Wiskunde en Informatica (2005)
- [165] Savcenco, V., Savcenco, E.: Multirate numerical integration for parabolic pdes. In: Simos, T.E., Psihoyios, G., Tsitouras, C. (eds.) *AIP Conference Proceedings*, 1048, 470–473 (2008) doi:10.1063/1.2990964
- [166] Schlegel, M., Knoth, O., Arnold, M., Wolke, R.: Implementation of multirate time integration methods for air pollution modelling. *Geosci. Model Dev.* **5**(6), 1395–1405 (2012) doi:10.5194/gmd-5-1395-2012
- [167] Schmich, M.: Adaptive finite element methods for computing nonstationary incompressible flows. Ph.D. thesis, University of Heidelberg (2009) urn:nbn:de:bsz:16-opus-102001
- [168] Schmich, M., Vexler, B.: Adaptivity with dynamic meshes for space-time finite element discretizations of parabolic equations. *SIAM J. Sci. Comput.* **30**(1), 369–393 (2008) doi:10.1137/060670468
- [169] Schwegler, K.: Adaptive goal-oriented error control for stabilized approximations of convection-dominated problems, Ph.D. thesis, Helmut Schmidt University Hamburg, (2014) urn:nbn:de:gbv:705-opus-30861

- [170] Showalter, R.E. Monotone operators in Banach space and nonlinear partial differential equations. Math. Surveys Monogr. 49, Amer. Math. Soc., Providence, Rhode Island (1997)
- [171] Sohr, H.: The Navier-Stokes equations. An elementary functional analytic approach. Birkhäuser, Basel (2001)
- [172] Tang, H.Z., Warnecke, G.: High resolution schemes for conservation laws and convection-diffusion equations with varying time and space grids. J. Comput. Math. **24**(2), 121-140 (2006)
- [173] Temam, R.: Navier-Stokes equations: Theory and numerical analysis. AMS Chelsea Publishing, Providence, Rhode Island (2001)
- [174] Thomée, V.: Galerkin finite element methods for parabolic problems. 2nd edn. In: Springer Series in Computational Mathematics, vol. 25, Springer, Berlin Heidelberg (2006)
- [175] Tobiska, L., Verfürth, R.: Robust *a posteriori* error estimates for stabilized finite element methods. IMA J. Numer. Anal. **35**(4), 1652–1671 (2015) doi:10.1093/imanum/dru060
- [176] van der Vegt, J.J.W., Rhebergen, S.: Hp-multigrid as smoother algorithm for higher order discontinuous Galerkin discretizations of advection dominated flows. Part I: Multilevel analysis. J. Comput. Phys. **231**(22), 7537–7563 (2012) doi:10.1016/j.jcp.2012.05.038
- [177] van der Vegt, J.J.W., Rhebergen, S.: Hp-multigrid as smoother algorithm for higher order discontinuous Galerkin discretizations of advection dominated flows. Part II: Optimization of the Runge-Kutta smoother. J. Comput. Phys. **231**(22), 7537–7563 (2012) doi:10.1016/j.jcp.2012.05.037
- [178] Verfürth, R.: A review of a posteriori error estimation and adaptive mesh-refinement techniques. Wiley-Teubner Series Advances in Numerical Mathematics. Wiley-Teubner, New York, Stuttgart (1996)
- [179] Verfürth, R.: A posteriori error estimators for convection-diffusion equations. Numer. Math. **80**(4), 641–663 (1998) doi:10.1007/s002110050381
- [180] Verfürth, R.: A posteriori error estimation techniques for finite element methods. Oxford University Press, Oxford (2013)

- [181] Verfürth, R.: Robust a posteriori error estimates for stationary convection-diffusion equations. *SIAM J. Numer. Anal.* **43**, 1766–1782 (2005) doi:10.1137/040604261
- [182] Verfürth, R.: Robust a posteriori error estimates for nonstationary convection-diffusion equations. *SIAM J. Numer. Anal.* **43**, 1783–1802 (2005) doi:10.1137/040604273
- [183] Wick, T.: Adaptive finite element simulation of fluid-structure interaction with applications to heart-valve dynamics. Ph.D. thesis, Universität Heidelberg (2012) urn:nbn:de:bsz:16-opus-129926
- [184] Wick, T.: Goal functional evaluations for phase-field fracture using PU-based DWR mesh adaptivity. *Comput. Mech.* **57**, 1017–1035 (2016) doi:10.1007/s00466-016-1275-1
- [185] Wick, T.: Dual-weighted residual a posteriori error estimates for a penalized phase-field slit discontinuity problem. *Comput. Methods Appl. Math.* **21**(3), 693–707 (2021) doi:10.1515/cmam-2020-0038
- [186] Wick, T., Wollner, W.: Optimization with nonstationary, nonlinear monolithic fluid-structure interaction. *Int. J. Numer. Methods Eng.* **122**(19), 5430–5449 (2020) doi:10.1002/nme.6372
- [187] Wloka, J.: *Partielle Differentialgleichungen*. B. G. Teubner, Stuttgart (1982)
- [188] Zeidler, E.: *Nonlinear functional analysis and its applications. Part II/A. Nonlinear monotone operators*, Springer, New York (1990)
- [189] Zeidler, E.: *Applied functional analysis: main principles and their applications. Applied Mathematical Sciences*, vol. 109, Springer, New York (1995)
- [190] Zhao, S., Wei, G.W.: A unified discontinuous Galerkin framework for time integration. *Math. Methods Appl. Sci.* **37**(7), 1042–1071 (2014) doi:10.1002/mma.2863
- [191] van Zuijlen, A.H., Bijl, H.: Implicit and explicit higher order time integration schemes for structural dynamics and fluid-structure interaction computations. *Computers & Structures* **83**(2-3), 93–105 (2005) doi:10.1016/j.compstruc.2004.06.003

